Research on Engineering Structures and Materials

www.jresm.org

Volume 10 Issue 4 December 2024

P-ISSN: 2148-9807 E-ISSN: 2149-4088

Research Group

The International Journal of **Research on Engineering Structures and Materials (RESM**) is a peer-reviewed open access journal (p-ISSN: 2148-9807; o-ISSN: 2149-4088) published by MIM Research Group. It is published in February, June, September, and December.

The main objective of RESM is to provide an International academic platform for researchers to share scientific results related to all aspects of mechanical, civil, and material engineering areas.

RESM aims the publication of original research articles, reviews, short communications technical reports, and letters to the editor on the latest developments in the related fields.

All expenditures for the publication of the manuscripts are most kindly reimbursed by *MIM Research Group*. Thus, authors do not need to pay for publishing their studies in the journal.

The scope of the journal covers (but not limited to) behavior of structures, machines and mechanical systems, vibration, impact loadings and structural dynamics, mechanics of materials (elasticity, plasticity, fracture mechanics), material science (structure and properties of concrete, metals, ceramics, composites, plastics, wood, etc.,), nano-materials performances of new and existing buildings and other structural systems, design of buildings and other structural systems, seismic behavior of buildings and other structural systems, repair and strengthening of structural systems, case studies and failure of structural systems, safety and reliability in structural and material engineering, use of new and innovative materials and techniques in energy systems and mechanical aspects of biological systems (biomechanics and biomimetics).

The topics covered in JRESM include:

- Structural Engineering
- Mechanical Engineering
- Material Engineering
- Earthquake Engineering
- Nano-technology
- Energy Systems (Focus on Renewable)
- Biomechanics and Biomimetics
- Environment (Material and Engineering System Related Issues)
- Computer Engineering and Data Science (Material and Engineering System-Related Issues)

Abstracting and Indexing
Please visit http://www.jresm.org for more information.

Graphics and Design

Mehmet Yılmaz myilmaz@jresm.net

RESEARCH on ENGINEERING STRUCTURES & MATERIALS

Research Group

RESEARCH on ENGINEERING STRUCTURES & MATERIALS

Editorial Board

Editorial Office

Publishing Manager		
Mehmet Yılmaz	MIM Research Group	Türkiye
Language Editors		
Gaye Kuru	Uşak University	Türkiye
Mete Çal	MIM Research Group	Türkiye

Asimina Athanatopoulou	Aristotle University	Greece
Atike İnce Yardımcı	Uşak University	Türkiye
Ayoub Souileh	University Mohammed V	Morocco
Berrin İkizler	Ege University	Türkiye
Billel Rebai	Abbes Laghrour University	Algeria
Breetha Yesudhas Jayakumari	Chennai Institute of Technology	India
Brijesh Singh	National Council for Cement and Building Materials	India
Bülent İmamoğlu	Gedik University	Türkiye
Can Gonenlı	Ege University	Türkiye
Catur Harsito	Universitas Sebelas Maret	Indonesia
Chella Gifta Christopher	National Engineering College Kovilpatti	India
Chıtaranjan Pany	Vikram Sarabhai Space Centre	India
Chinenye Elizabeth Okere	Federal University of Technology	Nigeria
Chuanjin Yu	Southwest Jiaotong University	China
Daniel Cruze	Mohamed Sathak A J College of Engineering	India
Davide Forcellini	University of San Marino	San Marino
Debasish Sen	Ahsanullah University of Science and Technology	Bangladesh
Deniz Uner	Middle East Technical University	Türkiye
Dhirendra Patel	Kalaniketan Polytechnic College	India
Dilay Uncu	Celal Bayar Üniversity	Türkiye
Dipankar Das	Tripura University	India
Diyar Qader	University of Kirkuk	Iraq
Abdul Razak Abdul Karim	Universiti Malaysia Sarawak	Malaysia
Anand Murthy Hc	Adama Science & Tech. University	Ethiopia
Vera Ilyina	Institute of Geology Karelian Research Centre	Russia
Dulce Franco Henriques	Instituto Politécnico de Lisboa	Portugal
Elavenil S	Vellore Institute of Technology	India
Elton Hala	Polytechnic University of Tirana	Albania
Emre Kemer	Usak University	Türkiye

Enea Mustafaraj	Epoka University, Tirana	Albania
Ercan Isık	Bitlis Eren University	Türkiye
Esra Özer	Tokat Gaziosmanpasa University	Türkiye
Essam Mohamed	South Valley University	Egypt
Fatoş Koç	Ege University	Türkiye
Federico Scafati	University of L'Aquila	Italy
Fokruddin Ahmad	Washington State University	USA
Gaurav Dhadse	G. H. Raisoni Institute of Engineering and Business Management	India
Guobo Wang	Wenzhou University	China
Gururaj Hatti	KLS Vishwanathrao Deshpande Institute of Technology	India
Guy Louarn	Université de Nantes	France
Habibe Demir	İskenderun Teknik University	Türkiye
Hadj Bekki	University Ibn Khaldoun of Tiaret	Algeria
Hakan Sarikaya	Uşak University	Türkiye
Hakan Ulker	Bursa Teknik University	Türkiye
Halil Murat Enginsoy	Çanakkale Onsekiz Mart University	Türkiye
Halil Yalcin Akdeniz	Eskisehir Osmangazi University	Türkiye
Hasan Ulus	Selcuk University	Türkiye
Hemadri Prasad Raju	Sree Vidyanikethan Engineering College	India
Hintsa G. Gebremariam	Addis Ababa University	Ethiopia
Hossein Kabir	University of Illinois	USA
Hussein Hamada	Al-Qalam University College	Iraq
I Gede Gegiranang Wiryadi	Universitas Mahasaraswati Denpasar	Indonesia
Ibrahim Sharaky	Taif University	Saudi Arabia
Ikram Kouidri	University of Relizane	Algeria
Indra Mawardi	Politeknik Negeri Lhokseumawe	Indonesia
Irakli Premti	Polytechnic University of Tirana	Albania
Isabel Milagre Martins	Laboratório Nacional de Engenharia Civil	Portugal

Ivana Štimac Grandić	University of Rijeka	Croatia
J. Jenix Rino	Anna University	India
J. Paulo Davim	University of Aveiro	Portugal
Jinxu Mo	Yangtze University	China
Jojok Widodo Soetjipto	Universitas Jember	Indonesia
Josephine Chang Hui Lai	Universiti Malaysia Sarawak	Malaysia
Juan Llorca-Schenk	University of Alicante	Spain
K. Ashwini	Jawaharlal Nehru Technological University Hyderabad	India
Kabiru Mustapha	Kwara State University	Nigeria
Kadir Gunaydın	GE Aviation Marmara Technology Center	Türkiye
Kamel Chaoui	Badji Mokhtar University	Algeria
Kanish Kapoor	Dr B R Ambedkar National Institute of Technology	India
Khairul Nizar Ismail	Universiti Malaysia Perlis	Malaysia
Konstantinos Kalfas	University of Texas at Tyler	USA
Lawrence Zahemen Tuleun	University of Ilorin	Nigeria
Lomesh Mahajan	Dr. Babasaheb Ambedkar Technological University	India
Lyamine Briki	University of Batna2	Algeria
M. Kalil Rahiman	Saveetha School of Engineering	India
Magdalini Titirla	Conservatoire National des Arts et Métiers	France
Maher Chakhari	Tunis El Manar University	Tunisia
Mahesh Gopal	Wollega University, Nekemte	Ethiopia
Maheswaran Chellapandian	Mepco Schlenk Engineering College	India
Mahmoud Mokhtar	Housing & Building National Research Center	Egypt
Majid Pouraminian	Islamic Azad University	Iran
Maria Richert	AGH University of Science and Technology	Poland
Marina Sunara	University of Split	Croatia
Marwa Enneffati	Université Angers	France
Md. Saiful Islam	Universiti Putra	Putra
Mehdi Panji	Islamic Azad University	Iran

Mehmet Ada	Uşak University	Türkiye
Mehmet Cemal Genes	Eastern Mediterranean University	Cyprus
Mehrab Nodehi	University of California Davis	USA
Mert Göksüzoğlu	SAMPA Advanced Parts for Commercial Vehicles	Türkiye
Mohammad .I Al Biajawi	Universiti Malaysia Pahang Al-Sultan Abdullah	Malaysia
Mohammad Afrazi	Tarbiat Modares University	Iran
Mohammad Naeim Moradi	Amirkabir University of Technology	Iran
Mohammad Saleh Baradaran	Islamic Azad University	Iran
Mohammed Bentahar	Tahar Moulay University of Saida	Algeria
Mohammed Sarhan	Mustansiriyah University	Iraq
Mohsen Hajizamani	Graduate University of Advanced Technology	Iran
Morchid Fatima Ezzahrae	University of Hassan II Casablanca	Morocco
Muhammad Bilal Khan	Ghulam Ishaq Khan Institute of Engineering Sciences and Technology	Pakistan
Mustafa Akpolat	Munzur University	Türkiye
Mustafa H. Omar	Bilad Alrafidain University College	Iraq
Mustafa Ozgunler	Mimar Sinan Fine Arts University	Türkiye
Mustaqqim Abdul Rahim	University Malaysia Perlis	Malaysia
Nadhim Hamah Sor	University of Garmian	Iraq
Nagaraj Ekabote	KLE Technological University	India
Nahida Nazim Musayeva	Azerbaijan National Academy of Sciences	Azerbaijan
Navdeep Singh	Dr. Babasaheb Ambedkar Technological University	India
Nebab - Mokhtar	University Hassiba Benbouali of Chlef	Algeria
Nghia P. Tran	The University of Melbourne	Australia
Nıtın Kumar	University of California Davis	USA
Olfa Maalej	Monastir University	Tunisia
Olumoyewa D. Atoyebı	Landmark University	Nigeria
Orhan Gülcan	General Electric Aerospace	Türkiye
Osman M. Ramadan	Cairo University, Giza	Egypt

Ozgur Avsar	Eskisehir Technical University	Türkiye
Özgür Demircan	Ondokuz Mayıs Üniversitesi	Türkiye
Partheeban Pachaivannan	Chennai Institute of Technology	India
Peng Gao	University of Massachusetts Lowell	USA
Peyman Beiranvand	Razi University	Iran
Piya Chotickai	Kasetsart University	Tailand
Pooja Sharma	Dr. Yashwant Singh Parmar University of Horticulture and Forestry	India
Subash Thanappan	KAAF University College	Ghana
Raif Sakin	Balıkesir University	Türkiye
Rajesh Kumar	KPR Institute of Engineering and Technology	India
Rajesh M.	Hindustan Institute of Technology and Science	India
Ramaswamy Palanivel	Shaqra University	Saudi Arabia
Rami Sldozian	University of Technology-Iraq	Iraq
Rasheed Abdulwahab	Kwara State University	Nigeria
Ravichandran M	K.Ramakrishnan College of Engineering	India
Revathi Srinivasan	Mepco Schlenk Engineering College	India
Riadh Bennaı	University Hassiba Benbouali of Chlef	Algeria
Rianti Dewi Sulamet-Ariobimo	Universitas Trisakti	Indonesia
Roberto Nascimbene	School of Advanced Studies IUSS Pavia	Italy
Royal Madan	Chandigarh University	India
S. Ali Faghidian	Islamic Azad University	Iran
Saeid Foroughi	Konya Technical University	Türkiye
Sahar Ismail	Saint Joseph University of Beirut	Lebanon
Sajjad Hassanpour Kasanagh	Middle East Technical University	Türkiye
Salmabanu Luhar	National Taipei University of Technology	Taiwan
Samer Adeeb	University of Alberta	Canada
Samia Bouzouaid	Kasdi Merbah University	Algeria
Samuel Awe	Automotive Components Floby AB	Sweden

Sangeetha Palanivelu	SSN College of Engineering	India
Sarmila Sahoo	Heritage Institute of Technology Kolkata	India
Sercan Serin	Osmaniye Korkut Ata University	Türkiye
Shaise K. John	College of Engineering Trivandrum	India
Shaohong Cheng	University of Windsor	Canada
Sharmin Reza Chowdhury	Ahsanullah University of Science and Technology	Bangladesh
Sivakumar N	SSN College of Engineering	India
Solomon Olalere Ajamu	Ladoke Akintola University	Nigeria
Somya Ranjan Patro	Indian Institute of Technology Delhi	India
Sonal Thakkar	Nirma University	India
Sophia Immanuel	National Institute of Technology Tiruchirappalli	India
Suliman Khan	NFC Institute of Engineering and Fertilizer Research	Pakistan
Sumanth Ratna Kandavalli	New York University	USA
Surajit Kumar Paul	Indian Institute of Technology	India
Susmita Naskar	University of Southampton	Englang
T.V. Reshma	GITAM School of Technology	India
Taha Rashid	Universiti Teknologi Malaysia	Malaysia
Tamer Saracyakupoglu	TUSAŞ Academy	Türkiye
Taqiy Eddine Boukelia	University of Jijel	Algeria
Tarun Kumar Rajak	Shri Shankaracharya Institute of Professional Management and Technology	India
Tasnia Ahmed	Military Institute of Science and Technology	Bangladesh
Thaer Alrudaini	University of Basrah	Iraq
Thı Loan Pham	Civil Engineering, Hai Phong University	Vietnamese
Thomás L. Resende	Federal University of Jequitinhonha and Mucuri Valleys	Brazil
Thomas Salonikios	The Institute of Engineering Seismology and Earthquake Engineering	Greece
Toufik Sebbagh	University of Skikda	Algeria
Tuan Anh Nguyen	Thuyloi University	Vietnamese

Upendra K. Mallela	İndian and Toubro Technology	India
Vedat Arda Küçük	Çankırı Karatekin University	Türkiye
Vıneeth Kumar T. V.	Siddaganga Institute of Technology	India
Víctor I. Fernandez-Davila	Pontifical Catholic University of Peru	Peru
Victor Rizov	University of Architecture	Bulgaria
Vincent Sam Jebadurai	Karunya Institute of Technology and Sciences	India
Wahyu Dwi Lestari	University of Pembangunan Nasional Veteran Jawa Timur	Indonesia
Waleed A Abbas	University of Technology, Baghdad	Iraq
Yamini Sreevalli I	Vellore Institute of Technology	India
Yang Feng	Xi'an Jiaotong University	China
Yang Yang	Southeast University	China
Yaser Acikbas	Uşak Üniversitesi	Türkiye
Yonatan Ayele Abera	Dilla University	Ethiopia
Yunika Kirana Abdul Khalik	University of Malaysia	Malaysia
Zafer Kaya	Dumlupınar University	Türkiye
Zahid Iqbal Khan	Universiti Teknologi Malaysia	Malaysia
Zikriye Ozbek	Çanakkale Onsekiz Mart University	Türkiye

In This Issue

Research on Engineering Structures & Materials
MIM Research Group Publications
P-ISSN: 2148-9807
E-ISSN: 2149-4088
http://www.jresm.org

ABSTRACTING / INDEXING

The international journal of Research on Engineering Structures and Materials (RESM) is currently Abstracted/Indexed by Asos Indeks, CiteFactor, Cosmos, CrossRef, Directory of Research Journal Indexing, Engineering Journals (ProQuest), EZB Electronic Journal Library, Global Impact Factor, Google Scholar, International Institute of Organized Research (I2OR), International Scientific Indexing (ISI), Materials Science & Engineering Database (ProQuest), Open Academic Journals Index, Publication Forum, Research BibleScientific Indexing Service, Root Indexing, Scopus, Ulakbim TR Index (Tubitak), Universal Impact Factor and under evaluation by many other respected indexes.

Check web site for current indexing info, www.jresm.org

Research on Engineering Structures & Materials
www.jresm.org
MIM Research Group

Research Article

Investigation on floor response spectra of a three-story building exposed to near- and far-field earthquakes

Vyshnavi Pesaralanka[a], Kameswara Rao Burugapalli[b], Surya Prakash Challagulla[*,c]

Department of Civil Engineering, Koneru Lakshmaiah Education Foundation, Vaddeswaram, Guntur, India

Article Info

Article history:

Received 07 Dec 2023
Accepted 18 Mar 2024

Keywords:

Non-structural component;
Floor response spectrum;
Peak component acceleration;
Near-field earthquakes;
Far-field earthquakes

Abstract

Historical earthquakes highlighted structural collapses and non-structural component (NSC) failures. This study aims to analyze NSC behavior during near and far-field earthquakes in a three-story building by studying elastic and inelastic acceleration responses. The investigation delves into floor response spectra and analyzes how NSCs affect floor acceleration responses, aiming to understand the performance of these components. The findings from the analysis indicated that the Floor Response Spectra (FRS) consistently align peaks with elastic and inelastic modal periods. Inelastic FRS notably show reduced floor spectral accelerations compared to elastic FRS. Near-field earthquakes induce 25-30% higher floor acceleration demands in NSCs compared to far-field earthquakes. Peak Component Acceleration (PCA) values differ significantly between near and far field earthquakes, with near-field ones exhibiting notably higher values across all floors. Higher damping ratios in NSCs lead to decreased peaks in the Component Dynamic Amplification Factor (CDAF) spectrum. The inelastic model notably reduces peak values of CDAF by approximately 49.53% to 69.3% for near-field and 51.81% to 64.47% for far-field earthquakes compared to the elastic model. In summary, the examination of peak floor responses against the formulation based on building codes highlights variations, with instances where the formulation either underestimates or overestimates the peak response demands.

1. Introduction

Buildings are attached with non-structural components (NSCs), which are not designed to withstand structural loads (1), have a vital role in ensuring earthquake resilience. The damage to NSCs can lead to substantial economic losses, both directly and indirectly, often surpassing the costs associated with the primary structural members. The damage to non-structural components (NSCs), which encompass crucial and valuable equipment, can greatly interrupt the operations of diverse structures, especially vital facilities like airports, hospitals, and sites of historical or cultural significance [2-3]. These results emphasize the critical necessity of assessing the seismic behavior of components alongside structural elements. Current standards and recommendations largely rely on practical approaches gleaned from previous encounters and engineering knowledge [4]. Hence, it is vital to design NSCs to endure seismic forces, guaranteeing their safety and the uninterrupted operation of buildings post-earthquake. This entails establishing the Floor Response Spectrum (FRS) at the juncture where the non-structural component connects with the main structure.

NSCs can be categorized into different types based on their failure [5]. While there are now precise methods available for accurately estimating seismic demand on both types of non-

*Corresponding author: chsuryaprakash@kluniversity.in
[a]orcid.org/0000-0003-1284-3139; [b]orcid.org/ 0000-0002-6161-2575; [c]orcid.org/0000-0003-0125-1488
DOI: http://dx.doi.org/10.17515/resm2024.115ea1207rs

structural components, simpler procedures are sometimes necessary in design scenarios [6]. National and international codes offer several straightforward formulas for calculating seismic demand on NSCs. Many seismic codes used in earthquake-prone areas aim to predict the maximum acceleration and thus the maximum inertial force caused by seismic shaking on NSCs. Therefore, this study focuses solely on acceleration-sensitive non-structural components. Examples of acceleration-sensitive non-structural components include suspended building utility systems like pipe systems and cable trays, as well as anchored or free-standing building utility systems or contents.

The floor response spectrum (FRS) method is an analytical approach that operates by separating various considerations [7–13]. Initially, the primary structure undergoes dynamic analysis independently, without factoring in the secondary system's influence. The acceleration response record from the particular floor where NSCs are affixed is employed as data for modeling the NSC and forming the floor response spectrum. As a result, the maximum force required for NSC design can be determined from the resulting FRS. Studies on the seismic performance of elements exposed to ground motion have demonstrated that the amplification of responses in the primary structure increases the likelihood of NSC damage [14]. Investigations into methods for generating FRS were initiated in the 1970s. Traditionally, various approaches treated the NSC and its supporting structure as single degree of freedom (SDOF) systems. Yasui et al. [15] introduced a method for creating smooth design floor response spectra using either the design spectra or ground response spectra as a reference point. They also developed and verified an innovative method for directly ascertaining floor acceleration spectra [16]. Wei Jiang et al. [17] established floor response spectra to assess the seismic demands on nuclear facilities, finding that FRS generated from time history analysis exhibited significant variations, especially in specific tuning scenarios. The investigation of floor response spectra for multi-story structures has been a subject of study [18–22]. Furthermore, the impact of stiffness irregularities on the FRS was examined [23], with the research revealing heightened acceleration amplification at the soft story level. While the relevant literature has documented a variety of FRS generation methods [17,21,24,25]none of them are capable of effectively assessing how the seismic performance of non-structural components is impacted under near and far-field earthquakes.

Prior research has mostly focused on how both structural and non-structural components respond seismically to typical ground motions. However, limited research has specifically addressed the seismic behavior of primary structures subjected to near- and far-field ground motions [26–31]. These investigations have revealed distinct behaviors of buildings under near field versus far field earthquakes. Consequently, there exists a crucial gap in understanding the seismic performance of non-structural components under both near and far-field earthquake conditions. As a result, there is a critical need to explore the seismic performance of non-structural components under both near and far field earthquake excitations. Therefore, this study aims to assess the impact of near and far field earthquake events on floor spectral accelerations. In the process of generating floor response spectra (FRS), the component dynamic amplification factors are particularly important, as they represent the extent to which NSCs are amplified. Consequently, these parameters and spectral data are examined within the context of a specific building model exposed to seismic forces. Subsequently, a comparative analysis is conducted to assess the disparities between the obtained amplification factors and those derived from code-based calculations.

The paper is organized as follows: Section 2 provides a concise overview of the structural model. Section 3 discusses the selection and scaling of ground motions and provides specific details pertinent to this research. In Section 4, the research findings are presented, with a focus on three key response parameters: floor response spectra, peak component

acceleration, and component dynamic amplification factors. The paper concludes in Section 5 with succinct summarizing remarks.

2. Structural Model

A 3-storey (Ground+2) reinforced concrete (RC), 3D moment-resisting bare frame building as shown in Fig. 1 has been considered in this analysis. Each floor height is assumed as 3 m. The building under consideration is a special moment-resisting frame (SMRF) with a consistent 4-meter bay width across all floors. The reinforced concrete (RC) is modelled with an M30 grade concrete, and the reinforcing steel is HYSD 500. Additionally, as per IS 875-Part 2 [32] guidelines, floor finish load and live load are considered to be 1.5 kN/m^2 and 3 kN/m^2, respectively. The initial sizes of columns and beams have been selected in compliance with IS 13920:2016 [33]. In this design, column dimensions are uniform at 350 mm × 350 mm, and beams are consistently sized at 300 mm × 300 mm for all frames. Additionally, the reinforced concrete (RC) slabs is standardized at 150 mm thickness. The structural model underwent analysis and design considerations for both gravity loads and earthquake forces, specifically in accordance with seismic Zone V conditions. This zone, characterized by a zone factor of 0.36, is associated with a hard soil profile. The design details are shown in Fig 2.

Fig. 1. Three-story building model

To evaluate the performance of the model, the elastic and inelastic responses of the bare frame were examined through time-history analysis, utilizing the finite element software package SeismoStruct (34). In linear modelling, beams and columns are represented as elastic frame elements using their gross moment of inertia. In nonlinear modelling, these elements are portrayed as inelastic plastic hinge force-based elements. Following the ASCE 41-17 [35] standard, the nonlinear characteristics of reinforced concrete (RC) elements are replicated using concentrated plastic hinges positioned at both ends of every member. The plastic hinge length, denoted as L_p, is defined in accordance with Paulay and Priestley [36] as being equal to half of the section depth. The actual structural geometry, incorporating the obtained reinforcement through design, is established to generate the moment-curvature diagram.

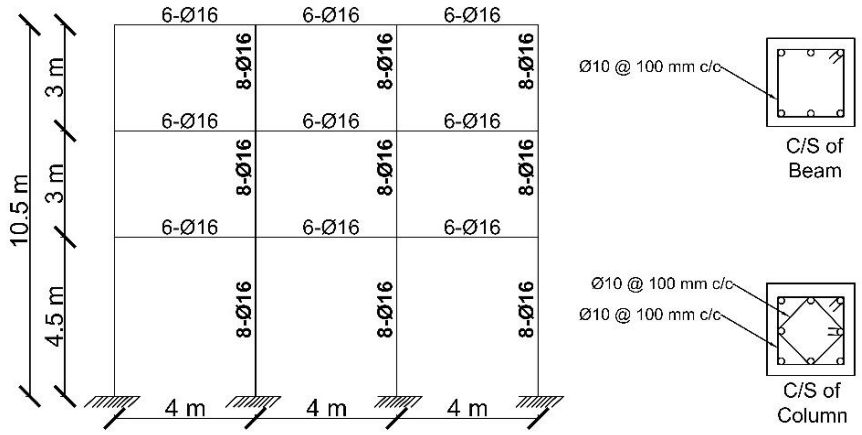

Fig. 2. Reinforcement details of a considered building model

The cracked stiffness of these nonlinear elements is determined following ASCE 41-17 guidelines, which specify the approach for calculating the stiffness of cracked sections for both columns and beams. Mander's model is used to describe the confined concrete's compressive behavior. Steel reinforcement in tension is represented by a bilinear model with isotropic strain hardening behavior. For modelling RC slabs, a rigid diaphragm approach is employed. To simulate the damping effects in the dynamic studies, a Rayleigh damping model has been set up, which accounts for 5% damping divided between the lowest and highest modes to obtain a total of 95% cumulative mass participation in both directions. The analysis considered fixed base conditions, without accounting for soil flexibility. The subsequent section outlines the process employed to choose the ground motion for the current study.

3. Ground Motions

Regarding the assessment of seismic response, realistic responses are generated by utilizing actual ground-motions. Therefore, for the current research, we have incorporated 20 horizontal ground motion excitations, as specified by ASCE 7-16 [37] tailored for hard soil conditions with a shear wave velocity (V_{s30}) greater than 350 m/sec. Additionally, for this study, we have chosen to employ a set of ground-motion records recommended in FEMA P695 [38]. These records will be used to carry out both linear and nonlinear dynamic analyses on the building structures under consideration. Among the set of 20 excitations, 11 of them are categorized as near-field ground motions, while the remaining are classified as far-field ground motions, as detailed in Table 1. According to the classification in FEMA P695, the far-field record set comprises ground motions originating from sites situated at a distance equal to or greater than 10 km from the fault rupture. In contrast, the near-field record set includes ground motions recorded at sites located within a distance of less than 10 km from the fault rupture, as determined by the Joyner-Boore distance (R_{jb}). The ground-motion records under consideration were obtained from sites with rock soil conditions, specifically falling within NEHRP site classes B and C.

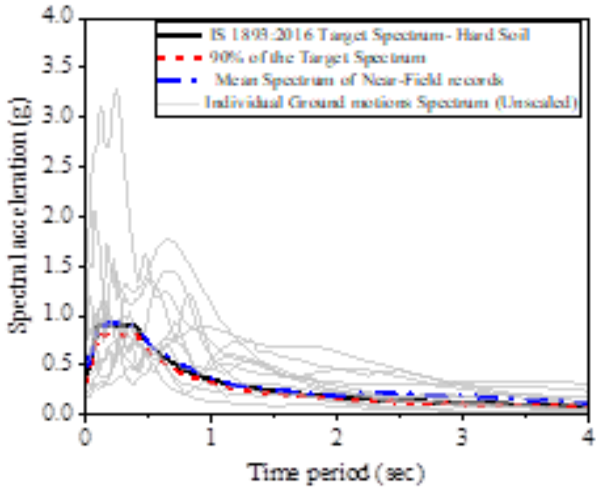

(a)

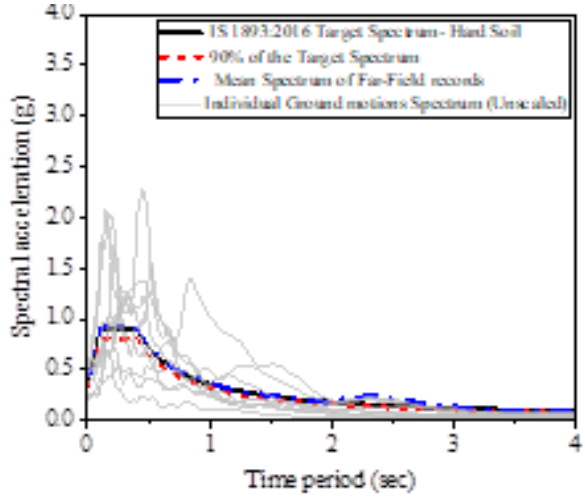

(b)

Fig. 3. Scaled ground motions mean spectra and the target spectrum (a) near-field data, (b) far-field data

These records are associated with moment magnitudes (M_w) ranging from 6.69 to 7.62, with an average magnitude of 7.05. Among the selected records, the closest distances to the fault rupture, calculated as the average Joyner-Boore distance, span from 0 to 26 km, with an average distance of 8.11 km. The epicentral distances (R_{epi}) for this chosen set of ground motions vary between 4.5 and 86 km, with an average distance of 33.4 km. The peak ground acceleration (PGA) values of these selected records range from 0.22 to 1.49 g, and their average PGA is 0.494 g. For more comprehensive information regarding these ground motions, further details can be found in FEMA P695. To achieve compatibility with the target response spectrum, which is the Zone V elastic design spectrum of IS 1893 (Part 1): 2016 [39], the chosen ground motion records were subjected to scaling.

Table 1. Details of near-field and far-field record sets for time-history analysis

S. No	RSN	Earthquake Name	Year	Station Name	M_w	R_{jb} (km)	V_{s30} (m/sec)	PGA (g)	R_{epi} (km)
Near field records									
1	292	Irpinia_ Italy-01	1980	Sturno (STN)	6.9	6.78	382	0.226	30.4
2	802	Loma Prieta	1989	Saratoga - Aloha Ave	6.93	7.58	380.89	0.514	27.2
3	821	Erzican_ Turkey	1992	Erzincan	6.69	0	352.05	0.386	9
4	828	Cape Mendocino	1992	Petrolia	7.01	0	422.17	0.597	4.5
5	879	Landers	1992	Lucerne	7.28	2.19	1369	0.725	44
6	1086	Northridge-01	1994	Sylmar - Olive View Med FF	6.69	1.74	440.54	0.604	16.8
7	1165	Kocaeli_ Turkey	1999	Izmit	7.51	3.62	811	0.165	5.3
8	1529	Chi-Chi_ Taiwan	1999	TCU102	7.62	1.49	714.27	0.303	45.6
9	496	Nahanni_ Canada	1985	Site 2	6.76	0	605.04	0.519	38.04
10	825	Cape Mendocino	1992	Cape Mendocino	7.01	0	567.78	1.49	33.98
11	1004	Northridge-01	1994	LA - Sepulveda VA Hospital	6.69	0	380.06	0.752	44.49
Far-field records									
1	953	Northridge	1994	Beverly Hills-Mulhol	6.7	9.4	356	0.52	13.3
2	1787	Hector Mine	1999	Hector	7.1	10.4	685	0.34	26.5
3	1111	Kobe, Japan	1995	Nishi-Akashi	6.9	7.1	609	0.51	8.7
4	1148	Kocaeli, Turkey	1999	Arcelik	7.5	10.6	523	0.22	53.7
5	900	Landers	1992	Yermo Fire Station	7.3	23.6	354	0.24	86
6	767	Loma Prieta	1989	Gilroy Array #3	6.9	12.2	350	0.56	31.4
7	1633	Manjil, Iran	1990	Abbar	7.4	12.6	724	0.51	40.4
8	1485	Chi-Chi, Taiwan	1999	TCU045	7.6	26	705	0.51	77.5
9	125	Friuli, Italy	1976	Tolmezzo	6.5	15	425	0.35	20.2

The process employed for this purpose involved the utilization of a time-domain spectral matching approach to generate earthquake excitations that align with the desired spectrum. Figure 3 illustrates the target spectrum as per IS 1893:2016, which are linked to 5% damping, along with the mean spectra of ground excitations. It is essential that the mean spectra remain over 90% of the target spectrum for the whole-time range, as per ASCE 7-16 requirements. It is evident (Fig. 3) that the mean spectra comfortably exceed this 90% threshold. Table 2 provides information regarding the modal periods and

cumulative modal mass participation ratios for a three-story building model in both linear and nonlinear analysis ranges.

Table 2. Details of time periods and cumulative mass participation ratios of considered models

Mode	Linear Model			Non-Linear Model		
	T (sec)	UX	UY	T (sec)	UX	UY
Mode 1(Y)	0.743	28.83	64.86	1.71	89.08	3.68
Mode 2(X)	0.742	93.85	93.77	1.70	92.79	92.74
Mode 3(Z)	0.635	93.92	93.92	1.40	92.83	92.82
Mode 4(X)	0.206	97.76	95.51	0.495	99.48	92.82
Mode 5(Y)	0.206	99.36	99.36	0.495	99.48	99.48
Mode 6(Z)	0.178	99.55	99.36	0.415	99.48	99.48
Mode7 (Y)	0.101	99.99	99.80	0.246	99.92	99.55
Mode 8(X)	0.101	99.99	99.99	0.246	99.99	99.99
Mode 9(Z)	0.089	99.99	99.99	0.214	99.99	99.99
Mode 10(X)	0.054	99.99	99.99	0.078	99.99	99.99

Note: T represents Time period, UX and UY are cumulative modal mass participation ratios along X and Y directions.

4. Results and Discussion

The behavior of non-structural components is examined in detail in the following sections. The key response parameters used to characterize the performance of these components include Floor Response Spectra (FRS), Peak Component Acceleration (PCA), and Component Dynamic Amplification Factors (CDAF). It is essential to highlight that this study does not consider component's nonlinearity and is specifically applicable to lightweight components that do not introduce dynamic feedback to the primary structure. In other words, interaction effects between non-structural components and the primary building structure are not considered in this analysis.

4.1 Floor Response Spectrum (FRS)

In the current research, the non-structural components (NSCs) under investigation are elastic single-degree-of-freedom (SDOF) systems. Dynamic interaction effects are disregarded since these NSCs are believed to have a mass much lower than that of the main structure. The methodology employed involves the use of Floor Response Spectra (FRS) as a decoupled approach, allowing for the independent assessment of both the structure and the NSCs in a specified manner. For this purpose, scaled near- and far-field ground motions serve as input data for both linear and non-linear time history analyses. Absolute acceleration responses are individually obtained for all floors and subsequently utilized as input to calculate the corresponding FRS for the NSCs. A 5% damping ratio is used to calculate these FRS, and the average findings for each floor are presented and evaluated. The average spectral acceleration (S_a, measured in g units) of a non-structural component (NSC) connected to a specific floor is graphed in relation to the vibration period (T_s, measured in seconds) for the building model depicted in Figure 4. When the FRS are plotted across an extensive variety of periods, it is predicted that the largest peaks in the spectrum would line up with the fundamental period of the main structure [40]. These observed peaks in the FRS correspond to the modal periods of the building model under consideration.

From Fig.4, it can be observed that the two peaks observed in the elastic and inelastic FRS are recorded close to the structure's elastic and inelastic modal periods (Table 3), respectively. This finding from this study is consistent with the outcomes of the previous research [11–13]. The Floor Response Spectra (FRS) exhibit a consistent trend of increasing magnitude from the first floor at the bottom to the third floor at the top. At first glance, it is evident that the floor spectral accelerations of the inelastic FRS—shown by dotted lines—are significantly lower than its elastic counterpart. The impact of both near-field and far-field excitations on the FRS is evident when observing the magnitude of the peaks. It is observed that, under far-field excitations, the FRS peaks corresponding to modal periods are noticeably lower in magnitude compared to those under near-field excitations.

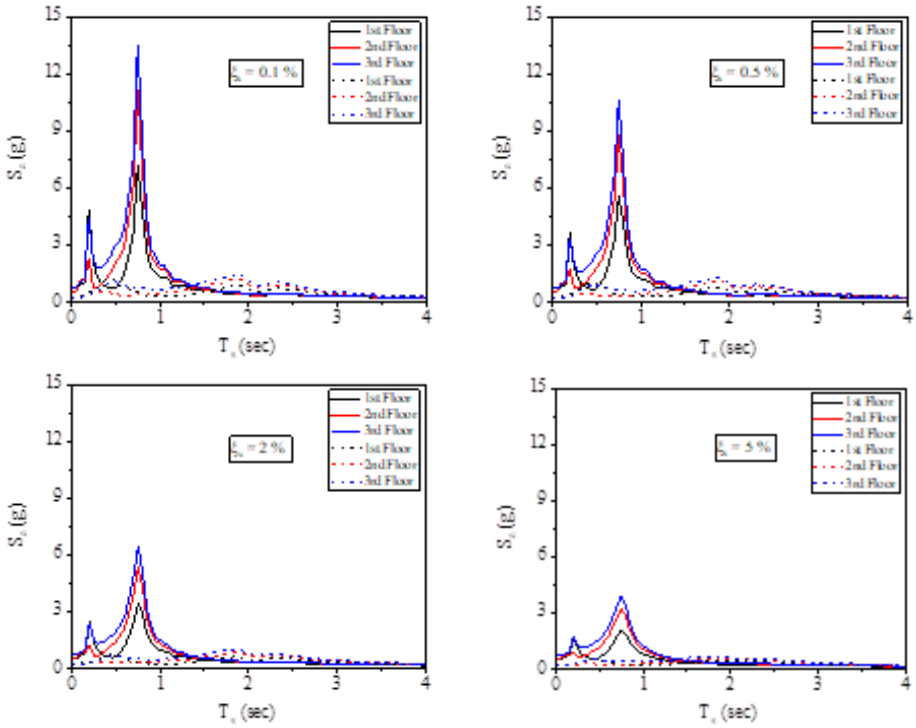

(a)

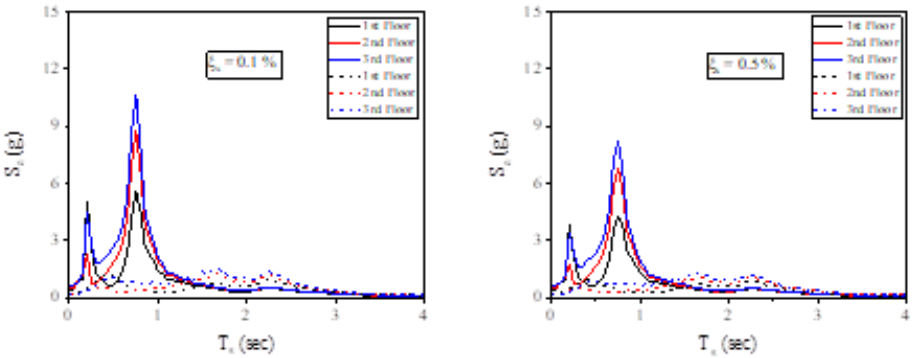

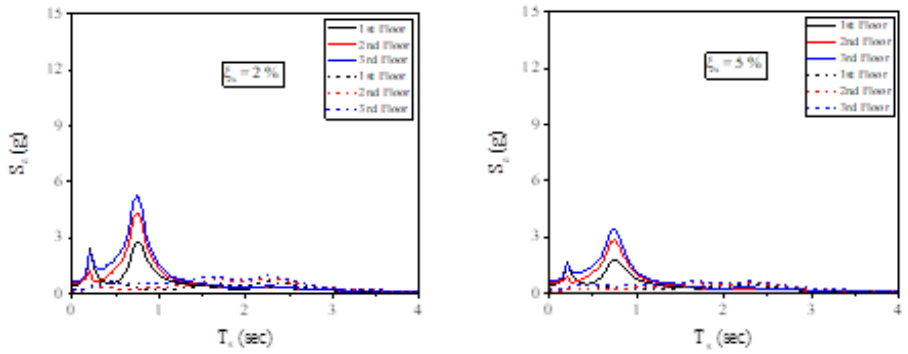

(b)

Fig. 4. Elastic (solid line) and inelastic (dashed line) FRS of 3-storey considered building model for (a) near-field data, (b) far-field data

As an illustration, when considering the higher floor level and an elastic FRS peak associated with the first fundamental period of a building model with a specified damping ratio for the non-structural component (ξ_s = 0.5%), the magnitudes of the floor spectral accelerations are 10.62 g and 8.19 g under near-field and far-field excitations, respectively. Likewise, for the higher floor level and an inelastic FRS peak associated with the first fundamental period of the same building model with the same damping ratio (ξ_s = 0.5%), the magnitudes of the spectral acceleration are 1.28 g and 1.19 g under near-field and far-field excitations, respectively. A significant decrease in floor spectral acceleration is evident when considering far-field excitations. The same pattern is observable for other damping ratios as well. Therefore, we can draw the conclusion that, regardless of the damping ratio of the non-structural component (NSC), near-field excitations lead to higher demands for floor accelerations when compared to far-field excitations. The proximity of the earthquake source plays a critical role in this outcome. Near-field earthquakes, which occur in close proximity to the building, tend to produce ground motions with higher amplitudes and more pronounced high-frequency content. These characteristics can induce higher spectral accelerations and amplification effects in the building's response. In contrast, far-field earthquakes, originating at a greater distance, generally result in ground motions with lower amplitudes and a broader range of frequencies. This typically leads to reduced demands for floor accelerations in the building's response. This conclusion underscores the importance of considering the source-to-site distance and the characteristics of the ground motion when assessing the seismic response of primary structures and non-structural components to withstand earthquakes.

4.2 Peak Component Acceleration

The highest ordinate in the floor response spectrum in the current investigation is referred to as the peak component acceleration (PCA), is subjected to a normalization process with the Peak Ground Acceleration (PGA). Subsequently, the PCA/PGA ratio is graphed in relation to the relative height (z/H, where z is the floor height and H is the total height of the building) of the building model.

Figure 5 highlights a consistent trend across both linear and non-linear analyses, demonstrating a direct relationship between floor elevation and seismic activity. It shows that seismic demands tend to increase as buildings rise, regardless of whether the analysis considers near or far field earthquakes. This suggests a crucial correlation between the floor level and the intensity of seismic effects.

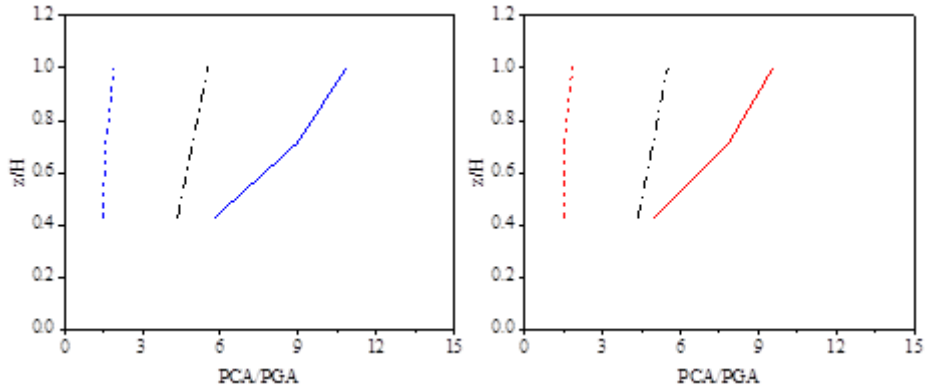

(a) (b)

Fig. 5. Comparison of elastic (solid line) and inelastic (dashed line) FRS of 3-storey considered building model with ASCE 7-16 (dashed-dotted line) formulation for (a) near-field data, (b) far-field data

The comparison between near and far field earthquakes reveals intriguing differences in seismic impact. Near field earthquakes exhibit significantly higher PCA values compared to far field earthquakes. This substantial difference—approximately 15.95% higher for the 1st floor, 14.12% for the 2nd floor, and 13.47% for the 3rd floor—emphasizes a much sharper variation in demands between floors during near field events. This heightened impact likely arises due to the closer proximity of near field earthquakes to the earthquake epicenter. Moreover, the examination of non-linear PCA values unveils additional intricacies. It highlights a nuanced impact, showing a slight decrease in impact on the 1st floor (approximately -1.86%) but a notable increase on the 2nd and 3rd floors (around 4.73% and 3.24% respectively) during near field earthquakes compared to far field earthquakes. These variations underscore the complex relationships in seismic effects across different floors during near field seismic events. Conversely, far field earthquakes showcase lower PCA values across all floors, suggesting a comparatively less pronounced variation in demands between different floor levels.

The PCA/PGA values obtained using the ASCE 7-16 formulation, as defined in Eq. (1), when compared to the results from linear analysis, consistently show lower values across both near and far field earthquake scenarios. This means that the ASCE 7-16 formulation tends to provide estimates of PCA demands that are lower than what the linear analysis suggests.

$$PCA/PGA = a_p\left(1+\frac{z}{H}\right) \tag{1}$$

where, a_p is the component amplification factor. As per the definition of ASCE 7–16, a_p for flexible NSCs with a time period longer than 0.06 sec is 2.5. The value of the a_p is 1 for NSCs whose time period is less than 0.06 sec.

Conversely, when compared to the results derived from non-linear analysis, the PCA values obtained from the ASCE 7-16 formulation tend to be higher across both near and far field earthquake scenarios. This indicates that the ASCE 7-16 formulation tends to overestimate the PCA demands compared to what the non-linear analysis reveals. So, in summary, the ASCE 7-16 formulation generally underestimates the seismic impact when compared to linear analysis and overestimates it when compared to non-linear analysis in both near and far field earthquake situations. As a result, the peak acceleration response of the NSCs cannot be reliably estimated using the present code-based linear formulation. To enhance

accuracy, there's a need to update the formulation to include considerations for both the non-linear behavior of the structure itself and the varied characteristics of ground motions that affect the structure's response during earthquakes.

4.3 Component Dynamic Amplification Factor (CDAF)

The analysis of component acceleration amplification in relation to the floor acceleration is covered in this section. Floor Response Spectra (FRSs) normalized by corresponding Peak Floor Accelerations (PFAs) are analyzed in this process. In Fig. 6, the FRS (elastic and in-elastic) of the building model at the first-floor level normalized by the corresponding PFA is depicted against the T_s. The ratio between FRS and PFA represents the Component Dynamic Amplification Factor (CDAF). The highest point on the CDAF spectrum represents the amplification factor. This study's CDAF for the building model is juxtaposed with the criteria outlined in ASCE 7–16 [37], FEMA P-750 (41) and EuroCode8 . According to ASCE 7–16, flexible NSCs with a time period exceeding 0.06 seconds have a [42]component amplification factor (a_p) of 2.5, while rigid NSCs (with a time period less than 0.06 seconds) have an amplification factor of 1.

Across various analysis types and seismic scenarios, a consistent observation emerges: an increase in the NSC's damping ratio correlates with a decrease in peaks within the CDAF spectrum. Furthermore, these spectra consistently exhibit peaks aligned with the building's modal periods. In near-field earthquakes, for the elastic model and selected NSC damping ratios (0.1%, 0.5%, 2%, and 5%), peak values within the CDAF spectrum associated with the first modal period range between 4.26 and 14.61, contrasting with the inelastic model's range of 2.15 to 4.49. Similarly, under far-field earthquakes, the elastic model's peak values vary from 3.76 to 13, while the inelastic model's range from 2 to 4.63 for the same damping ratios. In both seismic conditions, comparative analysis reveals distinct differences between elastic and inelastic models across various damping ratios. Under near-field earthquakes, the inelastic model showcases percentage decreases in peak values of approximately 49.53%, 56.14%, 64.89%, and 69.3% compared to the elastic model for damping ratios of 5%, 2%, 0.5%, and 0.1%, respectively. Correspondingly, in far-field earthquakes, these reductions amount to about 51.81%, 55.81%, 60.3%, and 64.47% for the same damping ratios. These consistent disparities underscore the significant impact of seismic conditions and damping ratios on the dynamic characteristics and spectral responses, emphasizing the distinct behavior between elastic and inelastic models within the system.

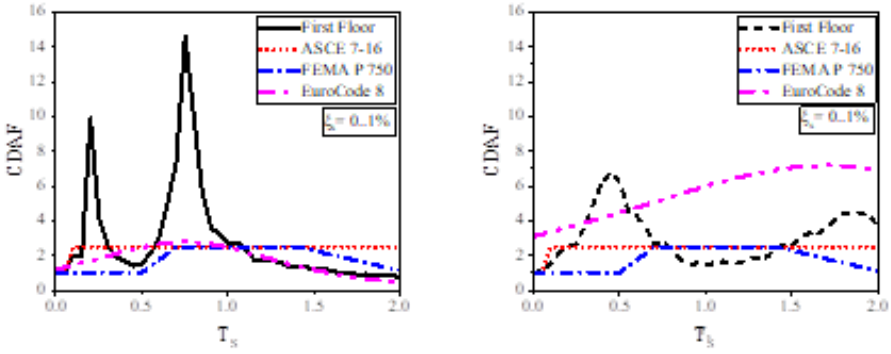

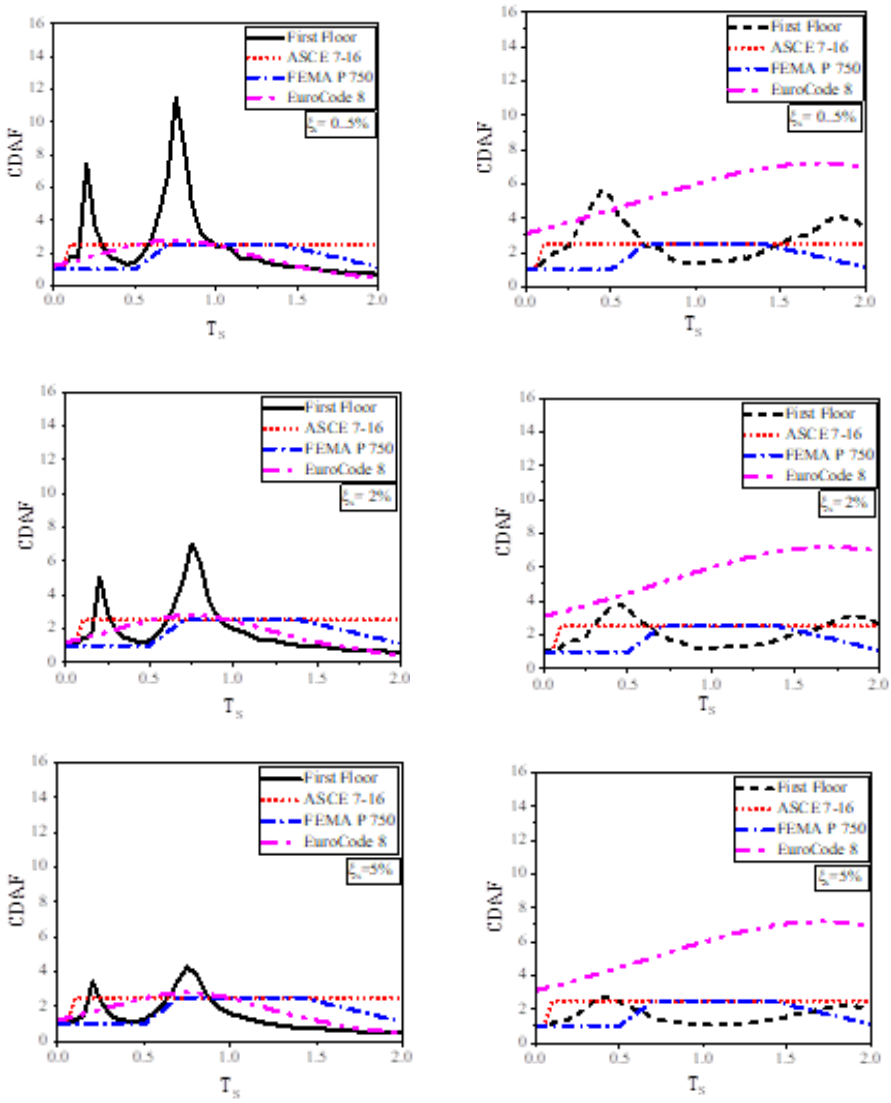
First Floor
ASCE 7-16
FEMA P 750
EuroCode 8
ξs= 0..5%
ξs= 2%
ξs=5%
ξs= 0..1%
CDAF
Ts

(a)

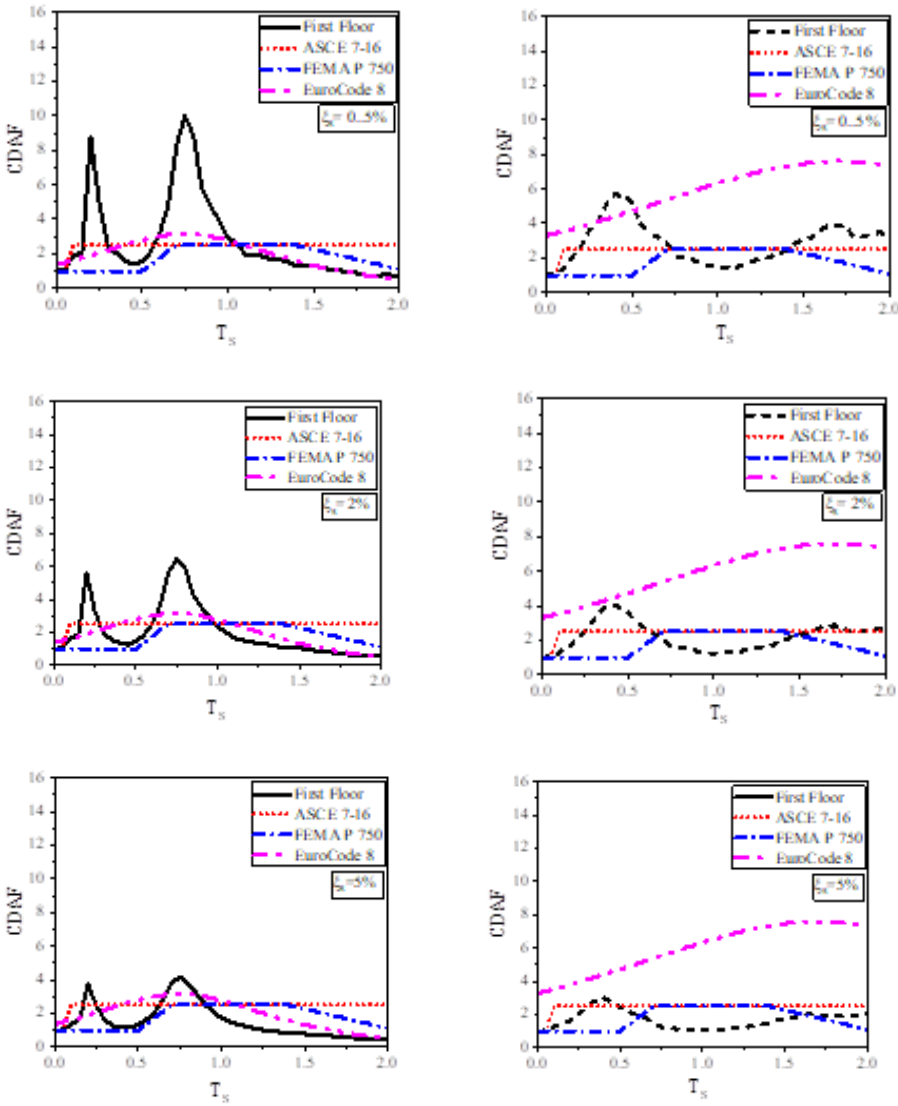

(b)

Fig. 6. Elastic (solid line) and inelastic (dashed line) CDAF spectrum for (a) near-field data, and (b) far-field data

The CDAF spectrum defined by the code-based formulation is plotted and compared against the simulated CDAF spectrum as shown in Fig. 6. In the elastic model, across near and far-field earthquake scenarios, the code-based formulation consistently underestimates the peak CDAF values corresponding to the building's modal periods. Conversely, within the inelastic model, the ASCE formulation consistently overestimates the peak CDAF associated with the first modal period, regardless of the earthquake type. However, both FEMA and Eurocode 8 formulations tend to underestimate the peak CDAF values for damping ratios of 0.1% and 0.5%, whereas for damping ratios of 2% and 5%, they exhibit an overestimation of the CDAF values. Therefore, based on the observed

discrepancies in peak CDAF values attributed to various earthquake types within the elastic and inelastic models, it becomes essential to refine the existing code-based formulation.

5. Conclusions

The current research focuses on analyzing a three-story building model under both near and far-field earthquake conditions. The main aim is to identify and measure the rise in floor acceleration, a crucial factor influencing the design of non-structural components in low-rise buildings for aforementioned earthquakes. The study yields noteworthy findings, summarized as follows:

- In both elastic and inelastic Floor Response Spectra (FRS), observed peaks consistently align closely with the structure's elastic and inelastic modal periods.
- The observed Floor Response Spectra (FRS) consistently depict an ascending trend in magnitude from the building's bottom to top floors. Compared to elastic FRS, the inelastic FRS notably show a considerable decrease in floor spectral accelerations.
- Near-field earthquakes induce 25-30% higher floor acceleration demands in non-structural components compared to far-field earthquakes.
- Near field seismic events exhibit significantly higher Peak Component Acceleration (PCA) values than far field earthquakes. Far field earthquakes display lower PCAs across all floors, suggesting less diverse demands between floor levels.
- Higher damping ratios in the non-structural component led to decreased peaks in the component dynamic amplification factor (CDAF) spectrum. In near-field earthquakes, the inelastic model notably reduces peak values by roughly 49.53% to 69.3% across damping ratios of 0.1% to 5% compared to the elastic model. Similarly, under far-field earthquakes, reductions range from about 51.81% to 64.47% for the same damping ratios in the inelastic model compared to the elastic one.
- The code-based formulations consistently underestimate peak CDAF values in the elastic model, whereas the ASCE formulation consistently overestimates peaks in the inelastic model. FEMA P-750 and Eurocode 8 show varied estimations, either overestimating or underestimating based on specific damping ratios.

The findings of this study are constrained by the specific characteristics of the building model and the selected ground motions. It is important to note that this research focuses solely on the linear response of non-structural components (NSCs) as an initial exploration. To obtain more comprehensive and generalized results, future investigations should incorporate the nonlinear behavior of NSCs. Additionally, there is potential for extending the scope of research to include high-rise structures such as 10, 15, or 20-story buildings with various irregularities. By considering a broader range of building types and structural complexities, future studies can provide deeper insights into the seismic performance of NSCs across different scenarios.

Acknowledgement

The authors acknowledge that this study is supported by Department of Civil Engineering, Koneru Lakshmaiah Education Foundation (KLEF), Vaddeswaram, Guntur, India.

References

[1] Filiatrault A, Perrone D, Merino RJ, Calvi GM. Performance-based seismic design of nonstructural building elements. Journal of Earthquake Engineering. 2021;25(2):237–69.

[2] Shang Q, Wang T, Li J. Seismic fragility of flexible pipeline connections in a base isolated medical building. Earthquake Engineering and Engineering Vibration . 2019;18(4):903–16. https://doi.org/10.1007/s11803-019-0542-5
[3] Di Sarno L, Magliulo G, D'Angela D, Cosenza E. Experimental assessment of the seismic performance of hospital cabinets using shake table testing. Earthq Eng Struct Dyn . 2019 Jan 1;48(1):103–23. https://doi.org/10.1002/eqe.3127
[4] Anajafi H, Medina RA. Evaluation of ASCE 7 equations for designing acceleration-sensitive nonstructural components using data from instrumented buildings. Earthq Eng Struct Dyn . 2018 Apr 10;47(4):1075–94. https://doi.org/10.1002/eqe.3006
[5] Pardalopoulos SI, Pantazopoulou SJ. Seismic response of nonstructural components attached on multistorey buildings. Earthq Eng Struct Dyn. 2015;44(1):139–58.
[6] Perrone D, Andre F. Seismic demand on non-structural elements: Influence of masonry infills on floor response spectra. In: Proceedings 16th European Conference on Earthquake Engineering. 16th European Conference on Earthquake Engineering; 2018.
[7] Suarez LE, Singh MP. Floor response spectra with structure–equipment interaction effects by a mode synthesis approach. Earthq Eng Struct Dyn . 1987 Feb 1;15(2):141–58. https://doi.org/10.1002/eqe.4290150202
[8] Adam C. Dynamics of elastic–plastic shear frames with secondary structures: shake table and numerical studies. Earthq Eng Struct Dyn . 2001 Feb 1;30(2):257–77. https://doi.org/10.1002/1096-9845(200102)30:2<257::AID-EQE7>3.0.CO
[9] Menon A, Magenes G. Definition of Seismic Input for Out-of-Plane Response of Masonry Walls: I. Parametric Study. Journal of Earthquake Engineering . 2011 Jan 5;15(2):165–94. https://doi.org/10.1080/13632460903456981
[10] Challagulla SP, Bhargav NC, Parimi C. Evaluation of damping modification factors for floor response spectra via machine learning model. In: Structures. Elsevier; 2022. p. 679–90.
[11] Challagulla SP, Bhavani BD, Suluguru AK, Jameel M, Vicencio F. Influence of ground motion scaling on floor response spectra. Curr Sci. 2023;124(8):928.
[12] Challagulla SP, Kontoni DPN, Suluguru AK, Hossain I, Ramakrishna U, Jameel M. Assessing the Seismic Demands on Non-Structural Components Attached to Reinforced Concrete Frames. Applied Sciences. 2023;13(3):1817.
[13] Pesaralanka V, Challagulla SP, Vicencio F, Chandra Babu PS, Hossain I, Jameel M, et al. Influence of a Soft Story on the Seismic Response of Non-Structural Components. Sustainability (Switzerland). 2023 Feb 1;15(4).
[14] D'Angela D, Magliulo G, Cosenza E. Seismic damage assessment of unanchored nonstructural components taking into account the building response. Structural Safety . 2021; 93:102126. https://www.sciencedirect.com/science/article/pii/S0167473021000503
[15] Yasui Y, Yoshihara J, Takeda T, Miyamoto A. Direct Generation Method for Floor Response Spectra. In 1993. https://api.semanticscholar.org/CorpusID:199778698
[16] Vukobratović V, Fajfar P. A method for the direct determination of approximate floor response spectra for SDOF inelastic structures. Bulletin of Earthquake Engineering. 2015; 13:1405–24.
[17] Jiang W, Li B, Xie WC, Pandey MD. Generate floor response spectra: Part 1. Direct spectra-to-spectra method. Nuclear Engineering and Design . 2015; 293:525–46. https://www.sciencedirect.com/science/article/pii/S002954931500271X
[18] Calvi P, Sullivan T. Estimating floor spectra in multiple degree of freedom systems. Earthquakes and Structures. 2014 Jul 31; 7:17–38.
[19] Zhai CH, Zheng Z, Li S, Pan X, Xie LL. Seismic response of nonstructural components considering the near-fault pulse-like ground motions. Earthquake and Structures. 2016;10(5):1213–32.

[20] Petrone C, Magliulo G, Manfredi G. Floor response spectra in RC frame structures designed according to Eurocode 8. Bulletin of Earthquake Engineering . 2016;14(3):747–67. https://doi.org/10.1007/s10518-015-9846-7
[21] Berto L, Bovo M, Rocca I, Saetta A, Savoia M. Seismic safety of valuable non-structural elements in RC buildings: Floor Response Spectrum approaches. Eng Struct. 2020; 205:110081.
[22] Shang Q, Li J, Wang T. Floor acceleration response spectra of elastic reinforced concrete frames. Journal of Building Engineering. 2022; 45:103558.
[23] Landge M V, Ingle RK. Comparative study of floor response spectra for regular and irregular buildings subjected to earthquake. Asian Journal of Civil Engineering. 2021; 22:49–58.
[24] Singh MP, Suárez LE. Seismic response analysis of structure–equipment systems with non-classical damping effects. Earthq Eng Struct Dyn. 1987;15(7):871–88.
[25] Perez YM, Guerra EM, Bazan-Zurita E. Seismic Response Of Equipment Supported On Structures. 2015.
[26] Chanda A, Debbarma R. Probabilistic seismic analysis of base isolated buildings considering near and far field earthquake ground motions. Structure and Infrastructure Engineering. 2021;18(1):97–108.
[27] Davoodi M, Sadjadi M, Goljahani P, Kamalian M. Effects of near-field and far-field earthquakes on seismic response of sdof system considering soil structure interaction. In: 15th World Conference on Earthquake Engineering Lisbon, Portugal. 2012.
[28] Alhan C, Öncü-Davas S. Performance limits of seismically isolated buildings under near-field earthquakes. Eng Struct. 2016;116:83–94.
[29] Moghaddam PK, Manafpour AR. Effects of Far-and Near-Field Multiple Earthquakes on the RC Single Degree of Freedom Fragility Curves Using Different First Shock Scaling Methods. International Journal Of Engineering. 2018;31(9):1505–13.
[30] Faghihmaleki H, Ahmadian F, Roosta H. The effect of far field and near field earthquakes on the hysteresis energy and relative displacement of steel moment resisting frame structures. Journal of Building Pathology and Rehabilitation. 2017; 2:1–9.
[31] Tavakoli HR, Naghavi F, Goltabar AR. Dynamic responses of the base-fixed and isolated building frames under far-and near-fault earthquakes. Arab J Sci Eng. 2014; 39:2573–85.
[32] BIS Bureau of Indian Standards. IS 875-2 (1987): Code of Practice for Design Loads (Other Than Earthquake) For Buildings And Structures, Part 2: Imposed Loads.
[33] 2016 IS 13920: Ductile design and detailing of reinforced concrete structure subjected to seismic force. Bureau of Indian Standard (BIS). 2016;
[34] SeismoStruct S. Release-1-A Computer Program for Static and Dynamic Nonlinear Analysis of Framed Structures. 2016.
[35] Engineers AS of C. Seismic evaluation and retrofit of existing buildings. In American Society of Civil Engineers; 2017.
[36] Reinforced Concrete Buildings with Restricted Ductility. In: Seismic Design of Reinforced Concrete and Masonry Buildings . John Wiley & Sons, Ltd; 1992. p. 639–61. https://onlinelibrary.wiley.com/doi/abs/10.1002/9780470172841.ch8
[37] A. Minimum Design Loads and Associated Criteria for Buildings and Other Structures. 2016.
[38] ATC. Quantification of building seismic performance factors. Fema P695. 2009;(June):421.
[39] IS 875 (part 1). IS 875-1: Code of Practice For Design Loads (Other Than Earthquake) For Buildings And Structures, Part 1: Dead Loads. Bureau of Indian Standards, New Delhi. 1987;875(July):1–37.

[40] Shooshtari M, Saatcioglu M, Naumoski N, Foo S. Floor response spectra for seismic design of operational and functional components of concrete buildings in Canada. Canadian Journal of Civil Engineering. 2010 Oct 22; 37:1590–9.
[41] Washington DC. NEHRP (National Earthquake Hazards Reduction Program) Recommended Seismic Provisions for New Buildings and Other Structures (FEMA P-750) Prepared for the Federal Emergency Management Agency of the U.S. Department of Homeland Security By the Building Seismic Safety Council of the National Institute of Building Sciences Building Seismic Safety Council A council of the National Institute of Building Sciences . 2009. www.bssconline.org
[42] British Standards Institution., European Committee for Standardization., British Standards Institution. Standards Policy and Strategy Committee. Eurocode 8, design of structures for earthquake resistance. British Standards Institution; 2005.

Research on Engineering Structures & Materials
www.jresm.org
Research Group

Research Article

The effect of age and wear on the mechanical performance of HDPE 80 polyethylene pipes

Noureddine Haddad*, [a], Ahmed Belbah[b]

Department of Mechanical Engineering, Applied Mechanics of New Materials Laboratory (LMANM), University 8 Mai 1945, BP 401,24000 Guelma, Algeria

Article Info

Article history:

Received 25 Dec 2023
Accepted 27 Mar 2024

Keywords:

HDPE 80;
Wear;
Taguchi method;
Optimization;
Aging

Abstract

In this work, we studied the influence of accelerated aging in an aggressive environment of high-density polyethylene (HDPE 80) used for pipeline applications to distribute gas. Accelerated aging by ultraviolet irradiation of the wavelength lamps (λ = 365nm) for 240 hours at a temperature of 35°C exposed samples to solar radiation on the sand in southern Algeria for 12 months. The samples were subjected to weathering at -10 °C and 25°C for four different durations. To assess the weight loss capacity of semi-crystalline polymer behavior (HDPE 80) Under accelerated aging conditions, aging is carried out mainly according to three referenced methods: ISO 105 B02/B04, DIN 75202, and SAE J 1885. The Taguchi method and regression analysis were used. Several experiments were conducted on a vertical milling machine using a multi-factor L16 (4^1*2^3) orthogonal mixed matrix. An analysis of variance (ANOVA) was used to determine the effects of treatment: corrosion, weight loss, and loss of thickness. The parameters are influenced by the sandpaper's grain diameter, cutting speed, and compressive strength continuity over two hours, with each trial lasting 15 minutes. Using S/N ratios, optimal control factors were determined to minimize lost weight (P) and thickness loss (ΔL) due to abrasion of HDPE polyethylene pipes 80. At A3, B2, C2, D2 (i.e. degradation mode = UV, rotation speed = 355 rpm, load = 9.3 N, abrasive paper = 10.3 degrees) and A3, B1, C2, D1 (i.e. degradation mode = UV, rotation speed = 180 rpm, load = 4.65 N, and abrasive paper = 18.3 degrees), ideal conditions for weight and thickness loss were observed.

1. Introduction

In sliding pairs against metals and other materials, polymers are commonly utilized, the phenomenon of absorption and diffusion under constant conditions and at various stages is one factor that affects the aging of polyethylene (HDPE); this phenomenon was the subject of numerous investigations using samples made of equations for stress. Fragments of bottles made of HDPE material were also demonstrated using mechanical tensile tests, crimps, Using ABAQUS software, a study of the aging phenomena of high-density polymers was conducted, The findings revealed a pattern that lowers compressive strength [1]. As a result of interactions between the various species in the mixtures during decomposition, the degradation of HDPE 80 polymer material is aging. It can greatly alter the progressive degradation behavior of the components, which could result in deterioration. Additionally, compared to the natural components, the reactions speed up the pace of disintegration, making it more challenging to recover the required qualities of HDPE 80 polyethylene through treatment and causing severe damages, such as the bursting of HDPE 80

*Correspondingauthor: haddad.noureddine@univ-guelma.dz
[a]orcid.org/0000-0001-8299-8019; [b]orcid.org/ 0000-0002-1020-6024
DOI: http://dx.doi.org/10.17515/resm2024.131me1225rs

polyethylene natural gas pipelines [2]. In manufacturing and in the channels used to transport various soft liquids like water, gas, and oil, HDPE 80 polymer material is one of the plastic materials that cannot be done without. Under normal circumstances, corrosion is easily handled at a reasonable cost [3 and 4]. The results focused on the fatigue behavior of a group of thermoplastic polymers mixed with composite materials. They showed that the Walker bond was the best, as it fits the Smith-Watson-Topper link with the experimental data using SN curves through which the Baskin equation and correction [5]. Using Taguchi analysis and ANOVA, multiple correlations were performed using L18 (2*3*3) different effects (surface roughness, cutting tool wear, cutting speed, and feed). The results showed that plastics are significantly less resilient to premature aging, especially when friction and wear occur in different media, depending on how the sliding surface moves [6]. Results of the matrix (2*3*3) of the Taguchi method showed success in improving surface roughness and corrosion under the effect of cutting speed, suggesting that the aging of plastics by corrosion in some media may be associated with the roughness of contact surfaces and compression forces [7]. The improvement of the bending ability of CFRP sheets made of carbon fiber-reinforced polymer and its strengthening under the influence of RC beams may reach 100% compared to the control beam using the finite element method to develop a digital model for analysis. [8]. Reduces high abrasive wear loss and dry plastic deformation of Al-Si automotive alloys on a standard disc-mounted device by controlling the lubricating film used for a lower wear rate and coefficient of friction due to aging [9]. It was also observed after UV exposure to high-density polyethylene (HDPE) used in solar panels for periods of varying durations up to 1152 hours, as this material highlighted its resilience by maintaining its properties under sunlight with a slight change [10]. Some studies have dealt with the design of experiments for production engineering (DOE), manufacturing technology to improve metal cutting tools, and also touched on the use of contemporary methods in the design of experiments for production engineering and during a previous study, an inference of the amount of rainfall affecting grass growth rate was also obtained using DOE in statistical analysis. In the author's opinion, the user must learn the Design of Experience [DOE] method. [11 and 12]. Also, heat effects on the fatigue behavior of HDPE allow the calculation of average stress by creating a general fatigue model for this substance [13]. Plastic PET is an additive to improve hardness during exposure to different temperatures [14]. The polyamide material P66 high molecular mass is characterized by improving and enhancing its corrosion resistance on its steel counterpart, which occurs through friction between two bodies [15]. Adding nanofibers to an HDPE matrix in a specific proportion can also treat plastic deformation and increase wear resistance and toughness. This improves toughness during tensile and thermal friction wear [16]. When the substance used for tubes is damaged by the loss of fish from the diameter deficiency whale by up to 40%, you should improve and review [17]. Frictional wear was examined using nano-micro-lubrication tribology in relation to material surface wear, Wear gradually reduces as the material loses its surface properties due to contact with another surface during movement [18 and 19]. According to research results, the treatment of the friction phenomenon of HDPE polymers improves by adding TiN titan compounds, where the relationship between the specific corrosion rate of the added compounds is found [20]. The use of plastic in shopping bags and edibles increases the likelihood of environmental contamination and endangers the growth of wild and marine plants and animals [21]. A new model of mechanical properties degradation has been developed. The prepared model uses cumulative data for distribution functions to approximate experimental data by calculating factors that reduce mechanical properties after periodic exposure to plastics and composite fatigue [22]. The Gray Relation study was used to improve the corrosion study of multi-response carbon-carbide-filled epoxy composites under the influence of four factors [23]. Artificial neural networks were used to study the effect of the coefficient of friction and contact temperature on a 30% carbon fiber-reinforced polyetherketone compound. The effect of

the coefficient of friction on weight loss was compared to the contact temperature factor, the coefficient of friction was mainly affected, and the thermal factor also significantly affected weight loss. [24]. In a previous study of sliding wear of polypropylene (PP) with steel on a dry body, the addition of CNT to PP affected the corrosion performance using a scanning electron microscope. We discussed the phenomenon of corrosion, i.e., the loss of surfaces' properties during contact [25]. A study was also conducted on the polymer material's friction wear method in hip prosthetic applications. The polymer material was tested under contact conditions, sliding speed, and constant pressure to obtain the best results [26]. The difference was explained in the manuscript by adding text in the last paragraph of the introduction as follows: The Taguchi method and regression analysis were used under several experiments on a vertical milling machine using an L16 (4^1*2^3) multi-factor orthogonal mixed matrix with the effect of wear on the natural and industrial ambient conditions used. This research also presents a new method to study the effect of various factors on the life of HDPE 80 polyethylene used in natural gas transportation channels, including exposure to sunlight, freezing, heating, and ultraviolet radiation, compared to the initial state of HDPE polyethylene. During this study of the phenomenon of artificial and natural aging and frictional wear of gas distribution pipes made of high-density polyethylene HDPE80, we used the L16 (4^1*2^3) array of the Taguchi array to determine the conditions for conducting experiments and to determine the influencing factors such as coarse paper grain size, rotational speed, and compressive strength, in addition to determining the time for each experiment to minimize weight loss and avoid scratches on the surface.

2. Experimental Section Experimental Method and Study Material

High-density polyethylene (HDPE 80), which is well-known for its thickness of 11.5 mm, inner diameter of 176 mm, and outer diameter of 200 mm, was used for natural gas pipelines in this investigation, as indicated in Tab. 1. The thermal properties and measurements of the examined pipes are listed here. Wear samples made of the high-density polyethylene HDPE80 material are displayed in (Fig.1). in the shape of a disk of 10 mm in diameter and 4 mm in thickness.

Table 1. Properties of test materials [27]

Materials	Code	Density	Elastics modulus	Elongation	Fracture energy
High Density Polyethylene	HDPE	0.952	276	700	126
Middle Density Polyethylene	MDPE	0.945	207	740	129
low-density polyethylene	LDPE	0.938	130	630	79
Polyethylene 100	PE100	0.962	260	740	137

Table 2. Experimental conditions for the abrasive wear tests

Load (N)	4.65 and 9.3
Rotation speed of disc (rpm)	180 and 355
Mean contact pressure (MPa)	59.24×10−3 and 118.47×10−3
Radius of wear track on disc (mm)	42
Testing time (min)	1–15
Sliding distance (m)	13.2 – 33.9
Abrasive paper (μm)	1000 and 2000 (18. 3 and 10.3)

With the crushing technique, wear between the polyethylene material and the surface of the abrasive paper causes a layer to be deposited on the surface. Some properties must be determined during and after the experiment, as shown in Table 2.

3. Tribological Features

A vertical milling machine used for pin and disc wear tests, as shown in the schematic diagram in (Fig.1) [28], of the wear test apparatus, as discussed in previous studies by Guermazi (2008), Liu and al (2006), in tensile and wear experiments on samples of a polymer material, the wear experiments were carried out at a laboratory temperature of 21 °C and using abrasive paper with grain sizes 1000 and 2000 (grain sizes 18.3 and 10.3 µm). It is installed on the milling machine table, as shown in the picture [29]. The rotational speed was given at two consecutive speeds (180 and 355) revolutions per minute for the friction device that holds the compressed pin with a force of (9.3 and 4.65) Newton under spring pressure so that the samples are weighed before and after each experiment for two hours, respectively, divided by a quarter of an hour for each measurement. Then, with a high-precision scale of 10^-4g, the abrasive paper is also changed for each trial, the amount of weight loss is calculated by the difference after each test, and the thickness is measured with a micrometer.

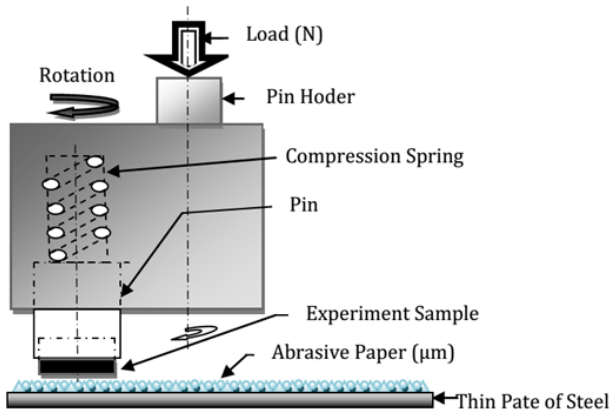

Fig.1. Schematic representation of the wear testing device

4. Accelerated Aging Procedure

The aging effect of the robust and diverse environment accelerates the behavior of semi-crystalline polymer (HDPE 80). The degradation behavior of the polymer material was analyzed by various methods and subjected to accelerated ultraviolet (UV) aging. Ultraviolet radiation decomposition of the lamps to wavelength (= 365 nm) in 240 hours at 35 °C, exposure to sand in southern Algeria for 12 months, and thermal aging in lousy weather at -10 °C and 25 °C for four different periods for three months for an entire year.

After the experiment, the weight (P) of the sample was determined with high precision (10-4 g) using an electronic balance (Eqn.1) while calculating the thickness loss (ΔL). A vernier caliper was used to correspond to the difference between the length value of the sample before and after the experiment (Eqn.2). The pressure value is kept constant using an elastic spring of a friction device.

$$P = P_n - P_{n-1} \tag{1}$$

P: weight loss value; Pn: Initial weight; Pn-1Weight After the test.

$$\Delta l = L_n - L_{n-1} \quad (2)$$

ΔL: elongation; Ln: the initial length; Ln-1: the length following the experiment.

5. Taguchi Method and Experimental Design

The Taguchi method is widely used in engineering analysis because it reduces the number of experiments with orthogonal matrices and the effects of uncontrollable factors. Moreover, it provides a scientific method for determining the weight loss during the wear of manufacturing materials [29]. By converting the quality analysis method into a signal-to-noise ratio (S/N) file, the Taguchi method is also used to calculate the empirical values of the various factors affecting the material used and the values available through the lowest loss, most effective. The best-used S/N ratio for each level [7] was used, and experiments were performed using Taguchi's method with a mixed orthogonal matrix. Table 3. Regression analysis on a vertical milling machine, and the L16 (4^1*2^3) multifactorial design Influence factors and their levels Table 4.

Table 3. Full factorial design with an orthogonal array of Taguchi L16(4^1*2^3)

N° of experiments	Factor (A)	Factor (B)	Factor (C)	Factor (D)
	(months*3)	(rpm)	(N)	(µm)
1	1	1	1	1
2	1	1	2	2
3	1	2	1	2
4	1	2	2	1
5	2	1	1	1
6	2	1	2	2
7	2	2	1	2
8	2	2	2	1
9	3	1	1	1
10	3	1	2	2
11	3	2	1	2
12	3	2	2	1
13	4	1	1	1
14	4	1	2	2
15	4	2	1	1
16	4	2	2	2

Table 4. Influence factors and their levels

Parameters	Symbol	Level 1	Level 2	Level 3	Level 4
Degradation modes (months)	A	3	6	9	12
Spindle speeds(rpm)	B	180	355	-	-
Load (N)	C	4.65	9.3	-	-
Abrasive paper (µm)	D	18. 3	10.3	-	-

The Taguchi technique calculates the deviation between theoretical and experimental values using a loss function. In addition, the signal-to-noise ratio (S/N) is calculated using this loss function (grams for weight loss and millimeters for thickness loss). The purpose of this study was to lessen the corrosion of the pipes under investigation since corrosion causes weight loss and surface scratches, both of which directly impact wear, particularly during the aging phases. As can be seen in (Eqn.3), the "Smaller is better" characteristic of lesser quality was employed (better minimize).

$$\eta = S/N_S = -10\log[\frac{1}{\eta}\sum_{i=1}^{\eta} y_i^2] \quad (3)$$

(S/N): Signal-to-noise ratio

6. Evaluate and Analyze the Results of The Experiments

6.1. Signal-to-Noise Ratio (S/N) Analysis

We analyzed all the results we reached using Takeshi's method in the field of experiment analysis charts using the Mini-Tab program analysis, where the results were within the applicable confidence interval, less than 5%, the probability value as shown in Table5. Weight loss (P) and thickness loss (ΔL) due to frictional wear were determined by experimentally designing each set of controls using Taguchi techniques, and signal-to-noise (S/N) ratios optimized the measured controls. Minimum weight and thickness loss due to corrosion are very important to improve product quality.

Table 5. Experimental findings and S/N ratio value

Degradation modes	B	C	D	P	S/N ratio for P	ΔL	S/N ratio for ΔL
	rpm	(N)	(μm)	(g)	(dB)	(mm)	(dB)
Raw material	180	4,65	1000	0,2910	10,7221	0,10	20,0000
Raw material	180	9,3	2000	0,1050	19,5762	0,05	26,0206
Raw material	355	4,65	2000	0,5170	5,7302	0,45	6,9357
Raw material	355	9,3	1000	0,4260	7,4118	0,20	13,9794
Ex -sunlight	180	4,65	1000	0,4990	6,0380	0,10	20,0000
Ex-sunlight	180	9,3	2000	0,7530	2,4641	0,30	10,4576
Ex-sunlight	355	4,65	2000	0,5710	4,8673	0,20	13,9794
Ex-sunlight	355	9,3	1000	0,8550	1,3607	0,35	9,1186
Ex-UV	180	4,65	1000	0,1350	17,3933	0,05	26,0206
Ex-UV	180	9,3	2000	0,1490	16,5363	0,10	20,0000
Ex-UV	355	4,65	2000	0,2480	12,1110	0,30	10,4576
Ex-UV	355	9,3	1000	0,0728	22,7574	0,15	16,4782
Ex-heat & cold	180	4,65	1000	0,4920	6,1607	0,25	12,0412
Ex-heat & cold	180	9,3	2000	0,2860	10,8727	0,10	20,0000
Ex-heat & cold	355	4,65	2000	0,1081	19,3235	0,45	6,9357
Ex-heat & cold	355	9,3	1000	0,1450	16,7726	0,40	7,9588

P (Weight loss total mean value) = 0.3531g and P (S/N ratio, total mean value) = 11.2561 dB. ΔL (thickness loss total mean value) = 0.22 mm and ΔL (S/N ratio, total mean value) = 15.0239 db. The "less is better" formula was used to calculate the S/N ratio bids. As shown in Tab 6. In terms of the values of the S/N ratios to monitor the weight loss and the decrease in the thickness of the tube after all the friction corrosion experiments were calculated by calculating the average values of the weight loss and the thickness, which P (Weight loss total mean value) = 0.3531g and P (S/N ratio, total mean value) = 11.2561 dB. ΔL (thickness loss total mean value) = 0.22 mm and ΔL (S/N ratio, total mean value) = 15.0239 db. The "less is better" formula calculates the S/N ratio bids. As shown in Table 6. The values of the S/N ratios to monitor the weight loss and the decrease in the tube thickness after all the friction corrosion experiments were calculated by calculating the average values of the weight loss and the thickness, respectively 0.3553 g and 0.22 mm. Similarly, the average values of the S/N ratio for weight loss and fish loss were calculated to be 11.2561 dB and 15.0239 dB, respectively, where we analyzed the effect of each control factor (deterioration mode, rotational speed, spring pressure force, and abrasive paper). Weight

loss and thickness loss were performed using a weight loss and the optimum thickness loss control factors “S/N” response schedule" as per Table 6.

Table 6. Experimental values for Optimal Levels of Weight Loss (P) and Values for Optimal Levels of Thickness Loss (ΔL) Control Factors

Levels	Weight Loss (P)				Thickness Loss (ΔL)			
	A (months*3)	B (rpm)	C (N)	D (µm)	A (months*3)	B (rpm)	C (N)	D (µm)
Leve1	10,860	11,220	10,293	11,077	16,73	**19,32**	14,55	**15,70**
Leve2	3,683	**11,292**	**12,219**	**11,435**	13,39	10,73	**15,50**	14,35
Leve3	**17,199**	-	-	-	**18,24**	-	-	-
Leve4	13,282	-	-	-	11,73	-	-	-
Delta	13,517	0,071	1,926	0,358	6,51	8,59	0,96	1,35
Rank	1	4	2	3	2	1	4	3

Loss of weight and thickness after 45 minutes of corrosion (Figs. A and B) show the optimal treatment parameters for the control factors to reduce the weight loss value as well as the value of the loss of thickness of pipes made of HDPE80 material, where the corrosion of natural gas transmission pipes can be easily determined as the level of each control factor is found, according to the S/N ratio, to be higher at levels of this control factor.

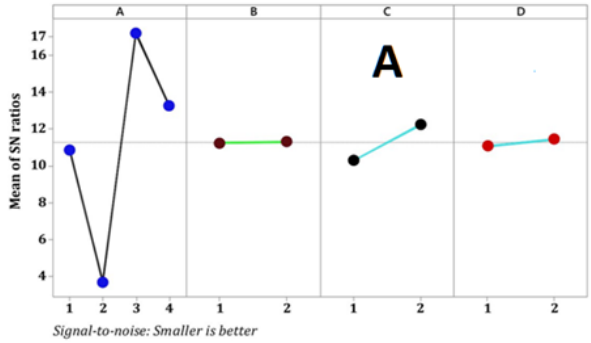

(a)

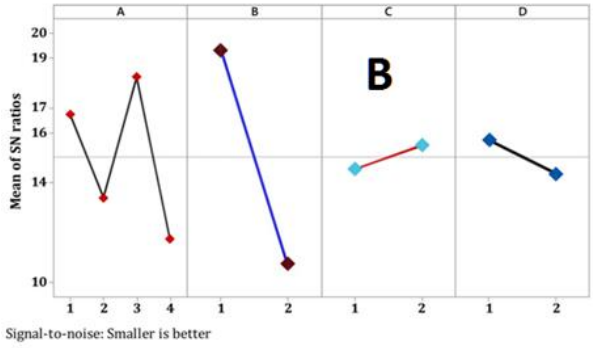

(b)

Fig. 2. (a) Effect of process parameters on the average S/N ratio for weight loss (P) and (b)effect of process parameters on the average S/N ratio for thickness loss (ΔL).

Accordingly, the stories and S/N ratios of factors influencing weight loss for HDPE80 were determined as factor A (level 3, S/N = 17,199), factor B (level 2, S/N = 11,292), factor C (level 2, S/N = 12,219), and factor D (level 2, S/N = 11,435). In other words, the optimal value obtained under the influence of UV aging agents (A3) is 355 rpm of rotating speed (B2), constant pressing force (C2), at a rate of 9.3 N, and using D abrasive paper with a grain size of 2000. (10.3µm) (Fig.2A). Similarly, the levels and S/N ratios of the factors give ΔL the best definition as Factor A (Level 3, S/N = 18, 24), Factor B (Level 1, S/N = 19, 32), Factor C (Level 2, S/N = 15,50), and the D factor (Level 1, S/N = 15,70). In other words, the friction factors affecting the thickness loss of HDPE80 material were demonstrated, as the highest ΔL value was obtained using (A3) UV, with a rotational speed of (B2) of 180 rpm, with a continuous compressive force (C2) at a rate of 9.3 N, and using D abrasive paper with a grain size of 1000 (18.3 m) (Fig. 2B).

Exposure to radiation emitted from a UV lamp with a wavelength equal to (=365 nm) increases weight loss and thickness in the friction zone, where the most influential factor in premature aging and, thus, weight loss and thickness of the studied tubes were observed. Effect on the weight loss, and the increase in the compressive strength rate causedCaused a significant increase in the value of the lost weight. [9], this feature causes rapid wear of plastic materials during processing and shortens their life of use.

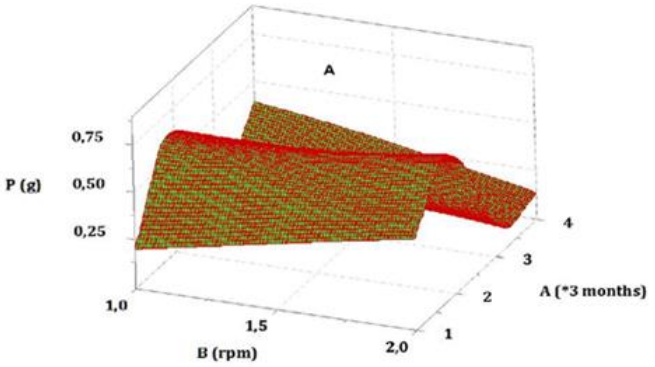

(a)

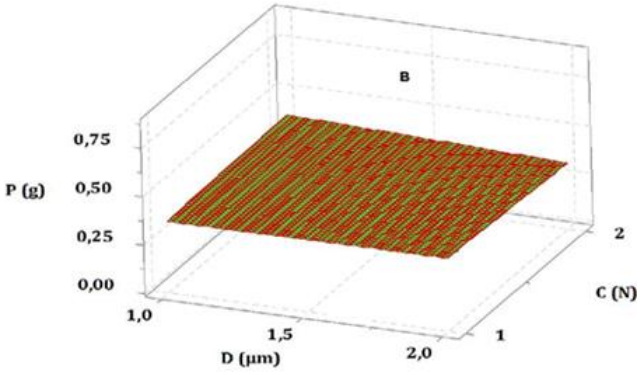

(b)

Fig. 3. Effect of the Weight loss (P) parameters A (B: Spindle speeds,A: Modes of degradation months) and B (D: abrasive paper ,C: Load pressure)

Also, the low rotational speed and the abrasive paper grains with smaller diameters affected the thickness loss value of the tested tubes, as well as the high compressive strength, which directly affected the thickness loss, as shown in (Fig.3) and (Fig.4) that show the effects of the control factors that using The Taguchi method validated the results obtained from experimental studies.Figure 4. Effect of the Weight loss parameters (P) (B: Spindle speeds,A: Modes of degradation months) and (D: abrasive paper ,C: Load pressure).

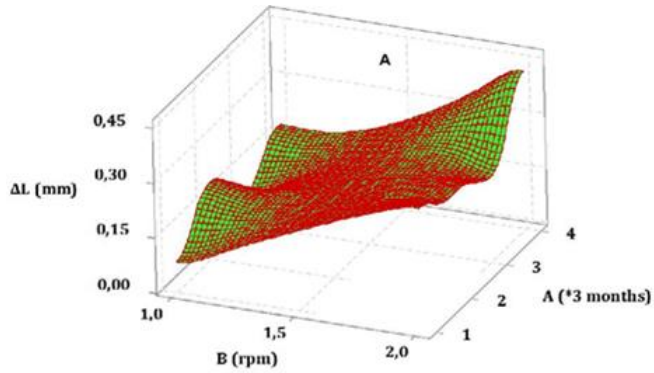

(a)

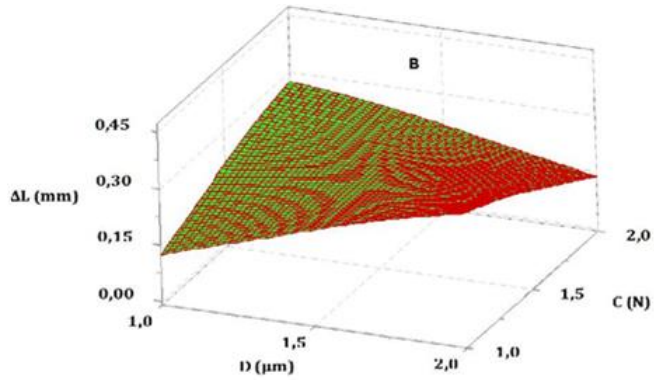

(b)

Fig. 4. Effect of the thickness loss (ΔL) parameters A (B: Spindle speeds,A: Modes of degradation months) and B (D: abrasive paper ,C: Load pressure)

6.2. Method Anova and Taguchi Analysis

ANOVA is a statistical method used to determine the individual interactions of all the control factors in a test design. In this study, ANOVA was used to analyze the effect of the degradation of HDPE80 pipes during the process, 6 months and 60 hours of exposure to ultraviolet radiation, rotational speeds, pressure forces, and an abrasive medium with grains of different diameters (10.3 and 18.3 µm).

The ANOVA results for weight loss and thickness loss are presented in Table7. This analysis was performed with a significance level of 5% and a confidence level of 95%. The significance of the control factors is determined in an ANOVA by comparing the control factors. The fourth column of the table shows the percentage of the contribution value of

each factor, which indicates the degree of impact on process performance. According to Table 6, the percentage contributions of factors A, B, C, and D to mass loss were found to be 63,86%, 0,10%, 0,74%, and 0,16%, respectively. Thus, the most important factor affecting mass loss was rotational speed (factor, 63,86%). According to the ANOVA results, the percentage contributions of factors A, B, C, and D on thickness loss were found to be 16.99%, 47.70%, 0.95%, and 1.89%, respectively. This showed that the most effective factor in corrosion was load pressure (B-factor, 47.70%). The error percentage was considerably low at 35,13% and 32,47% for P and ΔL respectively.

Table 7. Taguchi Analysis for Weight Loss (P) and thickness loss (ΔL) versus A; B; C; D

Source	DF	Weigh Loss (P)			Thickness Loss (ΔL)		
		Contribution	Seq MS	F-Value	Contribution	Seq MS	F-Value
A	3	**63,86%**	**0,136028**	**5,45**	16,99%	0,019838	1,57
B	1	0,10%	0,000652	0,03	**47,70%**	**0,167139**	**13,22**
C	1	0,74%	0,004747	0,19	0,95%	0,003314	0,26
D	1	0,16%	0,001034	0,04	1,89%	0,006631	0,52
Error	9	35,13%	0,024944	-	32,47%	0,012642	-
Total	15	100,00%	-	-	100,00%	-	-

7. Regression Analysis of Weight Loss and Thickness Loss

Regression analyses are employed for modeling and analysis of multiple variables when there is a link between a dependent variable and one or more independent variables [30].

In this study, the dependent variables are the weight lost (P) and the thickness lost due to wear of the material by friction (ΔL). In contrast, the independent variables are the deterioration mode (M) during four equal periods of one full year (3, 6, 9, and 12 months), two rotational speeds (V), two pressing forces (F), as well as the use of two types of abrasive paper as a coarse medium (A). The equations of weight loss, thickness of the material, corrosion of the studied surfaces, and regression analysis were used to obtain a prediction. These predictive equations were made for both linear and quadratic regression models. Predictive equations for handlebar weight and loss thickness wear obtained by the linear regression model are shown below Eqns (4; 4a) and Eqns (5; 5a).

$$P_L = 0{,}111 + 0{,}335\ M - 0{,}122\ V - 0{,}083\ F - 0{,}013\ A \tag{4}$$

$$\text{Model Summary} : (S = 0{,}165193\ ;\ R\text{-sq (adj)} = 81{,}48\% \ \text{ and } R\text{-sq (pred)} = 53{,}70\%\ ) \tag{4a}$$

$$\Delta L_L = 1{,}1412 + 0{,}0468\ M + 0{,}0201\ V + 0{,}0295\ F + 0{,}0432\ A \tag{5}$$

$$\text{Model Summary}: (S = 0{,}0144940\ ;\ R\text{-sq(adj)} = 98{,}80\% \text{ and } R\text{-sq(pred)} = 91{,}02\%) \tag{5a}$$

Here, the lost weight (P) and the lost thickness resulting from wing wear by friction (ΔL) are shown, respectively. In (Fig.5), The comparison of actual test results and predicted values, which the linear regression model obtained, are given, R^2 values of the equations which were obtained by the linear regression model for (P and ΔL) were found to be 81,48% 98,80% respectively.

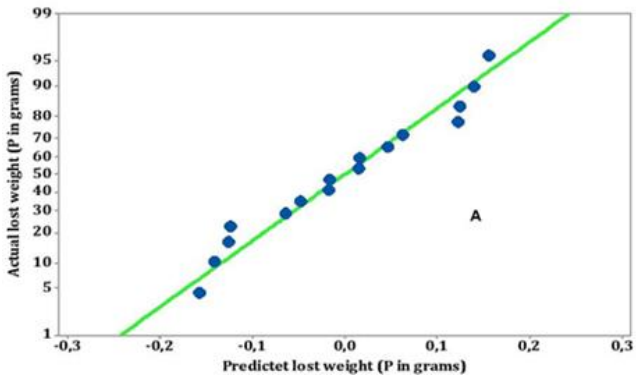

(a)

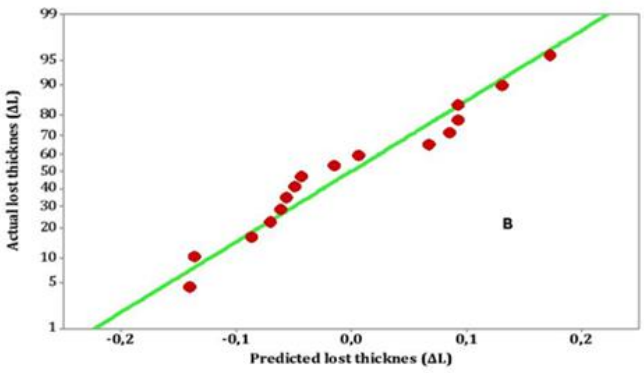

(b)

Fig.5. Comparison of the linear regression model with experimental results for the lost weight (PL) (a) and (b) the lost thickness resulting from wing wear by friction (ΔL)

The predictive equations for the quadratic regression of the lost weight (P) and the lost thickness resulting from wing wear by friction (ΔL) are given below: Eqns (6; 6a) and Eqs (7;7a).

$$P_q = 0{,}41 + 0{,}520\ M + 0{,}696\ V - 0{,}789F + 0{,}308\ A - 0{,}234\ M*V + 0{,}202\ M*F - 0{,}092M*P \quad (6)$$

$$(\text{Model Summary}: S = 0{,}141413;\ R\text{-sq(adj)} = 93{,}21\%\ \text{and}\ R\text{-sq(pred)} = 66{,}07\%) \quad (6a)$$

$$\Delta L_q = 1{,}3429 - 0{,}0153M + 0{,}0212V - 0{,}0290F - 0{,}02739A - 0{,}00643M*M + 0{,}02768M*F \quad (7)$$

$$(\text{Model Summary}: S = 0{,}0063214;\ R\text{-sq (adj)} = 99{,}89\%\ \text{and}\ R\text{-sq (pred)} = 98{,}29\%) \quad (7a)$$

Here Pq and ΔLq show the predictive equations for weight loss and thickness loss due to frictional wear of the material. In (Fig.6), The test results and comparison of the expected values obtained by the quadratic regression model are shown. It turns out that there is a perfect relationship between the predicted values and the test results. Were found to be 93,21% and 99,89%, respectively. Therefore, very expected values were obtained through the quadratic regression model compared to the linear regression model, which proved the success of the quadratic regression model in losing weight and thickness resulting from corrosion of the studied material.

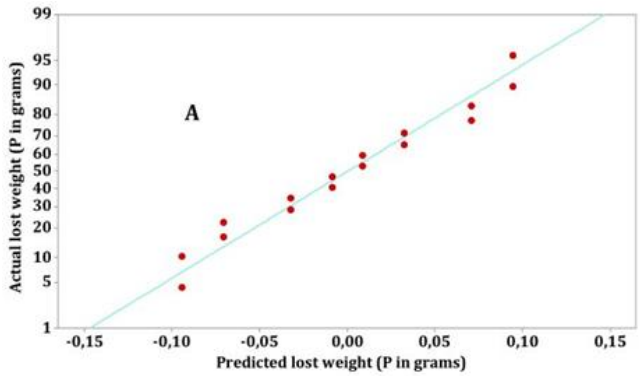

(a)

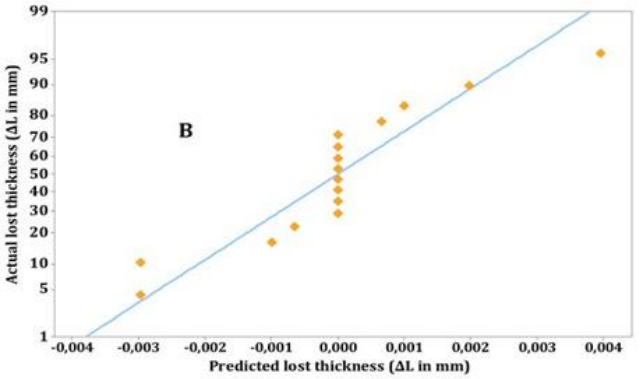

(b)

Fig. 6.Comparison of the quadratic regression model with experimental results for the lost weight (Pq) and the lost thickness resulting from wing wear by friction (ΔLq)

8. Confirmation of Experiments

Here is the overall rate for WLTMV and TLTMV for the total mean value of weight loss (P) in grams (g) and the total value of thickness loss (ΔL) in millimeters, respectively, during the experiment optimally Eqn.(8), and n is the number of control factors for the expected missing value. The results are clearly shown in Tabs. (8) show that the expected value agrees well with the experimental value.

Table 8. Weight loss total mean value (P), and Thickness loss total mean value (ΔL)

		Predicted A3, B2,C2 and D2	Experimental A3, B2,C2 and D2
WLTMV (g)	Mean value (P)	0.408	0.353
TLTMV (mm)	Mean value (ΔL)	0.167	0.22

$$\gamma = \gamma_m + \sum_{i=1}^{\eta} (\gamma_I - \gamma_m) \quad (8)$$

Where:

γ_m : The total mean value of weight loss and the total value of thickness loss (ΔL);

γ_I : The mean of WLTMV and TLTMV at an optimal level;

η : The number of control factors.

9. Conclusions

This work used the Taguchi method to determine optimal machining parameters. This is done by using friction and corrosion experiments, which contribute to the destruction of the polymer (HDPE 80) material by weight loss. After evaluating the experimental results using ANOVA, we found the following:

- The optimum levels of the control factors for minimizing the lost weight (P) and the lost thickness resulting from wing wear by friction (ΔL) using S/N rates were determined. The optimal conditions for lost weight and thickness were observed at A3, B2, C2, and D2 (i.e., Degradation mode = UV, Rotation speed = 355 rpm, Load = 9.3N, and Abrasive paper = 10.3 Grade) and A3, B1, C2, and D1(Degradation mode = UV, Rotation speed = 180 rpm, Load = 4.65 N and Abrasive paper = 18.3 Grade), respectively.

- A vertical milling machine was used, with several experiments conducted using a Taguchi L16 (4^1*2^3) multifactor design with a mixed orthogonal array. Analysis of variance (ANOVA) to determine corrosion due to weight loss and thickness loss for natural gas transportation pipe made of polyethylene (HDPE 80) under the influence of the parameters of abrasive paper grain diameter, cutting speed, and continuity of pressure force over two hours, with each experiment lasting 15 minutes before inspection.

- The results clearly showed that the exposure of the HDPE 80 material to ultraviolet radiation directly contributes to the deterioration of the material by losing its thickness and weight through friction and corrosion.

- According to the results of the statistical analysis, it was found that the medium of use is the most significant factor for Weight loss with a percentage contribution of 63,86% and that the cutting speed was the most critical parameter for thickness loss by wear with a percentage contribution of 47,70%.

- Developed quadratic regression models demonstrated a perfect relationship with high correlation coefficients (P = 0,661 and ΔL = 0.983) between the measured and predicted values for lost weight and thickness.

- After conducting experiments and analyzing their results, it was shown that the effect of aging under the deterioration factor of ultraviolet rays and sunlight on the surface weakens the corrosion resistance of the studied polyethylene. Suppose that aging under normal and accelerated conditions leads to the deterioration of the properties of polyethylene. Therefore, a potential model has been found that contributes to significant improvement in mechanical and terbological degradation. In future studies, the effect of different transported fluids on the deterioration of plastic materials will be studied by simulation under real-world conditions.

References

[1] Abbès F, Tran NG, Abbès B, Guo YQ. Modelling of the degradation of mechanical properties of high-density polyethylene-based packaging exposed to amyl acetate solution. Polymer Testing. 2017;59:449-461. https://doi.org/10.1016/j.polymertesting.2017.03.005

[2] La Mantia FP, Morreale M, Botta L, Mistretta MC, Ceraulo M, Scaffaro R. Degradation of polymer blends: A brief review. Polymer Degradation and Stability. 2017;145:79-92. https://doi.org/10.1016/j.polymdegradstab.2017.07.011

[3] Wong SL, Ngadi N, Abdullah TAT, Inuwa IM. Current state and future prospects of plastic waste as source of fuel: A review. Renewable and Sustainable Energy Reviews. 2015;50:1167-1180. https://doi.org/10.1016/j.rser.2015.04.063
[4] AnuarSharuddin SD, Abnisa F, Wan Daud WMA, Aroua MK. A review on pyrolysis of plastic wastes. Energy Conversion and Management. 2016;115:308-326. https://doi.org/10.1016/j.enconman.2016.02.037
[5] Lu Z, Feng B, Loh C. Fatigue behaviour and mean stress effect of thermoplastic polymers and composites. Frattura Ed IntegritaStrutturale. 2018;12(46):150-157. https://doi.org/10.3221/IGF-ESIS.46.15
[6] Dangnan F, Espejo C, Liskiewicz T, Gester M, Neville A. Friction and wear of additive manufactured polymers in dry contact. Journal of Manufacturing Processes. 2020;59:238-247. https://doi.org/10.1016/j.jmapro.2020.09.051
[7] Kivak T. Optimization of surface roughness and flank wear using the Taguchi method in milling of Hadfield steel with PVD and CVD coated inserts. Measurement: Journal of the International Measurement Confederation. 2014;50(1):19-28. https://doi.org/10.1016/j.measurement.2013.12.017
[8] Madqour M, Hassan H, Fawzy K. Finite element modeling of flexural behavior of reinforced concrete beams externally strengthened with CFRP sheets. Frattura Ed IntegritaStrutturale. 2021;15(59):62-77. https://doi.org/10.3221/IGF-ESIS.59.05
[9] Khan AA, Kaiser MS. Wear studies on Al-Si automotive alloy under dry, fresh and used engine oil sliding environments. Research on Engineering Structures and Materials. 2023;9(1):0-18. https://doi.org/10.17515/resm2022.505ma0816
[10] Sahu AK, Sudhakar K. Effect of UV exposure on bimodal HDPE floats for floating solar application. Journal of Materials Research and Technology. 2019;8(1):147-156. https://doi.org/10.1016/j.jmrt.2017.10.002
[11] Davim JP. Design of Experiments in Production Engineering. Springer, Portugal. 2016. ISBN 978-3-319-23837-1.
[12] Davim JP (Ed.). Statistical and Computational Techniques in Manufacturing. Springer, University of Aveiro Campus Santiago, Portugal. 2012. ISBN 978-3-642-25858-9.
[13] Amjadi M, Fatemi A. Creep and fatigue behaviors of High-Density Polyethylene (HDPE): Effects of temperature, mean stress, frequency, and processing technique. International Journal of Fatigue. 2020;141(May):105871. https://doi.org/10.1016/j.ijfatigue.2020.105871
[14] Bekhedda A, Merbouh M. Recycling of plastic waste polyethylene terephthalate (PET) as a modifier in asphalt mixture: study of Creep-Recovery at Low, Medium, and Hot Temperatures. Frattura Ed IntegritaStrutturale. 2022;16(60):438-450. https://doi.org/10.3221/IGF-ESIS.60.30
[15] Kunishima T, Nagai Y, Nagai S, Kurokawa T, Abry J, Fridrici V, Kapsa P. Effects of glass fiber properties and polymer molecular mass on the mechanical and tribological properties of a polyamide-66-based composite in contact with carbon steel under grease lubrication Ga. Wear. 2020;463(October). https://doi.org/10.1016/j.wear.2020.203500
[16] Dabees S, Tirth V, Mohamed A, Kamel BM. Wear performance and mechanical properties of MWCNT/HDPE nanocomposites for gearing. Integrative Medicine Research. 2020. https://doi.org/10.1016/j.jmrt.2020.09.129
[17] Khaisem M, Budhe S, de Barros S, Banea MD, Rohem NRF. Numerical analysis of repaired wall loss defect pipelines for optimum composite wrap thickness. Frattura Ed IntegritaStrutturale. 2023;17(63):153-168. https://doi.org/10.3221/IGF-ESIS.63.14
[19] Davim JP. Wear of Advanced Materials. Wiley-ISTE. March 2013. ISBN 978-1-118-56586-5.
[20] Teoh SH, Ong EH. Tensile and pressure rupture behaviour of flow-formed high density polyethylene pipes. 1995;36(1):101-107. https://doi.org/10.1016/0032-3861(95)90681-Q

[21] Chen Y, Awasthi AK, Wei F, Tan Q, Li J. Single-use plastics: Production, usage, disposal, and adverse impacts. Science of the Total Environment. 2021;752:141772. https://doi.org/10.1016/j.scitotenv.2020.141772
[22] Staroverov OA, Mugatarov AI, Yankin AS, Wildemann VE. Description of fatigue sensitivity curves and transition to critical states of polymer composites by cumulative distribution functions. Frattura Ed IntegritaStrutturale. 2023;17(63):91-99. https://doi.org/10.3221/IGF-ESIS.63.09
[23] Ramesh BN, Suresha B. Optimization of tribological parameters in abrasive wear mode of carbon-epoxy hybrid composites. Materials and Design. 2014;59:38-49. https://doi.org/10.1016/j.matdes.2014.02.023
[24] Liujie X, Davim JP. Prediction on tribological behaviour of composite PEEK-CF30 using artificial neural networks. 2007;189:374-378. https://doi.org/10.1016/j.jmatprotec.2007.02.019
[25] Gandhi RA, Palanikumar K, Ragunath BK, Davim JP. Role of carbon nanotubes (CNTs) in improving wear properties of polypropylene (PP) in dry sliding condition. Materials and Design. 2013;48:52-57. https://doi.org/10.1016/j.matdes.2012.08.081
[26] Davim JP, Marques N. Evaluation of tribological behaviour of polymeric materials for hip prostheses application. 2001;11(2):91-94. https://doi.org/10.1023/A:1016607400392
[27] Yabuki A, Sugita K, Matsumura M, Hirashima M. The anti-slurry erosion properties of polyethylene for sewerage pipe use. 2000:52-58. https://doi.org/10.1016/S0043-1648(00)00343-4
[28] Guermazi N, Elleuch K, Ayedi HF, Kapsa P. Aging effect on thermal, mechanical and tribological behaviour of polymeric coatings used for pipeline application. Journal of Materials Processing Technology. 2008;203(1-3):404-4. https://doi.org/10.1016/j.jmatprotec.2007.10.062
[29] Liu CZ, Wu JQ, Li JQ, Ren LQ, Tong J, Arnell AD. Tribological behaviours of PA/UHMWPE blend under dry and lubricating condition. Wear. 2006;260(1-2):109-115. https://doi.org/10.1016/j.wear.2004.12.044
[30] Cetin MH, Ozcelik B, Kuram E, Demirbas E. Evaluation of vegetable based cutting fluids with extreme pressure and cutting parameters in turning of AISI 304L by Taguchi method. Journal of Cleaner Production. 2011;19(17-18):2049-205. https://doi.org/10.1016/j.jclepro.2011.07.013

Research on Engineering Structures & Materials
www.jresm.org
Research Group

Research Article

Seismic response prediction using a hybrid unsupervised and supervised machine learning in case of 3D RC frame buildings

Benbokhari Abdellatif[1,a*], Benazouz Chikh[1,b] , Mébarki Ahmed[2,3,c]

[1]*Laboratoire des Travaux publics, ingénierie de Transport, environnement, Ecole Nationale Supérieure des Travaux Publics, Algeria*
[2]*UPEC, CNRS, Laboratory Modélisation et Simulation Multi Echelle, University Gustave Eiffel, France*
[3]*Nanjing Tech University, China*

Article Info

Article history:

Received 29 Dec 2023
Accepted 20 Mar 2024

Keywords:

Nonlinear dynamic analysis;
Machine learning;
Seismic response prediction;
Unsupervised algorithms;
Artificial neural networks

Abstract

The seismic vulnerability assessment represents an important step in monitoring the buildings' capacity and checking their performance during and after earthquake events. The Nonlinear Time History Analysis (NL-THA) is considered the most reliable method that is used to calculate the exact structural behavior of any building. However, this sophisticated method is known for its complexity, the use of Finite Element (FE) software, and computational time consuming, especially in the case of tall buildings. For that reason, An Artificial Neural network (ANN) is used to develop a new model able to predict the essential Engineering Demand Parameters (EDPs), i.e., the Maximum Base Shear (MBS), the Maximum Inter-story Drift (MIDR) and the Maximum Roof Drift Ratio (RDR). Unsupervised algorithms such as the Principal Component Analysis PCA and the Autoencoder are coupled with the ANN to reduce the dimensionality, improve the dataset quality, and reduce the irrelevant features. More than 192,000 buildings are analyzed using the NL-THA and eighty artificial ground motions (GMs) to generate the dataset. The buildings' characteristics are generated randomly from the selection range. The results showed that the Autoencoder-ANN model represents the highest performance compared to the PCA-ANN and ANN models. The Autoencoder-ANN model could quickly and accurately predict the seismic responses of unseen ground motions using only the building's characteristics and the GM parameters without using any FE software.

1. Introduction

Earthquakes are unpredictable phenomena that may occur anywhere and anytime. Their energy is released as seismic vibrations affecting the buildings and infrastructure, which can be devastating [1]. Several earthquakes have been recorded in the last decade, resulting in enormous human losses and severe damage to infrastructure and strategic buildings [2]. Therefore, the preparedness and seismic vulnerability assessment is mandatory to protect lives, reduce economic losses, and maintain the functionality of essential structures like bridges, hospitals, and emergency offices [3-4].

Many researchers developed methodologies and approaches to study and estimate structures' seismic vulnerability and fragility [5-11]. The most reliable and accurate approach is the Nonlinear Time History Analysis (NL-THA) [12]. This approach is based on solving a complicated differential equation of motion. The results of the NL-THA can be used to construct fragility curves by performing Incremental Dynamic Analysis (IDA) and probabilistic calculations. These curves represent the probability of exceeding a specific

*Corresponding author: a.benbokhari@enstp.edu.dz
[a]orcid.org/0000-0002-0819-0641; [b]orcid.org/0000-0002-7228-9224; [c]orcid.org/0000-0002-3361-2594
DOI: http://dx.doi.org/10.17515/resm2024.137me1229rs

Intensity Measure (IM) damage level. This process can be used to estimate the cost needed to rehabilitate buildings in case of an earthquake event. However, the NL-THA and the IDA are considered time-consuming approaches that require suitable hardware and expertise, making the assessment process complex and take a long time [13-14].

Many numerical, mechanical, and empirical approaches are proposed to estimate the seismic response and assess buildings' seismic vulnerability and fragility [15-18]. Nevertheless, these approaches may represent some substantial uncertainties and less accuracy than the NL-THA results. Several new techniques have been proposed, including using artificial intelligence and Machine Learning (ML) in this field. These techniques showed promising results and potential in terms of predictability and high accuracy of the seismic response and damageability assessment of structures [19-21].

Vafaei et al. [22] used the ANN to detect the seismic damage of concrete shear walls, and they found that the ANN model successfully predicted the damages induced by an earthquake. Morfidis et al. [23] proposed a rapid seismic damage prediction of RC buildings methodology using the ANN. They used 30 RC buildings and 65 ground motions to train the ANN model, and it was found that the ANN can predict the damage indices precisely for seen GMs and with acceptable results in the case of unseen buildings and GMs. Oh et al.[24] proposed an ANN-based seismic response prediction using artificial 2700 GMs, where they proposed a new parameter related to the frequency domain and the resonance area. The model was validated using a 2D Multi degrees of freedom structure, and the method showed high accuracy in predicting the MIDR. In addition, Won et al. [25] developed a machine-learning approach for predicting the seismic damage of an equivalent Single degree of freedom considering the soil-structure interaction. The results of their paper were that the ANN model managed to accurately predict the damage level using only the idealized bilinear capacity curve parameters, soil, and earthquake characteristics. Furthermore, Petros and Vitor [26] used the ANN to model the seismic vulnerability of building portfolios, where they found a remarkable prediction of the structural response, economic loss, and damage level. They mentioned in their work that the ANN was an accurate technique to be used as a probabilistic seismic risk assessment method. Seo et al. [27] and Hait et al. [28] use the ML models to assess the seismic vulnerability of irregular structures and derive fragility curves quicker.

Finally, Machine learning use was not only applied to buildings but on some infrastructures such as bridges [29-31].

Based on the literature review, The proposed ML models show a valuable and promising method for seismic response prediction as accurate as the NL-THA results. However, it is essential to note that the studies mentioned in the literature review have some limitations. They are based on a small range of building characteristics and lack generalization. Furthermore, in some of these works, their generalized models could have achieved higher accuracy. Additionally, in some other cases, the prediction process needs software modeling to calculate input characteristics like the center of torsion and the period vibration of the fundamental mode. Furthermore, this paper compared the performance of three ML models to investigate the impact of the use of unsupervised algorithms on the ML performance.

This paper presents a ML model that can predict three Engineering Demand Parameters (EDPs) using only the geometric and loading characteristics of structures with the artificial ground motions (AGMs) parameters, without the need for additional Finite Element (FE) calculations. The EDPs in question are the Maximum Base Shear (MBS), the Maximum Inter-story Drift (MIDR), and the Maximum Roof Drift Ratio (RDR). These parameters are crucial in designing structures, as they help engineers estimate the MBS and control the structure's performance using the MIDR and MRDR.

The proposed method generates a dataset using OpenSees and performs over 192,000 Non-Linear Time-History Analyses (NL-THA). The characteristics of the buildings are selected randomly from a range of options, including the Number of Stories (Ns), Number of Bays in x-x direction (Nbx), Number of Bays in y-y direction (Nby), Story Height (Hs), Bays' Length in x-x direction (Lbx), Bays' Length in y-y direction (Lby), Column Dimensions (b,h), Beam Dimensions (b1,h1), Reinforcement Area of Column (As_col), Reinforcement Area of Beams (As_beam), Compression Strength of Concrete (fc28), Yielding Limit Stress of Rebars (fy), Permanent Surface Load (G), and Live Surface Load (Q). To perform the NL-THA and generate the dataset, the method generates eighty artificial and synthetic GMs and matches them to the target response spectrum (EuroCode-8).

Three ANN models are used to establish the relationship between the inputs and outputs. The first model uses the original dataset as input data. In the second model, a Principal Component Analysis (PCA) is applied to the input data to identify the principal components, which are then used as inputs. The third model utilizes an Autoencoder technique to capture the essential features of the dataset and reduce its dimensionality. To evaluate the models' predictability, 80 AGMs are generated and matched to the same target response spectrum. These AGMs are then used to perform a NL-THA on three case study buildings. Finally, the accuracy of the models in fragility assessment is determined by generating 3D fragility surfaces using the NL-THA and the three ANN models.

2. Methodology

This work aims to develop an ANN model to predict the maximum seismic response of a 3D RC frame building subjected to unseen GMs. In order to reach the objective, the first step is to create the dataset with OpenSees. The 3D model will be subjected to eighty AGMs, and NL-THA will be performed to calculate the MBS, MIDR, and MRDR. Figure 1 shows that the methodology is based on three main steps, which are explained in detail in the following sections.

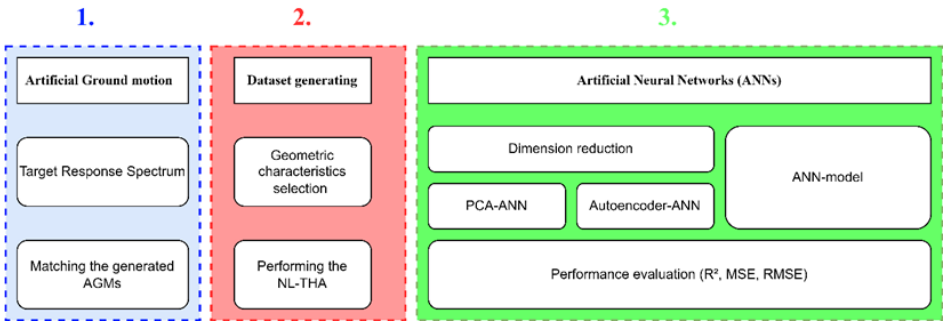

Fig. 1. The flowchart of the used methodology

2.1. Ground Motion Selection

The ground motion selection represents an essential step in performing a fragility assessment, mainly when we aim to construct fragility curves [32] [33]. Choosing the proper seismic record is challenging for analysts, especially when dealing with actual ground motion records [34]. In some cases, the studied area does not have the required ground motion records. In addition, real GMs may have a long duration, and that will affect the NL-THA calculation time. Therefore, using a generated ground motion is the best alternative to solve these problems. Artificial and synthetic ground motions are different algorithms used to generate unreal ground motion that satisfies some conditions. The user

can fix the earthquake parameters for synthetic accelerograms, e.g.: near/ far -field, moment magnitude, and soil parameters [35]. Only the shape envelope and the accelerogram duration are needed for the artificial GMs to generate a GM. For this study, eighty AGMs have been generated and matched to an EC8 target response spectrum. The target spectrum is generated using the EC8, considering the following parameters:

- Ground acceleration (A_g): 0.2 (g)
- Spectrum type: Type I.
- Importance class: II.

Figure 2 illustrates the mean-matched response spectra, the generated GMs, and the target response spectrum. Table A.1 represents the earthquake parameters of the generated GMs. Twenty-one parameters in Table 1 characterize the ground motions used in the ANN.

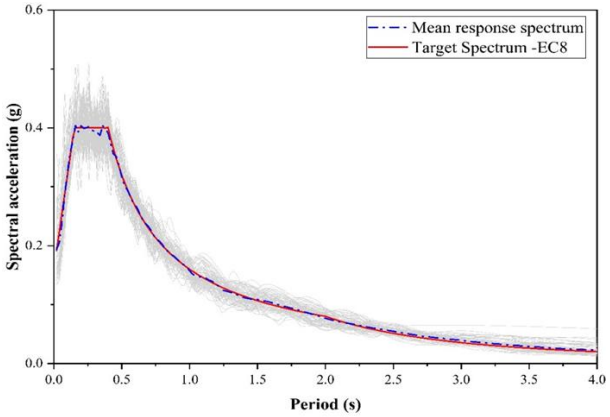

Fig. 2. The generated ground motions and their mean response spectrum and the target spectrum

Table 1. The ground motion characteristics

	Definition	Equation
PGA	Peak ground acceleration	= Max |acceleration(t)|
PGV	Peak ground velocity	= Max |velocity(t)|
PGD	Peak ground displacement	= Max |displacement(t)|
E_{cum}	Cumulative energy	$= \int_0^{t=end} acceleration(t)^2.dt$
I_a	Arias intensity	$= \frac{\pi}{2g}\int_0^{Td} acceleration(t)^2 dt$
CAV	Cumulative Absolute velocity	$= \int_0^{Tmax} \|a(t)\|dt$
Sa	Spectral acceleration (T1)	$= (\frac{2\pi}{T1})^2 \times Sd\ (T1)$
Sv	Spectral velocity (T1)	$= (\frac{2\pi}{T1}) \times Sd\ (T1)$
Sd	Spectral displacement (T1)	$=\frac{1}{m\times\omega}\max\left(\left\|\int_0^t p(\tau)\, e^{-\zeta\omega_n(t-\tau)} \sin[\omega_D\,(t-\tau)]\, d\tau\right|\right)$
U_T	Uniform duration	The cumulative duration of exceeding 5% of PGA

B_T	Bracket duration	The total duration between the first and the last exceedance of a 5% of PGA.
HI	Housner intensity	$= \int_{0.1}^{2.5} PSV\ (\zeta = 5\%, T) dT$
PP	predominant period	The period corresponding to the maximum Sa ($\zeta = 5\%$)
SD	Significant duration	The duration interval between 5% and 95% of the cumulative intensity arias
ASI	Acceleration Spectrum Intensity	$= \int_{0.1}^{0.5} Sa\ (\zeta = 5\%, T)\ dT$
VSI	Velocity Spectrum Intensity	$= \int_{0.1}^{0.5} Sv\ (\zeta = 5\%, T)\ dT$
DSI	Displacement Spectrum Intensity	$= \int_{0.1}^{0.5} Sd\ (\zeta = 5\%, T)\ dT$
SI	Response spectrum intensity	$= \int_{0.1}^{2.5} Sv\ (\zeta = 5\%, T)\ dT$
D_f	Dominant frequency	The frequency that carries out the highest amount of energy
B_w	Bandwidth	The difference between the lower and upper frequencies of a certain thresholds (-3db)
f_c	central frequency	The mean frequency between the upper and the lower frequencies.

2.2. Dataset Generation with The Nonlinear Time-History Analysis

NLTHA is a type of dynamic structural analysis used to simulate complex multiple support excitations at certain points on the structure. It is one of the most reliable methods used to calculate the exact structural behavior of any building during an earthquake event. It is based on solving a complicated differential equation of motion, and its results can be used to construct fragility curves by performing the Incremental Dynamic Analysis (IDA) and probabilistic calculations. However, the NL-THA is known for its complexity, the use of Finite Element (FE) software, and computational time-consuming, especially in the case of tall buildings. The outputs of this analysis can be an engineering demand parameter (EDPs) such as IDR, RDR or story displacement in a form of time series. OpenSees can be used to perform this analysis and to generate the dataset needed for this study.

The followed process of generating the dataset using OpenSees is illustrated in Figure 3 and explained below:

- Start by creating a model in OpenSees. For a time, history analysis, this would include defining nodes and elements, assigning boundary conditions, specifying material properties and assembling the system into a model.
- Create the ground motion records that represent earthquake loading on your structure then format and transform them such that they can be used in OpenSees as prescribed loading. a scale factor should be specified in this step to scale the ground motion, and their characteristics should be calculated and recorded (PGA, PGV, PGD, Ecum, Ia, CAV…etc.)
- Specify the type of analysis, the solution algorithm (e.g.: KrylovNewton, SecantNewton , ModifiedNewton , RaphsonNewton) , the integrator , and the the convergence test (e.g.; NormDispIncr, RelativeEnergyIncr, EnergyIncr, RelativeNormUnbalance.

Run the simulation in OpenSees after specifying the control node, direction, number of degrees of freedom and the needed responses (e.g., acceleration, velocity, displacement, reactions, drift).

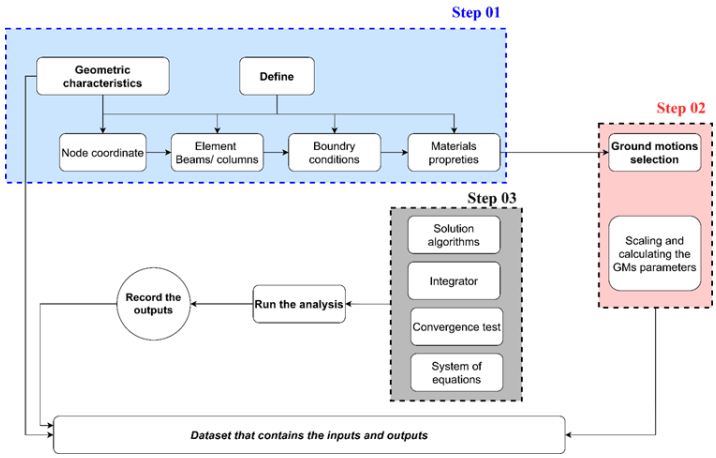

Fig. 3. The followed process on OpenSees to perform the NLTHA

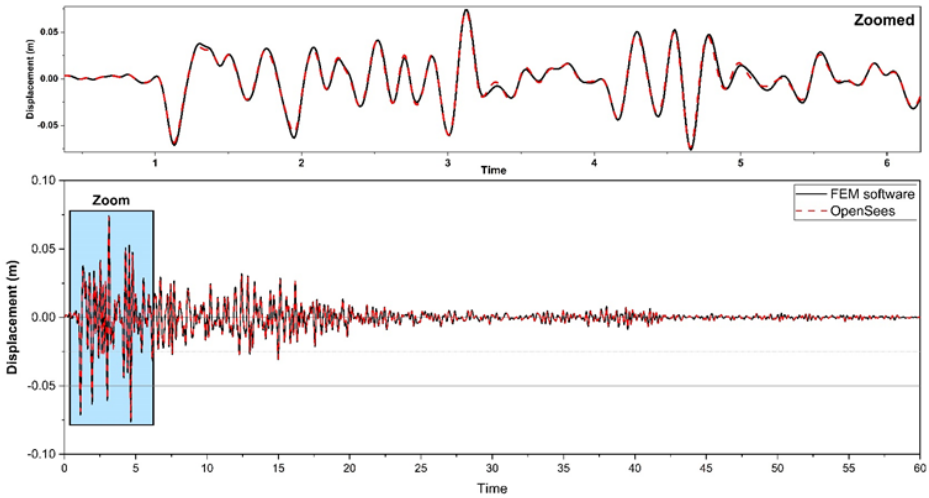

Fig. 4. The displacement history of a 4-story RC frame subjected to El-Centro GM scaled to PGA = 0.4g

Figure 4 illustrates the displacement time history of a 4-story RC frame building subjected to El-Centro ground motion scaled to PGA = 0.4 g using FEM software and OpenSees. It shows that the OpenSees model accurately estimates and find the displacement response of the validation model.

The dataset is generated using OpenSees by performing the NL-THA. The buildings are created by randomly selecting their geometric and material characteristics from the selection range, as shown in Table 2. The geometric and material characteristics are illustrated in Figure 5. In this work, it is considered that we have two types of loads (permanent load (G) and live load (Q)). The yielding and the ultimate strain of the concrete are -0.2% and -0.35%, and "concrete02" is used in OpenSees. A 200 GPa is the young

modulus of the reinforcement steel with a zero-post yielding ratio, and the "Steel02" is used in OpenSees.

Table 2. The structural characteristics and the selection range (min, max and step)

Parameter	Unit	Min	Step	Max
Ns	-	1	1	10
Hs	m	3	0.2	4
Nbx	-	1	1	6
Lbx	m	3.5	0.5	6
Nby	-	1	1	6
Lby	m	3.5	0.5	6
h	cm	25	0.05	100
b	cm	25	0.05	100
h1	cm	25	0.05	50
b1	cm	25	0.05	50
As_col	cm^2	9.0432	0.2512	64.3072
As_beam	cm^2	9.0432	0.2512	64.3072
G	kN/m^2	1	1	6
Q	kN/m^2	1	1	6
fc28	MPa	25	5	45
fy	GPa	350	50	550

After selecting the required geometric and material characteristics and selecting the GM, and scaling it, an NL-THA is performed, and the seismic response is captured, i.e., MBS, MISDR, and MRDR. These characteristics and the seismic response represent the input and the outputs that will be used in the machine-learning algorithms. As a result, a dataset has been generated that contains 192,092 NL-THA using eighty artificial and synthetic GMs, and this dataset should be preprocessed before using it in the ML.

Figure 6 displays a heatmap which shows the correlation between the various features of the dataset, including inputs and outputs. Upon examining the heatmap, it becomes apparent that there is a strong positive correlation between the MIDR and the ground motion parameters such as PGA, PGV, Ecum, Ai, CAV, Sa, Sv, HI, ASI, VSI, DSI, and SI. Conversely, there is a negative correlation between the MIDR and structural geometry parameters such as h, b, N_{bx}, N_{by}, and b_1. The MRDR exhibits the same correlation with the GMs parameters and structural geometry as the MIDR. This correlation helps to identify the most critical features that impact the performance or damage incurred during an earthquake event. For the MBS, It is affected positively with the earthquake parameters (PGA, PGV, Ecum, AI, ASI, VSI, DSI, SI) and negatively with the structural geometry (Nbx, Nby and As_column).

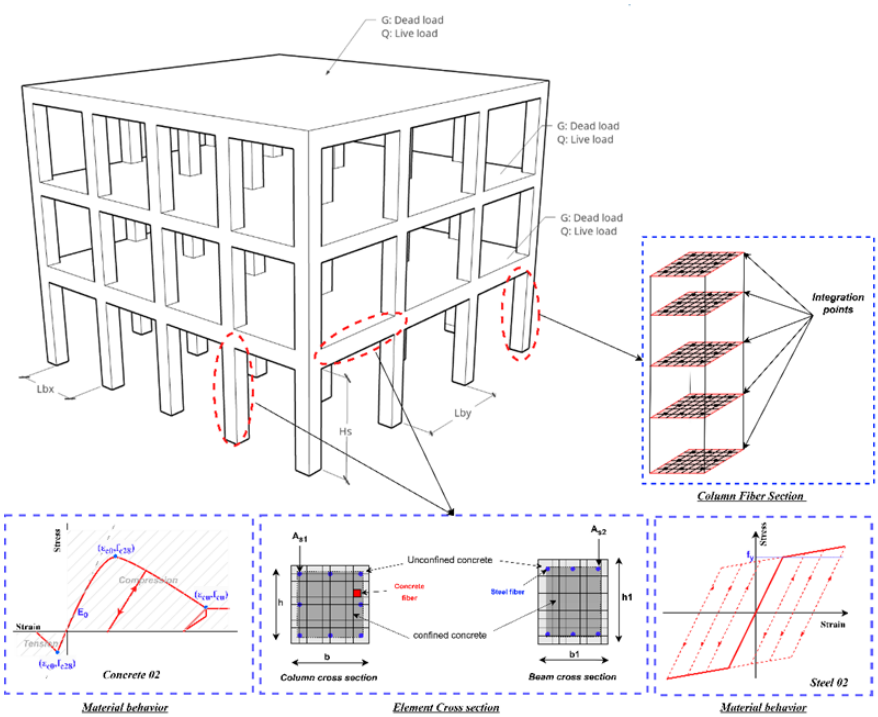

Fig. 5. The geometric characteristics of the 3D RC frame building

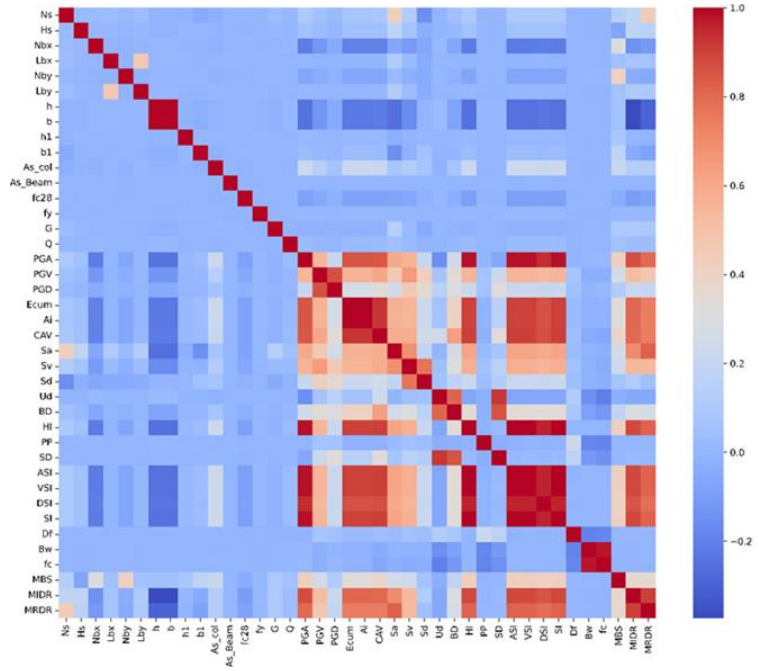

Fig. 6. The degree of correlation between the generated dataset features (inputs and outputs)

2.3. Principal Component Analysis (PCA)

The PCA is one of the most used techniques for dimensionality reduction. It is an unsupervised machine learning algorithm that aims to capture the principal components of the dataset. The data reorientation allows us to use fewer dimensions without losing much information. In addition, this technique may reduce the data noises and the irrelevant features that can affect the training time, the performance, and the hyperparameters optimization of the ANN. The PCA is based on transforming the correlated variables into uncorrelated new variables using a linear combination. The eigenvalues and the cumulative variability of each principal component are illustrated in Figure 7. If 90% of the variability is fixed as a threshold, twenty principal components will be used as inputs of the ANN model.

2.4. Autoencoder Algorithm

The autoencoder is a type of ANN used for unsupervised learning and dimensionality reduction. It is highly used in various domains, including text, voice, and image data analysis. It can capture the essential characteristics of the data and reduce the input features without losing the information. It is based on transforming the input data into a new compressed dataset by the encoder. Then, the decoder reconstructs the original data from the compressed data. By doing so, the noises or any redundant information can be discarded from the dataset. Compared to the PCA, the autoencoder algorithm is used when the correlation between the dataset variables is nonlinear using a nonlinear activation function such as: (Tanh, sigmoid). Figure 8 illustrates the structure of the autoencoder algorithm. The bottleneck or the code layer will have 20 neurons, the same number as the PCA's selected principal components, to compare the performance of the ANN using both methods.

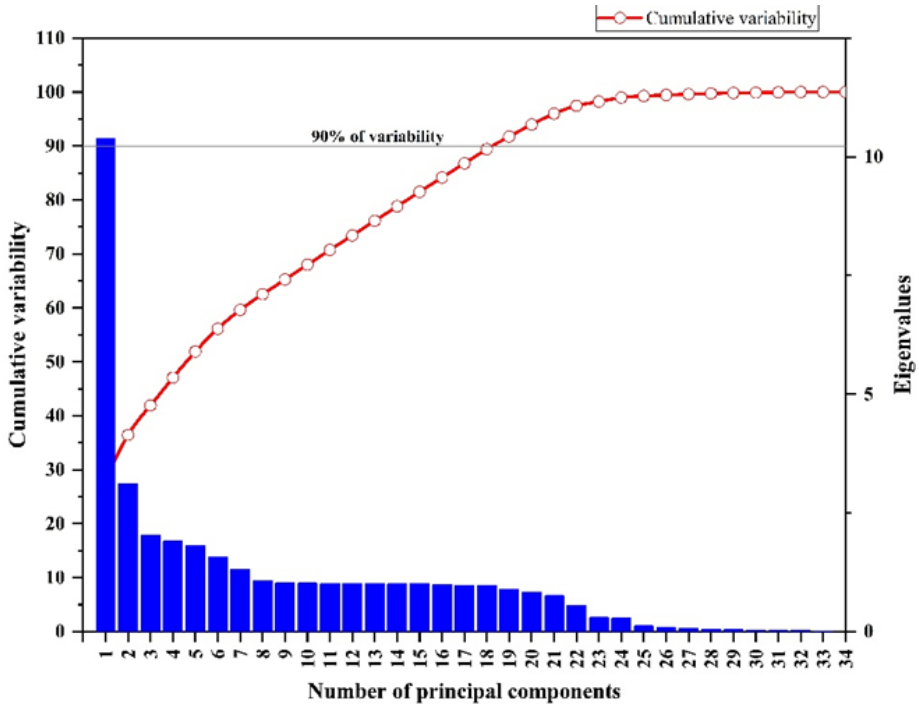

Fig. 7. Eigenvalues and the cumulative variability of the dataset

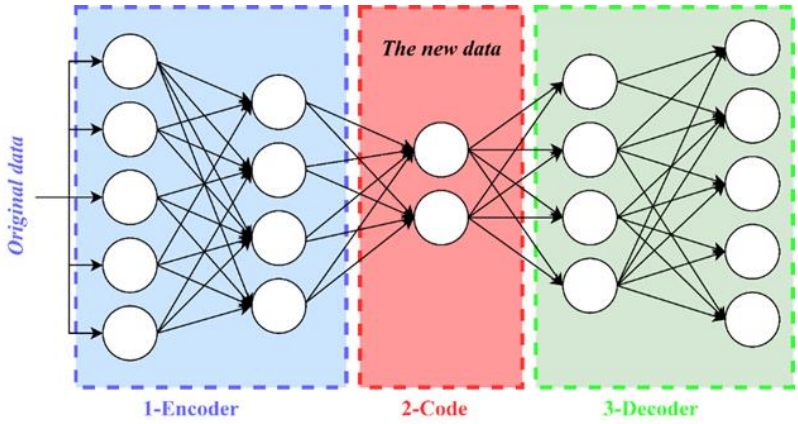

Fig. 8. The autoencoder structure

2.5. Artificial Neural Networks (ANN)

The ANN is supervised machine learning based on training the model on a dataset containing inputs and outputs and testing its performance in predicting unseen cases. It is composed of an input layer, hidden layers, and output layers. The input layer will contain the earthquake and the building characteristics or the transformed input features using the PCA or the autoencoder. A backpropagation (BP) algorithm will train the ANN model. The hidden layers (HL) contain intermediate neurons, and the number of hidden layers and number of neurons (NN) should be optimized to avoid the underfitting or overfitting of the ANN model. The output layer contains three neurons representing the seismic responses (MBS, MIDR, and MRDR). An "Adam" algorithm is used as an optimization algorithm, and "ReLu and Linear" activation functions are used for the hidden and output layers, respectively. The hyperparameters (HL/ NN) are selected by performing the ANN several times, changing them randomly, and selecting the best combination that corresponds to the highest correlation coefficient (R^2) and the lowest mean squared error (MSE). Figure 9 illustrates the ANN structures and the used activation functions.

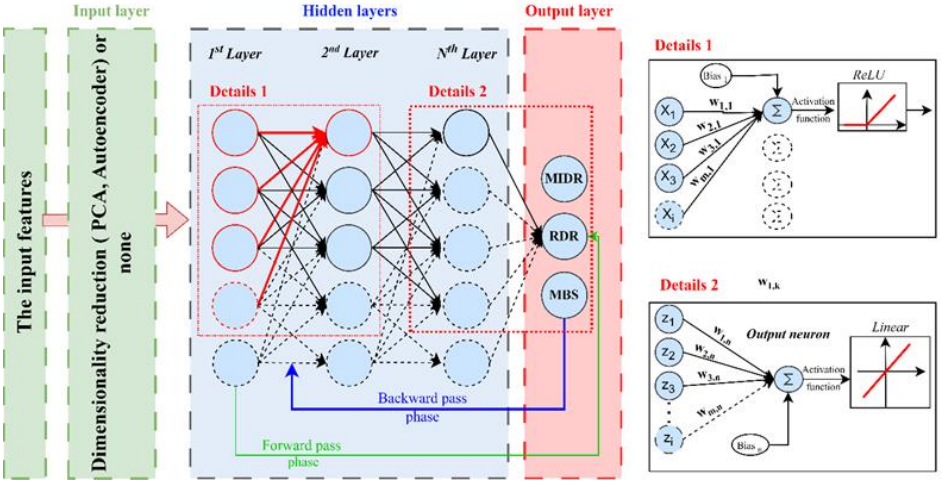

Fig. 9. the structure of the ANN

2.6. Performance of the ANNs

In order to find the best model that can predict the seismic responses accurately, three ANN models have been performed (ANN, PCA-ANN, and Autoencoder-ANN). The dataset is split into training (80%), testing (10%), and validation data (10%). The performance of the ANN will be evaluated using the correlation coefficient (R^2), mean squared error (MSE), and root mean squared error (RMSE), as they are shown in Table 3, where:

$y_{ANN,i}$: is the predicted seismic response.

$y_{NLTHA,i}$: is the calculated seismic response.

$\overline{y_{ANN,i}}$: is the mean value of the predicted seismic response.

$\overline{y_{NLTHA,i}}$: is the mean value of the calculated seismic response.

Table 3. the formulas of the performance coefficients

Performance coefficient	Formula
R^2	$=\frac{\sum(y_{ANN,i}-\overline{y_{ANN,i}})(y_{NLTHA,i}-\overline{y_{NLTHA,i}})}{\sqrt{\sum(y_{ANN,i}-\overline{y_{ANN,i}})^2(y_{NLTHA,i}-\overline{y_{NLTHA,i}})^2}}$
MSE	$=\frac{1}{N}\sum(y_{ANN,i}-y_{NLTHA,i})$
RMSE	$=\sqrt{\frac{1}{N}\sum(y_{ANN,i}-y_{NLTHA,i})}$

Firstly, the ANN model is trained on the generated dataset directly without using any unsupervised techniques (PCA or Autoencoder). It aims to compare the results of using the ANN model with hybrid ANN models regarding predictability. Secondly, a hybrid PCA-ANN model is performed using a dimensionality reduction and twenty principal components (reducing the dimensions from 37 to 20). Finally, another hybrid Autoencoder-ANN model is trained where a coder layer holds 20 neurons (20 dimensions). All the models' hyperparameters have been optimized using random selection and choosing the best combinations. Table 4 summarizes the hyperparameters used in these three models. Table 5 illustrates the performance of the ANN models, where the results represent the mean values of training, testing, and validating.

Table 4. The hyperparameters of the three ANN models

ANN model	Number of neurons	Number hidden layers	Learning rate	Activation function
ANN	60	4	0.01	Relu & linear
PCA-ANN	30	3	0.01	Relu & linear
Autoencoder-ANN	35	2	0.01	Relu & linear

Table 5. The performance of the ANN, PCA-ANN, and Autoencoder-ANN

	MBS			MIDR			MRDR		
	ANN	Auto-ANN	PCA-ANN	ANN	Auto-ANN	PCA-ANN	ANN	Auto-ANN	PCA-ANN
R^2	0.972	0.985	0.986	0.976	0.989	0.9913	0.9745	0.984	0.988
MSE	0.0018	7.6E-05	0.013	0.0017	0.00013	0.0087	0.0051	0.00011	0.0117
RMSE	0.042	0.0086	0.111	0.042	0.0113	0.090	0.071	0.0106	0.1045

Overfitting is a common problem that may occur during the training of ANN model. This can be caused due to the bad selection of hyperparameters such as the number of neurons or number of hidden layers. The overfitting is captured when the performance of the validation data diverges from the training performance as shown in Figure 10. It is represented in a high performance of the training process and low performance of validation data. In Figure 11 depicts the evolution of loss function (MSE) in function of number of epochs for the three ML models.

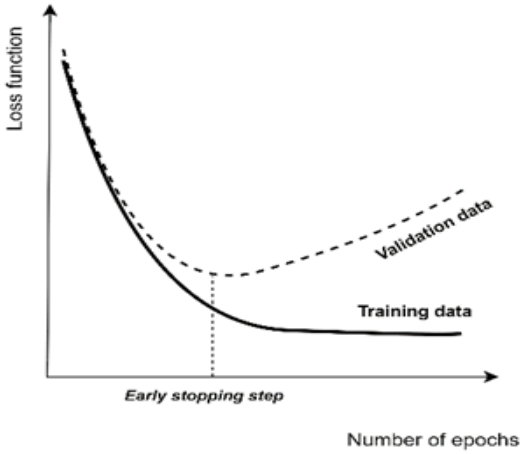

Fig.10 Overfitting in ML models illustration

2.7. Performance of the ANN-Models to Unseen GMs

This section aims to test the performance of the ANNs when the buildings are subjected to 30 unseen GMs. These AGMs matched the identical target response spectra, as shown in Figure 12. Three buildings will be used as a case study (low-, mid-, and high-rise) to check the predictability of the ANN models to unseen cases. IDA curves will be generated and compared to the predicted ones. The 3D fragility surfaces will be constructed using the IDA curves of the MISDR and the MRDR, and then a comparison between these surfaces will be made. The characteristics of the case study buildings are shown in Table 6.

Table 6. The geometric and material characteristics of the case study buildings (low-, mid-, and high-rise)

Parameter	Low-rise	mid-rise	High-rise	Parameter	Low-rise	mid-rise	High-rise
Ns	3	6	9	h1 (m)	0.4	0.45	0.45
Hs (m)	3	3	3	b1 (m)	0.3	0.3	0.35
Nbx	4	4	4	As_col (cm^2)	30.39	30.39	49.23
Lbx (m)	3.2	3.2	3.2	As_beam (cm^2)	25.12	25.12	36.17
Nby	3	3	3	fc28 (MPa)	35	35	35
Lby (m)	3.2	3.2	3.2	fy (GPa)	500	500	500
h (m)	0.4	0.45	0.65	G (kN/m^2)	3	3	3
b (m)	0.4	0.45	0.65	Q (kN/m^2)	1	1	1

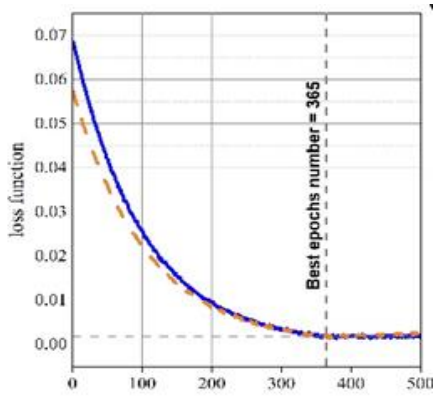
loss function
Best epochs number = 365

(a)

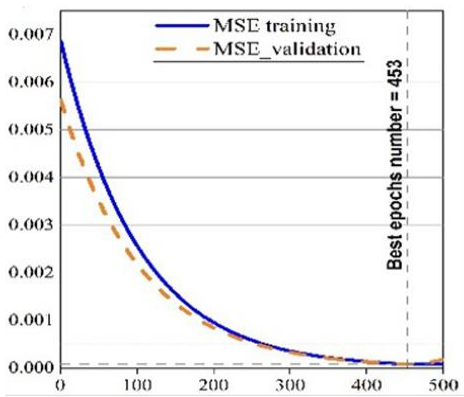
MSE training
MSE_validation
Best epochs number = 453

(b)

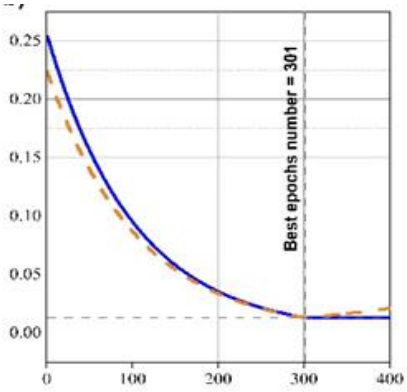
Best epochs number = 301

(c)

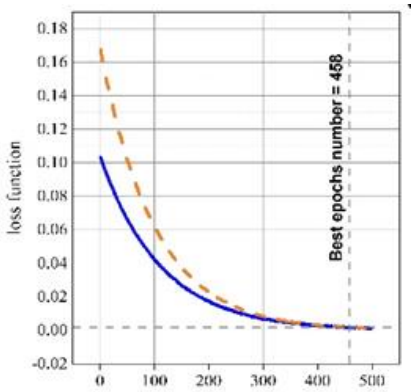
loss function
Best epochs number = 458

(d)

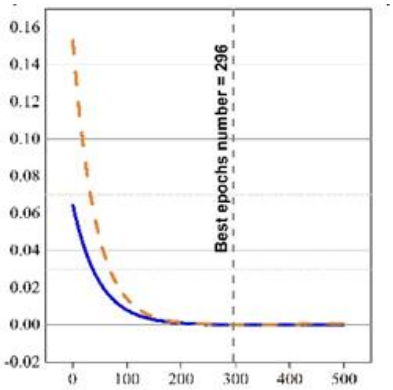
Best epochs number = 296

(e)

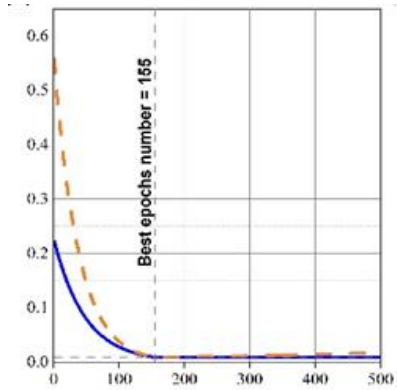
Best epochs number = 155

(f)

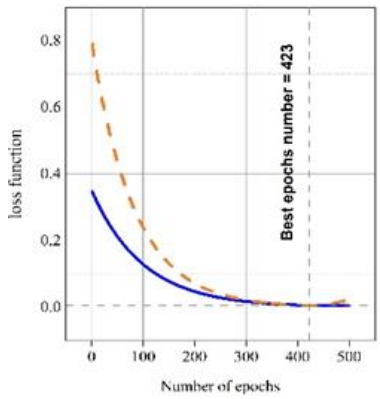

(g)

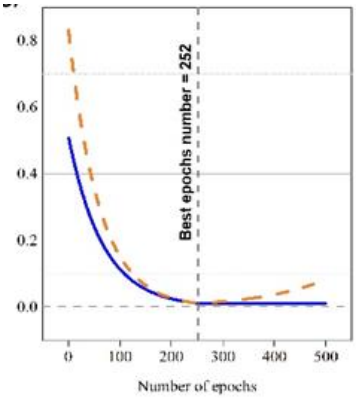

(h)

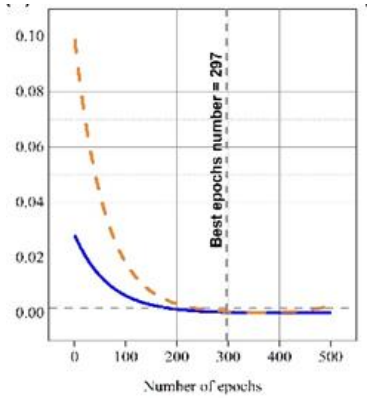

(i)

Fig. 11. Loss function in terms of number of epochs and the best performance position: a) ANN model for predicting the MBS, b) Auto-ANN model for predicting the MBS, c) PCA-ANN model for predicting the MBS, d) ANN model for predicting the MRDR, e) Auto-ANN model for predicting the MRDR, f) PCA-ANN model for predicting the MRDR, g) ANN model for predicting the MIDR, h) Auto-ANN model for predicting the MIDR, i) PCA-ANN model for predicting the MIDR

3. Results

The goal of this paper is not only to predict the seismic response but to generalize the prediction of the outputs based on the training dataset only. In the case study, three buildings were selected to perform the IDA, construct the fragility surfaces, and test the ANN models to predict seismic responses under unseen GMs. Figure 13, Figure 14, and Figure 15 illustrate the IDA points of the three buildings using the NL-THA and the ANN models. The performance criteria of the prediction of the MBS, MIDR and MRDR of the ANN model, PCA-ANN model and Autoencoder-ANN model is summarized in Table 7-8-9.

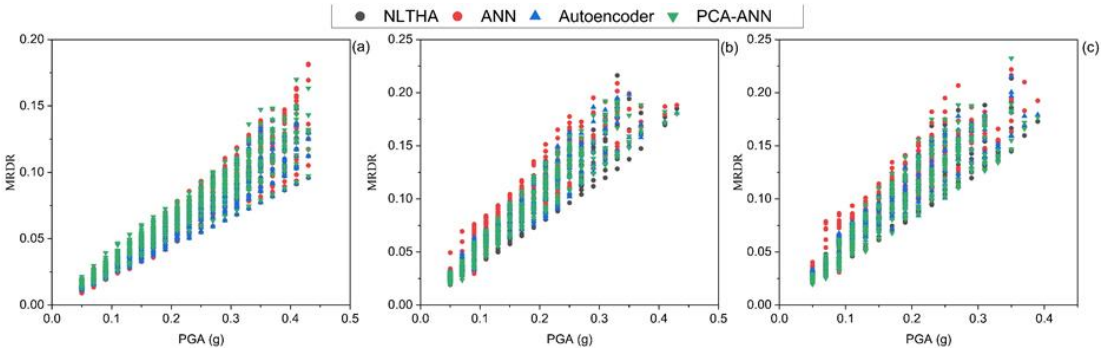

Fig. 13 the MRDR for the three models: a) low-rise, b) mid-rise and c) high-rise

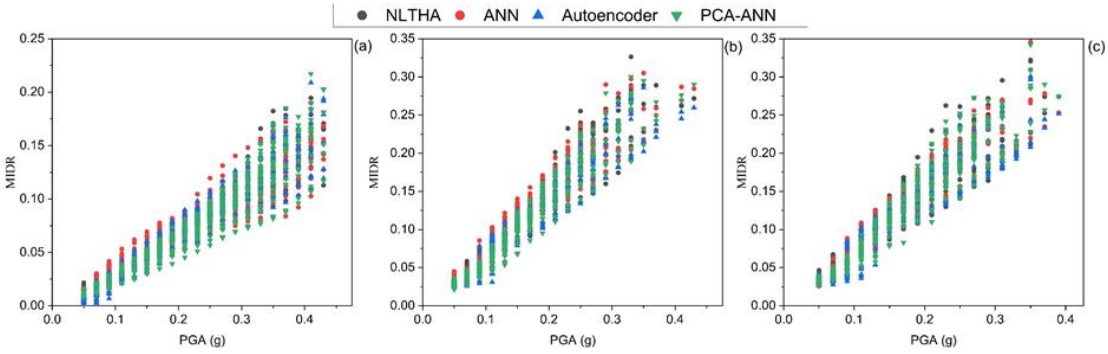

Fig. 14.The MIDR prediction for the three models: a) low-rise, b) mid-rise and c) high-rise

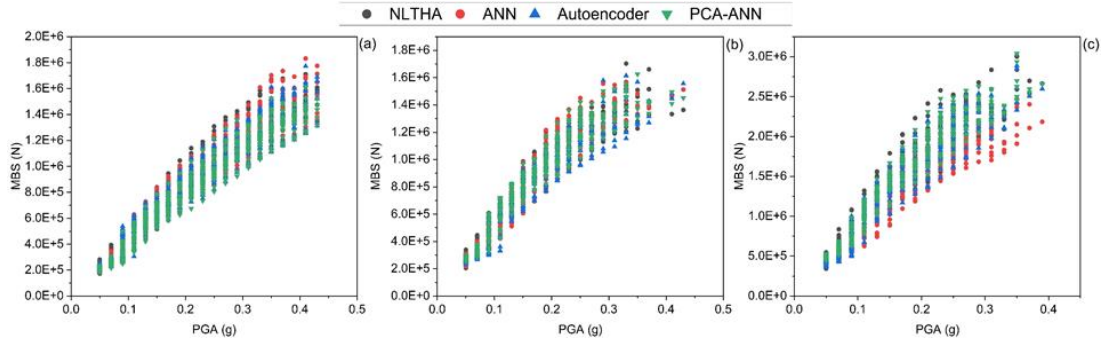

Fig. 15. The MBS prediction for the three models: a) low-rise, b) mid-rise and c) high-rise

Figure 16, Figure 17, Figure 18, Figure 19, Figure 20 and Figure 21 represent the 3D fragility surfaces constructed using the NL-THA and the ANN models for low-, mid-, and high-rise buildings. The accuracy of the prediction of these 3D fragility surfaces is calculated using the same performance criteria (R^2, MSE, and RMSE), and they are summarized in Table 10 and Table 11 for MIDR and MRDR.

Table 7. The performance of the ANN to predict the MBS to unseen GMs.

	MBS								
	Low-rise			Mid-rise			High-rise		
	ANN	Auto-ANN	PCA-ANN	ANN	Auto-ANN	PCA-ANN	ANN	Auto-ANN	PCA-ANN
R^2	0.850	0.964	0.964	0.931	0.965	0.931	0.822	0.964	0.954
MSE	0.025	0.002	0.017	0.016	0.005	0.009	0.084	0.017	0.034
RMSE	0.158	0.051	0.133	0.127	0.072	0.097	0.291	0.133	0.185

Table 8. The performance of the ANN to predict the MIDR to unseen GMs.

	MIDR								
	Low-rise			Mid-rise			High-rise		
	ANN	Auto-ANN	PCA-ANN	ANN	Auto-ANN	PCA-ANN	ANN	Auto-ANN	PCA-ANN
R^2	0.91	0.94	0.93	0.93	0.959	0.958	0.938	0.9550	0.94
MSE	0.0006	9.6E-05	1.0E-04	3.0E-04	8.7E-04	1.90E-04	1.22E-03	1.89E-04	2.48E-04
RMSE	0.025	0.0098	0.0103	0.0174	0.0296	0.0137	0.0348	0.0137	0.0157

Table 9. The performance of the ANN to predict the MRDR to unseen GMs.

	MRDR								
	Low-rise			Mid-rise			High-rise		
	ANN	Auto-ANN	PCA-ANN	ANN	Auto-ANN	PCA-ANN	ANN	Auto-ANN	PCA-ANN
R^2	0.708	0.90	0.909	0.861	0.961	0.962	0.878	0.968	0.9549
MSE	0.0003	0.0001	0.00096	0.0002	7.18E-05	7.07E-04	2.20E-04	5.84E-04	8.16E-05
RMSE	0.0174	0.0101	0.0311	0.0160	0.0084	0.0265	0.0148	0.0241	0.0090

Table 10. The accuracy of the 3D fragility surfaces prediction (MIDR).

	MIDR								
	Low-rise			Mid-rise			High-rise		
	ANN	Auto-ANN	PCA-ANN	ANN	Auto-ANN	PCA-ANN	ANN	Auto-ANN	PCA-ANN
R^2	0.6014	0.9512	0.9139	0.833	0.9917	0.9830	0.971	0.9719	0.9716
MSE	0.0808	0.0007	0.0098	0.059	0.0018	0.0035	0.006	0.0061	0.0062
RMSE	0.2842	0.0258	0.0989	0.244	0.0425	0.0595	0.078	0.0778	0.0784

Table 11. The accuracy of the 3D fragility surfaces prediction (MRDR).

	MRDR								
	Low-rise			Mid-rise			High-rise		
	ANN	Auto-ANN	PCA-ANN	ANN	Auto-ANN	PCA-ANN	ANN	Auto-ANN	PCA-ANN
R^2	0.8361	0.9713	0.9422	0.8993	0.9908	0.9414	0.9052	0.9937	0.9316
MSE	0.0583	0.0062	0.0126	0.0216	0.0020	0.0127	0.0202	0.0013	0.0149
RMSE	0.2416	0.0785	0.1122	0.1471	0.0449	0.1127	0.1420	0.0367	0.1222

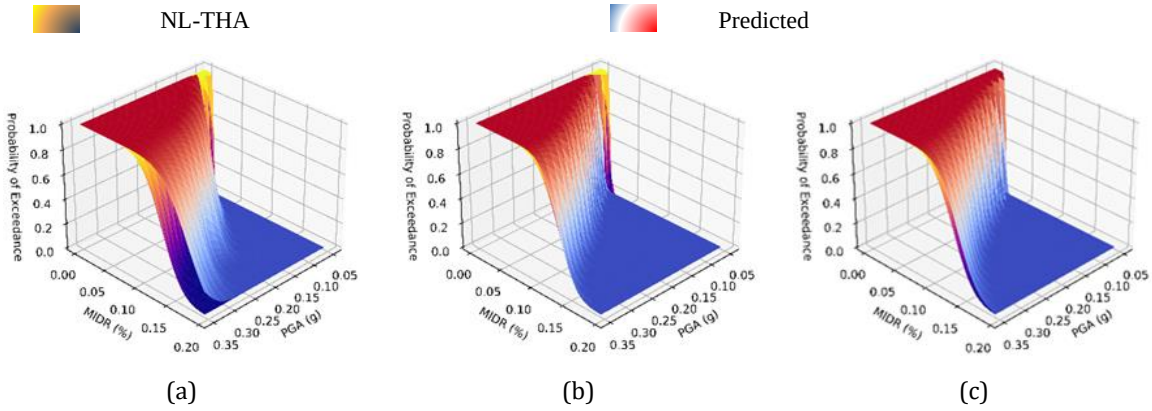

(a) (b) (c)

Fig. 16. 3D Fragility surfaces (NL-THA and ANNs) of the MIDR for low-rise building: a) ANN, b) Autoencoder-ANN and c) PCA-ANN

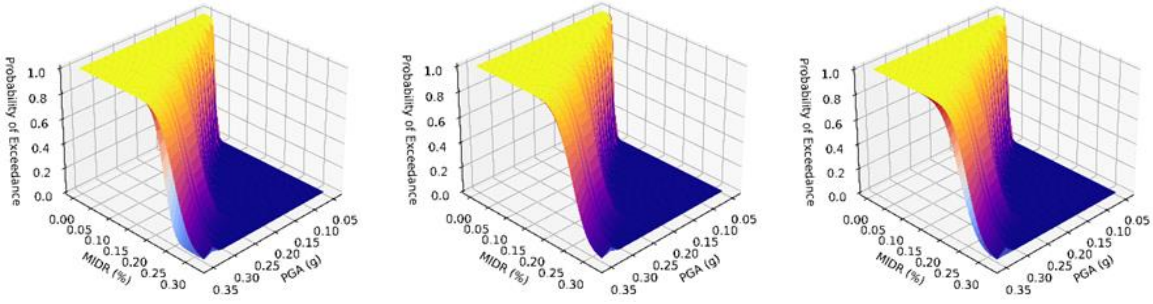

(a) (b) (c)

Fig. 17. 3D Fragility surfaces (NL-THA and ANNs) of the MIDR for mid-rise building: a) ANN, b) Autoencoder-ANN and c) PCA-ANN

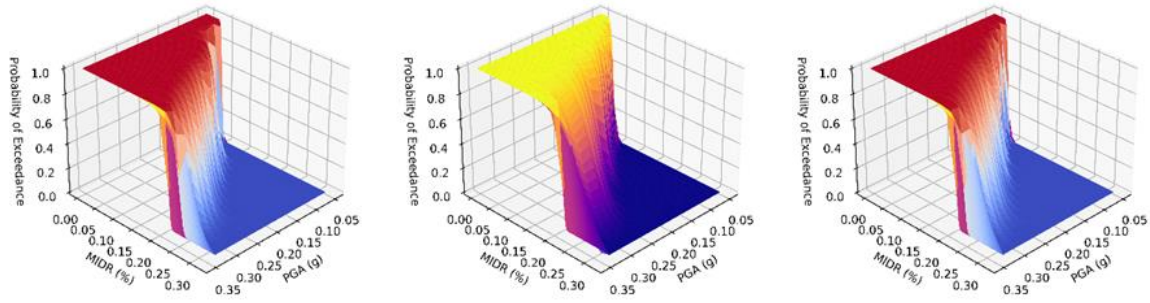

(a) (b) (c)

Fig. 18. 3D Fragility surfaces (NL-THA and ANNs) of the MIDR for high-rise building: a) ANN, b) Autoencoder-ANN and c) PCA-ANN

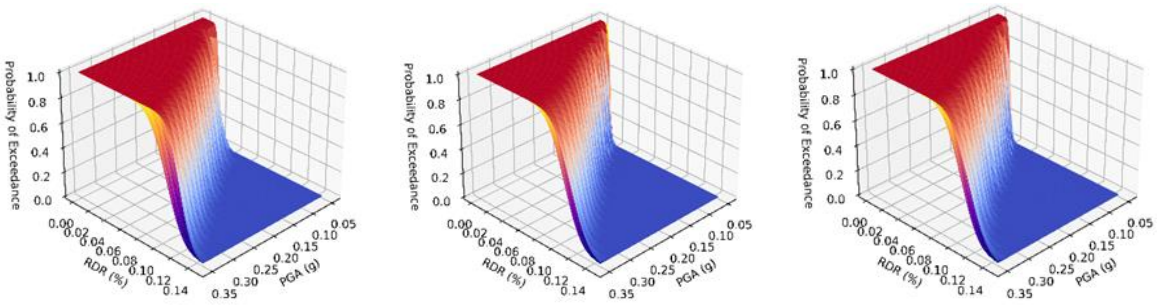

(a) (b) (c)

Fig.19. 3D Fragility surfaces (NL-THA and ANNs) of the MRDR for low-rise building: a) ANN, b) Autoencoder-ANN and c) PCA-ANN

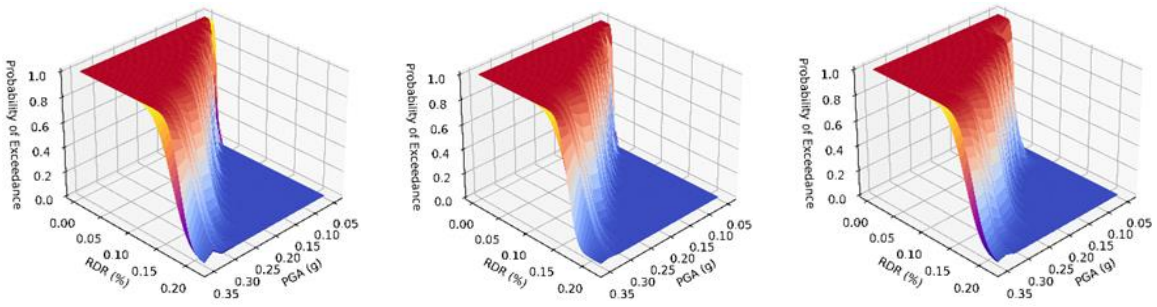

(a) (b) (c)

Fig. 20. 3D Fragility surfaces (NL-THA and ANNs) of the MRDR for mid-rise building: a) ANN, b) Autoencoder-ANN and c) PCA-ANN

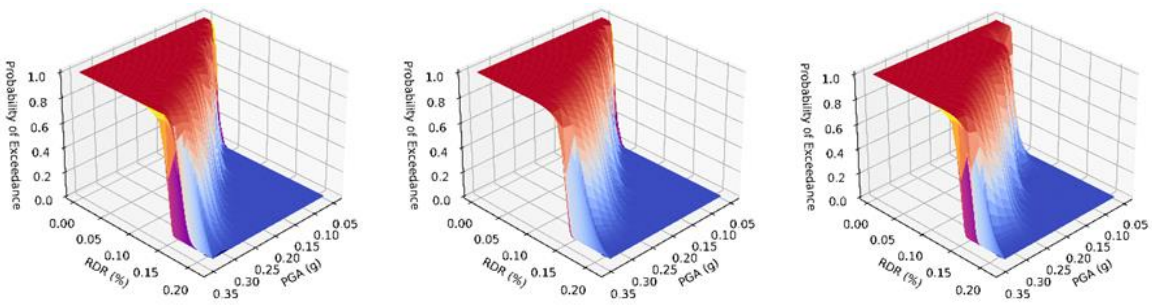

(a) (b) (c)

Fig. 21. 3D Fragility surfaces (NL-THA and ANNs) of the MRDR for mid-rise building: a) ANN, b) Autoencoder-ANN and c) PCA-ANN

4.Discussion

The seismic response is essential for the vulnerability and fragility assessment of new and existing buildings. The NL-THA is considered the most reliable and accurate method to achieve an exact investigation. However, this method is not always suitable due to its complexity and time-consuming. Therefore, many works have been proposed to facilitate the assessment process using techniques like machine learning algorithms. In this paper,

an ANN model has been developed to predict the seismic responses (MBS, MIDR, and MRDR) of RC frame buildings using only the building geometry and earthquake characteristics. It aims to offer analysts a rapid and fast alternative to predict the building's performance and calculate the probability of exceeding a certain damage level.

The paper starts by generating a dataset with more than 190,000 NL-THA performed, and three ANN models were trained (ANN, Autoencoder-ANN, PCA-ANN). Table 5 illustrates that three ANN models achieved a good performance level with correlation coefficients exceeding 97%. The Autoencoder-ANN model showed the lowest MSE and RMSE (0.00007,0.000131 and 0.00011) for MBS, MIDR, and MRDR, respectively. For the PCA-ANN model showed the highest correlation coefficients (98%, 99%, and 98%) during the training process, and the MSE is higher than the ANN's (0.0013,0.0087 and 0.011761) for MBS, MIDR, and MRDR. The hybrid models (PCA and Autoencoder) performed better in training, testing, and validation than the ANNs. Only twenty dimensions have been used to train the ANN. In addition, the dimensionality reduction allowed us to reduce and optimize the ANN model's hyperparameters, as shown in Table 4, which made the training process faster and less complex. This improvement is caused to the ability of the unsupervised techniques to capture the principal components (in the case of the PCA) or the essential features of the dataset (in the case of the Autoencoder). The proposed model was tested on unseen GMs since the work aims to develop an accurate, fast, and generalized method that can be used as an alternative to the NL-THA. Three buildings with different heights were used as a case study, and thirty artificial GMs matched to the same target response spectrum were used to perform the analysis.

Figure 13, Figure 14, and Figure 15 illustrate the IDA points of the (MBS, MIDR, and MRDR) versus the incremented seismic intensity (PGA). Table 7, Table 8, and Table 9 summarized the performance of the prediction. The results showed that the Autoencoder-ANN model has the highest rate of predictability regarding R^2 and MSE. The PCA-ANN model also showed high accuracy in terms of R^2 and MSE and slightly less than the Autoencoder's accuracy. The ANN model showed good predictability but remarkably less than the previous hybrid models for all the ANN models and all three buildings. It can be concluded that using these unsupervised techniques enhanced the accuracy of the prediction, even for unseen GMs.

The 3D fragility surfaces were constructed using the IDA results and compared to the NL-THA fragility surfaces. Figure 16, Figure 17, and Figure 18 illustrate the 3D fragility surfaces of the MIDR using the ANN, Autoencoder-ANN, and PCA-ANN for low-, mid-, and high-rise buildings. Figure 19, Figure 20, and Figure 21 illustrate the 3D fragility surfaces of the MRDR using the ANN, Autoencoder-ANN, and PCA-ANN for low-, mid-, and high-rise buildings. The accuracy of these surfaces to the exact surfaces is summarized in Table 10 and Table 11 for the MIDR and MRDR, respectively. According to these Figures and the tables, it can be noticed that the Autoencoder and the PCA models accurately predict the fragility of surfaces with an R^2> 95% where the Autoencoder models represented the highest correlation coefficient of 95%, 99%,97% for the MIDR and 97%, 99%, and 99% for the MRDR, and the lowest MSE 0.0007,0.0018 and 0.0061 for the MIDR and 0.0062, 0.002 and 0.0013 for the MRDR. The PCA-ANN model also showed high accuracy and slightly less than the Autoencoder-ANN model, with an R^2 of 91%,98%, and 97% for the MIDR and 94%, 94%, and 93% for the MRDR. For the ANN models, they showed an acceptable correlation with an R^2 of 83%, 89%, and 90% for the MRDR and 60%, 83%, and 97% for the MIDR and an MSE of 0.08, 0.05, and 0.0062 for the MIDR and 0.5, 0.02 and 0.02 for the MRDR.

Given these results, the Autoencoder-ANN is the most suitable hybrid method to predict seismic responses. Its accuracy is not limited to seen GMs but to unseen ones. Also, the

PCA-ANN model presented an excellent model, slightly less accurate than the Autoencoder regarding the predictability of the IDA points and fragility surfaces. The use of the hybrid models improved the accuracy and optimized the ANN's hyperparameters, making the ANN model more generalized to unseen scenarios.

5.Conclusion

The paper presents a new approach for predicting seismic responses with high speed and accuracy. The approach utilizes unsupervised algorithms and Artificial Neural Networks (ANN) to predict critical seismic parameters such as MBS, MIDR and MRDR. This new approach can be helpful in the field of earthquake engineering and research, as it can provide better understanding of the seismic behavior of structures.

The paper compares the performance of three different ML models. The first model is an ANN without any modification to the input features. The second model is a combination of an autoencoder and an ANN, where autoencoder algorithm is used to obtain the input features for ANN. The third model is a combination of Principal Component Analysis (PCA) and ANN, where PCA is used to reorient and reduce the input data. These ML models are compared with the NLTHA results in terms of R^2, MSE and RMSE.

The comparative study provides several insights into the performance of different models:

- The ML-based approach presented a quick alternative to the NLTHA, where it can be used as an alternative by the engineers to fast assess the seismic response of RC frame buildings without the need for modeling to processing time.
- The use of hybrid approaches as PCA-ANN and Autoencoder-ANN made the prediction more accurate and enhanced the performance and outputs results and reduced the MSE.
- The ML models were able to reach a high accuracy by using only the geometry characteristics which mean that the engineer can use it on the field without the need to any calculations or FEM software.
- The Autoencoder made the ANN training more accurate, and it reduced the MSE remarkably compared to PCA-ANN and ANN models.
- The use of hybrid models made the ANN training much faster and less complex due to the dimensionality reduction and data reorientation and make the ANN train on the principal components.
- The hybrid model reduces the hyperparameter numbers such as number of neurons and number of hidden layers due to the input features reduction.
- The ML-based can be a useful tool for vulnerability and fragility assessments due to it high accuracy and reduce computational time and its simplicity.

The hybrid model is a useful tool for quickly investigating the seismic vulnerability and fragility of structures. However, it should be noted that the accuracy of the model's predictions is limited to reinforced concrete frame structures with specific geometry characteristics mentioned in the paper. To ensure accurate results, it is recommended not to use parameters that exceed the upper bound of the training dataset. Doing so may affect the accuracy of the model's predictions.

Appendix A

Table A1. The eighty artificial ground motions and their characteristics used to generate the dataset.

GMs	PGA (g)	PGV (cm/sec)	PGD (cm)	AI	Ic	CAV (cm/sec)	VSI (cm)	HI (cm)	A95 (g)	PP (sec)	SD (sec)
GM 1	0.16	14.11	20.11	0.52	0.04	567.24	59.85	55.06	0.15	0.40	12.78
GM 2	0.19	14.32	9.15	0.51	0.04	545.23	61.57	57.10	0.19	0.20	11.38
GM 3	0.19	14.66	13.81	0.50	0.04	543.61	63.62	58.87	0.18	0.18	12.02
GM 4	0.22	18.64	15.45	0.52	0.04	554.85	61.65	56.96	0.22	0.26	11.88
GM 5	0.21	15.38	31.25	0.47	0.04	531.61	61.30	54.65	0.21	0.38	11.99
GM 6	0.18	13.76	8.97	0.53	0.04	561.33	63.73	57.84	0.17	0.22	11.86
GM 7	0.23	13.48	10.61	0.46	0.04	525.61	64.23	59.44	0.23	0.20	11.65
GM 8	0.21	16.43	18.57	0.50	0.04	543.66	61.33	56.10	0.21	0.18	12.40
GM 9	0.17	13.75	14.87	0.43	0.03	501.45	59.01	54.77	0.17	0.40	10.55
GM 10	0.18	13.25	7.55	0.35	0.03	439.99	63.80	57.74	0.18	0.36	9.65
GM 11	0.15	14.28	7.21	0.41	0.03	490.52	60.75	55.85	0.15	0.22	10.96
GM 12	0.19	13.93	6.34	0.50	0.04	546.92	62.42	58.53	0.19	0.26	12.25
GM 13	0.17	14.99	7.42	0.55	0.04	560.44	64.80	60.13	0.17	0.16	10.45
GM 14	0.19	12.39	4.40	0.41	0.03	468.87	64.58	58.89	0.18	0.26	10.14
GM 15	0.17	15.18	8.90	0.33	0.03	418.10	59.98	55.27	0.17	0.16	9.40
GM 16	0.18	16.73	12.04	0.39	0.03	472.72	61.43	56.29	0.17	0.20	10.20
GM 17	0.21	15.10	6.76	0.34	0.03	422.32	61.96	56.02	0.20	0.32	9.08
GM 18	0.16	12.79	9.33	0.50	0.04	587.56	59.82	55.51	0.15	0.40	14.25
GM 19	0.19	16.89	20.74	0.47	0.03	558.46	65.73	59.56	0.19	0.36	13.36
GM 20	0.16	13.91	9.36	0.49	0.04	588.11	61.13	56.49	0.16	0.22	15.16
GM 21	0.16	14.25	5.40	0.57	0.04	628.21	62.70	58.45	0.15	0.16	14.80
GM 22	0.18	13.23	8.54	0.51	0.04	579.00	64.44	59.07	0.18	0.26	13.76
GM 23	0.20	14.88	13.59	0.58	0.04	588.32	64.21	59.57	0.19	0.18	12.84
GM 24	0.17	12.02	8.39	0.40	0.03	515.35	59.72	56.04	0.17	0.16	14.70
GM 25	0.17	17.88	11.52	0.49	0.04	579.15	61.86	57.78	0.16	0.20	13.85
GM 26	0.19	14.01	12.36	0.39	0.03	508.24	57.89	54.05	0.19	0.32	14.31
GM 27	0.15	22.68	53.92	0.43	0.03	494.46	58.71	55.17	0.14	0.28	10.62
GM 28	0.15	15.24	4.38	0.40	0.03	468.88	61.65	57.47	0.15	0.34	10.34
GM 29	0.18	24.89	32.01	0.46	0.04	524.63	62.76	57.31	0.17	0.30	16.74
GM 30	0.24	16.87	7.59	0.44	0.03	492.32	61.89	57.19	0.24	0.16	10.35
GM 31	0.18	11.58	7.91	0.40	0.03	453.14	64.66	58.25	0.17	0.38	10.04
GM 32	0.18	29.46	41.92	0.37	0.03	443.87	57.01	55.76	0.17	0.22	9.66

GM 33	0.20	20.19	24.56	0.41	0.03	477.89	61.34	58.43	0.20	0.38	10.57
GM 34	0.24	15.01	6.42	0.51	0.04	561.26	60.64	56.34	0.24	0.16	12.83
GM 35	0.19	16.13	10.13	0.32	0.03	408.98	58.44	54.50	0.19	0.18	10.54
GM 36	0.16	12.97	6.89	0.40	0.03	564.23	61.60	53.14	0.16	0.36	14.24
GM 37	0.17	104.02	300.93	0.63	0.04	785.25	48.45	52.69	0.17	0.30	16.41
GM 38	0.18	12.77	9.02	0.43	0.03	586.99	56.76	51.90	0.17	0.24	13.71
GM 39	0.17	12.85	11.58	0.46	0.03	612.88	58.90	52.80	0.16	0.30	14.16
GM 40	0.15	33.28	90.36	0.44	0.03	593.89	58.27	53.39	0.15	0.32	14.39
GM 41	0.13	11.18	7.23	0.41	0.03	588.53	54.63	52.33	0.13	0.40	13.90
GM 42	0.15	38.52	124.98	0.47	0.03	680.39	56.90	53.23	0.15	0.36	20.67
GM 43	0.17	15.18	19.05	0.44	0.03	623.98	57.08	54.43	0.16	0.30	15.23
GM 44	0.13	30.39	130.65	0.59	0.03	905.73	57.45	53.37	0.13	0.28	24.96
GM 45	0.18	30.64	121.62	0.50	0.04	545.28	61.88	56.41	0.18	0.38	12.40
GM 46	0.15	13.73	26.47	0.60	0.03	906.12	57.12	53.26	0.14	0.32	24.16
GM 47	0.16	37.30	210.98	0.67	0.04	996.46	58.37	54.64	0.15	0.28	25.90
GM 48	0.15	16.38	10.19	0.70	0.04	983.07	60.61	54.21	0.15	0.24	23.87
GM 49	0.14	10.51	13.95	0.65	0.04	963.25	58.47	53.19	0.14	0.28	25.55
GM 50	0.14	41.64	159.92	0.67	0.04	1037.31	54.92	53.06	0.14	0.18	30.23
GM 51	0.15	13.97	21.95	0.63	0.03	943.91	57.09	52.38	0.15	0.26	25.03
GM 52	0.15	31.67	201.03	0.65	0.04	967.57	55.53	53.23	0.14	0.16	25.46
GM 53	0.14	16.77	29.56	0.70	0.04	991.50	62.04	56.74	0.13	0.24	25.21
GM 54	0.15	21.46	114.56	0.66	0.04	950.93	62.88	59.05	0.15	0.24	24.22
GM 55	0.16	15.49	79.16	0.69	0.04	977.16	61.59	56.89	0.16	0.28	23.85
GM 56	0.19	12.23	7.14	0.45	0.04	510.95	62.72	57.80	0.18	0.22	12.88
GM 57	0.14	19.87	106.57	0.68	0.04	981.23	60.71	54.27	0.14	0.24	24.55
GM 58	0.14	23.68	129.52	0.69	0.04	1006.77	60.98	56.66	0.14	0.26	26.05
GM 59	0.14	22.31	147.84	0.68	0.04	1025.23	56.65	52.42	0.14	0.40	28.88
GM 60	0.17	28.67	186.34	0.69	0.04	989.14	59.66	56.10	0.16	0.32	25.36
GM 61	0.14	14.10	40.27	0.70	0.04	991.06	60.10	55.87	0.14	0.16	24.87
GM 62	0.17	16.89	44.37	0.43	0.03	592.90	63.35	54.69	0.17	0.36	14.49
GM 63	0.16	12.64	3.39	0.52	0.03	660.31	61.54	55.08	0.16	0.36	14.55
GM 64	0.18	14.31	18.33	0.47	0.03	617.75	60.10	54.91	0.17	0.28	13.93
GM 65	0.17	11.51	15.65	0.47	0.03	624.10	60.11	53.38	0.16	0.28	14.42
GM 66	0.16	12.85	10.56	0.46	0.03	607.56	60.32	54.61	0.15	0.20	14.17
GM 67	0.22	24.04	38.87	0.48	0.04	541.49	63.77	59.20	0.21	0.20	12.39
GM 68	0.14	12.78	10.24	0.46	0.03	630.85	57.82	54.31	0.13	0.40	14.72
GM 69	0.16	22.10	58.72	0.45	0.03	595.52	63.40	57.76	0.15	0.32	13.75

GM 70	0.19	158.68	1376.71	0.67	0.04	876.57	52.93	55.44	0.19	0.30	25.31
GM 71	0.16	13.53	6.32	0.40	0.03	560.41	61.40	52.97	0.16	0.46	14.14
GM 72	0.16	38.57	116.48	0.52	0.03	676.30	58.32	54.42	0.15	0.30	15.47
GM 73	0.19	13.18	8.14	0.46	0.03	606.51	57.80	52.84	0.18	0.24	13.71
GM 74	0.17	12.60	10.78	0.46	0.03	614.91	58.90	52.79	0.17	0.30	14.16
GM 75	0.15	11.51	17.89	0.48	0.03	640.40	59.84	54.59	0.15	0.32	15.12
GM 76	0.14	12.42	8.64	0.46	0.03	620.74	56.73	54.02	0.13	0.40	14.24
GM 77	0.16	13.93	14.37	0.42	0.03	564.42	60.17	53.84	0.15	0.36	13.24
GM 78	0.19	15.51	10.81	0.39	0.03	478.98	60.31	55.50	0.18	0.18	13.59
GM 79	0.18	23.61	32.97	0.45	0.03	639.30	55.32	53.26	0.17	0.30	16.54
GM 80	0.19	15.27	13.54	0.50	0.04	542.96	63.50	57.38	0.18	0.24	11.56

References

[1] Benbokhari A, Benazouz C, A M, R M. Seismic vulnerability and fragility assessment of a strategic building in Algeria. Jun. 2023.

[2] Naddaf M. Turkey-Syria earthquake: what scientists know. Nature. 2023 [Epub ahead of print]. doi: 10.1038/d41586-023-00364-y. https://doi.org/10.1038/d41586-023-00364-y

[3] Petak W. Earthquake Resilience through Mitigation: A System Approach. Jan. 2002.

[4] Full article: Review of Seismic Risk Mitigation Policies in Earthquake-Prone Countries: Lessons for Earthquake Resilience in the United States. [Accessed Jul. 07, 2023]. [Online]. Available: https://www.tandfonline.com/doi/full/10.1080/13632469.2021.1911889

[5] Kassem MM, Mohamed Nazri F, Noroozinejad Farsangi E. Development of seismic vulnerability index methodology for reinforced concrete buildings based on nonlinear parametric analyses. MethodsX. Jan. 2019;6:199-211. https://doi.org/10.1016/j.mex.2019.01.006

[6] Li SQ, Chen YS, Liu HB, Del Gaudio C. Empirical seismic vulnerability assessment model of typical urban buildings. Bull Earthquake Eng. Mar. 2023;21(4):2217-2257. https://doi.org/10.1007/s10518-022-01585-8

[7] Aggarwal Y, Saha SK. An improved rapid visual screening method for seismic vulnerability assessment of reinforced concrete buildings in Indian Himalayan region. Bull Earthquake Eng. Jan. 2023;21(1):319-347. https://doi.org/10.1007/s10518-022-01537-2

[8] HAZUS-MH Flood Loss Estimation Methodology. II. Damage and Loss Assessment. Nat Hazards Rev. 2006;7(2):72. https://doi.org/10.1061/(ASCE)1527-6988(2006)7:2(72)

[9] Lantada N et al. Seismic hazard and risk scenarios for Barcelona, Spain, using the Risk-UE vulnerability index method. Bull Earthquake Eng. Apr. 2010;8(2):201-229. https://doi.org/10.1007/s10518-009-9148-z

[10] Kassem MM, Mohamed Nazri F, Noroozinejad Farsangi E. Development of seismic vulnerability index methodology for reinforced concrete buildings based on nonlinear parametric analyses. MethodsX. Jan. 2019;6:199-211. https://doi.org/10.1016/j.mex.2019.01.006

[11] Alilou AAR, Pouraminian M. Seismic Fragility Assessment of RC Frame Equipped by Visco-Elastic Dampers Using NLTHA and FNA. AJEAS. Jul. 2019;12(3):359-367. https://doi.org/10.3844/ajeassp.2019.359.367

[12] Chang SY. Accuracy of Time History Analysis of Impulses. J Struct Eng. Mar. 2003;129(3):357-372. https://doi.org/10.1061/(ASCE)0733-9445(2003)129:3(357)
[13] Progressive Analysis Procedure for Progressive Collapse. J Perform Constr Facil. 2004;18(2):79. https://doi.org/10.1061/(ASCE)0887-3828(2004)18:2(79)
[14] Rahgozar N, Pouraminian M, Rahgozar N. Reliability-based seismic assessment of controlled rocking steel cores. J Build Eng. Dec. 2021;44:102623. https://doi.org/10.1016/j.jobe.2021.102623
[15] A pushover seismic analysis method for asymmetric and tall buildings. J Chin Inst Eng. 2015;38(8). https://doi.org/10.1080/02533839.2015.1056553
[16] Pushover procedure for seismic analysis of buildings. Prog Struct Eng Mater. 1998;1(3-4). https://doi.org/10.1002/pse.2260010317
[17] Rosti A, Rota M, Penna A. An empirical seismic vulnerability model. Bull Earthquake Eng. Jun. 2022;20(8):4147-4173. https://doi.org/10.1007/s10518-022-01374-3
[18] Seismic vulnerability assessment using regional empirical data. Earthquake Eng Struct Dyn. [Accessed Jul. 07, 2023]. [Online]. Available: https://onlinelibrary.wiley.com/doi/abs/10.1002/eqe.572
[19] Asgarkhani N, Kazemi F, Jakubczyk-Gałczyńska A, Mohebi B, Jankowski R. Seismic response and performance prediction of steel buckling-restrained braced frames using machine-learning methods. Eng Appl Artif Intell. Feb. 2024;128:107388. https://doi.org/10.1016/j.engappai.2023.107388
[20] Gholizadeh S, Salajegheh J, Salajegheh E. An intelligent neural system for predicting structural response subject to earthquakes. Advances in Engineering Software. 2009 Aug;40(8):630-9. https://doi.org/10.1016/j.advengsoft.2008.11.008
[21] Buildings, Predicting Dynamic Response of Structures under Earthquake Loads Using Logical Analysis of Data. Accessed: Feb. 24, 2024. https://www.mdpi.com/2075-5309/8/4/61
[22] Vafaei M, bin Adnan A, Abd. Rahman AB. Real-time Seismic Damage Detection of Concrete Shear Walls Using Artificial Neural Networks. Journal of Earthquake Engineering. 2013 Jan;17(1):137-54. https://doi.org/10.1080/13632469.2012.713559
[23] Morfidis K, Kostinakis K. Approaches to the rapid seismic damage prediction of r/c buildings using artificial neural networks. Engineering Structures. 2018 Jun;165:120-41. https://doi.org/10.1016/j.engstruct.2018.03.028
[24] Oh BK, Glisic B, Park SW, Park HS. Neural network-based seismic response prediction model for building structures using artificial earthquakes. Journal of Sound and Vibration. 2020 Mar;468:115109. https://doi.org/10.1016/j.jsv.2019.115109
[25] Won J, Shin J. Machine learning-based approach for seismic damage prediction method of building structures considering soil-structure interaction. Sustainability (Switzerland). 2021;13(8). https://doi.org/10.3390/su13084334
[26] Kalakonas P, Silva V. Seismic vulnerability modelling of building portfolios using artificial neural networks. Earthquake Engineering & Structural Dynamics. 2022;51(2):310-27. https://doi.org/10.1002/eqe.3567
[27] Seo J, Dueñas-Osorio L, Craig JI, Goodno BJ. Metamodel-based regional vulnerability estimate of irregular steel moment-frame structures subjected to earthquake events. Engineering Structures. 2012 Dec;45:585-97. https://doi.org/10.1016/j.engstruct.2012.07.003
[28] Hait P, Sil A, Choudhury S. Seismic damage assessment and prediction using artificial neural network of RC building considering irregularities. Journal of Structural Integrity and Maintenance. 2020 Jan;5(1):51-69. https://doi.org/10.1080/24705314.2019.1692167
[29] Mangalathu S, Heo G, Jeon J-S. Artificial neural network based multi-dimensional fragility development of skewed concrete bridge classes. Engineering Structures. 2018 May;162:166-76. https://doi.org/10.1016/j.engstruct.2018.01.053

[30] Baylon M, Garduque J, Lineses R, Loriaga N. Seismic Vulnerability Assessment of Gilbert Bridge in Laoag, Ilocos Norte Using Capacity -Spectrum Method. 2020.
[31] Rachedi M, Matallah M, Kotronis P. Seismic behavior & risk assessment of an existing bridge considering soil-structure interaction using artificial neural networks. Engineering Structures. 2021 Apr;232:111800. https://doi.org/10.1016/j.engstruct.2020.111800
[32] Belejo A, Barbosa AR, Bento R. Influence of ground motion duration on damage index-based fragility assessment of a plan-asymmetric non-ductile reinforced concrete building. Engineering Structures. 2017 Nov;151:682-703. https://doi.org/10.1016/j.engstruct.2017.08.042
[33] Jalayer F, Ebrahimian H, Miano A, Manfredi G, Sezen H. Analytical fragility assessment using unscaled ground motion records. Earthquake Engineering & Structural Dynamics. 2017;46(15):2639-63. https://doi.org/10.1002/eqe.2922
[34] A probabilistic approach to ground-motion selection for engineering design | Bulletin of the Seismological Society of America | GeoScienceWorld. Accessed: Jul. 07, 2023.
[35] Evaluation of ground motion selection and modification procedures using synthetic ground motions - Kwong - 2015 - Earthquake Engineering & Structural Dynamics - Wiley Online Library. Accessed: Jul. 07, 2023.

Research on Engineering Structures & Materials
www.jresm.org
Research Group

Research Article

Investigation of the influence of mineral fillers on the structural and mechanical characteristics of polyethylene high-density (PEHD) composites reinforced with alumina and talc

Fatma Zohra Benabid*[1,a], Said Mohamed El Cheikh Mohamed Salem[1, b], Oum Keltoum Mallem[1, c], Foued Zouai[2,d]

[1]*Laboratory of Multiphase Polymeric Materials (LMPMP), Department of Process Engineering, Faculty of Technology, Ferhat ABBAS University Sétif1, Algeria*
[2]*Biopharmacy and Pharmacotechnics Laboratory, Faculty of Medicine, Sétif, Algeria*

Article Info

Article history:

Received 04 Jan 2024
Accepted 13 Mar 2024

Keywords:

Composites;
Alumina;
Talc;
Binary fillers;
Co-mixing;
Synergistic effect

Abstract

This study explores the impact of incorporating a blend of alumina and talc, ranging from 1 to 7%, into high-density polyethylene (HDPE) to modify its structural, rheological, and mechanical properties. Comparative evaluations with HDPE/Alumina and HDPE/Talc composites were conducted. The dual-filler combination was achieved through dry grinding, followed by melt processing with a Brabender plastograph. FTIR spectroscopy analysis of HDPE/ (alumina + talc) composites revealed interactions between aluminum and oxygen, with a peak at 700 cm-1 indicating alumina integration into the HDPE matrix, influencing composite properties. Impact strength decreased with talc inclusion but significantly improved with alumina. Notably, a 5% blend of HDPE/(alumina-talc) fillers exhibited the highest impact resistance. Tensile stress showed peaks at 1% talc content and a 3% filler mixture, emphasizing synergistic effects and talc's superiority over alumina. Synergism in elongation at break was observed for HDPE/ (alumina + talc) composites. Additionally, HDPE/Alumina composites displayed the highest modulus of elasticity, while HDPE/(Alumina + Talc) composites had the highest melt flow index. Surface treatments promoted uniform filler dispersion within the HDPE matrix, enhancing mechanical properties. Overall, composites with binary fillers harnessed synergistic effects, combining advantages from both components.

1. Introduction

In modern engineering, the versatility of materials is paramount, with engineers adapting materials to suit the evolving needs of society and the demands of cutting-edge technologies. The advancement of macromolecular materials, ignited by the advent of synthetic polymers, has spurred the emergence of new materials, revolutionizing industries over recent decades [1, 2]. Polymers, now integral to multitude everyday objects, have progressively supplanted traditional materials such as mineral glasses, ceramics, and metals, owing to their superior attributes in terms of both lightweight construction and durability. In this dissertation, our focus centers on high-density polyethylene (HDPE).

*Corresponding author: fzbenabid@yahoo.fr
[a] orcid.org/0000-0001-9755-6360; [b] orcid.org/0009-0009-8975-0767; [c] orcid.org/0009-0003-2734-0769; [d]orcid.org/0009-0009-3656-9702
DOI: http://dx.doi.org/10.17515/resm2024.140me0104rs

Polymer composites are complex materials comprised of two or more distinct phases, typically featuring a polymer matrix and reinforcing or filler components. This structural composition enhances properties beyond those of individual constituents. Thermoplastics are often favored over thermosets due to their recyclability and thermoformability. Conventional fillers, such as glass, aramid, and carbon fibers, along with additives like calcium carbonate, play a pivotal role in creating robust yet lightweight materials, thus driving advancements in composite technology [3]. The manufacturing process of composite materials involves several stages that integrate blending components possessing diverse physicochemical properties. These stages typically encompass intricate procedures such as material selection, mixing, polymerization, and molding. Each step contributes to the final composite's desired characteristics, ensuring optimal performance and functionality in various applications [4]. Fillers can incorporate particles, layered materials, fibers, or clusters that are enclosed within natural or synthetic polymers. These polymer composites exhibit significant promise for applications across various industries such as aeronautics, automotive manufacturing, cement production, electronics, medical equipment, consumer goods, and packaging. This is owing to their outstanding properties, which are enhanced by the presence of reinforced fillers [5].

The incorporation of fillers into polymers stands as a key technique for enhancing the properties of finished products and broadening the scope of plastic material applications. Moreover, it represents a cost-effective approach to crafting materials tailored to highly specific needs. Mineral fillers are renowned for their ability to enhance electrical conductivity, thermal resistance, and mechanical strength [6, 7]. Within the scope of this study, our attention is drawn to two mineral fillers: alumina, talc, and their amalgamation. Research conducted by F.Z. Benabid and colleagues [8] has revealed that incorporating alumina (Al_2O_3) into low-density polyethylene (LDPE) enhances its thermal stability and impact resistance. Conversely, O.K. Mallem et al. [9] found that the addition of talc improves the tensile strength of composites. Mechanical treatment of mineral fillers, typically employed, aims to enhance the quality of polymer/filler interfaces, ensuring effective dispersion. Moreover, the researchers [8, 9] demonstrated that severe grinding provides a more effective solution for increasing the specific surface area of the mineral.

According to K. Liu et al. [10], treating talc significantly enhances the Charpy impact strength and tensile strength of polypropylene/talc composites. Polyethylene (PE) finds extensive use across a spectrum of applications. Within the confines of this study, the combination of alumina and talc is introduced into HDPE to enhance specific properties, paving the way for potential applications.

The main objective of this research is to explore the impact of incorporating alumina, talc, and their combination (synergistic advantages) on the properties of HDPE, and to evaluate the efficacy of blending these two additives a distinctive aspect of this initiative. The method of co-mixing through grinding is a fast and economical approach utilized to reduce production costs, prevent filler agglomeration, and improve dispersion within the HDPE matrix.

2. Experiment

2.1. Materials

The polyethylene selected for this study is sourced as HDPE HYA 600 Blow Molding Resin, belonging to the ExxonMobil group- Chemical Company 22777 Springwoods Village Parkway Spring, TX 77389-1425. USA, and is provided in granule form with a density of 0.96 g/cm^3. Talc, specified as ETFINE 8CF, is provided by FOURNIER COMPOSITES SA (ZA DE RAGON 5 RUE DE COULOMB, 44119 TREILLIERES, FRANCE). with a particle size (d80) of approximately 38 μm and a whiteness of 85%.

The alumina GF68527187 used in this study is procured from Sigma-Aldrich Corporation PO Box 14508 Saint Louis, MO 63178 United States.

2.2. Preparation of Polymer/Filler Composites

In the process of creating polymer/filler composites, blends based on high-density polyethylene (HDPE) were meticulously crafted through melt processing. This was achieved using a Brabender plastograph operating at a temperature of 220°C and a rotational speed of 30 rpm for 10 minutes. The composites were systematically prepared, incorporating varying filler proportions (alumina, talc, alumina-talc mixture) set at 1, 3, 5, and 7%.

Following the production process, the resulting composites underwent grinding using a DREHER Brabender mechanical grinder, followed by compression molding to create thin films and test specimens. The preparation of these specimens for diverse mechanical tests involved the utilization of automatic compression press from the CARVER brand. The tests, including tensile and impact assessments, were conducted under specific working conditions: a plate temperature of 200°C, a preheating duration of 10 minutes, a compression time of 5 minutes, and subsequent air-cooling. Sample dimensions conform to ASTM standards.

2.3. Characterization

Infrared analyses (IR) are a crucial tool for discerning the intricacies of chemical bonds within materials. This method involves exciting molecular bonds in a sample using infrared radiation with wavelengths between 2.5 and 5 μm and frequencies from 4500 to 400 cm^{-1}. The specific absorptions within this frequency range offer valuable insights into the compound's structural composition. When the radiation frequency aligns with molecular vibrations, emitted energy is absorbed by the bonds, producing characteristic transmission bands representing elongation and angular deformation vibrations, such as rocking, scissoring, wagging, and twisting [11- 13]. The analyzes were carried out using a "Perkin Elmer 1000" type device with a resolution of 4 cm^{-1}. The different spectra present the transmittance (%) as a function of the wave number (cm^{-1}).

The experimentation involved the utilization of a Charpy testing apparatus, comprising a robust module with a hammer situated at its free end, a designated space for the test specimen, and an indicator dial to measure the absorbed energy during the impact, as outlined in reference [14-16]. This testing device is fundamental in assessing the impact resistance of materials, providing valuable data on their mechanical properties under specific conditions. The non-impact notched specimens were prepared with dimensions of 63x12.7x3mm^3. The Charpy test is conducted using a device of type CEAST 6546/000 with an energy of 7.5 joules.

The tensile test, a pivotal mechanical examination, serves to assess a material's deformation capacity when subjected to fluctuating stress levels. In this destructive procedure, a gradually increasing deformation is applied at a constant rate, and the corresponding force needed for this deformation is measured. This critical test is executed under ambient temperature conditions, as referenced in [17-20]. Through the tensile test, valuable insights into a material's mechanical behavior and its response to varying stresses can be garnered. The tensile specimens, manufactured with dimensions (115x13x3mm), are subjected to the tensile test controlled by a computer. After having fixed the initial length at a value of 115mm, the specimen is embedded between the two jaws, one of which is fixed and connected to a 2000N force sensor. The other jaw is mobile and connected to a drive system having a stretching speed of 5.$mm.min^{-1}$.

The Melt Flow Index (MFI) is a widely employed method in the plastics industry for characterizing thermoplastic materials. Using a melt flow meter, this technique measures the mass of molten polymer flowing under a calibrated load for a specific duration, providing a key indicator of viscosity and molecular weight. Known for its speed and comparability, MFI is crucial for the practical study of a polymer's molten state behavior [21]. The experiments utilized a "MELT-INDEXER" model 5 apparatus, featuring a vertical cylinder in an oven with a standard die. Tests were conducted under a 2.16 kg load at 200°C with Melt flow index (g/10 min)

3. Results and Discussion

3.1. Chemical Structure Analysis

3.1.1. Fourier Transform Infrared Spectroscopy (FTIR)

The Infrared (IR) analysis relies on exciting the molecular bonds of a sample using infrared radiation with frequencies ranging from 4500 to 400 cm^{-1}.

- HDPE/Filler Composites

Fig. 1, depicting the FTIR spectra of HDPE/Al_2O_3 composites incorporating fillers in the range of 1 to 7%, reveals noteworthy trends. The distinctive HDPE bands manifest as a prominent peak between 2800-3000 cm^{-1}, corresponding to the elongation vibration (C-H) of polyethylene, and a peak around 1480 cm^{-1}, indicative of the deformation vibration (C-H) of the polyethylene (CH_2) group. Absorptions within the range of 700-750 cm^{-1} signify the rotational vibration (CH_2) of polyethylene.

The distinctive HDPE bands previously elucidated persist in HDPE/Al_2O_3 composites spectra, albeit with a subtle decline in intensity correlating with an escalating filler content. Notably, the discernible alteration lies in the emergence of two distinct peaks indicative of alumina. Specifically, in the 500-400 cm^{-1} range, there is a manifestation of peaks attributed to Al-O bonds, signifying the interaction between aluminum and oxygen within the composite [22]. Additionally, a discernible peak at 700 cm^{-1} corresponds to the Al-OH bond [22], further elucidating the integration of alumina into the HDPE matrix. These observed shifts in the spectra signify the influence of alumina content on the composite.

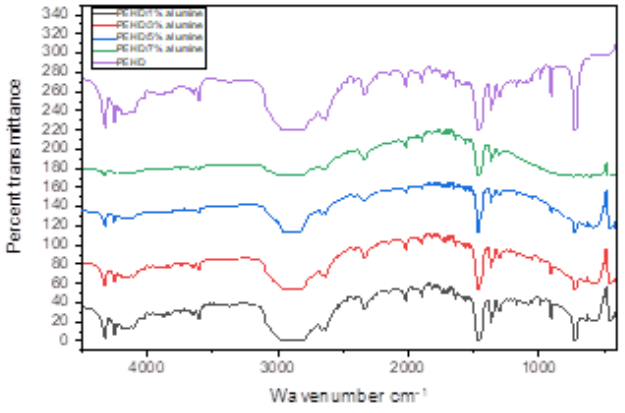

Fig. 1. FTIR spectra of HDPE/alumina composites

The findings from the FTIR spectroscopy analysis of HDPE/ (alumina+talc) composites are presented in Fig. 2. The spectral profile depicted mirrors the characteristic peaks of HDPE and alumina. Notably, the spectrum exhibits the concurrent presence of new absorbance

peaks attributed to talc, indicating their successful dispersion within the HDPE matrix. For talc, the peak at 3700 cm^{-1} is assigned to the surface hydroxyl groups as Si-OH and Mg-OH. The stretching band at 966 cm^{-1} is attributed to the Si-O tetrahedral layer and those at 3674, 664 and 549 cm^{-1} to the MgO/MgOH octahedral layer. The siloxane group (Si–O–Si and Mg–O–Si) stretching vibrational bands exist with intense peaks 460- 420 cm^{-1} [9]. This amalgamation signifies the formation of the HDPE/(alumina-talc) composite, elucidating the compositional synergy of the individual components in the resulting material.

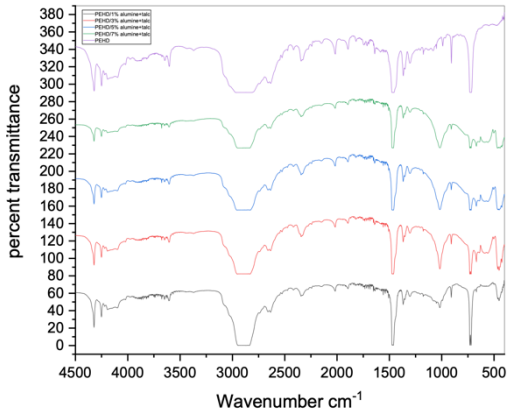

Fig. 2. FTIR spectra of HDPE/alumina+talc composites

3.2. Mechanical Properties

3.2.1. Impact Strength

The impact strength values ak (smooth specimens) of unloaded HDPE samples (ak=9.169 J/cm^2) and composites loaded with 1%, 3%, 5% and 7%, was investigated. Fig. 4 provides a comprehensive overview of the impact strength variation, specifically the Charpy impact strength, across different composites. The results unveil a distinct trend, wherein the introduction of talc is associated with a reduction in impact strength. Conversely, the inclusion of alumina demonstrates a noteworthy enhancement in the impact strength of the composites. This finding aligns with the observations made by Tuen et al [23], who reported superior flexural strength but diminished impact resistance in talc-based composites when compared to their $CaCO_3$-based counterparts.

Remarkably, a pivotal observation surfaces concerning the composite containing a 5% blend of the two HDPE/(alumina-talc) fillers, registering the highest impact resistance value (ak=13.15 J/cm^2). This improvement can be attributed to the finely granulated nature achieved through meticulous grinding during the blending process of the two fillers. This process results in a high specific surface area and an optimized interface [23, 24]. The absence of filler/matrix interaction favors particle/particle interaction, preventing an increase in the particle size of the fillers (brittle zones). This intricate combination mitigates brittleness in the material, underscoring the significance of the blending process in optimizing the composite's mechanical properties.

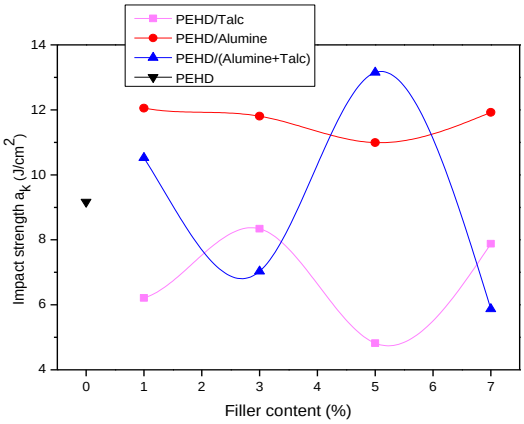

Fig. 3. Variation in Charpy ak impact strength (J/cm^2) of HDPE and its composites as a function of filler content

3.2.2. Tensile Test

Figs. 4-5 and 6 show the variations in tensile properties, i.e. stress at break, and strain at break and modulus of elasticity of the different compositions respectively. From the obtained results, it can be seen that the incorporation of fillers (alumina, talc and their mixtures) in the HDPE matrix has considerably affected its tensile properties.

- Stress at Break

The ultimate tensile stress values for HDPE/mineral filler composites were investigated σr (HDPE)=17.5 MPa Fig. 4 shows an increase in tensile strength, except for an optimum at 1% talc content and a second optimum at 3% mixture of the two fillers (synergism effect), with no improvement for the other composites. It should be noted that talc composition values are higher than those for alumina.

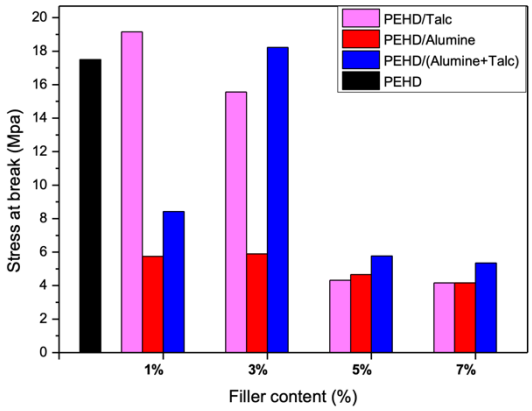

Fig. 4. Variation in Stress at break of HDPE and its composites

- Strain at Break

From Fig 5, we can deduce that there is no improvement in elongation at break by incorporating fillers compared with virgin HDPE.A decrease in this property is indeed

noticeable for composites with higher filler content, which have the lowest values of elongation at break. Synergism in elongation at break was observed for the HDPE/(alumina+talc) composite with 3, 5 and 7% filler content, compared with the two HDPE/alumina and HDPE/talc composites. More than a synergetic effect, this improvement is due to the fine particle size obtained after milling, as larger particles provide more stress concentrations where a crack can be initiated more easily [22, 23], and in addition to this, the presence of aggregates also creates brittle zones. This means that composites containing a mixture of two fillers have the best dispersion of fine particles in the polymer matrix compared to composites with separate fillers.

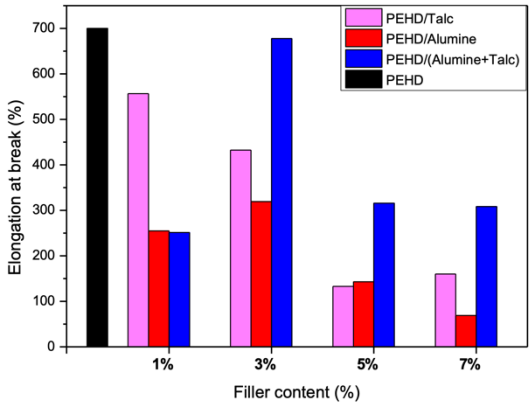

Fig. 5. Variation in elongation at break for HDPE and its composites

- Modulus of Elasticity

The best results in terms of modulus of elasticity were observed for composites containing 5% alumina, 1% talc and 7% mix of two fillers (Fig. 6). It was also found that the highest value of modulus of elasticity E (1200 MPa) was observed for the composite containing 5% alumina and consequently the increase in HDPE stiffness by the addition of fillers.

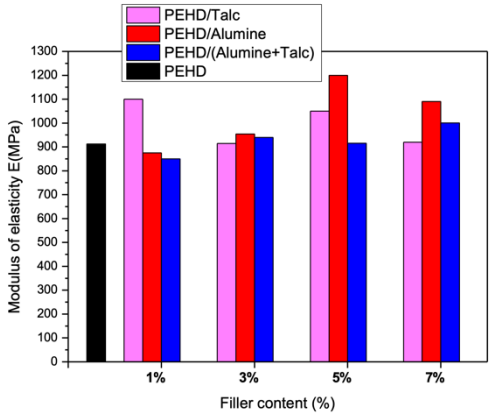

Fig. 6. Variation in modulus of elasticity of HDPE and its composites

The research shows that adding fillers like talc and alumina, or their mix, affects HDPE's tensile properties significantly, even in small amounts. Good dispersion and increased surface area of the fillers toughen the HDPE matrix. Just 1% of untreated talc can improve

HDPE's mechanical properties, likely due to its hydrophobic nature aiding deformation resistance.

Blending the fillers makes the material stiffer, stronger, and more stretchable before breaking, compared to using them separately, thanks to effective dispersion post-grinding. Chemically and mechanically treated talc, alumina, and their mix enhance certain properties of rigid HDPE, showing a synergistic effect when combined.

3.2.3. Rheological Analysis

- Melt Flow Index

The melt flow index is a simple parameter to obtain, and a very useful one which gives us an indication of a polymer's viscosity, branching rate, free volume between chains and degree of crystallinity. Fig. 7 shows the variation in melt index at a temperature of 200°C under a 2.16 kg load for the various HDPE/filler composites.

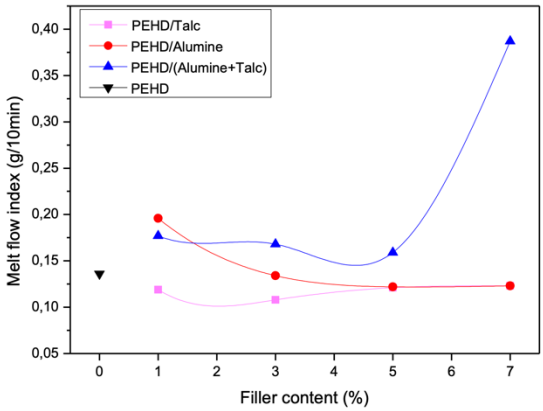

Fig. 7. Variations in the melt flow index of HDPE / filler composites as a function of filler ratio

Fig. 7 shows that the incorporation of talc causes a decrease in the melt flow index of the HDPE/Talc composite, and that the melt flow index value decreases with increasing alumina content, resulting in an increase in viscosity. The composite with binary fillers, on the other hand, has the highest melt flow index value. This is due to the fine particle size obtained by grinding during the preparation of the mixture of the two fillers, which facilitates the orientation of the flow and therefore favors the flow (melt flow) of the material [22]. The good particle dispersion in this case remarkably reduces the Van Der Waals forces between the polymer chains (polymer-polymer interactions), which facilitates the movement of the polymer chains and consequently facilitates flow, with a reduction in HDPE viscosity [25].

4. Conclusions

The aim of this work was to develop high-density polyethylene/(alumina-talc)-based composites, in order to study the effect of such mineral fillers on the properties of the polymers. By way of comparison, HDPE/alumina and HDPE/talc composites were also prepared and studied. From the various results obtained, it can be concluded that:

- Infrared results showed the appearance of new peaks characteristic of the mineral, which proves the presence of alumina and talc in the matrix (HDPE).

- The results of the impact test showed that the impact resistance of the composites decreased with increasing mineral loading due to the formation of particle aggregates in the matrix. The alumina-based composites showed good impact resistance talc-based composites, with the best impact resistance coming from composites containing a 5% mixture of the two fillers (synergism).
- On the other hand, the results of the tensile test showed an increase in stress at break only for composites with 1% talc and 3% mixtures of the two fillers, and a decrease in deformation at break of the composites as a function of the filler ratio, but there was some improvement in modulus of elasticity, implying that the incorporation of fillers imparts a certain stiffness to HDPE.
- HDPE/talc/Alumina co-filler composites combined good properties of both (synergism effect) in comparison with HDPE/talc and HDPE/alumina ones. The excellent dispersion of the filler's particles in HDPE matrix as well as the efficient treatment (dry co-mixing) lead to the enhancement of the mechanical PVC properties.
- Measurement of the melt flow index of various composite formulations showed that the incorporation of a mixture of two fillers resulted in an increase in the melt flow index and hence a reduction in composite viscosity represented by the HDPE/(alumina + talc) composite at 7% of the filler ratio, confirming the results of the mechanical tests that binary-filler composites offer good filler dispersion thanks to the fine particle size obtained by the grinding performed to prepare the mixture of two fillers. Mechanical test results showed that fine particle size has a significant effect on improving mechanical properties.

References

[1] Etienne S, David L. Introduction à la physique des polymères. Paris: Dunod; 2012.
[2] Gibson RF. A review of recent research on mechanics of multifunctional composite materials and structures. Composite Structures. 2010;92(12):2793-2810. https://doi.org/10.1016/j.compstruct.2010.05.003
[3] Khan ZI, Habib U, Mohamad ZB, Rahmat AR, Abdullah NA. Mechanical and thermal properties of sepiolite strengthened thermoplastic polymer nanocomposites: A comprehensive review. Alexandria Engineering Journal. 2022;61(2):975-90. https://doi.org/10.1016/j.aej.2021.06.015
[4] Khan ZI, Mohamad Z, Rahmat AR, Habib U. Synthesis and Characterization of Composite Materials with Enhanced Thermo-Mechanical Properties for Unmanned Aerial Vehicles (Uavs) and Aerospace Technologies. Pertanika Journal of Science & Technology. 2021;29(3). https://doi.org/10.47836/pjst.29.3.15
[5] Khan ZI, Habib U, Mohamad ZB, Khan I. Mechanical and thermal properties of a newly developed sepiolite filler-filled rPET/PA11 thermoplastic nanocomposites. Results in Engineering. 2023:101731. https://doi.org/10.1016/j.rineng.2023.101731
[6] Lertimolnun MW. Réalisation de nanocomposites polypropylène/argile par extrusion bivis [dissertation]. Paris: Ecole des Mines de Paris; 2006.
[7] Anderson C, et al. Synergistic Effects of Alumina and Talc Fillers in High-Density Polyethylene: A Comprehensive Study. Composite Science. 2020;28(3):201-215.
[8] Benabid FZ, Mallem OK, Zouai F, Cagiao ME, Benachour D. Effect of the Mechanical Treatment of Alumina on Thermal, Morphological and Dielectric Properties of LDPE/Al2O3 Composites. South African Journal of Chemistry. 2018;71:150-154. https://doi.org/10.17159/0379-4350/2018/v71a19
[9] Mallem OK, Zouai F, Gumus OY, Benabid FZ, Bedeloglu AC, Benachour D. Synergistic effect of Talc/Calcined kaolin binary fillers on rigid PVC: Improved Properties of PVC Composites. Journal of Vinyl and Additive Technology. 2021;27(4):881-893. https://doi.org/10.1002/vnl.21858

[10] Liu K, Stadlbauer W, Zitzenbachera G, Paulikb C, Burgstaller C. AIP Conf. Proc. 2016;1713:120008.
[11] Smith J, et al. Infrared Spectroscopy as a Tool for Analyzing Chemical Bonds in Materials. Journal of Analytical Chemistry. 35(2):123-140.
[12] Johnson M, et al. Fundamentals of Infrared Spectroscopy and Its Applications in Material Science. Spectroscopy Reviews. 2010;42(3):201-225.
[13] Brown A, et al. Applications of Infrared Spectroscopy in Polymer Chemistry. Polymer Science. 28(4):301-320.
[14] Johnson M, et al. Advancements in Charpy Testing: A Comprehensive Review. Materials Science Journal. 40(2):210-225.
[15] Smith J, et al. Charpy Apparatus Innovations for Enhanced Impact Testing. Journal of Mechanical Engineering. 28(3):301-320.
[16] Brown A, et al. Impact Resistance Assessment Using Charpy Testing: Methodology and Applications. Polymer Testing. 35(4):401-415.
[17] Jacquot B. Propriétés mécaniques des Biomatériaux utilisés en Odontologie [Internet]. Campus Odontologie, Société Francophone des Biomatériaux Dentaires (SFBD); 2008 [cité le 23 juin 2022]. http://campus.cerimes.fr/odontologie/enseignement/chap4/site/html/3.html
[18] Smith J, et al. Tensile Testing: Principles and Applications in Material Science. Journal of Mechanical Engineering. 40(2):210-225.
[19] Johnson M, et al. Deformation Behavior Analysis through Tensile Testing at Ambient Temperature. Materials Science Journal. 28(3):301-320.
[20] Brown A, et al. Room Temperature Tensile Testing: Methodology and Significance in Material Characterization. Polymer Testing. 35(4):401-415.
[21] Peurton F. Thermoplastic Matrix Nanocomposites and Platelet Reinforcements: Elaboration-Structure-Properties Relationships [dissertation]. Lille: University of Science and Technology Lille 1; 2008.
[22] Mallem OK. Etude des propriétés physico-chimiques des composites PP/Al2O3 et PEBD/Al2O3 [master's thesis]. Sétif-1: Ferhat ABBAS University; 2015.
[23] Tuen BS, Hassan A, Abu Bakar AM. Mechanical properties of talc- and (calcium carbonate)-filled poly(vinyl chloride) hybrid composites. Journal of Vinyl and Additive Technology. 2012;18(2):76-86. https://doi.org/10.1002/vnl.20280
[24] Bikiaris DN, Vassiliou A, Pavlidou E, Karayannidis GP. Compatibilisation of PP-g- MA copolymer on iPP/SiO2 nanocomposites prepared by melt mixing. European Polymer Journal. 2005;41:1965-1978. https://doi.org/10.1016/j.eurpolymj.2005.03.008
[25] Mallem OK. Effets des nanocharges sur l'amélioration des propriétés du PVC : Elaboration et caractérisation des nanocomposites PVC/Nanocharges (Talc et kaolin) [dissertation]. Sétif-1: Ferhat ABBAS University; 2022.

Research on Engineering Structures & Materials
www.jresm.org
MIM Research Group

Review Article

Environmental control system (ECS) design approach for collective nuclear, biological, and chemical (NBC) protection in military aircraft: A review

Emre Güler[a]

Türk Havacılık Uzay Sanayi (TUSAŞ), Ankara, Türkiye

Article Info

Article history:

Received 07 Feb 2024
Accepted 18 Mar 2024

Keywords:

ECS;
NBC protection;
Military aircraft;
Contamination;
Collective protection;
Closed loop configuration

Abstract

This comprehensive review paper delves into Environmental Control System (ECS) design strategies tailored for collective Nuclear, Biological, and Chemical (NBC) protection in military aircraft, exploring key elements such as hardening, air-tight construction, and filtering within the framework of open-loop or closed-loop ECS configurations. Initially, the paper elucidates the NBC protection requirements stipulated in commonly applied regulations such as MIL-HDBK-516C, DEFSTAN, and EMACC, highlighting the imperative for ventilation air to be devoid of contaminants, as mandated by these regulations. Subsequently, the paper delineates the strategic framework for NBC defense in the military aerospace industry, emphasizing the principles of avoidance, protection, and decontamination. A comparative analysis between individual and collective protection strategies underscores the comprehensiveness of the latter, prompting a recommendation for ECS design approaches grounded in the principles of collective protection, namely hardening, air-tight construction, and filtering. Furthermore, the paper provides insights into the configurations of open-loop and partial closed-loop ECS, elucidating their architectures for NBC protection. A comparative evaluation of these configurations enables the identification of pertinent parameters crucial for informed selection. In conclusion, the paper posits that the partial closed-loop ECS configuration exhibits greater promise in delivering enhanced NBC protection compared to the open-loop configuration, particularly in military aircraft applications operating in NBC environments.

1. Introduction

The Environmental Control System (ECS) stands as a cornerstone in the operational effectiveness of military aircraft, ensuring optimal conditions for both crew and equipment. Responsible for regulating temperature, pressure, humidity, ventilation, and air quality within the cockpit, the ECS plays a vital role in sustaining mission readiness. However, conventional ECS designs may fall short in safeguarding against the hazardous effects of nuclear, biological, or chemical (NBC) attacks.

In light of these challenges, a unique design approach becomes imperative to retrofit ECS systems for collective NBC protection within military aircraft. This paper presents a departure from conventional literature by offering a comprehensive review that explicitly addresses the specialized requirements of ECS systems for NBC protection, a topic that has garnered relatively limited attention in existing studies. The paper covers the following topics: (1) the overview of the NBC threat and the NBC protection's concept, (2) the requirements and specifications of the ECS for the NBC protection, (3) the current

*Corresponding author: emrelug@gmail.com
[a] orcid.org/0000-0003-4938-9320
DOI: http://dx.doi.org/10.17515/resm2024.176st0207rv

technologies and methods for the ECS design and analysis, and (4) the promising ECS configuration for the lowest risk of the contamination with NBC agents.

The paper covers the following topics: (1) the overview of the NBC threat and the NBC protection's concept, (2) the requirements and specifications of the ECS for the NBC protection, (3) the current technologies and methods for the ECS design and analysis, and (4) the promising ECS configuration for the lowest risk of the contamination with NBC agents.

Through a systematic review, this paper not only synthesizes existing knowledge but also breaks new ground by providing original insights into the intricacies of ECS design as it pertains to NBC protection in military aviation. By identifying gaps and limitations in the current state-of-the-art, it lays the groundwork for potential solutions and recommendations aimed at optimizing ECS performance and fostering innovation. Drawing from advancements in fluid mechanics, thermodynamics, heat transfer and filtration, this paper endeavors to contribute to the collective knowledge base, thereby inspiring further research and development in this critical and complex domain.

2. ECS Design Approaches for Collective NBC Protection in Aircraft

The term NBC refers to the condition in which the threat is posed by nuclear (N), biological (B), and chemical (C) substances or agents [1]. It replaced the term of ABC (atomic, biological, and chemical) that emerged in 1950s since the nuclear warfare is more complex, requiring more specific terms than atomic [2-4]. Chemical, Biological, Radiological, and Nuclear (CBRN) have also emerged to cover the wide range of potential hazards. The article will focus on the term of NBC.

An NBC incident is expressed as an unintentional (accidental) or deliberate (enemy aggression) release of nuclear, biological, or chemical agents [5]. Contamination resulting from the NBC incident, can be transmitted through radiation, vapor, and desorption [6]. Radiation is a form of electromagnetic energy with different wavelengths, as shown in Figure 1[7].

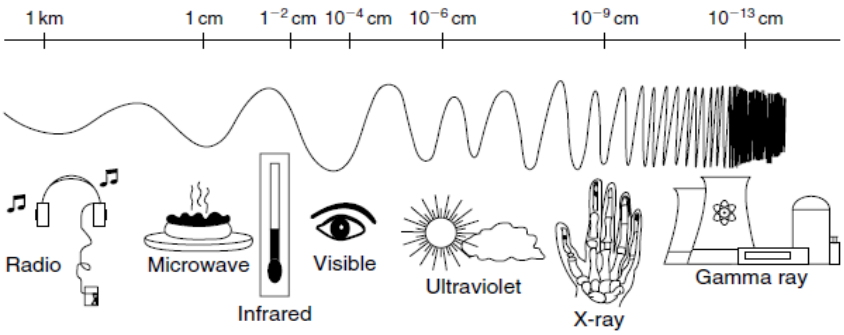

Fig. 1. Electromagnetic Spectrum [8]

Nuclear radiation is unique due to its ionizing capability to remove an electron from the orbit of a target atom or molecule, as shown in Figure 2. Ionization occurs when high energy alpha or beta particles or gamma rays transfer enough energy to remove the electron from orbit.

In nuclear incidents, the particles of alpha, beta, and gamma rays are released into the environment [9]. The ionizing capabilities of these products vary, and they are defined with

the specific ionization value, which is the average number of ion pairs per unit length along the path as shown in Table 1.

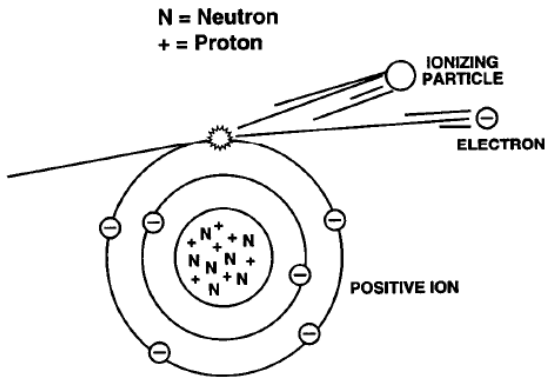

Fig. 2. Removal of an Electron due to Ionizing Particle [8]

The penetration capabilities of nuclear radiation, as depicted in Figure 3, play a crucial role in assessing their impact on human health beyond their ionizing potential. Alpha particles, due to their size, cannot penetrate human skin, thus presenting no immediate external hazard; however, inhalation poses a significant threat. In contrast, beta particles, being smaller, can penetrate multiple layers of skin, resulting in skin burns known as beta burns. Gamma rays, with their ability to traverse several inches through human tissue, pose a considerable risk to human health, often leading to fatal consequences.

Table 1.Specific Ionization of Radiation [10]

Radiation	Range in air	Speeds	Specific ionization
Alpha	5-7 cm	3,200-32,000 km/sec	20,000-50,000 ion pairs/cm
Beta	200-800 cm	25-99% speed of light	50-500 ion pairs/cm
Gamma	Use of half-thickness	Speed of light 300,000 km/sec	5-8 ion pairs/cm

The biological impact of ionization on the human body is profound. When water molecules within human tissue become ionized, they generate free radicals of hydrogen and hydroxyl, which can induce cellular damage, alter cell structures, and spur the production of abnormal cells. Beyond the perilous effects of nuclear substances on human health, they harbor the potential to wreak havoc on aviation electronics, jeopardizing their functionality and even causing operational standstills through mechanisms like ionization, displacement damage, and chemical reactions. Nuclear radiation has the capability to ionize atoms and molecules within electronic devices. A single charged particle can liberate numerous electrons from an atom or molecule, introducing unwanted electrical disturbances known as electronic noise [12], which can disrupt accurate signaling in digital circuits [13-16]. Moreover, nuclear radiation can harm the crystal lattice of semiconductor materials within electronic devices, resulting in defects that ensnare charge carriers and impede electron mobility. Additionally, nuclear radiation can instigate chemical reactions that culminate in the formation of corrosive byproducts within electronic devices [17-21].

Table 2. Potential Biological Agents [24]

Group	Disease	Likely Methods of Dissemination	Incubation Time	Duration of Illness	Lethality
Bacteria	Anthrax	Spores in aerosols	1-6 days	3-5 days	High
	Brucellosis	1. Aerosol 2. Sabotage	Days to months	Weeks to years	Low
	Cholera	1. Aerosol 2. Sabotage	1-5 days	1 or more weeks	Moderate to high
	Melioidosis	Aerosol	Days to years	4-20 days	Variable
	Plague	1. Aerosol 2. Infected vectors	2-3 days	1-2 days	Very high
	Tularemia	Aerosol	2- 10 days	2 or more weeks	Moderate if untreated
	Typhoid Fever	1. Aerosol 2. Sabotage	7-21 days	Several weeks	Moderate if untreated
Rickettsiae	Epidemic Typhus	1. Aerosol 2. Infected vectors	6-16 days	Weeks to months	High
	Q-Fever	1. Aerosol 2. Sabotage	10-20 days	2 days to 2 weeks	Very low
	Scrub Typhus	1. Aerosol 2. Infected vectors	4-15 days	Up to 16 days	Low
Chlamydia	Psittacosis	Aerosol	4-15 days	Weeks to months	Very low
	Coccidioidomycosis	Aerosol	1-2 weeks	Weeks to months	Low
	Histoplasmosis	Aerosol	1-2 weeks	Weeks to months	Low
Viruses	Chikun-Gunya Fever	Aerosol	2-6 days	2 weeks	Very low
	Crimean-Congo Hemorrhagic Fever	Aerosol	3-12 days	Days to weeks	High
	Dengue Fever	Aerosol	3-6 days	Days to weeks	Low
	Eastern Equine Encephalitis	Aerosol	5-15 days	1-3 weeks	High

During biological incidents, hazardous agents including bacteria, viruses, and toxins, as outlined in Table 2, can be discharged into the environment [22-23], triggering substantial adverse effects on human health. Additionally, these biological agents pose a notable threat to avionics systems. They have the potential to develop biofilms on surfaces, disrupting signaling processes and impeding performance. Moreover, these biofilms can act as barriers, diminishing the cooling efficiency of avionics. Furthermore, they may infiltrate organic components within avionics, such as sealants and lubricants, leading to leaks and other operational malfunctions [25-29]. In chemical incidents, hazardous chemical substances such as the nerve, blister, choking, or blood agents, may be released [30]. The

lethality of NBC agents presents how fatal they are, considering that it varies with agent type, exposure type, dosage, and individual susceptibility, as shown in Table 3.

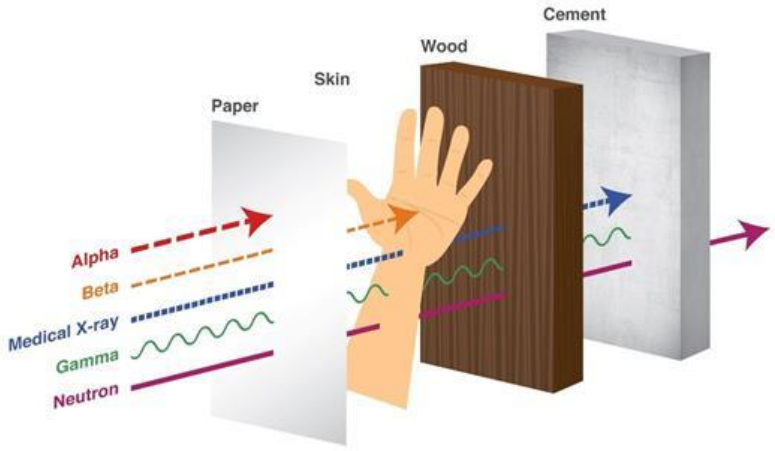

Fig. 3. Penetrating Capabilities of Nuclear Substances [11]

Table 3. Lethality of NBC Agents [31-39]

Group	Agent	Lethality Rate
Nuclear Agents	Including alpha, beta particles, and gamma ray	Fatal
Biological Agents	Anthrax (spores, inhaled)	10-80%
	Ebola (direct contact with bodily fluids)	50-90%
	Plague (pneumonic form)	90-100%
	Smallpox (inhaled)	30-60%
	Botulinum Toxin	60-90%
Chemical Agents	Methylphosphonothioic acid (nerve agent, inhaled)	90-100%
	Sarin (nerve agent, inhaled)	70-90%
	Mustard gas (blister agent, inhaled)	50-70%
	Chlorine gas (choking agent, inhaled)	10-30%
	Cyanide (blood agent, inhaled)	90-100%

NBC effects on human health are variable with respect to type of agent, its dosage, and route of exposure [40]. Different types of NBC agents lead to distinct effects, such as irradiation from radiation exposure, infection from exposure to live biological agents, and intoxication from chemical exposure [41-42]. The toxic effects of the agents upon humans range from sickness to death, temporary or long-term and often manifest within seconds or minutes of exposure. However, avionics may not exhibit signs of any degradation for long periods, such as weeks or months. NBC impact on avionics may be more significant since decontamination process would give additional damage when the equipment is washed in a corrosive solution [24].

In the current era, the clandestine pursuit of scientific studies and the escalation of regional arms races without adequate arms control measures are a great concern since their consequences may result in catastrophic conditions [43]. In the civil world, the case of the

coronavirus is the most recent example of a situation that caused the whole world to lock down. Moreover, the widening gap in military power between nations may prompt less advantaged states to seek a balance of power through the development of NBC weaponry. The deployment of tactical nuclear weapons in the Russia-Ukraine war and North Korea's nuclear missile tests are some of the examples that sustain this concern today. In such circumstances, aircraft crew and avionics may be exposed to NBC agents since military air vehicles are at the forefront of military operations or war.

NBC's threat is more likely than ever, whether it is due to an accident or an enemy's aggression. For this reason, NBC defense measures play a pivotal role in the design and certification process of military aircraft, ensuring compliance with NBC protection standards. These standards are delineated in various widely recognized regulations, including MIL-HDBK-516C from the U.S., DEF-STAN from the U.K., and EMACC from the European Union.

MIL-HDBK-516C states that [44] "Verify that the operators'/crew members' breathing air is protected from contamination in all forms, including oil leakage in the engine and nuclear, biological, and chemical (NBC) warfare conditions". Similarly, EMACC gives an explanation that [45] "NBC protection equipment and procedures shall be provided so that ventilation air is free from the contaminants".

Furthermore, DEF-STAN claims that [46] "The Aircraft and its installed equipment shall be designed to be operated by personnel wearing full CBRN and laser protective clothing. If full CBRN protective clothing is not worn by the aircrew, then the Aircraft shall be equipped with a system capable of supplying suitably pressurized and filtered air to the crew such that the crew are properly protected against the effects of CBRN hazards (CW agent liquid and vapor, BW agent in the form of aerosol and nuclear hazards in the form of dust). Appropriate levels of protection are required for the eyes, the skin, and the nasal tract". The top-down approach to NBC defense, as depicted in Figure 4, delineates a strategy centered on key principles: avoidance, decontamination, and protection [47].

NBC avoidance entails the utilization of stand-off or remotely located detectors that can interface with the aircraft, enabling the identification of potential threats and facilitating the selection of alternate flight paths to evade contamination. Decontamination procedures involve exposing aircraft components to contaminants during flight in an NBC environment, followed by thorough decontamination using specialized solutions upon landing. In contrast, protection involves designing aircraft components to withstand exposure to NBC agents during flight, obviating the need for post-mission decontamination on the ground. Various methods, including individual, collective, and hybrid approaches, are employed for protection against NBC threats. Since aircraft crew and avionics are exposed to the NBC agents through ECS, the system-level design provides extensive protection against the NBC agents.

Individual protection necessitates the use of specialized equipment, including a respiratory system and a protective suit [48]. For respiratory protection in aircraft applications, M40 masks are commonly utilized, offering comprehensive protection for the respiratory tract, eyes, and face against NBC agents. These masks feature an elastic head harness, binocular eye lenses, front and side voice meters, and a filter canister [49]. Similarly, the mission-oriented protective posture (MOPP) serves as the designated protective suit against NBC agents, comprising an overgarment, hood, mask, over boots, and gloves [50].

However, individual protection poses significant risks to both avionics and crew health. While crew members are safeguarded, avionics remain vulnerable to NBC threats and must undergo subsequent decontamination, necessitating meticulous precautions during

maintenance procedures. Moreover, wearing protective equipment during flight can induce discomfort and potential hazards for crew members, including inaccurate fitting of equipment, overheating, and slipping of respirators on sweaty faces [51].

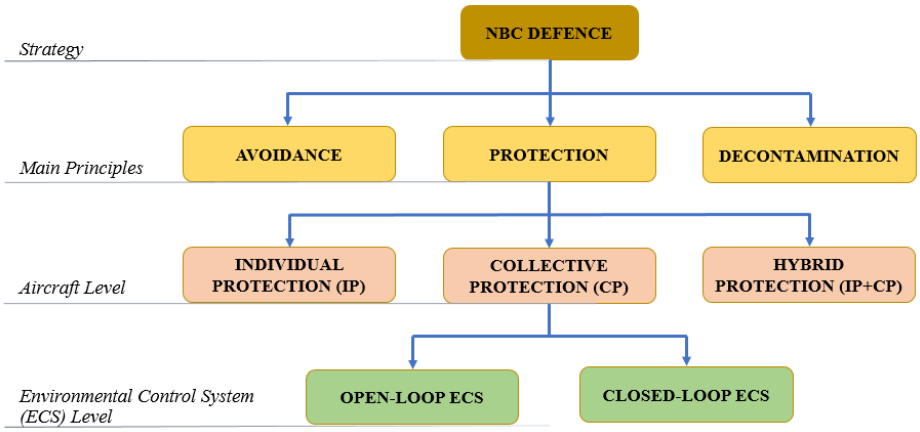

Fig. 4. Top Down Approach for NBC Defense [24]

In addition, the study [52] has shown that protective mask and clothing with significant weight usually decrease the time to sustain a particular activity level. Individual protection equipment may cause overheating in the body. It is estimated that the body temperature increases by 5°C for personnel in an NBC protection suit [53]. Many studies on the human thermal response [54-62] have demonstrated that the humans can tolerate a 630J heat load at a body temperature of 40°C. Exceeding this limit can lead the body to collapse. Furthermore, the degradation in mental performance, such as impairment in judgment, occurs at body temperatures below that limit. Thus, the crew cannot recognize his or her involvement in a dangerous situation [63].

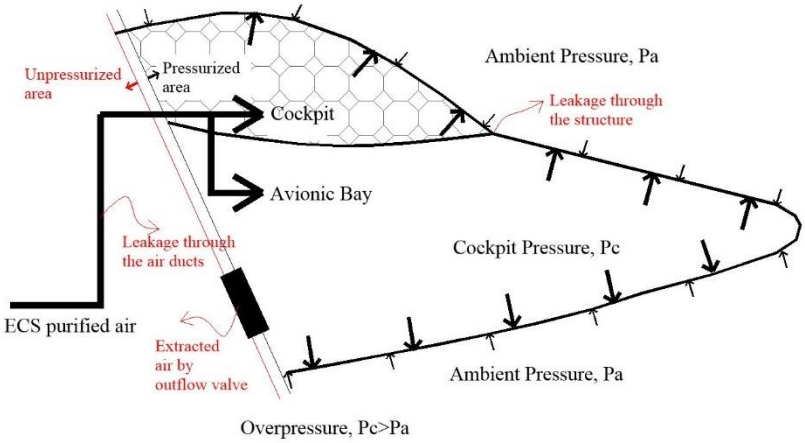

Fig. 5. Schematic of Overpressure in Aircraft [64]

In contrast, collective protection offers a more comprehensive protection mechanism. The collective protection in aircraft points to overpressure system, which is the build-up of purified air in the aircraft, as shown in Figure 5. ECS supplies purified or filtered air to crew and avionic bay, ensuring a comfortable environment and the cooling of avionics, respectively. Outflow valves discharge a portion of the supplied air outside to maintain

pressure within the cockpit within safe limits. Additionally, some air leakage occurs through the aircraft's structure and air supply ducts passing through unpressurized compartments. The air leakage may be estimated using the Eq (1) [65]:

$$W_D = 123 \times P_C \times Z \times CA / \sqrt{T_C} \quad (1)$$

where,W_D: Estimated leakage rate (lbs./min), P_C: Cabin pressure (psia), Z: Function of pressure ratio between cabin and ambient and it is between 0,53 and 1 and it is taken 0,256 for the pressure ratios equal to 0,53 and lower than 0,53, CA: Equivalent leakage area, (in^2), T_C:Cabin temperature (^oR).Z, the function of pressure ratio between cabin and ambient in Equation (1), is calculated with pressure values of ambient and cabin and specific air heat ratio in Equation (2).

$$Z = \sqrt{\left(\frac{P_A}{P_C}\right)^{2/k} - \left(\frac{P_A}{P_C}\right)^{(k+1)/k}} \quad (2)$$

where, P_C: Cabin pressure (psia), P_A: Ambient pressure (psia), k: Air specific heat ratio, c_p/c_v.

The structure, doors, windows, air ducts, and other openings within an aircraft are meticulously designed to ensure an air-tight seal, minimizing any potential leakage. The volume of air supplied by the Environmental Control System (ECS) exceeds the combined amount of discharged air and air leakage, thereby maintaining a positive pressure differential within the aircraft compared to the contaminated external environment. This positive pressure creates an overpressure environment, effectively preventing the infiltration of contaminated air into the aircraft during NBC scenarios. As a result, both crew members and avionics can operate without the need for stringent individual protection equipment, thereby mitigating the risk of contamination [24].

The ECS is engineered with the concept of either an open-loop configuration or partial closed-loop configurations, facilitating the establishment of overpressure and collective protection within the aircraft. Alongside these configurations, a third concept, the closed-loop configuration, is employed solely for the cooling of the cockpit and avionics. In this setup, air is not drawn from the external environment but instead continuously recirculated, refrigerated, and utilized for cooling purposes within the cockpit and avionics compartments, as illustrated in Figure 6. However, since maintaining overpressure in the cockpit necessitates compensating for air leakage, the closed-loop ECS configuration may not be suitable. Therefore, this article focuses on the partial closed-loop configuration over the closed-loop option.

In the partial closed-loop ECS configuration, engine bleed air is drawn into the system, where it undergoes refrigeration to cool the cockpit and avionic components. The cooled air is then recirculated within the system, as illustrated in Figure 8. The system draws additional engine air if necessary to compensate for any leakage and to replenish oxygen levels.

In open-loop configuration, the source for supply air is usually engine bleed air over the flight. ECS continually gathers engine bleed air, subjecting it to refrigeration, and subsequently employs it to cool the cabin, cockpit, and avionics, as depicted in Figure 7. Collective NBC protection necessitates the ECS's design to have certain prerequisites, including hardening, air-tight construction, and filtering, to guarantee that any degradation will not occur in the system over its entire operation in an NBC environment.

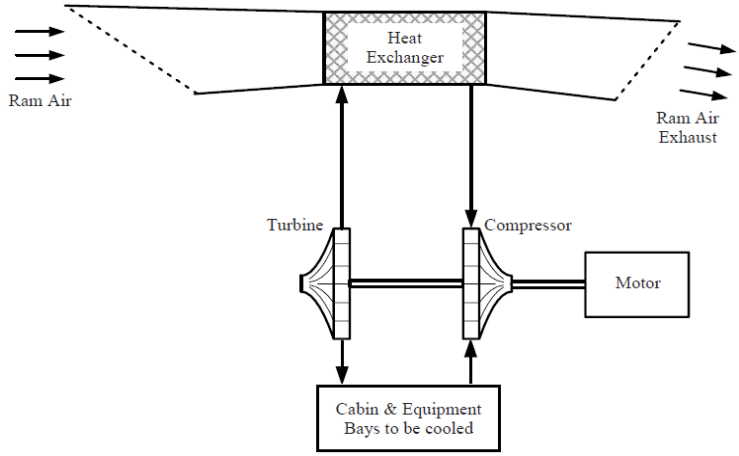

Fig. 6. Configuration of Closed-loop ECS [66]

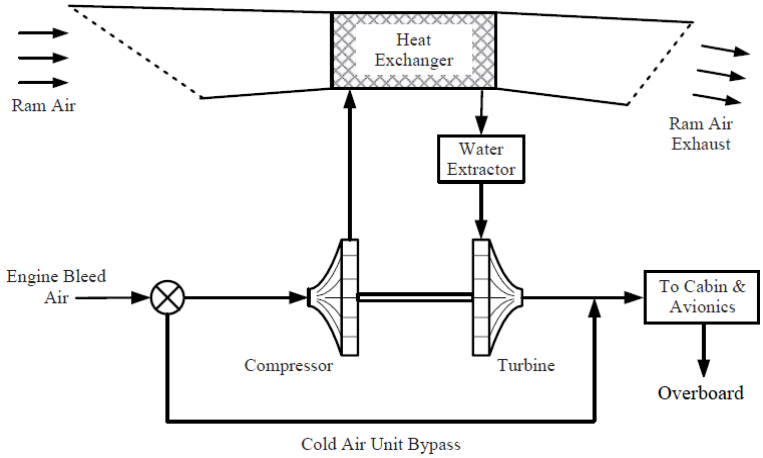

Fig. 7. Configuration of Open-loop ECS [66]

ECS needs the hardening requirements to have resistance to the nuclear, biological, and chemical agents using the approved NBC-resistant materials and design without any structural or functional degradation. Material selection is critical, with emphasis on minimizing the outgassing rate - the gradual release of trapped, dissolved, or absorbed gas from materials under extreme pressure and temperature conditions [67, 68]. Low pressure and high temperature are the proper conditions to trigger the outgassing phenomena. The buildup of the outgassed products causes the enclosed environment to be hazardous to the crew when the allowable limit is exceeded. Moreover, particles released by outgassing may interfere with the avionics and may degrade avionics' performance in the aircraft. Therefore, material selection with respect to outgassing rate is one of the control methods to reduce the quantity of toxic products in aircraft. Materials like solvents, resins, adhesives, and polymers are more susceptible to outgassing phenomena, while metals are the least susceptible to it. The molecular structure defines the susceptibility to the outgassing. A material is less susceptible to outgassing if it is more compact and stable when subjected to extreme environmental conditions. In addition to material selection, the design of hardening methods plays a crucial role in NBC protection.

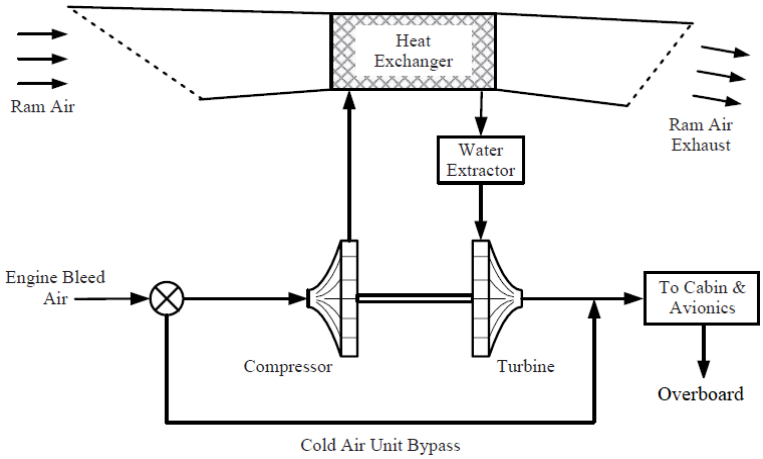

Fig. 8. Configuration of Partial Closed-loop ECS [66]

Recommended hardening practices for the ECS include sealing lapped surfaces, fasteners, and recesses around fastener heads, as well as shielding electrical connectors [24].Most of the military ECS designs allow cockpit cooling air to flow through the avionics to provide forced cooling to the air-cooled avionics. Therefore, contaminated cooling air may threaten the avionics. At least the following practices are recommended to diminish the impacts of the contaminants on the avionics:

- Drain holes are removed if possible.
- All printed circuit boards have a conformal coating, a protective thin polymeric film such as acrylic, epoxy, silicone, polyurethane, polyester, and perylene [69-71]. It is recommended to provide the coating with the thickness as shown in Table 4.
- The cold plate design is integrated into the avionics to eliminate the contact of contaminated cooling air with the electronic components. A cold plate is a heat exchanger that takes the heat released from the electronic component via heat conduction [73].

Table 4. Recommended Thickness of Polymerics for Conformal Coating [72]

Type of Coating	Thickness (inch)
Acrylic, Epoxy, and Polyurethane	0.002 ± 0.001
Silicone	0.005 ± 0.003
Parylene	0.0006 ± 0.0001

Ensuring air-tightness is paramount for aircraft when implementing collective NBC protection measures [74]. To achieve this, controlling leakage through sealing is recommended. The efficacy of a seal relies on the properties of both the constructed material and the materials it interacts with, thereby providing dependable sealing. When selecting seals, factors such as temperature, pressure, manufacturing method, sealed fluid, and application locations should be carefully considered [75]. It is imperative to choose seal types and materials resistant to NBC agents, considering their specific strengths and limitations, and aligning them with the application locations to prevent the ingress of NBC agents into the aircraft, as outlined in Table 5. Additionally, components of the ECS exposed to ultraviolet light and ozone should possess resistance to prevent seal failure.

Table 5. Typical Sealing Mechanisms on ECS Components for NBC Protection [76-78]

NBC Agents' Ingress Route	Requirements for Seals	Recommended Seals
Bleed air	- Resistance to high temperature (300-600ºC). - Resistance to high pressure (20-50psi). - Withstand vibration. - Resistance to chemical agents (oil, hydraulic fluids, etc.).	Metal-elastomer seal with a backup O-ring
Air inlet/outlets	- Resistance to chemical agents. - Resistance to corrosion.	Labyrinth seal with NBC-resistant materials
Air ducts' joints, connections, and access panel	- Resistance to chemical agents. - Withstand vibration.	O-ring seals or gaskets with NBC-resistant materials
Air filters	- Resistance to chemical agents. - Resistance to high and low temperatures. - Resistance to pressure differentials.	O-ring seals or gaskets with NBC-resistant materials
Valves	- Compensating for axial, lateral, and angular movements in the valve. - Resistance to chemical agents, corrosion. - Resistance to pressure differentials, high and low temperatures, and vibration.	Diaphragm seals, bellows seals.
Heat exchangers	- Resistance to chemical agents. - Resistance to high and low temperatures. - Resistance to pressure differentials.	Gaskets, flanges, and O-rings with NBC-resistant materials

Seal materials such as fluorinated and butyl rubbers usually resist the NBC agents. On the other hand, silicone, polyolefins, polysulfides, and Buna-N materials easily sorb the agents due to their porous atomic structure [24]. Therefore, they are not the best materials for the seals in the overall NBC protection. Air filtering is another requirement in the collective NBC protection since it separates the contaminants from the air supplied to the pressurized compartments. There are three main concepts of NBC filters namely non-regenerable, agent destruction, and regenerable filters as illustrated in Figure 9.

Non-regenerable filters are low-pressure and high-pressure carbon filters, which are based on the use of activated carbon bed technology. They consist of a high-efficiency particulate filter (HEPA) and carbon adsorption bed, as shown in Figure 10. Contaminated air passes through the HEPA filter in which at least 99.97% of aerosol particles (solid and liquid) with a size of 0.3 microns or larger hold, including bacteria and viruses. In other words, The HEPA filter's size limits its ability to completely remove aerosol particles smaller than 0.3μm. Filters no longer meet the specification requirements since their "removal effectiveness" gradually decreases during operation, necessitating their regular replacement [79]. Besides, the HEPA filter has a limitation that does not remove gaseous contaminants or volatile organic compounds. For this reason, an activated carbon bed is attached to a HEPA filter to hold the contaminated molecules on the surface with the principle of adsorption method.

The filter still has some limitations, as follows:

- It may not hold the contaminant particles of which the size is smaller than 0.3 microns.

- It may not provide a high level of protection against chemicals with vapor pressure between 10 mmHg and 100 mmHg. Furthermore, it will certainly not provide a significant protection against the chemicals with vapor pressure higher than 100 mmHg [80].
- It must be replaced when dirty, which may cause a logistical burden.
- There is a concern that new chemical agents, called, as carbon breakers, fall outside the protection capability of carbon filters.

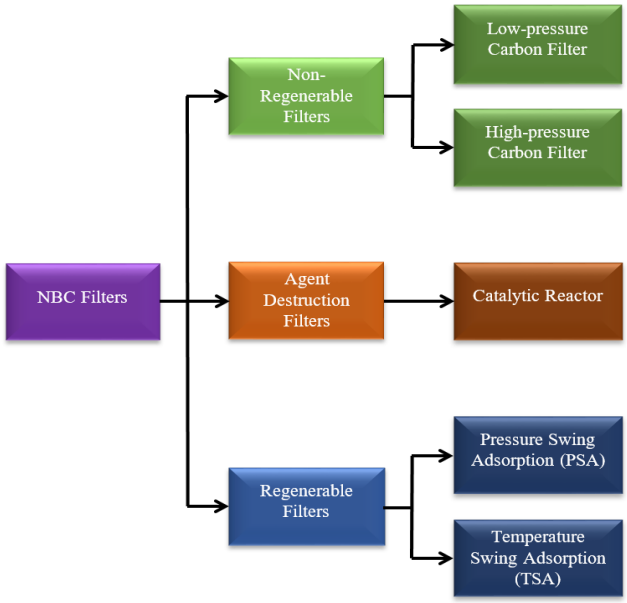

Fig. 9. Tree Diagram of Concepts of NBC Filters [24]

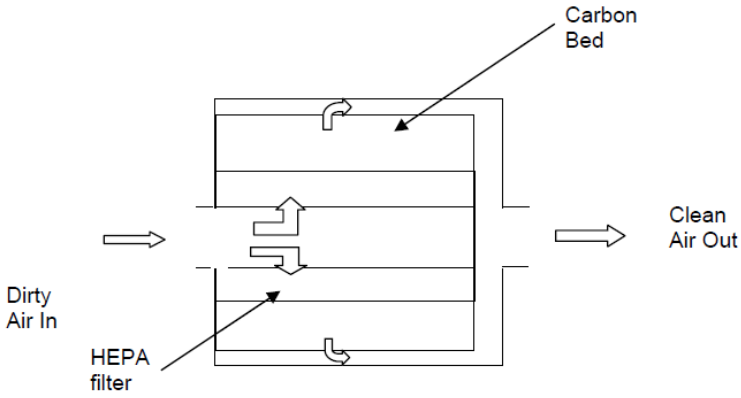

Fig. 10. Illustration of a Typical Carbon Filter [24]

Another type of NBC filter, the agent destruction filter, works with the catalytic oxidation method. It removes the contaminants through a chemical reaction between them and the catalyst. In Figure 11, bleed air is preheated to the ideal temperature for the oxidation reaction. Then, heated air is directed to the catalyst bed which has a metal catalyst that promotes the oxidation of contaminant agents. A catalyst is not altered since it is usually

stable and made of specialized materials such as platinum or palladium [81]. The oxidation breaks down the agents into less harmful byproducts such as carbon dioxide and water. Finally, it comes to the post-treatment filter, which prevents fine particles not completely oxidized during the catalytic process.

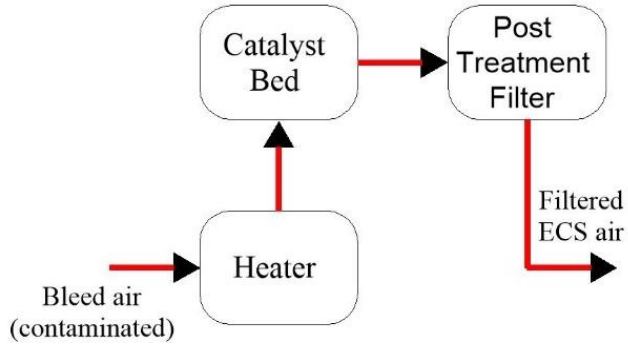

Fig. 11. Illustration of a Typical Catalytic Oxidation System [24]

The last type of NBC filters is the regenerable filter. It has sorption technologies based on pressure swing adsorption (PSA) and temperature swing adsorption (TSA) methods. A typical PSA system used two beds for adsorption, one is online, and the other is offline. It has three steps for each bed in the cycle: production, depressurization, and purge, as shown in Figure 12.

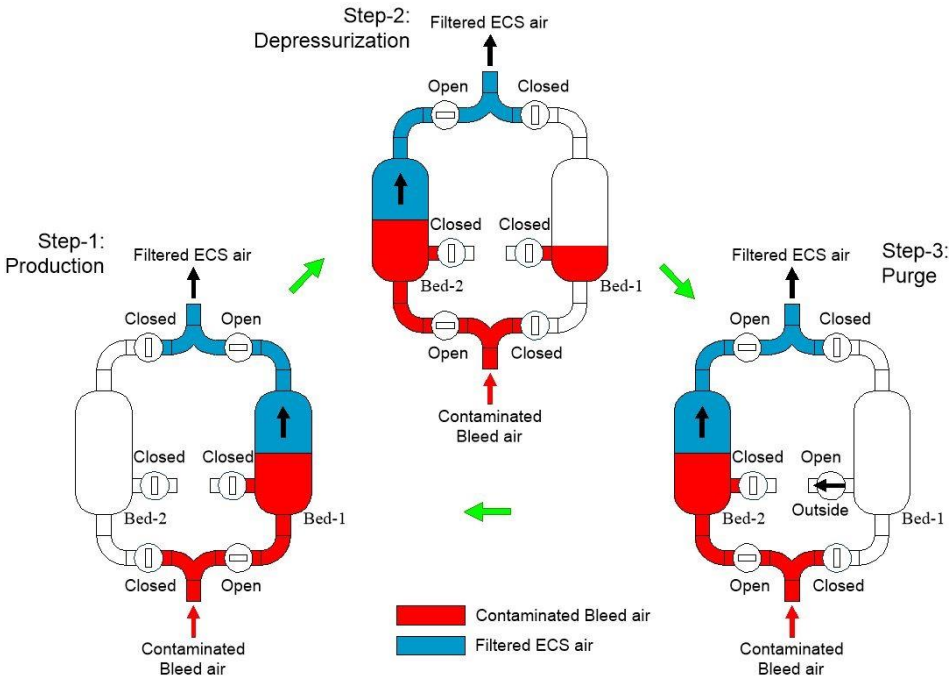

Fig. 12. Illustration of a Typical PSA cycle [82]

Step 1, which is production, involves a supply of contaminated air from the outside to the bed-1 (vessel) containing an adsorbent in high pressure. High pressure keeps the contaminants on the surface of the adsorbent; the purified air is fed to the cockpit. When the bed-1 is full of contaminated air, the air supply is directed to the bed-2 in Step-2 which

is depressurization. The inlet and outlet lines of the bed-1 are closed, and the pressure inside the vessel decreases prior to the purge. When the pressure is decreased in the vessel, the contaminants held on the surface are released and exhausted to the outside by the purge valve in Step 3, which is purge. These three steps repeat themselves in a loop based on the pressure change in the vessel which is called the pressure swing method. TSA uses a similar method with PSA except that it is based on temperature cycles instead of pressure cycles.

In an open-loop configuration, ECS continuously draws air from external sources, primarily through the engine bleed port [83]. Subsequently, it filters the air, refrigerates it, distributes it to pressurized compartments, and eventually discharges it overboard [84, 85]. Given that bleed air originates from the ambient environment, it may contain contaminants if the aircraft is operating within an NBC environment. Consequently, it is imperative to decontaminate the bleed air before supplying it to the cockpit and avionics bay. Although high temperatures (ranging from 400 to 650°C for the high-pressure stage) encountered in the engine bleed air can eliminate certain NBC contaminants, some may still bypass this process due to short dwell times in the bleed air system [24]. To address this, NBC filters are installed along the conditioned bleed air lines before supplying air to the cockpit and avionics bay, as depicted in Figure 13. This approach, known as "Clean Cockpit and Clean Avionics Bays," ensures effective NBC protection [24].

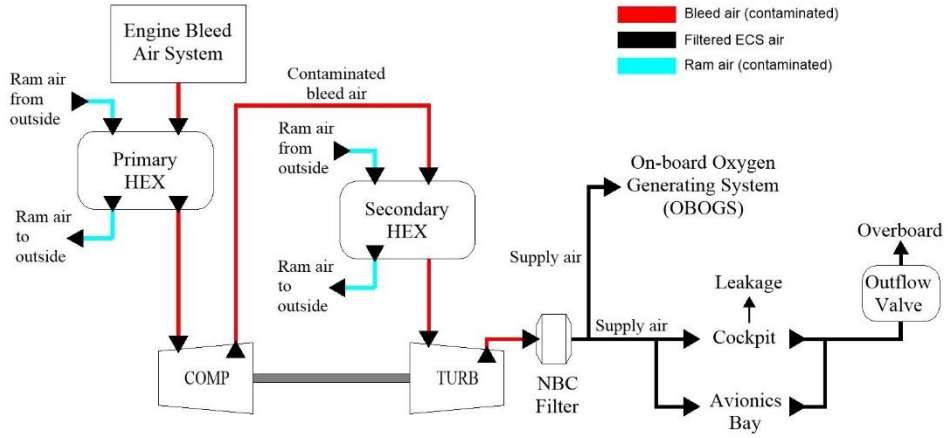

Fig. 13. Illustration of an Open-Loop ECS Configuration with NBC Filter [64]

In a more prevalent configuration, the NBC filter is positioned downstream of the compressor, ensuring purified air is supplied to both the cockpit and the avionics bay. However, in this setup, ECS components located upstream of the NBC filter may be vulnerable to contamination risks. To mitigate this, decontamination procedures can be implemented for the components situated upstream of the NBC filter on the ground, thus mitigating the risk of contamination. Alternatively, positioning the NBC filter upstream of the compressor can provide enhanced protection, albeit requiring stringent qualification standards for the filter to operate reliably, including resistance to high temperatures and pressures. Nonetheless, this placement may potentially compromise the compressor's performance due to significant pressure reduction caused by the NBC filter.

In contrast to the open-loop ECS configuration, the partial closed-loop ECS configuration does not continually draw bleed air. Instead, it draws air once and recirculates it within the cockpit, reducing reliance on bleed air [86]. Compensating for air leakage from pressurized compartments, excess air dump through outflow valves, and supplying air to the oxygen generating system is achieved through bleed air supply, as illustrated in Figure

14. NBC filters are strategically positioned upstream of the ECS mixing manifold to eliminate contaminants before the air is supplied to compartments and other customer services such as On-Board Oxygen Generating Systems (OBOGS). Additional filters may be incorporated into the cockpit recirculation airline if deemed necessary.

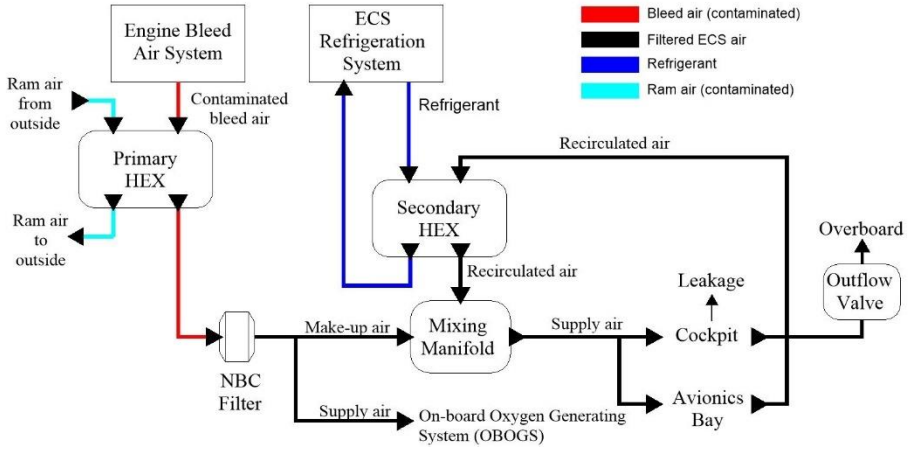

Fig. 14. Illustration of a Partial Closed-Loop ECS Configuration with NBC Filter [64]

It is crucial to carefully consider the selection of ECS configuration, considering various factors such as aircraft capabilities, mission duration, mission risk, and the required level of NBC protection. Different configurations offer distinct advantages in ensuring a safe environment within the aircraft, as summarized in Table 6.

Aircraft limitations, including ECS weight, power budget, and installation area, must be considered. In this context, the open-loop ECS configuration typically proves to be a more suitable solution for small aircraft, whereas the partial closed-loop ECS configuration offers comprehensive NBC protection for larger aircraft.

Mission duration is another critical parameter influencing ECS configuration selection for NBC protection. For short-duration missions with acceptable risk levels, the open-loop ECS configuration may suffice, as NBC effects on the aircraft are typically brief. Conversely, for longer missions where the risk of NBC contamination is higher, the partial closed-loop ECS configuration is recommended to provide enhanced protection.

The sizing of the NBC filter is determined by the flow rate of contaminated air passing through it. In the open-loop ECS configuration, the filter must be sized to accommodate all outside air supplied to the cockpit, while in the partial closed-loop ECS configuration, it is sized only for the make-up air flow rate since air circulates within the cockpit. Additionally, the open-loop configuration is more prone to filter saturation due to higher contaminant concentrations, increasing maintenance workload and risk. Maintenance requirements thus play a crucial role in ECS configuration selection.

In terms of NBC contamination exposure, the open-loop ECS exposes the cockpit air directly to NBC contaminants, as it filters all outside air. In contrast, the partial closed-loop configuration limits direct contact with contaminants, as air circulates within the cockpit, with contact occurring only when make-up air is required.

Table 6. Comparison of open-loop and partial closed-loop ECS configurations

Parameter *	Open-loop ECS configuration	Partial Closed-loop ECS configuration
Aircraft capability	Fit to small aircraft	Fit to larger aircraft
Mission's duration	Fit to the short missions	Fit to the longer missions
NBC risk	Fit to the missions with low NBC risk	Fit to the missions with high NBC risk
Filter Capacity	All air	Make-up air
Filter Failure	Higher possibility of filter saturation due to the high concentration of the contaminants	Lower possibility of filter clogging
Maintenance workload	Higher due to a higher risk of contamination	Lower due to lower risk of contamination
Contaminated air	All air direct contact with contaminated air has a higher risk of contamination.	Make-up air direct contact with contaminated air lowers the risk of contamination.

*: Parameters are selected considering the health risk due to contamination. Performance and cost parameters, such as bleed air penalty, weight, noise, fuel consumption, complexity, and cost, are not considered since they may depend on the specific information from the aircraft's manufacturer or component's supplier.

3. Conclusions

Collective NBC protection in military aircraft offers significant advantages by eliminating the need for individual NBC protection equipment, thereby enhancing crew safety and operational efficiency. This approach not only safeguards crew members from the discomfort and potential risks associated with individual protective gear but also ensures the integrity of avionics systems by obviating the need for post-flight decontamination.

To optimize the effectiveness of collective NBC protection, key design concepts such as hardening, air-tight construction, and advanced filtering mechanisms must be incorporated into the Environmental Control System (ECS). These features enable the ECS to maintain full operational capability throughout the entirety of a mission in an NBC environment, without degradation.

Furthermore, the selection between open-loop and partial closed-loop ECS configurations should be based on careful consideration of aircraft capabilities, mission duration, risk factors, and the desired level of protection. While open-loop ECS offers advantages in terms of weight, power, and installation area constraints, it provides less comprehensive protection compared to partial closed-loop ECS, particularly during extended missions where the risk of NBC contamination is higher.

The size and maintenance requirements of NBC filters are directly influenced by airflow rates, with open-loop ECS necessitating larger filters due to the filtration of all outside air. However, partial closed-loop ECS configurations require smaller filters, as they only filter make-up air. Additionally, the risk of filter saturation and failure is mitigated in partial closed-loop ECS, reducing maintenance workload and enhancing overall system reliability.

Ultimately, the adoption of a partial closed-loop ECS configuration presents a lower risk of contamination throughout the duration of a flight, as recirculated air remains isolated from NBC contaminants. By carefully considering these factors and implementing appropriate design strategies, military aircraft can ensure robust collective NBC protection while

maintaining operational flexibility and efficiency. The findings of this review present a wealth of opportunities for future research and development in the realm of collective NBC protection for military aircraft. Building upon the insights gleaned from this study, researchers can delve deeper into several areas ripe for exploration.

Firstly, further investigations could focus on refining and optimizing the design concepts of hardening, air-tight construction, and filtering within ECS systems to ensure uninterrupted operational capability throughout extended durations in NBC environments. By honing these design elements, future studies can strive to enhance the effectiveness and reliability of collective NBC protection measures.

Moreover, there is a pressing need for research into the development of advanced ECS configurations that strike a delicate balance between protection efficacy and resource constraints. Studies could delve into exploring innovative approaches to ECS design, considering factors such as aircraft capabilities, mission duration, and risk levels to tailor solutions that maximize protection while minimizing associated burdens on weight, power, and installation space. Additionally, investigations into the performance and durability of NBC filters within ECS systems warrant attention. Future studies may seek to optimize filter sizing and airflow rates to mitigate the risk of premature saturation and failure, thereby reducing maintenance workload and enhancing overall system reliability.

Furthermore, comparative studies between open-loop and partial closed-loop ECS configurations could provide valuable insights into the trade-offs between protection levels and operational constraints. By systematically evaluating the performance and effectiveness of these configurations under various mission scenarios, researchers can inform decision-making processes regarding ECS selection and deployment strategies.

Overall, the outcomes of this review serve as a catalyst for further inquiry and innovation in the field of collective NBC protection for military aircraft. Through collaborative efforts and interdisciplinary research endeavors, the potential exists to propel advancements that safeguard both crew and aircraft against the evolving threats of NBC contamination.

Nomenclature

ABC	Atomic, biological, and chemical
CBRN	Chemical, biological, radiological, and nuclear
ECS	Environmental control system
EMACC	European military airworthiness certification criteria
HEPA	High-efficiency particulate filter
MOPP	Mission-oriented protective posture
NBC	Nuclear, biological, and chemical
OBOGS	On-board oxygen generating system
PSA	Pressure swing adsorption
TSA	Temperature swing adsorption

References

[1] European Commission Joint Research Centre (JRC). Chemical, biological, radiological and nuclear hazards. [Internet]. [cited 2024 Jan 16]. Available from: [https://commission.europa.eu/about-european-commission/departments-and-executive-agencies/joint-research-centre_en].

[2] Robinson JP, editor. The Routledge Handbook of Nuclear, Biological and Chemical Weapons. Routledge; 2009.
[3] Oppenheimer A, editor. Jane's nuclear, biological and chemical defence 2010-2011. Jane's Information Group; 2010.
[4] Garrett BC, Hart J. Historical dictionary of nuclear, biological, and chemical warfare. Lanham, MD: Scarecrow Press; 2007.
[5] Federal Office for Civil Protection (FOCP). The NBC Protection. [Internet]. [cited 2024 Jan 16]. Available from: [https://www.nccs.admin.ch/nccs/en/home/the-nccs/about-the-nccs/organisation/members-and-partners/federal-office-for-civil-protection-FOCP.html]
[6] U.S. Army. NBC Decontamination. [Internet]. [cited 2024 Jan 16]. Available from: [https://www.army.mil/]
[7] Clements BW. Nuclear and radiological disasters. In: Disasters and public health. Elsevier; 2023. p. 211-236. https://doi.org/10.1016/B978-1-85617-612-5.00014-7
[8]National Aeronautics and Space Administration. Introduction to the Electromagnetic Spectrum. NASA Science. [Internet]. [cited 2024 Jan 16]. Available from: [https://science.nasa.gov/ems/01_intro/].
[9] Morton H, Johnson C. Chemical, biological, radiological and nuclear major incidents. Surgery (Oxford). 2021;39(7):416-422. https://doi.org/10.1016/j.mpsur.2021.05.005
[10] U.S. Department of the Army. Field Manual 8-9. U.S. Government Printing Office; 1996.
[11] National Environment Agency. Radiation basics. [Internet]. Available from: https://www.nea.gov.sg/our-services/radiation-safety/understanding-radiation/radiation-basics. Last accessed: 16 January 2024.
[12]Motchenbacher CD, Connelly JA. Low-noise electronic system design. Wiley Interscience; 1993. ISBN: 0-471-57742-1.
[13] Adams GE, Smith TD. The effects of radiation on electronic systems. Springer Netherlands; 1981.
[14] Berger HW. Radiation effects in semiconductors. CRC Press; 2000.
[15] Messenger SR. Single-event effects in integrated circuits. Springer Science & Business Media; 2004.
[16] Dodd PE, Masuda M, Virtanen A. Radiation hardening techniques for emerging technologies. Nature Electronics. 2022;5(4):268-281. doi:10.1038/s41928-022-00804-y.
[17] Saltmarsh RB. Nuclear radiation effects on electronic components. In: Macdonald JR, editor. Radiation effects in electronics. CRC Press; 1999; 215-275.
[18] Murgai VS. Radiation effects in semiconductor devices. In: Hamamatsu HC, Sawaki N, editors. Radiation effects on semiconductors. Springer Netherlands; 2001. p. 217-240.
[19] Lanford WA. Ionizing radiation effects on materials and devices. In: Macdonald JR, Freeman WT, editors. Radiation effects in electronics. CRC Press; 2007; 277-317.
[20] Solovyev AV. Protection of electronic systems from nuclear radiation. Springer-Verlag New York Inc; 2011.
[21] Bulinski AT, Petrenko AA. Radiation hardening of electronics. CRC Press; 2013.
[22] Saalbach KP. Biological warfare. In: Schaechter M, editor. Encyclopedia of microbiology. 4th ed. Elsevier; 2019. p. 520-525. https://doi.org/10.1016/B978-0-12-801238-3.62160-8
[23] Shuvo II, Dolez PI. Design of a military protective suit against biological agents. In: Hu F, Miao J, editors. The Textile Institute Book Series. Academic Press; 2023; 141-176. https://doi.org/10.1016/B978-0-323-91593-9.00009-2
[24] Society of Automotive Engineers. NBC Protection Considerations for ECS design (SAE AIR 4362A). 2014.
[25] Aly MA. Biocontamination of Avionics: A Review of Current Knowledge and Future Directions. MDPI; 2018.
[26] Patel KK. Biological effects on avionics and aircraft systems. Springer Nature; 2020.

[27] Chen CH. Protecting avionics from biological threats: A comprehensive guide. InTech; 2021.
[28] Smith JJ. Biological contamination of avionics: Prevention, detection, and response. CRC Press; 2022.
[29] Ali NA. The challenges and opportunities of protecting avionics from biological agents. Frontiers. 2023.
[30] U.S. Department of the Army. Chemical, biological, radiological, and nuclear platoons (ATP 3-11.74). 2011.
[31] Fletcher CD. Effects of ionizing radiation on living tissues. Oxford University Press; 1997.
[32] Narayanan VR. Biological Effects of Radiation. Elsevier; 2008.
[33] United Nations Scientific Committee on the Effects of Atomic Radiation (UNSCEAR). The health effects of radiation exposure. United Nations; 2020.
[34] Murray PR, Rosenthal KS, Pfaller MA. Medical microbiology. 9th ed. Elsevier; 2020.
[35] Russell DA. The anthrax handbook. Springer-Verlag New York Inc; 2003.
[36] Luchansky DB. Botulinum Neurotoxins. Marcel Dekker Inc; 2000.
[37] Gupta RC. Handbook of toxicology of chemical warfare agents. Academic Press; 2009.
[38] Wilkinson TC. Chemical warfare agents: Toxicology and treatment. Medical Chemical Publishing; 2004.
[39] Sidell FR, Goodman EH, Willson TD, editors. Medical aspects of chemical warfare. Office of the Surgeon General, U.S. Army Medical Department, Center for Countermeasures; 2009.
[40] The International Federation of Red Cross and Red Crescent Societies (IFRC). Chemical, biological, radiological and nuclear (CBRN) hazards; 2022.
[41] Bland SA. Chemical, Biological, Radiological and Nuclear (CBRN) Casualty Management Principles. In: Conflict and Catastrophe Medicine. Springer; 2013. p. 747-770. https://doi.org/10.1007/978-1-4471-2927-1_46
[42] Doran BM. The Human and Environmental Effects of CBRN Weapons [Student Theses, Fordham University]. Fordham Research Commons; 2015.
[43] Klare MT. The Next Great Arms Race. Foreign Affairs. 1993;72(3):136–152. https://doi.org/10.2307/20045628
[44] Department of Defense. Airworthiness Certification Criteria (MIL-HDBK-516C); 2014.
[45] European Defence Agency. European Military Airworthiness Certification Criteria (EMACC); 2018.
[46] U.K. Ministry of Defence. Certification Specifications for Airworthiness Part 13: Military Common Fit Equipment (00-970); 2020.
[47] Zahradníček R, Otřísal P, Skaličan Z. CBRN consequence management: New approach and possibilities of participation of chemical units. Security and Defence Quarterly. 2016;10(1):147-163. https://doi.org/10.5604/23008741.1215432
[48] U.S. Department of Army. Field Manual: NATO Handbook on the Medical Aspects of NBC Defensive Operations (FM 8-9). U.S. Army Medical Department; 1996.
[49] U.S. Department of Army. Field Manual: NBC Protection (FM 3-4/11-9). U.S. Army Medical Department; 1992.
[50] U.S. Department of Army. Field Manual: Multiservice Tactics, Techniques, and Procedures for Nuclear, Biological, and Chemical (NBC) Protection (FM 3-11.4). U.S. Army Medical Department; 2003.
[51] Janssen L, Johnson AT, Johnson JS. Chemical, Biological, Radiological, and Nuclear (CBRN) Respiratory Protection Handbook. National Institute for Occupational Safety and Health; 2018.
[52] Johnson AT, et al. Respirator masks protect health but impact performance: a review. Journal of Biological Engineering. 2016;10(1):125-136. https://doi.org/10.1186/s13036-016-0025-4
[53] Department of Defense. Human Engineering (MIL-STD-1472G); 2012.

[54] Buchberg H, Harrah CB. Conduction Cooling of the Human Body - A Biothermal Analysis. In: Thermal Problems in Biotechnology. ASME Symposium Series; 1968. p. 82-95.
[55] Cole RD. Heat Stroke During Training with Nuclear, Biological and Chemical protective Clothing: Case Report. Military Medicine. 1983;148(7):624-625. doi:10.1093/milmed/148.7.624. https://doi.org/10.1093/milmed/148.7.624
[56] Fanger PO, Nevins RG, McNall PE. Predicted and Measured Heat Losses and Thermal Comfort Conditions for Human Beings. In: Thermal Problems in Biotechnology. Winter Annual Meeting of the ASME; 1968. p. 111-126.
[57] Harrison MH, Higenbottam C. Heat Stress in an Aircraft Cockpit During Ground Standby. Aviation, Space, and Environmental Medicine. 1977;48(6):519-523.
[58] Hwang CL, Konz SA. Engineering Models of the Human Thermoregulatory System- A Review. IEEE Transactions on Biomedical Engineering. 1977;24(4):309-25. https://doi.org/10.1109/TBME.1977.326137
[59] Stribley R, Nunneley SA. Physiological requirements for design of environmental control systems: Control of heat stress in high performance aircraft. ASME Paper presented at the Intersociety Conference on Environmental Systems (78-ENAS-22); 1978. p. 1-8.
[60] Wing JF. Upper Thermal Tolerance Limits for Unimpaired Mental Performance. Aerospace Medicine. 1965;36(10):960-964.
[61] Wissler EH. Mathematical Simulation of Human Thermal Behavior Using Whole Body Models. In: Heat Transfer in Medicine and Biology. Springer, New York, NY; 1985. p. 325-374.
[62] Shender BS. Predictions of Human Tolerance to Heat Stress While Wearing Advanced Integrated Suit Concepts During Simulated Realistic Combat Scenarios. Naval Air Warfare Center, Aircraft Division Warminster Report No. NAWCADWAR-94136-60; 1993.
[63] Johnson AT. Biomechanics and exercise physiology: quantitative modeling. Boca Raton, FL: Taylor & Francis; 2007. https://doi.org/10.1201/b15850
[64] Güler E. Compliance Strategy for the Certification of Environmental Control System in Military Applications. Mühendis ve Makina; 2024. https://doi.org/10.46399/muhendismakina.1257053
[65] Society of Automotive Engineers Standard. Airplane Cabin Pressurization (SAE ARP 367C); 1963.
[66] Moir I, Seabridge A. Environmental control systems. In: Aircraft systems. 3rd ed. John Wiley & Sons; 2022. p. 259-295.
[67] Pedley MD. Materials and Processes Branch. In: Safety Design for Space Systems. Elsevier; 2023. p. 401-420. https://doi.org/10.1016/B978-0-323-95654-3.00028-6
[68] National Aeronautics and Space Administration (NASA) Standard. Flammability, Odor, Offgassing, and Compatibility Requirements and Test Procedures for Materials in Environments that Support Combustion (NASA STD 6001); 1998.
[69] Society of Automotive Engineers Standard. Conformal Coatings for Panels, Printed Circuit and Panels, Electronic Circuit
[70] Snedeker KG, Pike TW. Electronic circuit protection technology. CRC Press; 1984.
[71] Haba M. Conformal coating technology for improved circuit reliability. TT Electronics; 2018.
[72] Department of Defense. Insulating Compound, Electrical (For Coating Printed Circuit Assemblies). (MIL-I-46058C); 1966.
[73] Society of Automotive Engineers Standard. Cooling of Military Avionic Equipment (SAE AIR 1277B); 2005.
[74] Department of Defense. CB Collective Protection of Mobile Vehicles, Vans and Shelters (MIL-HDBK-753); 1971.
[75] Ernsberger RR, editor. Handbook of seals and sealing. Elsevier; 2014.

[76] Anderson JD Jr, Raymer JC. Aerospace Engineering. McGraw-Hill Education; 2014.
[77] Sauter R, Shevell WS. Aircraft Environmental Control Systems. American Institute of Aeronautics and Astronautics; 2012.
[78] Boer ER, Schijve JL. Aerospace seals: A handbook for design and engineering. Elsevier; 2011.
[79] Saraçyakupoğlu T. Major Units and Systems in Aircraft. In: Kuşhan MC, Gürgen S, Sofuoğlu MA, editors. Materials, Structures and Manufacturing for Aircraft. Sustainable Aviation. Springer; 2022. https://doi.org/10.1007/978-3-030-91873-6_10
[80]Morrison RW. NBC Filter Performance. U.S. Army Soldier and Biological Chemical Command; 2001. https://doi.org/10.21236/ADA397007
[81] Tarraf M, Soltan M, Elweteedy A. Gas Phase Air Cleaning Using Catalytic Oxidation. In: International Conference on Aerospace Sciences and Aviation Technology; 2013. https://doi.org/10.21608/asat.2013.22271
[82] Singh B, Singh VV, Boopathi M, Shah D. Pressure swing adsorption based air filtration/purification systems for NBC collective protection. Defence Life Science Journal. 2016;01(2): https://doi.org/10.14429/dlsj.1.10737
[83] Society of Automotive Engineers Standard. SAE Aerospace Applied Thermodynamics Manual Aerothermodynamic Systems Engineering and Design (SAE AIR 1168-3A); 2019.
[84] Giorgi L. Design of Innovative Environmental Control Systems for high-speed commercial aviation [Master's thesis]. The University of Politecnico di Torino Research Repository; 2019.
[85] Poudel S. Modelling of a Generic Aircraft Environmental Control System in Modelica [Master's thesis]. Diva Portal Research Repository, Linköping University; 2019.
[86] Edgar JM, Campbell B. Evaluation and Control of an Integrated Closed Environmental Control System (ICECS). SAE Transactions. 1990;99:545–560. https://doi.org/10.4271/901237

Research on Engineering Structures & Materials
www.jresm.org
Research Group

Research Article

Probabilistic investigation of the pounding effect in steel moment resisting frames with equal and unequal heights

Abbasali Sadeghi[*1,a], Hamid Kazemi[2,b], Mohammad Hossein Razmkhah[3,c], Amirreza Sadeghi[4,d]

[1]*Department of Civil Engineering, Birjand Branch, Islamic Azad University, Birjand, Iran*
[2]*Department of Civil Engineering, Mashhad Branch, Islamic Azad University, Mashhad, Iran*
[3]*Department of Civil Engineering, Semnan University, Semnan, Iran*
[4]*Department of Civil Engineering, University of Birjand, Birjand, Iran*

Article Info

Article history:

Received 12 Oct 2023
Accepted 23 Mar 2024

Keywords:

Steel moment resisting frame (SMRF);
Pounding;
Gap;
Incremental dynamic analysis (IDA);
Fragility curve;
Kriging meta-model

Abstract

In this research, the influence of the pounding phenomenon of two adjacent steel moment resisting frames (SMRFs) with 2 and 5-story with an intermediate ductility is investigated by considering equal and unequal heights under seismic excitations. In this way, two scenarios are applied. The first and second scenarios are related to the pounding of two SMRFs with an equal height (both frames with 2-story) and an unequal height (2-story and 5-story frames), respectively. In the following, at first, sensitivity analysis is conducted by the Monte Carlo simulation (MCS) method. Then, the collapse performance of the studied SMRFs is evaluated by incremental dynamic analysis (IDA), and fragility curves under 14 far-fault records and also, the failure probability is predicted by the Kriging meta-model. The results of sensitivity analysis indicate that the yield strength of cross-sections and dead load were the greatest effect on failure probability computation. Also, in the statistical level of 50%, the collapse probability of SMRFs with an equal height is 17% compared to the SMRFs with an unequal height. Also, the results of the Kriging meta-model show that the failure probability is increased by 65% in an unequal height versus an equal height.

1. Introduction

Today, in cities with high population density, the minimum gap among adjacent structures is an important issue due to the fluctuation of buildings during seismic excitations, and various codes in this field have specified the minimum distance to prevent buildings from colliding [1, 2]. The conducted studies in the field of structural damage in past earthquakes show that adjacent buildings with partial discontinuity or with a common wall between two structures may suffer serious damage during an earthquake and even go to the point of collapse [3, 4]. Kamal and Inel showed that pounding phenomenon may alter the dynamic features of two adjacent buildings significantly [5]. The pounding problem was first numerically modeled for single-degree-of-freedom (SDOF) structures [6-8], and then for multi-degree-of-freedom (MDOF) structures, these analyses were performed numerically with concentrated mass [9, 10], and then for three adjacent buildings, numerical analyses related to pounding were also performed [11, 12]. Past earthquakes have shown that the pounding issue is a serious topic for tall buildings in the vicinity whose floors are not on the same level [13-17]. Another important reason for the pounding issue

*Corresponding author: abbasali.sadeghi@mshdiau.ac.ir
[a] orcid.org/0000-0002-3016-9080; [b] orcid.org/0000-0003-2590-1051; [c] orcid.org/0000-0001-5463-308X; [d] orcid.org/0009-0007-0468-7718
DOI: http://dx.doi.org/10.17515/resm2024.07ma1012rs

is that different natural frequencies of adjacent buildings may vibrate out of phase [5]. Eftychia et al. [19] evaluated the influence of base isolation on the impact of two buildings and Forcellini [20] studied the effect of the interaction of soil and structure on the pounding phenomenon. The results of this research showed that the deformation of the soil during an earthquake causes the pounding phenomenon is intensified. Also, past studies about steel moment resisting frames (SMRFs) are presented in the following. The fragility behavior of SMRFs is evaluated subjected to vehicle impact by Sadeghi et al. [21] and in another research by Sadeghi et al. [22], the weight of SMRFs is optimized under vehicle collision by using optimization algorithms. Saberi et al. [23] assessed the effect of fire on SMRFs. The results of this paper showed that by varying each of the factors, the damage modes are changed considering to the thickness of connections under fire loadings.

2. Research Significance

By reviewing past technical studies, it is revealed that the debated topic is novel and new. Therefore, in this paper, as a research significance and contribution part, the effect of pounding phenomenon between two adjacent SMRFs with equal and unequal heights has been investigated by presenting the probabilistic framework. In this way, two scenarios are utilized. The first and second scenarios are related to the pounding of two SMRFs with an equal height (both frames with 2-story) and an unequal height (2-story and 5-story frames), respectively.

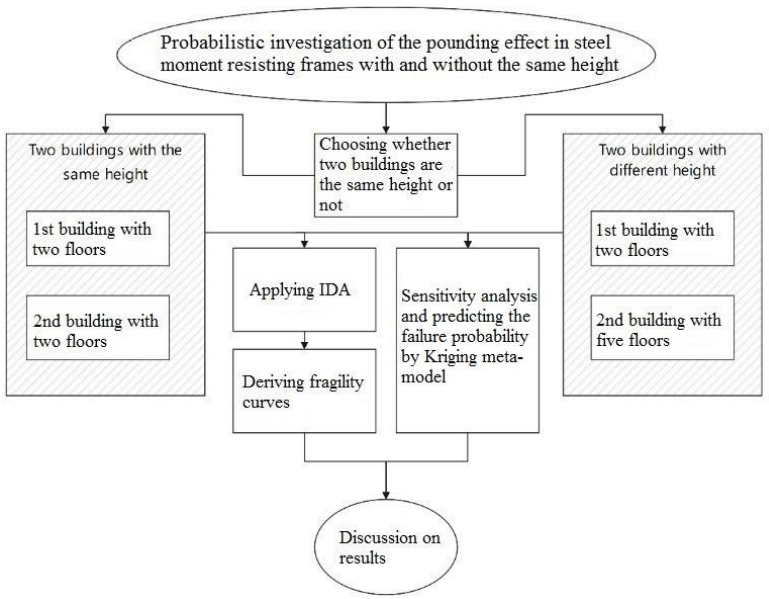

Fig. 1. The flowchart of the current research

In the following, the sensitivity analysis of random variables of SMRFs is performed under the influence of pounding phenomenon and the effective random variables are specified by using the Monte Carlo simulation (MCS) method, then, incremental dynamic analysis (IDA) has been performed in OpenSees software [24] under 14 far-fault records to evaluate this issue probabilistically, and the amount of damage has been assessed by using the fragility curves. In the following, for the first time, the Kriging meta-model is used to

predict the failure probability for studied SMRFs. It is noted that the probabilistic framework for SMRFs with and without an equal height under the effect of pounding has not been investigated from this point of view. Fig. 1 indicates the flowchart of this research.

3. Theoretical Fundamentals

In this part, the technical concepts related to present a probabilistic framework of SMRFs with equal and unequal heights under the effect of pounding phenomenon are introduced. In this route, the technical fundamentals such as IDA, fragility curves, MCS method, sensitivity analysis, and Kriging meta-model are elaborated point by point.

3.1 IDA and Fragility Curves

IDA is a probabilistic numerical method for assessing the performance of structures against seismic records. The volume of produced data is huge in this method and presents the probabilistic framework for indicating the seismic behavior of structures. In this method, the intensity of earthquake records is amplified incrementally until the structural responses of structures achieve the intended performance levels. In The following, the fragility curve expresses the probability of failure corresponding to a certain damage mode in several levels of seismic excitations. In fact, the fragility curve describes the ratio between the intensity of the earthquake and the level of possible seismic damage. To accurately determine such a ratio, it is important to choose the correct intensity of the earthquake in the location of the structure [25, 26]. In this paper, for IDA, damage measure and intensity measure are assumed to be the maximum drift ratio of the SMRFs and 5% damped first mode spectral acceleration, $S_a(T_1, 5\%)$, respectively, and fragility curves are depicted just for the collapse performance (CP) level. As a result, the collapse capacity of SMRFs with equal and unequal heights are computed under the occurrence of the pounding phenomenon. In the present research, fragility curves are depicted by assessing the results of IDAs curves, the statistical approaches are conducted in EasyFit software to extract fragility curves based on collapse limit state. For the above circumstances, fragility curves are achieved according to Eq (1) [25]:

$$Fragility\ (x) = P[S_a \geq S_{a,c} / S_a = x] = P[S_{a,c} \leq x] \quad (1)$$

In Eq (1), the function Fragility (x) is the value of the collapse limit state achieved by fragility curve for spectral acceleration (x) and showing collapse capacity of the *SMRFs*. The parameters S_a and $S_{a,c}$ are spectral acceleration and collapse capacity of *SMRFs*, respectively.

3.2 MCS Method

MCS is a probabilistic method to compute the failure probability of structures. This method is widely used in reliability engineering. According to fundamentals of this method, MCS solves structural problems by statistical sampling of random parameters in mathematical way. In this way, Eq (2) shows the failure probability (P_f) of structural problems by using MCS method. Parameters x and g (x) are named as the uncertain quantities and the performance function of the structural systems, respectively [27].

$$P_f = \int_{g(x)\leq 0}^{\blacksquare} f_x(x)dx = \int_{\mathbb{X}}^{\blacksquare} \mathbb{I}_{g(x)\leq 0}(x)\ f_x(x)\ dx = \mathbb{E}_f\ (\mathbb{I}_{g(x)\leq 0}\ (x)) \quad (2)$$

Based on Eq (2), the parameters of $\mathbb{E}_f\ and\ f_x$ are defined as the expectation operator and the probability density function of uncertainties x and the functions $g(x) \leq 0\ and\ \mathbb{I}_{g(x)\leq 0}\ are$ indicated as the failure set and an index.

3.3 Sensitivity Analysis

In simulation methods, sensitivity analysis is often evaluated by computing the rate of change of failure probability to the statistical characteristics of each variable $\partial P_f / \partial P$ (P can be the mean or standard deviation of each variable) [27, 28]. The easiest way to estimate the results of sensitivity analysis by considering the simulation method is to use the MCS method based on Eq (3). By using the MCS, the rate of the above changes can be calculated with a single simulation (which estimates the failure probability) as follows:

$$\frac{\partial P_f}{\partial p} = \frac{\partial}{\partial p} \int I[g\,(x) < 0]\, f_{x(p)}(x) dx \tag{3}$$

In Eq (3), (f_x) is the probability density function of parameters and (I) is the counter vector. The need to derive the probability density function is one of the disadvantages of estimating sensitivity results by using Eq (3).

3.4 Kriging Meta-Model

The status of structural systems such as SMRF is evaluated in terms of reliability analysis by computing the failure probability mathematically. These failure probabilities are usually determined by structural damage levels. Therefore, the Kriging meta-model is an interpolation method to predict the response of specific data. Kriging meta-model approximates a function using a combination of basic functions. For interested readers, the surplus explanations about this method are presented in reference [27].

4. Modeling Verification

In this research, to verify the modeling procedure of the pounding phenomenon, the extracted results of OpenSees software are compared with the experimental results of Takabatake et al. (2014) [29]. In this regard, the investigated models are two three-dimensional 4-story samples with one span named F-A and F-B, 4. The global dimensions of these frames are 0.20 m, 0.15 m, and 0.60 m for width, depth and height, respectively. For more information about the features of experimental models, interested readers can refer to the research of Takabatake et al. (2014) [29]. The schematic view of the adjacent frames is presented in Fig. 2. The experimental and numerical models are indicated in Fig. 2 (a) and (b), respectively. In this research, for structural members, fiber cross-section has been used as an extended plasticity model. In these members, instead of the plasticization of the materials in certain points of the structure (such as points in the beam, which is near the column), the plasticization of the materials is considered distributed throughout the length of the member. In current paper, non-linear force beam-column members have been used to model the beam and column members. In the following, the number of threaded sections is 200 and the number of integration points along the length of the beam-column members is assumed to be 5. In the following, nonlinear dynamic time history analysis is conducted under the El-Centro earthquake record (1940). This record is scaled based on the maximum acceleration of 0.5 m/sec^2. Also, the number of time steps is equal to 6000 with a step of one to ten thousand. The considered damping for the models is as described in Reference [29]. In this regard, a model ELCN 2-0-0 in which only impact effects between two structures were included was selected to verify the results of analytical modeling. In addition, the GAP element has been used between two structures instead of the aluminum element. The comparison of the numerical modeling results of this paper and the reference model [29] is presented in Tables 1 and 2. In Table 1, the percentage of conformity of the period results of the reference model and the constructed model in OpenSees software is presented and in Table 2, the percentage of conformity of the maximum impact force of the two experimental and numerical models are compared with each other. The error rate of numerical modeling process versus Experimental setup in period and maximum impact

force is 3.48% and 3.19%, respectively. As a result, the outputs of the numerical modeling are in good agreement with the experimental results.

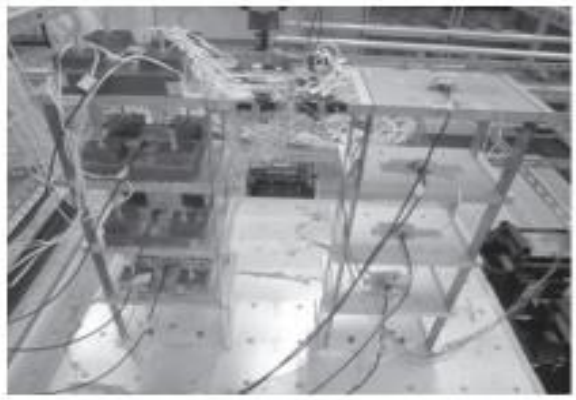

(a)

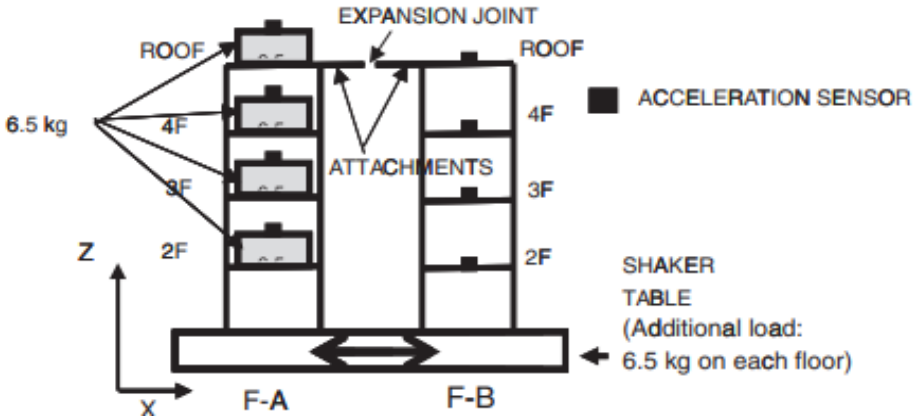

(b)

Fig. 2. The process of experiment [29] (a) The global view of experimental setup, (b) The schematic view of pounding phenomenon

Table 1. The comparison of period values of numerical and reference model [29]

Sample	F-A	F-B
Reference paper [29]	0.287 sec	0.135 sec
Present paper	0.277 sec	0.124 sec
Error rate (%)	3.48	8.14

Table 2. The comparison of maximum impact force values of numerical and reference model

Outputs	Maximum impact force
Reference paper [29]	61.48 kN
Present paper	63.51 kN

Error rate (%)	3.19

5. Modeling Procedure

In this study, 2 and 5-story SMRFs with intermediate ductility are designed based on ASCE07 [30] and AISC-360 [31]. Soil type D is considered for the designing procedure. The seismicity of the model was very high with high importance. The values of 1500 and 600 kg/m^2 are assumed for dead and live loads, respectively. The used steel in the structural components was ST37 with values of 200 GPa, 240 MPa, and 370 MPa for elasticity modulus, yield stress, and ultimate stress, respectively. For structural modeling, the Steel01 model is considered with a post-yielding stiffness of 3% [32]. Fig. 3 shows the building plan and determination of the exterior frame enclosed in the red rectangle. Fig. 4 (a) and (b) indicates the two-dimensional elevation of SMRFs with 2 and 5-story, respectively. Also, the designed cross-sections of structural components are introduced in Table 3.

In this research, to evaluate the performance of adjacent SMRFs under the effect of pounding caused by an earthquake, as equal height samples, two adjacent 2-story SMRFs and as unequal height samples, two adjacent 2 and 5-story SMRFs are considered. In modeling the impact of two frames on each other, the gap between the two frames is used according to the relations provided in ASCE07 [30]. For simulating the gap in this research, the nonlinear viscoelastic model is used [33, 34]. The Hertz contact model is utilized to consider the energy loss during impact. According to Fig. 5, a non-linear damper is built in parallel with the non-linear spring in this model and damping is omitted during the return phase. Therefore, energy loss in the return phase is not considered. ZeroLength element is used for impact modeling. This element is used to connect two nodes. In this element, until the gap between the two structures is filled, no force is created and the amount of slip and damping is zero.

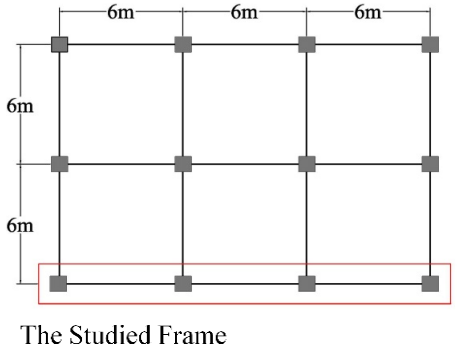

Fig. 3. Building plan view and location of the studied frame

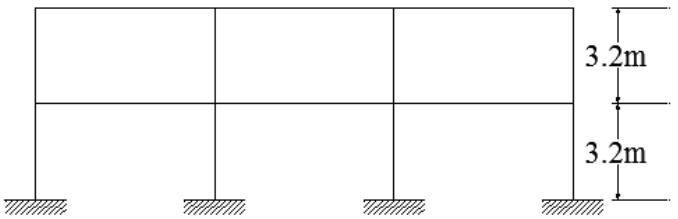

(a)

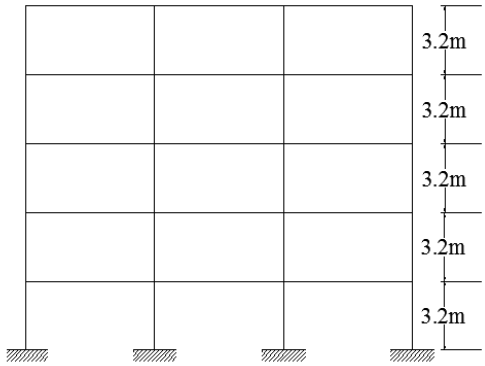

(b)

Fig. 4. The two-dimensional elevation of the studied models (a) 2-story SMRF, (b) 5-story SMRF

Table 3. The designed cross sections of structural components of the studied SMRFs

SMRF	Story	Beam		Column	
		Side span	Middle span	Side span	Middle span
2-story	1st story	IPE200	IPE220	BOX200*20	BOX200*20
	2nd story	IPE180	IPE200	BOX200*18	BOX200*18
5-story	1st story	IPE260	IPE280	BOX200*22	BOX200*25
	2nd story	IPE260	IPE260	BOX200*20	BOX200*22
	3rd story	IPE240	IPE260	BOX200*18	BOX200*20
	4th and 5th stories	IPE220	IPE240	BOX200*16	BOX200*16

After two structures collide with each other and by creating compression in the spring, a negative (compressive) force is created. After the separation of the two structures, the force returns to zero and no force is transferred in the tension state. For this element, elastoplastic properties are used in OpenSees software. Finally, Figs. 6 and 7 illustrate the configuration of two adjacent SMRFs with and without an equal height.

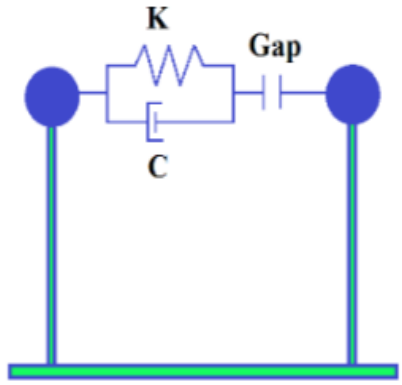

Fig. 5. The schematic of pounding model in adjacent SMRFs [33]

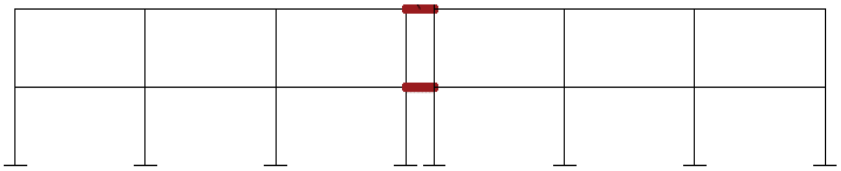

Fig. 6. The configuration of two adjacent SMRFs with an equal height

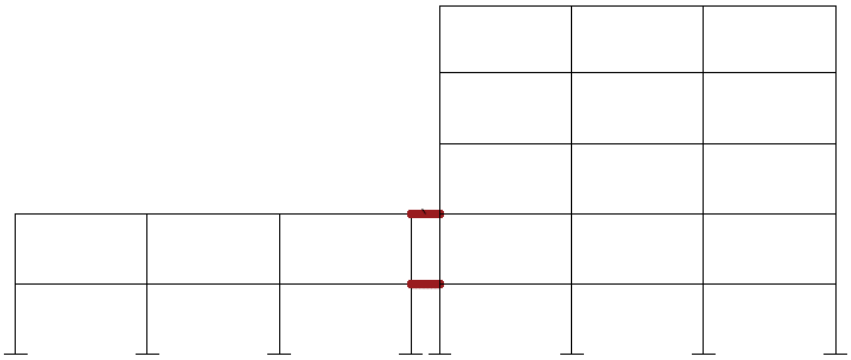

Fig. 7. The configuration of two adjacent SMRFs with an unequal height

5.1 Limit State Function

In this study, the failure probability is calculated based on the Kriging meta-model, taking into account the structural uncertainties for the pounding scenarios of adjacent SMRFs. To calculate the failure probability, since the considered structural system is non-linear, simulation methods are used to increase the accuracy. Therefore, it is necessary to determine the points in the health and failure areas first. For this purpose, the limit state function (LSF) of the reliability problem should be evaluated by structural analysis. At each time of structural analysis, random variables are defined according to Table 4 for the investigated structural models under the scenario of pounding of adjacent SMRFs based on the selected distribution. To save time, before calculating the failure probability, a sensitivity analysis is done and the random variables that have a negligible dependence on the change of the LSF are removed and other influential variables are considered definitively. The proposed LSF for the investigated models in this research is presented in the scenario of pounding of the adjacent SMRFs according to Eq (4):

$$g_1 = 0.1 - (Max(Drift)) \tag{4}$$

In Eq (4), Max (Drift) is the maximum drift of the structure at each time of analysis and the value of 0.1 is the collapse limit of the structure based on the regulations. Now, if $g_1>0$ after the analysis, the sample is in the healthy area, and if $g_1 \leq 0$, the sample is in the failure area. According to the different seismic codes, the values of drift equivalent to different performance levels of SMRFs have been presented [35, 36]. In transient deformations, drifts of 0.7%, 2.5%, 5%, and 10% show Immediate Occupancy (IO), Life Safety (LS), Collapse Prevention (CP), and Collapse (C) performance levels, respectively.

Table 4. The statistical features of random variables in this study

Category	Symbol	Description	Unit	PDF	Mean	c. o. v or σ	Reference
Gravity Load	DL	Dead load	kg/m	N*	1500	0.1	[37, 38]
	LL	Live load	kg/m	G*	600	0.4	[37, 38]
Material	F_y	Yield strength	MPa	LN*	240	0.07	[37, 39]
	E	Elasticity modulus	MPa	LN	$2*10^5$	0.03	[40, 41]
	ξ	Damping ratio	-	LN	5%	40	[41]
	ρ	Specific weight	kg/m^3	LN	7890	0.1	[39]
	ϑ	Poisson ratio	-	LN	0.3	0.1	[39]
Geometric	L	Beam length	m	N	6	0.0304	[39, 40]
	H	Column height	m	N	3.2	0.0304	[39, 40]

* N: Normal, LN: Lognormal, G: Gamma

5.2 Ground Motion Records

One of the main issues in evaluating the nonlinear dynamic analysis of structures is the selection of earthquakes and their number to obtain the results with appropriate accuracy. FEMA P 695 [42] suggests a set of near-fault and far-fault earthquake records for nonlinear dynamic analyses. This code presents the suitable earthquake records with different natures for calculating the collapse probability of structure. In this study, IDA has been performed with small and controlled steps.

Table 5. The features of the studied earthquakes

ID No.	Date	Event	Station	Magnitude (M_w)	Component	PGA[1] (g)	PGV[2] (cm/s^2)
R1	1994	Northridge, CA	Beverly Hills-Mulhol	6.7	NORTH/ MUL009	0.42	59
R2					NORTH/ MUL279	0.52	63
R3	1994	Northridge, CA	Canyon Country-WLC	6.7	000	0.41	43
R4					NORTH/ LOS270	0.48	45
R5	1999	Duzce, Turkey	Bolu	7.1	DUZCE/ BOL000	0.73	56
R6					DUZCE/ BOL090	0.82	62
R7	1999	Hector Mine, CA	Hector	7.1	HECTOR/ HEC000	0.27	29
R8					HECTOR/ HEC090	0.34	42
R9	1979	Imperial Valley, CA	Delta	6.5	IMPVAL/ H-DLT262	0.24	26
R10					IMPVAL/ H-DLT352	0.35	33
R11	1979	Imperial Valley, CA	El Centro Array # 11	6.5	IMPVAL/ H-E11140	0.36	35

R12					IMPVAL/ H-E11230	0.38	42
R13	1995	Kobe, Japan	Nishi-Akashi	6.9	KOBE/ NIS000	0.50	37
R14					KOBE/ NIS090	0.51	37

[1] Peak ground acceleration
[2] Peak ground velocity

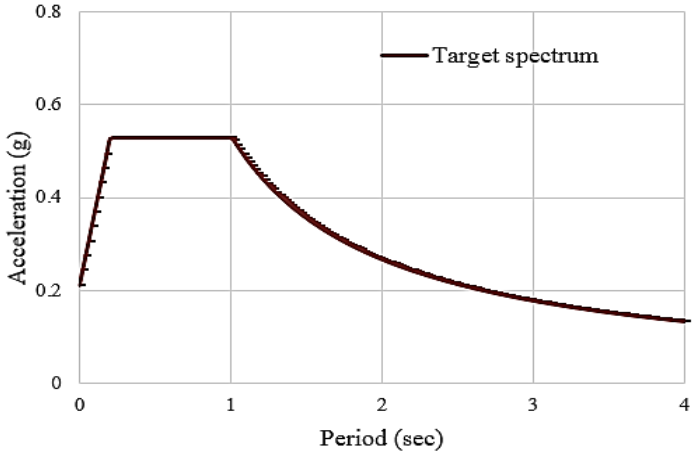

Fig. 8. Target spectrum of ASCE07 [30]

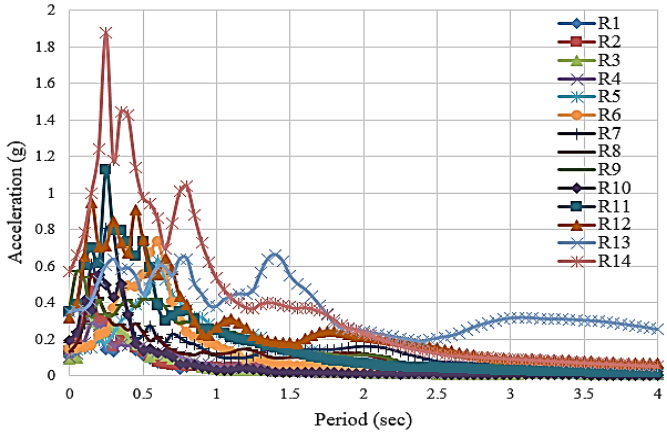

Fig. 9. Elastic acceleration spectrum for 5% damping of earthquake records used in this research

It is noted that IDA is a set of time history nonlinear dynamic analyses under different numerous records therefore selection of seismic records is an important step to assess the performance of structures probabilistically. Some researchers evaluate the influence of the features, content and number of the seismic excitations on the analysis results [43-50]. In this paper, these records are first scaled according to the peak ground velocity (PGV). Then, the spectral acceleration of all records in the period of the first mode of the structure (S_a (T_1, 5%)) was scaled. Also, target spectrum and an elastic acceleration spectrum for 5% damping of earthquake records used in this research are depicted based on Figs. 8 and 9. In this study, IDA is performed and IDA curves are plotted. In the following, for calculating

the seismic collapse capacity, the fragility curves of SMRFs adjacent to each other in two scenarios are obtained. Table 5 shows the features of the studied earthquakes.

6. Results and Discussion

6.1 Results of The Sensitivity Analysis

In this part, the sensitivity analysis of random parameters of studied SMRFs such as dead load, live load, yield strength, elasticity modulus, damping ratio, specific weight, Poisson ratio, beam length, and column height is checked by MCS method. In this way, the variation rate of failure probability to the statistical characteristics of each mentioned variable is assessed. The sensitivity analysis is performed by calling the LSF 100,000 times and by evaluating the rate of change of the failure probability compared to the changes of each random parameter, and the results of the sensitivity analysis are also presented in Table 6. It can be seen that for the desired models under the effect of pounding, the parameters with uncertainty of the yield strength of the cross-sections, and the dead load have the greatest effect and Poisson's ratio, the specific weight of the cross-sections, and the live load have the least effect on the calculation of failure probability.

Table 6. The results of the sensitivity analysis of the SMRF models under the effect of pounding

No.	Failure Probability Variation for Each Variable	
1	$(\partial Pf)/(\partial DL)$	0.0086146
2	$(\partial Pf)/(\partial LL)$	0.000064689
3	$(\partial Pf)/(\partial Fy)$	-0.032309
4	$(\partial Pf)/(\partial E)$	0.000090022
5	$(\partial Pf)/(\partial \xi)$	-0.000075751
6	$(\partial Pf)/(\partial \rho)$	-0.00006656
7	$(\partial Pf)/(\partial \vartheta)$	0.000037615
8	$(\partial Pf)/(\partial L)$	0.00021061
9	$(\partial Pf)/(\partial H)$	0.00066004

6.2 Results of IDA and Fragility Curves

According to Figs. 10 and 11, IDA curves of SMRFs with equal and unequal heights are presented under 7 pairs of far-fault earthquake records (equivalent to 14 earthquake record components) in OpenSees software. In addition, the fragility curves of the mentioned models are shown in Fig. 12.

According to Fig. 12, it can be seen that the seismic collapse capacity of SMRFs adjacent to each other with equal heights is high and they have more values of spectral acceleration versus adjacent SMRFs with unequal heights. Table 7 shows the spectral accelerations of the mentioned SMRFs for different statistical levels of 16%, 50%, and 84%.

Also, by conducting numerous time history nonlinear dynamic analyses, the comparison of maximum values of story displacement, story drift, story acceleration, and impact force of two adjacent SMRFs with the equal and unequal heights are reported based on Figs. 13 to 16. The extracted seismic responses of the studied models indicate that critical values of story displacement, story drift, story acceleration, and impact force are related to the two adjacent SMRFs with the unequal heights.

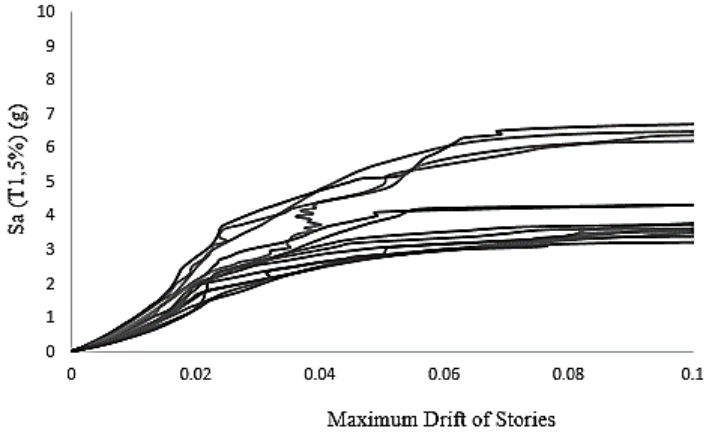

Fig. 10. IDA curves of two adjacent SMRFs with an equal height

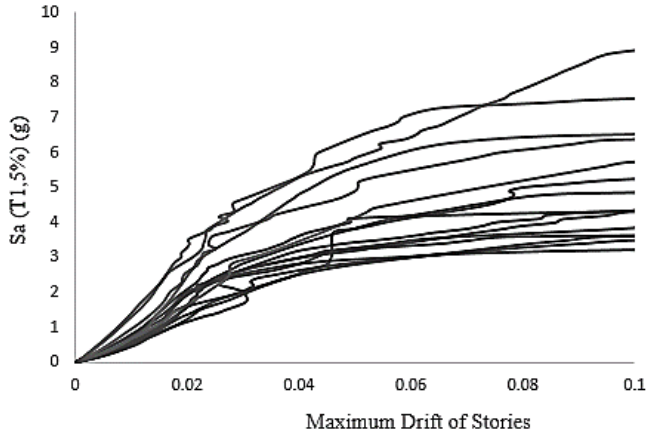

Fig. 11. IDA curves of two adjacent SMRFs with an unequal height

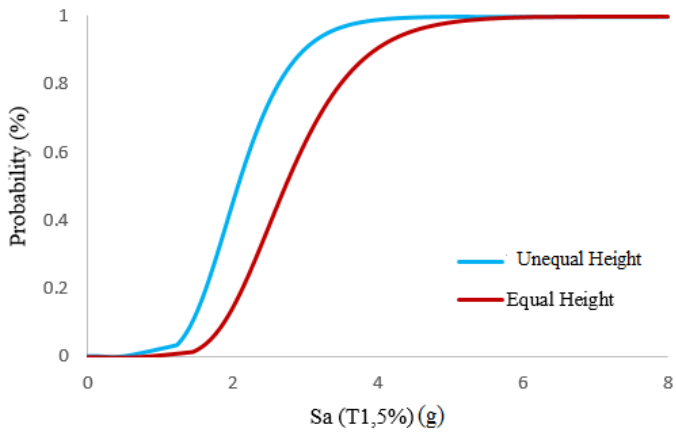

Fig. 12. Fragility curves of two adjacent SMRFs with the equal and unequal heights

Table 7. The spectral acceleration of SMRFs under the effect of pounding

Statistical levels	SMRFs with equal heights (g)	SMRFs with unequal heights (g)
16%	2	1.6
50%	2.3	1.9
84%	3.9	2.4

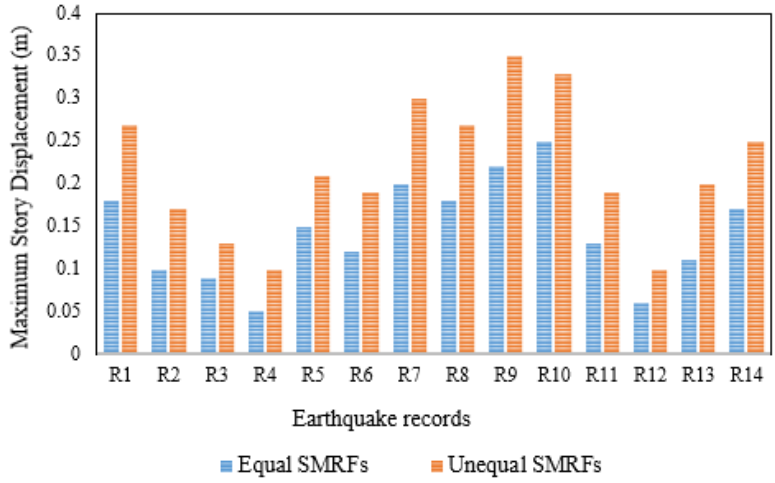

Fig. 13. Comparison of maximum story displacement of two adjacent SMRFs with the equal and unequal heights

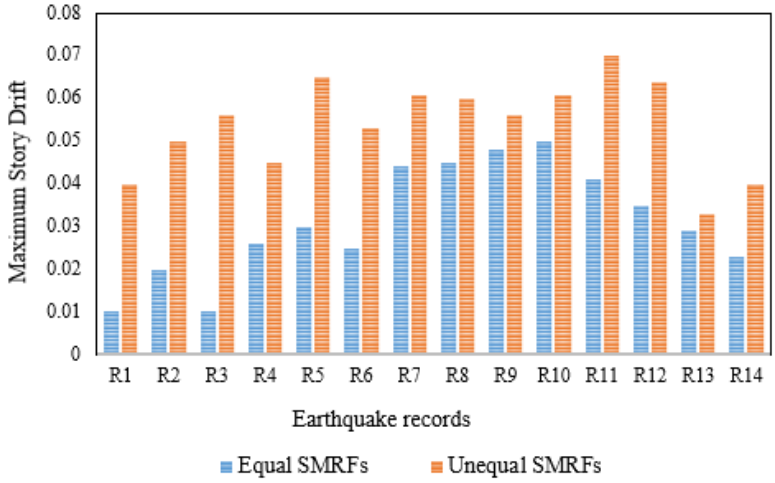

Fig. 14. Comparison of maximum story drift of two adjacent SMRFs with the equal and unequal heights

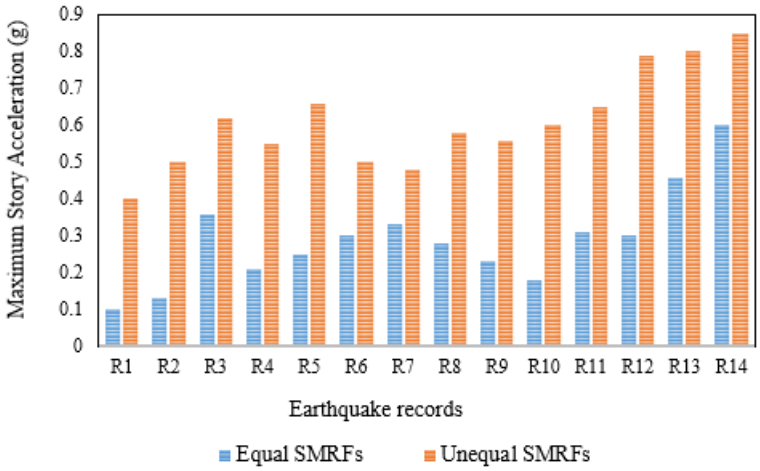

Fig. 15. Comparison of maximum story acceleration of two adjacent SMRFs with the equal and unequal heights

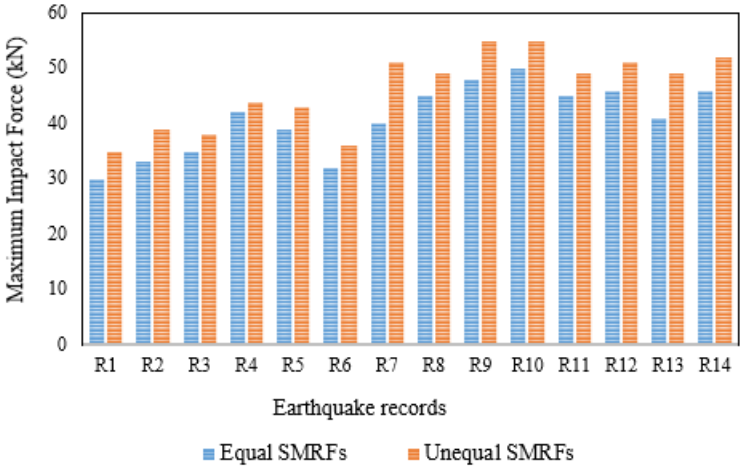

Fig. 16. Comparison of maximum impact force of two adjacent SMRFs with the equal and unequal heights

6.3 Results of Kriging Meta-Model

In this study, for preparing the meta-model, 3000 random samples are produced based on the statistical distribution of each random parameter placed in Table 4. Since the LSF of this research is based on drift. As a result, the drift of selected SMRFs is computed and in this regard, 2000 random samples and the corresponding drift of mentioned SMRFs are opted to train the Kriging meta-model. The remaining samples are utilized to test the Kriging meta-model for predicting the drift values of SMRFs based on LSF. In the following, MCS with 100,000 simulations is conducted for evaluating the reliability of the SMRFs with the equal and unequal heights. The accuracy of the findings given by the Kriging meta-model can be verified by the MCS. Table 8 indicates the results of the reliability analysis of the SMRFs with the equal and unequal heights by using MCS and Kriging meta-model. By comparing the results in Table 8, it is clear that Kriging meta-model can predict the failure probability of SMRFs with the equal and unequal heights by high validity, and accuracy versus MCS, and It can significantly decrease the computational time with far fewer the

number of samples than MCS. It is also found that the results of SMRFs with equal heights have a higher reliability index than the SMRFs with unequal heights. Also, It is noted that the parameters such as (β), (P_f), and (#g call) are the reliability index, failure probability, and the number of calling LSF, respectively.

Table 8. Reliability analysis results of the studied SMRFs using the MCS and Kriging meta-model

	SMRFs with equal heights		SMRFs with unequal heights	
Simulation Method	MCS	Kriging	MCS	Kriging
β	2.80	2.79	2.64	2.63
P_f	2.5×10^{-3}	2.6×10^{-3}	4.2×10^{-3}	4.3×10^{-3}
#g call	10^5	2000	10^5	2000

It is noted that the reliability analysis using the MCS method with 100,000 simulations is really time consuming therefore the Kriging meta-model can decrease the computational time significantly in comparison with MCS. In the following, by using Kriging meta-model, taking into account the uncertainties based on Table 4, the failure probability values of SMRFs with equal and unequal heights are extracted due to 14 far-fault earthquake records. These values are specified in Table 9. The total results of Table 9 indicate that the failure probability of SMRFs with an unequal height is high in comparison of SMRFs with an equal height.

Table 9. The failure probabilities of SMRFs under the effect of pounding by using Kriging meta-model

No.	SMRFs with an equal height	SMRFs with an unequal height
1	0.0026	0.0043
2	0.0021	0.0035
3	0.0024	0.0040
4	0.0022	0.0042
5	0.0022	0.0041
6	0.0018	0.0033
7	0.0017	0.0035
8	0.0021	0.0032
9	0.0015	0.0036
10	0.0022	0.0040
11	0.0024	0.0039
12	0.0018	0.0036
13	0.0024	0.0035
14	0.0021	0.0029

7. Conclusions

Pounding is one of the most common phenomenon during an earthquake that causes significant damage to adjacent SMRFs. In this research, SMRFs with the equal and unequal heights are placed adjacent to each other, taking into account the gap, and their failure probability is calculated by using nonlinear dynamic analyses and Kriging meta-model. Sensitivity analysis is done to specify the important variables in failure probability

computation. Also, by using IDA and fragility curves, the collapse capacity is determined at different statistical levels. The key findings of this paper are presented in the following:

- The sensitivity analysis indicates that the variables with uncertainty of the yield strength of the cross-sections and the dead load have the greatest effect and Poisson's ratio, the specific weight of the cross-sections, and the live load have the least effect on the calculation of failure probability.
- The collapse capacity of the adjacent SMRFs with the equal heights has increased at the statistical levels of 16%, 50%, and 84% compared to the adjacent SMRFs with the unequal heights by 20%, 17%, and 90%, respectively.
- For different spectral accelerations, the collapse probability of the adjacent SMRFs with the unequal height is higher than that of equal height.
- The results of Kriging meta-model indicate that the failure probability is increased by 65% in SMRFs with an unequal height versus an equal height.
- The results of reliability analysis and fragility curves reveal that the collapse capacity of the adjacent SMRFs with the equal height is higher than that of unequal height.
- The application of Kriging meta-model is confirmed with MCS. This meta-model can decrease the computational time significantly in comparison with MCS. Hence, Kriging is an exact probabilistic way for reliability assessment of pounding issues in adjacent SMRFs.
- As recommendations for future works, the authors propose to assess the seismic performance of the adjacent SMRFs with the equal and unequal heights (various stories) under the influence of pounding by considering soil-structure-interaction (SSI) by using reliability and fragility analyses.

References

[1] Favvata MJ. Minimum required separation gap for adjacent RC frames with potential inter-story seismic pounding. Engineering Structures, 2017; 152: 643-659. https://doi.org/10.1016/j.engstruct.2017.09.025

[2] Lin JH. Separation distance to avoid seismic pounding of adjacent buildings. Earthquake engineering & structural dynamics, 1997; 26(3): 395-403. https://doi.org/10.1002/(SICI)1096-9845(199703)26:3%3C395::AID-EQE655%3E3.0.CO;2-F

[3] Kasai K, Maison BF. Building pounding damage during the 1989 Loma Prieta earthquake. Engineering structures, 1997; 19(3): 195-207. https://doi.org/10.1016/S0141-0296(96)00082-X

[4] Sorrentino L, Cattari S, Da Porto F, Magenes G, Penna A. Seismic behaviour of ordinary masonry buildings during the 2016 central Italy earthquakes. Bulletin of Earthquake Engineering, 2019; 17(10): 5583-5607. https://doi.org/10.1007/s10518-018-0370-4

[5] Kamal M, Inel M. Simplified approaches for estimation of required seismic separation distance between adjacent reinforced concrete buildings. Engineering Structures, 2022; 252: 113610. https://doi.org/10.1016/j.engstruct.2021.113610

[6] Naderpour H, Barros R, Khatami S, Jankowski R. Numerical study on pounding between two adjacent buildings under earthquake excitation. Shock and vibration, 2016. https://doi.org/10.1155/2016/1504783

[7] Anagnostopoulos SA. Pounding of buildings in series during earthquakes. Earthquake engineering & structural dynamics, 1988; 16(3): 443-456. https://doi.org/10.1002/eqe.4290160311

[8] Jankowski R. Impact force spectrum for damage assessment of earthquake-induced structural pounding. Key Engineering Materials, 2005; 293: 711-718. https://doi.org/10.4028/www.scientific.net/KEM.293-294.711

[9] Anagnostopoulos SA, Spiliopoulos KV. An investigation of earthquake induced pounding between adjacent buildings. Earthquake engineering & structural dynamics, 1992; 21(4): 289-302. https://doi.org/10.1002/eqe.4290210402
[10] Maison BF, Kasai K. Dynamics of pounding when two buildings collide. Earthquake engineering & structural dynamics, 1992; 21(9): 771-786. https://doi.org/10.1002/eqe.4290210903
[11] El-Khoriby S, Seleemah A, Elwardany H, Jankowski R. Experimental and numerical study on pounding of structures in series. Advances in Structural Engineering: Dynamics, 2015: 1073-1089. https://doi.org/10.1007/978-81-322-2193-7_84
[12] Jankowski R, Seleemah A, El-Khoriby S, Elwardany H. Experimental study on pounding between structures during damaging earthquakes. Key Engineering Materials, 2015; 627: 249-252. https://doi.org/10.4028/www.scientific.net/KEM.627.249
[13] Stone WC, Yoke FY, Celebi M, Hanks T, Leyendecker EV. Engineering Aspects of the September 19, 1985 Mexico Earthquake (NBS BSS 165), 1987.
[14]Kasai K, Jeng V, Patel P, Munshi J, Maison B. Seismic pounding effects-survey and analysis. Earthquake Engineering, 1992.
[15] Cole G, Dhakal R, Carr A, Bull D. Interbuilding pounding damage observed in the 2010 Darfield earthquake. Bulletin of the New Zealand Society for Earthquake Engineering, 2010; 43(4): 382-386. https://doi.org/10.5459/bnzsee.43.4.382-386
[16] Cole G, Dhakal R, Chouw N. Building Pounding Damage Observed in the 2011 Christchurch earthquake Christchurch Earthquake. Earthquake Engng Struct Dy, 2012; 41(5): 893-913. https://doi.org/10.1002/eqe.1164
[17] Dizhur D, et al., Performance of masonry buildings and churches in the 22 February 2011 Christchurch earthquake. Bulletin of the New Zealand Society for Earthquake Engineering, 2011; 44(4): 279-296. https://doi.org/10.5459/bnzsee.44.4.279-296
[18] Maniatakis CA, Spyrakos CC, Kiriakopoulos PD, Tsellos KP. Seismic response of a historic church considering pounding phenomena. Bulletin of Earthquake Engineering, 2018; 16: 2913-2941. https://doi.org/10.1007/s10518-017-0293-5
[19] Mavronicola EA, Polycarpou PC, Komodromos P. Effect of ground motion directionality on the seismic response of base isolated buildings pounding against adjacent structures. Engineering Structures, 2020; 207: 110202. https://doi.org/10.1016/j.engstruct.2020.110202
[20] Forcellini D. The role of Soil Structure Interaction (SSI) on the risk of pounding between low-rise buildings. Structures, 2023; 56: 105014. https://doi.org/10.1016/j.istruc.2023.105014
[21] Sadeghi A, Kazemi H, Mehdizadeh K, Jadali F. Fragility analysis of steel moment-resisting frames subjected to impact actions. Journal of Building Pathology and Rehabilitation, 2022; 7(26). https://doi.org/10.1007/s41024-022-00165-2
[22] Sadeghi A, Kazemi H, Samadi M. Single and multi-objective optimization of steel moment-resisting frame buildings under vehicle impact using evolutionary algorithms. Journal of Building Pathology and Rehabilitation, 2021; 6(21). https://doi.org/10.1007/s41024-021-00117-2
[23] Saberi H, Saberi V, Khodamoradi N, Pouraminian M, Sadeghi A. Effect of detailing on performance of steel T-connection under fire loading. Journal of Building Pathology and Rehabilitation, 2022; 7(7). https://doi.org/10.1007/s41024-021-00147-w
[24] OpenSees, Open System for Earthquake Engineering Simulation Manual, Pacific Earthquake Engineering Research Center, University of California, Berkeley, CA, 2007. http://opensees.berkeley.edu
[25] Mehdizadeh K, Karamodin A, Sadeghi A. Progressive sidesway collapse analysis of steel moment-resisting frames under earthquake excitations. Iranian Journal of Science and Technology, Transactions of Civil Engineering, 2020; 44: 1209-1221. https://doi.org/10.1007/s40996-020-00374-0

[26] Yancheshmeh BS, Adeli MM. A probabilistic approach for seismic demand estimation of steel moment frames considering capacity uncertainty. Asian J Civ Eng, 2023; 24: 2669–2691. https://doi.org/10.1007/s42107-023-00623-3
[27] Sadeghi A, Kazemi H, Samadi M. Reliability and Reliability-based Sensitivity Analyses of Steel Moment-Resisting Frame Structure subjected to Extreme Actions. Frattura ed Integrità Strutturale, 2020; 15(57): 138–159. https://doi.org/10.3221/IGF-ESIS.57.12
[28] Naji A. Sensitivity and fragility analysis of steel moment frames subjected to progressive collapse. Asian J Civ Eng, 2018; 19: 595–606. https://doi.org/10.1007/s42107-018-0045-0
[29]Takabatake H, Yasui M, Nakagawa Y, Kishida A. Relaxation method for pounding action between adjacent buildings at expansion joint. Earthq Eng Struct Dyn, 2014; 43(9): 1381–1400. https://doi.org/10.1002/eqe.2402
[30] ASCE07, Minimum design loads for buildings and other structures, New York: American Society of Civil Engineers, 2016.
[31] AISC 360, Specifications for structural steel buildings, Chicago: American Institute of Steel Construction, 2016.
[32] Kim J, Park J, Lee T. Sensitivity analysis of steel buildings subjected to column loss. Engineering Structures, 2011; 33(2): 421–432. https://doi.org/10.1016/j.engstruct.2010.10.025
[33] Madani B, Behnamfar F, TajmirRiahi H. Dynamic response of structures subjected to pounding and structure–soil–structure interaction. Soil Dynamics and Earthquake Engineering, 2015; 78: 46–60. https://doi.org/10.1016/j.soildyn.2015.07.002
[34] Jankowski R. Non-linear viscoelastic modelling of earthquake-induced structural pounding. Earthquake Eng Struct Dynam, 2005; 34(6): 595–611. https://doi.org/10.1002/eqe.434
[35] FEMA 356, Pre-Standard and Commentary for the seismic Rehabilitation of Buildings, Washington D.C. Federal Emergency Management Agency, USA, 2000.
[36] FEMA 273, NEHRP Guidelines for Seismic Rehabilitation of Buildings, Washington, D.C. Federal Emergency Management Agency, USA, 1997.
[37]Javidan MM, Kang H, Isobe D, Kim J. Computationally efficient framework for probabilistic collapse analysis of structures under extreme actions. Engineering Structures, 2018; 172, 440–452. https://doi.org/10.1016/j.engstruct.2018.06.022
[38] Ellingwood B, Galambos TV, MacGregor JG, Cornell CA. Development of a probability based load criterion for American National Standard A58 – building code requirement for minimum design loads in buildings and other structures. Washington, DC: National Bureau of Standards, Dept. of Commerce, 1980.
[39] JCSS, Joint Committee on Structural Safety, Probabilistic model code, 2001.
[40] CEN, European Committee for Standardization, EN 10034:1993.
[41] Zhang X, Liu J, Yan Y, Pandey M. An Effective Approach for Reliability-Based Sensitivity Analysis with the Principle of Maximum Entropy and Fractional Moments. Entropy, 2019; 21(7): 649. https://doi.org/10.3390/e21070649
[42]FEMA P695. Quantification of building seismic performance factors, Federal Emergency Management Agency, Washington, DC, USA, 2009.
[43] Iervolino I, Maddaloni G, Cosenza E. Eurocode-8 compliant real record sets for seismic analysis of structures. J Earthq Eng, 2008; 12:54–90. https://doi.org/10.1080/13632460701457173
[44] Kayhan AH, Demir A, Palanci M. Multi-functional solution model for spectrum compatible ground motion record selection using stochastic harmony search algorithm. Bull Earthquake Eng, 2022; 20: 6407–6440. https://doi.org/10.1007/s10518-022-01450-8

[45] Iervolino I, Maddaloni G, Cosenza E. A note on selection of time-histories for seismic analysis of bridges in Eurocode 8. J Earthq Eng, 2009; 13(8):1125–1152. https://doi.org/10.1080/13632460902792428
[46] Kayhan AH, Demir A, Palanci M. Statistical evaluation of maximum displacement demands of SDOF systems by code-compatible nonlinear time history analysis. Soil Dyn Earthq Eng, 2018;115:513–30. https://doi.org/10.1016/j.soildyn.2018.09.008
[47] Reyes JC, Kalkan E. How many records should be used in an ASCE/SEI-7 ground motion scaling procedure? Earthq Spectra, 2012; 28(3):1223–42. https://doi.org/10.1193/1.4000066
[48] Demir A. Investigation of the effect of real ground motion record number on seismic response of regular and vertically irregular RC frames. Structures, 2022; 39: 1074–91. https://doi.org/10.1016/j.istruc.2022.03.091
[49] Demir A, Palanci M, Kayhan AH. Evaluation of Supplementary Constraints on Dispersion of EDPs Using Real Ground Motion Record Sets. Arab J Sci Eng, 2020; 45: 8379–8401. https://doi.org/10.1007/s13369-020-04719-9
[50] Demir A, Kayhan AH, Palanci M. Response- and probability-based evaluation of spectrally matched ground motion selection strategies for bi-directional dynamic analysis of low- to mid-rise RC buildings. Structures, 2023; 58. https://doi.org/10.1016/j.istruc.2023.105533

Research on Engineering Structures & Materials
www.jresm.org
Research Group

Research Article

Flux potentials of local talc in low voltage electro-porcelain insulator production

Ifeanyi Uchegbulam[*1,a], Agbo Sunday Chukwuemeka[2,b], Onyinyechi Pauline Elenwo[3, c], Emmanuel Owoichoechi Momoh[4,d]

[1]*Production Tech., School of Science Laboratory Technology, University of Port Harcourt, Choba, Nigeria*
[2]*Ceramics Research and Production Department, Projects Development Institute (PRODA) Enugu, Nigeria*
[3]*Physics Department, Faculty of Science, University of Port Harcourt, Choba PMB 5323, Nigeria*
[4]*Faculty of Environment Science and Economy, University of Exeter, Streatham Campus, Exeter, UK*

Article Info

Article history:

Received 04 Dec 2023
Accepted 22 Mar 2024

Keywords:

Ceramic;
Porcelain insulator;
Talc;
Feldspar;
Sintering;
Voltage

Abstract

Increasing demand for accessories like porcelain electric insulators have continued in developing countries causing overdependence on imported products. Meanwhile, raw materials for their local production are available in commercial quantities with high firing temperature being the major challenge. Hence, the need for fluxing agents that can reduce the working temperature led to the investigation of Talc as a partial replacement of conventional Feldspar. An optimum replacement of 10% Feldspar with Talc was adopted, and this recipe showed microstructurally enriched glassy phase, primary and secondary Mullite with other crystalline phases like Cristobalite, Microcline and Albite at 1200°C with micropores evident in both the Talc and Feldspar formulations. The produced insulator fired at 1200°C offered an optimum thermal conductivity of 0.2768W/mK with reductions in water absorption, apparent porosity and linear shrinkage by 78.29%, 76.02% and 19.75% respectively with a 9.48% rise in bulk density. The electrical performance comprised Inception, Withstand and Breakdown Voltages of 10.2 kV, 14 kV and 20 kV respectively at leakage currents of 0.2 mA, 1.2 mA and 2 mA accordingly. With a withstand voltage above 11 kV and breakdown voltage below 22 kV, this pin-type porcelain insulator will find wide application in both electric substations and end user load points like commercial and residential electric power lines. The novelty lies on the fluxing and filler potentials of Talc as a locally-sourced mineral in porcelain insulator production which increases the market value of Nigerian Talc while reducing importation, costs of energy and raw materials in porcelain production.

1. Introduction

Porcelain is one of the engineering materials that have passed through ages without losing its relevance despite the development of modern plastic and glassy materials. This sustained significance can be linked to its durability and adaptability to harsh environmental situations. They are extensively used for chemical, heat and electrical resistant purposes. Their mechanical properties, corrosion resistance, low water affinity, high heat resistance, and high electrical resistivity are responsible for their excellent performance in refractories, laggings, tiles, kitchen and sanitary wares.

They also demonstrate excellent chemical resistance (as laboratory wares), thermal shock (as pestles), beautiful textures (when glazed for decorative uses) as well as fatigue resistance (in dentistry). As non-conductors of electricity, porcelain insulators find

*Corresponding author: uche.aberdeen.ac.uk@gmail.com
[a] orcid.org/0000-0002-0836-3370; [b] orcid.org/0000-0002-7803-0950; [c] orcid.org/0009-0009-7226-9635; [d]orcid.org/0000-0003-3432-1366
DOI: http://dx.doi.org/10.17515/resm2024.96ma1204rs

satisfactory usage in unlimited indoor electrical applications as well as outdoor uses as high voltage insulations like overhead power transmission and distribution lines, bushings for transformers, etc.

In service, a Porcelain Electric Insulator is exposed to very harsh environmental conditions like heat, rain, humidity, dust etc. For instance, while establishing the need for formulating a corrosion control protocol for insulators, it was noticed in [1] that relative humidity plays key roles in insulator electrolytic corrosion. Similarly, in [2], it was reported that corrosion of porcelain insulating systems are mainly dependent on geographic locations with the cap components of the insulators degrading by galvanic corrosion mechanism while the pin corrodes by both crevice and electrolytic corrosion mechanisms. Other studies such as [3], studied the biological contamination of electrical insulators by alga Chlorella vulgaris. Their findings showed the adverse effect of bio-contamination which reduced the flashover voltage by 12% and increased the leakage currents up to 80%. In [4], artificial neural network was used to predict the flashover voltage of humidity and pollution induced surface contaminations of porcelain insulators.

These challenges have motivated researchers and scientists to investigate diverse improvement techniques to enhance the performance of Porcelain insulators through material formulations and production methods. Since sintering temperature also known as firing or working temperature complemented with formulation recipe are the principal factors responsible for the precipitation of crystalline phases, which in turn dictates the properties of porcelain materials, it becomes imperative to understand the relationship between these factors for performance optimization. Several authors have investigated the partial replacement and variation of the amount of quartz, Feldspar, kaolin and ball clay in porcelain recipes. In [5], the use of micro additives as fillers to enhance the electrical properties of ceramic-glass insulators was studied while [6], used recycled waste glass from broken car glasses as a replacement of K-Feldspar for the production of porcelain. Their findings showed improvements in microhardness and dielectric properties. Remarkably, [7] in their use of cullet to substitute the Feldspar component found that this measure offered excellent dielectric strength at a lower kiln temperature. Similarly, the partial replacement of Feldspar with sodium bicarbonate has also been reported in [8], which reduced sintering temperature and improve dielectric performance of porcelain insulators. Mineral raw materials are potential substitutes to the felspathic component of porcelain formulation. These materials like Talc have been used for other industrial purposes and is both available and affordable in commercial quantities in Nigeria. Talc is a soft and light-weight mineral with its mineralogical occurrence mainly from the metamorphosis of other rocks. It is a secondary mineral from either carbonate of magnesium like dolomite and magnesite or oxides of silicon such as serpentine and tremolite. This is why it is generally recognized as hydrated magnesium silicate $Mg_3Si_4O_{10}(OH)_2$ [9,10]. It has several uses ranging from cosmetics, agriculture, industrial lubrication, electrical wire insulation and even anticaking agent in drug tablets molding. It is a soft and whitish mineral when ground. The physico-chemical properties like softness, hydrophobicity, low thermal and electrical conductivity with high crystallinity and specific surface area of Talc suggest its suitability as a fluxing material in porcelain production. Talc as a magnesium-rich phyllosilicate has found extensive industrial applications for making plastics, detergents, paint, paper, pharmaceuticals, pesticides, rubber, cosmetics, ceramics, adhesives, part of animal feed and acts as a hydroTalcite in the petroleum industry [11-13].

Hence, in this study, the use of Talc as a partial replacement of Feldspar in formulation of porcelain insulator recipes and how this affects the physical properties, thermal stability and electrical performance of the insulator were investigated.

2. Materials and Methods

2.1 Material characterization

The raw materials were obtained from local Nigerian communities: Kaolin from the Projects Development Institute's mineral store, Talc from Kenyatta Industrial market and Silica from Iva Pottery all in Enugu state while the Ball clay was obtained from Ehime Mbano in Imo state and Feldspar from Okene in Kogi state. These materials were identified at the Projects Development Institute at minimum purity levels of 97.3%, 98.5%, 97.4% and 95.8% for Kaolin, Talc, Silica and Ball clay respectively. The methodology employed in this study is illustrated in the overview of Figure 1.

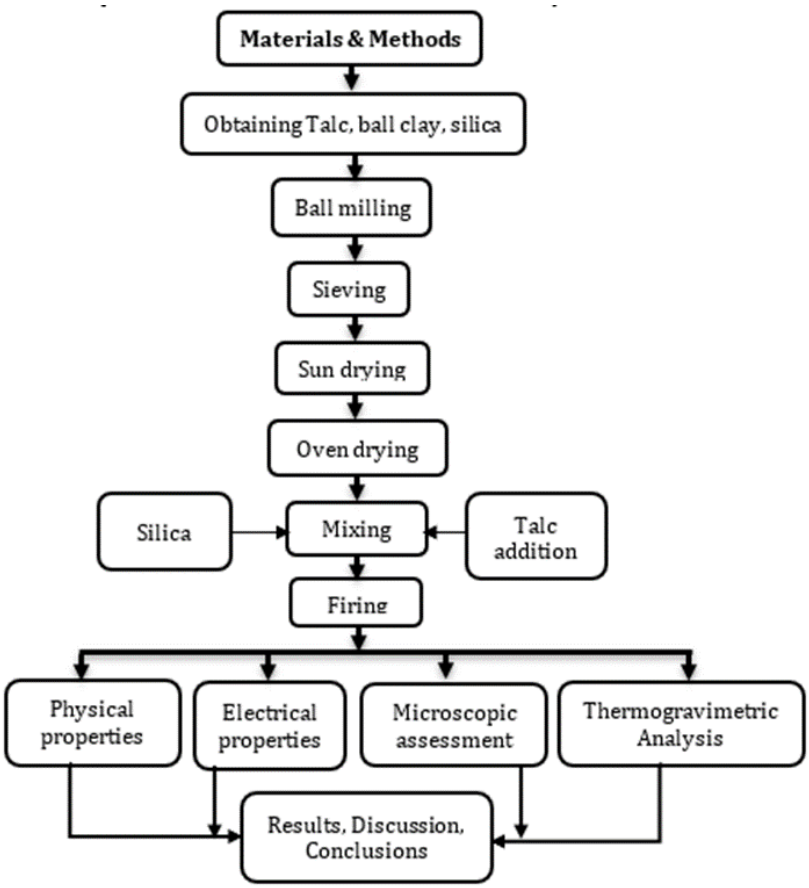

Fig. 1. Overview of the study

2.2 Slip formulation and Molding into Porcelain Insulator

The kaolin, ball clay and silica were in fixed amounts of 40%, 10% and 25% respectively, while Feldspar and Talc were varied as shown in Table 1. These starting materials were obtained as lumpy coarse powders and were crushed in a ball mill to obtain finer particle sizes.

Further processing was carried out by soaking in distilled water, vigorous stirring to achieve adequate dissolution, and filtering (through a 0.425 mm mesh sieve) to get rid of organic matter. This procedure was followed by allowing the sediments to settle. The

floated water was then run off to isolate other suspended solids and residual organic matter after which the condensed clay was sun-dried for 5 hours prior to oven drying at 100 °C for 3 hours. The dried clay was later pulverized and sifted through a 0.18mm sieve. With the recipe in Table 1, 1.6kg of the clay sample was used as the base raw material with the other materials added to achieve different slurries. The sample codes are shown in Table 1. Subsequently, 2g of Sodium Silicate (Na_2SiO_3) was added to each blended mixture of powders in order to inhibit flocculation of suspended solids. The powders were then kneaded in appropriate amount of water into plastic slip until ready for molding.

Table 1. Formulation of Porcelain insulator

Code	Kaolin	Ball clay	Silica	Feldspar	Talc
A	40	10	25	25	0
B	40	10	25	23	2
C	40	10	25	21	4
D	40	10	25	19	6
E	40	10	25	17	8
F	40	10	25	15	10

With these conditions, the slip was poured into a plaster-of-Paris mold consistent with the industrial dimensions of porcelain insulators. The slip was poured until the mold gate was full. Extra slip was added after two hours to supplement mass reduction due to absorbed water. The mold was left to set for 5 hours, after which the cast porcelain was removed from the mold and fettled to obtain a smooth surface finish.

Fig. 2. The produced porcelain insulators at different levels of glazing

The green compacts were oven dried at 120°C for 2 hours to get rid of mechanically bound water prior to Bisque firing up to 900°C for 3 hours to obtain the adequate porcelain sinter following the procedure conducted in [14]. To achieve the characteristic brown colored impervious glaze, the fired bisques were immediately dipped into a glaze slurry made from Feldspar, Silica, clay, borax, zinc oxide and cobalt oxide. The dipping process was carried out by immersing the fettled green compact into a container of the glaze compound. The glaze-coated compact was sun-dried for 2 hours and fired up to 900°C for 1 hour and allowed to cool under ambient conditions. This glazing process was repeated to ensure high glaze penetration and adherence on the fettled surface. This was followed by a Gloss-firing at 1200°C in an electric kiln at a ramp of 5°C/min and dwell time of 150 minutes. The sintered porcelain products were allowed to cool to room temperature within the kiln for about 15 hours after which the produced porcelain insulators were taken out of the kiln.

Industrial sized samples were made so that their properties can be compared to those of commercial products in the market.

2.3 Molding of Test Pieces and The Porcelain Insulator

To mold test pieces for physical analysis, three metallic molds were used. The molds were firstly lubricated for ease of retrieving of the green compact. Different mold patterns were produced: the cylindrical patterns of 3.5ø x 3 cm, and short rectangular patterns of 8 x 4 x 1.5 cm while the longer rectangular patterns were of 9.5 x 2 x 1.5 cm. Three (3) samples each of the three sets of test pieces were used for the physical analyses.

2.4 Physical Analysis

Physical properties such as making water, water absorption, porosity, shrinkage, apparent and bulk density of the pellets at different firing temperatures were analyzed in accordance with the requirements of ASTM C20-00 [15], for water absorption, apparent porosity, apparent density, and bulk density.

2.4.1 Making Water

The making water is a very important parameter in slip casting as it represents the amount of water needed to make a plastic slip from the mixture of raw materials. In this study, the making water was determined by weighing the cylindrical test pieces immediately after molding and this weight was recorded as the wet weight (w_o). After this, the test pieces were air-dried for 24hrs, then oven-dried at 105°C until a constant weight was recorded as W_i. The making moisture was then estimated from Eq. 1.

$$Making\ Moisture\ (\%) = \frac{W_0 - W_i}{W_0} \times 100 \tag{1}$$

2.4.2 Water Absorption

As a vital parameter, the water absorption (W_a) which demonstrates the extent of curing of the porcelain when fired was also evaluated. This was carried out by measuring the post-drying weight (wd). The post-dried samples were then soaked in water for 1 hour, cleaned and reweighed as weight after soaking in water as (ww). Eq. 2 was used to evaluate the water absorption of the samples.

$$W_a\ (\%) = \frac{W_w - W_d}{W_d} \times 100 \tag{2}$$

2.4.3 Apparent Porosity

The void composition of porcelain insulator largely affects their dielectric strengths. Both accessible and remote pores make up the total porosity of porcelain products.

The apparent porosity test was carried out in accordance with the requirement of ASTM C20-00, (2015), [15]. The samples were suspended in a beaker of water, with their weights measured via a lever balance. The suspended weight was recorded as W_s while the dry weight wd and the wet weight ww were measured in line with the procedure described in section 2.4.2. Eq. 3 was used to evaluate the apparent porosity of the samples.

$$Apparent\ Porosity\ (\%) = \frac{W_w - W_d}{W_w - W_s} \times 100 \tag{3}$$

2.4.4 Shrinkage

The linear shrinkage of ceramic products could lead to excessive dimensional instability, thereby, adversely affecting the performance of the finished product. Therefore, analysis of shrinkage is very important in the design of ceramic components. In this study, the shrinkages of the samples were estimated by measuring the sample lengths before and after kiln firing in line with ASTM C356-17, [16]. A vernier caliper was used to insert a 0.5 cm mark on each of the rectangular test pieces and this was recorded as the original length L_o (in cm). The test pieces were then sun-dried outdoor in still air for 7days. The samples were then transferred into an oven and at 105^{o}C until a constant weight was obtained. The contraction from the 5cm mark was recorded as the dried length, L_d (in cm). Finally, the dried samples were fired to sintering temperatures. The determination of shrinkage was conducted for samples kiln-fired at 1000^{o}C and 1200^{o}C while the shrinkage of the test pieces was determined by measuring the change in the distance between the initial 5 mm markings. The final length after firing was recorded as the fired length, L_f (in cm). The different variants of the shrinkage were then estimated using Eqs. 4, 5 and 6. This procedure was consistent with other studies [14, 17].

$$Wet - Dry\ Shrinkage\ (\%) = \frac{L_o - L_d}{L_o} \times 100 \quad (4)$$

$$Dry - Fired\ Shrinkage\ (\%) = \frac{L_d - L_f}{L_d} \times 100 \quad (5)$$

$$Total\ Shrinkage\ (\%) = \frac{L_o - L_f}{L_o} \times 100 \quad (6)$$

2.4.5 Apparent and Bulk Density

The apparent and bulk densities of the samples were estimated using Eqs 7 and 8 following the procedure described in sections 2.4.2 and 2.4.3. Table 4 presents the results of the apparent and bulk densities of the samples.

$$Apparent\ Density\ (\%) = \frac{W_d}{W_d - W_s}\ x\ 100 \quad (7)$$

$$Bulk\ Density\ (\%) = \frac{W_d}{W_w - W_s}\ x\ 100 \quad (8)$$

Where W_d, W_s and W_w are previously defined in sections 2.4.2 and 2.4.3.

2.5 Microscopic Evaluation

The samples were polished with a moist emery cloth, cleaned and sun-dried prior to microscopic examination using Keyence VH-Z450/VH-6300 Digital Microscope with VH-Z450 High-Range Zoom Lens at 500X magnification.

2.6 Thermal Analysis

The thermal property of the clay samples was analyzed with Shimadzu DTG-60H model (TA Instruments, USA) using differential scanning calorimetry (DSC) and a simultaneous thermal analyzer (Differential Thermal Analysis-Thermogravimetric Analysis, DTA/TGA). The DTG procedure was carried out by heating the clay samples from room temperature to 1200 °C at a ramp of 10 °C/min under a steady air flow of 50 ml/h. A 3.002mg sample was introduced into a Platinum cup, heated in comparison to a reference crucible and cooled at instrument cooling rate to obtain DSC and DTA/TGA curves that reveal the

thermal profiles at different mineralogical transformation during the firing of the produced insulator.

2.7 Electrical Analysis

The main aim of the electrical analysis on the porcelain bodies was to determine their insulating properties. The parameters tested were the dielectric inception voltage, withstand voltage and breakdown voltage as well as the leakage currents at these various voltage limits. These were carried out using BAUR PGK 260 HB AC/DC HV test set, Austria, by applying electrodes at the ends of the porcelain insulator and results presented in section 3.6.

3. Results and Discussion

3.1 Material Characterization

This result of chemical composition (see Table 2) shows that silica (SiO_2) and alumina (Al_2O_3) are the principal oxides found in the raw materials while other oxides were present in negligible quantities. This result agrees with findings in [7] and [18]. Remarkably, flux content in Feldspar (K_2O-Na_2O) sums up to 13.21% which is greater than the 12% threshold [18] for porcelain insulators. Also, the high potash and soda contents of the Feldspar with low lime composition shows that the Feldspar is not a "lime Feldspar".

Table 2. Chemical composition of the starting raw materials in % oxide constituents

Component (%)	Kaolin Clay	Feldspar	Iva-pottery sand
SiO_2	60.0	64.65	74.15
Al_2O_3	21.0	16.1	13.73
Fe_2O_3	0.5	1.86	0.005
Na_2O	0.031	2.99	-
K_2O	0.75	10.22	-
TiO_2	0.9	1.4	1.3
LOI	11.34	1.62	0.61

3.2 Water Absorption, Making Water and Apparent Porosity

As the Talc content increased from 0 to 10% and were fired up to 1000 ^oC, it was observed that the apparent porosity was gradually increasing. This may be due to the linear expansion that occurred within 1000 ^oC causing crack nucleation, thereby, adding to the micropore density (i.e., the number of micropores per unit volume of porcelain). However, as the firing temperature was increased to 1200^oC, a significant reduction in apparent porosity, was observed. Evidently, these pores collapse as most of the porcelain materials melt at temperatures above 1000^oC. Figure 3 revealed that water absorption increased at 1000^oC but reduced at 1200^oC. This indicates that there is a correlation between porosity and water absorption such that increase in apparent porosity creates more pores that causes water ingress, hence, increases water absorption. Conversely, as the apparent porosity reduces, there are less pore spaces to accommodate absorbed water thereby causing the reduction in the percentage water absorption. Figure 3 also revealed that the 10% Talc concentration offered the least porosity and water absorption at 1200^oC due to the reduced apparent porosity from 12.09 % in the Feldspar-rich recipe to 2.90 % in 10% Talc substitution and a consequent 76.02 % reduction in apparent porosity. In addition, water absorption was reduced from 6.88 % in the Feldspar-rich recipe to 1.49 % in the 10 % Talc substitution resulting in a 78.29 % reduction in water absorption. This trend in reduction of both apparent porosity and water absorption at higher temperatures is consistent with previous studies [7, 19].

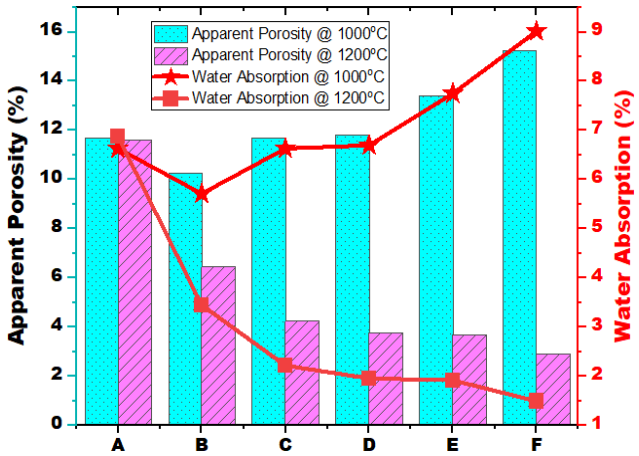

Fig. 3. Apparent porosity and water absorption of PPE insulator as functions of firing temperature (1000 - 1200°C)

3.3 Linear Shrinkage, Apparent and Bulk Density

At 1000°C, the linear shrinkage increased until 6% Talc but then decreased as the Talc content approached 10 % (see Figure 4 (a)). As temperature increased, release of glassy crystallites occurred along with entrapped gases [7] and this caused the steady increase in linear shrinkage. However, as the Talc content increased from 2 %, reduction of sintering temperature occurs and this inhibits shrinkage, although this phenomenon does not apply to Talc contents above 6%. In other words, fluxing impact cannot resist linear shrinkage below 6% Talc as demonstrated in Figure 4 (a). From Figure 4 (b), bulk density slightly reduced as the Talc content increased from 0 to 10 % as a result of the effect of the fluxing characteristics of the Talc which reduced the sintering temperature. Although the reduction in the sintering temperature at 1000°C did not favor densification, The densification was so rapid at 1200°C and subdued the lowering of sintering temperature induced by the increasing Talc content. Reduction in volume caused dimensional reduction viz-a-vis linear shrinkage as well as the enhanced densification noticed in the produced porcelain insulators at 1200°C.

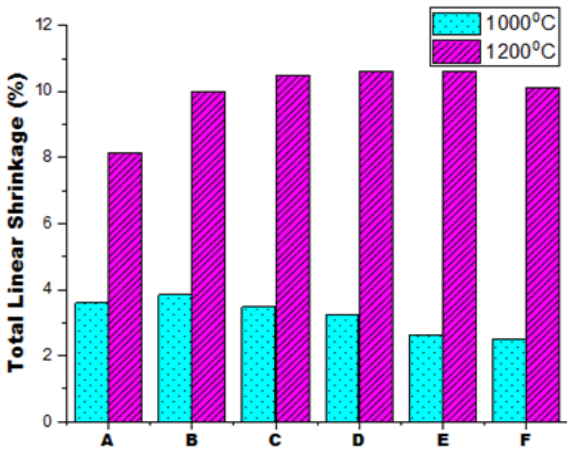

(a)

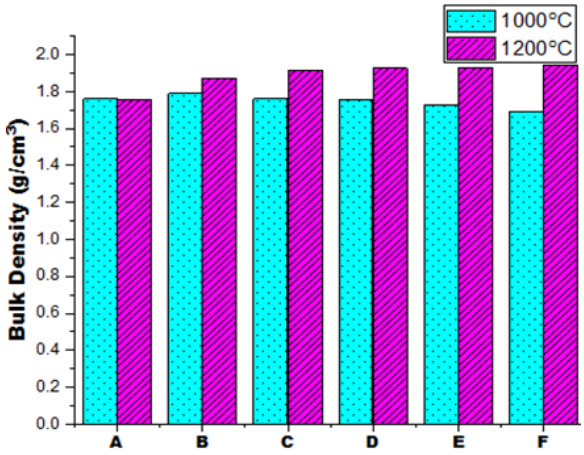

(b)

Fig. 4. Total linear shrinkage (a) and bulk density (b) of PPE insulator as functions of firing temperature at 1000 and 1200°C

Figure 4 also revealed that the 10% Talc concentration offered the least linear shrinkage and highest bulk density at 1200°C. It is noteworthy that total linear shrinkage increased from 8.13 % in the feldspar-rich recipe to 10.13 % in the 10 % talc substitution thereby leading to 19.75 % increase in total linear shrinkage. Likewise, bulk density increased from 1.76 % in the feldspar-rich recipe to 1.94 % in the 10% talc substitution leading to a 9.48 % rise in bulk density. This declining linear shrinkage with increase in bulk density due to pore volume reductions at 1200°C were also reported in other studies [7].

3.4 Thermal analysis

The DTA/TGA curves in Figure 5 presents the simultaneous weight loss with rise of firing temperature in real time for the produced porcelain insulator. The DTA/TGA curves demonstrated the physico-chemical transformation regime that occur during a typical kaolin calcination through endothermic and exothermic reactions as shown in Figure 5. From Figure 5, the first endothermic peak occurred at -98°C and can be attributed to the release of surface bound water in line with [20] with approximately 0.89 % weight loss indicated by the TGA curve.

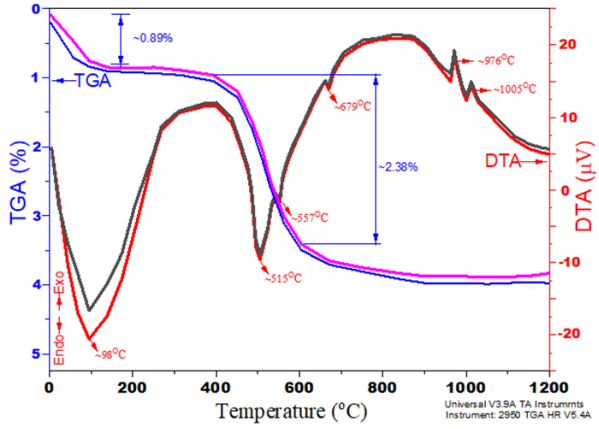

Fig. 5. Thermal profile (TGA/DTA) of produced porcelain insulator

The second endothermic peak occurred at -51°C and is linked to the dehydroxylation of kaolinte by the removal of structural hydroxyl groups which reorganized the octahedral layers of the kaolin into the tetrahedral configuration of metakaolin. This resulted in a corresponding weight loss of 2.38 %. The dehydroxylation of kaolinte occurred until 772.8°C in the study of [19], 448.8°C in [21], 553°C in [22] and 569°C in [23]. These discrepancies can be linked to the differing raw materials, differences in processing methods, as well as ambient conditions. The total weight loss of in the porcelain body in this study was 3.27 %; consisting of 0.89% from loss of physically bound water and 2.38 % loss of chemically bound water during the decomposition of the porcelain clays. The dehydroxylation of kaolinite is the first chemical transformation in the porcelain production, this thermal reaction is represented by Eq. 9 [19, 24].

$$Al_2O_3.2SiO_2.2H_2O \xrightarrow{\sim 515^0C} Al_2O_3.2SiO_2. + 2H_2O_{(g)} \uparrow \quad (9)$$

Furthermore, an endothermic peak occurred at 557°C which can be linked to the polymorphic transformation of α to β of quartz. This allotropic phase transition was also reported at 573°C in both [20] and [22]. These reductions in thermal reactions can be attributed to the fluxing properties of Talc used as a replacement of Feldspar in this study. The last noticeable endothermic peak was seen at 679°C which was linked to the sharp change at the onset of sintering and formation of glassy crystallites in the porcelain body. Then, the first noticeable exothermic peak was clear at 976°C corresponding to Al-Si spinel crystallization from the metakaolin and/or other amorphous Si-containing γ-Al_2O_3. This was reported at 999.6°C in [22] which still maintained the fluxing functions of Talc in the porcelain body. Meanwhile, this was the second thermophysical reaction and is represented by Eq 10 [19, 24].

$$2(Al_2O_3.2SiO_2) \xrightarrow{\sim 976^0C} 2Al_2O_3.3SiO_2. + SiO_{2\,(amorphous)} \quad (10)$$

Finally, the expansive nucleation of mullite from the further decomposition of kaolin was seen to earlier commence at 1005°C similar to the study in [23] which occurred at 1050°C and 1084°C in [25].

This establishes the potentials of Talc as a fluxing replacement of Feldspar in porcelain formulation and the corresponding reaction is represented in Eq. 11 [19, 24].

$$3(2Al_2O_3.3SiO_2) \xrightarrow{\sim 1005^0C} 2(3Al_2O_3.2SiO_2 + 5SiO_2 \quad (11)$$

Finally, the gradual rise in densification as the temperature approached 1200°C can be linked to the crystallization of stable crystals like cristobalite from the amorphous quartz and seepage of mullite melts into the porcelain pores as illustrated in Eq. 12 [19, 24].

$$SiO_{2\,(amorphous)} \xrightarrow{\sim 1200^0C} SiO_{2\,(Cristobalite)} \quad (12)$$

These results demonstrate that the thermal behavior of the porcelain body was consistent with its mineralogical transformations. According to the TGA/DTA thermal profiles (Figure 5), mullite nucleation which fills up micropores and cristobalite crystallization which occurred at 1005°C and 1200°C, respectively, were volumetric reduction mechanisms. In addition, Figure 6 shows the thermal conductivity of the produced porcelain insulator which indicates the allowable heat flux that the insulator can withstand. This allowable heat flux is a significant measure of its thermal and electric shock resistance.

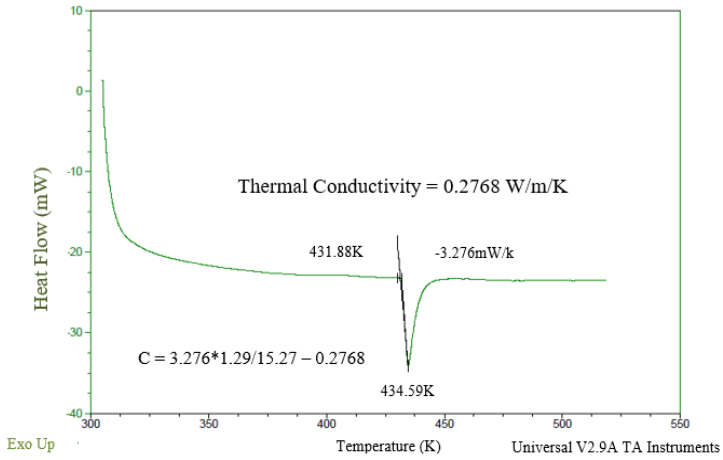

Fig. 6. Thermal conductivity (DSC) of the produced porcelain insulator

Figure 6 shows that the thermal conductivity measured from the differential scanning calorimetric analysis reveals a thermal conductivity of 0.2768 W/mK. This low thermal conductivity or high thermal resistivity demonstrates the insulator's thermal stability under harsh temperature conditions and as well as capacity to withstand thermal shocks. This thermal stability can be linked to the 13.21% flux content recorded in the starting materials which was higher than the recommended threshold of 12% recorded in [18] for porcelain insulator production.

3.5 Microscopic evaluation

The microstructural analysis of the produced porcelain insulator was presented in Figure 7 which agrees with the chemical analysis of the raw minerals in table 2 and the properties of the produced insulator in figures 2-6. In figure 7, A = Albite; PM = Primary Mullite; P = Pores; C = Cristobalite; SM = Secondary Mullite; M = Microcline. Figure 7 demonstrated the components of the Feldspar bedrock being more of potash Feldspar than soda Feldspar. The potash enrichment was revealed in the microcline with a characteristic green colour while its soda

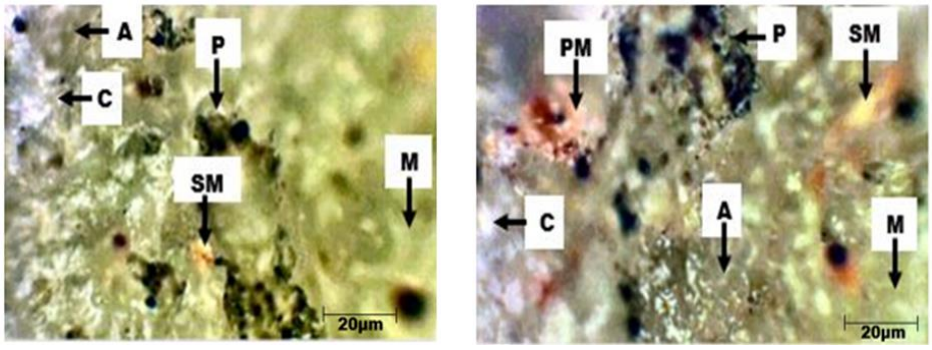

(a) (b)

Fig. 7. Microstructural evaluation of the PPE insulator (a) No Talc (b) 10% Talc at 1200°C

Feldspar represented as albite can be distinctively seen as gray colors. The Talc-rich sample was rich in both the greenish Microcline (M) and gray Albite (A) due to the relative abundance of Feldspar in Figure 7 (a) than the Talc rich Figure 7 (b).

The Talc in Figure 7 (b) had more thermal effect than mineralogical contribution to the porcelain properties. Instead, Figure 7 (b) shows richer contents of brownish Primary Mullite (PM) and golden Secondary Mullite (SM). The glassy Cristobalite (C) was more in the Talc enriched porcelain (Figure 7 (b)) than the Feldspar dominated Figure 7 (a). The gray Albite was significant in Figure 7 (b) while the greenly microcline reduced despite the reduction of their source (Feldspar) in the porcelain (Figure 7 (b)). This will be investigated in subsequent studies. Closed Pores (P) were seen as dark regions which are present in both microstructures. According to [8], the amount of crystalline mullite and glassy phases generated during kiln firing of porcelain insulators control the dielectric strength of the insulators which should be moderate to avoid ionic conductions that will reduce the insulating propensities of the insulator. Since, the substitution of Feldspar with Talc led to more mullite and glassy cristobalite, the dielectric strength of the produced porcelain insulator with the presence of Talc in comparison with the sample without Talc as discovered in this study. In addition, the higher densification due to Talc content can also be linked to the earlier mullite transformations and their seepage into the porcelain pores. In line with table 2, apart from Alumina and Silica as the fundamental components of clay minerals, the next components were Potash and Soda with Potash being higher showing that the raw Feldspar used was alkali in nature. According to [26], Feldspar's alkalinity increases porcelain vitrification and melt's fluidity leading to unrestricted and rapid nucleation of crystals. In this light, the high fluidity enhances permeation into micropores leading to reductions in both porosity and water absorption with higher densification as recorded in figures 3. As a partial replacement of Feldspar, Talc has acted as both a fluxing agent and as a filler that displaces interconnected pores. This dual purpose is responsible for the 76.02 and 78.29 % reductions in apparent porosity and water absorption respectively.

3.6 Electrical Analysis

To investigate the effect of Feldspar replacement with Talc in electro-porcelain insulators, the electrical properties of the insulators produced was tested and the results are presented in Table 3. The inception voltage can be defined as the minimum voltage loading at which a partial electric current is discharged through the insulator. The withstand voltage is the permissible voltage the insulator material can resist in static air at room temperature up to three minutes, while the breakdown voltage is a measure of the least voltage that can collapse the insulator's current resisting ability. Table 3 shows satisfactory voltage and current results as compared to IEC 60168 standards. Their break down voltage of 20 kV shows that they cannot be suitable for 22 kV and higher transmission lines while a withstand voltage of 14 kV shows their electrical capacity for 11 kV insulation. In addition, the glazed surface offers self-cleaning properties against dust, acid rain, high humidity and other environmentally adverse effects. Being made from local raw materials provides cost effectiveness and simplicity in production and installation. Hence, they can find wide application in 11 kV power distribution and sub-transmission lines, that is, they are ideal for all distribution lines and low voltage sub-transmission lines. Therefore, the aim of producing a low-voltage electro-porcelain insulator with Talc modified properties was successfully achieved.

In this study, electrically insulating and thermally stable porcelain insulator was produced from Nigerian local minerals by substituting its Feldspar content with Talc. The effect of sintering temperatures at 1000 ^{o}C and 1200 ^{o}C was studied. Locally sourced minerals from of Nigerian origin obtained as lumps were pulverized into homogenized powders through

ball milling with a slurry made after adding 2g of Na_2SiO_3 to inhibit flocculation of suspended solids and resulting to suitable slip for casting the porcelain.

Table 3. Electric test results

Description	Voltage (kV)	Leakage Current (mA)	Remarks
Inception	10.2	0.2	Satisfactory
Withstand	14	1.2	Satisfactory
Breakdown	20	2	Satisfactory

4. Conclusion

The kaolin, ball clay and silica contents were fixed at 40 %, 10 % and 25 % respectively, with the remaining 25 % Feldspar partially replaced with Talc for each formulation. Results showed a linear relationship between porosity and firing temperature at 1200°C. There was also a direct relationship between apparent porosity and water absorption such that increase in apparent porosity gave rise to higher water ingress. Linear shrinkage and bulk density were also linearly related to the working temperature. Interestingly, the 10% replacement of Feldspar with Talc offered the least porosity, water absorption and linear shrinkage but highest bulk density all at 120°C. Also, at this recipe, an insulator thermal conductivity of 0.2768 W/mK was obtained. This low thermal conductivity or high thermal resistivity demonstrates the insulator thermal stability under elevated temperature and as well as capacity to withstand thermal shocks. At these optimal conditions, the microstructural evaluation revealed that the 10 % Talc at 1200°C was enriched with a glassy phase, primary and secondary mullite and other crystalline phases like cristobalite, albite and microcline as well as albite but with micropores evident in both Talc and Feldspar recipes. Thermal profile of the produced insulator showed four endothermic and two exothermic peaks where mineralogical transformations validated the microstructural results in addition to weight loss and thermal conductivity results. Since the produced porcelain insulator was thermally stable up to 1200°C, the potentials of Talc as a cheap substitute of Feldspar in porcelain production is substantiated. Also, electrical performance of the porcelain insulator was rated satisfactory with Inception, Withstand and Breakdown Voltages of 10.2 kV, 14 kV and 20 kV respectively and at leakage currents of 0.2 mA, 1.2 mA and 2 mA, respectively. Despite reduction in working temperature due to the introduction of Talc, these electrical properties demonstrate the insulator's potentials for use in distribution lines and low voltage sub-transmission lines. The potentials of Talc and other local flux materials as a cheap substitute for Feldspar in the production of porcelain insulators for high voltage transmission lines can be achieved which are within our considerations for future work. Generally, the use of the local materials and the recipe from this study would reduce importation, the costs of raw materials and energy in production. These prospects will be easier to realize if collaborations between industry and academia is enhanced especially in the country of this research. For instance, this study was funded by the personal contribution of funds by the authors, hence the study was limited to the tests reported. Future studies will encompass microscopic and spectroscopic examinations of the locally produced insulators.

References

[1] Yang D, Cao B, Li Z, Yang L, Wu Y, On-line monitoring, data analysis for electrolytic corrosion of ±800 kV high, International Journal of Electrical Power and Energy Systems, 2021; 131(107097). https://doi.org/10.1016/j.ijepes.2021.107097

[2] Kim T, Lee Y, Sanyal S, Woo J, Choi I, Yi J, Mechanism of Corrosion in Porcelain Insulators and Its Effect on the Lifetime, Applied Science, 2020; 10(423). https://doi.org/10.3390/app10010423

[3]Rojas HE, Pérez CD, León AF, Cantor LF, Electrical performance of Distribution insulators with chlorella vulgaris growth on its surface, Ingeniería e Investigación, 2015; 35(1):21-27. https://doi.org/10.15446/ing.investig.v35n1Sup.53578

[4] Salem A, Rahisham A, Waheed G, Samir A, Salem A, Prediction Flashover Voltage on Polluted Porcelain Insulator Using ANN, Computers,Materials & Continua Tech Science Press, 2021; 68(3). https://doi.org/10.32604/cmc.2021.016988

[5] Hsieh M, Chen W, Hsu C, Wu C, High-voltage insulation and dielectric properties of ceramic-glass composites, Journal of Asian Ceramic Societies, 2022; 10(3): 739-743. https://doi.org/10.1080/21870764.2022.2123522

[6] Belhoucheta K, Bayadia A, Belhouchetb H, Maximina R, Improvement of mechanical and dielectric properties of porcelain insulators using economic raw materials, Boletin De La sociedad Sociedad Espanola De Ceramica Y Vidrio, 2019; 58: 28-37. https://doi.org/10.1016/j.bsecv.2018.05.004

[7] Tullu AM, Terfasa TT, Zerfe EA, Tadese M, Beyene E, Abebe AM, Adoshe DM, Effect of cullet on firing temperature and dielectric properties of porcelain insulator, Heliyon, 2022; 8(2). https://doi.org/10.1016/j.heliyon.2022.e08922

[8] Beyene E, Tiruneh SN, Andoshe DM, Abebe AM, Tullu AM, Partial substitution of Feldspar by alkaline-rich materials in the electrical porcelain insulator for reduction of processing temperature, Materials Research Express, 2022. 9. https://doi.org/10.1088/2053-1591/ac7301

[9] Sanz J, Tomasa O, Jimenez-Franco A, Sidki-Rius N, Talc. In: Elements and Mineral Resources, 2022; 391-393. https://doi.org/10.1007/978-3-030-85889-6_98

[10] Abdel-Rahman AM, El-Desoky HM, Shalaby BNA, Awad HA, Ene A, Heikal MA, El-Awny H, Fahmy W, Taalab SA, Zakaly HMH, Ultramafic Rocks and Their Alteration Products From Northwestern Allaqi Province, Southeastern Desert, Egypt: Petrology, Mineralogy, and Geochemistry. Front. Earth Sci., 2022; 10. https://doi.org/10.3389/feart.2022.894582

[11] Baba AA, Ibrahim AS, Bale RB, Adekola FA, Alabi AGF, Purification of a Nigerian Talc ore by acid leaching. Applied Clay Science, 2015; 114: 476-483. https://doi.org/10.1016/j.clay.2015.06.031

[12] Olajide-Kayode JO, Okunlola OA, Olatunji AS, Compositional Features and Industrial Assessment of Talcose Rocks of Itagunmodi-Igun Area, Southwestern Nigeria, Journal of Geoscience and Environment Protection, 2018; 6: 59-77 https://doi.org/10.4236/gep.2018.61005

[13] Emmanuel S A, Physicochemical Evaluation of Some Talc Mineral Deposits Collected From Four States In Nigeria, Journal of Chemical Society of Nigeria, 2022; 47(4): 712 - 717. https://doi.org/10.46602/jcsn.v47i4.779

[14] Mgbemere HE, Obidiegwu EO, Oginni AA, Production and Characterisation of Porcelain Insulator Modified with Talc and Bentonite, Nigerian Research Journal of Engineering and Environmental Sciences, 2020; 5(2): 659-671.

[15] ASTM C20-00, Standard Test Methods for Apparent Po¬rosity, Water Absorption, Apparent Specific Gravity and Bulk Density of Burned Refractory Brick and Shaped by Boiling Water, ASTM International, 2015.

[16] ASTM C356-17, Standard Test Method for Linear Shrink¬age of Preformed High Temperature Thermal Insulation Subject¬ed to Soaking Heat, ASTM International, 2017.
[17] Nwachukwu VC, Lawal SA, Investigating the Production Quality of Electrical Porcelain Insulators from Local Materials, IOP Confer. Ser.: Materials Science and Engineering, 2018; 413(012076). https://doi.org/10.1088/1757-899X/413/1/012076
[18] Moyo MG, Park E, Ceramic Raw Materials in Tanzania - Structure and Properties for Electrical Insulation Application, International Journal of Engineering Research & Technology, 2014; 3 (10).
[19] Xu X, Lao X, Wu J, Zhang Y, Xu X, Li K, Microstructural evolution, phase transformation, and variations in physical properties of coal series kaolin powder compact during firing, Applied Clay Science, 2015; 115: 76-86. https://doi.org/10.1016/j.clay.2015.07.031
[20] Herna'ndez MF, Violini MA, Serra MF, Conconi MS, Suarez G, Rendtorff MN, Boric acid (H3BO3) as flux agent of clay-based ceramics, B2O3 effect in clay thermal behavior and resultant ceramics properties, Journal of Thermal Analysis and Calorimetry, 2020; 139:1717-1729. https://doi.org/10.1007/s10973-019-08563-4
[21] Shanjun K, Yanmin W, Zhidong P, Chengyun N, Shulong Z, Recycling of polished tile waste as a main raw material in porcelain tiles, Journal of Cleaner Production, 2016; 115: 238-244. https://doi.org/10.1016/j.jclepro.2015.12.064
[22] Valmir J, Michelle F, Wherllyson PG, Romualdo R, Gelmires A, Hélio L, Lisiane N, Porous mullite blocks with compositions containing kaolin and alumina waste, Ceramics International, 2016; 42(14): 15471-15478. https://doi.org/10.1016/j.ceramint.2016.06.199
[23] Garcia-Valles M, Alfonso P, Martínez S, Núria R, Mineralogical and Thermal Characterization of Kaolinitic Clays from Terra Alta (Catalonia, Spain). Minerals, 2020; 10: 142. https://doi.org/10.3390/min10020142
[24] Krupa P, Malinarič S, Thermal Properties of green alumina porcelain. Ceramics International, 2015; 41: 3254-3258. https://doi.org/10.1016/j.ceramint.2014.11.015
[25] De Aza AH, Turrillas X, Rodriguez MA, Pena DP.Time-resolved powder neutron diffraction study of the phase Transformation sequence of kaolinite to mullite. Journal of the European Ceramic Society, 2014; 34: 1409-1421. https://doi.org/10.1016/j.jeurceramsoc.2013.10.034
[26] Njoya, D, Tadjuidje FS, Ndzana EJA, Pountouonchi, A., Tessier-Doyen, N., and Lecomte-Nana, G. Effect of Flux Content and Heating Rate on The Microstructure and Technological Properties of Mayouom (Western-Cameroon) Kaolinite Clay Based Ceramics. Journal of Asian Ceramic Societies, 2017; 5 (4): 422-426. https://doi.org/10.1016/j.jascer.2017.09.004

Research on Engineering Structures & Materials
www.jresm.org
Research Group

Research Article

Experimental study on the effect of colloidal nano silica in self-compacting concrete containing ground granulated blast furnace slag

K. Shyam Sundar Murty*[,a], G.V. Rama Rao[b], S. Adiseshu[c]

Department of Civil Engineering, Andhra University, Visakhapatnam, India

Article Info

Article history:

Received 02 Dec 2023
Accepted 23 Mar 2024

Keywords:

Colloidal nano silica;
Self-compacting concrete;
Flowability

Abstract

Self-compacting concrete (SCC) is profusely utilized in building construction due to its unique design and mechanism of flow without segregation by occupying the corners and preventing the voids to achieve better compaction and mechanical strength. This work addresses the effect of colloidal nano-silica (NS) of size 5-40nm with an active nano solids content of 32% on SCC containing Ground Granulated Blast Furnace Slag (GGBFS) and Ordinary Portland Cement as binders in addition to NS. The liquid content of 68% in NS was added to the water content in the mix. The ratios of NS were evaluated at 0%,0.5%,1%,1.5%, 2% and GGBFS as 20% by weight of binder in concrete. The water to binder ratio was 0.33 with a water and binder content of 184kg/m^3 and 557.58 kg/m^3. The optimum mix was 1.5% NS based on the concrete's slump and compressive strength at 28 days. The slump was reduced with a rise in NS beyond 1.5% due to the accumulation of NS particles causing the reduction in flowability. The density of SCC for all the mixes was satisfactory. The compressive strength of optimum SCC, $M_2$1.5NS20G was decreased by 5.88% and increased by 0.49% and 2.45% at 7, 28 and 91 days to that of the reference mix whereas its split tensile strength was risen by 31.13%, 9.27%, and 12.41% and flexural strength was risen by 5.8% and reduced by 8.17% and 4.06% to that of the reference mix at aforementioned durations. The SEM and XRD analyses were conducted on the optimum hardened SCC mix at 28 days in which the presence of Calcium silicate hydrate compounds of different crystalline structures, viz., Ettringite, and Portlandite were observed. The SCC designed in the work can be used for structural applications such as beam-column joints.

1. Introduction

Self-compacting concrete (SCC) is extensively utilized in the construction sector and was first proposed in 1986 with the development of the first prototype in 1988 in Japan using the materials available in the market, to solve labour scarcity, achieve durable structures with good compaction without vibration, thereby reducing the voids in members and at the junctions of congested reinforcements [1-4]. The method uses a superplasticizer, meagre aggregate content, and a lower ratio of water and powder to attain self-compaction, high deformability, viscosity, and hindrance to segregation during the concrete flow through the congested reinforcement [1-2]. As the gap between the particles diminishes, the number of collisions per unit of time, interparticle contact and internal stress rise as the concrete deforms, especially near obstructions [1]. The thickening of shear in SCC, which is caused by the cluster formations of Brownian motion of small particles that lead the viscosity to increase the shear rate, is significant to be considered to prevent the damage of mixers, conduits, and pipes [7]. The packing density of total

*Corresponding author: kssundar.phd@andhrauniversity.edu.in
[a] orcid.org/0000-0001-5138-9448; [b] orcid.org/0000-0002-3443-8890; [c] orcid.org/0000-0001-9415-0453
DOI: http://dx.doi.org/10.17515/resm2024.105me1204rs

aggregate in SCC lies between 50% and 60% to decrease the relation between them and limit the shear deformation of concrete [1-2]. The pressure transferability occurs when mortar undergoes normal stress between coarse aggregate particles [1,5]. The reduction in shear deformation of mortar relies on the solid particles' behaviour in the mortar [6]. Industrial waste such as GGBFS, fly ash, etc. containing pozzolanic behaviour are used in SCC, to avoid their disposal onto the land [9]. The enhancement of the strengths of SCC depends on the proportion of SCM to be replaced or added to the cement [9-13]. There were no standard guidelines for the Self-Compacting concrete mix design during its entry into the construction market and the construction companies had proposed their procedures for the concrete [14]. In the year 2005, guidelines were proposed for SCC, receiving international recognition [15]. India had also adopted the guidelines for SCC in IS 10262:2019 Concrete Mix Design Proportions [16].

GGBFS, a final byproduct obtained from steel making, contains calcium oxide and silica in major proportions, and alumina and Magnesia in minor proportions. 'The hydraulic capability of GGBFS was first discovered by Emil Langen in Germany in 1862' and its commercial production was commenced in 1865 [17]. Later, it was widely spread across Europe to produce Portland slag cement to be used in underground structures to oppose the aggressive conditions in the ground [17]. The grinding of GGBFS was carried out by two processes viz. wet process [18], with limitations having developed by Victor Trief in Belgium, and dry process that was further adopted successfully [17]. The hydraulic activity of GGBFS depends on the chemical composition that determines its basicity index with the quick lime-to-silica ratio to be greater than 1[19] and it is enhanced with increasing calcium, magnesium, and aluminum oxide ranges and diminished with rising silica in water [20]. GGBFS causes variations in hydration products due to C-S-H gel, resulting in larger pore volumes in the cement matrix, high water absorption, and reduced strength. The activated alumina further reacts with portlandite and gypsum to produce Ettringite [21,22]. GGBFS has a superior water reduction effect and reduces the time-dependent loss of slump flow and fluidity [23]. Workability is reduced by the huge surface area with uneven surface texture of GGBFS [24]. Superplasticizer (SP) improves the performance of fresh mixture and disperses the powder particles through steric repulsion and its adsorption on cement particles might lower the initial hydration resulting in slow setting as well as initial strength growth of the paste [25]. GGBFS occupies the spaces in the aggregate to form denser concrete and influences the development of strength in SCC which depends on water-to-cement (w/c) ratio and quantity of GGBFS with the former's increase leading to the increase in the latter at the three different percentages of slag [26]. Compression, split tension and flexure of concrete are increased up to 20% substitution of GGBFS beyond which they are reduced due to a dearth of flowability [24, 26, 27] and dilution effect that forms the alkali–silica reaction with a huge amount of unreactive silica present in GGBFS [28]. The alkali-silica reaction stresses the concrete to enlarge forming the cracks [29].

Colloidal nano silica (NS), obtained from the Weber Stober process [30], contains dense, 'amorphous hydroxylated silica particles' of size 1-100 nm in an aqueous form [31], is used in the construction sector [32,33]. The vast specific surface area of NS contributes to an aggregate-cement binder [34] and entails a high water–cement ratio. A higher quantity of PCE-based super-plasticizer is used to enhance flow properties to reduce particle agglomeration, and improper dispersion, and improve workability [35,43]. PCE improves NS dispersion and compressive strength of mortar and lowers the porosity and dangerous voids in hardened cement paste [36]. Well–dispersed nanoparticles activate to improve the hydration and consume the portlandite to form excess C-S-H gel during pozzolanic reactions [37-39] and thicken the cement paste [39]. The concrete's initial age strength is increased and its initial and final setting times are shortened by nano silica particles [40].

The ITZ is also improved by the packing of smaller particles in all voids to decrease permeability [41]. When the amount of NS increases, the slump reduces due to the formation of silanol groups and inadequate water [42]. Adding up to 2% to 3% of NS as a replacement for cement in concrete can enhance its strength by leveraging its pozzolanic reactivity and filling action [43-45].

Considering the previous research works on colloidal nano silica, it has been noted that the separate addition of NS solids content to binder materials and NS liquid content to the water and their effect on the workability and mechanical strengths of SCC were not discussed. The objective of the current research work is to investigate workability properties, mechanical strength properties and microstructural analysis of the high-strength self-compacting concrete of Grade 50 incorporated with cement, GGBFS and colloidal nano silica (32% solids and 68% liquid) as cementitious materials and Auramix 300 plus as superplasticizer of PCE type.

2. Experimental Work

2.1 Materials

Ordinary Portland Cement 53 grade of KCP brand, confirming to IS 269:2015 [49] and GGBFS, confirming to IS 16714-2018 [50], the by-product of Visakhapatnam Steel Plant, were used in concrete mix and their chemical and physical characteristics are presented in Table 1 and Table 2 respectively. Colloidal Nano silica, designated as CemSyn XTX*, having a specific gravity of 1.22, was manufactured and procured from Beechems, Kanpur, Uttar Pradesh, India. The solid particles visible in Transmission Electron Microscopy image as shown in Fig. 1, contain active nano silica with liquid among them.

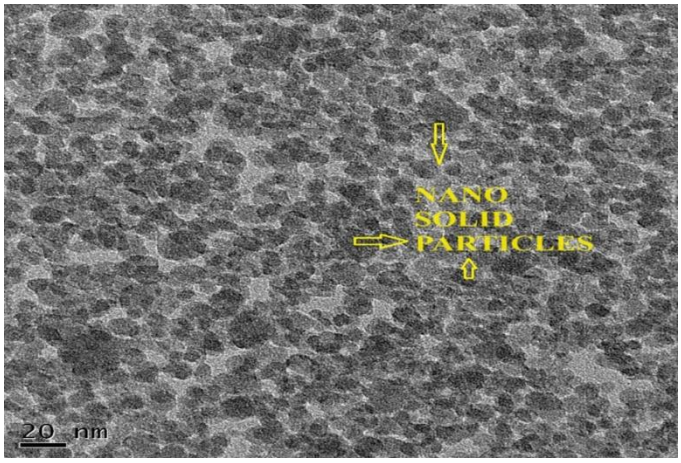

Fig. 1. TEM image of Colloidal Nano Silica

Coarse aggregate of size 10mm, having specific gravity 2.88, confirming to IS 383:2016 [51], was obtained from Anjani Stone Crushers, Duddupalem, Anakapalli, India. River sand of type Zone – II having Fineness modulus 2.66 and specific gravity 2.61, confirming to IS 383:2016, was utilized as fine aggregate in concrete mix [51]. Chemical admixture, Auramix 300 Plus of specific gravity 1.08**, which contains Viscosity Modifying Admixture procured from FOSROC, confirming to IS 9103-1999 [52], was used in SCC. Potable water was used during the concrete mixing.

Table 1. Chemical characteristics

Sl. No.	Characteristic	OPC 53***	Requirements as per IS 269:2015	GGBFS****	Requirements as per IS 16714:2018
1	Lime Saturation Factor	0.92	0.8-1.02	-	-
2	Ratio of percentage of Alumina to that of Iron Oxide	1.24	Min. 0.66	-	-
3	Insoluble Residue (% by mass)	0.47	Max. 5.0	0.78	Max. 3.0
4	Magnesia (% by mass)	1.10	Max. 6.0	8.86	Max. 17
5	Sulphuric Anhydride (% by mass)	1.74	Max. 3.5	0.66	Max. 3
6	Total loss of ignition (%)	1.24	Max. 4.0	NIL	Max. 3
7	Chlorides (%)	0.002	Max. 0.1	0.012	Max. 0.1
8	Manganese Oxide (%)	-	-	0.72	Max. 5.5
9	Sulphide Sulphur (%)	-	-	0.78	Max. 2

Table 2. Physical characteristics

Sl. No.	Characteristic	OPC 53	Requirements as per IS 269:2015	GGBFS	Requirements as per BS 6699:1992
1	Fineness (m^2/kg)	299***	Min. 225	342****	Min. 275
2	Soundness LeChatelier Expansion(mm)	0.5	Max. 10	NIL	Max. 10
3	Initial Setting Time (min.)	165	Min. 30	185	More than 30
4	Normal Consistency (%)	29.5	-	29	-
5	Specific gravity	3.13	-	2.9	-
6	Compressive strength (MPa) 7 days	49	Min. 37	29	Min. 12.0
	28 days	60	Min. 53	49	Min. 32.5

Courtesy: *Bee Chems, Kanpur, Uttar Pradesh, India

**FOSROC constructive solutions

***KCP Cement Limited, Andhra Pradesh, India

**** Sri Vishnu Sai Saravana Enterprises, Autonagar, Visakhapatnam, India

2.2 SCC Mix Design

In this research work, with reference to IS 10262:2019 [16], the standard deviation of concrete of Grade is 5N/mm^2. The mean target strength of the concrete of grade 50 is 58.25 N/mm^2. The entrapped air content was taken as 1.5% of the volume of concrete for the nominal aggregate maximum size of 10mm. GGBFS was taken at a proportion of 20% [24,26,27] and the solids content in colloidal nano silica was taken in different proportions of 0%, 0.5%, 1%,1.5% and 2% by weight of the binder content and liquid content was added to the potable water by calculating it separately. The remaining proportion of the binder material contains cement. Based on the trials, the water to binder ratio was adopted to be 0.33 with the binder material and water content as 557.57 kg/m^3 and 184 kg/m^3. The influence of GGBFS on the fresh SCC depends on the fineness and admixture proportion as it retains water at increased fineness to lower fluidity and slump flow [24,26,27]. The admixture was considered 0.5% for concrete containing 0% NS and 0.7% for concrete containing the rest of the proportions of NS by weight of binder content. The mixes were given notation as mentioned in Table 3. The fines required were then calculated. The percentage of particles passing through 0.125 mm IS sieve was 3%. The total aggregate quantity was obtained in which fine aggregate lies within the limits of 48% to 60%. Water to-powder ratio was within the limits.

Table 3. Quantity of constituents in SCC

Mix Notation / Constituents	$M_2$0NS 20G	$M_2$0.5NS 20G	$M_2$1NS 20G	$M_2$1.5NS 20G	$M_2$2NS 20G
Cement (kg/m^3)	446.06	445.17	444.28	443.38	442.49
GGBFS (kg/m^3)	111.52	111.52	111.52	111.52	111.52
NS (kg/m^3)	0	2.79	5.58	8.36	11.15
NS(Solids) (kg/m^3)	0	0.89	1.78	2.68	3.57
NS(Liquids) (kg/m^3)	0	1.89	3.79	5.69	7.58
Water (kg/m^3)	184	184	184	184	184
Fine Aggregate (kg/m^3)	814.14	814.14	814.14	814.14	814.14
Coarse Aggregate (kg/m^3)	879.9	871.17	865.41	859.65	853.89
Chemical Admixture (kg/m^3)	2.79	3.90	3.90	3.90	3.9
water-binder ratio	0.33	0.33	0.33	0.33	0.33
Fines required (kg/m^3)	24.42	24.42	24.42	24.42	24.42
Powder content (kg/m^3)	582	582	582	582	582
Water powder ratio by volume	0.97	0.96	0.96	0.96	0.96

M_2 0NS 20G M_2 = M 50 0NS = 0% NS 20G = 20% GGBFS

The constituents were mixed in the concrete mixer. The fresh concrete was tested for its workability after mixing as shown in Fig.2. The flow table was allowed to rotate and subjected to impact as shown in Fig.2(a). The concrete was spread horizontally throughout the circumference of the table considering a maximum distance(mm) between the far ends to be slump indicating the flowability as shown in Fig.2(b). The concrete was poured into the V-Funnel to find the viscosity by counting down the time taken (s) to pass through it as shown in Fig.2(c) and in the L-Box through the vertical duct to pass down and move in the horizontal portion to study the passing ability as shown in Fig.2(d) [16].

2.3 Preparation of Test Specimens

A total of 45 standard cube specimens of size 150mm x150mmx150mm were cast with the fresh concrete of the five different mixes. They were placed in ambient curing for 24 hours at 27±2°C and then in water curing after demoulding for the different durations of 7, 28, and 91 days [53]. Three specimens of all five mixes were tested for the compressive strength for the corresponding durations. The same procedure was repeated for 45 standard cylindrical specimens of size 150mm diameter and 300 mm length to test for Split Tensile strength and 45 standard prism specimens of size 100mm x 100mm x500mm to test for flexural strength [53]. The notations for the specimens were considered as $M_2$0NS20G (reference mix), $M_2$0.5NS20G, $M_2$1NS20G, $M_2$1.5NS20G and $M_2$2NS20G.

3. Results and Discussions

3.1 Workability Tests on SCC

The workability test values of SCC are mentioned in Table 4. The slump of M_2 0NS20G is classified as SF1 and $M_2$0.5NS20G, $M_2$1NS20G and $M_2$1.5NS20G are classified as SF2 [16]. The slump flow of $M_2$2NS20G was very less due to the assemblage of NS particles in the mix. The mix, M_2 0.5 NS 20G, passed completely through the L-box like a liquid [16]. The viscosity of all the mixes exceeded 25 seconds i.e., V2 [16]

Table 4. Fresh properties of SCC

Mix Notation	Slump(mm)	h_1(mm)	h_2(mm)	Passing Ability (h_1/ h_2)	Viscosity(s)
M_2 0NS 20G	620	53	315	0.17	96.00
M_2 0.5 NS 20G	670	65	65	1.00	32.19
M_2 1NS 20G	670	55	128	0.43	28.40
M_2 1.5NS 20G	680	42	210	0.20	64.95
M_2 2NS 20G	500	40	270	0.15	60.12

(a)

(b)

(c) (d)

Fig. 2 Workability tests on scc (a) flow table equipment, (b) slump flow, (c) viscosity test, and (d) passing ability test using L-Box

3.2 Compressive Strength

The strength of $M_20.5NS20G$, $M_21NS20G$, $M_21.5NS20G$ and $M_22NS20G$ was decreased by 9.25%, 4.20%, 5.88%, and 17.09% to that of the reference mix, $M_20NS20G$ at 7 days and the tests were conducted on 300T compression testing machine as shown in Fig.4. Similarly, the strength of $M_20.5NS20G$, $M_21NS20G$, $M_22NS20G$ was decreased by 7.60%, 6.52%, 4.34% and $M_21.5NS20G$ increased by 0.49% of that of the reference mix at 28 days. The strength of $M_20.5NS20G$, $M_21NS20G$, $M_22NS20G$ was decreased by 5.89%, 3.20%, 11.92% and $M_21.5NS20G$ increased by 2.45% to that of the reference mix at 91 days respectively as shown in Fig.3.

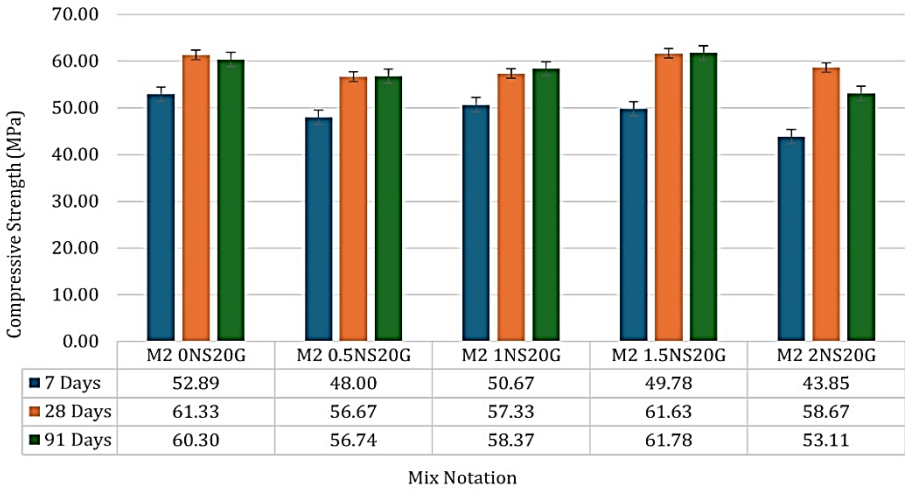

	M2 0NS20G	M2 0.5NS20G	M2 1NS20G	M2 1.5NS20G	M2 2NS20G
7 Days	52.89	48.00	50.67	49.78	43.85
28 Days	61.33	56.67	57.33	61.63	58.67
91 Days	60.30	56.74	58.37	61.78	53.11

Fig. 3. Variation of compressive strength of SCC at 7,28,91 days

The reduction in strengths of 0.5%,1% NS concrete might be due to the possible lack of dispersion of nanoparticles, which can lead to weak zones [47]. It has been noted that there

is a minor difference in the strength between the reference and optimum mixes except in the slump values and the minute enhancement of compressive strength in the optimum mix was increased by pozzolanic reactivity and the generation of extra C-S-H gel [46]. The mix containing 2% NS in pozzolanic reaction is diminished by its agglomeration and changes the original amorphous C-S-H gel into tobermorite leading to reduced compressive strength [47].

Fig. 4. Compressive strength test using 300T CTM

3.3 Split Tensile Strength

The strength of SCC mixes of $M_20.5NS20G$ and $M_21NS20G$ was decreased by 10.38%, 18.87% and $M_21.5NS20G$, $M_22NS20G$ increased by 31.13% and 20.75% that of the reference mix, $M_20NS20G$ at 7 days and the tests were conducted on 300T compression testing machine as shown in Fig.6.

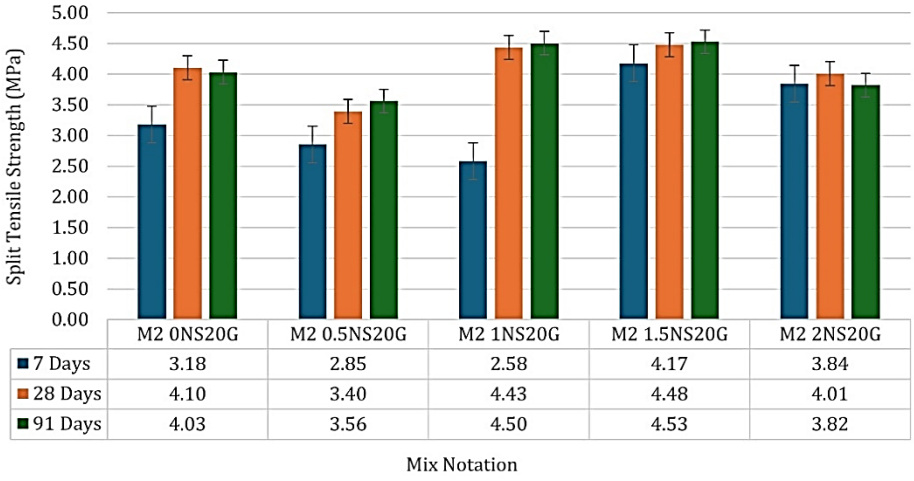

	M2 0NS20G	M2 0.5NS20G	M2 1NS20G	M2 1.5NS20G	M2 2NS20G
7 Days	3.18	2.85	2.58	4.17	3.84
28 Days	4.10	3.40	4.43	4.48	4.01
91 Days	4.03	3.56	4.50	4.53	3.82

Fig. 5. Variation of split tensile strength of SCC at 7,28,91 days

Similarly, the strength of $M_20.5NS20G$, $M_22NS20G$ was decreased by 17.07%, 2.19% and M21NS20G and $M_21.5NS20G$ was increased by 8.05%, 9.27% to that of the reference mix

at 28 days. The strength of $M_20.5NS20G$, $M_22NS20G$ was decreased by 11.66%, 5.21% and $M_21NS20G$, $M_21.5NS20G$ increased by 11.66%, 12.41% to that of the reference mix at 91 days respectively as shown in Fig.5. The cause of strength variance when compared to reference mix might be due to the improper nanoparticle dispersion that form weak portions [47]. When the proportion of NS exceeds 1.5%, the excess silica is leached out due to the liberated lime during cement hydration which leads to strength reduction [46,47].

Fig. 6. Split tensile strength test using 300T CTM

3.4 Flexural Strength

The strength of SCC mixes of $M_20.5NS20G$, $M_22NS20G$ was decreased by 0.70%, 3.51% and $M_21NS20G$, $M_21.5NS20G$ increased by 5.62%, 5.80% to that of the reference mix, $M_20NS20G$ at 7 days and the tests were carried out on 100T universal testing machine. The strength of $M_20.5NS20G$, $M_21NS20G$, $M_21.5NS20G$ and $M_22NS20G$ was decreased by 13.44%, 8.56%, 8.17% and13.44% to that of the reference mix at 28 days.

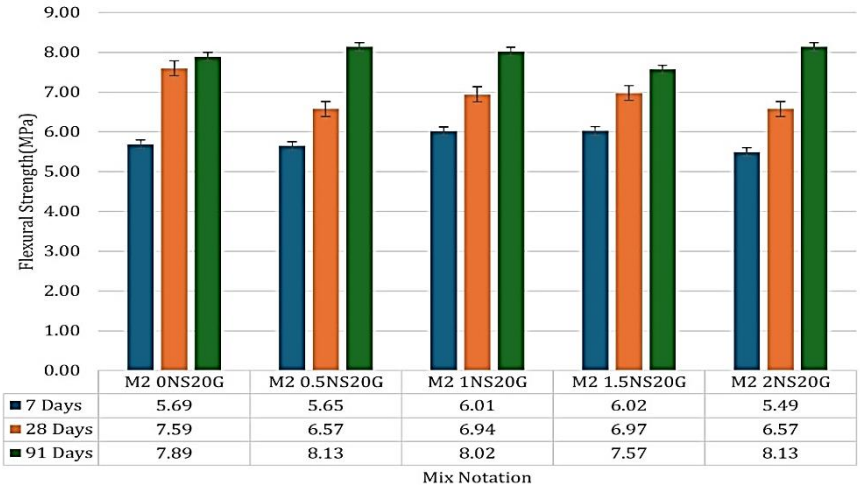

Fig. 7Variation of flexural strength of SCC at 7,28,91 days

The strength of $M_2$1.5NS20G was decreased by 4.06% and $M_2$0.5NS20G, $M_2$1NS20G, $M_2$2NS20G increased by 3.04%, 1.65%, 3.04% that of reference mix at 91 days respectively as shown in Fig.7. Due to the rapid utilization of portlandite produced during the early age hydration of cement due to the high NS reactivity, the flexural strength increased up to 1.5% [48]. However, at 28 days, it decreased in comparison to the reference mix, but it still exceeded the estimated flexural strength as per IS 456:2000 [54] and the required slump was achieved.

Fig. 8. Flexural strength test using 100T UTM

3.5 Microstructural studies on SCC

Scanning Electron Microscopy (SEM) and X-ray Diffraction (XRD) tests were conducted on the optimum SCC mix, $M_2$1.5NS20G at 28 days, to study the compounds present in the concrete. The sample from the cube specimen was taken and ground into the powder using the impact testing equipment and then, it was sieved through 75 micron IS Sieve. The fine powder passed through the sieve was collected for the tests. The powder was compressed to a pill and dispersed in volatile solvent and placed on mounting pin for the test. Scanning Electron Microscope (SEM) test is an instrument used to produce a magnified image to study the internal structure of the material by ejecting electrons instead of light from an electron gun with much higher resolution due to the usage of electromagnets to control the degree of magnification to generate X-rays, backscattered and secondary electrons for image detection.

Fig.9 illustrates the needle-shaped crystals of calcium tri sulfoaluminate or Ettringite, large prismatic crystals of calcium hydroxide and fiber-shaped C-S-H which enhanced strength of concrete. Similarly, NS enhanced the C-S-H gel formation and reduced calcium hydroxide to form a dense concrete structure [37-39].

X-Ray Diffraction [55] is a method to find compounds present in the sample by emitting X-rays from a X-ray tube that is placed on a goniometer along with sample, optics and detector. The powdered sample was placed on a glass slide in sample holder. The number of X-rays scattered by the sample is counted at each angle 2θ by the detector and its position is recorded as 2θ. The X-ray intensity is recorded as counts per unit time. The equipment is connected to Panalytical XPert High Score software (ICDD indexed) to identify the compounds as shown in Fig.10. The long-range order with sharp maxima and peak position indicates the crystalline nature. with Etrringite (Hexacalcium aluminate trisulfate hydrate), Xonotlite and Thaumasite (Calcium silicate hydrates), Yeelimite

(Calcium sulfo aluminate) were identified as crystalline compounds with the parameters of the intensity (height of the peak), Full Width of Half Maximum (crystalline size) and detector angle (2θ).

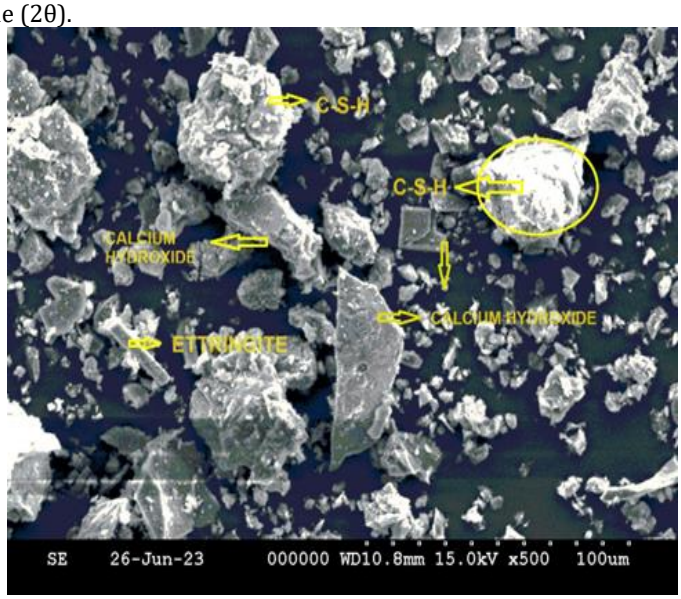

Fig. 9. SEM image of 28 days hardened SCC, $M_2$1.5NS20G

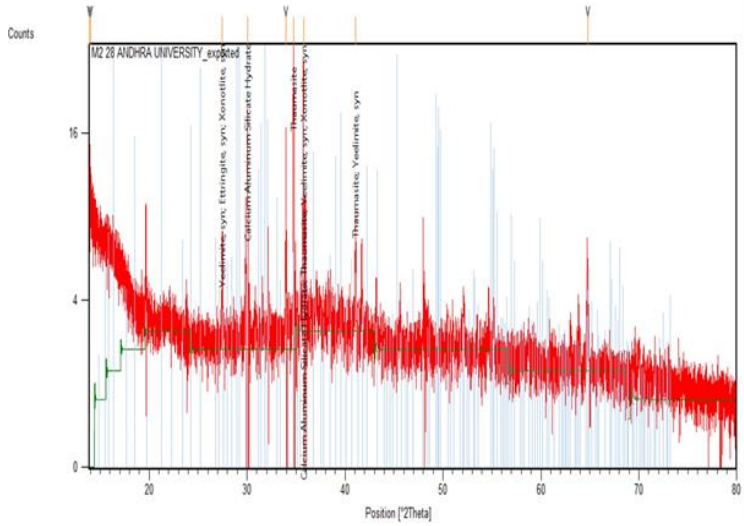

Fig. 10. XRD pattern of 28 days SCC, $M_2$1.5NS20G

4. Conclusions

- The slump of the SCC was maximum at 1.5% NS as a binder, beyond which the NS solid particles accumulated and reduced the flow of SCC and the additional amount of superplasticizer (>0.7% of binder material) must be added to maintain the workability of the mix beyond 1.5% NS.

- The compressive strength of optimum SCC was reduced by 5.88% at 7 days and was increased by 0.49% and 2.45% at 28 days and 91 days to that of the reference mix respectively. Despite the minor rise in optimum strength compared to reference mix, the high slump value of the optimum mix was achieved with a significant difference. NS, having a very small particle in size, enhanced the strength due to good pozzolanic activity and filled the voids in SCC, including ITZ, and formed extra C-S-H gel.
- The split tensile strength of optimum SCC at 7, 28 and 91 days was increased by 31.13%, 9.27% and 12.41% to that of the reference mix respectively. When the proportion of NS exceeds 1.5%, the excess silica was leached out due to the liberated lime during cement hydration and strength reduction.
- The flexural strength of optimum SCC was decreased by 8.17% and 4.06% at 28 days and 91 days whereas it was increased by 5.8% at 7 days to that of the reference mix respectively. Its increase of up to 1.5% compared to other NS mixes was due to the quick utilization of portlandite liberated during the cement hydration at early ages due to the high reactivity of NS. Although the flexural strength of the optimum mix is less than that of the reference mix, it exceeded the estimated strength value and achieved the required slump.
- Due to its greater specific surface area, NS functions as a binder between cement and aggregate, shortening the initial and final setting time and improving early age strength.
- SEM and XRD pictures indicated calcium hydroxide and calcium silicate hydrate compounds with different crystalline structures. Strength is primarily due to these compounds. NS also increased C-S-H gel development and lowered calcium hydroxide, resulting in a compact concrete structure.

5. Scope for further study

- The current research can be expanded by incorporating a higher concentration of solid particles in the NS and examining its impact on the characteristics of SCC.
- The effect of adding another binder material in SCC in addition to the existing ones, can be investigated.

References

[1] Okamura H, Ouchi M. Self-Compacting Concrete. Journal of Advanced Concrete Technology 2003;1:5–15. https://doi.org/10.3151/jact.1.5

[2] Hajime Okamura (Prof.) & Kazumasa Ozawa (Assoc. Prof.) Self-Compacting High Performance Concrete, Structural Engineering International, 1996,6:4, 269-270, https://doi.org/10.2749/101686696780496292

[3] Ozawa,K.,Maekawa,K.,Kunishima,M.,and Okamura,H.Development of high-performance concrete based on the durability design of concrete structures.Proceedings of the second East- Asia and Pacific Conference on Structural Engineering and Construction 1989;(EASEC-2), 1, 445-450.

[4] Okamura, H., Maekawa, K., and Ozawa, K.High Performance Concrete.Gihodo Publishing.1993; https://www.researchgate.net/publication/285281222_Development_of_High_Performance_Concrete

[5] Ouchi, M. and Edamatsu, Y. A Simple evaluation method for interaction between coarse aggregate and mortar particles in self-compacting concrete. Transaction of JCI. 2000; https://www.rilem.net/images/publis/pro007-011.pdf

[6] Nagamoto, N., and Ozawa, K.Mixture properties of Self-compacting, High-performance concrete.ACI International, 1997; SP-172, 623-636.

https://www.concrete.org/publications/internationalconcreteabstractsportal/m/details/id/6155
[7] Feys D, Verhoeven R, De Schutter G. Why is fresh self-compacting concrete shear thickening? Cement and Concrete Research 2009;39:510–23. https://doi.org/10.1016/j.cemconres.2009.03.004
[8] Nandhini K, Karthikeyan J. A review on sustainable production of self-compacting concrete utilizing industrial by-products as cementitious materials. Innovative Infrastructure Solutions 2022;7. https://doi.org/10.1007/s41062-022-00792-1
[9] Mahalingam B, Nagamani K, Kannan LS, Mohammed Haneefa K, Bahurudeen A. Assessment of hardened characteristics of raw fly ash blended self-compacting concrete. Perspectives in Science 2016;8:709–11. https://doi.org/10.1016/j.pisc.2016.06.066
[10] Esquinas AR, Ledesma EF, Otero R, Jiménez JR, Fernández JM. Mechanical behaviour of self-compacting concrete made with non-conforming fly ash from coal-fired power plants. Construction and Building Materials 2018;182:385–98. https://doi.org/10.1016/j.conbuildmat.2018.06.094
[11] Altoubat S, Talha Junaid M, Leblouba M, Badran D. Effectiveness of fly ash on the restrained shrinkage cracking resistance of self-compacting concrete. Cement and Concrete Composites 2017;79:9–20. https://doi.org/10.1016/j.cemconcomp.2017.01.010
[12] Benaicha M, Roguiez X, Jalbaud O, Burtschell Y, Alaoui AH. Influence of silica fume and viscosity modifying agent on the mechanical and rheological behavior of self compacting concrete. Construction and Building Materials 2015;84:103–10. https://doi.org/10.1016/j.conbuildmat.2015.03.061
[13] Fakhri M, Yousefian F, Amoosoltani E, Aliha MRM, Berto F. Combined effects of recycled crumb rubber and silica fume on mechanical properties and mode I fracture toughness of self-compacting concrete. Fatigue & Fracture of Engineering Materials & Structures 2021;44:2659–73. https://doi.org/10.1111/ffe.13521
[14] Geert De Schutter, Peter J.M.Bartos, Peter Domone, John Gibbs. Self-Compacting Concrete. Whittles Publishing, CRC Press, 2008:16-17,ISBN 978-1904445-30-2.
[15] EFNARC:2005 Specification and Guidelines for Self-Compacting Concrete
[16] IS 10262:2019 Indian Standard Concrete Mix Proportioning – Guidelines (Second Revision)
[17] Dennis Higgins Fifty Years of Experience in the UK using GGBS as an addition to concrete. International RILEM Conference series on Material Science – MATSCI, Aachen 2010 – Vol.III AdIPoc pg.15-20. https://www.rilem.net/images/publis/pro077-002.pdf
[18] The Trief cement process: corrosion-resisting concrete in U.K. Anti-Corrosion Methods and Materials 1955; 2:199–199. https://doi.org/10.1108/eb019071
[19] Nkinamubanzi, P.C.; Baalbaki, M.; Bickley, J.; Aitcin, P.C.The Use of Slag for Making High Performance Concrete. In Proceedings of the 6th NCB International Seminar on Cement and Bulding Materials, New Delhi, India, 24–27,1998
[20] Pal SC, Mukherjee A, Pathak SR. Investigation of hydraulic activity of ground granulated blast furnace slag in concrete. Cement and Concrete Research 2003;33:1481–6. https://doi.org/10.1016/s0008-8846(03)00062-0
[21] Provis, J.L.; Van Deventer, J.S.Alkali Activated Materials: State-of-the-Art Report; RILEM TC 224-AAM; Springer: Dordrecht, 2014:Volume 13, ISBN 978-94-007-7671-5.
[22] Provis JL, Palomo A, Shi C. Advances in understanding alkali-activated materials. Cement and Concrete Research 2015;78:110–25. https://doi.org/10.1016/j.cemconres.2015.04.013
[23] Boukendakdji O, Kadri E-H, Kenai S. Effects of granulated blast furnace slag and superplasticizer type on the fresh properties and compressive strength of self-

compacting concrete. Cement and Concrete Composites 2012;34:583–90. https://doi.org/10.1016/j.cemconcomp.2011.08.013
[24] Patra RK, Mukharjee BB. Influence of incorporation of granulated blast furnace slag as replacement of fine aggregate on properties of concrete. Journal of Cleaner Production 2017;165:468–76. https://doi.org/10.1016/j.jclepro.2017.07.125
[25] Zhang Y, Kong X. Correlations of the dispersing capability of NSF and PCE types of superplasticizer and their impacts on cement hydration with the adsorption in fresh cement pastes. Cement and Concrete Research 2015;69:1–9. https://doi.org/10.1016/j.cemconres.2014.11.009
[26] Dadsetan S, Bai J. Mechanical and microstructural properties of self-compacting concrete blended with metakaolin, ground granulated blast-furnace slag and fly ash. Construction and Building Materials 2017;146:658–67. https://doi.org/10.1016/j.conbuildmat.2017.04.158
[27] Ganesh P, Murthy AR. Tensile behaviour and durability aspects of sustainable ultra-high performance concrete incorporated with GGBS as cementitious material. Construction and Building Materials 2019;197:667–80. https://doi.org/10.1016/j.conbuildmat.2018.11.240
[28] Mehta P.K. Greening of the Concrete Industry for Sustainable Development. Concr. Int. 24, 23–28,2002.
[29] Ahmad J, Martínez-García R, Szelag M, de-Prado-Gil J, Marzouki R, Alqurashi M, et al. Effects of Steel Fibers (SF) and Ground Granulated Blast Furnace Slag (GGBS) on Recycled Aggregate Concrete. Materials 2021;14:7497. https://doi.org/10.3390/ma14247497
[30] Stöber W, Fink A, Bohn E. Controlled growth of monodisperse silica spheres in the micron size range. Journal of Colloid and Interface Science 1968;26:62–9. https://doi.org/10.1016/0021-9797(68)90272-5
[31] Garg Rishav, Garg Rajni, Bansal M, Aggarwal Y. Experimental study on strength and microstructure of mortar in presence of micro and nano-silica. Materials Today: Proceedings 2021;43:769–77. https://doi.org/10.1016/j.matpr.2020.06.167
[32] P. P. A, Nayak DK, Sangoju B, Kumar R, Kumar V. Effect of nano-silica in concrete; a review. Construction and Building Materials 2021;278:122347. https://doi.org/10.1016/j.conbuildmat.2021.122347
[33] Singh LP, Bhattacharyya SK, Kumar R, Mishra G, Sharma U, Singh G, et al. Sol-Gel processing of silica nanoparticles and their applications. Advances in Colloid and Interface Science 2014;214:17–37. https://doi.org/10.1016/j.cis.2014.10.007
[34] Wang XF, Huang YJ, Wu GY, Fang C, Li DW, Han NX, et al. Effect of nano-SiO2 on strength, shrinkage and cracking sensitivity of lightweight aggregate concrete. Construction and Building Materials 2018;175:115–25. https://doi.org/10.1016/j.conbuildmat.2018.04.113
[35] Zareei SA, Ameri F, Bahrami N, Shoaei P, Moosaei HR, Salemi N. Performance of sustainable high strength concrete with basic oxygen steel-making (BOS) slag and nano-silica. Journal of Building Engineering 2019;25:100791. https://doi.org/10.1016/j.jobe.2019.100791
[36] Qian Y, De Schutter G. Enhancing thixotropy of fresh cement pastes with nanoclay in presence of polycarboxylate ether superplasticizer (PCE). Cement and Concrete Research 2018;111:15–22. https://doi.org/10.1016/j.cemconres.2018.06.013
[37] Zahiri F, Eskandari-Naddaf H. Optimizing the compressive strength of concrete containing micro-silica, nano-silica, and polypropylene fibers using extreme vertices mixture design. Frontiers of Structural and Civil Engineering 2019;13:821–30. https://doi.org/10.1007/s11709-019-0518-6
[38] Björnström J, Martinelli A, Matic A, Börjesson L, Panas I. Accelerating effects of colloidal nano-silica for beneficial calcium–silicate–hydrate formation in cement.

Chemical Physics Letters 2004;392:242–8. https://doi.org/10.1016/j.cplett.2004.05.071
[39] Ltifi M , Guefrech A, Mounanga P, Khelidj A.Experimental study of the effect of addition of nano-silica on the behaviour of cement mortars Mounir. Procedia Engineering;2011;10:900–905. https://doi.org/10.1016/j.proeng.2011.04.148
[40] Zhang M-H, Islam J, Peethamparan S. Use of nano-silica to increase early strength and reduce setting time of concretes with high volumes of slag. Cement and Concrete Composites 2012;34:650–62. https://doi.org/10.1016/j.cemconcomp.2012.02.005
[41] Sharkawi AM, Abd-Elaty MA, Khalifa OH. Synergistic influence of micro-nano silica mixture on durability performance of cementious materials. Construction and Building Materials 2018;164:579–88. https://doi.org/10.1016/j.conbuildmat.2018.01.013
[42] Mukharjee BB, Barai SV. Influence of Incorporation of Colloidal Nano-Silica on Behaviour of Concrete. Iranian Journal of Science and Technology, Transactions of Civil Engineering 2020;44:657–68. https://doi.org/10.1007/s40996-020-00382-0
[43] Nazar i A, Riahi S.Microstructural, thermal, physical and mechanical behavior of the self-compacting concrete containing SiO2 nanoparticles. Mater Sci Eng A 2010;527:7663–72. https://doi.org/10.1016/j.msea.2010.08.095
[44] Nazar i A, Riahi S. The role of SiO2 nanoparticles and ground granulated blast furnace slag admixtures on physical, thermal and mechanical properties of self-compacting concrete. Mater Sci Eng A 2011;528:2149-2157. https://doi.org/10.1016/j.msea.2010.11.064
[45] Amin M, Abu el-hassan K. Effect of using different types of nano materials on mechanical properties of high strength concrete. Construction and Building Materials 2015;80:116–24. https://doi.org/10.1016/j.conbuildmat.2014.12.075
[46] Khaloo A, Mobini MH, Hosseini P. Influence of different types of nano-SiO2 particles on properties of high-performance concrete. Construction and Building Materials 2016;113:188–201. https://doi.org/10.1016/j.conbuildmat.2016.03.041
[47] Najigivi A, Khaloo A, Iraji zad A, Abdul Rashid S. Investigating the effects of using different types of SiO2 nanoparticles on the mechanical properties of binary blended concrete. Composites Part B: Engineering 2013;54:52–8. https://doi.org/10.1016/j.compositesb.2013.04.035
[48] Amin M, Abu el-hassan K. Effect of using different types of nano materials on mechanical properties of high strength concrete. Construction and Building Materials 2015;80:116–24. https://doi.org/10.1016/j.conbuildmat.2014.12.075
[49] IS 269:2015 Ordinary Portland Cement – Specification (Sixth revision)
[50] IS 16714-2018 Ground Granulated Blast Furnace Slag for use in cement, mortar and concrete - Specification
[51] IS 383:2016 Coarse and Fine aggregate for concrete – Specification (Third revision)
[52] IS 9103:1999 Concrete admixtures – Specification (First revision)
[53] IS 516 (Part 1/Sec 1): 2021 Hardened Concrete -Methods of Test Part 1 Testing of Strength of Hardened Concrete Section 1 Compressive, Flexural and Split Tensile Strength (First Revision)
[54] IS 456:2000 Plain and Reinforced concrete- Code of practice (fourth revision)
[55] B.D.Cullity, S.R.Stock Elements of X-ray diffraction – Third edition.2014:191-200, ISBN 13: 978-1-292-04054-7

Research on Engineering Structures & Materials
www.jresm.org
Research Group

Research Article

Experimental study on the utilization of construction and demolition waste of recycled aggregate with GGBS and I-Crete in pavement quality concrete

B. Chitti Babu[*,a], K. Durga Rani[b]

Civil Engineering Department, Andhra University, Visakhapatnam, Andhra Pradesh, India

Article Info

Article history:

Received 20 Nov 2023
Accepted 27 Mar 2024

Keywords:

Recycled coarse aggregate;
Mechanical properties of fresh and hardened concrete;
Water absorption;
UPV;
GGBS;
I-Crete

Abstract

This study investigates the mechanical properties of M40 concrete in Pavement Quality Concrete (PQC) by incorporating Recycled Aggregates (RA) from construction, demolition waste and industrial wastes, such as GGBS and I-Crete, for sustainable pavement construction. The research explores varying proportions of RA (25% to 100% by weight in 25% intervals). Results show concrete mechanical strength decreases with higher RA proportions but all mixes still meet target strength criteria (compressive, flexural, split tensile) at 7, 28, and 90 days of curing. Further testing on 100% RA (MRCA-100) with GGBS admixture from 5% to 35% in 5% increments found strength improves significantly up to 10% GGBS replacement by cement weight, with subsequent decreases at higher percentages Initially. Then introducing the mineral additive, I-Crete at 2% by weight of cement in 15% to 35% GGBS range results in notable strength enhancement, peaking at 25% GGBS replacement. Ultrasonic pulse velocity (UPV) and water absorption tests showed similar trends in 28-day strength across all mixes. Increased strength from better bonding was observed, with Scanning Electron Microscopy (SEM) showing enhanced hydration and bonding due to mineral admixture and additive. These findings underscore the efficacy of such additives in enhancing the mechanical strength of sustainable PQC.

1. Introduction

In recent years, the construction industry has expanded significantly, focusing increasingly on sustainability and environmental accountability. This change has especially improved the attractiveness of using recycled materials in construction projects. Among these materials, Recycled aggregates (RA) have emerged as a viable and promising solution for promoting sustainable construction practices. RA encompasses crushed concrete, brick and other construction debris that have undergone a process of careful processing and preparation for reuse as a sustainable alternative. By repurposing these materials, the construction industry can substantially diminish the demand for virgin resources, mitigate waste generation, and lessen the environmental impact of construction activities.

The encapsulated mortar around the RAC (Recycled aggregate concrete) possesses a lower density than the virgin aggregate [1]. The specific gravity of the RAC was reported to be between 2.35 to 2.58, sometimes nearly equivalent to conventional aggregate [2,3]. The specific gravity of the collection material is 2.60, which is less than that of the virgin aggregate as shown in Table 1. The RAC has water absorption of1.80%, which is much

*Correspondingauthor: bchittibabu.rs@andhrauniversity.edu.in
[a]orcid.org/0009-0003-0718-050X; [b]orcid.org/0009-0004-1847-6012;
DOI: http://dx.doi.org/10.17515/resm2024.87me1110rs

higher than that of the virgin aggregate. The presence of adhered mortar in Recycled Aggregate Concrete (RAC) is primarily responsible for its porous nature, which results in higher levels of water absorption [3, 31]. Furthermore, another study [4] has reported even greater water absorption rates in RAC. The physical and mechanical properties of the RAC were judged to be less satisfactory than those of conventional aggregate due to the presence of residual mortar around the aggregate. This residual mortar is responsible for the weak structure observed in the RAC [5,6].

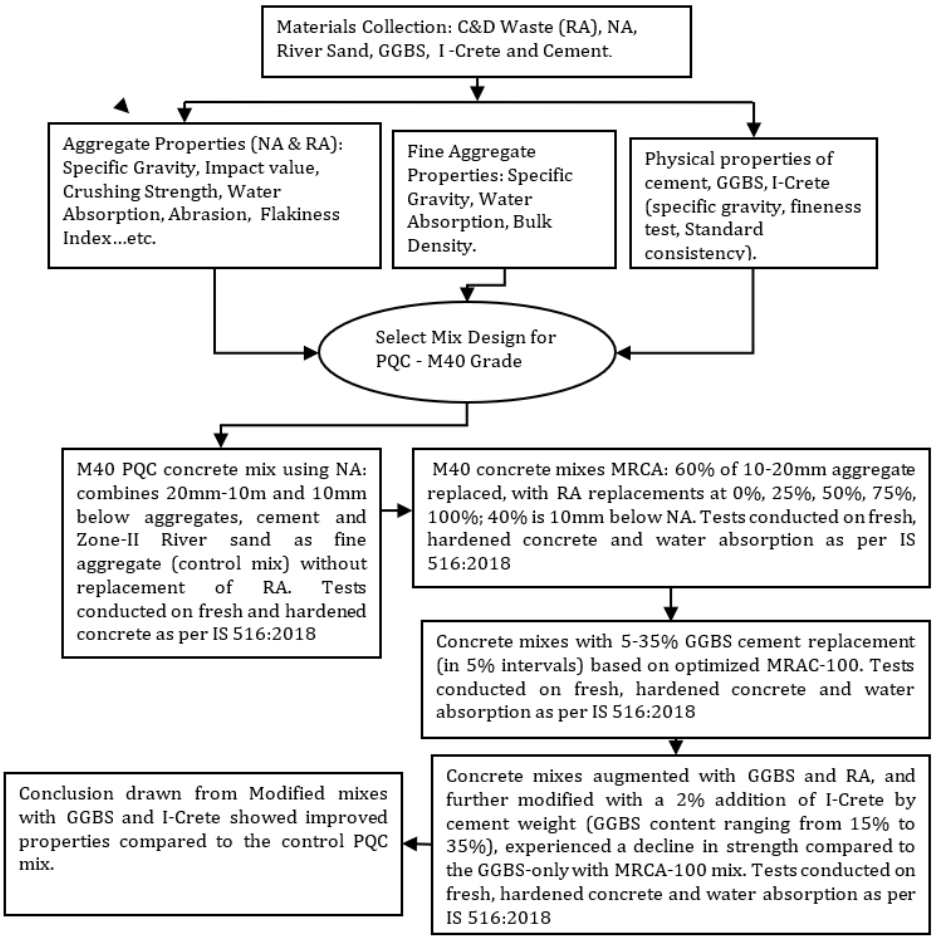

Fig. 1. Demonstration of detailed application of the methodology

Due to the poor mechanical properties of the RAC, the compressive strength has been reduced by 15 to 20% compared to conventional concrete when using 100% replacements[6].The physical and mechanical properties of RA with different percentages of replacement RA as shown in Table 1 and its combined gradation with Natural aggregate (NA) of aggregate as shown in Table 3.It follows all permissible limits according to relevant codes and MORTH (Ministry of Road and Transportation Highways) specifications. Additionally, about a 20% to 25% reduction in strength was reported for replacements of 25%, 50%, 75%, and 100%.However, it has been suggested that recycled aggregate can be used in medium-strength concrete by incorporating 25% RAC with a uniform water-cement ratio [2]. The aggregate impact values increase as the replacement of RA increases

[2, 7]. All the impact values are within the permissible limits asper code specifications IS:383-2016 [8, 9]and MORTH [10]. The compressive strength and flexural strength of the concrete with 25% replacement of RAC as coarse aggregate and 50% replacement as fine aggregate were observed to be in the range of 30% to 40% and 15% to 40%, respectively [11]. Replacing the virgin aggregate with RA leads to a decline in strength, despite achieving the target strength with its semi-porous structure. The increase in strength can be achieved through the incorporation of other supplementary materials such as Ground Granulated Blast Furnace Slag (GGBS).

GGBS is a widely used stabilized cementitious substitute material in the construction industry. It is obtained as a by-product of the iron and steel industry through the granulation of molten blast furnace slag. To enhance durability, a two-stage mixing process was employed, replacing 30% of the cement with GGBS and 50% with coal fly ash [12]. The strength can also be obtained with cement replacement made with 10% metakaolin and 15% GGBS. Alternatively, the desired strength can also be attained by replacing cement with 10% metakaolin and 15% GGBS [13]. The inclusion of GGBS could potentially lead to an increase in strength, but it may not match the strength of conventional materials. Therefore, ongoing studies are being conducted to enhance the strength by combining RAC and GGBS [14]. A decrease in the 28-day compressive strength of RA concrete mixtures containing only GGBS was observed initially, but these mixtures gained strength at a later stage [15]. The present study aims to improve the strength of RAC by using cement mineral admixture and mineral additive such as GGBS and I-Crete to make eco-friendly concrete that reduces the carbon footprint in PQC.

I-Crete complies with ASTM C1797 [16]: IS2645[17] and itis a mixture of additional cementitious ingredients and naturally existing minerals. It is a very reactive, high-quality addition for concrete applications because of its chemical makeup and well-regulated particle size retention on a 45-micronsieve of less than 10% [17, 18]. The physical properties for GGBS, Cement and I-Crete as shown in Table 2. The following flow chart depicts in detail the procedure to implement the methodology in Fig. 1.

1.1 Research Significance

Several studies have been conducted on the utility of recycled aggregate in concrete application, but limited research has been carried out on pavement application. Hence in this study, an attempt was made to use recycled aggregate as partial replacement of natural aggregate in PQC. In addition to replacing coarse aggregate, cement was replaced with GGBS and I-Crete to reduce carbon imprint in PQC. The optimal design mix is arrived at through laboratory investigations such as mechanical, water absorption and microscopic studies.

2. Experimental Program

This paper presents an experimental initiative conducted to investigate the performance of Pavement Quality Concrete (PQC) incorporating recycled aggregate and GGBS mineral admixture and I-Crete mineral additive. The study aims to assess the effects of these materials as partial replacements for cement in M40 grade PQC.

2.1. Material Used in The Study

RA was collected from the construction and demolition waste processing plant in Hyderabad, Telangana. It has a nominal size of 20-10 mm and exhibits high water absorption of 1.8% along with lower physical and mechanical properties and density compared to conventional aggregates. But they fall within the acceptable limits stated by IS 383-2016 [8] and the Ministry of Road and Transportation Highways (MORTH) [10]. In the present study, RA is used in the mix under Saturated Surface Dry (SSD) conditions. The

properties of RA and conventional aggregates are presented in Table1. River sand confirming to Zone-II [8] is used as fine aggregate Table 4 and its properties such as specific gravity, water absorption and bulk density are presented in Table5.OPC 53 grade is used as the bonding material, which is collected from the local vendor in Visakhapatnam. The physical and mechanical properties of the cement are carried out in according to the IS 12269: 2013 [19]. The cement supplementary materials, such as GGBS and I-Crete used in this study, were acquired from Sri Vishnu Sai Saravana Enterprises in Visakhapatnam and Navodaya Sciences Pvt Ltd in Chennai, respectively. The properties of Cement, GGBS, and I-Crete are depicted in Table2. The chemical composition of GGBS, Cement, and I-Crete is shown in Table 6. The potable water was used following IS 456-2000 [20] for the design mix and curing. CONPLAST SP 430 was used as a chemical admixture with a specific gravity of 1.20 with no chloride content and less than 1.5% air. The materials selected for the study, as shown in the Fig. 2.

Table 1. Physical and mechanical properties of coarse aggregate

Properties	100% NA	50% NA + 50% RA	100% RA	Permissible limits as per standard specifications of MORTH and IS:383-2016
Bulk density (kg/m^3)	1800	1750	1600	1200-1800
Specific gravity	2.84	2.75	2.60	2.5 to 3
Fineness modulus	7.06	7.135	7.15	6-7.5
Water absorption (%)	0.30	0.90	1.80	2
Flakiness Index (%)	13	12	11	25
Elongation Index (%)	11	13	14	25
Aggregate impact value (%)	18.96	22.72	23.40	30
Aggregate crushing value (%)	18.01	22.41	25.47	30
Angularity number	2	2.7	3	10
Abrasion resistance (%)	20	24.4	25.26	30
Soundness test (mm)	0.5	0.9	1.2	10mm

Table 2. Description of physical properties of cement, GGBS, and I-Crete

Test/ Material	Specific gravity	Fineness (m^2/kg)	Initial setting time (min)	Final setting time (min)	Consistency
Cement	3.15	260	165	230	30
GGBS	2.90	340	190	322	32
I-Crete	2.43	-	125	205	22

Table 3. Combined aggregate gradation for pavement quality concrete: as per IRC-44-2017

Sieve size (mm)	A combined Natural aggregate of 20mm nominal size (% ge of finer)	Combined Recycled aggregate 20mm nominal size (% ge of finer)	IRC44-2017 (19mm nominal size) (% ge of finer)
37.5	100	100	100
31.50	100	100	100
26.50	100	100	100
19	97.84	100	90-100
9.50	56.14	61.64	48-78
4.75	32.47	35.5	30-58
0.6	19.24	21.34	8-35
0.15	2.57	1.34	0-12
0.075 (wet sieving)	0	0	0-5 0-2

Table 4. Fine aggregate gradation for pavement quality concrete

Sieve size (mm)	% Of finer	Zone-IIas per IRC -44-2017
10	100	100
4.75	98	90-100
2.36	85	75-100
1.18	65	55-90
0.600	60	35-59
0.300	25	8-30
0.150	2	0-10

Table 5. Physical and mechanical properties of fine aggregate (River Sand)

Properties	Test value	As per IS 383-2016
Specific gravity	2.61	2.5 to 3.0
Bulk density- compacted	1780	1680 to 1920 kg/m^3
Bulk density –Loose	1580	1440 to 1680 kg/m^3
Water absorption	1.06	1-2%

Table 6. Chemical composition of cement, GGBS, I-Crete

Material	SiO_2 (%)	Fe_2O_3 (%)	Al_2O_3 (%)	Cao (%)	MgO (%)	Other (%)
Cement	22.5	0.3	6.5	62.5	3.2	5
GGBS	47.65	0.0	7.50	24.11	4.81	15.93
I-Crete	47.56	0.57	6.04	15.59	2.46	27.78

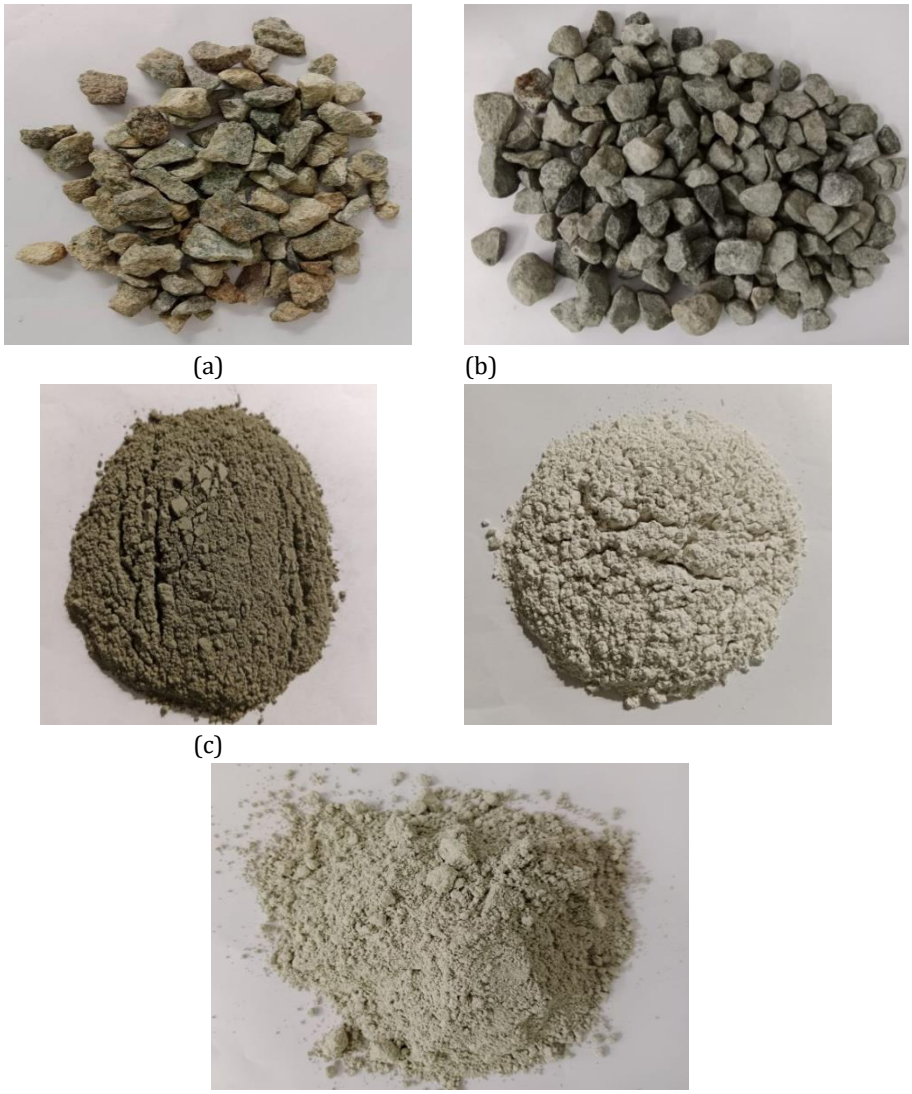

Fig. 2. Images of the materials used in the current study (a) recycledaggregate, (b) natural aggregate, (c) cement, (d) ggbs and (e)I – crete

2.2 Mix Design

The complete mix design for M40 grade was carried out as per the specification provided inIRC-44-2017 [21] and IRC 15-2017 [22], incorporating the provisions of IS 10262-2019[23] for pavement quality concrete. The quantification for each design mix as shown in Table 7. The experimental procedure was performed in four stages, as follows:

- Stage 1: The PQC M-40 grade concrete mix uses natural aggregates, with no recycled aggregates or cementitious materials, serving as the control mix.
- Stage 2: The concrete mixture consisted of a 60% replacement of 10-20mm size aggregate in proportions of 0%, 25%, 50%, 75%, and 100% with RAC, while the remaining 40% was filled with a conventional aggregate size of 10mm.

- Stage 3: Concrete mixtures were prepared with GGBS as a cement replacement ranging from 5% to 35 % at 5% intervals, with 100% recycled aggregate.

- Stage 4: Concrete mixtures were prepared using GGBS 15%-35% at 5% intervals and with 100% RA, and with the addition of I-Crete at a 2% dosage by weight of cement.

2.3 Studies on Fresh Concrete

The workability of the freshly prepared concrete mixtures, composed of different proportions of Natural Aggregates (NA), Recycled Aggregate concrete (RAC), GGBS and I-Crete, was determined by using slump cone and compaction factor apparatus as per IS 1199(part-I):2018[24] and the experimental results are presented in Fig.3 and Fig.4 respectively.

2.4 Studies on Hardened Concrete

Destructive and Non-Destructive tests were performed on the hardened concrete to evaluate the quality and strength of the different concrete mixtures. The Non-Destructive tests (NDT), such as the UPV (Ultrasonic Pulse Velocity) test were performed after 28 days of curing as per IS 516 Part 5: Sec 1: 2018 [25]. Water absorption was determined after28 days of curing as per IS 516:Part 1:2018[25]. The compressive strength test was carried out following the standard procedure IS516:Part 1:2018[25]. Cube moulds of standard size of 150mm x 150mm x 150mm were cast to perform the compressive strength test. The maximum load corresponding to the failure of the specimen divided by the cross-sectional area of the specimen is recorded as the Compressive strength. Split tensile strength was carried out in compliance with IS 516 Part 1:2018[25]. Standard cylindrical specimens with a size of 150mm diameter x 300mm height were cast for each concrete mix. Prisms of the standard size 100mm x100mmx500mm were cast according to IS 516 Part 1:2018[25]. For each mix proportion, three replicates were cast, and the specimens were cured for 7, 28, and 90 days respectively.

Table 7. The quantification for each design mix

Notation	Mineral admixture and mineral additive (kg/m³)				Recycled agg. (10mm-20mm) (60% of recycled agg.) replacement (kg/m³)		40%0f 10mm size agg. (kg/m³)	Total Coarse agg. (kg/m³)	Cement (kg/m³)	Water ltr/m³	Fine agg. (River sand) (kg/m³)
Type of Mix ID	GGBS		I-Crete								
	%	kg	%	kg	%	kg	Kg	kg	kg	ltr/m³	kg/m³
MNAC	0	0	0	0	0	0	509.20	1273	411	156	651
MRAC 25	0	0	0	0	25	176	504.80	1262	411	156	651
MRAC 50	0	0	0	0	50	352	498.40	1246	411	156	651
MRAC 75	0	0	0	0	75	528	492	1230	411	156	651
MRAC 100	0	0	0	0	100	728	485.20	1213	411	156	651
MRAC-100 +5% GGBS	5	20.55	0	0	100	728	485.20	1213	390.45	156	651

MRAC-100 +10% GGBS	10	40.10	0	0	100	728	485.20	1213	370.90	156	651
MRAC-100 +15% GGBS	15	61.65	0	0	100	728	485.20	1213	349.35	156	651
MRAC-100 +15% GGBS +2% I	15	61.65	2	8.22	100	728	485.20	1213	341.13	156	651
MRAC-100 +20% GGBS +2% I	20	82.20	2	8.22	100	728	485.20	1213	341.13	156	651
MRAC-100 +25% GGBS +2% I	25	102.75	2	8.22	100	728	485.20	1213	341.13	156	651
MRAC-100 +30% GGBS +2% I	30	123.30	2	8.22	100	728	485.20	1213	341.13	156	651

3. Results and Discussions

3.1 Studies on Fresh Concrete Mix

The slump values and compaction factors were observed to decrease with an increase in RA content as shown in Fig. 3 and Fig.4respectively. The slump values and compaction factors, with a uniform water-to-cement ratio (w/c) of 0.38 and 0.7% of super-plasticizer, ranging from 45mm to 38mm slump values and 0.89 to 0.79 compaction factor values respectively, as the RA replacement percentage increased from 0 to 100%. The decrease in slump can be attributed to the higher water absorption and porous structure of MRAC (Mix with Recycled Aggregate Concrete). Furthermore, with the inclusion of GGBS in addition to the 100% MRAC replacement, the slump value decreased to 30mm[9, 26, 27, 28,29].The compaction factor decreased to 0.73.As the proportion of the RAC rises, there is a corresponding decline in the compaction factor[30].This decrease can be attributed to the higher specific surface area of GGBS compared to cement which in turn requires more water to become workable [21, 28,].

There was no appreciable change in slump observed with the incorporation of I-Crete. It can be noted that adding 2% of I-Crete, which is a marginal amount, hardly influenced the slump and compaction factor. However, the observed slump values are within the permissible limits (30±15 mm) stipulated by the IRC 15-2017[22], and for achieving the necessary workability control in pavement quality concrete, compaction is more appropriate than slump values. As per IS 456-2000[20], suggested IS 1199(part-I):2018 [24] for PQC is 0.75 to 0.80. In most cases, the compaction factor values of the above mix follow the recommended range.

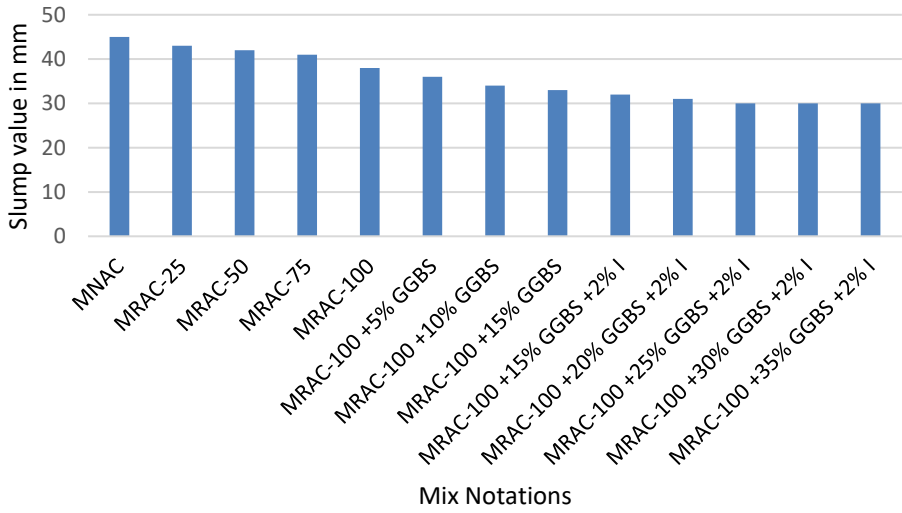

Fig. 3. Variations of slump values for different mixes

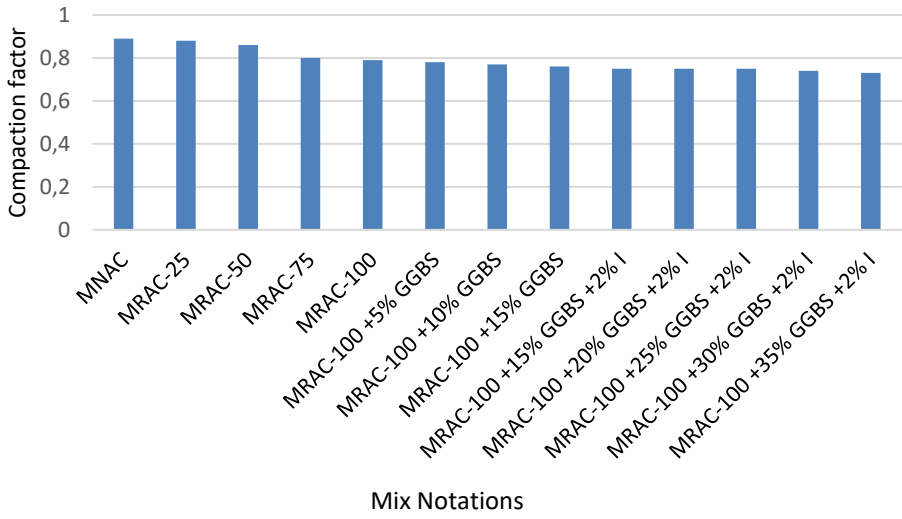

Fig. 4. Variation of compaction factor for different mixes

3.2 Studies on Hardened Concrete

3.2.1 Compressive Strength

Compressive strength of the concrete mixtures was carried out in the laboratory as perIS516:2018[25]. When replaced with RAC up to 100% with 25% intervals, The 7 days compressive strength of (MNAC, MRAC-25, MRAC-50, MRAC-75, MRAC-100) decreases from 38.32 MPa to 35.35 MPa, the percentage of reduction compressive strength is when compared MNAC mix to MRCA-100 is 7.75%. The exhibited a decrease from 51.10 MPa to 48.43 MPa at 28 days curing and 53.01 MPa to 50.05 MPa at 90 days curing, as indicated in

Table 8. The reduction in compressive strength can be attributed to the fact that the available free surface on the RAC for cement adhesion has been diminished. This reduction is a result of the pre-attached mortar on the RAC, which creates a weakened Interfacial Transition Zone (ITZ), thus leading to a compromised bonding mechanism [9, 27]. Additionally, the texture of the RAC is porous, resulting in higher water absorption and lower mechanical strength in comparison to conventional aggregates [31]. Despite these factors, the total observed percentage decrease in strength was 5.58% at 100% RAC when compared to conventional concrete. Nevertheless, the achieved strength still satisfied the required target strength specified by the IRC58:2017[32] code provisions. Subsequent investigations involved the incorporation of GGBS as a cement replacement in conjunction with 100% RAC replacement.

GGBS was introduced in varying proportions, ranging from 5% to 35% with a 5% increment. The decision to employ 100% RAC replacement was made based on its ability to attain the target strength, thus maximizing the effective utilization of RAC for sustainable concrete construction. A maximum increase in compressive strength of 0.97% was noted in the case of 10% GGBS inclusion (MRAC100+10% GGBS) when compared to 100% RAC (MRAC-100) alone. However, as the GGBS content was further increased, a subsequent decrease in strength was observed. The Same trend follow in 7 days of curing. The observed strength enhancement resulting from the inclusion of GGBS can be attributed to its higher specific surface area, which facilitates the formation of efficient reactive hydration products in conjunction with the cement [20]. However, surpassing the 10% GGBS leads to an increase in voids within the mixture, consequently causing a decline in strength. Despite identifying the optimized GGBS content at 10% through analysis, the aim to minimize carbon footprint prompted the utilization of the maximum GGBS proportion, some research findings indicate that the optimal results in terms of compressive strength for rigid pavement were achieved when GGBS was used as a partial replacement for cement, specifically up to 15%. Notably, at a 10% replacement level, a substantial 12% increase in compressive strength was observed [33]. Efforts were undertaken to balance the strength with that of conventional aggregate.

Fig. 5. Compressive strength test

To counteract the diminishing strength, the introduction of I-Crete commenced at the 15% GGBS inclusion level. This development could potentially represent a significant stride towards reducing carbon emissions and establishing sustainable methods for the effective utilization of waste materials [31]. Maintaining a constant 2% I-Crete content, the

assessment of strength was conducted by progressively increasing the GGBS content up to 35%. Notably, commendable compressive strengths of the 7 days of early-stage strength are at MRCA-100+20%GGBS+2I gained early strength 38 MPa and it is nearly equal to the MNAC mix. The reason for developing early strength is that I-Create is a composite pozzolanic material that develops good bonding strength in the early stages. The 51.11 MPa and 52.88 MPa were observed at 28 and 90 days of curing with a GGBS content of 25% and an I-Crete content of 2%. These values align with the compressive strength of the conventional concrete mixtures (MNAC) as shown in Fig. 6. Compressive strength test setup with specimen shown in Fig. 5.

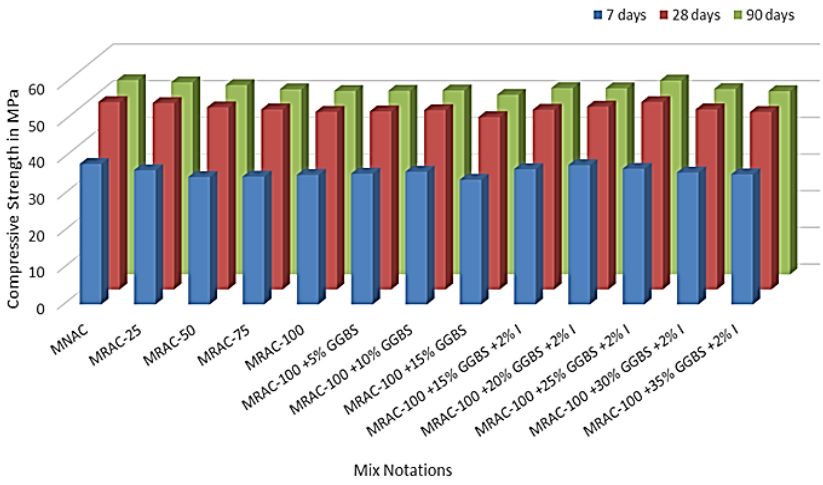

Fig. 6. Variation of compressive strength with different curing periods for different mixes

3.2.2 Split Tensile Strength

The trend observed in split tensile strength followed as that of the compressive strength. The 7 days split tensile strength of (MNAC, MRAC-25, MRAC-50, MRAC-75, MRAC-100) decreases from 3.78 MPa to 2.69 MPa, the percentage of reduction is when compared MNAC mix to MRCA-100 is 28.83% decreased. The most notable reduction in tensile strength was seen at 100% RAC, amounting to a decline of 28.83%, as indicated in Table 8. The split tensile strength exhibits a decreasing trend as the replacement ratio of RAC increases [34,35]. Subsequently, the introduction of GGBS to the 100% (MRAC-100) mixture increased in tensile strength. This increase can be attributed to the inter-particle bonding between cement and GGBS, which leads to reduced porosity and enhanced tensile strength. The most significant increase, amounting to 20.64%, was observed with a 10% GGBS replacement of cement at the 90-day mark. The incorporation of slag cement has been noted to elevate the tensile strength of RAC by a significant 25% compared to RAC without these mineral admixtures [36], followed by a subsequent decrease with higher GGBS content. To counter the decline in strength [33]. I-Crete was incorporated into the concrete mixtures starting from 15% GGBS, Strength enhancement was observed with increasing I-Crete content, up to 25% GGBS, paralleling the trends seen in the compressive strength observations. The 7 days of early stage split tensile strength is at MRCA-100+20%GGBS+2I gained early strength 3.90MPa and it is more than to the MNAC mix. The reason for developing early strength is that I-Create is a composite pozzolanic material that develops good bonding strength in the early stages.

The 4.20 MPa and 5.10 MPa were observed at 28 and 90 days of curing with a GGBS content of 25% and an I-Crete content of 2%. These values align with the split tensile strength of the conventional concrete mixtures (MNAC) as the trend is shown in Fig. 8. Split tensile strength test setup with specimen shown in Fig. 7.

Fig. 7. Split tensile strength test

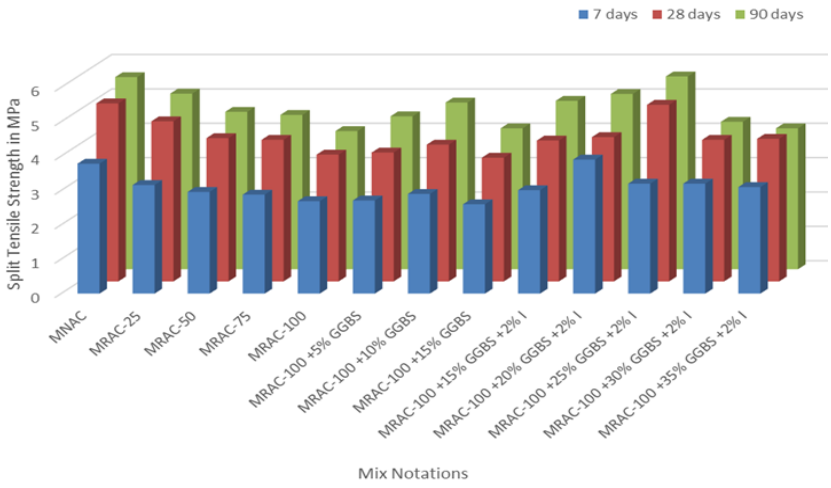

Fig. 8. Variation of split tensile strength with different curing periods for different mixes

3.2.3 Flexural Strength

Flexural strength plays a vital role in the design of rigid pavement, especially when subjected to the effects of multi-axle repetitions. These repetitions can lead to phenomena such as bottom-up and top-down cracking, which are further influenced by concurrent diurnal and seasonal temperature variations. The primary application of concrete's flexural strength lies in the calculation of the stress ratio. This ratio serves as a determinant for the number of repetitions required to induce cracking. For design purposes, the 90-day flexural strength is typically chosen, as concrete continues to gain strength during this period. IRC 58-2015 [32] recommends a flexural strength of 4.5 MPa at 28 days, and at 90 days, the flexural strength should be 1.1 times that of the 28-day strength. The 7 days

flexural strength of (MNAC, MRAC-25, MRAC-50, MRAC-75, MRAC-100) decreases from 4.33MPa to 3.64MPa, the percentage of reduction is when compared MNAC mix to MRCA-100 is 15.93%. All the mixtures achieved a flexural strength of more than 4.5 MPa at 28 days, thereby satisfying the design criteria as per IRC58-2015[32]. In the current analysis, the flexural strength after a 90-day curing period ranged from 1.02 to 1.10 times the flexural strength at 28 days for mixtures containing RAC replacement.

The introduction of 2% I-Crete resulted in a range of approximately 1.03 to 1.19 times the strength at 28 days. The flexural strengths of all the mixtures exhibited similar trends to those observed in compressive strength. The flexural strengths of all the mixes followed similar trends as that of the compressive strength. The highest reduction in strength occurred in MRAC100, amounting to 17.90% in RCA mixtures alone. The flexural strength of RAC exhibits a diminishing trend as the replacement ratio of RA increases. [28, 37, 38]. Conversely, an increase in strength of 7.38% was noted when comparing MRCA100 to the mix with 10% GGBS inclusion (MRAC100+10%GGBS) [39]. The strength equivalent to MNAC was achieved in the MRAC100+25%GGBS+2%I mixture, measuring 5.98 MPa at 28 days and 6.65 MPa at 90 days, the trend as shown in Fig. 10. Flexural strength test setup with specimen shown in Fig. 9.

Fig. 9. Flexural strength test

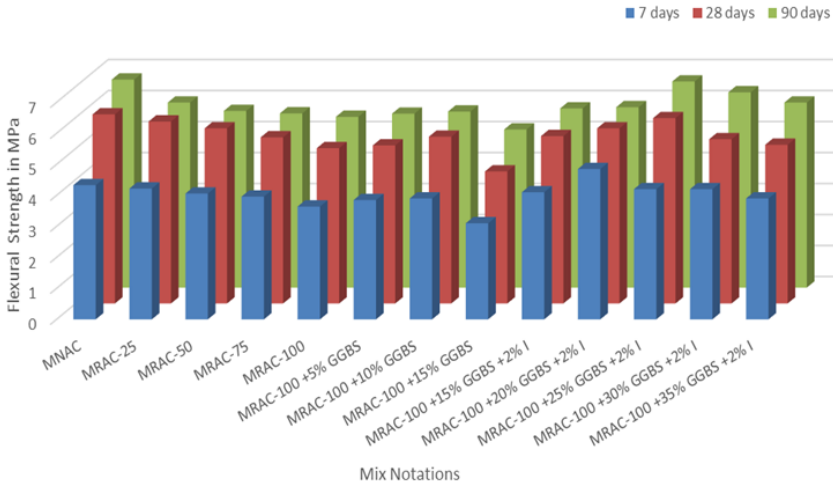

Fig. 10. Variation of flexural strength with different curing periods for different mixes

3.2.4 Correlation Between Compressive Strength and Flexural Strength

A correlation, with a coefficient of 0.9481, has been obtained between compressive strength and flexural strength for all concrete mixtures, as shown in Fig. 11. It has also been observed that there is a power function relationship between compressive strength and flexural strength in one of the studies, characterized by a correlation coefficient of 0.89[40]. With the correlation established in this study, it is possible to estimate the compressive strength of all mixtures based on their flexural strength.

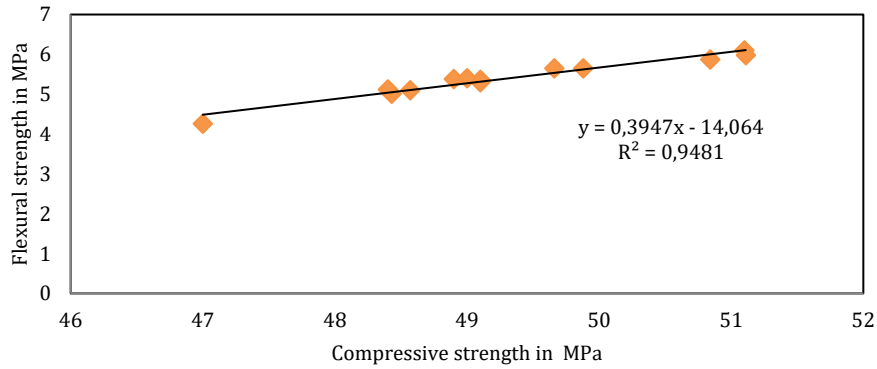

Fig. 11. Correlation graph between compressive strength and flexural strength for all mixes

3.2.5 Correlation Between Compressive Strength and Split Tensile Strength

For all concrete combinations, a high association between compressive strength and split tensile strength has been found, with a coefficient of 0.8413, as indicated in Figure 12. Additionally, it has been noted that one of the researches shows a power function relationship with a correlation coefficient of 0.89 [40] between compressive strength and split tensile strength. It is now feasible to determine the compressive strength of any mixes based on their split tensile strength owing to the correlation discovered in this research.

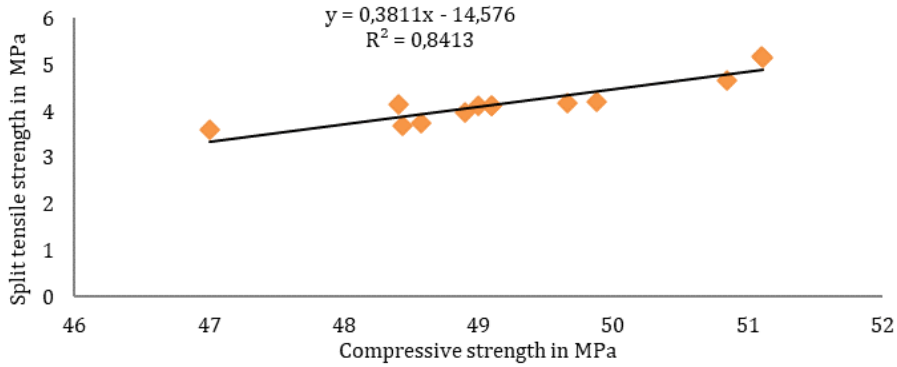

Fig. 12.Correlation graph between compressive strength and split tensile strength for all mixes

Table 8. Mechanical properties of concrete mixes under study

Mix designation	Compressive strength (MPa)			Flexural strength (MPa)			Split tensile strength(MPa)			Water absorption (%)	UPV for 28 days in (m/s)
	7 days	28 days	90 days	7 days	28 days	90 days	7 days	28 days	90 days	28 days	
MNAC	38.32	51.10	53.01	4.33	6.10	6.71	3.78	5.18	5.59	0.94	5043
MRAC-25	36.60	50.84	52.41	4.22	5.87	5.97	3.16	4.66	5.11	1.12	4958
MRAC-50	34.76	49.66	51.63	4.06	5.65	5.70	2.96	4.17	4.58	1.60	4881
MRAC-75	34.86	49.10	50.50	3.96	5.36	5.62	2.88	4.12	4.49	1.80	4820
MRAC-100	35.35	48.43	49.00	3.64	5.01	5.51	2.69	3.69	4.02	1.20	4617
MRAC-100 +5% GGBS	35.67	48.57	50.10	3.85	5.10	5.61	2.71	3.75	4.45	1.90	4663
MRAC-100 +10% GGBS	36.2	48.90	51.20	3.90	5.38	5.68	2.90	3.98	4.85	1.15	4748
MRAC-100 +15% GGBS	34.00	47.00	49.00	3.10	4.26	5.10	2.60	3.60	4.10	1.10	4636
MRAC-100 +15% GGBS +2% I	36.90	49.00	50.85	4.10	5.40	5.78	3.01	4.10	4.90	1.05	4776
MRAC-100 +20% GGBS +2% I	38.00	49.88	50.78	4.85	5.65	5.82	3.90	4.20	5.10	1.01	4900
MRAC-100 +25% GGBS +2% I	37.00	51.11	52.88	4.20	5.98	6.65	3.20	5.14	5.61	0.90	5002
MRAC-100 +30% GGBS +2% I	36.00	49.10	50.60	4.20	5.30	6.30	3.20	4.12	4.29	1.01	4950
MRAC-100 +35% GGBS +2% I	35.50	48.40	50.01	3.90	5.12	5.97	3.10	4.15	4.10	1.00	4750

3.2.6Water Absorption

In the conventional concrete mix design, the MNAC water absorption percentage after28 days of curing is found to be 0.94%. However, as the percentage of recycled aggregate in the mix increases, the water absorption also increases [9, 27]. For MRAC-100, the water absorption rate is 1.2%, which is higher than the conventional mix. This represents a 32.5%increase in water absorption compared to the conventional concrete mix. This higher water absorption adversely affects the concrete, leading to poor workability, significant slump loss, and the potential for concrete pumping blockages. It has been observed that incorporating different mineral admixtures tends to reduce the water absorption percentage, and the degree of reduction varies depending on the properties of the included mineral admixture and mineral additive. In the case of concrete mixes with GGBS, the observed water absorption value for MRAC-100+25% GGBS+2I is only 0.9%, and it is lower than that of MNAC mix, while for mixes with GGBS, this value is approximately 1.9% and 1.15% for MRCA-100+5% GGBS and MRCA-100+ 10% GGBS, respectively. This improvement in water absorption parameters can be attributed to the presence of ultrafine particles in the mineral admixture and mineral additive, which refines the pore structure of the concrete, making it less permeable. This, in turn, leads to better strength development in concrete, as discussed in the results for compressive, flexural, and split tensile strength as shown in Fig. 12.

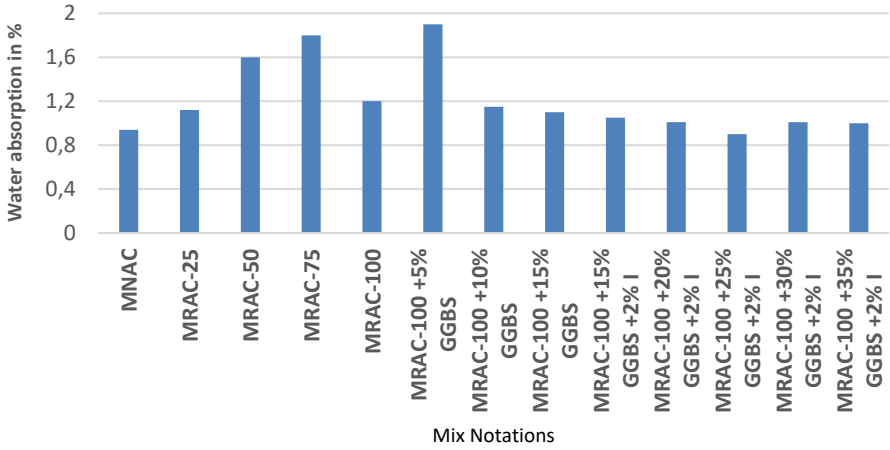

Fig: 12. Variation of water absorption with different curing periods for different mixes

3.2.8 Ultrasonic Pulse Velocity

Indian Road Congress (IRC) provides guidelines for quality control of pavement materials and construction, including the use of Ultrasonic Pulse Velocity (UPV) for assessing the quality of PQC as shown in Fig. 14. These guidelines help ensure that the concrete used in road construction meets the required standards and specifications IS 516 part5-2018[25]. The test setup for cube as shown in Fig. 13.

Fig. 13. Ultrasonic pulse velocity test

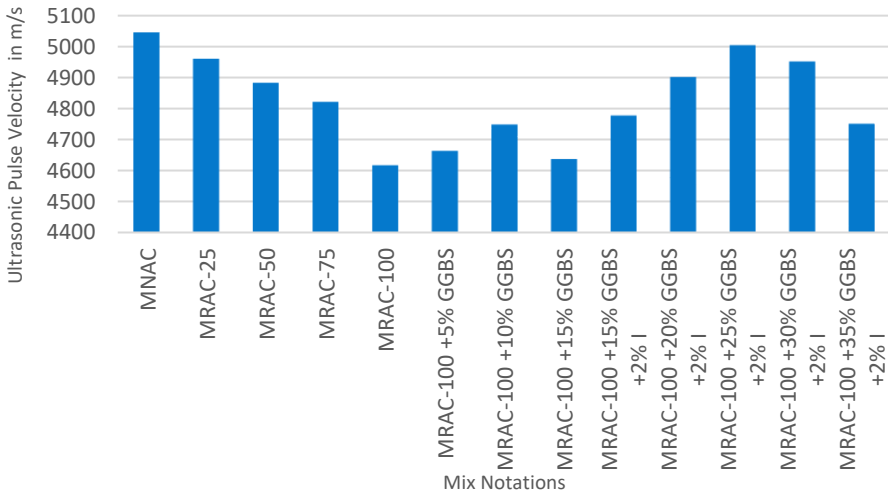

Fig. 14. Ultrasonic pulse velocity for various mixes

4. Scanning Electron Microscopic (SEM) Analysis

Scanning Electron Microscopy (SEM) is one of the most adaptable technologies available for observing and analyzing the micro structural characteristics of solid materials. SEM is used to provide high-resolution photographs of an object's form and to detect spatial differences in chemical composition. SEM investigations of the fracture surfaces of concrete constructed from RAC with varying mineral contents were performed [41]. These composites were included in a study at a curing age of 28 days. In Fig. 15 (a), the SEM imaging of the MNAC mix show the microstructure at the virgin aggregate-concrete-cement interface, revealing the formation of Calcium-Silicate-Hydrate (C-S-H) gel and other hydrated compounds. The existence of hexagonal and fine bundle-type structures implies that hydroxide compounds and C-S-H gels are abundant. In Fig. 15(b) the microstructure of MRAC-100 diverges from that of normal concrete due to the presence of adhered mortar from the old cement matrix. This results in the formation of two Interfacial Transition Zones (ITZ): one between natural aggregates (NA) and the old cement matrix,

and another between the new cement matrix [42, 43]. The MRAC-100 mix's SEM picture displays an abundance of needle-like ettringite and hexagonal calcium hydroxide particles. Incomplete hydration is responsible for the occurrence of an excess of calcium hydroxide particles, voids, and the ITZ. This loss of strength is attributed to a weaker ITZ caused by weakly adhered mortar surrounding the recycled aggregate particles, which interferes with aggregate bonding and reduces the overall strength. Utilizing SSD aggregates has been observed to notably diminish the micro pores in concrete. This is attributed to the fact that SSD aggregates, having no absorbed water during the casting process, do not release entrapped air during the concrete setting [44]. Prior research has efficiently summarized the analysis of Recycled Aggregate Concrete (RAC) with pozzolanic materials; Chemical admixtures boost ITZ density. Pozzolanic reactions with anhydrate $Ca(OH)_2$ generate secondary C-S-H gel, improving MRAC structural weaknesses [27, 44-47]. Indications show that the mean and median particle sizes of GGBS and I-Crete particles are spherical in shape. SEM images were obtained for GGBS Fig. 15(d) and I-Crete Fig. 15(e). Spherical particles increase ITZ in concrete by increasing packing efficiency, reducing voids, and more uniformly dispersing stresses. Their smooth surface and greater workability aid in bonding, resulting in a stronger ITZ. SEM image Fig. 15(c) of MRCA-100+25% GGBS+2I reveals an increase in C-S-H and Calcium Hydroxide (CH) content in the mix. GGBS and I-Crete have pozzolanic qualities that, when added to concrete, accelerate the hydration process and increase the amount of hydration products.

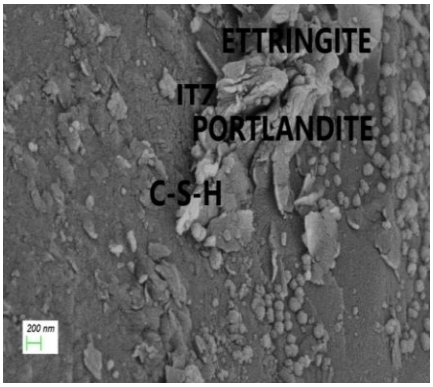

(a)

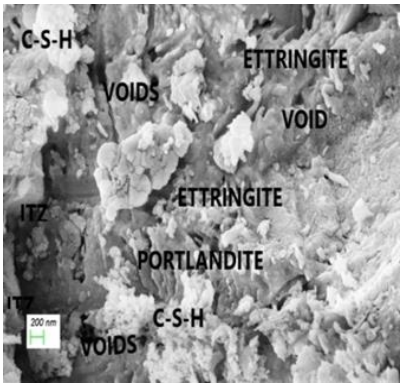

(b)

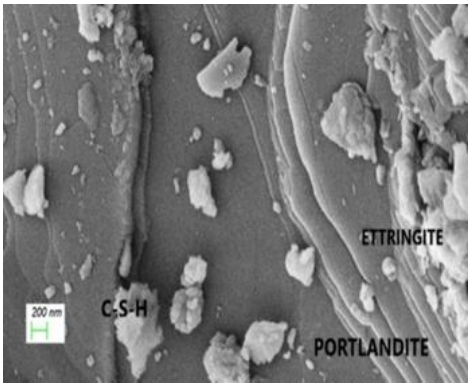

(c)

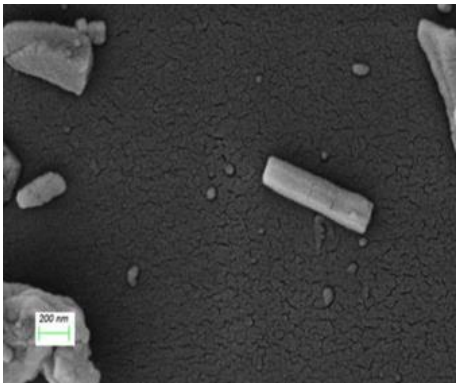

(d)

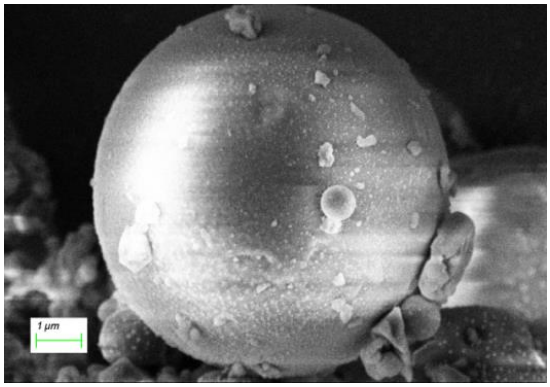

(e)

Fig. 15. SEM Images(a) MNAC mix, (b) MRCA – 100 mix, (c) MRCA – 100+25% GGBS + 2I, (d) GGBS and (e) I – Crete

The enhanced strength metrics, particularly in compressive and flexural strength, clearly demonstrate the strength of the ITZ. This improvement in flexural strength (as shown in Table 8) is especially desired because the concrete mix has been specifically formulated for stiff pavement applications. Increased durability is also a result of the decrease of voids.

5. Conclusion

The laboratory study yields the following conclusions.

- Studies conducted on fresh concrete with increasing amounts of RA have shown a decrease in the compaction factor from 0.89 to 0.79 and the slump also followed a similar trend, decreasing from 45 mm to 38 mm. further replacement of cement up to 10%GGBS, also showed a decrease in compaction factor from 0.79 to 0.73 and slump reduction from 38mm to 30mm. However, the inclusion of I-Crete had no appreciable effect on the properties of fresh concrete.
- The replacement of NA with RA decreased the performance of RAC. Compressive strength decreased by 5.22% to 7.84% across all curing durations, while flexural strength and split tensile strength decreased by 15.93% to 17.88% and 28.08% to 28.83%, respectively. However, the required target strength was met.
- GGBS replacement levels increased from 5% to 35% in 5% intervals, with MRCA-100 being the most efficient. MRCA-100 with GGBS demonstrated up to a 10% improvement in compressive strength, with results ranging from 0.96% to 4.29% for all phases of curing when compared to the MRCA-100 mix. Flexural strength and split tensile strength increased by 2.99% to 6.87%, and 7.24% to 7.28%, respectively, throughout all curing times This increase can be attributed to the inter-particle bonding between cement and GGBS, which leads to reduced porosity and enhanced compressive strength, tensile strength and flexural strength. However, strength began to decline after GGBS replacement levels were above 15%.
- Adding 2% I-Crete to MRCA-100 with 15% to 35% GGBS in 5% intervals showed increases in compressive, split tensile, and flexural strength by 5.24% to 7.33%, 28.34% to 31.02% and 16.22% to 24.94% respectively increased in the MRCA-100+25%GGBS+2I mix exhibited these improvements over MRCA-100 across 7, 28 and 90-day curing periods. The reason for developing strength is that I-Create is a composite pozzolanic material that develops good bonding strength in the early and later stages. The optimal replacement of 25% GGBS and 2% I-Crete in RAC mixes not

only improves strength but also drops prices and adverse environmental impacts, as GGBS is an industrial by-product.

- In conventional concrete, 28-day cured MNAC specimens had a water absorption rate of 0.94%. But MRCA-100 exhibits a 32.5% rise to 1.2%, due to increased RA concentration. Adding mineral admixtures such as GGBS and I-Crete helps to limit water absorption. The UPV test target result is exceptional in all I-Crete and virgin mixtures, and good in others, indicating that they fulfill IS:516 specifications.
- The SEM image of the 28-day-cured MNAC mix reveals a complex microstructure at the interface of virgin aggregate, concrete, and cement, including gels made up of C-S-H and hydrated compounds with hexagonal and fine bundle-type structures. In MRAC-100, the inclusion of needle-like ettringite and hexagonal calcium hydroxide particles indicates insufficient hydration and a weak ITZ, resulting in decreasing strength. SEM pictures of GGBS and I-Crete reveal spherical particles and, when mixed in MRCA-100+25% GGBS+2I, an increase in C-S-H and CH. Their pozzolanic capabilities increase hydration while also improving pavement bonding as well as structure quality.

References

[1] Limbachiya MC, Leelawat T, Dhir RK. Use of recycled concrete aggregate in high-strength concrete. Materials and structures. 2000 Nov;33:574-80 https://doi.org/10.1007/BF02480538

[2] Rahman IA, Hamdam H, Zaidi AM. Assessment of recycled aggregate concrete. Modern Applied Science. 2009 Oct;3(10):47-54. https://doi.org/10.5539/mas.v3n10p4 7

[3] Shayan A, Xu A. Performance and properties of structural concrete made with recycled concrete aggregate. Materials Journal. 2003 Sep 1;100(5):371-80 https://doi.org/10.14359/12812

[4] Sagoe-Crentsil KK, Brown T, Taylor AH. Performance of concrete made with commercially produced coarse recycled concrete aggregate. Cement and concrete research. 2001 May 1;31(5):707-12. https://doi.org/10.1016/S0008-8846(00)00476-2

[5] Tavakoli M, Soroushian P. Strengths of recycled aggregate concrete made using field-demolished concrete as aggregate. Materials Journal. 1996 Mar 1;93(2):178-81. https://doi.org/10.14359/9802

[6] Sonawane TR, Pimplikar SS. Use of recycled aggregate concrete. IOSR Journal of Mechanical and Civil Engineering. 2013 Jan;52(59).

[7] Jindal A, Ransinchung GD, Kumar P. Recycled Concrete Aggregates for Rigid Pavements: A Review. InInternational Conference on Sustainable Civil Infrastructure (ICSCI 2014), IIT Hyderabad 2014 Oct 17.

[8] IS 383:2016 Coarse aggregate and fine aggregate for Concrete -Specification.

[9] IRC: 121-2017: Guidelines for use of construction and demolition waste in road sector.

[10] MORTH (Ministry of Road Transportation & Highways), specification for road and bridge works .

[11] Ahmed B, Sultana TT, Hasan AS, Tabassum H. Assessment of Recycling Aggregate as Construction Materials. International Journal of Advanced Scientific Engineering and Technological Research. 2013 Jan 1;2(3)..

[12] Biswal US, Dinakar P. A mix design procedure for fly ash and ground granulated blast furnace slag based treated recycled aggregate concrete. Cleaner Engineering and Technology. 2021 Dec 1;5:100314. https://doi.org/10.1016/j.clet.2021.100314

[13] Tiwari PK, Sharma P, Sharma N, Verma M. An experimental investigation on metakaoline GGBS based concrete with recycled coarse aggregate. Materials Today: Proceedings. 2021 Jan 1;43:1025-30. https://doi.org/10.1016/j.matpr.2020.07.691

[14] Shamass R, Rispoli O, Limbachiya V, Kovacs R. Mechanical and GWP assessment of concrete using Blast Furnace Slag, Silica Fume and recycled aggregate. Case Studies in Construction Materials. 2023 Jul 1;18:e02164. https://doi.org/10.1016/j.cscm.2023.e02164
[15] Sharma P, Verma M, Sharma N. Examine the mechanical properties of recycled coarse aggregate with MK GGBS. In IOP conference series: materials science and engineering 2021 Apr 1 (Vol. 1116, No. 1, p. 012152). IOP Publishing. https://doi.org/10.1088/1757-899X/1116/1/012152
[16] Designation: C1797 − 17 Standard Specification for Ground Calcium Carbonate and Aggregate Mineral Fillers for use in Hydraulic Cement Concrete1
[17] IS 2645: 2003, Integral Waterproofing Compounds for Cement Mortar and Concrete-Specification.
[18] I-Crete: https://www.ecomaterials.in/products-I-Crete.php.
[19] IS 12269: 2013 Ordinary Portland cement, 53 Grade - Specification.
[20] IS 456-2000 Plain and Reinforced Concrete code of practice.
[21] IRC 44-2017 Guidelines for Cement Concrete Mix design for pavements.
[22] IRC 15 - 2017 Code of practice for construction of jointed plain Concrete Pavements
[23] IS 10262: 2019 Concrete Mix proportioning guidelines
[24] IS 1199 (part-I):2018 Fresh Concrete -Methods of sampling, Testing and analysis.
[25] IS 516-2018 Methods of testing for Strength of concrete.
[26] Majhi RK, Nayak AN, Mukharjee BB. Development of sustainable concrete using recycled coarse aggregate and ground granulated blast furnace slag. Construction and Building Materials. 2018 Jan 20;159:417-30. https://doi.org/10.1016/j.conbuildmat.2017.10.118
[27] Jindal A, Ransinchung GD. Behavioural study of pavement quality concrete containing construction, industrial and agricultural wastes. International Journal of Pavement Research and Technology. 2018 Sep 1;11(5):488-501. https://doi.org/10.1016/j.ijprt.2018.03.007
[28] Kumar R. Influence of recycled coarse aggregate derived from construction and demolition waste (CDW) on abrasion resistance of pavement concrete. Construction and Building Materials. 2017 Jul 1;142:248-55. https://doi.org/10.1016/j.conbuildmat.2017.03.077
[29] Kisku N, Joshi H, Ansari M, Panda SK, Nayak S, Dutta SC. A critical review and assessment for usage of recycled aggregate as sustainable construction material. Construction and building materials. 2017 Jan 30;131:721-40. https://doi.org/10.1016/j.conbuildmat.2016.11.029
[30] Abera YS. Performance of concrete materials containing recycled aggregate from construction and demolition waste. Results in Materials. 2022 Jun 1;14:100278. https://doi.org/10.1016/j.rinma.2022.100278
[31] Wang B, Yan L, Fu Q, Kasal B. A comprehensive review on recycled aggregate and recycled aggregate concrete. Resources, Conservation and Recycling. 2021 Aug 1;171:105565. https://doi.org/10.1016/j.resconrec.2021.105565
[32]. IRC-58-2015 Guidline for the Design of Plain Jointed Rigid Pavements Design for Highways
[33] Lall A, Jha AK. An experimental study on strength properties of concrete by using GGBS for the construction of rigid pavement. International Journal of Innovative Research in Technology and Management. 2020;4(6):60-8.
[34] Kou SC, Poon CS. Long-term mechanical and durability properties of recycled aggregate concrete prepared with the incorporation of fly ash. Cement and Concrete Composites. 2013 Mar 1;37:12-9. https://doi.org/10.1016/j.cemconcomp.2012.12.011
[35] Kou SC, Poon CS, Agrela F. Comparisons of natural and recycled aggregate concretes prepared with the addition of different mineral admixtures. Cement and Concrete

Composites. 2011 Sep 1;33(8):788-95. https://doi.org/10.1016/j.cemconcomp.2011.05.009
[36] Tabsh SW, Abdelfatah AS. Influence of recycled concrete aggregates on strength properties of concrete. Construction and building materials. 2009 Feb 1;23(2):1163-7..
[37] Padmini AK, Ramamurthy K, Mathews MS. Influence of parent concrete on the properties of recycled aggregate concrete. Construction and building materials. 2009 Feb 1;23(2):829-36. https://doi.org/10.1016/j.conbuildmat.2008.06.007
[38] Heeralal M, Kumar RP, Rao YV. Flexural fatigue characteristics of steel fiber reinforced recycled aggregate concrete (SFRRAC). Facta universitatis-series: Architecture and Civil Engineering. 2009;7(1):19-33. https://doi.org/10.2298/FUACE0901019H
[39] Deepa PR, Anup J. Experimental Study on the Effect of Recycled Aggregate and GGBS on Flexural Behaviour of Reinforced Concrete Beam. Applied Mechanics and Materials. 2017 Feb 15;857:101-6. https://doi.org/10.4028/www.scientific.net/AMM.857.101
[40] Govardhan C, Gayathri V. Experimental Investigation on Ternary Blended Recycled Aggregate Concrete Using Glass Fibers. Buildings. 2023 Aug 1;13(8):1961. https://doi.org/10.3390/buildings13081961
[41] Designation: C1723 - 10 Standard Guide for Examination of Hardened Concrete Using Scanning Electron Microscopy1
[42] Padmini AK, Ramamurthy K, Mathews MS. Influence of parent concrete on the properties of recycled aggregate concrete. Construction and building materials. 2009 Feb 1;23(2):829-36. https://doi.org/10.1016/j.conbuildmat.2008.03.006
[43] Bonifazi G, Capobianco G, Serranti S, Eggimann M, Wagner E, Di Maio F, Lotfi S. The ITZ in concrete with natural and recycled aggregates: Study of microstructures based on image and SEM analysis. Proc. 15th Euroseminar Microsc. Appl. to Build. Mater. 2015 Jun:299-308.
[44] Leite MB, Monteiro PJ. Microstructural analysis of recycled concrete using X-ray microtomography. Cement and Concrete Research. 2016 Mar 1;81:38-48. https://doi.org/10.1016/j.cemconres.2015.11.010
[45] Kong D, Lei T, Zheng J, Ma C, Jiang J, Jiang J. Effect and mechanism of surface-coating pozzalanics materials around aggregate on properties and ITZ microstructure of recycled aggregate concrete. Construction and building materials. 2010 May 1;24(5):701-8. https://doi.org/10.1016/j.conbuildmat.2009.10.038
[46] Duan P, Shui Z, Chen W, Shen C. Effects of metakaolin, silica fume and slag on pore structure, interfacial transition zone and compressive strength of concrete. Construction and Building Materials. 2013 Jul 1;44:1-6.. https://doi.org/10.1016/j.conbuildmat.2013.02.075
[47] Plank J, Sakai E, Miao CW, Yu C, Hong JX. Chemical admixtures-Chemistry, applications and their impact on concrete microstructure and durability. Cement and concrete research. 2015 Dec 1;78:81-99. https://doi.org/10.1016/j.cemconres.2015.05.016

Research on Engineering Structures & Materials
www.jresm.org
Research Group

Research Article

Investigation of strength and durability performance of concrete with varying crude oil waste ratios

Qosai Sahib Radi Marshdi[1,a], Ali Jaafar Dakhil[2,b], Zainab Al-Khafaji[3,4,c,*]

[1]*Dept. of Water Resources Management Eng., College of Eng., Al-Qasim Green University, Babylon, Iraq*
[2]*Dept. of Roads and Transport Eng., College of Engineering, University of Al-Qadisiyah, Al Diwaniyah, Iraq*
[3]*Imam Ja'afar Al-Sadiq University, Qahira, Baghdad, Iraq*
[4]*Dept. of Civil Eng., Faculty of Eng. and Built Environment, Universiti Kebangsaan Malaysia, Malaysia*

Article Info

Article history:

Received 11 Dec 2023
Accepted 21 Mar 2024

Keywords:

Crude oil (CRO);
Chemical analysis;
Physical properties;
Normal concrete;
Reactive powder concrete;
Pollution

Abstract

The influence of crude oil (CRO) pollution on concrete compressive strength and durability performance is evaluated in this work. Due to CRO contamination on its compositions, concrete exposed to oil-prone areas may lead to considerable changes in its properties. Experimental work has been conducted, and several cubes of concrete with varying ratios of CRO pollution were treated to study the impact of pollution on the mechanical characteristics of the concrete. The current research methodology consists of preparing contaminants by mixing CRO in different ratios with fine aggregates and mixing it with other raw materials to produce polluted concrete. Twelve CRO ratios (0, 1, 2, 2.5, 3, 4, 5, 6, 10, 15, 20, and 25%) were utilized to test typical concrete slump, compressive, and tensile strength. Then, the same concrete procedure and testing were repeated by utilizing 2% CRO in the case of reactive powder concrete. The chemical test was also utilized to identify the changes in concrete composition for the three samples (standard concrete without CRO, standard concrete with 2% CRO, and reactive powder concrete sample). The experimental tests illustrated that a ratio of 2% of CRO in standard concrete improves compressive and tensile strength, while utilizing the same ratio in reactive powder concrete reduces strength. On the other hand, utilizing 2% CRO illustrates that the internal sulfate amount has been increased for both normal and reactive powder concrete compared with normal concrete samples without CRO, which refers to a reduction in concrete durability.

Introduction

Concrete is a combination of cement, aggregate (coarse and fine), and water and is unquestionably the most frequently utilized material in the development of civil engineering projects [1,2]. The slurry (water and cement) binds the aggregate together to form a solid mass; the paste hardens due to a hydration reaction (for example, the chemical reaction of water and cement) [3]. It is a versatile construction and building material utilized for various purposes [4]. Several elements, such as additives and admixtures, may be utilized to modify the characteristics of the concrete to get the desired outcome property, depending on the engineer's specifications or requirements [5,6]. Crude oil (CRO) is among the most significant energy sources influencing any country's economy. Oil leaks throughout oil production and extraction are becoming severe global environmental issues, as seen in Fig. 1. The frequency of oil spills. Other environmental issues contribute to a decline in agricultural production, notably in the fishing industry, as illustrated in Fig. 2 [7], where the loss of the annual revenue from fishing activities has been reduced with

*Corresponding author: p123005@siswa.ukm.edu.my
[a] orcid.org/0000-0002-0532-9812; [b] orcid.org/0000-0002-3598-261X; [c] orcid.org/0000-0002-5450-7312
DOI: http://dx.doi.org/10.17515/resm2024.122me1211rs

time due to the spill of large quantities of oil in the water during the last 40 years. For instance, large volumes of oily effluent are generated as part of production processes, contaminating neighboring materials such as sand [8].

Consequently, CRO pollution directly impacts sand erosion, water penetration, and the potential for groundfire [9]. Sand's physio-chemical qualities are also affected by CRO pollution [10]. Sharma and Reddy [11] found that as the density of the fluid filling the gaps rises and the fluid viscosity decreases, the intrinsic permeability (k) of contaminated sand increases. Because the sand's permeability expanded as the CRO's viscosity reduced, the CRO spread quickly, affecting a broader area. Moreover, CRO pollution is more likely to reach subsurface water. According to many investigations, groundwater pollution by CRO and other petroleum-based liquids has become a common concern [12].

Fig. 1. The CRO spill in water

Some researchers consider utilizing oil-polluted sand in cement and concrete manufacturing as a sustainable, green, and cost-effective solution. With the development, the final product can be employed in various technical applications [13]. Ajagbe et al. [14] studied the impact of CRO on concrete compressive strength, where it was found that 25 %of CRO pollution resulted in a loss of 90 %compressive strength. Another investigation utilized oil solidification utilizing the direct immobilization approach. Some research has been done to see whether utilizing polluted sand in a building is functional.

Moreover, multiple studies [15–17] have investigated the impacts of various light CRO pollution %(0.5, 1, 2, 4, 6, 8, 10, and 20% by weight) on the mechanical microstructure and characteristics of produced concrete. These investigations found that at a contamination level of up to 6%, concrete with minor CRO contamination may preserve most of its compressive and splitting tensile strength. A good connection between the steel concrete and reinforcement may be formed due to this oil pollution.

The impacts of utilized motor oil on concrete characteristics and behavior are investigated by Hamad et al. [18]. The impact of utilized motor oil on hardened and fresh concrete features has been studied. The findings illustrated that utilizing motor oil improved the fluidity and slump of the concrete mixture and the air content of new concrete, acting as an air-entraining agent. The strength qualities of hardened concrete have been affected less by adding oil once a chemical-based air-entraining additive was applied. They discovered that adding used engine oil to concrete mixture materials did not influence the structural behavior of reinforced elements, as the ultimate loading or displacement diagrams were not changed. Ayininuola [19] investigated the impact of gas oil and bitumen on the concrete's compressive strength in which sand was polluted with gas and bitumen at various weight proportions. Oil-subjected concrete exhibits a reduction in compressive strength over time. According to Jassim and Jawad [20], the maximum decrease in the strength magnitudes of high and normal concrete samples subjected to gas and CRO for four months was approximately 25.19 %and 12.86%, respectively.

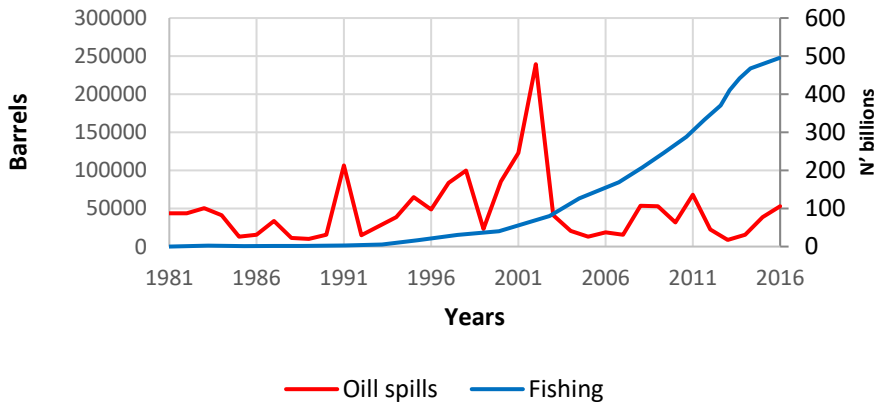

Fig. 2. Relationship between oil spill in water and reduction of fishing activity [7]

Ajagbe et al. [14] evaluated the concrete's compressive strength utilizing fine aggregates polluted with CRO at various percentages of the sand utilized in the combination. As the proportion of contaminants increased, the findings revealed a modest rise in concrete strength and increased loss rate. Abousnina et al. [17] observed that when fine sand concrete was polluted with light CRO, the cohesiveness rose dramatically to 1 %oil pollution and subsequently declined as the percentage of CRO grew. However, the frictional angle fell by 1%. The mortar with 1 %oil pollution had the maximum compressive strength, whereas mortar with 10 % had just an 18 %drop in strength compared to unpolluted specimens. Depending on Osuji and Nwankwo [21], the existence of CRO in concretes prevents the creation of bonds between component minerals, resulting in segregation. Consequently, the existence of CRO in concrete caused differences in workability. The greater the CRO amount in the fine aggregates, the more workable it is. In addition, compared to controlling cubes, polluted concrete cubes had lower compressive strengths, which illustrates that CRO is a compressive strength inhibitor in concrete manufacturing. The lower the compressive strength, the greater the CRO percentage in the fine aggregates. The ideal CRO pollution for normal compressive strength is as low as 0.3 percent [21].

Compared to the controlling concrete's slump, Shafiq et al. [22] observed that adding utilized motor oil raised the concrete slump by 18%to 38%and air amount by 26 to 58 percent. The oxygen permeability and porosity of concretes utilizing motor oil also decreased. In addition, the compressive strength achieved was similar to that of the control sample. Shahrabadi1 and Vafaei [23] investigated the compressive strengths of typical normal-weight concrete utilizing kerosene-contaminated sands. In all exposure settings investigated, they observed that 2 %of kerosene-polluted specimens had a loss in concrete compressive strength of up to 27%.

Because of its exceptional durability and strength characteristics, reactive powder concrete (RPC), a high-performance fiber-reinforced concrete, is receiving increasing attention these days. Recent studies have demonstrated that utilizing steel fibers as reinforcement has effectively overcome concrete fragility [24]. Therefore, high-resistance concrete reinforced with fiber (UHPSFRC) is a good alternative for its favorite features, such as high resistance against pressure and tensility [25].

In an RPC blend mix proportion, the coarse aggregates of traditional concrete are eliminated, requiring that the amounts of silica fume, Portland cement, and fine aggregate be significantly increased to enhance the homogeneity and improve the concrete granular

mixture density. After being exposed to CRO products, Tuama et al. [5] looked at the mechanical characteristics of the hardened concrete mixture for reactive powder concrete (RPC) and regular concrete (NSC). After 180 days of exposure, two categories of CRO products (gas oil and kerosene) have been examined. The findings demonstrated that the mechanical properties (modulus of elasticity and modulus of rupture) of the RPC mix, which were reduced by around (3.41-6.32%) compared to the control RPC mix, were not significantly impacted by exposure to each petroleum product. After being exposed to petroleum products for the same amount of time, the NSC mix lost around (13.82-21.95%) of its mechanical properties (modulus of elasticity and modulus of rupture) compared with the control NSC mixture.

Oil spills and leaks constantly happen, especially in facilities that store, transport, or process oil products. Contamination may arise in several ways, but the most crucial consideration when dealing with polluted concrete (apart from environmental concerns) is whether the building is still structurally sound. Furthermore, the concrete underneath these leaks or spills changed. However, more research is needed on the exposure of concrete to CRO products and comparing the behavior of both concrete and reactive powder concrete after exposure to CRO. Therefore, the main goal of the current research is to explore the changes in concrete properties, strength, and durability caused by adding different CRO ratios to the concrete mixture (0, 1, 2, 2.5, 3, 4, 5, 6, 10, 15, 20, and 25%). After that, A 2% CRO ratio was selected to be mixed with reactive powder concrete to investigate the differences between normal and reactive powder concretes. The current research focused on investigating the behavior of fresh and hardened concretes (normal and reactive powder concretes) after exposure to CRO.

2. Experimental Works

2.1 Materials

2.1.1 Cement

Ordinary Portland Cement [26] has been utilized in the research to work as a binder material in the presence of water, and the chemical and physical characteristics of OPC are shown in Tables 1 and 2.

Table 1. Compounds and chemical analysis of cement

Chemical analysis	Percentage by Weight	Limitation of (EN 197-1:2011)
Lime (CaO)	62.79	---
Silica (SiO2)	20.58	---
Alumina (Al2O3)	5.6	---
Iron Oxide (Fe2O3)	3.28	---
Magnesia (MgO)	2.79	5% max
Sulfate (SO3)	2.35	2.5 if C3A ≤5 2.8 if C3A >5
Chloride content	0.02	≤ 0.10 %
Loss on Ignition (L.O.I.)	1.94	5% max
Insoluble Residue (I.R.)	1.00	---
Lime Saturation Factor (L.S.F.)	0.9	---
Main Compounds (Bogue's Equation)		
Tricalcium Silicate (C3S)	50.12	---
Dicalcium Silicate (C2S)	21.26	---
Tricalcium Aluminate (C3A)	9.29	---
Tetracalcium Aluminoferrite (C4AF)	9.98	---

Table 2. Physical Krasta cement features

Physical features	Test findings	Limitation of (EN 197-1:2011)
Specific Surface Area (Blaine Method) m2/kg	314	
Setting times (hr: min)	Initial=122	≥ 45 min
	Final=3:13	≤ 10 hrs
Soundness Utilizing Autoclave Method	0.61	≤ 10 mm
Compressive Strengths		
2 Days (MPa)	21.0	> 20
28 Days (MPa)	45.8	≤ 42.5

2.1.2 Water

For concreting, fresh, drinkable water has been utilized; the water facilitated the cement hydration, resulting in the concrete setting and hardening.

2.1.3 Fine Aggregate

In this work, natural sand was used as fine aggregate. The chemical and mechanical properties of sand are given in Table 3. The fine aggregate used has gradation that lies within the upper and lower limits of the ASTM C33/C33M specification [27] and Iraqi specification (IQ.S 45/1984) zone (2), as shown in Table 4. Fine aggregate has been tested at Al-Mustaqbal University in the Construction Material Laboratories.

Table 3. Chemical and mechanical properties of fine aggregate

Properties	Test results	IQ. S No. 45/1984 zone (2)
Specific gravity	2.6	------
Fineness modulus	3.8	≤ 5 %
Sulfate content SO_3	0.22%	≤ 0.5 %
Absorption	2%	------

Table 4. Grading of fine aggregate

Sieve no.	Sieve size (mm)	Passing %		
		Fine aggregate	IQ. S No. 45 Zone (2)	ASTM C 33/C 33M
3/8 in	9.5	100	100	100
NO.4	4.75	91	90 - 100	90 - 100
NO.8	2.36	83	75 - 100	80 - 100
NO.16	1.18	74.8	55 - 90	50 - 85
NO.30	0.60	57.2	35 - 59	25 - 60
NO.50	0.30	24.2	8 - 30	5 - 30
NO.100	0.15	7.2	0 - 10	0 - 10

2.1.4 Coarse Aggregate (Gravel)

This work used coarse aggregate with a maximum aggregate size of 19 mm. The coarse aggregate was cleaned, washed with drinkable water, and dried before use. The mechanical and chemical properties of coarse aggregate are given in Table 5. The sieve analysis of coarse aggregate lies within the lower and upper limits of the Iraqi specification (IQ.S No.45/1984) [28], as shown in Table 6.

Table 5. Mechanical and chemical properties of coarse aggregate

Properties	Test results	IQ. S No. 45/1984
Specific gravity	2.66	------

Sulfate content SO3	0.03%	≤ 0.1 %
Absorption	0.6%	------
Clay content	0.2%	≤ 3%

Table 6. Grading of coarse aggregate

Sieve Size (mm)	Passing %	
	Coarse aggregate	IQ. S No. 45/1984
37.5	100	100
19	100	100 - 95
9.5	43	60 - 30
5.0	3	10 - 0

2.1.5 Crude Oil

Crude oil (CRO) utilized in the current study has been selected from length= 1.3 cm and diameter= 0.02 cm Refinery of Al-Durra and kept in air-tight steel and plastic containers to prevent losses and contamination. Table 7 demonstrates the features of CRO utilized. It has American Petroleum Institute gravity (API gravity) =11.43, specific gravity=0.99, density= 62 lbs/cu ft, and viscosity=4.8 centipoise at 30 ^{0}C.

Table 7. Feature of Al-Dura CRO

Factors	Value
Gravity Degree	< 35
Specific Gravity 15 degrees centigrade	0.812
Sulfur amount (% by weight)	0.30
% by volume	0.40
Wax amount (% by weight)	7.0
Carbon Residue (% by weight)	2.10
Melting point (degree centigrade)	57
Viscosity (21-degree centigrade)	6.81
Acidity (Mg/KOH/g)	0.05

2.2 Preparation of Concrete Mixture

In compliance with the British Standards, a concrete mix design with a water-cement ratio of 0.5 has been selected and batched in weight. The mix design includes specimens of 0 % contaminated cubes cured in freshwater as a control, 0 % contaminated cubes cured in Al-Dura CRO-polluted water as a control, and various levels of artificially contaminated cubes cured in freshwater (1, 2, 2.5, 3, 4, 5, 6, 10, 15, 20, and 25) percent. These three specimens have been compared regarding newly mixed concrete and compressed strength in hardened concrete. The concrete ingredients were mixed in a clean, dry manual tilting drum, yielding 144 cubes. Table 8 illustrates the material mix proportions. After identifying the optimum CRO percentage that causes an increase in the compressive strength of standard concrete, the same CRO proportion (2%) was utilized for reactive powder concretes, as illustrated in Table 9. On the other hand, the reactive powder concrete specimens were tested in two conditions: the first without CRO and the second with the addition of 2% CRO.

Table 8. Standard concrete mix design for 1 m^3 concrete

Mix ID	Cement (kg/m3)	Sand (kg/m3)	Gravel (m3)	Water (kg/m3)	CRO Proportion	CRO (kg/m3)
NM 1	300	650	1200	150	0%	0
NM 2	300	650	1200	150	1%	6.5

NM 3	300	650	1200	150	2%	13
NM 4	300	650	1200	150	2.5%	16.25
NM 5	300	650	1200	150	3%	19.5
NM 6	300	650	1200	150	4%	26
NM 7	300	650	1200	150	5%	32.5
NM 8	300	650	1200	150	6%	39
NM 9	300	650	1200	150	10%	65
NM 10	300	650	1200	150	15%	97.5
NM 11	300	650	1200	150	20%	130
NM 12	300	650	1200	150	25%	162.5

Table 9. Reactive powder concrete mix design

Mix ID	Cement (kg/m3)	Sand (kg/m3)	Silica Fume (kg/m^3)	Water (kg/m^3)	Super Plasticizer3 by Wt. of Cementitious (%)	CRO (kg/m3)
RM	980	10504	245	156.8	7	13

2.3 Workability and Slump Test

A slump mold in the shape of a frustum of a cone 30.5 cm high, 20.3 cm base diameter, with a smaller hole of 10.2 cm diameter at the top - was utilized to produce the slump result. The mold had a smooth surface and was equipped with appropriate fort parts and grips to make lifting easier. The mold was securely held against its base, and three layers of concrete were poured into it. A standard 1.6 cm diameter steel rod has been utilized to tamper with every layer 25 times. The cone was gently inverted and dumped onto a flat plate after filling it. The slump is the reduction in the height of the slumping concrete's center, which was analyzed and evaluated to the closest 0.5 cm, as shown in Fig. 3.

Fig. 3. Slump test

2.4 Physical Tests

2.4.1 Concrete Strength Test

Concrete's great compressibility is one of its most distinguishing features. The compressibility of a concrete cube with dimensions of 150 x 150 x 150mm to produce specific compressive strengths following 28 days has traditionally been referred to as the concrete performance test. Various procedures may determine the concrete's compressive

strength, including direct and indirect methods and destructive and nondestructive tests. The destructive technique utilized in this study was the cube compressive test with a size of 15x15x15 cm based on ASTM standard [29], as shown in Fig. 4, and reactive powder concretes were tested at 7, 14, 28, and 56 days.

2.4.2 Splitting Tensile Strength

This test uses six cylinders with a 15 cm diameter and 30 cm height to measure tensile strength based on ASTM [30], as shown in Fig. 4. Every age uses three cylinders, and the reading for that age is determined by averaging the readings from the three cylinders. Splitting Tensile strength tests are performed on specimens of reactive powder concrete and regular concrete at 28 and 56 days.

Fig. 4. Photograph of compressive strength testing and splitting tensile strength

2.5 Chemical Tests

The samples of the two concrete types, standard concrete (NM 1 and NM3) and reactive powder concrete (MR), representing samples exposed to CRO, were the most effective. Fig. 5 illustrates the test device, which gives the concentration of the materials involved in the composition of the samples.

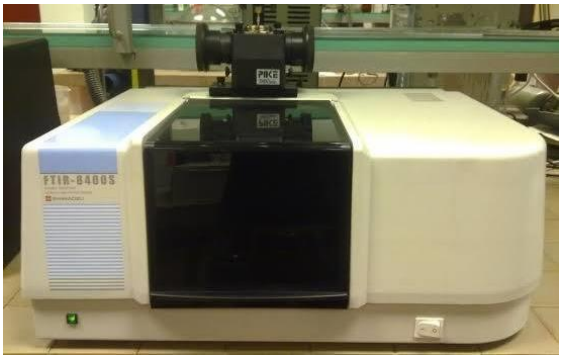

Fig. 5. Chemical testing apparatus

3. Results and Discussion

3.1 Workability and (Slump Test) Results

When the slump values recorded for every polluted specimen are compared to the 20 mm value recorded for the controlling specimen, as demonstrated in Table 10, the polluted specimens exhibit higher slump. This observation is because sand is generally utilized in

concrete mixtures with a dry surface, but CRO increases the liquids in the produced mixture. The slump values increase with increasing CRO in the fine aggregate for both standard and reactive powder concrete. With 6 to 25 % CRO pollution, the concrete slump ultimately crumbled. It is also safe to assume that CRO caused the rise in the slump and interfered with the cement-water binding interactions, delaying or inhibiting the complete hydration of the cement particles [31,32]. Increased slump value is compatible with increased workability from very low to high when utilizing 25 % CRO as an additive on regular concrete. However, it caused a slight increase in the workability and slump value for reactive powder concrete due to the presence of a superplasticizer, which already added more workability to the concrete mix.

Table 10. The slump test findings for normal and reactive powder concrete

Sample ID	Slump mm	Workability [33]
NM 1	20	Very low
NM 2	45	Low
NM 3	50	Low
NM 4	55	Medium
NM 5	60	Medium
NM 6	85	Medium
NM 7	105	High
NM 8	120	High
NM 9	165	High
NM 10	178	High
NM 11	180	Very High
NM 12	200	Very High
RM0	80	Medium
RM	85	Medium

3.2 Compressive Strength Test Results

Fig. 6 reveals the compressive strength findings for different CRO ratios at 7, 14, 28, and 56 curing days. Sample NM3 with 2% CRO presents the best compressive strength for all selected ages, while sample NM7 with 25% presents the worst compressive strength due to the prevention of bonds between the cement hydration gel. On the other hand, the reactive powder concrete samples have been tested in two conditions. The loss of moisture and subsequent decrease in water content/moisture might prohibit the concrete cube from absorbing water during curing in water, which could explain the fall in strength. The phenomenon affects the cement hydration reaction of the concrete cubes. A limited strength enhancement of the concrete with CRO might have resulted from the dilatation of the gel and the weakness of the cohesive forces in the paste [14,34]. The negative impact of CRO is due to the contamination of fine aggregate with CRO, a component of the concrete's matrix microstructure.

The strength dropped once the concrete was exposed to CRO [35,36]. Therefore, sand that contains more than 15% CRO by weight findings has less than 42 % strength, as experimentally detected for unpolluted concrete, and should not be utilized for most construction applications (road, bridge, loaded elements) and used just for unloaded elements. The change in the compressive strength can be obtained from Equation 1 and the findings illustrated in Table 11. Nevertheless, efforts might be necessary to enhance the strength of the CRO concrete utilized in low-strength applications with less than 5%contamination. However, a CRO application on reactive powder concrete significantly decreased compressive strength compared with standard concrete with the same CRO

ratio, as demonstrated in Fig. 7 and Table 11, which illustrates the highest increase in compressive strength for all selected curing ages.

$$\text{Change in (Fc, Fsp, Fr, Ec)\%} = \left(\frac{\text{(Fc,Fsp, Fr, Ec)}}{\text{(Fc, Fsp, Fr, Ec) (at air)}} \times 100 - 100\right)\% \quad (1)$$

Based on [37], a single formula, which is presented below, was utilized to establish a connection between the data on strength and the properties of durability:

$$DI = \frac{a}{(f_c')^b} \quad (2)$$

Whereas DI is the durability index (for example, water penetration depth (mm), chloride permeability (Coulombs), or the coefficient of chloride diffusion, De; f_c' the compressive strength; and a=1400 and b=2.18 are the experiential constants for normal concrete; and (a=1000000 and b=2.78) for reactive powder concrete. A good correlation was noted between compressive strength and durability characteristics, which is expressed in the above expression. However, increasing the compressive strength causes an increase in the concrete's durability due to reducing its permeability. Fig. 8 illustrates that increasing the durability index refers to a reduction in compressive strength; the durability index at 7 curing days is the highest, and increasing the curing days to 14, 28, and 56 reduces the durability index significantly. However, applying crude oil in reactive powder concrete shows a negative impact on the durability index that is shown in Fig. 9.

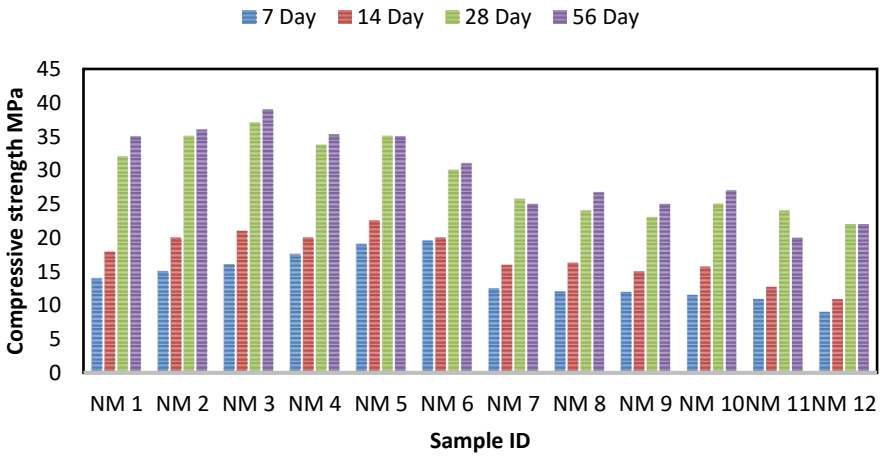

Fig. 6. Compressive strengths of standard concrete with or without CRO contamination

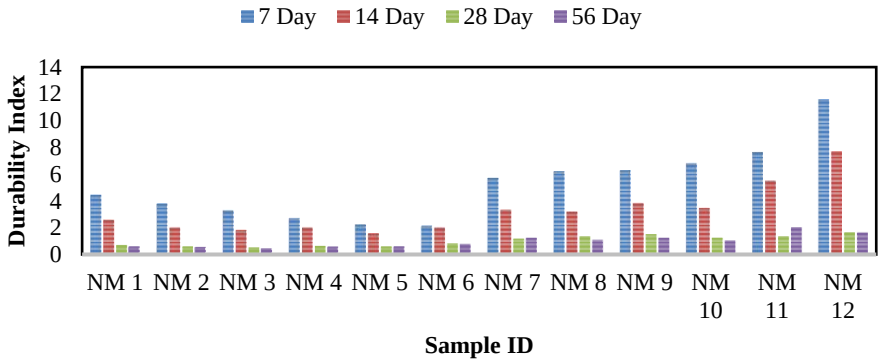

Fig. 7. Durability index for normal concrete samples with different CRO ratios

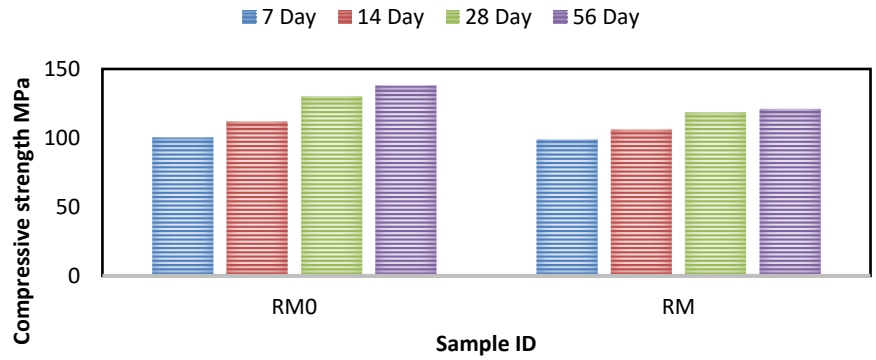

Fig. 8. Compressive strengths of reactive powder concrete with or without CRO contamination

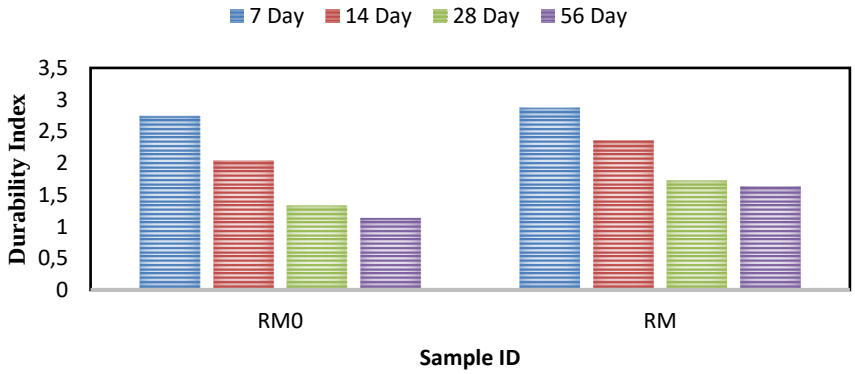

Fig. 9. Durability index for reactive concrete samples with different CRO ratios

Table 11. The change in the compressive strength values.

Sample ID	Improvement percentage %			
	7 Day	14 Day	28 Day	56 Day
NM 1	0.00	0.00	0.00	0.00
NM 2	7.45	11.73	9.38	2.86
NM 3	14.61	17.32	15.63	11.37
NM 4	25.36	11.73	5.31	0.86
NM 5	36.10	25.70	9.38	0.00
NM 6	39.69	11.73	-6.25	-11.43
NM 7	-10.82	-10.89	-19.59	-28.57
NM 8	-14.04	-9.05	-25.00	-23.71
NM 9	-14.54	-16.20	-28.13	-28.57
NM 10	-17.62	-12.29	-21.88	-22.86
NM 11	-21.92	-29.05	-25.00	-42.86
NM 12	-35.53	-39.11	-31.25	-37.14
RM	-1.67	-5.10	-8.92	-12.31

3.3 Tensile Strength Results

The behavior of the standard concrete after exposure to different CRO ratios in both tensile and compressive strength is illustrated in Table 12 and Fig. 10, with enhanced tensile strength after applying less than 4% of CRO. Fig. 10 illustrates the tensile strength in all selected CRO ratios for standard concrete at 28 and 56 curing ages, improving as the concrete ages. However, samples NM2, NM3, NM4, and NM5 illustrate increased tensile strength for two selected periods. Sample NM3, with a 2% CRO ratio, has the highest value, while samples NM6-NM12 illustrate a significant decrease in the tensile strength of standard concrete samples, and sample NM12 records the lowest value. Relying on the works of Bangham [38], Onabolu [39] found that the loss in surface energy brought on by the CRO adsorption onto the surface of C-S-H gel might also have had a role in the material's decreased compressive strength. The control (curing) medium's strength values have always been more significant once compared to the other values. In contrast, the other curing media degrade with time as the curing age rises. Utilizing 2% CRO improves tensile strength in a standard concrete sample. Utilizing the same ratio in reactive power concrete leads to decreased tensile resistance at 28 and 56 curing ages, as demonstrated in Fig. 11 and Table 12.

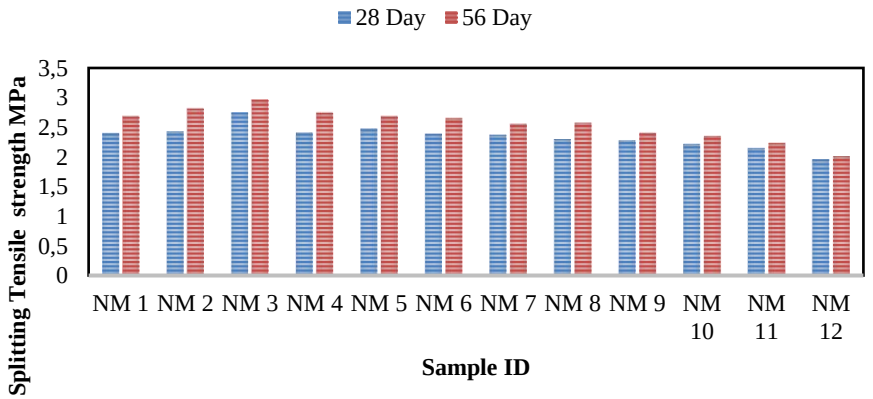

Fig. 10. Tensile strengths of standard concrete with or without CRO contamination

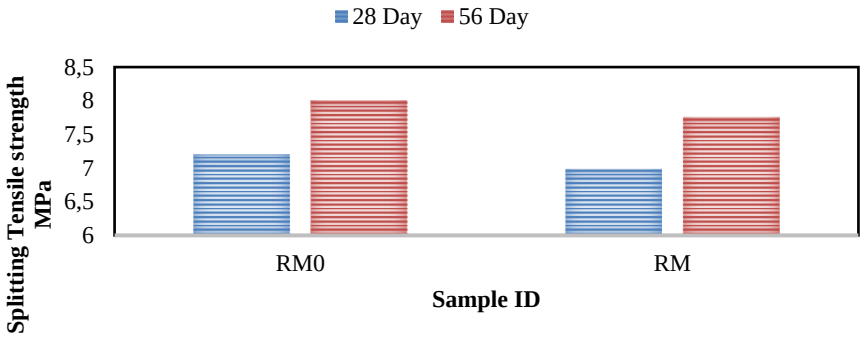

Fig. 11. Tensile Strengths of reactive powder concrete with or without CRO contamination

Table 12. The change in the tensile strength values

Sample ID	Improvement percentage %	
	28 Day	56 Day
NM 1	0.00	0.00
NM 2	1.25	4.85
NM 3	14.58	10.45
NM 4	0.42	2.24
NM 5	3.33	0.00
NM 6	-0.42	-1.12
NM 7	-1.25	-4.85
NM 8	-4.17	-4.10
NM 9	-5.00	-10.45
NM 10	-7.50	-12.31
NM 11	-10.42	-16.79
NM 12	-18.33	-25.00
RM	-3.10	-3.13

3.4 Chemical Observation

By analyzing interactions between the concrete matrix components utilizing the FTIR spectroscopy method [40], it was possible to quantify their chemical compatibility before and after exposure to CRO. The chemical linkages in the composite materials may be examined utilizing FTIR. The findings of the chemical tests demonstrated a significant increase in the concentration of sulfate in normal concrete sample NM1 with the absence of CRO (1424.79 cm-1), as illustrated in Fig. 12, and both samples of normal and reactive powder concrete after exposure to CRO (1900 and 1850.4 cm-1) as illustrated in Fig. 13 and 14, respectively. The concentration of sulfates may harm the concrete, and its reaction with concrete components is accompanied by an increase in volume, which leads to the cracking of the concrete. Sulfate attack is one of the leading contributors to the reduction in durability of concrete. The resistance of concrete materials to sulfate attack may typically be determined by laboratory testing by looking at factors such as the loss of mass, the drop in strength, and the expanding strain of concrete specimens. On the other hand, one cannot utilize these signs to make a quantitative prediction about the carrying capability of actual concrete buildings that are being attacked by sulfate [41] immediately. Based on Figs (13-14), utilizing CRO causes an increase in internal sulfate amount in concrete in comparison with normal concrete without CRO; therefore, utilizing CRO leads

to reduced durability due to increased sulfate amounts, and these results are compatible with results obtained by [40].

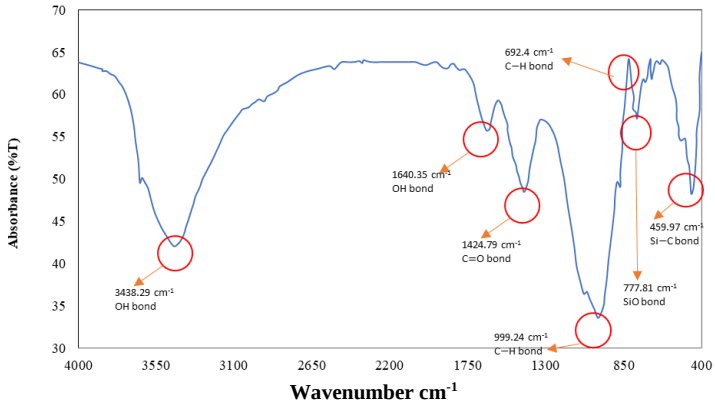

Fig. 12. Chemical analysis for standard concrete without CRO sample (NM1)

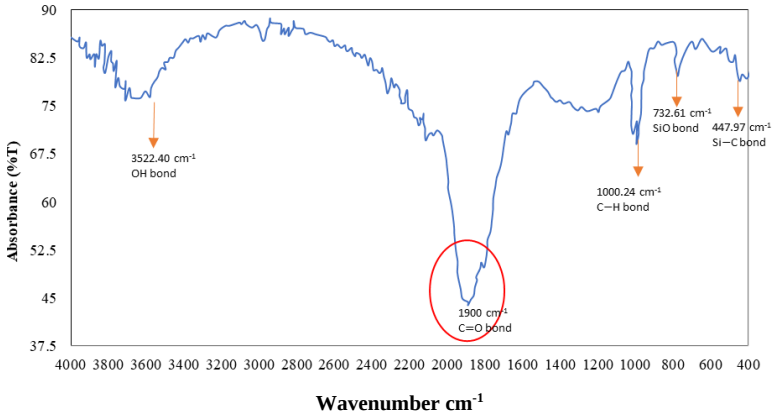

Fig. 13. Chemical analysis for standard concrete with 2% CRO sample (NM3)

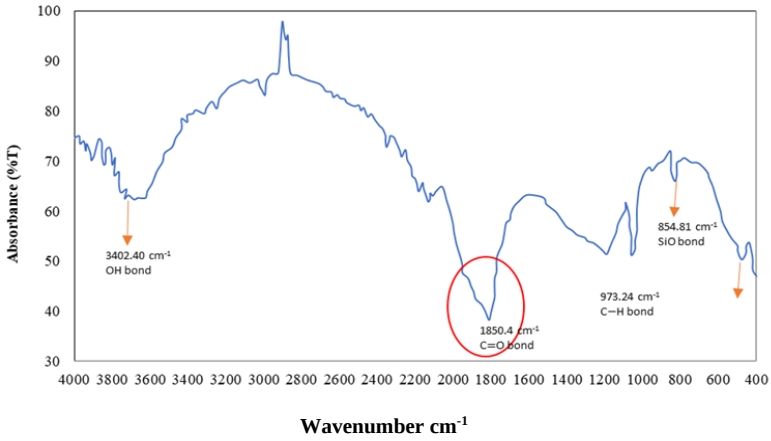

Fig. 14. Chemical analysis for reactive powder concrete with 2% CRO sample (RM)

4. Conclusion

The impact of CRO contamination on concrete compressive strength has been studied, and the following points were concluded from the study:

- CRO was found to influence the concrete's strength depending on the different practical and analytical procedures utilized. Once concrete meets liquids other than potable or fresh water, it is proven harmful to the cement-based material, mainly for OPC. Its low environmental and chemical resistance and low compressive strength due to slow strength development lead to early deterioration.
- The magnitude of the concrete slump rises incompatible with the quantity of polluted CRO ratio for both standard and reactive powder concrete.
- The concrete strength varies depending on the quantity of CRO utilized, and a ratio of 2 % was found to be an enhancement ratio that caused an increase in the compressive strength.
- The compressive strength of reactive powder concrete deteriorated after exposure to 2% of CRO; the lowest compressive strength was obtained after 56 curing days.
- The durability index increased slightly when utilizing 2% CRO based on the durability index, but the internal sulfate amount has increased compared with normal concrete without CRO.

References

[1] Al Zand AW, Hosseinpour E, Badaruzzaman WHW, Ali MM, Yaseen ZM, Hanoon AN. Performance of the novel C-purlin tubular beams filled with recycled-lightweight concrete strengthened with CFRP sheet. Journal of Building Engineering 2021. https://doi.org/10.1016/j.jobe.2021.102532

[2] Nedeljković M, Visser J, Šavija B, Valcke S, Schlangen E. Use of fine recycled concrete aggregates in concrete: A critical review. Journal of Building Engineering 2021. https://doi.org/10.1016/j.jobe.2021.102196

[3] Yaphary YL, Lu J-X, Chengbin X, Shen P, Ali HA, Xuan D, et al. Characteristics and production of semi-dry lightweight concrete with cold bonded aggregates made from recycling concrete slurry waste (CSW) and municipal solid waste incineration bottom ash (MSWIBA). Journal of Building Engineering 2022;45:103434. https://doi.org/10.1016/j.jobe.2021.103434

[4] Ramesh BM, Vongole RM, Nagraj Y, Naganna SR, Sreedhara BM, Mailar G, et al. Valorization of incinerator bottom ash for the production of resource-efficient eco-friendly concrete: Performance and toxicological characterization. Architecture, Structures and Construction 2021. https://doi.org/10.1007/s44150-021-00006-9

[5] Tuama WK, Kadhum MM, Alwash NA, Al-Khafaji ZS, Abdulraheem MS. RPC Effect of Crude Oil Products on the Mechanical Characteristics of Reactive-Powder and Normal-Strength Concrete. Periodica Polytechnica Civil Engineering 2020. https://doi.org/10.3311/PPci.15580

[6] Falah MW, Hafedh AA, Hussein SA, Al-Khafaji ZS, Shubbar AA, Nasr MS. The Combined Effect of CKD and Silica Fume on the Mechanical and Durability Performance of Cement Mortar. Key Engineering Materials, vol. 895, Trans Tech Publ; 2021, p. 59-67. https://doi.org/10.4028/www.scientific.net/KEM.895.59

[7] Bello AT, Amadi J. Oil Pollution and Bio-Diversity Conservation in Nigeria: An Assessment of Legal Framework. Journal of Geoscience and Environment Protection 2019;7:354. https://doi.org/10.4236/gep.2019.78024

[8] Khosravi E, Ghasemzadeh H, Sabour MR, Yazdani H. Geotechnical properties of gas oil-contaminated kaolinite. Engineering Geology 2013;166:11-6. https://doi.org/10.1016/j.enggeo.2013.08.004

[9] Shakesby RA, Wallbrink PJ, Doerr SH, English PM, Chafer CJ, Humphreys GS, et al. Distinctiveness of wildfire effects on soil erosion in south-east Australian eucalypt forests assessed in a global context. Forest Ecology and Management 2007;238:347-64. https://doi.org/10.1016/j.foreco.2006.10.029
[10] Osuji LC, Ezebuiro PE. Hydrocarbon contamination of a typical mangrove floor in Niger Delta, Nigeria. International Journal of Environmental Science & Technology 2006;3:313-20. https://doi.org/10.1007/BF03325939
[11] Sharma HD, Reddy KR. Geoenvironmental engineering: site remediation, waste containment, and emerging waste management technologies. John Wiley & Sons; 2004.
[12] Delin GN. Groundwater contamination by crude oil near Bemidji, Minnesota. US Department of the Interior, US Geological Survey; 1998. https://doi.org/10.3133/fs08498
[13] Abousnina R, Manalo A, Lokuge W, Zhang Z. Effects of light crude oil contamination on the physical and mechanical properties of geopolymer cement mortar. Cement and Concrete Composites 2018; 90: 136-49. https://doi.org/10.1016/j.cemconcomp.2018.04.001
[14] Ajagbe WO, Omokehinde OS, Alade GA, Agbede OA. Effect of crude oil impacted sand on compressive strength of concrete. Construction and Building Materials 2012;26:9-12. https://doi.org/10.1016/j.conbuildmat.2011.06.028
[15] Abousnina R, Manalo A, Lokuge W, Al-Jabri KS. Properties and structural behavior of concrete containing fine sand contaminated with light crude oil. Construction and Building Materials 2018;189:1214-31. https://doi.org/10.1016/j.conbuildmat.2018.09.089
[16] Abousnina R, Manalo A, Ferdous W, Lokuge W, Benabed B, Al-Jabri KS. Characteristics, strength development, and microstructure of cement mortar containing oil-contaminated sand. Construction and Building Materials 2020;252:119155. https://doi.org/10.1016/j.conbuildmat.2020.119155
[17] Abousnina RM, Manalo A, Lokuge W, Shiau J. Oil contaminated sand: an emerging and sustainable construction material. Procedia Engineering 2015;118:1119-26. https://doi.org/10.1016/j.proeng.2015.08.453
[18] Hamad BS, Rteil AA, El-Fadel M. Effect of used engine oil on properties of fresh and hardened concrete. Construction and Building Materials 2003;17:311-8. https://doi.org/10.1016/S0950-0618(03)00002-3
[19] Ayininuola GM. Influence of diesel oil and bitumen on compressive strength of concrete. Journal of Civil Engineering 2009;37:65-71.
[20] A Jawad F, Jasim AT. Effect Of Oil On Strength Of Normal And High Performanc Concrete. Al-Qadisiyah Journal for Engineering Sciences 2010;3:24-32.
[21] Osuji SO, Nwankwo E. Effect of crude oil contamination on the compressive strength of concrete. Nigerian Journal of Technology 2015;34:259-65. https://doi.org/10.4314/njt.v34i2.7
[22] Shafiq N, Nuruddin MF, Beddu S. Properties of concrete containing used engine oil. International Journal of Sustainable Construction Engineering and Technology 2011;2.
[23] Shahrabadi H, Vafaei D. Effect of kerosene impacted sand on compressive strength of concrete in different exposure conditions. J Mater Environ Sci 2015;6:2665-72.
[24] Shubbar HA, Alwash NA. The fire exposure effect on hybrid reinforced reactive powder concrete columns. Civil Engineering Journal (Iran) 2020;6:363-74. https://doi.org/10.28991/cej-2020-03091476
[25] Meng Q, Wu C, Li J, Liu Z, Wu P, Yang Y, et al. Steel/basalt rebar reinforced Ultra-High Performance Concrete components against methane-air explosion loads. Composites Part B: Engineering 2020;198:108215. https://doi.org/10.1016/j.compositesb.2020.108215
[26] Institution BS. Specification for ordinary and rapid-hardening Portland cement. British Standards Institution; 1988.

[27] ASTM C. C 33-86; Standard Specification for Concrete Aggregates, Annual Book of ASTM Standards. ASTM: West Conshohocken, PA, USA 1986.
[28] IQS. No. 45, Aggregate from natural sources for concrete and construction. Iraqi Specif 1984.
[29] ASTM C. 109. Standard Test Method for Compressive Strength of Hydraulic Cement Mortars (Using 2in or [50-Mm] Cube Specimens)', Annual Book of ASTM Standards, USA 2013.
[30] ASTM C. 496-96. Standard Test Method for Splitting Tensile Strength of Cylindrical Concrete Specimens 1996.
[31] Pollard SJT, Montgomery DM, Sollars CJ, Perry R. Organic compounds in the cement-based stabilisation/solidification of hazardous mixed wastes-Mechanistic and process considerations. Journal of Hazardous Materials 1991;28:313-27. https://doi.org/10.1016/0304-3894(91)87082-D
[32] Asna MZ. Optimization of solidifications/stabilization for petroleum-based waste using blended cement/Asna Mohd Zain 2013.
[33] Neville AM, Brooks JJ. Concrete Technology (2nd Indian reprint) 2002.
[34] Faiyadh FI. Properties of oil-saturated concrete. 1980.
[35] Ejeh SP, Uche OAU. Effect of crude oil spill on compressive strength of concrete materials. Journal of Applied Sciences Research 2009;5:1756-61.
[36] Abdul Ahad RB, Mohammed AA. Compressive and tensile strength of concrete loaded and soaked in crude oil 2000.
[37] Al-Amoudi OSB, Al-Kutti WA, Ahmad S, Maslehuddin M. Correlation between compressive strength and certain durability indices of plain and blended cement concretes. Cement and Concrete Composites 2009;31:672-6. https://doi.org/10.1016/j.cemconcomp.2009.05.005
[38] Bangham DH. The swelling and shrinkage of porous materials and the role of surface forces in determining technical strength. Symposium Society Chemical Industry, 1946.
[39] Onabolu OA. Effects of hot crude oil on concrete for offshore storage applications 1986.
[40] Horgnies M, Chen JJ, Bouillon C. Overview about the use of Fourier transform infrared spectroscopy to study cementitious materials. WIT Trans Eng Sci 2013;77:251-62. https://doi.org/10.2495/MC130221
[41] Cheng H, Liu T, Zou D, Zhou A. Compressive strength assessment of sulfate-attacked concrete by using sulfate ions distributions. Construction and Building Materials 2021;293:123550. https://doi.org/10.1016/j.conbuildmat.2021.123550

Research on Engineering Structures & Materials
www.jresm.org
Research Group

Research Article

A novel high order theory for static bending of functionally graded (FG) beams subjected to various mechanical loads

Mourad Chitour[1,a], Faicel Khadraoui[1,b], Khelifa Mansouri[1,c], Billel Rebai[2,d], Abderrahmane Menasria[2,e], Amina Zemmouri[3,f], Sofiane Touati[1,g], Haithem Boumediri[*4,h]

[1]*Mechanical Engineering Department, Abbes Laghrour University, BP. 1252, Khenchela 4004, Algeria*
[2]*Civil Engineering Department, Abbes Laghrour University, BP. 1252, Khenchela 4004, Algeria*
[3]*Mechanical Engineering Department Badji Mokhtar Annaba University, Mechanics of Materials and Plant Maintenance Research Laboratory (LR3MI), Algeria*
[4]*Institut des sciences et des Techniques Appliquées (ISTA), Université Constantine 1, Algeria*

Article Info

Article history:

Received 04 Jan 2024
Accepted 31 Mar 2024

Keywords:

Functionally graded beams;
Virtual works;
Navier's method;
Deflection analysis;
Stress analysis

Abstract

This study develops a new higher-order shear deformation theory (HSDT) to analyze the static behavior of functionally graded (FG) beams under various mechanical loading conditions. The new theory is meticulously designed to effectively represent complexities in stress, strain, and deformation analysis, with a focus on maintaining or enhancing accuracy while reducing the computational burden for practical applications. The material properties of the FG beams are assumed to vary continuously across the thickness as per a power law distribution (P-FGM). The governing equilibrium equations are derived using the principle of virtual work. Navier's solution method is then utilized to obtain the analytical solutions. Extensive numerical studies are conducted to study the influences of key geometric and material parameters on the static response. The deflection, axial stress and tangential stress distributions are computed for different combinations of length-to- thickness ratio, material grading index, and applied loads. The results are validated by comparison with existing literature where good agreement is observed, demonstrating the accuracy of the proposed HSDT formulation. Parametric analyses provide useful insights into the individual and coupled effects of beam slenderness, material inhomogeneity and transverse loading on the static performance of P-FGM beams. This study enhances understanding of the structural behavior of FG beams through an efficient and accurate analytical approach.

1. Introduction

Functionally graded materials (FGMs) comprise a class of advanced composites distinguished by continuous spatial variations in composition and microstructure, resulting in corresponding property gradients across the volume [1,2]. This concept enables tailored optimization of material response and functionality by customizing the microstructural distribution. FGMs serve to mitigate challenges arising from the use of composite materials with abrupt interfaces in harsh conditions. These issues encompass stress singularities, property mismatches, inadequate adhesion, and delamination [3]. Owing to these advantages, FGMs have garnered substantial interest and adoption across diverse fields such as civil engineering, aerospace, automotive industry, general engineering applications, nuclear power plants, and more [4,5]. The graded morphology

*Corresponding author: haithem.boumediri@umc.edu.dz
[a] orcid.org/0009-0009-9087-680X; [b] orcid.org/0009-0002-3175-4377; [c] orcid.org/0000-0002-8523-6578; [d] orcid.org/0000-0003-3739-2784; [e] orcid.org/0009-0008-3507-0128; [f] orcid.org/0000-0002-6262-747X; [g] orcid.org/0000-0001-9791-0964; [h] orcid.org/0000-0002-9578-0948
DOI: http://dx.doi.org/10.17515/resm2024.141me0104rs

provides new dimensions for designing next-generation materials to meet demanding thermomechanical requirements across an array of critical applications.

Several researchers have dedicated their efforts to the mechanical analysis of Functionally Graded (FG) materials, specifically focusing on plates, beams, and shells. Their investigations have employed a range of theories and methods, encompassing both analytical and numerical approaches grounded in classical principles such as first-order shear deformation theory, higher-order shear deformation theories, and the Quasi-3D theory. In the context of FG beams, their studies have delved into the examination of free vibration and bending characteristics. Theoretical frameworks employed in these studies include well-established models such as the Euler-Bernoulli theory and the utilization of Timoshenko beam elements [6-9].

U. Kumar Kar and J. Srinivas have pioneered an elasticity solution for a rotating micro-beam subjected to thermo-mechanical loading. Their innovative approach incorporates bi-directional functional grading with graphene nanoplatelets (FG-GNPs), showcasing the potential for enhanced structural performance in challenging environments [10]. Zenkour [11] provided a precise solution for plates composed of FGM using a generalized sinusoidal shear deformation theory. Pei-Liang B et al. [12] employed a new FEM framework to analyze the mechanical responses of nanobeams made of axially functionally-graded material (FGM) under different boundary conditions. Chitour et al. [13] introduced a novel hyperbolic quasi-3D shear deformation plate theory for analyzing the bending behavior of functionally graded sandwich plate structures submitted to sinusoidal loads, while Chikh et al. [14] investigated the static response and free vibration of a functionally graded beam on elastic foundations. Thai et al. [15] explored the free vibration and bending of FG beams using higher-order beam theories, and a refined plate theory was developed for examining thermoelastic effects and wave propagation in functionally graded plates.

Ongoing research extends to dynamic analysis [16,17], stability behavior [18,19], and formulation of theories considering additional effects like porosity [20]. Investigations into beams with variable thickness and nonuniform geometries have also been undertaken [21-22]. Simultaneously, the sustained research focus on FGM beams in the mechanics, materials, and structures communities highlights their potential for tailored gradation patterns and advanced responses. This ongoing interest underscores the pivotal role FGMs play in advancing material science and structural design methodologies across various engineering applications [23-27].

This study unfolds through two integral components: a comprehensive comparative analysis and an in-depth parametric investigation. The primary objective of the comparative study is to elucidate and validate the precision and efficiency of the employed high-order shear deformation theory by systematically contrasting it with existing theories. In contrast, the parametric study systematically dissects the mechanical behavior of functionally graded beams under a spectrum of mechanical loads. It meticulously considers various factors, such as the material index (k) linked to the power-law distribution of Young's modulus, the thickness ratio (L/h) of the beams, and the specific beam type. This approach empowers the comparative evaluation, ensuring the theoretical formulation's accuracy is substantiated against alternative methodologies. Additionally, the parametric studies methodically delve into examining the influences of parameters, including the power-law distribution index, thickness ratio, beam configuration, and loading conditions, on the mechanical response of FGM beams. The study explores the coupled effects of material gradation, geometry, and external stimuli on static and dynamic performance metrics, providing a nuanced understanding of the interplay between these influential factors. This multi-faceted approach enhances the study's comprehensiveness and contributes to advancing the understanding of functionally graded beams' intricate

mechanical behavior. The integration of a comparative framework and a thorough parametric exploration not only substantiates the theory's precision but also provides valuable insights into the nuanced factors influencing the mechanical response of functionally graded beams

2. Geometry of A Functionally Graded Beams

An FG beam possesses a length (L) and a rectangular cross-section denoted by b × h, where (b) represents the width and (h) corresponds to the height [15]. The coordinates x, y, and z correspond to the length, width, and height of the beam, respectively, as depicted in Figure 1.

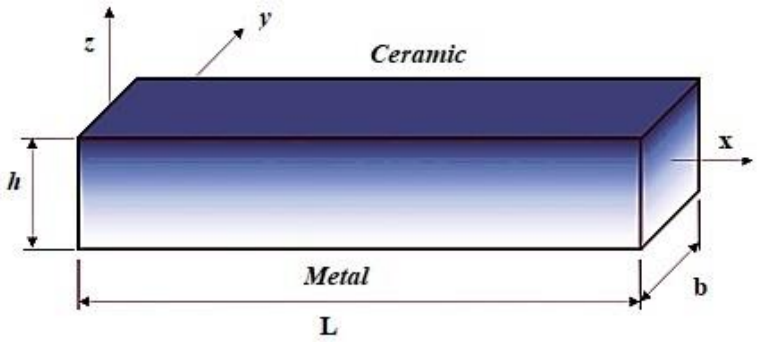

Fig. 1. Geometry and coordinate system of FG beam

The effective material properties of FGM beams, including Young's modulus (E) and mass density (ρ) that undergo smooth variations solely in the z direction. are expressed by [28]:

$$P(z) = P_m + (P_c - P_m)V_c \qquad -\frac{h}{2} \le z \le \frac{h}{2} \tag{1}$$

$$V(z) = (\frac{z}{h} + \frac{1}{2})^k, \quad V_c + V_m = 1 \tag{2}$$

The FGMs' volume fraction is assumed to conform to a power-law function along the thickness direction.

3. Displacement Field and Constitutive Equations

In this study, the emphasis is on investigating the displacement model of FG beams. A high-order shear strain theory, commonly known as the refined theory, is utilized to represent the model. The representation of the displacement model is encapsulated in the following equation:

$$\begin{aligned} u(x,z) &= u_0(x) - z\frac{\partial w_0(x)}{\partial x} + KA\, f(z)\frac{\partial \theta(x)}{\partial x} \\ w(x,z) &= w_0(x) \end{aligned} \tag{3}$$

uo, w and θ Are the three unknown displacement of the mid-plane of the FG beams. The specific form of the shape function f(z) is assumed by Himeur et al [29]:

$$f(z)=\sin\left(\left(\frac{z}{h}\right)-\left(\frac{4z^3}{3h^2}\right)\right) \tag{4}$$

The kinematic relations corresponding to the displacement field described in Equation (3), relying on the principles of small-strain elasticity theory, are expressed as follows:

$$\begin{aligned}\varepsilon_{xx}&=\frac{\partial u_0(x)}{\partial x}-z\frac{\partial^2 w_0(x)}{\partial x^2}+KA\,f(z)\frac{\partial\theta^2(x)}{\partial x^2}\\ \gamma_{xz}&=KA\,g(z)\frac{\partial\theta(x)}{\partial x}\end{aligned} \tag{5}$$

Where:

$$g(z)=\left(\frac{\partial f(z)}{\partial z}\right) \tag{6}$$

Based on 2D displacement field expressed in Eq. (5), the linear constitutive relations of FGM beams are assumed as:

$$\begin{Bmatrix}\sigma_{xx}\\ \tau_{xz}\end{Bmatrix}=\begin{bmatrix}C_{11} & 0\\ 0 & C_{55}\end{bmatrix}\begin{Bmatrix}\varepsilon_{xx}\\ \gamma_{xz}\end{Bmatrix} \tag{7}$$

Where:

$$\begin{aligned}C_{11}&==E(z)\\ C_{55}&=E(z)/2(1+\nu)\end{aligned} \tag{8}$$

4. Displacement Field and Constitutive Equations

The principal equations of equilibrium are employing the concept of virtual displacements as follows Merdaci et al [30]:

$$\delta V_{tot}=\int_V\left[\sigma_{xx}\delta\varepsilon_{xx}+\tau_{xz}\delta\gamma_{xz}\right]dV-\int_{\Omega}q\delta w(x)d\Omega=0 \tag{9}$$

Through the integration of Equations (5) and (7) into Equation (9) across the thickness of the beams, a rephrased representation of Equation (9) is as follows:

$$\int\left[N_{xx}\frac{\partial u_0}{\partial x}-M_{xx}\frac{\partial^2 w_0}{\partial x^2}+KA\,S_{xx}\frac{\partial^2\theta}{\partial x^2}+KA\,Q_{xz}\frac{\partial\theta}{\partial x}\right]dx-\int\left[q\delta w_0\right]dx \tag{10}$$

Where *q* is the distributed transverse load. The stress resultants *Nxx, Mxx, Sxx and Qxz* are defined by:

$$N_{xx} = \int \sigma_{xx} dz$$
$$M_{xx} = \int \sigma_{xx} z dz$$
$$S_{xx} = \int \sigma_{xx} f(z) dz \qquad (11)$$
$$Q_{xz} = \int \tau_{xx} f'(z) dz$$

By substituting Equation (5) and Equation (7) into Equation (11), the stress and moment resultants Nxx, Mxx, Sxx and Qxz are defined as follows

$$\begin{aligned} N_{xx} &= A_{11}\frac{\partial u_0}{\partial x} - B_{11}\frac{\partial^2 w_0}{\partial x^2} + KAC_{11}^S\frac{\partial^2 q}{\partial x^2} \\ M_{xx} &= B_{11}\frac{\partial u_0}{\partial x} - D_{11}\frac{\partial^2 w_0}{\partial x^2} + KAF_{11}\frac{\partial^2 q}{\partial x^2} \\ S_{xx} &= C_{11}^S\frac{\partial u_0}{\partial x} - F_{11}\frac{\partial^2 w_0}{\partial x^2} + KAH_{11}\frac{\partial^2 q}{\partial x^2} \\ Q_{xz} &= KAG_{55}\frac{\partial q}{\partial x} \end{aligned} \qquad (12)$$

Where the stiffness components are given as follows

$$\left\{A_{11}, B_{11}, C_{11}^S, D_{11}, F_{11}, H_{11}\right\} = \int C_{11}\left\{1, z, f(z), z^2, z f(z), f^2(z)\right\} dz, \qquad G_{55} = \int C_{55} g^2(z) dz \qquad (13)$$

By performing integration by parts on Equation (10) and setting ($\delta u0$, $\delta w0$, $\delta\theta$) equal to zero, the principal differential equations from Equation (14) are obtained:

$$\begin{aligned} \delta u_0 &: \frac{\partial N_{xx}}{\partial x} = 0 \\ \delta w_0 &: \frac{\partial^2 M_{xx}}{\partial x^2} + q = 0 \\ \delta\theta &: \frac{-(KA)\partial^2 P_{xx}}{\partial x^2} + \frac{(KA)\,\partial Q_{xz}}{\partial x} = 0 \end{aligned} \qquad (14)$$

By inserting Equation (12) and Equation (13) into Equation (14), the principal equations are expressed as follows:

$$\begin{aligned} & A_{11}\frac{\partial^2 u_0}{\partial x^2} - B_{11}\frac{\partial^3 w_0}{\partial x^3} + KAC_{11}^S\frac{\partial^3\theta}{\partial x^3} \\ & B_{11}\frac{\partial^3 u_0}{\partial x^3} - D_{11}\frac{\partial^4 w_0}{\partial x^4} + KAF_{11}\frac{\partial^4\theta}{\partial x^4} + q = 0 \\ & -C_{11}^S\frac{\partial^3 u_0}{\partial x^3} + F_{11}\frac{\partial^4 w_0}{\partial x^4} - KAH_{11}\frac{\partial^4\theta}{\partial x^4} + KAG_{55}\frac{\partial^2\theta}{\partial x^2} = 0 \end{aligned} \qquad (15)$$

5. Analytical Solution

Beams are typically categorized based on the type of support they receive. In the case of simply supported FG beams, the analytical solution to the partial differential equation is achieved using the Navier method, which relies on the double Fourier series. The variables *u0, v0 and θ*, can be expressed by assuming the following variations.

$$\begin{Bmatrix} u_0 \\ v_0 \\ \theta \end{Bmatrix} = \sum_{n=1}^{\infty} \begin{Bmatrix} U_m \cos(\lambda x) \\ W_m \sin(\lambda x) \\ X_m \sin(\lambda x) \end{Bmatrix} \tag{16}$$

Where λ=mπ/a; *Um, Wm and Xm* represent arbitrary parameters to be determined. Also, the transverse load *q* is expanded in a Fourier series as:

$$q_m = \frac{2}{a}\int_0^a q(x)\sin(\lambda x)\,dx \tag{17}$$

The values of *qm* using Equation (17) are set as follows:

- Sinusoidally distributed load

$$q_m = q_0, \qquad m = 1 \tag{18}$$

- Uniform distributed load

$$q_m = \frac{4q_0}{m\pi} \tag{19}$$

- Central patch load

$$q_m = \frac{4\,q_0}{m\pi}\sin\left(m\,\pi\,0.02\left(l/2\right)\right) \tag{20}$$

- Central concentrated load

$$q_m = \frac{4\,Q_0}{a}\sin\left(m\,\pi/2\right); \quad Q_0 = q_0\,l \tag{21}$$

By substituting Equation (16) and Equation (17) into Equation (22), the resulting equations are as follows:

$$\left[L\right] = \begin{bmatrix} L_{11} & L_{12} & L_{13} \\ L_{12} & L_{22} & L_{23} \\ L_{13} & L_{23} & L_{33} \end{bmatrix} \begin{Bmatrix} U_m \\ W_m \\ X_m \end{Bmatrix} = \begin{Bmatrix} 0 \\ q_m \\ 0 \end{Bmatrix} \tag{22}$$

The elements Lij are expressed as follows:

$$
\begin{aligned}
L_{11} &= -4A_{11}\lambda^2 \\
L_{12} &= -8B_{11}\lambda^3 \\
L_{13} &= -8K_1A\,C^s_{11}\lambda^3 \\
L_{22} &= -8D_{11}\lambda^4 \\
L_{23} &= 8K_1AF_{11}\lambda^4 \\
L_{33} &= -8H_{11}K_1A\lambda^4 - 2G_{55}K_1A\lambda^2
\end{aligned}
\tag{23}
$$

6. Numerical Results and Discussion

The analysis focuses on the bending behavior response of simply-supported FG beams under various loading conditions, encompassing sinusoidal distributed, uniform, central patch, and concentrated loads. Multiple parametric studies are undertaken, and the obtained solutions are juxtaposed with available data from existing literature. The present FGM beams investigated in this study consist of a composite blend comprising Alumina (Al2O3) as the ceramic phase and Aluminum (Al) as the metal phase. The mechanical properties, including Young's modulus and Poisson's ratio, are specified in Table 1. To facilitate the analysis, the vertical displacement and stresses of the beams under various distributed loads (q) are expressed in non-dimensional terms. This allows for a more convenient comparison and understanding of the results.

Table 1. Material properties used in the FG Beams [31]

Properties	Alumina (Al2O3)	Aluminum (Al)
Young's modulus E (GPa)	380	70
Poisson's ratio ν	0.3	0.3

6.1 Validation of The Results

Tables 2, 3, and 4 provide the non-dimensional numerical results for the deflection, axial, and tangential stress of the Functionally Graded Material (FGM) beams under uniform and sinusoidal loads. These results are presented for various values of the power law index (k). The model excels in comparison to other shear deformation theories, specifically for thick beams and those with a higher power law index, due to its inclusion of thickness stretching effects. The findings indicate that a higher power law index results in a greater stiffness for FGM beams, resulting in reduced deflection and stress under uniform load. This understanding is vital for customizing FGM beams for specific purposes, as a higher power law index offers advantages such as increased stiffness and the ability to withstand higher axial loads.

Table 2. The maximum non-dimensional central deflection of FG SS beams (under uniform distribution load)

L/h	Method	*K*					
		0	0.5	1	2	5	10
5	Chikh Abdelbaki [32]	3.1654	4.8285	6.2594	8.0675	9.8271	10.9375
	Li et al. [33]	3.1657	4.8292	6.2599	8.0602	9.7802	10.8979
	Present	3.1653	4.8285	6.2594	8.0682	9.8317	10.9400
20	Chikh Abdelbaki [32]	2.8962	4.4644	5.8049	7.4420	8.8181	9.6905
	Li et al. [33]	2.8962	4.4645	5.8049	7.4415	8.8151	9.6879
	Present	2.8963	4.4642	5.8052	7.4419	8.8181	9.6906

Table 3. The maximum non-dimensional axial stresses of FG SS beams (subjected to an evenly distributed load)

L/h	Method	K					
		0	0.5	1	2	5	10
5	Chikh Abdelbaki [32]	3.8017	4.9920	5.8831	6.8819	8.1095	9.7111
	Li et al. [33]	3.8020	4.9925	5.8837	6.8812	8.1030	9.7063
	Present	3.8035	4.9943	5.8877	6.8853	8.1146	9.7158
20	Chikh Abdelbaki [32]	15.0129	19.7003	23.2052	27.0989	31.8127	38.1383
	Li et al. [33]	15.0130	19.7005	23.2054	27.0989	31.8112	38.1372
	Present	15.0133	19.7008	23.2059	27.1001	31.8136	38.1398

Table 4. The maximum non-dimensional tangential stresses of FG SS beams (Subjected to a load uniformly distributed)

L/h	Method	K					
		0	0.5	1	2	5	10
5	Chikh Abdelbaki [32]	0.7312	0.7484	0.7312	0.6685	0.5883	0.6445
	Li et al. [33]	0.7500	0.7676	0.7500	0.6787	0.5790	0.6436
	Present	0.7422	0.7592	0.7428	0.6802	0.6008	0.6570
20	Chikh Abdelbaki [32]	0.7429	0.7599	0.7429	0.6802	0.5998	0.6572
	Li et al. [33]	0.7500	0.7676	0.7500	0.6787	0.5790	0.6436
	Present	0.7565	0.7695	0.7540	0.6930	0.6130	0.6130

Tables 5, 6, and 7 meticulously detail the outcomes for functionally graded (FG) beams subjected to sinusoidal loads, unraveling the nuanced effects of varying power law index values. The presentation extends beyond mere reporting, incorporating a comprehensive systematic comparison with results from established beam theories, such as Chikh Abdelbaki [32], Li et al. [33], L. Hadji et al. [34], Sayyad et al. [35], and Reddy [36]. This exhaustive evaluation underscores the precision and reliability of the proposed high-order shear deformation theory in predicting the static bending behavior of FG beams under sinusoidal loads.

A granular analysis of the outcomes unveils insightful trends, particularly in the realm of deflection. Notably, there is a discernible increase in deflection with a rising volume fraction index, as evidenced in both Table 2 and Table 5. This insight underscores the pronounced influence of the power law index on the bending behavior of FG beams. The correlation is further elucidated—a higher power law index corresponds to a higher concentration of metal in the beam, resulting in a decrease in the beam's stiffness. Consequently, the beam deflects more under the same load. Similarly, the in-plane normal stress (σxx) consistently decreases with a diminishing volume fraction index (k), as observed in Table 3 and Table 6. This observation sheds light on the intricate relationship between the power law index and the distribution of normal stress within FG beams. The linkage becomes clearer—a lower power law index corresponds to a higher concentration of ceramic in the beam, which, having a lower modulus of elasticity than metal, leads to less stress under the same load.

$$\bar{w} = 100\frac{E_m h^3}{q_0 l^4} w\left(\frac{l}{2}\right), \bar{\sigma}_{xx} = \frac{h}{q_0 l}\sigma_{xx}\left(\frac{l}{2}, \frac{h}{2}\right), , \bar{\tau}_{xz} = \frac{h}{q_0 l}\tau_{xz}(0,0). \quad (24)$$

The examination of non-dimensional tangential stresses in Table 4 and Table 7 further enriches the understanding, revealing a decrement in these stresses as the volume fraction index (k) increases. These findings collectively contribute to a nuanced comprehension of the power law index's impact on various stress components within FG beams under

sinusoidal loads. The mechanistic connection emerges—a higher power law index translates to a higher concentration of metal in the beam, resulting in a higher shear modulus than ceramic and, consequently, less shear stress under the same load.

Table 5. The maximum non-dimensional central deflection of FG SS beams under a sinusoidal load

L/h	Method	K			
		0	1	5	10
5	Hadji et al. [34]	2.5019	4.9458	7.7715	8.6526
	Sayyad et al. [35]	2.5019	4.9441	7.7739	8.6539
	Reddy [36]	2.5020	4.9458	7.7723	8.6530
	Present	2.5019	4.9458	7.7752	8.6544
20	Hadji et al. [34]	2.2839	4.5774	6.9539	7.6421
	Sayyad et al. [35]	2.2839	4.5774	6.9541	7.6422
	Reddy [36]	2.2838	4.5773	6.9540	7.6421
	Present	2.2839	4.5776	6.9538	7.6425

Table 6. The maximum non-dimensional axial stresses of FG SS beams under a sinusoidal load.

L/h	Method	K			
		0	1	5	10
5	Hadji et al. [34]	3.0913	4.7851	6.6047	7.9069
	Sayyad et al. [35]	3.0922	4.7867	6.6079	7.9102
	Reddy [36]	3.0916	4.7857	6.6057	7.9080
	Present	3.0927	4.7877	6.6092	7.9118
20	Hadji et al. [34]	12.171	18.814	25.794	30.923
	Sayyad et al. [35]	12.171	18.814	25.795	30.923
	Reddy [36]	12.171	18.813	25.794	30.999
	Present	12.171	18.815	25.796	30.923

Table 7. The maximum non-dimensional tangential stresses of FG SS beams under a sinusoidal load.

L/h	Method	K			
		0	1	5	10
5	Hadji et al. [34]	0.4755	0.4755	0.3840	0.4208
	Sayyad et al. [35]	0.4800	0.5248	0.5274	0.4237
	Reddy [36]	0.4769	0.5243	0.5314	0.4226
	Present	0.4836	0.4836	0.3928	0.4294
20	Hadji et al. [34]	0.4760	0.4760	0.3847	0.4215
	Sayyad et al. [35]	0.4806	0.5245	0.5313	0.4263
	Reddy [36]	0.4774	0.5249	0.5323	0.4233
	Present	0.4842	0.4842	0.3934	0.4302

The difference in deflection between the present method and other methods Chikh Abdelbaki [32] and Li et al. [33] as a function of the power law index k is illustrated in Figures 2 (a, b). The deviation between the deflections of FGM beams estimated by the present method and other methods depends on the power law index (k).

The difference between methods for the estimated deflection values reaches a maximum of (0.0515 for L/h = 5 and 0.003 for L/h = 20) for k = 5. Between the present method and Li et al [32] method, the difference reaches up to 0.0046 for L/h = 5 and 0.0 for L/h = 20. Between the present method and Chikh Abdelbaki [32] method, the difference is 0.008 for L/h = 5 and 0.0004 for L/h = 20, both for a value of k < 2. The difference is insignificant between methods, with the gap not exceeding 0.008 for l/h = 5 and 0.0004 for L/h = 20.

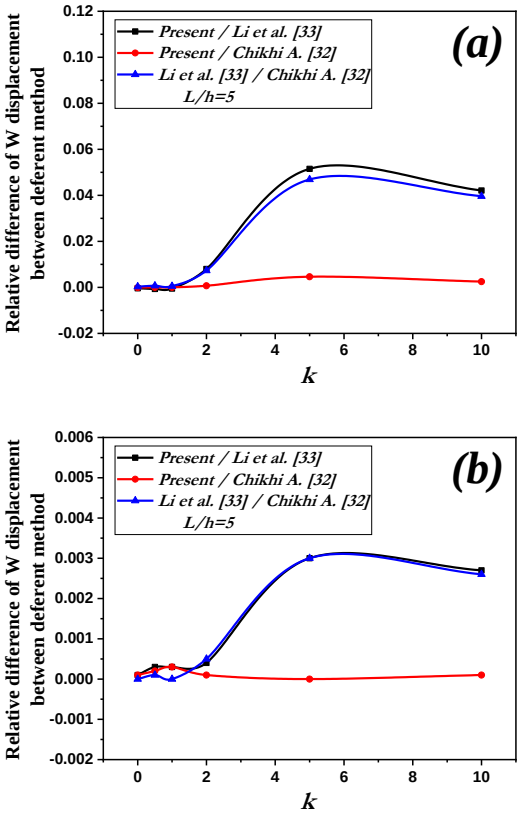

Fig. 2. Difference of non-dimensional center deflections w between different methods as a function of the power-law index k of FG S-S beams under uniform load: (a) L/h=5, (b) L/h=20

FG beams with side-to-thickness ratio L/h=5,20 is chosen in Figures 3 (a, b) and 4 (a, b). It can be seen that the deviation on the axial and tangential stress between the present model and previous one Chikh Abdelbaki [32] and Li et al. [33] is bigger for k>2 than that on for k<2. Moreover, it is also observed that the deviation on the axial and tangential stress between the present model and previous is effectively significant for thick FG s beams. The comparative analysis indicates a close correspondence between the results obtained from the proposed beam theory and the actual solutions, notably aligning well with the works of Chikh Abdelbaki [32] and Li et al. [33]. Consequently, the new beams theory can be applied to analyze the bending of FG beams.

In Figures 5, 6, 7, and 8, the effect of various types of mechanical loads (sinusoidal distributed, uniform, central patch, and concentrated load) on non-dimensional center deflections and axial stress and transversal stress is depicted, for simply supported FG beams. Figure 5 gives the changing rules of the central deflection with the power law index k. Central deflection increases monotonically with the rising value of power law index k. Meanwhile, these curves would tend to be a steady value in a value of k=5. It means that, the increasing of power law index k (beam rich in metal) would reduce the mechanical resistance of structures, rather than increasing the central deflection.

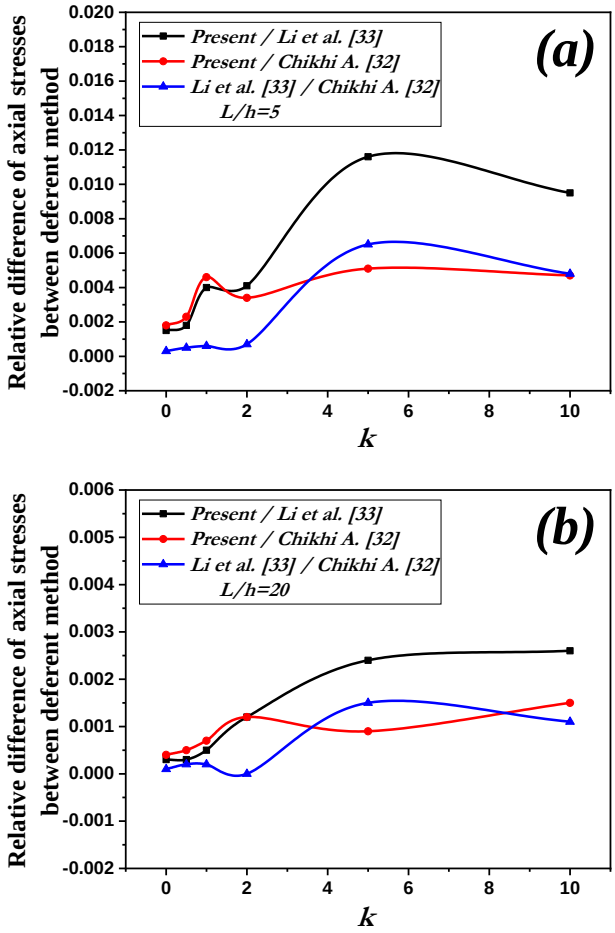

Fig. 3. Difference of non-dimensional axial stress between different methods as a function of the power-law index k of FG S-S beams subjected to an evenly distributed load: (a) L/h=5, (b) L/h=20

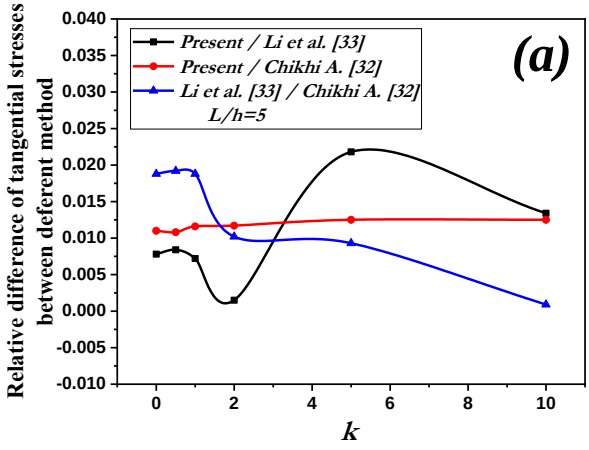

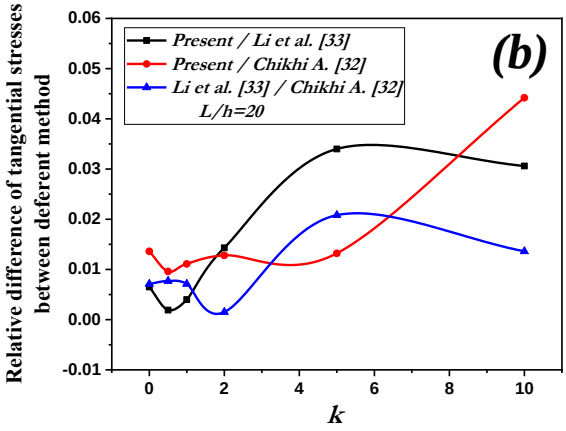

Fig. 4. Difference of tangential stress between different methods as a function of the power-law index k of FG S-S beams subjected to a load uniformly distributed: (a) L/h=5, (b) L/h=20)

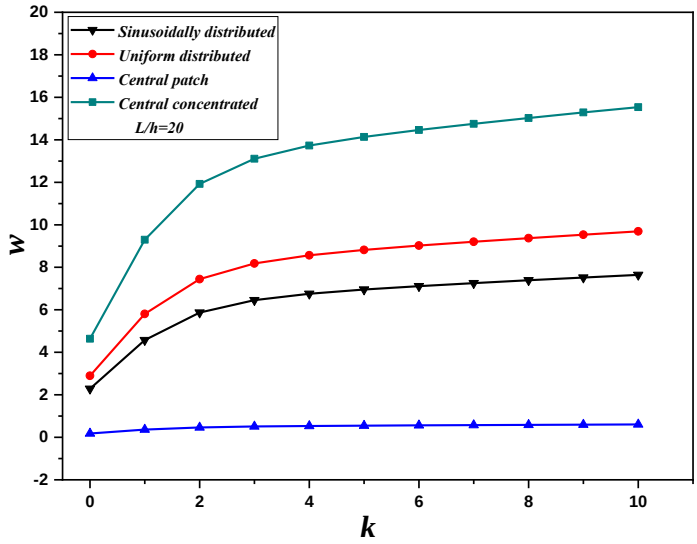

Fig. 5. Variation of the non-dimensional central deflection w versus the power-law index k of FG beams (L/h=20) exposed to diverse mechanical loading types

Figures 7 show the effect of various types of mechanical loads on distribution of normal stresses across the thickness of the FGM beam. The volume fraction exponent considered is equal to k= 1 for these results. From Figure 7 the normal stresses show that the beam works in compression up to z/h = 0.17 cases of L/h =5 and 0.14 cases of L/h=20. Then, beyond this value, the beam works only in tension. The maximum values of these stresses (longitudinal stresses), occur on the upper and lower surfaces of the plate.

In Figure 8, the non-dimensional transverse shear stresses τxz are plotted for various types of mechanical loads. the maximum transverse shear stress is directly dependent on the type of loads. Additionally, the shear stress values are relatively higher in the case of concentrated load.

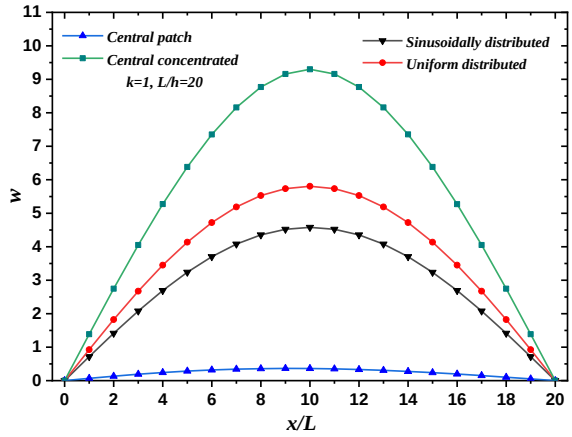

Fig. 6. Variation of the non-dimensional deflection along the length direction (L/h =20, k=1) of FG beams subjected to various types of mechanical load

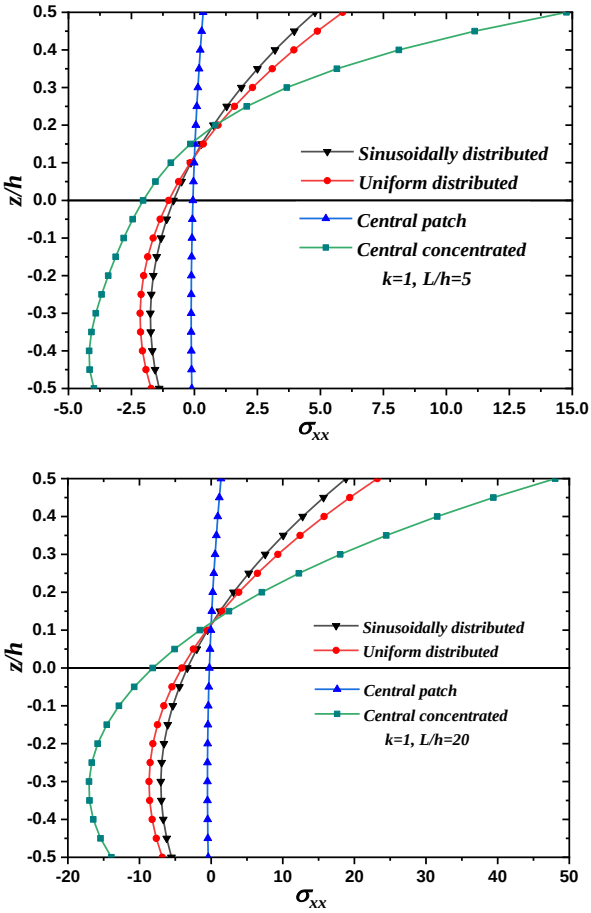

Fig. 7. Effect of various types of mechanical loads on distribution of normal stresses across the thickness of the FG beam

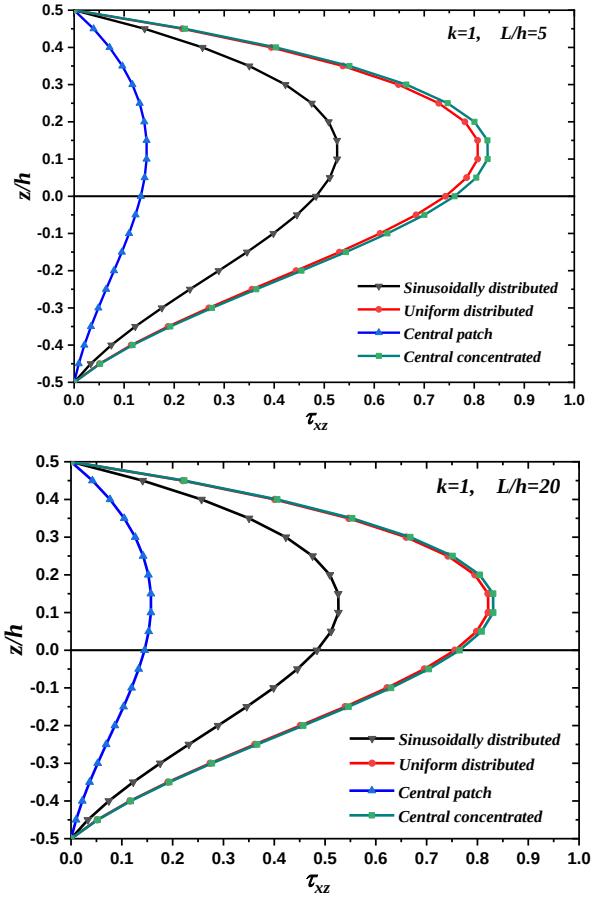

Fig. 8. effect of various types of mechanical loads on distribution of transverse shear stress across the thickness of the FG beam

7. Conclusions

This paper introduces a groundbreaking high-order shear deformation theory tailored for the static bending analysis of functionally graded (FG) beams under diverse mechanical loads. The formulation of this novel theory is meticulous, aiming to precisely capture the intricate stress, strain, and deformation behaviors inherent in FG beams, all while maintaining computational efficiency for practical applications. The governing equations, derived through the principle of virtual work, are solved analytically using Navier's method, providing a robust analytical solution that enhances our understanding of FG beam behavior.

The proposed theory undergoes extensive numerical validation, comparing favorably with existing analytical solutions and higher-order shear deformation theories. This substantiates the theory's superiority in terms of accuracy and efficiency in predicting static responses. Parametric studies investigate the individual and coupled effects of beam slenderness, material grading index, and applied load type on deflection, axial stress, and transverse shear stress distributions. The outcomes illuminate the significance of considering the thickness stretching effect, particularly for thicker beams and those with

higher power law indices, providing valuable insights into the nuanced structural behavior of FG beams.

A pivotal finding in this study reveals that an augmentation in the power-law index (k) correlates with a reduction in mechanical resistance, attributed to an increased volume fraction of metal (Vm), without a proportionate rise in central deflection. This nuanced relationship between material composition and mechanical behavior underscores the intricate nature of FG beams. The proposed theory surpasses Higher-Order Shear Deformation Theory (HSDT) in accuracy and efficiency, especially in scenarios involving thick beams and higher power law indices where the thickness stretching effect is more pronounced.

The numerical examples presented confirm the theory's accuracy in predicting deflections and stresses in FG beams subjected to uniformly distributed loads. Additionally, load type influences are explored, highlighting higher deflection and shear stress values under concentrated loads. In conclusion, the analytical solutions provided by the proposed high-order theory constitute a robust framework for comprehensively analyzing the static bending of FG beams under various mechanical loads. The theory's reliability, accuracy, and computational efficiency position it as an invaluable tool for advancing research in composite materials and structural mechanics.

References

[1] Akbaş, Ş D. Free vibration and bending of functionally graded beams resting on elastic foundation. Research on Engineering Structures and Materials, 2015; 1: 25-37. https://doi.org/10.17515/resm2015.03st0107

[2] Birman V, Byrd LW. Modeling and analysis of functionally graded materials and structures, Applied Mechanics Reviews, 2007; 60: 195-216. https://doi.org/10.1115/1.2777164

[3] Mahamood RM, Akinlabi ET. Additive manufacturing of functionally graded materials. Functionally graded materials, 2017; 47-68. https://doi.org/10.1007/978-3-319-53756-6_4

[4] Anandakumar G, Kim JH. On the modal behavior of a three-dimensional functionally graded cantilever beam: Poisson's ratio and material sampling effects. Compos. Struct, 2010; 92: 1358-1371. https://doi.org/10.1016/j.compstruct.2009.11.020

[5] Sahu RK, Sondhi L, Bhowmick S, Madan R. Deformation and stress analysis of rotating functionally graded hollow cylindrical body for variable heat generation. Res. Eng. Struct. Mater; 2023, 9: 597-616. https://doi.org/10.17515/resm2022.470me0713

[6] Alshorbagy AE, Eltaher MA, Mahmoud FF. Free vibration characteristics of a functionally graded beam by finite element method. App Math Model, 2011; 35: 412-25. https://doi.org/10.1016/j.apm.2010.07.006

[7] Eltaher MA, Emam SA, Mahmoud FF. Free vibration analysis of functionally graded size-dependent nanobeams. Appl Math Comput, 2012; 218: 7406-20. https://doi.org/10.1016/j.amc.2011.12.090

[8] Falsonea G, La Valle G. Dynamic and buckling of functionally graded beams based on a homogenization theory. Res. Eng. Struct. Mater., 2021; 7: 523-538. https://doi.org/10.17515/resm2021.259st0216

[9] Filippi M., Carrera E., Zenkour A. M. Static analyses of FGM beams by various theories and finite elements. Compos Part B-Eng. 2015; 72 1-9. https://doi.org/10.1016/j.compositesb.2014.12.004

[10] Uttam Kumar K., Srinivas. J. Vibration analysis of Bi-directional FG-GNPs reinforced rotating micro-beam under Thermo-mechanical loading. Materials Today, Proceedings, 2023; 78: 752-759. https://doi.org/10.1016/j.matpr.2022.10.227

[11] Zenkour AM. Generalised shear deformation theory for bending analysis of functionally graded plates, Appl. Math. Model., 2006; 30: 67-84. https://doi.org/10.1016/j.apm.2005.03.009
[12] Pei-Liang B, Hai Q, Tiantang Y. A new finite element method framework for axially functionally-graded nanobeam with stress-driven two-phase nonlocal integral model, Composite Structures, 2022; 295: 115769 https://doi.org/10.1016/j.compstruct.2022.115769
[13] Chitour M, Benguediab S, Bouhadra A, Bourada F, Benguediab M, Tounsi A. Effect of variable volume fraction distribution and geometrical parameters on the bending behavior of sandwich plates with FG isotropic face sheets, Mechanics Based Design of Structures and Machines, 2023; 51. https://doi.org/10.1080/15397734.2023.2197036
[14] Chikh A. Investigations in static response and free vibration of a functionally graded beam resting on elastic foundations, Frattura ed Integrità Strutturale. 2020; 51 115-126. https://doi.org/10.3221/IGF-ESIS.51.09
[15] Thai H.T, and Vo T. P. Bending and free vibration of functionally graded beams using various higher-order shear deformation beam theories. International Journal of Mechanical Sciences, 2012; 62: 57-66. https://doi.org/10.1016/j.ijmecsci.2012.05.014
[16] Khorramabadi, M.K., Jalilian, M.M. Dynamic stability analysis of functionally graded epoxy/clay nanocomposite beams subjected to periodic axial loads. J Braz. Soc. Mech. Sci. Eng., 2023; 45-61. https://doi.org/10.1007/s40430-022-03984-z
[17] Karmi Y, Tekili S, Khadri Y, Boumediri H. Vibroacoustic analysis in the thermal environment of PCLD sandwich beams with frequency and temperature dependent viscoelastic cores. Journal of Vibration Engineering & Technologies, 2023; 1-20. https://doi.org/10.1007/s42417-023-01065-6
[18] Attia A, Bousahla AA, Tounsi A, Mahmoud SR, Alwabli AS. A refined four variable plate theory for thermoelastic analysis of FGM plates resting on variable elastic foundations. Struct Eng Mech., 2018; 6 5: 453-464.
[19] Li SR, Batra RC. Relations between buckling loads of functionally graded Timoshenko and homogeneous Euler-Bernoulli beams, Composite Structures, 2013; 95: 5-9. https://doi.org/10.1016/j.compstruct.2012.07.027
[20] Benferhat R, Daouadji TH, Mansour MS. Free vibration analysis of FGM plates resting on the elastic foundation and based on the neutral surface concept using higher order shear deformation theory, Comptes Rendus Mechanique, 2016; 344: 631-641. https://doi.org/10.1016/j.crme.2016.03.002
[21] Yepeng X, Tiantang Y, Ding Z. Two-dimensional elasticity solution for bending of functionally graded beams with variable thickness, Meccanica, 2014; 49: 2479-2489. https://doi.org/10.1007/s11012-014-9958-1
[22] Rebai B. Contribution to study the effect of (Reuss, LRVE, Tamura) models on the axial and shear stress of sandwich FGM plate (Ti-6A1-4V/ZrO2) subjected on linear and nonlinear thermal loads, AIMS Materials Science, 2023;10: 26-39. https://doi.org/10.3934/matersci.2023002
[23] Esfahani SE, Kiani Y, Eslami MR. Non-linear thermal stability analysis of temperature dependent FGM beams supported on non-linear hardening elastic foundations, International Journal of Mechanical Sciences, 2013; 69: 10-20. https://doi.org/10.1016/j.ijmecsci.2013.01.007
[24] Arbind A, Reddy JN, Srinivasa AR. Modified couple stress-based third-order theory for nonlinear analysis of functionally graded beams, Latin American Journal of Solids and Structures; 2014; 11: 459-487. https://doi.org/10.1590/S1679-78252014000300006
[25] Aboudi J, Arnold SM, Pindera MJ. Response of functionally graded composites to thermal gradients, Composites Engineering, 1994; 4: 1-18. https://doi.org/10.1016/0961-9526(94)90003-5

[26] Giunta G, Crisafulli D, Belouettar S, Carrera E. A thermo-mechanical analysis of functionally graded beams via hierarchical modelling, Composite Structures, 2013; 95: 676-690. https://doi.org/10.1016/j.compstruct.2012.08.013
[27] Atteshamuddin SS., Yuwaraj MG. Bending, buckling and free vibration of laminated composite and sandwich beams: A critical review of literature, Composite Structures. 2017;171: 486-504. https://doi.org/10.1016/j.compstruct.2017.03.053
[28] Chitour M, Bouhadra A, Benguediab S, Saoudi A, Menasria AR, Tounsi A. Effect of Phase Contrast and Geometrical Parameters on Bending Behavior of Sandwich Beams with FG Isotropic Face Sheets, Journal Of Nano- And Electronic Physics, 2022: 14: 05016(6pp). https://doi.org/10.21272/jnep.14(5).05016
[29] Himeur N, Mamen B, Benguediab S, Bouhadra A, Menasria A, Bouchouicha B, Bourada F, Benguediab M, Tounsi A. Coupled effect of variable Winkler-Pasternak foundations on bending behavior of FG plates exposed to several types of loading, Steel Compost. Struct., 2022; 44: 339-355.
[30] Merdaci S, Mostefa AH, Beldjelili Y, Merazi M, Boutaleb S, Hellal H. Analytical solution for statif bending analyses of functionally grades plates with porosities. Frattura ed Integrità Strutturale. 2021; 15: 55. https://doi.org/10.3221/IGF-ESIS.55.05
[31] Menasria A, Bouhadra A, Tounsi A, Bousahl AA, Mahmoud SR. A new and simple HSDT for thermal stability analysis of FG sandwich plates. Steel and Composite Structures, 2017; 25: 157-175.
[32] Chikh A. Analysis of static behavior of a P-FGM Beam, Journal of Materials and Engineering Structures, 2019; 6: 513-524.
[33] Li XF, Wang BL, Han JC. A higher-order theory for static and dynamic analyses of functionally graded beams. Archive of Applied Mechanics. 2010; 80: 1197-1212. https://doi.org/10.1007/s00419-010-0435-6
[34] Hadji L, Bernard F, Zouatnia N. Bending and Free Vibration Analysis of Porous-Functionally Graded (PFG) Beams Resting on Elastic Foundations. Fluid Dynamic and Material Process. 2023; 19: 1043-1054. https://doi.org/10.32604/fdmp.2022.022327
[35] Sayyad AS., Ghugal YM. Analytical solutions for bending, buckling, and vibration analyses of exponential functionally graded higher order beams. Asian Journal of Civil Engineering, 2018; 19: 607-623. https://doi.org/10.1007/s42107-018-0046-z
[36] Reddy JN. A simple higher order theory for laminated composite plates. ASME Journal of Applied Mechanics, 1984; 51: 745-75 2. https://doi.org/10.1115/1.3167719

Research on Engineering Structures & Materials
www.jresm.org
MIM Research Group

Research Article

Dynamic behavior of high damping rubber bearings and lead rubber bearings under near-fault earthquakes

Dhirendra Patel[*,a], Rajesh Kumar[b] , Vishal Kumar Mourya[c], Gaurav Pandey[d]

Department of Civil Engineering, Indian Institute of Technology-BHU, Varanasi, India

Article Info

Article history:

Received 25 Feb 2024
Accepted 05 Apr 2024

Keywords:

Base isolation;
High damping rubber bearing;
Lead rubber bearing;
ABAQUS;
Earthquakes

Abstract

Civil engineering structures are susceptible to natural calamities such as earthquakes, floods, and strong winds. Base isolation is a proven method for protecting structures during earthquakes. It involves inserting a flexible layer between the foundation and superstructure to isolate the structure from earthquakes, thereby changing the system's dynamic characteristics. The present study compares the dynamic performance of passive base isolators, specifically High Damping Rubber Bearings (HDRBs) and Lead Rubber Bearings (LRBs), under near-fault ground motion conditions to assess their effectiveness in reducing seismic impact on structures. The isolator is first analyzed using a static general approach and validated against existing literature before undergoing dynamic analysis. In this research, the LRB isolation system is analyzed using a dynamic explicit approach in ABAQUS, while the HDRB is analyzed using a dynamic implicit approach. The behavior of these isolators is studied under seismic events such as those from the Imperial Valley, Managua, Loma Prieta, Northridge, and Kocaeli ground motions. The results indicate that LRBs significantly reduce acceleration at the top of the bearing compared to HDRBs. The maximum reductions in response are 68.42% for the Kocaeli earthquake in case of LRBs and 61.80% for the Northridge earthquake in case of HDRBs. The LRB shows a minimum acceleration response reduction of 57.24%, while for HDRB, it is 24.47% for the Imperial Valley records in both cases.

1. Introduction

Earthquakes are ancient, unpredictable hazards that disrupt the ground, affecting structures and systems, often with significant consequences. Structural designers and engineers face a challenge in mitigating these effects. Extensive research has led to strategies to strengthen structures against seismic forces. This vulnerability is often observed in existing buildings where some storeys lack walls, making them susceptible to larger earthquake forces and increased lateral deformations. Worldwide, buildings collapse during earthquakes, requiring costly retrofitting to extend their service life [1].

Seismic hazard in regions is determined by geological, tectonic, and statistical data. Key parameters include earthquake epicenter, hypocenter, duration, source parameters, and intensities. Earthquakes are crucial for testing structural behavior under horizontal loads [2]. Studies conducted in the Balkan countries and neighboring regions, like Turkey and Iran, have experienced destructive earthquakes in recent years, causing significant damage and even building collapse [3]. Post-disaster studies are essential for assessing earthquake hazards, understanding factors affecting building performance, and guiding urban

*Corresponding author: dhirendrapatel.rs.civ17@itbhu.ac.in
[a] orcid.org/0009-0004-1633-2437; [b] orcid.org/0000-0001-5145-588X; [c] orcid.org/0009-0009-4348-9911; [d] orcid.org/0009-0008-3750-3097
DOI: http://dx.doi.org/10.17515/resm2024.194ea0225rs

planning and structural design [4]. Furthermore, a study was conducted to examined seismic damage to masonry buildings, focusing on low and mid-rise masonry residential buildings in Albania constructed between 1940 and 1990 under pre-modern seismic codes. The study aims to compare their seismic behavior under near-field and far-field earthquake scenarios [5].

Base isolation employs specially designed devices between the superstructure and foundation to isolate the structure from seismic motion as shown in Fig. 1 [6-8]. Seismic isolation is a technique aimed at diminishing inertial forces generated within a structure during earthquake ground shaking. It achieves a shift in the fundamental period of vibration by uncoupling the superstructure from the supporting foundation through the use of isolators, elements that are laterally flexible yet vertically stiff [9]. Decoupling involves extending a building's natural vibration period, reducing spectral acceleration (Fig. 2). This shift in the structural time-period, depicted in Fig. 3, results in greater relative displacements [10]. Seismic Base Isolation (BI) is an innovative, globally adopted approach in earthquake-resistant design.

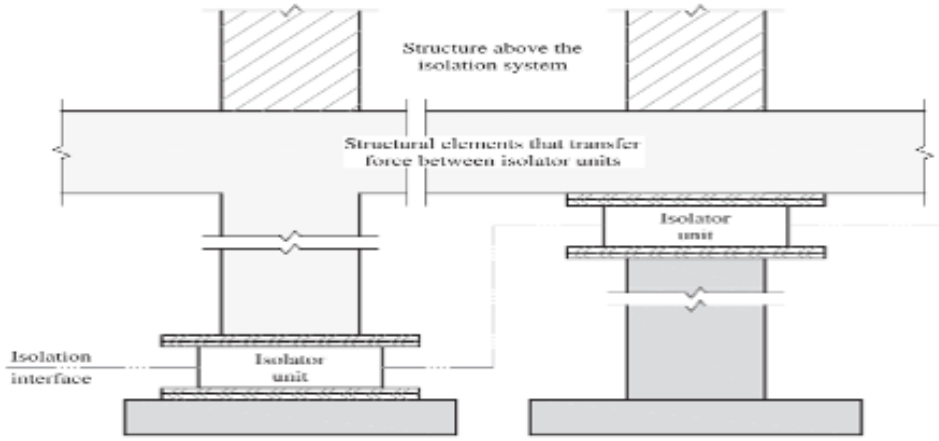

Fig. 1. Base Isolation terminology (ASCE 7-16)

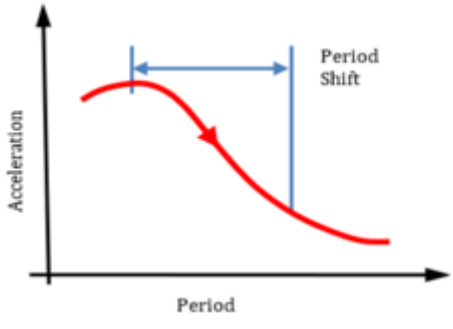

Fig. 2. Time period shift

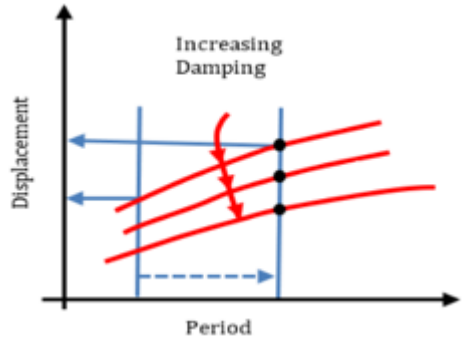

Fig. 3. Displacement design response spectra

The two primary techniques for earthquake resistance in structures are conventional earthquake-resistant design and seismic isolation. Conventional methods strengthen structures with features like shear walls or braced frames but can lead to issues like excessive floor acceleration or inter-story drifts. Seismic isolation, especially base

isolation, is increasingly popular for protecting structures in earthquake-prone areas from intense ground motion [11].

The rubber material is derived from Hevea brasiliensis latex, natural rubber, initially known as "Caoutchouc," was termed "rubber" by Joseph Priestley in 1770. Fisher introduced "elastomer" in 1939 for synthetic rubber-like materials. Charles Goodyear's 1839 vulcanization discovery and DuPont's 1931 Neoprene creation revolutionized rubber properties. Fillers, accelerators, anti-ozonants, and antioxidants improve rubber compounds. Natural rubber pads absorbed impact in a Melbourne rail bridge in 1889. Eugene Freyssinet's 1954 patent paved the way for widely used multilayer rubber bearings in earthquake-resistant designs [12]. In 1981, Robinson integrated lead cores into rubber bearings, resulting in the creation of Lead Rubber Bearings (LRBs), aimed at improving energy dissipation [13]. The HDRB is exemplified by the 1985 Foothill Communities Law and Justice Center, offer high stiffness and damping at low shear strains and increased resilience under major earthquakes. Modeling HDRB behavior in seismic design considers factors like creep, rate dependence, mechanical properties, manufacturing variations, and environmental influences [14].

HDRBs are characterized by their ability to provide high stiffness and damping at small shear strains, effectively reducing their behavior to service and wind loads. They also exhibit low shear stiffness but with suitable damping capability at the design displacement level. As displacement amplitudes intensified, HDRBs show a notable increase in stiffness and damping, which is beneficial in restraining movements during major ground motions [12]. When modeling HDRB behavior in seismic isolation systems, it is essential to consider various factors. Creep, a significant consideration, makes the response of these devices rate reliable. Additionally, mechanical features can be affected by manufacturing variations, contact pressure, loading and strain history, temperature fluctuations, and aging effects. HDRB along with low-damping natural rubber bearings and LRBs, are usually implemented as seismic base-isolation system [14]. The complex structure of HDRBs involves adding fine carbon blocks, oils, resins, and other fillers to natural rubber, enhancing their damping properties. This modification leads to non-linear hysteretic material behavior during earthquake loads, posing challenges in accurately representing their actual performance [15]. Laminated elastomeric bearings, featuring rubber and steel layers bonded through vulcanization, are widely used. The inclusion of steel shim layers enhances vertical stiffness with minimal impact on shear stiffness. However, excessive damping at smaller displacements may affect the system's overall effectiveness and internal equipment [10]. The study analyzed two adjacent three-story buildings in India's highest seismic zone: one on a Lead Rubber Bearing (LRB) base isolator and the other a conventional RC framed structure. Real earthquake responses from 2006 to 2007 were recorded. The LRB building had a frequency 2.6 times lower than the conventional one, with a response reduction of 4 to 5 times. Structure-soil-structure interaction was observed in the LRB building's response, aligning with the nearby structure's frequency. Numerical simulations and soil modeling validated the results. During a larger earthquake with a PGA of 0.26 g, the LRB building's response acceleration was about 4.1 times lower than the conventional structures [16]. Furthermore, the effect of soil-structure interaction is studied [17-19].

The choice of a suitable material model and the determination of its parameters significantly impact the accuracy and reliability of finite element analysis results for rubber components like tires, engine mounts, and rubber bearings. Typically, two types of mechanical models are employed for rubber materials: hyper-elastic and hyper-viscoelastic models. The former is suitable for simpler problems where time effects can be disregarded, while the latter is essential for analyses involving time-dependent factors, such as dissipated energy determination in cyclic loading (hysteresis). Despite extensive

research on hyper-elastic models, hyper-viscoelastic models have received less attention, and further work is needed to document and determine their parameters adequately.

The study was conducted to evaluates seismic-isolated bridges using LRBs under near-field earthquake with discrete pulse responses. It examines maximum isolator displacements (MIDs) and maximum isolator forces (MIFs), accounting for LRB yield strength deterioration due to heating. The comparison includes deteriorating and non-deteriorating conditions, employing bounding analyses. Nonlinear response history analyses, considering different soil conditions, reveal that lower bound analyses tend to overestimate MIDs, especially for LRBs with higher Q/W ratios, during near-field earthquakes with increased velocity pulses [20]. The paper also investigates the impact of lead core heating on LRB-isolated bridges under near-field ground motions, validating bounding analyses for designing maximum isolator force and displacement envelopes. Results indicate that temperature rise in the lead core correlates with higher magnitudes and more near-fault earthquakes pulses, decreasing with greater distances from the fault. [21]. Earthquake excitations were applied to a 20-story RC and a 3-story steel structure to investigate the impact of isolator characteristics, including isolation period and characteristic strength-to-weight ratio, on the behaviour of the superstructures [22]. LRB base-isolated buildings, designed with optimal yield strength ratios, demonstrate robust seismic performance, even in mega earthquake scenarios, surpassing structures using critical yield strength and second shape coefficients [23]. Rubber material parameters are derived from laboratory tests, including uniaxial tensile and relaxation tests. The 3D-FE model of the bearing is then compared with an analytical ABAQUS CAE model for LRB isolators, showing good agreement in shear behaviour [24]. The inclusion of a lead core in a lead rubber bearing (LRB) improves its performance by enabling energy dissipation, enhancing damping characteristics, increasing vertical stiffness, and ensuring overall reliability. The lead core is engineered to plastically deform under lateral loads, effectively absorbing substantial energy during seismic events and minimizing force transmission to the structure. This deformation isolates the structure from ground motion, reducing the likelihood of structural damage. Furthermore, the lead core boosts the bearing's vertical stiffness, supporting the structure and ensuring stability under varying loads.

RRB (rubber bearing with steel rings) is implemented in 3 to 6-story steel and concrete building, compared to fixed and isolated base structures with LRB. Abaqus is used for finite element modelling, showing average effective stiffness of 110.88 (ton/m) for LRB and 82.48 (ton/m) for RRB, with damping at 18.44% for LRB and 47.02% for RRB. Nonlinear time history analysis with earthquake records reveals RRB isolated base structures achieve reductions in acceleration by 42.16%, 43.36%, 51.83%, and 57.16% for 3, 4, 5, and 6-story buildings. Shear reductions are 55.5%, 47.16%, 37.93%, and 56.83%, and drift decreases are 35.33%, 50%, 54.5%, and 59.66% for 3, 4, 5, and 6-story structures [25]. The research refines the estimation of yield strength and confinement of lead cores in Lead Rubber Bearings (LRB). Prototype tests reveal variability, challenging the traditional use of a standard lead yield value (7-10 MPa). The study validates a newly developed equation for estimating yield strength based on lead core confinement. Comparisons with prototype tests demonstrate a good match, with differences mostly within ±5% [26]. The value-based seismic design framework to optimize the geometrical and mechanical characteristics of LRBs has been studied. Considering construction cost and seismic consequences as key components, the optimization problem accounts for multiple LRB failure modes, such as strength weakening, axial buckling, and rubber rupture [27]. The study assesses the influence of LRB and HDRB on structures using nonlinear finite element analyses with SAP 2000. Isolator designs follow the UBC code [28]. This research presents a novel approach for designing base-isolated buildings in line with Algerian seismic regulations. The method combines the linear equivalent approach for design displacement using an iterative

process with time history analysis. Numerical modelling, compared with global regulations, validates the approach, demonstrating satisfactory results in design displacement and base shear force alignment [29]. The study was conducted to investigate the impact of pulse-like ground motions on seismically isolated buildings using three near-fault record sets with varying pulse periods. Two seismically isolated RC buildings were designed following ASCE-7-16 standards. Each records spectrum was scaled to the Risk-Targeted Maximum Considered Earthquake level spectrum using the amplitude scaled approach in the scaling period range of ASCE 7–16. The buildings were then subjected bidirectionally to the scaled records. Results for two different scaling period ranges were compared to assess their effects on isolator displacements [30]. Moreover, a 40-story building subjected to near-fault and far-field strong motion records were examined. Results compared various factors such as story drift ratios, wall shear stresses, and beam rotations. It is common to reduce shear wall thickness at upper levels, but this study found that doing so can lead to early elastic capacity in the core-wall, altering post-yield shear force redistribution below the yielding level [31]. The study was conducted to developed fragility curve for five building by using FEMA P695. It found a strong link between isolation unit collapse probability and the isolation system displacement ratio. Simple, highly correlated equations were developed to estimate required displacement capacity for specific risk-target levels. These equations were validated against two building models and compared with IDA results, showing their applicability for the preliminary design of mid-rise isolated reinforced concrete buildings [32].

This study employs Abaqus CAE 2020 software to validate the static analysis of the LRB model with existing experimental and numerical analysis. Subsequently, the LRB and HDRBs are analyzed for dynamic response, comparing acceleration responses at the base and top of the loading plate under ground motion inputs. For dynamic analysis, five near-fault earthquakes are selected from PEER NGA West2 records. Despite extensive research on various isolation systems, including LRBs and HDRBs, there is a notable scarcity of studies examining the dynamic performance in relation to their mechanical characteristics and material properties. This study investigates the impact of seismic isolators, specifically HDRBs and LRBs, on key seismic parameters. The uniqueness of the work lies in its comparative analysis of these base isolators under various seismic events, providing valuable insights for isolator design. A micro modelling of the isolator is performed using finite element modelling software ABAQUS, and both LRBs and HDRBs are subjected to different near-fault ground motions to gain insights into their dynamic response. The results are compared with the input earthquake values, and the response reduction is presented as a percentage decrease in acceleration response. Additionally, the time-displacement response is provided for the Imperial Valley and Managua earthquake records.

2. Theory and Design of LRB and HDRB for Finite Element Dynamic Analysis

A FEM holds the potential to serve as a robust tool for advancing our understanding of the local behavior of seismic isolation devices. Kelly applied FE modeling to investigate the variation in lateral force-displacement response under increasing axial load, employing a 2-D model [33]. Imbimbo and Luca [34] conducted FE analyses on circular elastomeric bearings subjected to vertical loads. Doudoumis [35] employed numerical modeling, utilizing finite element micromodels, for Lead-Rubber Bearings, revealing enhanced possibilities for a detailed study of stress, strain, and available strength. Despite these advancements, there has been a lack of comprehensive comparison between theoretical and numerical models for laminated rubber bearings in previous finite element modeling efforts. This research addresses this gap by first detailing the process of 3-D FE analysis modeling for a laminated rubber bearing. Subsequently, through a comparison of the FE

analysis outcomes with experimental findings, the validity of the models is demonstrated. The analysis procedure for the current study is depicted in the Fig. 4.

3. Material Properties, Dimensions and Loading Condition

When selecting numerical models for LRBs and HDRBs in Abaqus, prioritize accuracy, reliability, and compatibility. The materials for models must be chosen that accurately represent hyper elastic rubber and lead behavior under dynamic loading, ensuring they can perform dynamic analysis and simulate contact with surrounding structures accurately. The models must be validated against experimental data, consider computational efficiency for numerical simulation in Abaqus.

Fig. 4. The flow chart illustrates the analysis procedure of the present study

The LRB used in this study is the Skellerup150 isolator, which is listed in the Skellerup Industries manufacturer's catalogue [36]. The inclusion of steel in rubber isolators is crucial for mitigating excessive strains under vertical loads and is commonly represented as an elastoplastic material. Steel's properties include a yield stress of 240 MPa, a Poisson's ratio of 0.3, and an elastic modulus of 210 GPa. Lead, with a crystal structure undergoing alterations with increasing displacement, is characterized by a yield stress of 19.5 MPa, a Poisson's ratio of 0.43, and a modulus of elasticity of 18000 MPa. The assembly comprises two top and bottom loading steel plates, each with a diameter of 601 mm and a thickness

of 31.8 mm. Additionally, there are two fixing steel plates (top and bottom) with a diameter of 431 mm and a thickness of 25.4 mm. The configuration includes 11 rubber layers, each with a diameter of 431 mm and a thickness of 9 .5 mm, as well as 10 steel shims measuring 431 mm in diameter and 3.0 mm in thickness. At the core is a central lead core with a diameter of 116.8 mm and a height of 185 mm. According to the specifications, the design compressive load is 667 kN, and the lateral design displacement is 0.1524 m [35].

Before moving to dynamic analysis, a preliminary static analysis is performed to optimize the dimensions of the bearing. The analysis of the LRB is conducted using ABAQUS CAE (User's Manual V6.14). Initially, the model is subjected to vertical static loadings. After applying a vertical compressive load of 667 kN, a cyclic horizontal displacement with an amplitude of ±1524 mm is applied, based on the specified dimensions. The analysis includes analytical results from numerical simulations conducted in Abaqus. A comparison is made with the force-displacement curves provided by the manufacturer and Doudoumins 2005, illustrated in Fig. 5.

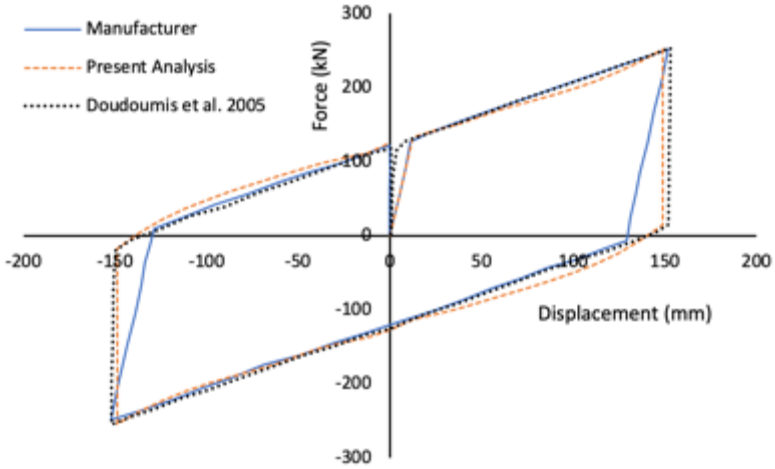

Fig. 5. Comparison of the force-displacement curves obtained from analytical (Abaqus), experimental and Doudoumis et al. results

3.1 Selecting a Rubber Constitutive Model for Dynamic Analysis

Rubber is identified as an incompressible material, retaining a constant volume during deformations, which classifies it as isochoric. In rubber compounds, volume alterations are minimal, nearing incompressibility. This results in a Poisson's ratio of 0.5, constraining the use of classical computational mechanics for stress and strain calculations. The elastic characteristics of rubber in terms of potential strain energy function U in terms of Green's deviatoric strain invariants are as follows:

$$U = f(I_1, I_2, I_3) \tag{1}$$

I_1, I_2, I_3 are first, second and third deviatoric strain invariant of the green deformation tensor in terms of $\lambda_1, \lambda_2, \lambda_3$.

$$I_1 = \lambda_1^2 + \lambda_2^2 + \lambda_3^2 \tag{2}$$

$$I_2 = \lambda_1^2\lambda_2^2 + \lambda_2^2\lambda_3^2 + \lambda_3^2\lambda_1^2 \tag{3}$$

$$I_3 = \lambda_1^2\lambda_2^2\lambda_3^2 \tag{4}$$

The rubber's hyper-elasticity is characterized by the Yeoh model, and its damping response is modeled using the Prony series viscosity model. A comprehensive overview of both the Yeoh hyper-elasticity model and the Prony series viscosity model is available in the accompanying Table1 and Table 2.

3.1.1 Yeoh Model

The strain energy function for the Yeoh model

$$U = C_{10}(\bar{I}_1 - 3) + C_{20}(\bar{I}_1 - 3)^2 + C_{30}(\bar{I}_1 - 3)^3 + \frac{1}{D_1}(J^{el} - 1)^2 + \frac{1}{D_2}(J^{el} - 1)^4 + \frac{1}{D_3}(J^{el} - 1)^6 \tag{5}$$

For N=3, the equation can be written as:

$$U = \sum_{i=1}^{3} C_{10}(\bar{I}_1 - 3)^i + \sum_{i=1}^{3} \frac{1}{D_i}(J^{el} - 1)^{2i} \tag{6}$$

C_{i0}, D_i are material constants, N= material constant (positive numbers N=1,2,3), μ, λ_m and D, are temperature-dependent parameters $D = \frac{2}{K}$; and $\bar{I}_1 = \bar{\lambda}_1^2 + \bar{\lambda}_2^2 + \bar{\lambda}_3^2$ and $\bar{I}_2 = \bar{\lambda}_1^{(-2)} + \bar{\lambda}_2^{(-2)} + \bar{\lambda}_3^{(-2)}$, where $\bar{\lambda}_i = J^{-\frac{1}{3}}\lambda_i$; J= Jacobean determinant where $J = \lambda_1\lambda_2\lambda_3$, J^{el} is the elastic volume ratio, and K is the bulk modulus.

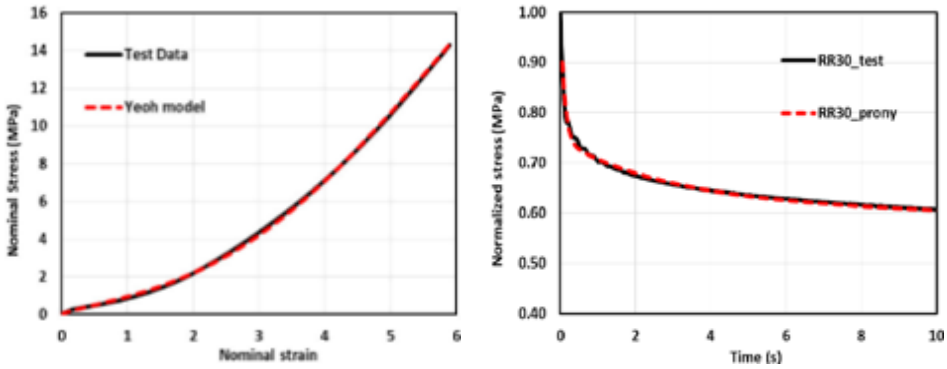

(a) (b)

Fig. 6. The uniaxial tensile test (a) results (black line) for the rubber specimen, along with the relaxation test results (b), are compared with their respective numerical models, represented by the red line

Table 1. Parameters for the Yeoh hyper-elasticity model applied to rubber material [24]

C_{10}	C_{20}	C_{30}
0.206	0.013	-0.000059

Table 2. Coefficients for the Prony series in rubber specimens [24]

i	G_i	t_i
1	0.25	0.103
2	0.11	2.664
3	0.08	26.06
4	0.25	924.24

The μ_i and α_i are constants which depend upon shear behaviour and D_i is compressibility. Fig. 6 displays the rubber specimen's strain-stress curve (black line), with Fig. 6(a) demonstrating alignment between test data and the Yeoh model. In Fig. 6(b), the relaxation data is compared with the Prony model [24].

4. Mechanical Parameters of LRB and HDRB

Total thickness of rubber

$$T_r = nt_r \tag{7}$$

where n is number of rubber layers, t_r is the thickness of the single rubber layer and T_r is total rubber layer thickness. Total height of the elastomeric rubber bearing;

$$h = nt_r + (n-1)t_s \tag{8}$$

where n is number of rubber layers, t_r is the thickness of the single rubber layer, t_s thickness of single layer steel shim and T_r is total rubber layer thickness. Bonded rubber area;

$$A = \frac{\pi}{4}[(D_0 + t_c)^2 - D_i^2] \tag{9}$$

Where, t_c is the rubber cover thickness, D_0 is the outer diameter and D_i is the inner thickness or lead core diameter (for LRB and for HDRB $D_i = 0$)

The zero-displacement force intercept (Q_d) in a LRB is determined by the shear yield strength of the lead (σ_L) and the area of cross-section for the lead plug (A_L). The characteristics strength for the bearing;

$$Q_d = \sigma_L A_L \tag{10}$$

The second-slope stiffness (K_d) refers to the elastomeric component stiffness of the bearing. At a specific horizontal displacement (d), the effective or secant stiffness of the LRB is given by:

$$K_{eff} = \frac{Q_d}{d} + K_d \tag{11}$$

Shape factor, is defined individually for a rubber layer as:

$$S = \frac{D_o - D_i}{4t_r} \tag{12}$$

The steel shims confine the rubber at the bond interface. The shim spacing (or thickness of rubber layer) regulates the bulging around the perimeter, influencing the compression modulus (E_c) of the elastomeric layer.

$$E_c = \left(\frac{1}{6GS^2F} + \frac{4}{3K_{bulk}}\right)^{-1} \tag{13}$$

Where, G is shear modulus, K_{bulk} is bulk modulus of rubber, S is shape factor, central hole factor $F = \frac{(r_d)^2+1}{(r_d-1)^2} + \frac{1+r_d}{(1-r_d)ln(r_d)}$, $r_d = \frac{D_o}{D_i}$

The tight arrangement of steel plates, or thin rubber layers, generates a substantial shape factor, leading to increased vertical stiffness.

$$K_v = \frac{AE_c}{T_r} \tag{14}$$

The overall rubber thickness (T_r) serves to offer the essential low horizontal stiffness required to extend the fundamental period of the system. Simultaneously, the tight arrangement of intermediate steel plates contributes substantial vertical stiffness and shear modulus is given as G and bonded rubber area (A). It's important to note that the steel shim plates do not influence the calculated horizontal stiffness of the bearing.

$$K_h = \frac{GA}{T_r} \tag{15}$$

Torsional Stiffness

$$K_t = \frac{2GI_s}{h} \tag{16}$$

Effective Period

$$T_{eff} = 2\pi\sqrt{\frac{W}{K_{eff}.g}} \tag{17}$$

Where, W is the seismic weight of the structure supported by the isolation unit g is gravitational acceleration.

Effective stiffness

$$K_{eff} = \frac{W}{g}\left(\frac{2\pi}{T}\right)^2 \tag{18}$$

Hysteresis loop defined the energy dissipation per cycle,

$$W_D = 2\pi K_{eff}\beta D^2 \tag{19}$$

The energy dissipated per loading cycle (E_{loop}) and the effective stiffness (K_{eff}) is determined based on the peak displacements, Δ^+ and Δ^-.

$$\beta_{eff} = \frac{2}{\pi}\frac{E_{loop}}{K_{eff}(|\Delta^+| + |\Delta^-|)^2} \tag{20}$$

Damping reduction factor

$$\frac{1}{B} = 0.25\left(1 - ln\beta_{eff}\right) \tag{21}$$

The design and construction of the isolation system must ensure resilience to, at the very least, the maximum displacement D ascertained through the upper and lower bound characteristics, particularly in the most critical horizontal response direction.

$$D = \frac{gS_aT_{eff}^2}{4\pi^2 B} \tag{22}$$

The force-deflection properties of an isolation system should be determined through cyclic load tests conducted on prototype isolation unit. For each loading cycle, the effective stiffness of the isolator, denoted as K_{eff}, must be calculated as per the specified

$$K_{eff} = \frac{|F^+| + |F^-|}{|\Delta^+| + |\Delta^-|} \tag{23}$$

Here, F^+ represents the positive force at the maximum positive displacement Δ^+, and F^- denotes the negative force at the minimum negative displacement Δ^- as shown in Fig. 7.

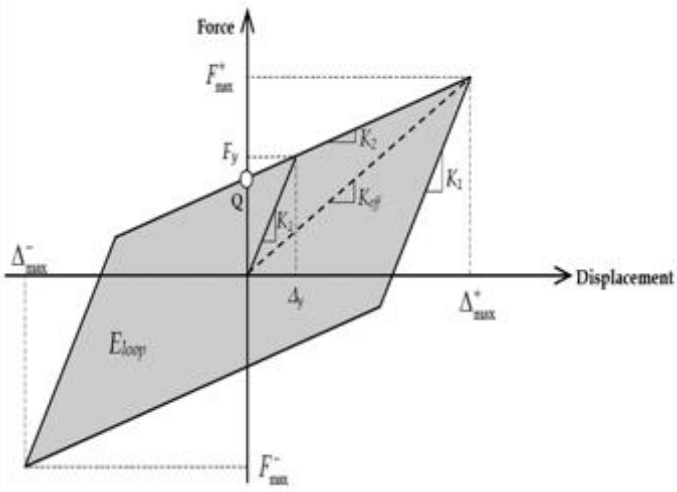

Fig. 7. Force-displacement hysteretic characteristic of an isolator (IS 1893 Part 6)

4.1. Modelling of HDRB for Dynamic Analysis

The HDRB was modeled in Abaqus CAE 2020 software, with its four parts (Loading Plate, Fixing Plate, Steel Plate, and Rubber Plate as shown in Fig. 8) created according to properties outlined in the 'Material Properties and Dimensions' section. The model was constructed in the Parts module, with material characteristics such as Poisson's coefficient, modulus of elasticity, density, and plastic properties, including visco-elastic coefficients and Yeoh model coefficients are defined. These properties were assigned to the respective sections, and the parts were assembled together.

To facilitate the dynamic analysis, two reference points are positioned at the centroids of the top and bottom surfaces of the model as shown in Fig. 9. The degrees of freedom for these surfaces are linked to their corresponding reference points. These reference points serve as anchors for applying boundary conditions and loading scenarios to the bearing. The simulation applied a general method with analysis procedure as Dynamic Implicit in the step module. The Interaction module in ABAQUS serves to define contact behaviors, such as friction or heat, between layers.

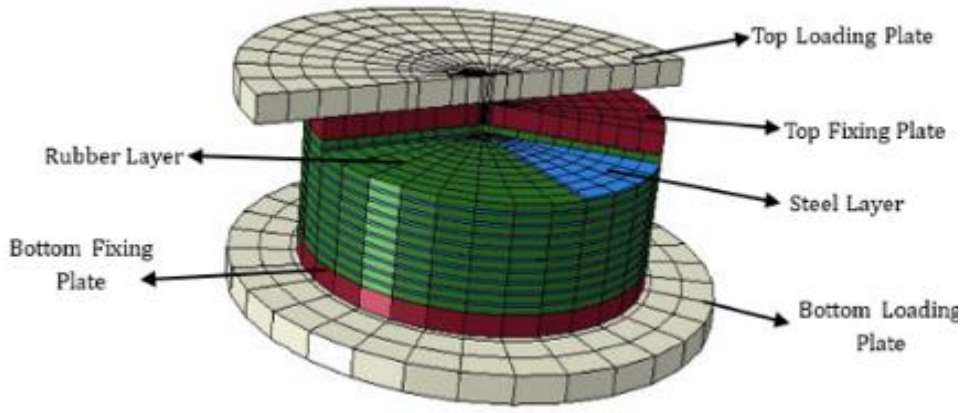

Fig. 8. Schematic representation of the HDRB with its components

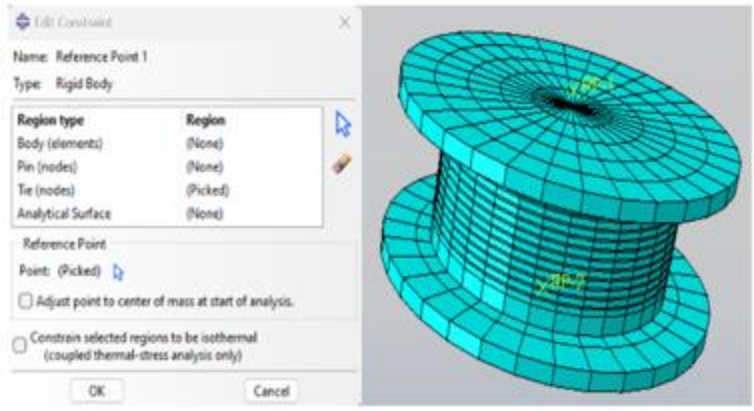

Fig. 9. Diagram depicts the reference point RP1 and RP2 at the top and bottom of the bearing

It also allows for the specification of how degrees of freedom are constrained and how parts are connected. In this study, the Tie constraint is utilized to attach the parts of the isolators, ensuring their cohesive movement as a single unit. The bearing was meshed to create 9222 elements. For the steel material, the C3D8R *Hex* element type (an 8-node linear brick with reduced integration and hourglass control) was selected, while for the visco-hyperelastic rubber material, the C3D20H *Hex* element type (a 20-node quadratic brick with hybrid linear pressure) was chosen. A concentrated force of 667kN was applied at the top of the loading plate of the bearing, and ground motion was applied at its bottom surface.

4.2. Modelling of Lead Rubber Bearing for Dynamic Analysis

The Lead Rubber Bearing was modelled in Abaqus CAE 2020 software, with its four parts (Loading Plate, Fixing Plate, Lead Core, Steel Plate, and Rubber Plate as shown in Fig. 10) created based on properties outlined in the 'Material Properties and Dimensions' section. The simulation used a general method with analysis procedure is used as Dynamic Explicit in the step module, employing Tie constraints to connect the parts.

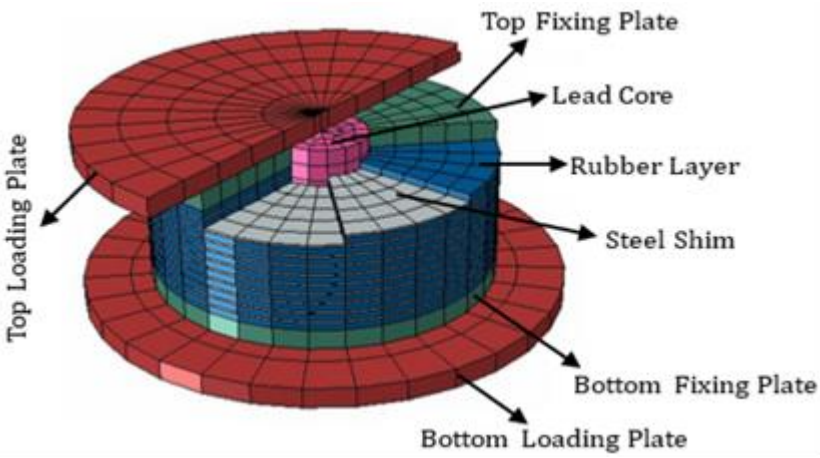

Fig. 10. Schematic representation of lead rubber bearing

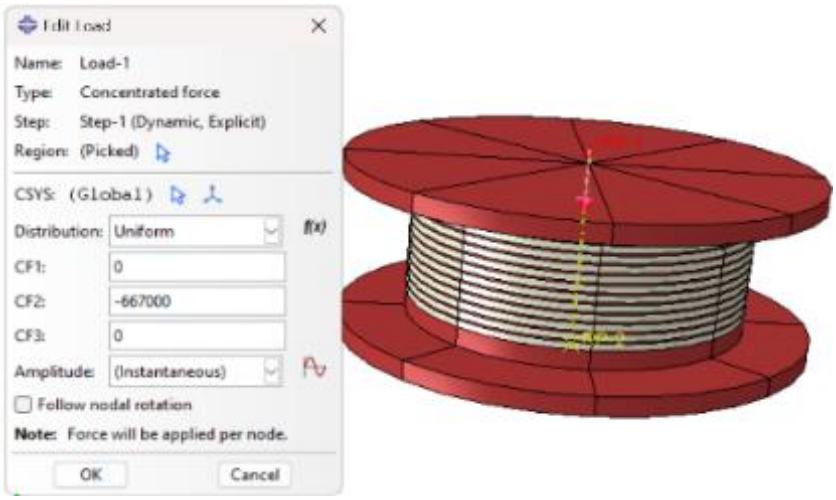

Fig. 11. Diagram depicts the applied concentrated load on LRB

The bearing was meshed with 4424 *Hex* elements, using the C3D8R element type (an 8-node linear brick with reduced integration and hourglass control). A concentrated force of 667kN was applied at the top of the loading plate of the bearing as shown in Fig. 11, and ground motion was applied at its bottom surface.

5. Properties of the Near-Fault Ground Motions

To examine the seismic performance of rubber bearings under earthquake excitations, five intense near-field ground motion records were chosen from the Pacific Earthquake Engineering Research Center [37], as listed in the Table 3. Near-fault ground motions are discerned by their long-period pulses and substantial ground displacements, which are notably greater than those observed in far-fault ground motions. Using the following earthquake specifications: Magnitude 7 > M_w > 6.0 and Distance (R) < 10 km, a search was conducted in the PEER NGA West2 Ground Motion Database. The input earthquake records are shown in Fig. 12 for Imperial Valley records and acceleration response spectra, Fig. 13 represents Managua record and acceleration response spectra, Fig. 14 represents Loma Prieta records and acceleration response spectra, Fig. 15 represents The Kocaeli records and acceleration response spectra and Fig. 16 represents Northridge records and acceleration response spectra. The Fourier Amplitude Spectrum for time history records is shown in Fig. 17.

Table 3. Properties of the applied near-fault ground motions Records

S. No.	Earthquake Record	Station Name	Year	Mechanism	RSN	Magnitude (M_w)	R_{jb} (km)	R_{rup} (km)	V_s30 (m/s)	PGA (g)	PGV (cm/s)	PGD (cm)
1.	Imperial Valley	El Centro Array #9	1940	Strike slip	6	6.95	6.09	6.09	213.4	0.233	31.29	18.44
2.	Managua, Nicaragua	Managua, ESSO	1972	Strike slip	95	6.24	3.51	4.06	288.7	0.354	28.41	6.096
3.	Loma Prieta	Saratoga,	1989	Reverse Oblique	802	6.93	7.58	8.5	380.8	0.369	47.32	26.53
4.	Northridge	Arleta Nordhoff	1994	Reverse	949	6.69	3.3	8.66	297.7	0.329	29.28	9.49
5.	The Kocaeli	Yarmica	1999	Strike Slip	1176	7.51	1.38	4.83	297	0.285	70.86	63.12

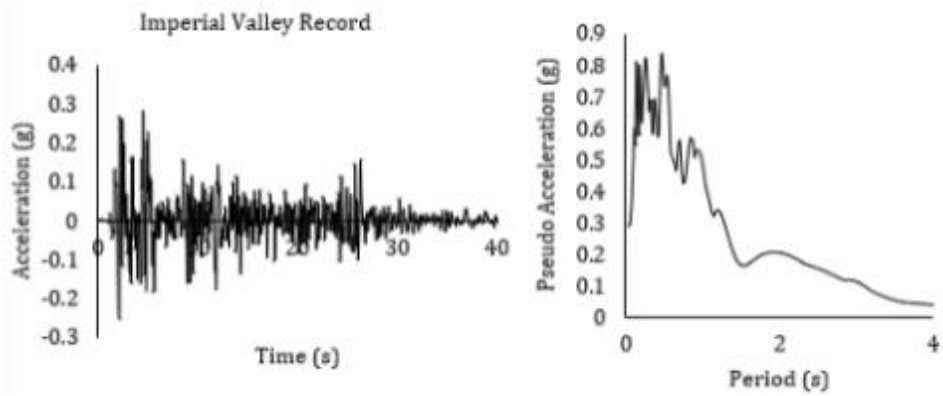

Fig. 12. Time histories recorded during the earthquake of Imperial Valley and Acceleration Response Spectra

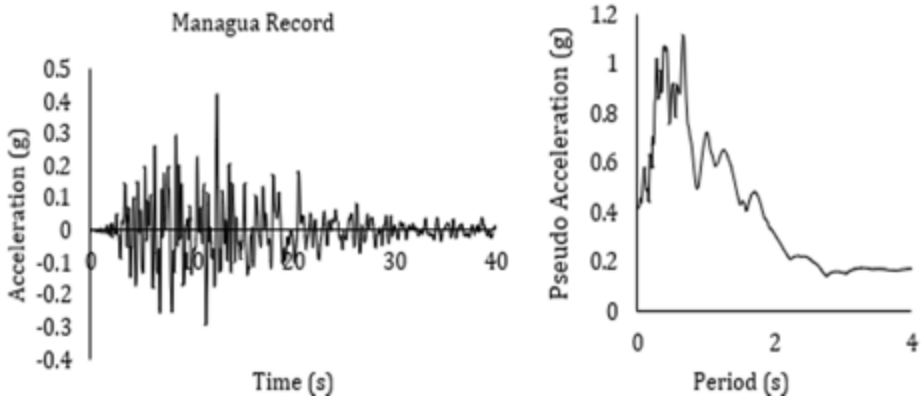

Fig. 13. Time histories recorded during the earthquake of Managua and Acceleration Response Spectra

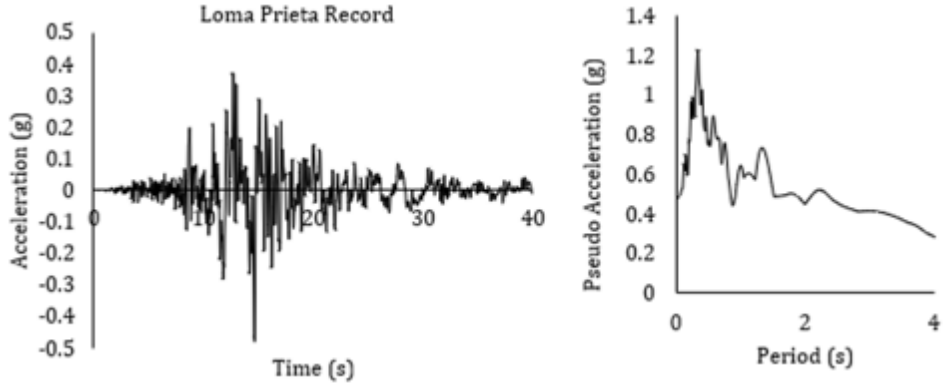

Fig. 14. Time histories recorded during the earthquake of Loma Prieta and Acceleration Response Spectra

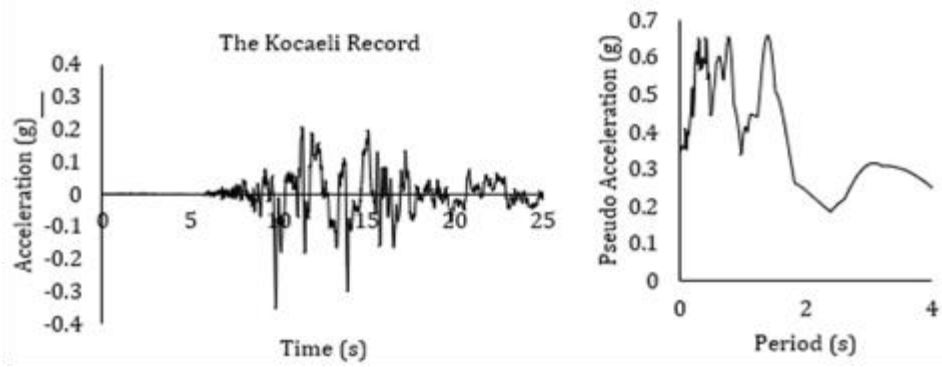

Fig. 15. Time histories recorded during the earthquake of The Kocaeli and Acceleration Response Spectra

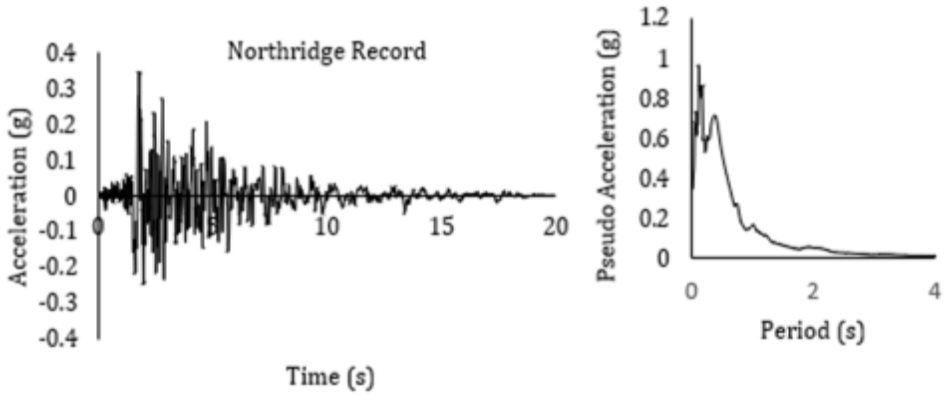

Fig. 16. Time histories recorded during the earthquake of Northridge and Acceleration Response Spectra

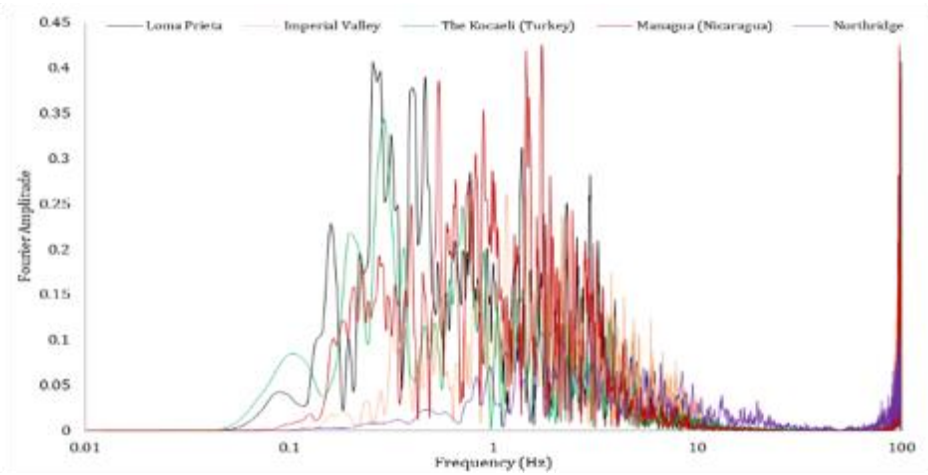

Fig. 17. Fourier amplitude spectrum of various time history records

6. Comparison of the Acceleration Response

The study examined the key features of the bearings and compared the input earthquakes reduced at the top of both LRBs and HDRBs. The inclusion of a lead core in the rubber bearing significantly decreased earthquake responses. The comparative results of Imperial Valley, Managua, Kocaeli, Northridge and Loma Prieta are shown in Fig. 18, Fig. 19, Fig. 20, Fig. 21 and Fig. 22, respectively. The bearings exhibited effective behavior during the input time history earthquakes, with maximum response reductions of 68.42% for the Kocaeli earthquake in the case of LRBs and 61.80% for the Northridge earthquake in the case of HDRBs.

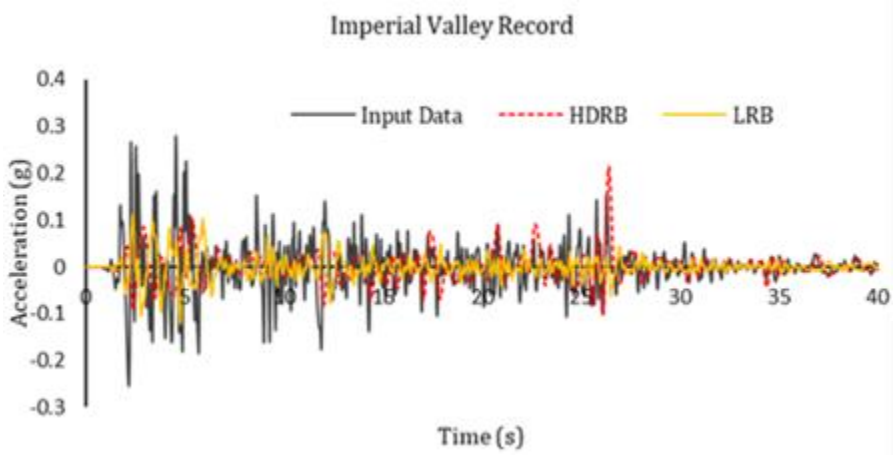

Fig. 18. Comparison of the Top bearing acceleration obtained from the dynamic analysis of the HDRB and LRB models under the input Imperial Valley earthquake

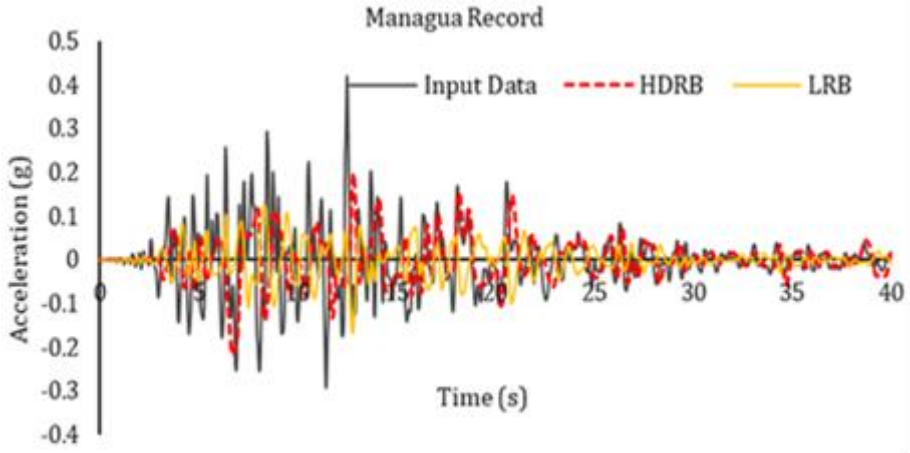

Fig. 19. Comparison of the Top bearing acceleration obtained from the dynamic analysis of the HDRB and LRB models under the input Managua earthquake

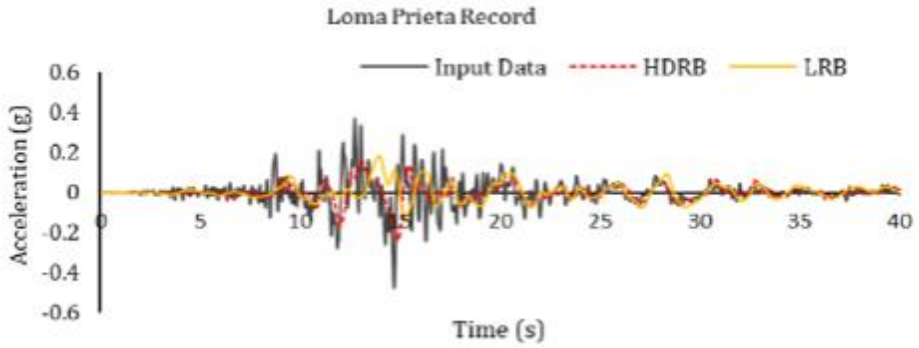

Fig. 20. Comparison of the Top bearing acceleration obtained from the dynamic analysis of the HDRB and LRB models under the input Loma Prieta earthquake

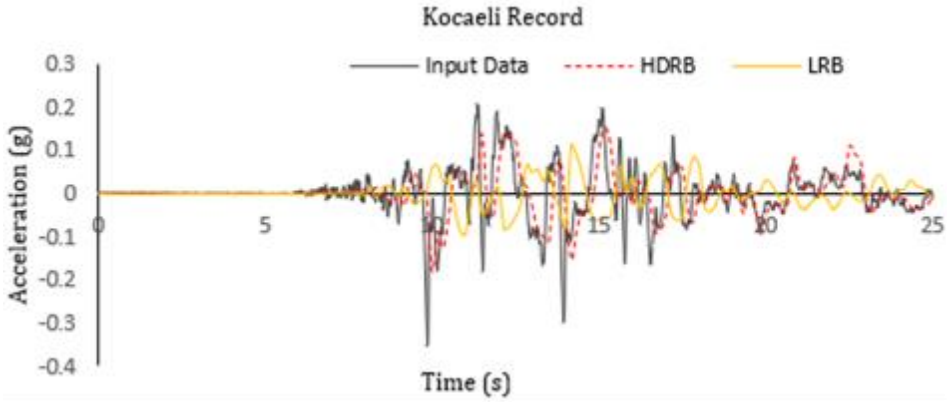

Fig. 21. Comparison of the Top bearing acceleration obtained from the dynamic analysis of the HDRB and LRB models under the input The Kocaeli earthquake

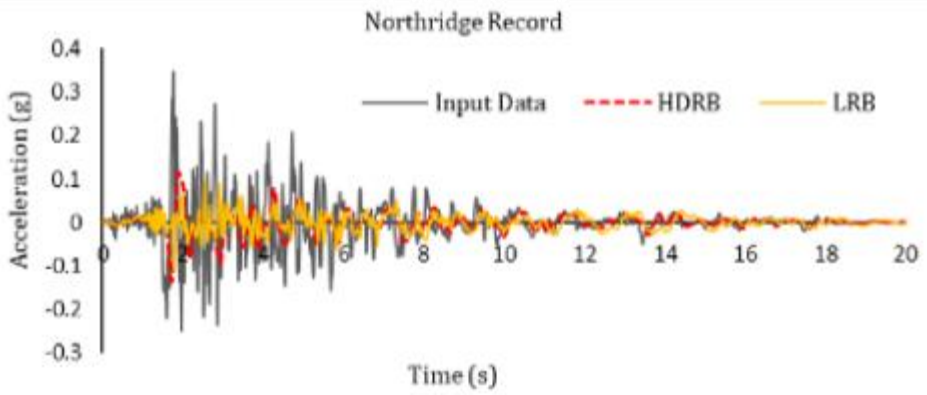

Fig. 22. Comparison of the Top bearing acceleration obtained from the dynamic analysis of the HDRB and LRB models under the input Northridge earthquake

7. Result and Discussion

The LRB undergoes a general static analysis procedure under a vertically concentrated load and subjected to cyclic lateral load, with the bottom end of the bearing fixed. A force-displacement curve is generated, and the results are compared with experimental and literature data. It was noted that the analyzed model closely aligns with both the manufacturer's specifications and previously analyzed results. Following optimization of the model for static analysis, the bearing is subsequently analyzed for dynamic behavior. The studies were performed [15][38-40] to evaluate the dynamic efficiency of the LRBs and HDRBs. The study conducted by Belbachir [11] shows a 54% reduction in acceleration for the HDRB+FVD isolated system compared to the fixed-base structure. The nonlinear dynamic analysis conducted on a fixed-base RC structure and three different base-isolated RC structures (employing HDRB, LRB, and elastomeric spring damper systems) provided the basis for a comparative analysis. This analysis includes the time history of base acceleration, base shear, base displacements, inter-storey drifts over time, and peak base shear values for each system [38]. Further, the study was performed to assessed dynamic responses of isolated structures, including crack distribution, acceleration, displacement, internal forces of bearings, and beam strains near failure. Sudden bearing failure, coupled with horizontal earthquakes, led to significant vertical deformation and impact. This affected adjacent and non-adjacent bearings, increasing the risk of overturning collapse. Vertical and low-frequency earthquake components notably influenced dynamic responses and damages, especially at bearing failure points [39]. In this study, the isolated bearing was simulated using ABAQUS CAE 2020 and subjected to time history records from the Imperial Valley, Managua, Loma Prieta, Northridge, and The Kocaeli events.

7.1 Validation of LRB and Analysis of HDRB

The response of the Lead Rubber Bearing (LRB) has been validated against experimental results from the manufacturer and numerical simulation analysis by Doudoumis using ADINA, as illustrated in Fig. 5. Additionally, a numerical simulation of the HDRB was conducted to analyze its force-displacement response as shown in Fig. 23. As the bearing undergoes cyclic loading, it exhibits a characteristic behavior in which the applied force increases progressively with displacement.

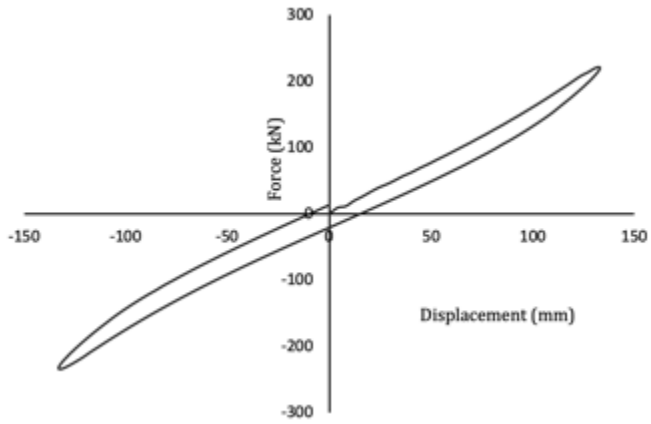

Fig. 23. Force-Displacement curve of the HDRB subject to horizontal cyclic loading

This is accompanied by a gradual stiffening of the bearing structure. Consequently, the displacement of the bearing is met with resistance, resulting in a nonlinear response where the force needed to induce further displacement increases gradually. This behavior is a

result of the high damping features of the rubber material within the bearing, which effectively dissipates energy and attenuates vibrations, contributing to the overall stability and performance of the bearing system. The analysis of HDRB and LRB revealed that the lead core in the LRB substantially enhances its performance. The static analysis showed good agreement between the analytical results and the experimental data, validating the precision of the models. These findings confirm the suitability of the numerical models for further dynamic analyses. Moreover, it highlights the efficacy of both LRBs and HDRBs in fortifying structures against seismic forces, emphasizing their role in bolstering structural resilience.

7.2 Acceleration Response

The results, based on accelerations at the top loading plate of the bearing, indicate that the isolation system was effectively activated during seismic events, ensuring the decoupling of motion between the superstructure and the foundations. Numerical analysis shows that the lead rubber bearing achieved a higher reduction in response compared to the HDRB. Specifically, the reduced acceleration responses in percentage are shown in Table 4 and the acceleration response in terms of 'g' for input, HDRB and LRB are shown in Fig. 24.

Table 4. Shows the acceleration response reduction for HDRB and LRB for input earthquake records

S.No.	Earthquake Records	HDRB response	LRB response
1.	The Kocaeli	48.42%	68.42%
2.	Imperial Valley	24.47%	57.24%
3.	Managua	48.35%	60.39%
4.	Loma Prieta	51.42%	62.05%
5.	Northridge	61.80%	68.41%

A notable decrease in the acceleration response at the top of the bearing was observed. This phenomenon indicates the effective dissipation of energy within the bearings, leading to reduced transmission of forces and vibrations to the superstructure. Such behavior is a key characteristic of these bearings, highlighting their ability to absorb and dissipate seismic energy, thereby safeguarding the structure against excessive vibrations.

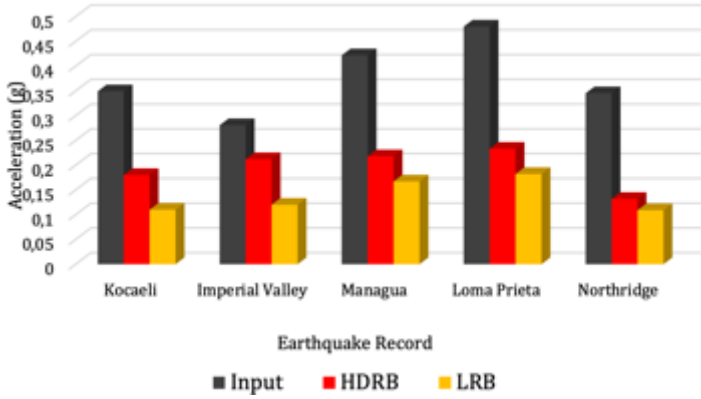

Fig. 24. Maximum acceleration at the top of the bearing with different input of the Time History earthquakes

7.3 Displacement Response

The displacement response at the top of the bearing is crucial for understanding structural behavior under seismic loading. It reveals how effectively bearings accommodate deformations and isolate the superstructure. A minimal or decreasing displacement indicates efficient energy dissipation and structural flexibility, reducing transmitted seismic forces. This highlights LRBs and HDRBs' ability to enhance seismic capacity by mitigating ground motion impact and preventing excessive deformations.

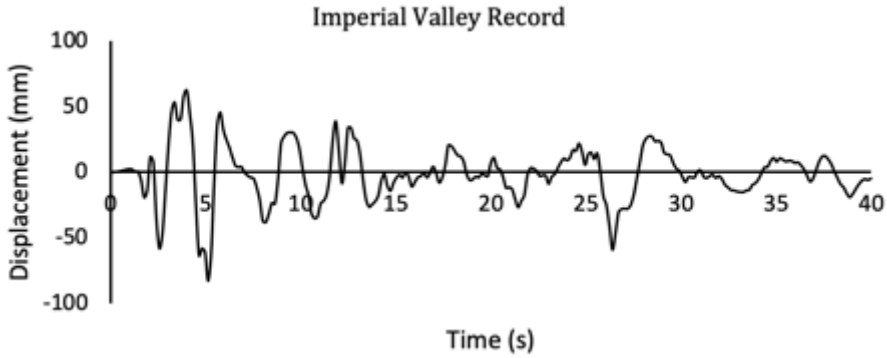

Fig. 25. The displacement response of the lead rubber bearing for time history function Imperial Valley

To prevent the overturning of isolators, it is crucial to restrict the horizontal displacement of the isolator. As per Chinese Code for the Seismic Design of Buildings, the maximum horizontal displacement of a rubber bearing during a ground motion should not exceed 0.55 times its effective diameter [41]. The displacement responses of the LRB for the Imperial Valley earthquake and the HDRB for the Managua earthquake, as illustrated in the respective Fig. 25 and Fig. 26, are provided. However, these responses, being at the top of the bearing, may not entirely reflect the actual behavior as it would occur within a complete building-bearings system.

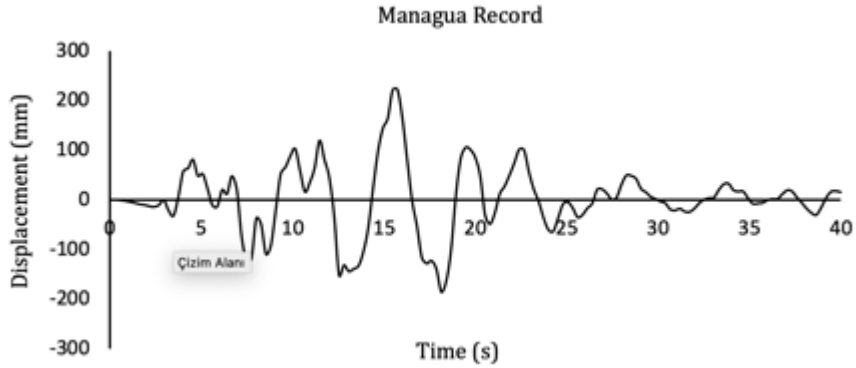

Fig. 26. The displacement response of the high damping rubber bearing for time history function Managua

8. Conclusion

In summary, the study comprehensively validated two types of isolators, LRBs and HDRBs, through a meticulous process involving static and dynamic analyses using 3D Finite Element (FE) models in Abaqus. The dynamic analysis revealed promising results, particularly in terms of acceleration and displacement responses. The bearings exhibited efficient energy dissipation, leading to reduced transmitted forces and vibrations to the superstructure. Furthermore, they demonstrated the capacity to withstand significant deformations, effectively protecting the superstructure from ground motion. These findings, presented in terms of the acceleration reduction within the bearing, highlight the effectiveness of LRBs and HDRBs in enhancing the seismic resilience of structures. This suggests their potential to mitigate ground motion impacts and prevent excessive structural deformations.

The hysteresis curves of HDRB show a smaller area compared to LRBs, indicating an unexpected lower energy dissipation capacity under similar shear deformation conditions. The horizontal shear performances of both types of bearings are illustrated in the force-displacement curve as shown in Fig. 4 for LRB and Fig. 21 for HDRB, indicating that the HDRB has a lower horizontal stiffness than the LRB under equivalent vertical loading and shear strain. This implies that, with an equal total rubber thickness, the steel plates in the HDRB exert less constraint force on the rubbers compared to the lead core in the LRB. The presence of the lead core enhances the energy dissipation capacity of the LRB.This study validates that both isolators significantly diminish the destructive effects of earthquakes, with LRBs showing superior performance over HDRBs. The maximum reductions in response are 68.42% for the Kocaeli earthquake in the case of LRBs and 61.80% for the Northridge earthquake in the case of HDRBs. The reduction in acceleration response at the top of the bearing is indicative of the bearings' effectiveness in mitigating the impact of seismic forces on the structure. This emphasizes their pivotal role in enhancing the collective seismic performance and safety of the structure.

In influence of near field ground motion excitation, the peak displacement for LRB under the Imperial Valley ground motion is 62.577mm, while for HDRB under the Managua earthquake record, it is 221.052mm.

Finite element micromodels provide detailed insights into the stress, strain, and strength characteristics of LRBs and HDRBs, aiding in the understanding of their mechanical behavior and facilitating improvements in their design. The inclusion of a lead core in LRBs alters stress and strain distribution, highlighting the necessity of micromodels for their study. It is essential to validate basic assumptions regarding material properties and fabrication details to ensure the accuracy of the analysis.

Dynamic analysis of HDRBs and LRBs in Abaqus is limited by the accuracy of material models for dynamic loading, large deformations, and high loading rates. Contact modeling, crucial for HDRBs and LRBs, can be challenging to accurately represent in Abaqus, impacting overall performance assessment. Additionally, results may be affected by material and interaction properties of the models, with dynamic analyses being computationally time consuming for complex models.

This research addresses the gap in the literature by focusing specifically on LRBs and HDRBs, applying ABAQUS software package for numerical simulations and finite element micro analysis. The results include a comparative analysis of the reduction in input earthquake forces, laying the foundation for future research in this field.

Future research in the analysis of HDRBs and LRBs using Abaqus should emphasize the development of more accurate material models, enhancements in contact algorithms, and

the refinement of dynamic loading simulations. Incorporating viscoelastic properties alongside other hyperelastic material models could be simulated numerically to identify the most optimized and improve models with enhanced precision and accuracy. It is crucial to conduct comprehensive experimental studies and parametric analyses to validate results and gain insights into the impact of various design parameters.

References

[1] Khan BL, Azeem M, Usman M, Farooq SH, Hanif A, Fawad M. Effect of near and far field earthquakes on performance of various base isolation systems. Procedia Struct Integr. 2019;18:108–18.

[2] Işık E. Comparative investigation of seismic and structural parameters of earthquakes (M ≥ 6) after 1900 in Turkey. Arab J Geosci. 2022;15(10):971.

[3] Bilgin H, Hadzima-Nyarko M, Isik E, Ozmen HB, Harirchian E. A comparative study on the seismic provisions of different codes for RC buildings. Struct Eng Mech. 2022;83(2):195–206.

[4] Akar F, Işık E, Avcil F, Büyüksaraç A, Arkan E, İzol R. Geotechnical and Structural Damages Caused by the 2023 Kahramanmaraş Earthquakes in Gölbaşı (Adıyaman). Appl Sci. 2024;14(5):2165.

[5] Bilgin H. Effects of near-fault and far-fault ground motions on nonlinear dynamic response and seismic damage of masonry structures. Eng Struct. 2024;300(November 2023):117200. https://doi.org/10.1016/j.engstruct.2023.117200

[6] Standards ASCE/SEI 7-16. Minimum Design Loads and Associated Criteria for Buildings and Other Structures. ASCE Standard.

[7] Sheikh H, Van Engelen NC, Ruparathna R. A review of base isolation systems with adaptive characteristics. Structures. 2022;38(March):1542–55. https://doi.org/10.1016/j.istruc.2022.02.067

[8] Weisman J, Warn GP, Asce AM. Stability of Elastomeric and Lead-Rubber Seismic Isolation Bearings. J Struct Eng. 2012;138(2):215–23.

[9] Zhang C, Ali A. The advancement of seismic isolation and energy dissipation mechanisms based on friction. Soil Dyn Earthq Eng. 2021;146(11):106746. https://doi.org/10.1016/j.soildyn.2021.106746

[10] Patel D, Mourya VK, Pandey G, Kumar R. Advancements in base isolation for seismic mitigation : Perspectives on elastomeric and lead rubber bearings. Res Eng Struct Mater. 2024;1–33 http://dx.doi.org/10.17515/resm2024.15ma0927rv

[11] Belbachir A, Benanane A, Ouazir A, Harrat ZR, Hadzima-Nyarko M, Radu D, et al. Enhancing the Seismic Response of Residential RC Buildings with an Innovative Base Isolation Technique. Sustain. 2023;15(15).

[12] Markou AA, Manolis GD. Mechanical models for shear behavior in high damping rubber bearings. Soil Dyn Earthq Eng. 2016;90:221–6. http://dx.doi.org/10.1016/j.soildyn.2016.08.035

[13] Yoshida J, Abe M, Fujino Y. Constitutive Model of High Damping Rubber Materials. Doboku Gakkai Ronbunshu. 2002;2002(710):209–24.

[14] Clemente P, Bongiovanni G, Buffarini G, Saitta F, Gabriella M, Scafati F. Effectiveness of HDRB isolation systems under low energy earthquakes. Soil Dyn Earthq Eng. 2019;118(December 2018):207–20. https://doi.org/10.1016/j.soildyn.2018.12.018

[15] Alhan C, Gazi H, Kurtulu H. Significance of stiffening of high damping rubber bearings on the response of base-isolated buildings under near-fault earthquakes. Mech Syst Signal Process. 2016;

[16] Bandyopadhyay S, Parulekar YM, Sengupta A, Chattopadhyay J. Structure soil structure interaction of conventional and base-isolated building subjected to real earthquake. Structures. 2021;32(March):474–93.

https://doi.org/10.1016/j.istruc.2021.03.069
[17] Pandey G, Patel D, Mourya VK. A Review on Soil - Foundation - Interaction Models. J Rehabil Civ Eng. 2023;3(11):158–79. https://doi.org/10.22075/JRCE.2022.25247.1570
[18] Pandey G, Mourya VK, Patel D, Kumar R. Load sharing behaviour in piled-raft foundations over sand and clay : An experimental investigation. Res Eng Struct Mater. 2023;1–26. http://dx.doi.org/10.17515/resm2023.41me0714rs
[19] Mourya VK, Pandey G, Patel D, Kumar R. Approaches considering non-linearity in soil-foundation-interaction: A State of the Art Review. Res Eng Struct Mater. 2023;9(3):989–1013. http://dx.doi.org/10.17515/resm2023.646me0117
[20] Ozdemir G, Avsar O, Bayhan B. Change in response of bridges isolated with LRBs due to lead core heating. Soil Dyn Earthq Eng. 2011;31(7):921–9. http://dx.doi.org/10.1016/j.soildyn.2011.01.012
[21] Ozdemir G, Dicleli M. Effect of lead core heating on the seismic performance of bridges isolated with LRB in near-fault zones. Earthq Eng Struct Dyn. 2012;41(14):1989–2007.
[22] Arguc S, Avsar O, Ozdemir G. Effects of Lead Core Heating on the Superstructure Response of Isolated Buildings. J Struct Eng. 2017;143(10):04017145.
[23] Hu GJ, Ye K, Tang ZY. Design and analysis of LRB base-isolated building structure for multilevel performance targets. Structures. 2023;57(July):105236. https://doi.org/10.1016/j.istruc.2023.105236
[24] Basshofi Habieb A, Tavio T, Milani G, Wijaya U. 3D-Finite element modeling of lead rubber bearing using high damping material. MATEC Web Conf. 2019;276:01013.
[25] Behzad Talaeitaba S, Safaie M, Zamani R. Development and application of a new base isolation system in low-rise buildings. Structures. 2021;34(July):1684–709. https://doi.org/10.1016/j.istruc.2021.07.077
[26] Pourmasoud M, Park ARL, Hajirasouliha I, Lim J, Behzadi A. Validation of a New Equation to Estimate the Yield Strength of Lead Rubber Bearings. Procedia Struct Integr. 2022;44(2022):590–7. https://doi.org/10.1016/j.prostr.2023.01.077
[27] Rahgozar A, Estekanchi HE, Mirfarhadi SA. On optimal lead rubber base-isolation design for steel moment frames using value-based seismic design approach. Soil Dyn Earthq Eng. 2023;164(July 2022):107520. https://doi.org/10.1016/j.soildyn.2022.107520
[28] Saiful Islam ABM, Jameel M, Jummat MZ. Study on optimal isolation system and dynamic structural responses in multi-storey buildings. Int J Phys Sci. 2011;6(9):2219–28.
[29] Ounis HM, Ounis A, Djedoui N. A new approach for base isolation design in building codes. Asian J Civ Eng. 2019;20(6):901–9. https://doi.org/10.1007/s42107-019-00153-x
[30] Güneş N. Effects of near-fault pulse-like ground motions on seismically isolated buildings. J Build Eng. 2022;52(April):1–17.
[31] Güneş N, Ulucan ZÇ. Nonlinear dynamic response of a tall building to near-fault pulse-like ground motions. Bull Earthq Eng. 2019;17(6):2989–3013. https://doi.org/10.1007/s10518-019-00570-y
[32] Güneş N. Risk-targeted design of seismically isolated buildings. J Build Eng. 2022;46(August 2021):1–16.
[33] Kelly JM. Analysis of fiber-reinforced elastomeric isolators. J Seism Earthq Eng. 1999;2(1):19–34.
[34] Imbimbo M, De Luca A. F.E. stress analysis of rubber bearings under axial loads. Comput Struct. 1998;68(1–3):31–9.
[35] Doudoumis IN, Gravalas F. Analytical Modeling of Elastomeric Lead-Rubber Bearings with the use of Finite Element Micromodels. In: 5th GRACM International Congress on Computational Mechanics. 2005.

[36] Evaluation findings for skellerup base isolation elastomeric bearings. Technical evaluation report, (CERF report: HITEC 98-12), prepared by the Highway Innovative Technology Evaluation Center. 1998;
[37] PEER. User's manual for the peer ground motion database application. Pacific Earthq Eng Res Center Univ California, Berkeley. 2011;
[38] Cancellara D, Angelis F De. Nonlinear dynamic analysis for multi-storey RC structures with hybrid base isolation systems in presence of bi-directional ground motions. Compos Struct. 2016;154:464–92. http://dx.doi.org/10.1016/j.compstruct.2016.07.030
[39] Han B, Du Y, Hong N, Li H, Shi C. Shaking table test study on dynamic performance of a base-isolated frame structure under an isolation bearing removal scenario. Structures. 2023;48(January):1141–56.
[40] Tagliafierro B, Montuori R, Castellano MG. Shake table testing and numerical modelling of a steel pallet racking structure with a seismic isolation system. Thin-Walled Struct. 2021;164(October):107924. https://doi.org/10.1016/j.tws.2021.107924
[41] Zhang R, Wu M, Lu W, Li X, Lu X. Seismic retrofitting of a historic building by using an isolation system with a weak restoring force. Soil Dyn Earthq Eng. 2021;148(January):106836. https://doi.org/10.1016/j.soildyn.2021.106836

Research on Engineering Structures & Materials
www.jresm.org
MIM Research Group

Review Article

Harnessing microbes for self-healing concrete – A review

Farzin Asgharpour[*,1,3,a], Kadir Çakiral[2,3,b], Khaled Hamed Marar[1,c]

[1]*Dept. of Civil Eng., Eastern Mediterranean University, Famagusta, North Cyprus Via Mersin 10, 99628*
[2]*Dept. of Chemistry, Eastern Mediterranean University, North Cyprus Via Mersin 10, 99628, Turkey*
[3]*Faculty of Medicine, Eastern Mediterranean University, North Cyprus Via Mersin 10, 99628, Turkey*

Article Info

Article history:

Received 04 Mar 2024
Accepted 10 Apr 2024

Keywords:

Bacillus sp;
Bio-mediated repair;
Microbial concrete;
Self-healing concrete;
Sustainable construction

Abstract

This review explores the burgeoning field of microbially enhanced construction materials, with a special focus on self-healing concrete, through the lens of microbial biotechnology. Central to this discourse is the innovative use of bacteria, particularly Bacillus species, to address the pervasive issue of microcracks in concrete, a fundamental material in the construction industry. Traditional remedies, such as chemical admixtures and fiber reinforcements, offer partial solutions; however, self-healing concrete represents a paradigm shift, harnessing the natural calcite-precipitating ability of bacteria to autonomously repair cracks, thereby augmenting structural durability and longevity. Delving into the mechanics, the bacteria, embedded within the concrete matrix, remain dormant until crack formation triggers their metabolic pathways, leading to calcite production that effectively seals the fissures. This bio-mediated repair mechanism not only enhances the structural integrity of concrete but also aligns with sustainable construction practices by minimizing maintenance requirements and material wastage. The review extends beyond self-healing phenomena, encompassing broader applications of microbial technology in construction, including bio-concrete, bio-cement, and soil stabilization methods. These applications underscore the versatility of microbes in enhancing material properties such as compressive strength, tensile resilience, and water impermeability. Empirical evidence underscores the necessity of optimizing bacterial dosages and curing conditions to maximize the self-healing efficiency. Future research trajectories should aim to elucidate the complex interactions between microbial agents and concrete matrices, assess long-term performance, and evaluate the environmental and economic sustainability of microbial interventions in construction. The integration of microbial technology in construction materials heralds a new epoch of innovation, offering robust, sustainable, and resilient solutions to enduring challenges in the industry.

1. Introduction

In the evolving landscape of civil engineering, the quest for durable and sustainable building materials has become paramount, driven by the urgent need to address the environmental and structural challenges of modern construction. Concrete, the cornerstone of global infrastructure development, is under increasing scrutiny due to its vulnerability to degradation and the environmental impact of its production. This paper explores the utilization of microorganisms in construction materials and the methods employed to evaluate their effect on strength. Concrete, being the most extensively used building material in construction projects (1) is not without its challenges, including the presence of micro cracks (2). These micro cracks can reduce the workability of concrete and potentially lead to structural collapse and failure.

[*]Corresponding author: farzin.asgharpour@emu.edu.tr
[a]orcid.org/0000-0003-3380-8359; [b]orcid.org/0000-0003-4639-7528; [c]orcid.org/0000-0001-5650-2980
DOI: http://dx.doi.org/10.17515/resm2024.207ma0304rv

To address these challenges, various approaches have been employed, such as the use of chemical admixtures (3) and fiber concretes (4). Additionally, the concept of self-healing concrete has gained attention, aiming to minimize the need for manual maintenance. One promising self-healing approach involves the utilization of specific bacteria that operate independently within the concrete structure (2). When tensile forces exceed the concrete's strength, fractures occur (5). These fractures can serve as pathways for water ingress and the infiltration of toxic substances (6). Concrete cracks can be classified into two groups: non-hazardous cracks that are visually unappealing but do not pose a safety threat (7), and structural cracks that require careful attention to prevent significant harm to the overall structure. Self-healing concrete methods, such as bacterial reactions within the hardened concrete, have shown promise in mitigating the latter type of cracks (8).

Micro cracks typically range from 0.1 to 0.05 mm in width, and their presence allows the infiltration of water particles, acting as capillaries (9). When water droplets penetrate the cracks, partially or completely unreacted cement hydrates, leading to expansion and subsequent sealing of the crack (10). Recent studies, by Saravanan et al., have delved into the compressive strength development of geopolymer concrete using manufactured sand, highlighting the environmental benefits and performance efficiencies of alternative materials like geopolymer concrete in reducing carbon emissions associated with conventional cement usage (11). Similarly, the work of Chaitanya et al. on the self-healing characteristics of GGBS admixed concrete using Artificial Neural Networks underscores the innovative strategies being developed to enhance concrete's self-healing properties and reduce its carbon footprint (12).

Moreover, Cappellesso et al. (2023) reviewed the efficiency of self-healing concrete technologies, affirming the potential of microbial and chemical methods to extend the service life of concrete structures (13). The research on Ground Granulated Blast Furnace Slag (GGBS) in concrete by Subramanian et al. (2022) also emphasizes the improved flexural behavior and durability of concrete beams reinforced with polymer composites (14). In addition, the investigations into the prediction of self-healing characteristics of concrete with GGBS by M. Chaitanya et al. (2020) and the work of Aleem et al. on the properties of Geopolymer concrete with M-sand provide comprehensive insights into the advancements in concrete technology that contribute to more sustainable construction practices (15,16).

The exploration of self-healing concrete is important, particularly in the context of material costs and the judicious selection of optimal materials tailored to project requirements. Attaining high-quality self-healing concrete necessitates a thorough examination of prior studies to identify effective solutions. Understanding the response and workability of concrete, along with addressing challenges in healing or sealing cracks, remains a dilemma. Furthermore, self-healing concrete is recognized as a viable approach to minimize structural maintenance requirements. Following established methodologies outlined in previous literature can lead to reduced maintenance costs and alleviate environmental impacts associated with traditional repair methods, such as the production and transportation of materials. The field of bacterial concrete has rapidly evolved, offering innovative solutions for enhancing the durability and sustainability of construction materials. This technology is believed to not only promise extended lifespans for concrete structures but also align with environmental sustainability goals. The integration of bacterial spores into concrete matrices for self-healing purposes represents a significant breakthrough in construction material science (17).

This research assumes strategic significance by aiming to comprehensively assess and analyze the impacts of self-healing on key concrete properties, including compressive strength, tensile strength, and water absorption. The insights gleaned from this review are

pivotal for researchers, guiding the trajectory of advancements in self-healing concrete. Ultimately, this contributes to the development of infrastructure that is both more resilient and sustainable.

2. Application of Microbes in Construction

Microorganisms, particularly bacteria, have various applications in the construction industry. In other words, bacteria bring a world of possibilities to the construction industry, opening doors to innovative and sustainable practices. These tiny living organisms play a significant role in enhancing various aspects of construction materials and processes, paving the way for a more eco-friendly and resilient future (18).

Recent advancements in microbial applications for concrete have highlighted the efficacy of various bacterial strains, such as *Bacillus pseudofirmus* and *Bacillus cohnii*. These bacteria have been shown to significantly enhance concrete's durability through the process of calcium carbonate precipitation. This biogenic mineralization contributes to self-healing of micro-cracks, thereby extending the lifespan of concrete structures. The integration of these specific bacterial strains represents a promising development in sustainable construction materials (19). In the following, the most famous applications of microorganisms and using them in the construction is examined:

2.1. Self-Healing Concrete

In the domain of construction, self-healing concrete emerges as a captivating and groundbreaking innovation. Imagine concrete structures imbued with the extraordinary ability to mend themselves! This remarkable achievement is made possible through the incorporation of specific bacterial strains from the *Bacillus genus* into the concrete mix. These highly adept bacteria remain quiescent within the concrete until the emergence of cracks, at which point they are triggered into action. In a process akin to skilled artisans, they facilitate the production of calcium carbonate, serving as a natural adhesive that adeptly seals the cracks and fortifies the concrete's structural integrity. The enchantment of self-healing concrete extends beyond its capability to diminish maintenance requirements; it also bestows an extended lifespan upon our structures, imbuing them with heightened resilience and reliability as time unfolds (20,21).

2.2. Biodegradable Construction Materials

Microbes have emerged as a significant catalyst in the development of biodegradable construction materials, including bioplastics and biocomposites. The incorporation of these materials signifies a notable stride towards fostering eco-friendliness and mitigating the environmental impact of construction activities. Leveraging the remarkable potential of these microorganisms, we can fabricate bioplastics and biocomposites that epitomize a more environmentally sensitive approach to construction. The intrinsic value of these materials lies in their inherent propensity for natural degradation, leaving behind a minimal ecological footprint while contributing to the reduction of waste in construction projects. Such advancements underscore the crucial role of microorganisms in promoting sustainable practices within the construction industry (22–24).

2.3. Bioconcrete and Biocement

The fascinating world of bioconcrete and biocement unfolds as it harnesses the power of microbes in their production. Bioconcrete ingeniously incorporates bacteria capable of limestone production, fortifying the concrete and enhancing its durability. On the other hand, bio cement relies on microorganisms that induce calcite precipitation within the concrete matrix, bestowing it with heightened strength and resilience. Just imagine the potential of these microbe-powered wonders-construction materials that not only meet

our practical needs but also demonstrate a profound commitment to environmental stewardship. Through these advancements, we find ourselves on a path where sustainable construction practices and ecological well-being go hand in hand (18,25,26).

2.4. Soil Stabilization

The other microbial application in construction involves soil stabilization, where certain microbial species come to the rescue, especially in areas with weak or loose soil. These remarkable microorganisms possess the fantastic ability to fortify the soil, rendering it suitable and robust for construction purposes. By promoting microbial-induced calcite precipitation, we can establish a solid foundation for our building endeavors, ensuring stability and longevity in our construction projects. It's like nature's own construction crew working behind the scenes to strengthen the very ground we build upon (27–29).

3. History and Importance of Use of Microbes

In the history of concrete, the introduction of calcium-rich bacteria during the mixing stage has emerged as a significant development. These bacteria play a crucial role in the self-healing process of concrete. When cracks form within the concrete, the introduced bacteria initiate the precipitation of calcium carbonate. This natural process effectively seals the cracks and reinforces the overall structure. Consequently, bacterial concrete exhibits higher strength compared to conventional concrete. By leveraging a biotechnological approach centered around calcite precipitation, it becomes possible to enhance both the strength and durability of structural concrete (30,31).

The use of bacteria in concrete is an innovative method that harnesses the power of microbial activity to improve the performance and longevity of concrete structures. The formation of calcium carbonate through the action of bacteria leads to the creation of a more robust and resilient construction material (32–34). Self-healing concrete can be achieved through three main methods: natural, chemical, and biological. The biological method can be further categorized into three subcategories: bacteria, fungi, and viruses. Among these methods, the utilization of bacteria, particularly specific strains within the concrete, has garnered significant interest (35). Self-healing concrete can be achieved through three main methods: natural, chemical, and biological. The biological method can be further categorized into three subcategories: bacteria, fungi, and viruses. Among these methods, the utilization of bacteria, particularly specific strains within the concrete, has garnered significant interest (35,36). The historical development and increasing interest in using microbes, especially bacteria, in the self-healing process of concrete highlight the potential of biotechnological advancements in construction materials. By incorporating microbial activity, concrete can exhibit improved resilience and longevity, addressing the challenges associated with cracks and structural deterioration (37). The historical development of bio-concrete represents a significant milestone in construction material technology. This evolution from traditional concrete to bio-concrete highlights a shift towards sustainable, self-healing materials, emphasizing the crucial role of microbes in modern construction practices (38).

OPC accounted for approximately 12% of global CO_2 emissions in 2020. Alkali-activated slag (AAS) has emerged as a potentially sustainable alternative to ordinary OPC. Research suggests that producing AAS composites with intelligent properties, enabling maintenance and repair with minimal external assistance, may be a sustainable solution. Additionally, bacteria-based self-repairing represents a promising and sustainable alternative method for repairing and conducting regular maintenance (39).

3.1 Various Types of Bacteria Used in Concrete

Bacterial strains used in concrete are carefully selected for their ability to thrive in high-pH environments. Typically, microorganisms cannot survive in alkaline conditions with a pH value of 10 or higher (40,41). Table 1 provides a list of bacteria capable of withstanding pH levels equal to or greater than 10.

Table 1. Bacteria that can be usable in concrete in the alkaline environment (41)

No.	Type of the Bacteria	Compressive Strength (+ or -)	Application	References
1	*Sporosarcina Pasteurii*	+	Mortar Concrete Fly Ash	(42–46)
2	*Bacillus cereus*	NA	Mortar Concrete	(47–49)
3	*Bacillus flexus*	NA	Mortar	(50–52)
4	*Bacillus megaterium*	+	Concrete Bricks	(51,53–55)
5	*Bacillus sphaericus*	+	Mortar Concrete	(56–61)
6	*Bacillus halodurans*	NA	Concrete with 10% Cement kiln dust	(62,63)
7	*Bacillus cohnii*	+	Mortar	(64,65)
8	*Bacillus pseudofirmus*	-	Cement stone	(66,67)
9	*Bacillus subtilis*	+	Mortar Concrete	(68–71)
10	*Diaphorobacter nitroreducens*	-	Mortar	(61,72)
11	*Shewanella* sp.	+	Mortar	(73)
12	*Escherichia coli*	NA	Mortar Concrete	(74,75)
13	*Bacillus aureus*	+	Rice Husk Ash	(39)

Among these bacteria, those belonging to the *Bacillus* sp., such as *Bacillus subtilis* and *Bacillus megaterium*, are well-known for their ability to thrive in highly alkaline environments. In such conditions, these bacteria produce spores that resemble plant seeds. These spores have robust walls and remain dormant until cracks develop in the concrete, allowing water to penetrate the structure. When exposed to the pH range of 10 to 11.5, typical of highly alkaline concrete, these bacterial spores become active. Apart from *Bacillus* sp., other bacterial species have also been found to survive in alkaline environments (41,76).

In addition to pH, other factors play a role in the biochemical processes involving bacteria, including the concentration of Ca^{+2} ions, the presence of nucleation sites, and the

availability of dissolved inorganic carbon (77,78). Bacteria play a crucial role in creating an alkaline environment through various pathways, including autotrophic and heterotrophic processes. Among these pathways, enzymatic hydrolysis of urea, aerobic oxidation of organic carbon, and anoxic oxidation of organic carbon have been extensively studied and recognized as significant contributors to alkalinity generation. These processes are essential for establishing favorable conditions for bacteria to thrive and actively participate in the self-healing process of concrete. Extensive research has demonstrated the pivotal role of bacteria in creating an alkaline environment and promoting the healing capabilities of concrete structures (66,79–89).

The specific strains *Bacillus subtilis* and *Bacillus megaterium*, both gram-positive bacteria, are commonly employed in concrete applications. *Bacillus subtilis* possesses a remarkable ability to form highly resistant dormant endospores as a response to nutrient deprivation and environmental stresses. It is commonly found as a gut commensal in humans and can also be present in the upper layer of soil. On the other hand, *Bacillus megaterium*, besides being prevalent in soil, can be found in various environments, including certain food items like honey, as well as on surfaces such as clinical specimens, paper, and stone (90).

In the context of evaluating bacterial influence on concrete properties, it is imperative to discuss the concept of optical density (OD). Optical density is a quantitative measure of the attenuation of light as it passes through a sample containing particles or solutes. In microbiological assays, this measure is often used to estimate the concentration of bacteria within a culture by assessing the light absorption at a specific wavelength, typically 600 nm (OD_{600}). The attenuation is due to both the scattering and absorption of light by the bacterial cells, which corresponds to their concentration in the culture medium. The relevance of OD measurements in microbial concrete research lies in its ability to correlate bacterial concentrations with the observed effects on concrete's mechanical properties. In self-healing concrete, where bacterial activity is pivotal, an optimal OD value indicates the effective concentration of bacteria required to precipitate calcium carbonate to heal cracks and enhance the structural integrity of the concrete. It is this precise and careful calibration of bacterial density, ascertained through OD measurements, that allows for the targeted improvement of compressive strength and other key concrete properties.

By carefully selecting bacterial strains that can survive and thrive in alkaline environments, concrete applications can harness the self-healing properties of these microorganisms, contributing to the durability and resilience of concrete structures.

4. Results and discussions:

4.1 Compressive Strength

After using *Bacillus cereus* and *Bacillus subtilis*, it is observed that compressive strength of the concrete upsurged in both 7 and 28 days. However, the optimum amount of using these kinds of bacteria (optimum amount of *Bacillus cereus* and *Bacillus subtilis*) is 10^3 CFU/mL and 10^5 CFU/mL respectively (48).

The research utilized Ordinary Portland cement (OPC) with 25 grades along with two different bacterial strains, namely *Bacillus cereus* and *Bacillus subtilis*, in the study. Concrete cubes with dimensions of 150×150×150 mm was used for testing. The data presented in Fig. 1 demonstrates the impact of these bacteria on concrete strength.

It can be observed that the optimal concentration of *Bacillus cereus* resulted in a significant enhancement in concrete strength, with a notable 20% increase at both the 7-day and 28-day curing periods. Similarly, the application of *Bacillus subtilis* showcased even more promising results, exhibiting a remarkable 32% increase in concrete strength at the 7-day mark and a commendable 25% increase at the 28-day stage.

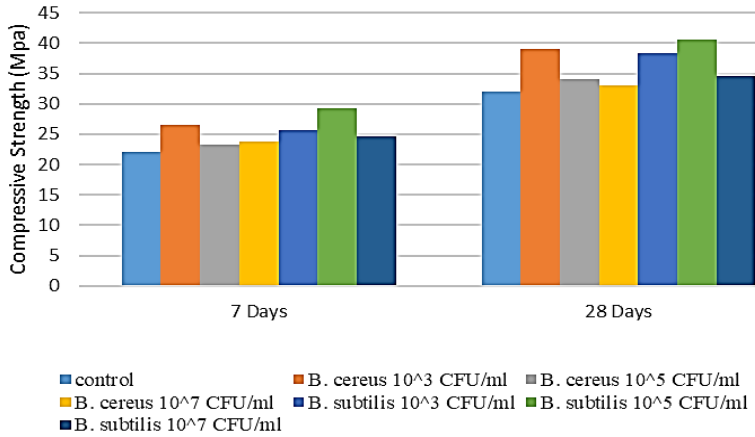

Fig. 1. A comparison about compressive strength of using different types of Bacillus cereus and Bacillus subtilis with different dosages (48)

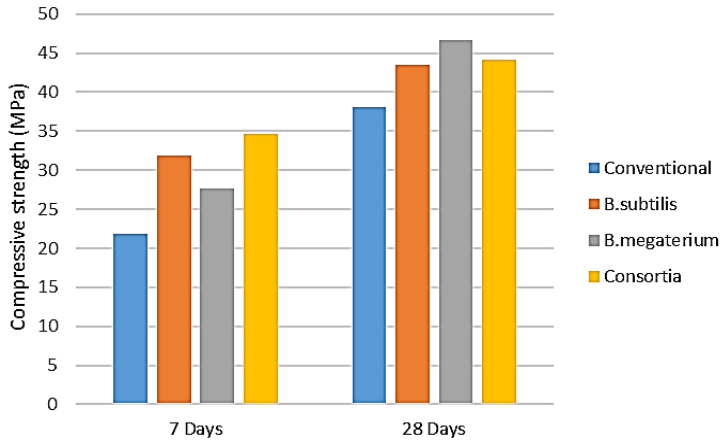

Fig. 2. comparison compressive strength of concrete with different types of bacteria (Bacillus subtilis and Bacillus megaterium) (91)

Based on Figure 2, compressive strength values for four different concrete batches tested at three different curing times: 7 days, 14 days, and 28 days. The concrete utilized is OPC 53 grade, molded into cubes with dimensions of 150mm per side. The chart demonstrates a distinct increase in compressive strength for each batch as the curing time extends from 7 days to 28 days. This suggests that the incorporation of Bacillus sp. Bacteria (specifically Bacillus subtilis and Bacillus megaterium) contributes positively to the strength development of concrete. For instance, Batch 1 shows an appreciable increase in strength at each testing interval, which indicates that the bacterial treatment could be influencing the curing process and improving the concrete's mechanical properties. This pattern is consistent across all batches, confirming the benefit of bacterial additives in concrete mixtures. The data signifies that both early age and longer-term strength properties are enhanced, highlighting the potential for these biological agents to improve construction materials' performance.

Also, it is observed that concrete batches treated with Bacillus megaterium initially demonstrate lower compressive strength at the 7-day mark compared to those treated

with Bacillus subtilis and the combined consortia. This initial lag suggests that Bacillus megaterium may have a slower start in the bio-mineralization process which contributes to the concrete's strength. However, as the curing period extends to 28 days, a remarkable phenomenon occurs: the Bacillus megaterium-treated batches exhibit superior compressive strength compared to their Bacillus subtilis counterparts and the consortia.

The reasons behind this trend could be multifold. It is possible that Bacillus megaterium engages in a more gradual but ultimately more effective calcium carbonate precipitation process, which is a critical factor in concrete strengthening. The delay in strength gain could also be attributed to the specific metabolic pathways of Bacillus megaterium that may take longer to kickstart but result in more robust crystal formation over time. Another aspect to consider is the possibility that Bacillus megaterium could be more effective at pore-filling within the concrete matrix, which becomes evident only in the later stages of curing.

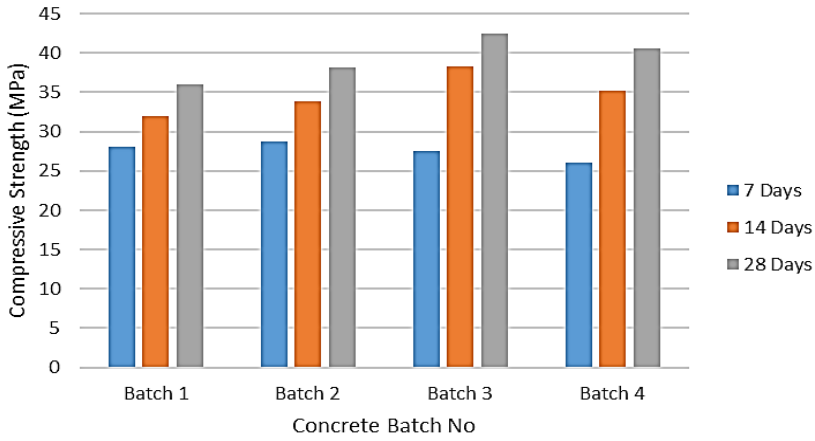

Fig. 3. Compressive strength of using Enterococcus faecalis, Bacillus sp. and mix of Enterococcus faecalis and Bacillus sp. per MPa (92)

In this experiment, the compressive strength of concrete was evaluated over an extended curing period by examining four distinct batches: Batch 1 (control), Batch 2 (*Enterococcus faecalis*), Batch 3 (*Bacillus* sp.), and Batch 4 (combination of *Bacillus* sp. and *Enterococcus faecalis*). The primary objective was to assess the impact of these bacterial compositions on the concrete's strength development. The cube specimens used in the study were 150mm ×150mm ×150mm, and Portland composite cement (PCC) was utilized. The presented graphical representation (Fig. 3) displayed the results obtained from the experiment, with Batch 3 (*Bacillus* sp.) demonstrating the most favorable and optimal outcomes in terms of compressive strength. Notably, the concrete's strength noticeably increased after 7 and 14 days of curing, with Batch 3 exhibiting the highest strength values among all the batches. The inclusion of *Bacillus* sp. at a 5% concentration proved to be effective in enhancing the concrete's compressive strength within the specified time frame. Through this analysis, valuable insights were gained regarding the influence of different bacterial additives on the concrete's performance, contributing to a deeper understanding of their role in enhancing the material's mechanical properties.

Fig. 4 presents the results of the compressive strength test, revealing a consistent enhancement in the strength of the various concrete samples over the curing duration. After 28 days of curing, the compressive strengths of the concrete specimens with different concentrations of *Bacillus subtilis* (0, 10^5, 10^7, and 10^9 cell/ml) were measured at 26.2 MPa,

29.9 MPa, 27.4 MPa, and 26.8 MPa, respectively. Notably, all the tested concretes exhibited higher compressive strengths than the target strength, with all samples incorporating different concentrations of *B. subtilis* outperforming the control sample.

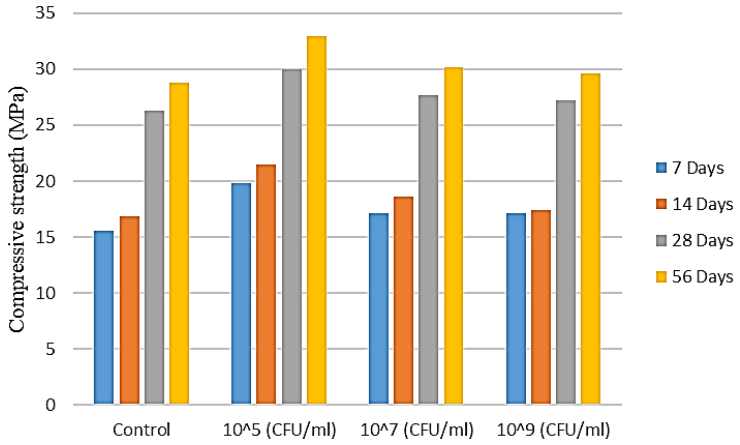

Fig. 4. Compressive strength of concretes with different concentrations of Bacillus subtilis (93)

The percentage increases in strength relative to the control sample were 14%, 5%, and 2% for *B. subtilis* concentrations of 10^5, 10^7, and 10^9, respectively, after 28 days of curing. Similarly, after 56 days of curing, the percentage increases in strength compared to the control sample were 13%, 4%, and 1% for *B. subtilis* concentrations of 10^5, 10^7, and 10^9, respectively, consistent with the 28-day curing results. The obtained results underwent statistical analysis using Analysis of Variance (ANOVA), confirming that both bacterial concentrations and curing duration significantly influenced the compressive strengths of the concrete samples ($p < 0.05$). This analysis highlights the critical role of these factors in determining the performance and quality of the concretes. It is worth noting that for this research, Portland cement (32.5 N) was used as the binder material.

Fig. 5 presents a comparison of different mixes, denoted as Mix 1 to Mix 5, with varying culture densities (OD_{600}) of 0, 0.107, 0.2, 0.637, and 1.221 respectively. The graphical representation highlights the relationship between compressive strengths and optical densities across various curing periods. The control specimen or Mix 1 exhibited compressive strengths of 20.1, 31.8, and 38.9 MPa at the age of 28 days, as per the designed strengths. Notably, all bacterial groups displayed an increase in compressive strength upon the addition of *B. subtilis*, with the highest values recorded in Mix 4 at 23.7, 35.6, and 42.5 MPa respectively.

The compressive strengths of Mix 1 at a curing period of 120 days were determined to be 30.6, 35.8, and 47.1 MPa, while Mix 4 exhibited superior performance compared to the other mixes with recorded values of 35.2, 43.2, and 57.2 MPa for the specified design strengths. Moreover, it illustrates the increase in strengths on the 28th day for different culture densities. It is evident that Mix 4, with a culture density of OD_{600}=0.637, displays a notable improvement across all design strengths. This can be attributed to the enhanced formation of mineral deposits within the internal structures of the concrete. Same results reported from Nivedhitha et. Al while they used the *Bacillus subtilis* for self-healing concrete (95).

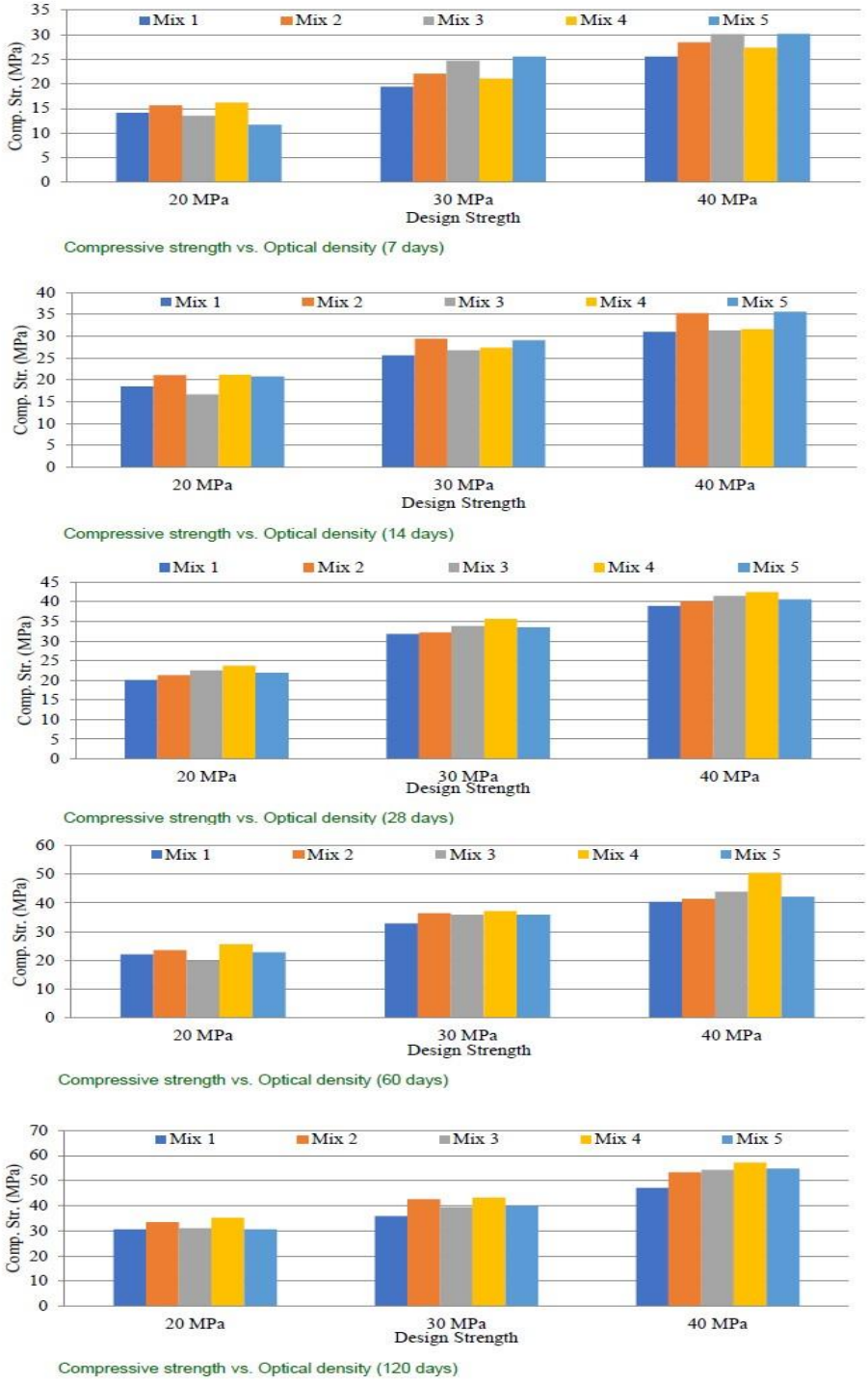

Fig. 5. Comparison of Compressive Strength and Optical Density of Bacillus subtilis (94)

In the domain of microbial-enhanced concrete, the introduction of *Bacillus subtilis* is of paramount significance, which could be elaborated in the context of the experimental observations discussed in Figure 2. Notably, this strain has demonstrated a consistent ability to increase the compressive strength across all bacterial groups. This enhancement is attributable to the unique properties of *Bacillus subtilis* that include promoting better cohesion in the cement matrix, instigating biogenic mineral precipitation, and fostering synergistic interactions within the microbial community embedded in the concrete. Such cohesive interactions are believed to reduce the porosity of concrete, thus densifying the matrix and enhancing the mechanical properties. Furthermore, *Bacillus subtilis* facilitates calcium carbonate precipitation, not merely as a crack-filling agent but as a means to bind concrete constituents more effectively, thereby improving compressive strength. Its ability to stimulate other beneficial bacteria within the concrete also contributes to a more robust and uniformly healed material. The intricacies of these interactions and their influence on the mechanical properties of concrete provide valuable insights into the biological mechanisms underpinning the improved durability and structural integrity of the construction material.

4.2 Tensile Strength

The inclusion of bacteria in concrete demonstrates a parallel effect on the tensile strength, mirroring the notable improvements observed in compressive strength. Tensile strength is an important measure of a material's ability to resist breaking under tension and is crucial for the overall structural integrity of concrete. Fig. 6 displays the outcomes of the tensile strength tests conducted on the concrete samples.

The results indicate that the presence of bacteria has a substantial and successful impact on the tensile strength of the concrete, particularly after a curing period of 7 and 28 days. It is worth noting that the tensile strength values are measured in megapascals (MPa). These findings further support the efficacy of bacteria in enhancing the tensile properties of the concrete over time. Fig. 7 presents a comparative analysis of several concrete mixes, labeled as Mix 1 to Mix 5, with each mix associated with different culture densities represented by the optical density at 600nm (OD_{600}) values.

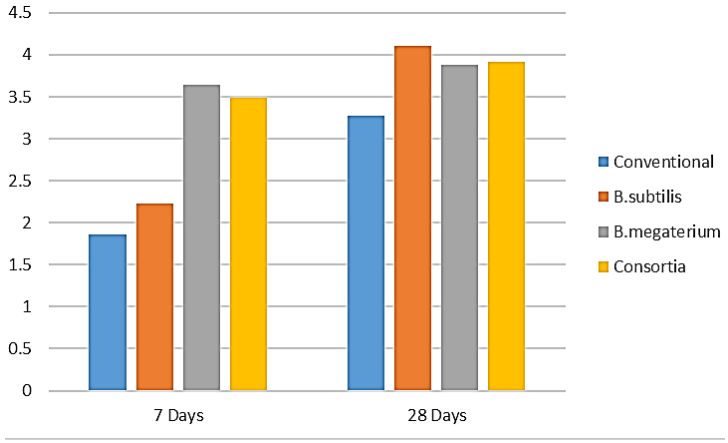

Fig. 6. Comparison tensile strength of concrete with different types of bacteria (Bacillus subtilis and Bacillus megaterium) (91)

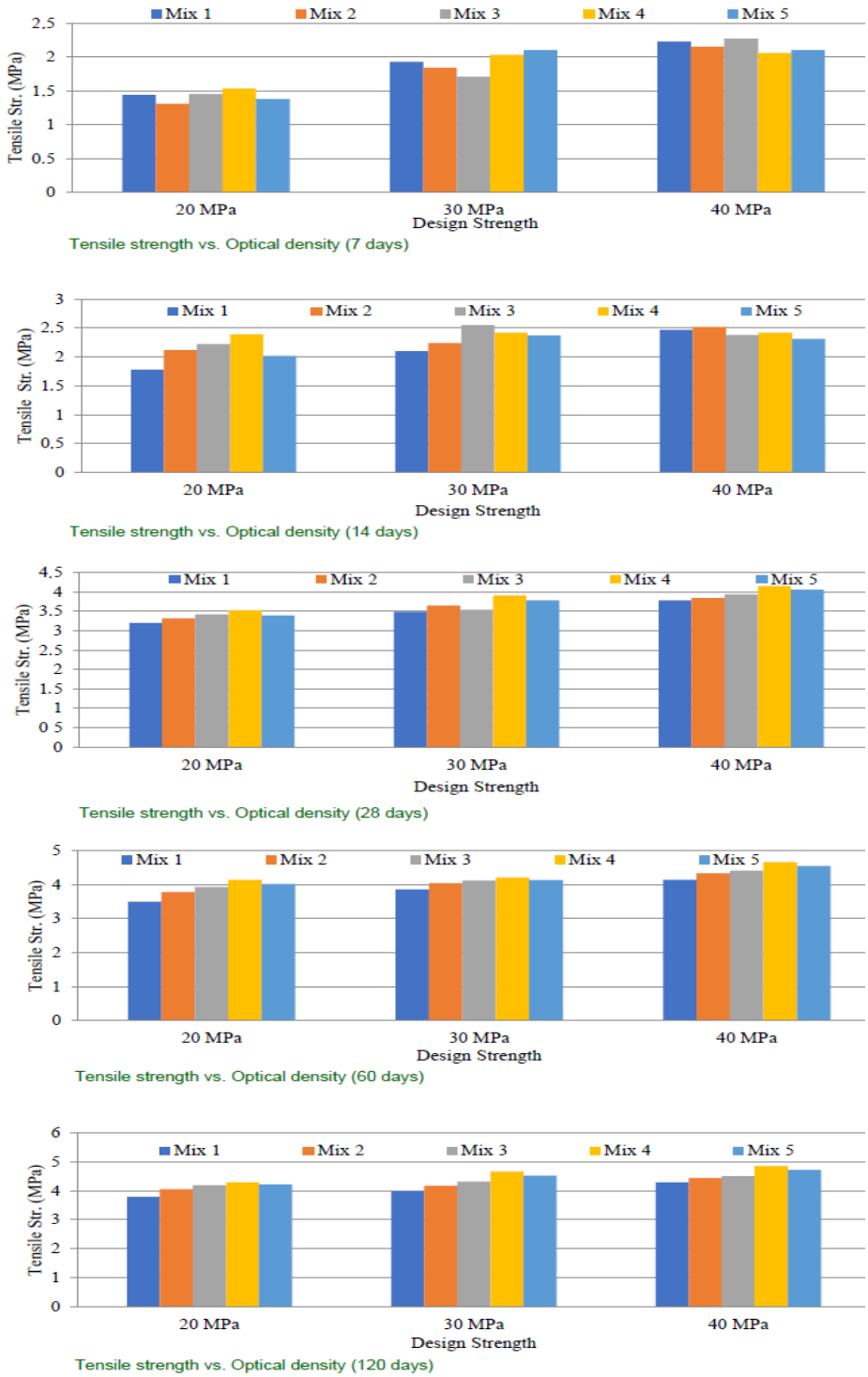

Fig. 7. Comparison of Tensile Strength and Optical Density of Bacillus subtilis (94)

The evaluated mixes correspond to OD_{600} values of 0, 0.107, 0.2, 0.637, and 1.221, respectively, enabling a thorough examination of how varying culture densities influence the performance and properties of the concrete. At a curing period of 28 days, mix 1 exhibited split tensile strengths of 3.2 MPa, 3.5 MPa, and 3.8 MPa for the specified design strengths. Notably, mix 4 demonstrated the highest increase in split tensile strength, reaching values of 3.5 MPa, 3.9 MPa, and 4.2 MPa, respectively, indicating a significant enhancement in its tensile properties compared to the other mixes. Moreover, after an extended curing period of 120 days, Mix 4 exhibited substantial improvements ranging from 13% to 18% in split tensile strength across all grades. This extended curing duration facilitated further development and strengthening of the concrete's tensile capabilities. The results underscore the effectiveness of Mix 4 in enhancing split tensile strength, suggesting its potential for applications requiring improved tensile performance in various construction projects. For this research, specimens were prepared using ordinary Portland cement (OPC) with strength class 42.5 N.

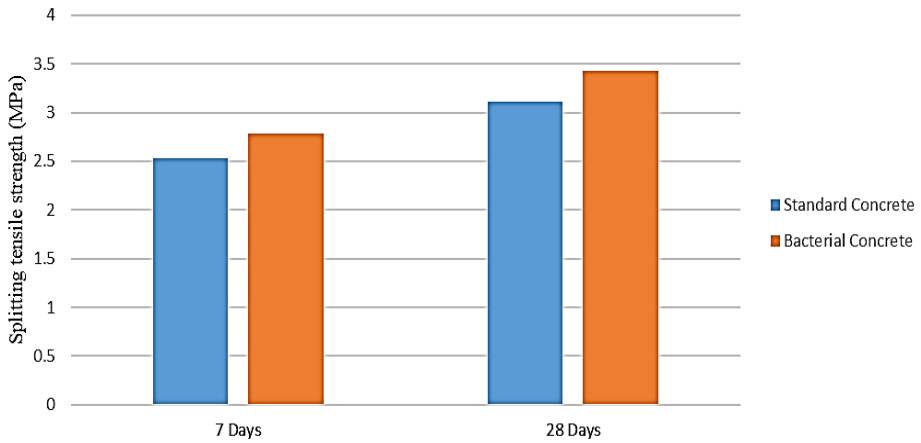

Fig. 8. splitting tensile strength of standard and Bacillus megaterium bacteria concrete. (96)

According to Fig 8, the addition of *Bacillus megaterium* into the concrete mixture results in a noticeable improvement in splitting tensile strength. The concrete samples with *Bacillus megaterium* showed an increase of 9.88% at 7 days and 10.28% at 28 days, compared to the standard concrete samples.

4.3 Water Absorption

Water absorption is a significant and widely recognized test for concrete. In this study, we will delve into the water absorption test while incorporating bacteria and examine their impact on the concrete's strength and the rehabilitation of micro cracks. This investigation aims to shed light on the potential benefits of utilizing bacteria in enhancing concrete properties and durability.

Fig. 9 illustrates the distinctions between Ordinary Portland Cement (OPC) and the addition of a pozzolan replacement, specifically calcined clay concrete (CC), with varying dosages of *Bacillus subtilis*. The incorporation of bacteria in calcined clay concrete led to a notable reduction in water absorption capacity compared to regular concrete and calcined clay concrete. Over a 28-day curing period, the inclusion of *B. subtilis* in calcined clay concrete resulted in water absorption reductions of 18.30%, 17.38%, and 13.59% for 10%, 15%, and 20% calcined clay replacements, respectively. These findings indicate that the water absorption of the specimens decreased in bacterial-infused CC when compared with

specimens without bacteria. The study utilized OPC grade 43 and casted M25 grade of concrete cubes with dimensions of 150×150×150 mm.

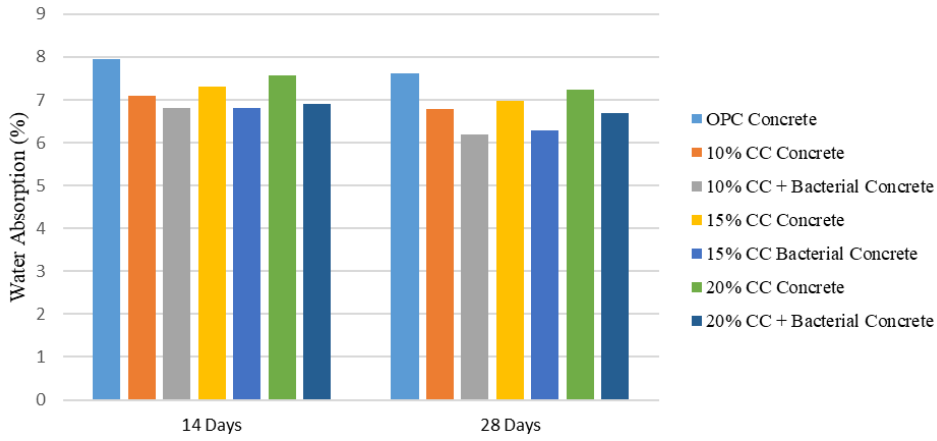

Fig. 9. Analysis of water absorption on calcined clay concrete and OPC in different dosages of bacteria. (97)

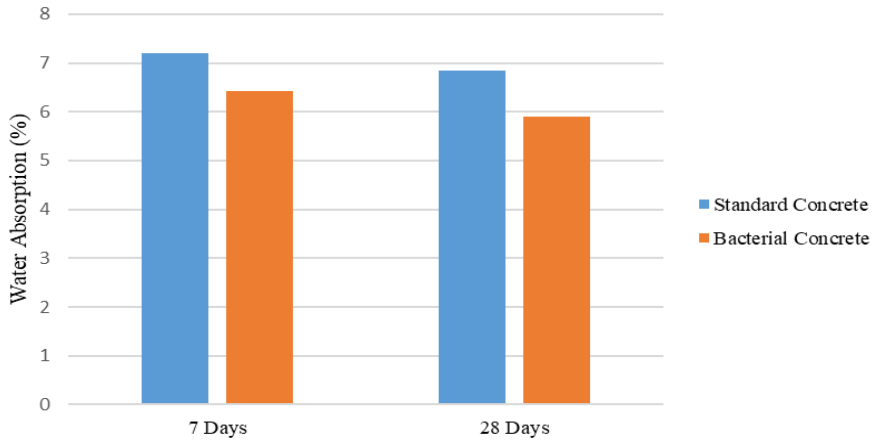

Fig. 10. Water absorption of standard and Bacillus megaterium concrete. (96)

In Fig. 10, the study utilized Ordinary Portland Cement (OPC) of grade 43, and *Bacillus megaterium* at a concentration of 10^8 CFU/mL was employed. The specimens were of size 150mm x 150mm x 150mm. The results demonstrate that when *B. megaterium* is incorporated into the concrete mix, it leads to a reduction in water absorption both at 7 and 28 days, by 5.25% and 7.35%, respectively, as compared to the control samples.

Based on the data presented in Table 2, a comparison was made regarding the impact of various bacterial types on water absorption. The results indicate that *Sporosarcina pasteurii* exhibited the highest effectiveness in reducing water absorption, achieving a remarkable reduction of up to 70%. On the other hand, other *Bacillus* sp. showed a water absorption reduction ranging from 45% to 50%. Consequently, it can be inferred that the selection of bacterial species does not significantly influence the water porosity variation.

Table 2. Water absorption of different bacteria after 28 days of curing. (98)

Type of the Bacteria	Researchers	Results of water absorption after 28 days
B. sphaericus	De Muynck et al. (99), Achal et al. (100)	The concrete sample exhibited a reduction of 45–50% compared to the controlled sample.
B. subtilis	Reddy et al. (101), Muhammad et al. (102), Pei et al. (103)	The concrete sample showed a reduction of nearly 50% compared to the controlled concrete sample.
B. megaterium	Dhamia et al. (53)	The concrete sample exhibited a decrease of 46% compared to the controlled concrete sample.
Sporosarcina pasteurii	Achal et al. (104), Pei et al. (105)	The concrete sample showed a reduction of 50-70% compared to the controlled concrete sample.
B. pseudofirmus	De Muynck et al. (99), Maheshwaran et al.	The concrete sample exhibited a 50% reduction compared to the controlled concrete sample.

Recent studies, as explored in 'Calcium Carbonate Precipitation by Different Bacterial Strains for Concrete Repair', have demonstrated the significant role of bacterial strains like *Bacillus sphaericus* and *Bacillus pasteurii* in enhancing concrete's compressive strength and reducing its water absorption. These strains facilitate the biomineralization process, leading to calcium carbonate formation that not only aids in sealing micro-cracks but also improves the overall structural integrity of the concrete. This innovative approach promises a new dimension in prolonging the durability of concrete structures, particularly in environments subjected to extensive wear and tear (106).

5. Discussion and Recommendation for Future Studies

The exploration into microbial concrete has laid a foundation for innovation within the construction industry, yet it is clear that we have only begun to unearth the full spectrum of its capabilities. Future research directives must be comprehensive and multifaceted to span the depths of this burgeoning field.

Firstly, the scope of microbial agents employed in concrete must be broadened. Diverse microorganisms, including fungi and algae, should be investigated for their unique biogenic processes that may yield more robust and resilient self-healing concrete formulations. Uncovering alternative biological pathways could pave the way for concrete that is not only self-repairing but also possesses enhanced mechanical properties.

Longitudinal studies are imperative to ascertain the long-term viability and efficacy of microbial concrete. Such studies should rigorously evaluate the performance of these

innovative materials against the rigors of environmental stresses encountered in situ, such as freeze-thaw cycles, corrosive chemical exposures, and abrasion. Understanding how microbial concrete withstands such conditions will inform the engineering of materials that can endure through decades rather than just years.

Further, there is an essential need to refine the delivery and maintenance of microbial concentrations within the concrete matrix. Innovative techniques, such as advanced encapsulation or the development of biofilms, must be optimized to balance the microbial activity with structural integrity. These methods should ensure the longevity of microbial viability and consistent healing action throughout the concrete's lifecycle.

Additionally, a thorough ecological and economic analysis is essential to evaluate the sustainability of microbial concrete. This encompasses a complete lifecycle assessment that addresses the environmental impacts from production to end-of-life recycling or disposal. The integration of such assessments will ensure that the advancement in construction materials technology is in concert with our sustainability objectives, minimizing the carbon footprint while maintaining cost-efficiency.

In the vein of scientific inquiry, there is an urgency to decode the biochemical intricacies of microbial calcite precipitation. Understanding the molecular mechanisms that govern this process could lead to the optimization of microbial consortia, tailored for enhanced self-healing efficiency. Investigating how Bacillus subtilis and other bacteria interact with varying concrete compositions will allow for broader application and more customized material solutions.

The path to harnessing the full potential of microbial technologies within construction materials is complex, demanding a confluence of expertise from disciplines such as microbiology, material science, and civil engineering. Collaborative research efforts must converge to innovate resilient, self-sustaining, and environmentally benign construction materials. As we stride toward this goal, we must also ensure that our scientific and engineering pursuits are scalable and transferable to practical applications, cementing the legacy of microbial concrete as a pillar of sustainable development in the construction industry.

6. Conclusion

The study meticulously explores the innovative integration of microbial technologies in the construction sector, specifically through the development of self-healing concrete utilizing bacterial agents. The investigation has illuminated the significant role of bacteria, notably the Bacillus species, in autonomously repairing microcracks that compromise the structural integrity of concrete. This self-healing mechanism, driven by the microbial-induced calcite precipitation process, not only seals cracks but also contributes to the long-term durability and strength of the concrete infrastructure.

Our comprehensive analysis has revealed that the incorporation of bacteria like Bacillus cereus and Bacillus subtilis leads to marked improvements in the compressive strength of concrete within the initial seven days of curing. This enhancement persists and becomes more pronounced with prolonged curing periods, underlining the enduring benefits of microbial action on the concrete's mechanical properties. The optimal bacterial dosages and specific curing conditions emerge as critical factors that significantly influence the efficacy of the self-healing process, necessitating further research to establish standardized protocols for practical applications.

Furthermore, the study extends beyond the immediate realm of self-healing concrete to explore broader applications of microbial interventions in construction materials. This includes the development of bioconcrete and biocement, which leverage microbial

activities for material fortification and sustainability. The soil stabilization techniques enhanced by microbial action also present a promising avenue for improving the foundational stability of construction sites, particularly in geotechnically challenging environments.

The empirical evidence gathered points to a substantial reduction in water absorption rates in microbially treated concrete, a factor that contributes to the material's resilience against environmental degradation and extends its service life. The nuanced interplay between bacterial concentration, culture density, and environmental conditions in dictating the performance of microbial concrete underscores the complexity of this innovative technology.

The integration of microbial technologies in the construction industry heralds a transformative era in material science, where sustainability, durability, and self-repairing capabilities become intrinsic characteristics of construction materials. The potential of bacteria-infused concrete to revolutionize building practices is immense, offering a sustainable solution to the perennial challenges of material degradation and environmental impact. However, the path to widespread adoption and optimization of these technologies are paved with challenges that necessitate meticulous research, standardized testing protocols, and a deeper understanding of microbial ecology within construction materials.

The dynamic interplay of bacterial agents within the concrete matrix heralds a complex ecosystem, whose understanding is pivotal for the optimization of material properties and engineering applications. Future investigations must delve into the nuanced mechanisms of bacterial interactions, with an emphasis on real-time dynamics and long-term impacts on structural resilience and durability. Moreover, the potential for an engineered synergy between diverse microbial species and concrete formulations beckons a new frontier in construction material science. To translate this pioneering research into tangible engineering practices, it is imperative to devise strategies for the scaled-up application that address economic feasibility, environmental considerations, and compatibility with existing construction methodologies. The pathway forward is collaborative and interdisciplinary, requiring concerted efforts from microbiologists, material scientists, and civil engineers, to harness the full spectrum of benefits offered by microbial technologies in construction.

While this study has provided valuable insights into the potential of microbial concrete, particularly focusing on self-healing properties and the role of Bacillus species, it acknowledges certain limitations. The experimental conditions under which the microbial concrete's performance was evaluated might not fully replicate the complex environmental conditions encountered in real-world applications. The longevity and sustainability of the microbial-induced healing process under varied climatic and loading conditions remain to be comprehensively understood. Additionally, while the study explored a range of bacterial species, the ecological impact of introducing these microorganisms into construction materials warrants further investigation to ensure that no adverse environmental consequences arise. Economic feasibility, scalability of the microbial application process, and the potential for microbial resistance development in the concrete matrix are aspects that need to be addressed in future research. These limitations underline the necessity for continued and extensive investigation into the dynamics of microbial concrete to optimize its application in the construction industry and to fully understand its environmental implications.

Acknowledgement

I would like to express my sincere gratitude to Associate Professor Dr. Mümtaz Güran for his exemplary guidance, invaluable teaching methods, and insightful contributions to both this paper and my thesis.

References

[1] Aytekin B, Mardani A, Yazıcı Ş. State-of-art review of bacteria-based self-healing concrete: Biomineralization process, crack healing, and mechanical properties. Constr Build Mater. 2023 May 16;378:131198. https://doi.org/10.1016/j.conbuildmat.2023.131198

[2] Shantilal Vekariya M, Pitroda J. Bacterial Concrete: New Era For Construction Industry. International Journal of Engineering Trends and Technology [Internet]. 2013;4(9). Available from: http://www.ijettjournal.org

[3] Natalli JF, Thomaz ECS, Mendes JC, Peixoto RAF. A review on the evolution of Portland cement and chemical admixtures in Brazil. Revista IBRACON de Estruturas e Materiais. 2021;14(6). https://doi.org/10.1590/s1983-41952021000600003

[4] Zhang P, Wang C, Gao Z, Wang F. A review on fracture properties of steel fiber reinforced concrete. Journal of Building Engineering. 2023 May 15;67:105975. https://doi.org/10.1016/j.jobe.2023.105975

[5] Mujalli MA, Dirar S, Mushtaha E, Hussien A, Maksoud A. Evaluation of the Tensile Characteristics and Bond Behaviour of Steel Fibre-Reinforced Concrete: An Overview. Fibers. 2022 Dec 2;10(12):104. https://doi.org/10.3390/fib10120104

[6] P.K. Mehta RWB. Building durable structures in the 21st century. 2001 Sep;36(9):57-63. https://doi.org/10.2115/fiber.57.P_36

[7] MOHD Mehndi S, Ahmad S, Mohd Mehndi Meraj Ahmad Khan S. Causes And Evaluation Of Cracks In Concrete Structures. In: International Journal of Technical Research and Applications. 2020. p. 29-33.

[8] Yang Z, Hollar J, He X, Shi X. Laboratory Assessment of a Self-Healing Cementitious Composite. Transportation Research Record: Journal of the Transportation Research Board. 2010 Jan 1;2142(1):9-17. https://doi.org/10.3141/2142-02

[9] Kandalkar M, Bhatkar M. Comparative Study of Self-Healing Concrete & Normal Concrete. International Research Journal of Engineering and Technology [Internet]. 2020; Available from: www.irjet.net

[10] Udhaya S, Vandhana Devi V, Philips J, Lija RL. Experimental study on bio-concrete for sustainable construction. Mater Today Proc. 2023 Apr 5; https://doi.org/10.1016/j.matpr.2023.03.676

[11] Saravanan S, Nagajothi S, Elavenil S. Investigation On Compressive Strength Development Of Geopolymer Concrete Using Manufactured Sand [Internet]. Vol. 18, Materials Today: Proceedings. 2019. https://doi.org/10.1016/j.matpr.2019.06.284

[12] Chaitanya M, Manikandan P, Prem Kumar V, Elavenil S, Vasugi V. Prediction of self-healing characteristics of GGBS admixed concrete using Artificial Neural Network. J Phys Conf Ser. 2020 Dec 1;1716(1):012019. https://doi.org/10.1088/1742-6596/1716/1/012019

[13] Cappellesso V, di Summa D, Pourhaji P, Prabhu Kannikachalam N, Dabral K, Ferrara L, et al. A review of the efficiency of self-healing concrete technologies for durable and sustainable concrete under realistic conditions. International Materials Reviews. 2023 Jul 4;68(5):556-603. https://doi.org/10.1080/09506608.2022.2145747

[14] Subramanian N, Solaiyan E, Sendrayaperumal A, Lakshmaiya N. Flexural behaviour of geopolymer concrete beams reinforced with BFRP and GFRP polymer composites. Advances in Structural Engineering. 2022 Apr 11;25(5):954-65. https://doi.org/10.1177/13694332211054229

[15] Chaitanya M, Manikandan P, Prem Kumar V, Elavenil S, Vasugi V. Prediction of self-healing characteristics of GGBS admixed concrete using Artificial Neural Network. J Phys Conf Ser. 2020 Dec 1;1716(1):012019. https://doi.org/10.1088/1742-6596/1716/1/012019
[16] Aleem A, Sundararajan V. Chemical Formulation of Geopolymer Concrete with M-Sand. International Journal of Research in Civil Engineering, Architecture & Design [Internet]. 2013 Oct;1(2):54-60. Available from: www.iaster.com
[17] Intarasoontron J, Pungrasmi W, Nuaklong P, Jongvivatsakul P, Likitlersuang S. Comparing performances of MICP bacterial vegetative cell and microencapsulated bacterial spore methods on concrete crack healing. Constr Build Mater. 2021 Oct;302:124227. https://doi.org/10.1016/j.conbuildmat.2021.124227
[18] Alemu D, Demiss W, Korsa G. Bacterial Performance in Crack Healing and its Role in Creating Sustainable Construction. Int J Microbiol. 2022 Jul 7;2022:1-10. https://doi.org/10.1155/2022/6907314
[19] Jongvivatsakul P, Janprasit K, Nuaklong P, Pungrasmi W, Likitlersuang S. Investigation of the crack healing performance in mortar using microbially induced calcium carbonate precipitation (MICP) method. Constr Build Mater. 2019 Jul;212:737-44. https://doi.org/10.1016/j.conbuildmat.2019.04.035
[20] Amran M, Onaizi AM, Fediuk R, Vatin NI, Muhammad Rashid RS, Abdelgader H, et al. Self-Healing Concrete as a Prospective Construction Material: A Review. Materials. 2022 Apr 29;15(9):3214. https://doi.org/10.3390/ma15093214
[21] Han B, Yu X, Ou J. Challenges of Self-Sensing Concrete. In: Self-Sensing Concrete in Smart Structures. Elsevier; 2014. p. 361-76. https://doi.org/10.1016/B978-0-12-800517-0.00011-3
[22] Ryłko-Polak I, Komala W, Białowiec A. The Reuse of Biomass and Industrial Waste in Biocomposite Construction Materials for Decreasing Natural Resource Use and Mitigating the Environmental Impact of the Construction Industry: A Review. Materials. 2022 Jun 8;15(12):4078. https://doi.org/10.3390/ma15124078
[23] JOHN M, THOMAS S. Biofibres and biocomposites. Carbohydr Polym. 2008 Feb 8;71(3):343-64. https://doi.org/10.1016/j.carbpol.2007.05.040
[24] Mohammed AABA, Omran AAB, Hasan Z, Ilyas RA, Sapuan SM. Wheat Biocomposite Extraction, Structure, Properties and Characterization: A Review. Polymers (Basel). 2021 Oct 21;13(21):3624. https://doi.org/10.3390/polym13213624
[25] Kashif Ur Rehman S, Mahmood F, Jameel M, Riaz N, Javed M, Salmi A, et al. A Biomineralization, Mechanical and Durability Features of Bacteria-Based Self-Healing Concrete-A State of the Art Review. Crystals (Basel). 2022 Aug 29;12(9):1222. https://doi.org/10.3390/cryst12091222
[26] Ahmed SO, Nasser AA, Abbas RN, Kamal MM, Zahran MA, Sorour NM. Production of bioconcrete with improved durability properties using Alkaliphilic Egyptian bacteria. 3 Biotech. 2021 May 22;11(5):231. https://doi.org/10.1007/s13205-021-02781-0
[27] Gowthaman S, Mitsuyama S, Nakashima K, Komatsu M, Kawasaki S. Biogeotechnical approach for slope soil stabilization using locally isolated bacteria and inexpensive low-grade chemicals: A feasibility study on Hokkaido expressway soil, Japan. Soils and Foundations. 2019 Apr;59(2):484-99. https://doi.org/10.1016/j.sandf.2018.12.010
[28] Ramachandran AL, Dubey AA, Dhami NK, Mukherjee A. Multiscale Study of Soil Stabilization Using Bacterial Biopolymers. Journal of Geotechnical and Geoenvironmental Engineering. 2021 Aug;147(8). https://doi.org/10.1061/(ASCE)GT.1943-5606.0002575
[29] Soundara B, Kulanthaivel P, Nithipandian S, Soundaryan V. A critical review on soil stabilization using bacteria. IOP Conf Ser Mater Sci Eng. 2020 Nov 1;955(1):012065. https://doi.org/10.1088/1757-899X/955/1/012065

[30] Sidiq A, Gravina R, Giustozzi F. Is concrete healing really efficient? A review. Constr Build Mater. 2019 Apr 30;205:257-73. https://doi.org/10.1016/j.conbuildmat.2019.02.002
[31] Kumar Jogi P, Vara Lakshmi TVS. Self healing concrete based on different bacteria: A review. Mater Today Proc. 2021;43:1246-52. https://doi.org/10.1016/j.matpr.2020.08.765
[32] Islam MdM, Hoque N, Islam M, Ibney Gias I. An Experimental Study on the Strength and Crack Healing Performance of E. coli Bacteria-Induced Microbial Concrete. Advances in Civil Engineering. 2022 Apr 15;2022:1-13. https://doi.org/10.1155/2022/3060230
[33] Sarkar M, Maiti M, Malik MA, Xu S. Evaluation of the crack-healing performance and durability of bacteria integrated alkali-activated fly ash composites. Journal of Building Engineering. 2022 Aug 15;54:104642. https://doi.org/10.1016/j.jobe.2022.104642
[34] Chen B, Sun W, Sun X, Cui C, Lai J, Wang Y, et al. Crack sealing evaluation of self-healing mortar with Sporosarcina pasteurii: Influence of bacterial concentration and air-entraining agent. Process Biochemistry. 2021 Aug 1;107:100-11. https://doi.org/10.1016/j.procbio.2021.05.001
[35] Abd Majid M, Ali Fulazzaky M, Tin Lee C. A Review of Self-healing Concrete Research Development. 2014.
[36] Wu M, Johannesson B, Geiker M. A review: Self-healing in cementitious materials and engineered cementitious composite as a self-healing material. Constr Build Mater. 2012 Mar 1;28(1):571-83. https://doi.org/10.1016/j.conbuildmat.2011.08.086
[37] Griño AA, M. Daly MaK, Ongpeng JMC. Bio-Influenced Self-Healing Mechanism in Concrete and Its Testing: A Review. Applied Sciences. 2020 Jul 27;10(15):5161. https://doi.org/10.3390/app10155161
[38] Nuaklong P, Jongvivatsakul P, Phanupornprapong V, Intarasoontron J, Shahzadi H, Pungrasmi W, et al. Self-repairing of shrinkage crack in mortar containing microencapsulated bacterial spores. Journal of Materials Research and Technology. 2023 Mar;23:3441-54. https://doi.org/10.1016/j.jmrt.2023.02.010
[39] Hammad N, Elnemr A, Shaaban IG. State-of-the-Art Report: The Self-Healing Capability of Alkali-Activated Slag (AAS) Concrete. Materials. 2023 Jun 14;16(12):4394. https://doi.org/10.3390/ma16124394
[40] Padan E, Bibi E, Ito M, Krulwich TA. Alkaline pH homeostasis in bacteria: New insights. Biochimica et Biophysica Acta (BBA) - Biomembranes. 2005 Nov;1717(2):67-88. https://doi.org/10.1016/j.bbamem.2005.09.010
[41] Kumari N, Kumari S, Malik S. SELF-HEALING CONCRETE-LIMITATIONS & OPPORTUNITIES. www.irjmets.com @International Research Journal of Modernization in Engineering [Internet]. 515. Available from: www.irjmets.com
[42] SK Ramachandran, V Ramakrishnan, SS Bang. Remediation of Concrete Using Microorganisms. ACI Mater J. 2001;98(1). https://doi.org/10.14359/10154
[43] Bang SS, Galinat JK, Ramakrishnan V. Calcite precipitation induced by polyurethane-immobilized Bacillus pasteurii. Enzyme Microb Technol. 2001 Mar;28(4-5):404-9. https://doi.org/10.1016/S0141-0229(00)00348-3
[44] Abo-El-Enein SA, Ali AH, Talkhan FN, Abdel-Gawwad HA. Application of microbial biocementation to improve the physico-mechanical properties of cement mortar. HBRC Journal. 2013 Apr 17;9(1):36-40. https://doi.org/10.1016/j.hbrcj.2012.10.004
[45] Chahal N, Siddique R, Rajor A. Influence of bacteria on the compressive strength, water absorption and rapid chloride permeability of fly ash concrete. Constr Build Mater. 2012 Mar;28(1):351-6. https://doi.org/10.1016/j.conbuildmat.2011.07.042
[46] Chen B, Sun W, Sun X, Cui C, Lai J, Wang Y, et al. Crack sealing evaluation of self-healing mortar with Sporosarcina pasteurii: Influence of bacterial concentration and air-entraining agent. Process Biochemistry. 2021 Aug;107:100-11. https://doi.org/10.1016/j.procbio.2021.05.001

[47] Maheswaran S, Dasuru SS, Murthy ARC, Bhuvaneshwari B, Kumar VR, Palani GS, et al. Strength improvement studies using new type wild strain Bacillus cereus on cement mortar. Curr Sci [Internet]. 2014;106(1):50-7. Available from: http://www.jstor.org/stable/24099862
[48] Mondal S, Das P, Kumar Chakraborty A. Application of Bacteria in Concrete. Mater Today Proc. 2017;4(9):9833-6. https://doi.org/10.1016/j.matpr.2017.06.276
[49] Rahaman S, Dutta JR, Bandyopadhyay M, Kar A. Laboratory Investigations to Optimize the Physicochemical Parameters for Bacillus cereus Inclusions in Concrete for Enhanced Compressive Strength and Chloride Resistance. Journal of The Institution of Engineers (India): Series A. 2022 Dec 6;103(4):1147-64. https://doi.org/10.1007/s40030-022-00685-7
[50] Jagadeesha Kumar B G, R Prabhakara, Pushpa H. Effect of Bacterial Calcite Precipitation on Compressive Strength of Mortar Cubes. 2013 Feb.
[51] Krishnapriya S, Venkatesh Babu DL, G. PA. Isolation and identification of bacteria to improve the strength of concrete. Microbiol Res. 2015 May;174:48-55. https://doi.org/10.1016/j.micres.2015.03.009
[52] Mahmoud HHA, Kalaba MH, El-Sherbiny GME, Mostafa AEA, Ouf MEA, Tawhed WMF. Sustainable repairing and improvement of concrete properties using artificial bacterial consortium. J Sustain Cem Based Mater. 2022 Nov 2;11(6):465-78. https://doi.org/10.1080/21650373.2021.2003908
[53] Dhami NK, Reddy MS, Mukherjee A. Improvement in strength properties of ash bricks by bacterial calcite. Ecol Eng. 2012 Feb;39:31-5. https://doi.org/10.1016/j.ecoleng.2011.11.011
[54] Andalib R, Abd Majid MZ, Hussin MW, Ponraj M, Keyvanfar A, Mirza J, et al. Optimum concentration of Bacillus megaterium for strengthening structural concrete. Constr Build Mater. 2016 Aug;118:180-93. https://doi.org/10.1016/j.conbuildmat.2016.04.142
[55] Ul Islam S, Waseem SA. Strength retrieval and microstructural characterization of Bacillus subtilis and Bacillus megaterium incorporated plain and reinforced concrete. Constr Build Mater. 2023 Nov;404:133331. https://doi.org/10.1016/j.conbuildmat.2023.133331
[56] Muynck D, Belie D, Verstraete W. Improvement Of Concrete Durability With The Aid Of Bacteria. In: Proceedings of the First International Conference on Self Healing Materials. Noordwijk aan Zee, The Netherlands; 2007.
[57] De Muynck W, Debrouwer D, De Belie N, Verstraete W. Bacterial carbonate precipitation improves the durability of cementitious materials. Cem Concr Res. 2008 Jul;38(7):1005-14. https://doi.org/10.1016/j.cemconres.2008.03.005
[58] Gavimath CC, Mali BM, Hooli VR, Mallpur JD, Patil AB, Gaddi DP, et al. Potential Application Of Bacteria To Improve The Strength Of Cement Concrete [Internet]. Vol. 3, International Journal of Advanced Biotechnology and Research. 2012. Available from: http://www.bipublication.com
[59] Wang JY, Soens H, Verstraete W, De Belie N. Self-healing concrete by use of microencapsulated bacterial spores. Cem Concr Res. 2014 Feb;56:139-52. https://doi.org/10.1016/j.cemconres.2013.11.009
[60] Mahat SB, Johari MAM, Mokhtar N, Kok Keong C, Idris MN, Wan Zakaria WZE, et al. Phenomena of Bacillus sphaericus LMG 22257 Activity and Its Influence on Properties of Portland Cement Mortar Exposed to Different Curing Media. Separations. 2022 Dec 29;10(1):19. https://doi.org/10.3390/separations10010019
[61] Erşan YÇ, Da Silva FB, Boon N, Verstraete W, De Belie N. Screening of bacteria and concrete compatible protection materials. Constr Build Mater. 2015 Jul;88:196-203. https://doi.org/10.1016/j.conbuildmat.2015.04.027

[62] Kunal, Siddique R, Rajor A. Influence of bacterial treated cement kiln dust on the properties of concrete. Constr Build Mater. 2014 Feb;52:42-51. https://doi.org/10.1016/j.conbuildmat.2013.11.034
[63] Durga CSS, Venkatesh C, Muralidhararao T, Bellum RR, Rao BNM. Estimation of durability properties of self-healing concrete influenced by different bacillus species. Research On Engineering Structures and Materials. 2023; https://doi.org/10.17515/resm2023.745st0423
[64] Sierra-Beltran MG, Jonkers HM, Schlangen E. Characterization of sustainable bio-based mortar for concrete repair. Constr Build Mater. 2014 Sep;67:344-52. https://doi.org/10.1016/j.conbuildmat.2014.01.012
[65] Dipendraditya K, Singh BK. Performance of Bacillus Cohnii Added Microbial Concrete. Civil Engineering and Architecture. 2023 Jan;11(1):525-30. https://doi.org/10.13189/cea.2023.110141
[66] Jonkers HM, Thijssen A, Muyzer G, Copuroglu O, Schlangen E. Application of bacteria as self-healing agent for the development of sustainable concrete. Ecol Eng. 2010 Feb 1;36(2):230-5. https://doi.org/10.1016/j.ecoleng.2008.12.036
[67] Nežerka V, Demo P, Schreiberová H, Ryparová P, Bílý P. Self-healing concrete: application of monod's approach for modeling Bacillus pseudofirmus growth curves. European Journal of Environmental and Civil Engineering. 2022 Dec 10;26(16):8229-41. https://doi.org/10.1080/19648189.2021.2021996
[68] Nugroho A, Satyarno I, Subyakto S. Bacteria as Self-Healing Agent in Mortar Cracks. Journal of Engineering and Technological Sciences. 2015 Jul;47(3):279-95. https://doi.org/10.5614/j.eng.technol.sci.2015.47.3.4
[69] Chakraborty AK, Mondal S. Bacterial concrete: A way to enhance the durability of concrete structures. Indian Concr J. 2017;91:30-6.
[70] Wiegert T, Homuth G, Versteeg S, Schumann W. Alkaline shock induces the Bacillus subtilisσW regulon. Mol Microbiol. 2001 Dec 21;41(1):59-71. https://doi.org/10.1046/j.1365-2958.2001.02489.x
[71] Karimi N, Mostofinejad D. Bacillus subtilis bacteria used in fiber reinforced concrete and their effects on concrete penetrability. Constr Build Mater. 2020 Jan;230:117051. https://doi.org/10.1016/j.conbuildmat.2019.117051
[72] Soysal A, Milla J, King GM, Hassan M, Rupnow T. Evaluating the Self-Healing Efficiency of Hydrogel-Encapsulated Bacteria in Concrete. Transportation Research Record: Journal of the Transportation Research Board. 2020 Jun 22;2674(6):113-23. https://doi.org/10.1177/0361198120917973
[73] Ghosh S, Biswas M, Chattopadhyay BD, Mandal S. Microbial activity on the microstructure of bacteria modified mortar. Cem Concr Compos. 2009 Feb;31(2):93-8. https://doi.org/10.1016/j.cemconcomp.2009.01.001
[74] Ghosh P, Mandal S, Bandyopadhyaya G, Chattopadhyay BD. Development of bioconcrete material using an enrichment culture of novel thermophilic anaerobic bacteria. Vol. 44, Indian Journal of Experimental Biology. 2006.
[75] Islam MdM, Hoque N, Islam M, Ibney Gias I. An Experimental Study on the Strength and Crack Healing Performance of E. coli Bacteria-Induced Microbial Concrete. Advances in Civil Engineering. 2022 Apr 15;2022:1-13. https://doi.org/10.1155/2022/3060230
[76] Cho WI, Chung MS. Bacillus spores: a review of their properties and inactivation processing technologies. Food Sci Biotechnol. 2020 Nov 6;29(11):1447-61. https://doi.org/10.1007/s10068-020-00809-4
[77] Stocks-Fischer S, Galinat JK, Bang SS. Microbiological precipitation of CaCO3. Soil Biol Biochem. 1999 Oct;31(11):1563-71. https://doi.org/10.1016/S0038-0717(99)00082-6

[78] Hammes F, Verstraete W. Key roles of pH and calcium metabolism in microbial carbonate precipitation [Internet]. Vol. 1, Re/Views in Environmental Science & Bio/Technology. 2002.
[79] Mondal S, Ghosh A (Dey). Spore-forming Bacillus subtilis vis-à-vis non-spore-forming Deinococcus radiodurans, a novel bacterium for self-healing of concrete structures: A comparative study. Constr Build Mater. 2021 Jan;266:121122. https://doi.org/10.1016/j.conbuildmat.2020.121122
[80] Wong LS. Microbial cementation of ureolytic bacteria from the genus Bacillus: a review of the bacterial application on cement-based materials for cleaner productio n. J Clean Prod. 2015 Apr 15;93:5-17. https://doi.org/10.1016/j.jclepro.2015.01.019
[81] Vijay K, Murmu M, Deo S V. Bacteria based self healing concrete - A review. Constr Build Mater. 2017 Oct;152:1008-14. https://doi.org/10.1016/j.conbuildmat.2017.07.040
[82] Tziviloglou E, Van Tittelboom K, Palin D, Wang J, Sierra-Beltrán MG, Erşan YÇ, et al. Bio-Based Self-Healing Concrete: From Research to Field Application. In 2016. p. 345-85. https://doi.org/10.1007/12_2015_332
[83] Li W, Dong B, Yang Z, Xu J, Chen Q, Li H, et al. Recent Advances in Intrinsic Self-Healing Cementitious Materials. Advanced Materials. 2018 Apr;30(17):1705679. https://doi.org/10.1002/adma.201705679
[84] Erşan YÇ, Van Tittelboom K, Boon N, De Belie N. Nitrite producing bacteria inhibit reinforcement bar corrosion in cementitious materials. Sci Rep. 2018 Dec 1;8(1). https://doi.org/10.1038/s41598-018-32463-6
[85] Erşan YÇ, Verbruggen H, De Graeve I, Verstraete W, De Belie N, Boon N. Nitrate reducing CaCO3 precipitating bacteria survive in mortar and inhibit steel corrosion. Cem Concr Res. 2016 May 1;83:19-30. https://doi.org/10.1016/j.cemconres.2016.01.009
[86] Xu J, Chen B, Xie T. Experimental and theoretical analysis of bubble departure behavior in narrow rectangular channel. Progress in Nuclear Energy. 2014 Nov 1;77:1-10. https://doi.org/10.1016/j.pnucene.2014.06.002
[87] Wang JY, De Belie N, Verstraete W. Diatomaceous earth as a protective vehicle for bacteria applied for self-healing concrete. J Ind Microbiol Biotechnol. 2012 Apr 1;39(4):567-77. https://doi.org/10.1007/s10295-011-1037-1
[88] Wiktor V, Jonkers HM. Quantification of crack-healing in novel bacteria-based self-healing concrete. Cem Concr Compos. 2011 Aug 1;33(7):763-70. https://doi.org/10.1016/j.cemconcomp.2011.03.012
[89] Mohammadi SA, Najafi H, Zolgharnian S, Sharifian S, Asasian-Kolur N. Biological oxidation methods for the removal of organic and inorganic contaminants from wastewater: A comprehensive review. Science of The Total Environment. 2022 Oct 15;843:157026. https://doi.org/10.1016/j.scitotenv.2022.157026
[90] Nicholson WL, Munakata N, Horneck G, Melosh HJ, Setlow P. Resistance of Bacillus Endospores to Extreme Terrestrial and Extraterrestrial Environments. Microbiology and Molecular Biology Reviews. 2000 Sep;64(3):548-72. https://doi.org/10.1128/MMBR.64.3.548-572.2000
[91] Nain N, Surabhi R, Yathish N V., Krishnamurthy V, Deepa T, Tharannum S. Enhancement in strength parameters of concrete by application of Bacillus bacteria. Constr Build Mater. 2019 Mar 30;202:904-8. https://doi.org/10.1016/j.conbuildmat.2019.01.059
[92] Anneza LH, Irwan JM, Othman N, Alshalif AF. Identification of Bacteria and the Effect on Compressive Strength of Concrete. MATEC Web of Conferences. 2016 Apr 1;47:01008. https://doi.org/10.1051/matecconf/20164701008
[93] Akindahunsi AA, Adeyemo SM, Adeoye A. The use of bacteria (Bacillus subtilis) in improving the mechanical properties of concrete. Journal of Building Pathology and Rehabilitation. 2021 Dec 15;6(1):16. https://doi.org/10.1007/s41024-021-00112-7

[94] Priyom SN, Islam MdM, Shumi W. Utilization of Bacillus Subtilis Bacteria for Improving Mechanical Properties of Concrete. Journal of the Civil Engineering Forum. 2020 Dec 29;1000(1000). https://doi.org/10.22146/jcef.60216
[95] Hussain ZA, Nivedhitha M, Hidhaya FA, Devi AR, Year Civil Engg F. Evaluation of Biocalcification and Strength Aspects in Bacterial Concrete with Bacillus Subtillis. International Journal of Engineering Research & Technology (IJERT) [Internet]. 2016 Nov;5(11). https://doi.org/10.17577/IJERTV5IS110018
[96] Parashar AK, Gupta A. Experimental study of the effect of bacillus megaterium bacteria on cement concrete. IOP Conf Ser Mater Sci Eng. 2021 Apr 1;1116(1):012168. https://doi.org/10.1088/1757-899X/1116/1/012168
[97] Parashar AK, Gupta N, Kishore K, Nagar PA. An experimental investigation on mechanical properties of calcined clay concrete embedded with bacillus subtilis. Mater Today Proc. 2021 Jan 1;44:129-34. https://doi.org/10.1016/j.matpr.2020.08.031
[98] Mutitu KD, Munyao MO, Wachira MJ, Mwirichia R, Thiong'o KJ, Marangu MJ. Effects of biocementation on some properties of cement-based materials incorporating Bacillus Species bacteria - a review. J Sustain Cem Based Mater. 2019 Sep 3;8(5):309-25. https://doi.org/10.1080/21650373.2019.1640141
[99] De Muynck W, De Belie N, Verstraete W. Microbial carbonate precipitation in construction materials: A review. Ecol Eng. 2010 Feb;36(2):118-36. https://doi.org/10.1016/j.ecoleng.2009.02.006
[100] Achal V, Pan X, Özyurt N. Improved strength and durability of fly ash-amended concrete by microbial calcite precipitation. Ecol Eng. 2011 Apr;37(4):554-9. https://doi.org/10.1016/j.ecoleng.2010.11.009
[101] V, Mukerjee A, Sudhakara Reddy M. Biogenic treatment improves the durability and remediates the cracks of concrete structures. Constr Build Mater. 2013 Nov;48:1-5. https://doi.org/10.1016/j.conbuildmat.2013.06.061
[102] Muhammad NZ, Keyvanfar A, Abd. Majid MZ, Shafaghat A, Mirza J. Waterproof performance of concrete: A critical review on implemented approaches. Constr Build Mater. 2015 Dec;101:80-90. https://doi.org/10.1016/j.conbuildmat.2015.10.048
[103] Pei R, Liu J, Wang S, Yang M. Use of bacterial cell walls to improve the mechanical performance of concrete. Cem Concr Compos. 2013 May;39:122-30. https://doi.org/10.1016/j.cemconcomp.2013.03.024
[104] Achal V, Pan X, Özyurt N. Improved strength and durability of fly ash-amended concrete by microbial calcite precipitation. Ecol Eng. 2011 Apr;37(4):554-9. https://doi.org/10.1016/j.ecoleng.2010.11.009
[105] Pei R, Liu J, Wang S, Yang M. Use of bacterial cell walls to improve the mechanical performance of concrete. Cem Concr Compos. 2013 May;39:122-30. https://doi.org/10.1016/j.cemconcomp.2013.03.024
[106] Pungrasmi W, Intarasoontron J, Jongvivatsakul P, Likitlersuang S. Evaluation of Microencapsulation Techniques for MICP Bacterial Spores Applied in Self-Healing Concrete. Sci Rep. 2019 Aug 28;9(1):12484. https://doi.org/10.1038/s41598-019-49002-6

Research on Engineering Structures & Materials
www.jresm.org
Research Group

Research Article

Influence of SiO_2 and nano graphene particles on the microstructure and mechanical behavior of A356 alloy metal composites

Samuel Dayanand[1,a], S Manjunath Yadav[1,b], Madeva Nagaral[2,c], Satish Babu Boppana[3,d], Manjunatha T H[4,e], V Auradi[5,f]

[1]*Dept. of Mechanical Engineering, Government Engineering College, Karnataka, India*
[2]*Aircraft Research and Design Centre, Hindustan Aeronautics Limited, Karnataka, India*
[3]*Dept. of Mechanical Eng., School of Eng. College, Presidency University, Karnataka, India*
[4]*Dept. of Mechanical Eng., Ballari Institute of Technology and Management, Karnataka, India*
[5]*Department of Mechanical Engineering, Siddaganga Institute of Technology, Karnataka, India*

Article Info

Article history:

Received 06 Nov 2023
Accepted 18 Apr 2024

Keywords:

A356 alloy;
Metal matrix composite;
Stir casting;
Tensile properties;
Silicon oxide;
Graphene

Abstract

The current research focuses on investigating the microstructural and mechanical properties of aluminum (Al) metal matrix composites (MMCs) reinforced with both silicon dioxide (SiO_2) and nano-graphene particles. The composite material was produced using a novel two stage stir cast metallurgy approach. In this study, a constant reinforcement of 1 wt. % nanographene was maintained, while the SiO2 content was independently varied at levels of 2.5, 5, and 7.5 wt. %. Employing scanning electron microscopy (SEM) tool, microstructural analyses were conducted, revealing a uniform dispersion of ceramic silicon dioxide (SiO2) and graphene particles within the as-cast A356 MMCs. Mechanical testing, following the ASTM standards, was carried out on the composites, specifically assessing tensile strength, yield strength, and percentage elongation to evaluate the properties of the Al-based MMCs. The findings of this study indicate a significant enhancement in both tensile and yield strength values for the fabricated composites by 60.64% and 82.78% respectively. However, it is important to note that the percentage elongation decreases as the reinforcement content in the composite increases.

1. Introduction

In recent times, there has been remarkable growth in the development of materials used for various engineering applications. Traditional engineering materials, which are often unmodified monolithic substances, may not be suitable for certain specialized applications. Consequently, composite materials have emerged as innovative solutions to meet the requirements of such applications [1]. Researchers are actively engaged in combining advanced materials and novel processing techniques to create a new category of metal matrix composites (MMCs). These customized composite materials find specific applications in sectors like aviation, defense, and the automotive industry, owing to their unique and significantly enhanced properties compared to solid materials. The distinctive properties of Al-based MMCs, such as their low weight and high strength, make them highly relevant in the realm of engineering materials. One of the most significant advantages of composite materials is the ability to tailor their properties by choosing suitable reinforcements [2]. Researchers have used a variety of matrices and reinforcement

*Corresponding author: madev.nagaral@gmail.com
[a] orcid.org/0000-0001-5279-3522; [b] orcid.org/0000-0003-2358-4005; [c] orcid.org/0000-0002-8248-7603; [d] orcid.org/0000-0002-1792-2621; [e] orcid.org/0000-0002-2794-797X; [f] orcid.org/0000-0001-6549-6340
DOI: http://dx.doi.org/10.17515/resm2024.73me1106rs

systems when dealing with MMCs. Powder metallurgy and liquid metallurgical techniques are employed to refine these composites [3, 4]. Integrating hard or soft ceramic or nonmetal reinforcements into aluminum alloy is a huge challenge, according to the research. By employing an optimized fabrication technique, wetting properties and homogenous reinforcement particle dispersion inside the matrix can be achieved in aluminum-based composites [5, 6]. Vasant Kumar et al. [7] investigated the impact of SiC particles inclusion on the mechanical behavior of Al2014 alloy composites. These composites were fabricated by using 5 and 10 wt. % of SiC particles with liquid metallurgy route. Al2014 alloy with 10 wt. % of SiC composites exhibited the superior properties.

Aluminum is the most commonly used matrix material for MMCs, as it offers several desirable attributes, including low density, excellent thermal and electrical conductivity, precipitation hardening capability, corrosion resistance, and high damping capacity. Moreover, it offers an extensive range of mechanical properties, depending on its chemical composition. Al-based MMCs are usually strengthened with ceramic particulates, such as Al_2O_3, SiC, B, AlB_2, TiB_2, BN, SiO_2, AlN, and others. Various fabrication methods, predominantly based on casting or powder metallurgy, are available for creating nano-size (or micro-size) particle/metal composites [8, 9]. However, achieving uniform dispersion of particles in liquid metal can be challenging. Furthermore, micro-level porosity, a common casting defect, can pose difficulties in creating micro-level geometries [10].

Silicon oxide (SiO_2) is one of the most cost-effective and readily available reinforcements, capable of retaining high strength at elevated temperatures and offering excellent mechanical and wear properties [11]. Silica has diverse applications in various fields, containing drug delivery systems, catalysis, biomedicine, imaging, chromatography, sensors, and as a filler in composite materials [12]. It is also used for porous silica ceramics, which serve as high-temperature dielectrics and thermal shields, with applications in aerospace and engineering [13]. Silica enhances the strength and hardness of ceramic materials [14]. Additionally, silica aerogel, due to its porous, ultra-lightweight, and nanostructured properties, is utilized in composite insulators and for water resistance, UV protection, fire resistance, and acoustic barriers [15]. Silica gel, known for its great specific surface area and gas adsorption capacity, is employed as an adsorbent for heavy metal removal from wastewater and the adsorption of volatile organic compounds. In various applications, silica nanoparticles are employed as super-hydrophobic materials by modifying their hydrophilic properties to hydrophobic ones [16].

Graphene, on the other hand, stands out due to its exceptional conductivity, high Young's modulus, high specific surface area, and high electron mobility. Carbon atoms are packed tightly into a honeycomb lattice arrangement in a single layer [17]. Since graphene's discovery, there has been constant investigation into new methods of synthesis to meet the needs of a wide range of industries, such as the automotive, green energy, electronics, biomedical, and catalyst fields [18]. To improve the thermal conductivity of aluminum matrices, graphene shows promise as a reinforcement due to its high thermal conductivity. Graphene tends to settle to the bottom and may not scatter uniformly [19], therefore there have been challenges in exploring graphene-reinforced composites utilizing liquid stirring methods. Researchers have been working to improve the mechanical and wear properties of MMCs by creating hybrid-reinforced variants. To fulfill the needs of future sophisticated applications, the next generation of such materials includes these hybrid aluminum AMCs [20].

Hybrid composites have been developed through additional testing, with the goal of improving mechanical qualities such as dimensional stability and heat and corrosion resistance by merging two or more reinforcement components [21]. Many hybrid composites have had their mechanical properties studied, and the results demonstrate that

the tensile strength, stiffness, and porosity all increase with the percentage of reinforcement in the matrix. Impact energy and composite density are both greatly reduced, however, with increasing reinforcing content. Several investigators were studied various properties of MMCs.

In their investigation, Knowels et al. [22] examined the mechanical properties of 6061 alloy that had been made using the powder metallurgy technique and had SiC nano particles added to it. The mechanical qualities are enhanced by the powder metallurgy process, which distributes the particles without clumping. The Young's modulus was greatly enhanced after 8 hours of heat treatment at 125˚C, which led to a strong connection between the particles and the matrix. A combination of high strength, hardness, and ductility was achieved by adding tiny SiC particles (less than 500 nm in size). An aluminum composite including Al_2O_3 particles was created by Dinesh Kumar Koli et al. [23] through the use of ultrasonic assisted casting. Maintaining the microstructure while controlling the grain size is no easy feat. Various processes are examined in this research. Better bonding, easier microstructure control, and reduced cost are all benefits of ultrasonic aided casting. Nano alumina particles, when added up to 4% by volume, increase the strength until it plateaus.

The copper composites enhanced with SiC were made by Mohsen et al. [24] utilizing the friction stir method. Through optical and scanning electron microscopy, the existence of SiC particles was captured. The incorporation of silicon carbide particles into the copper matrix improved its wear resistance. A study comparing the wear behavior of brake shoe linings made of grey cast iron and aluminum alloy 356 strengthened with a 25% silicon carbide metal matrix composite was carried out by Natarajan et al. [25]. Grey cast iron brake shoe linings from passenger cars were cut to a diameter of 10 mm and tested beside MMC coated with AA356-25 wt. % SiC particles. Researchers used the pin-on-disc technique to study tribological behavior and discovered that MMC wore out less quickly than grey cast iron. It was also discovered that, under same circumstances, the frictional force of MMC sliding was 20% greater than that of cast iron, which would improve braking.

The composition material studied by Raghu et al. [26] is made up of A356 alloy with silicon carbide particles in weight percentages of 3, 5, 7, and 10. The powder metallurgy procedure was used to process the material. Hardness, tensile strength, and compression strength all rose with increasing weight percentages of SiC particles, with maximum values shown at 10 weight percent of SiC, according to scanning electron microscopy data. The SiC was found to disperse very uniformly throughout the A356 matrix. At 10 weight percent SiC, the wear rate was likewise determined to be minimal. Using the salt metal reaction in-situ approach, Mingliang Wang et al. [27] created a composite of A356 matrix alloy and titanium di boride (TiB_2) particles in both their as-cast and T6 heat-treated forms. The characteristics of A356/TiB_2 composites were enhanced. As TiB_2 particles were added to the composite, a smaller average grain size was noted.

Given the distinct advantages of both graphene and silica, their integration has been projected to achieve superior properties. The synthesis of graphene-silica hybrid composites combines the strengths of both materials while mitigating issues related to graphene agglomeration [28]. Agglomeration can significantly reduce the surface area of graphene, diminishing its performance.

Based on the literature review wettability and agglomeration are the major problems in the processing of metal composites. In the present research to overcome these problems novel two step stir casting process has been adopted to prepare the hybrid composites. In this, instead of adding reinforcement particles in single step, entire reinforcement quantity is divided and added into the molten metal in two stages. Two-step process helps in developing good quality castings and enhances the properties. The combination of

graphene and silica effectively addresses this challenge and results in advanced functional materials. Such composites are extensively used in applications such as electrodes, catalysts, hydrogen storage, batteries, displays, adsorbents, and sensors. Notably, researchers have explored the mechanical possessions of composites using A356 with SiO_2 and graphene as reinforcements, which is a relatively less explored area [29].

2. Experimental Details

2.1 Matrix and Reinforcement Materials

In this particular study, A356 was designated as the matrix material due to its varied range of applications in the automotive and aviation industries. The A356 matrix was reinforced with a combination of silicon oxide (SiO_2) and graphene. Graphene was kept constant at 1 wt. %, while the SiO_2 content was varied at levels of 2.5, 5, and 7.5 wt. % of the matrix material, leading to the development of hybrid metal composites. The chemical composition of A356 is detailed in Table 1 and the A356 material was sourced from Fenfee Metallurgical Pvt. Ltd, located in Bangalore, Karnataka, India. The SiO_2 particles employed in this research had particle size of 35µm. Through the addition of varying percentages of the (SiO_2 + Graphene) mixture in different combinations, we successfully produced Al-SiO_2-Gr hybrid composites. Fig. 1 is indicating the process adopted to prepare A356 alloy composites.

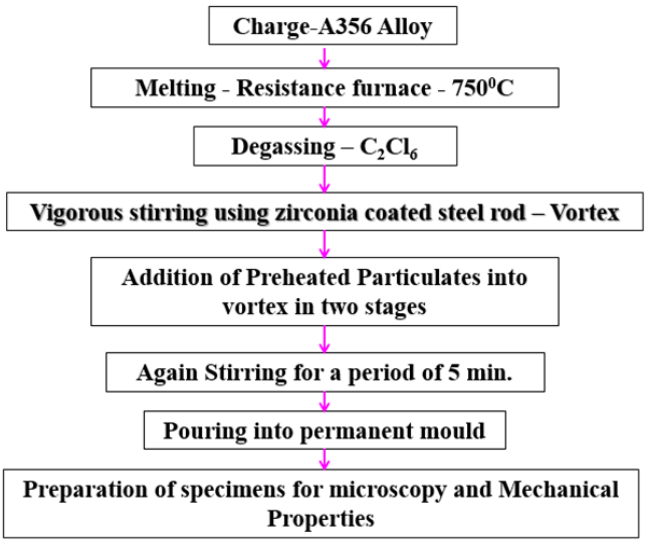

Fig. 1. Process of preparing A356 alloy hybrid composites

Table 1. Chemical composition of A356 alloy [30]

Constituent	Si	Mg	Fe	Cu	Zn	Mn	Ti	Al
Wt. %	7.5	0.45	0.2	0.2	0.1	0.1	0.05	Balance

2.2 Composite Fabrication

The specimen preparation involved employing the standard stir-casting method. In the production of each sample, 2000 grams of aluminum (A356) were melted using a graphite

crucible in an electric furnace with an argon environment, maintaining a temperature of 750°C. To achieve a homogeneous melt, the furnace temperature was consequently amplified to 850°C and maintained for 20 minutes. Furthermore, to enhance the wettability of the matrix alloy with the reinforcements, 0.5 wt.% of magnesium was introduced into the molten metal. In order to oxidize the surface of the SiO_2 particles, they underwent a baking process for 3-4 hours at a temperature of 200°C in a baking oven. This preheated powder was then fed into the molten metal at a consistent feed rate using Gr powder and mixed uniformly with the molten metal by a graphite stirrer rotating at 400 rpm for approximately 5 minutes.

(a) (b)

Fig. 2. Showing the (a) Molten metal in electric furnace (b) Cast iron die used to prepare samples

This ensured an even distribution of the particles throughout the metal. The constant reinforcement of graphene (1 wt.%) was introduced into the molten metal through an external sprue. The graphene and SiO_2, with particle sizes of 10 nm, were added to the molten matrix at varying wt.% levels (2.5, 5, and 7.5 wt.%). As the temperature of the molten metal increased to 850°C, the stirring speed was maintained at 500 rpm with a stirring time of 15 minutes to ensure the homogeneous distribution of the reinforcement in the molten matrix. Subsequently, the temperature was raised to 950°C, while the stirring speed and stirring time were increased to 600 rpm and 20 minutes, respectively, to achieve a uniform circulation of the strengthening in the matrix material. In order to avoid heterogeneity and facilitate proper cooling, the steel die was preheated to 350°C.

Fig. 3. A356 alloy hybrid composites

The synthesized aluminum hybrid composite slurry was then poured into the steel die and allowed to cool at atmospheric temperature. A 120 mm length and 15 mm diameter cast iron mold was used for pouring the liquid mixture. The resulting hybridized composite was permitted to harden at ambient temperature before being removed from the mold for

subsequent mechanical testing. Samples containing Gr and SiO_2 composites were prepared using the same procedure for the sake of comparison. Table 2 is representing various composites prepared using A356 alloy with nano graphene and SiO_2 particles. Material A is as-cast A356 alloy, B is A356 alloy with 1 wt. % of graphene and 2.5 wt. % of SiO_2 particles, C is A356 alloy with 1 wt. % of graphene and 5 wt. % of SiO_2 particles and finally, D is A356 alloy with 1 wt. % of graphene and 7.5 wt. % of SiO_2 particles reinforced composites. Fig. 2 (a) is showing the molten metal in the furnace, further Fig. 2(b) is representing cast iron die used to prepare composites. Fig. 3 indicates the prepared casting for the study.

Table 2. List of composites prepared for the study

Sl .No.	Material Code	Composition
1	A	As-Cast A356 Alloy
2	B	A356 + 1 wt. % Gr + 2.5 wt. % SiO2
3	C	A356 + 1 wt. % Gr + 5 wt. % SiO2
4	D	A356 + 1 wt. % Gr + 7.5 wt. % SiO2

2.3 Testing

A comprehensive microscopic analysis of the newly synthesized hybrid composites is crucial to gain a deeper understanding of their microstructural characteristics. To examine the microstructure of the Al-SiO_2-Gr hybrid composites, specimens were prepared following the ASTM standard for metallographic procedures. The microstructures were inspected using a scanning electron microscope (SEM). The samples were etched using Keller's Reagent (HF /HCl/HNO_3/H_2O), and emery paper with varying grades (400, 600, and 1000) was employed in the preparation process. SEM analysis was performed to measure the microstructure and the uniform dispersion of SiO_2 and graphene particles in the hybrid composites. For microstructural examination, cylindrical samples were produced, with dimensions of 10 mm in diameter and 5 mm in height for SEM images. The microstructure samples, as shown in Figure 4, were an integral part of the research, and the VEGAS TESCAN scanning electron microscope was used for microstructural analysis. The tensile properties of the composites were examined in accordance with the ASTM-E8 standard [31]. Furthermore, the tensile and compressive properties of the aluminum hybrid composite were evaluated following the ASTM E9 standard [32]. During the testing, ambient conditions were maintained, with temperatures ranging from 25°C to 30°C and relative humidity levels between 40% and 60%. A computerized universal testing machine (Instron 5982) equipped with a strain gauge extensometer was employed, and the tests were conducted at a constant cross-head speed of 1 mm/min at room temperature. Impact tests were showed using Charpy specimens measuring 56 × 10 × 10 mm, with a 3 mm notch depth, a tip radius of 0.30 mm, and angles of 45°, on impact testing machines. To obtain an average result, all specimens underwent three evaluations for both hardness and impact strength. Brinell hardness tests were carried out using a 5 mm ball diameter and a load-carrying capacity of 250 kg. The hardness test involved specimens measuring 15 mm in diameter and 10 mm in thickness.

3. Results and Discussion

In this current investigation, we have undertaken the synthesis of aluminum composites with SiO_2 and Graphene particles. The composition includes a consistent 1 wt.% of graphene and varying SiO_2 content at levels of 2.5, 5, and 7.5 wt.%, and the production method employed is the stir casting technique. Comprehensive experimental studies have been carried out, encompassing microstructural analysis, tensile strength assessment,

compressive strength evaluation, impact and hardness testing. The results and analysis of these synthesized hybrid composites are elaborated in the subsequent section.

3.1 Microstructural Analysis

To analyze the morphologies of SiO_2 and graphene particles, we employed SEM micrographs. SiO_2 particles exhibited spherical shapes, as apparent in the micrographs. Fig. 4 (a) to (d) illustrate the SEM micrographs of A356 alloy, A356-2.5 wt.% SiO2-1 wt.% graphene, A356-5 wt.% SiO2-1 wt.% graphene, and Al-7.5 wt.% SiO_2-1 wt.% graphene, respectively. The images in Fig. 4(b) and (d) depict SiO_2/graphene particles as round and spherical particles. The spherical morphology confirms the presence of SiO_2 particles and nano-graphene within the matrix. The grain boundaries in Fig. 4 (a) to (c) appear dendritic, suggesting an even dissemination of the reinforcing particles throughout the composite and alloy.

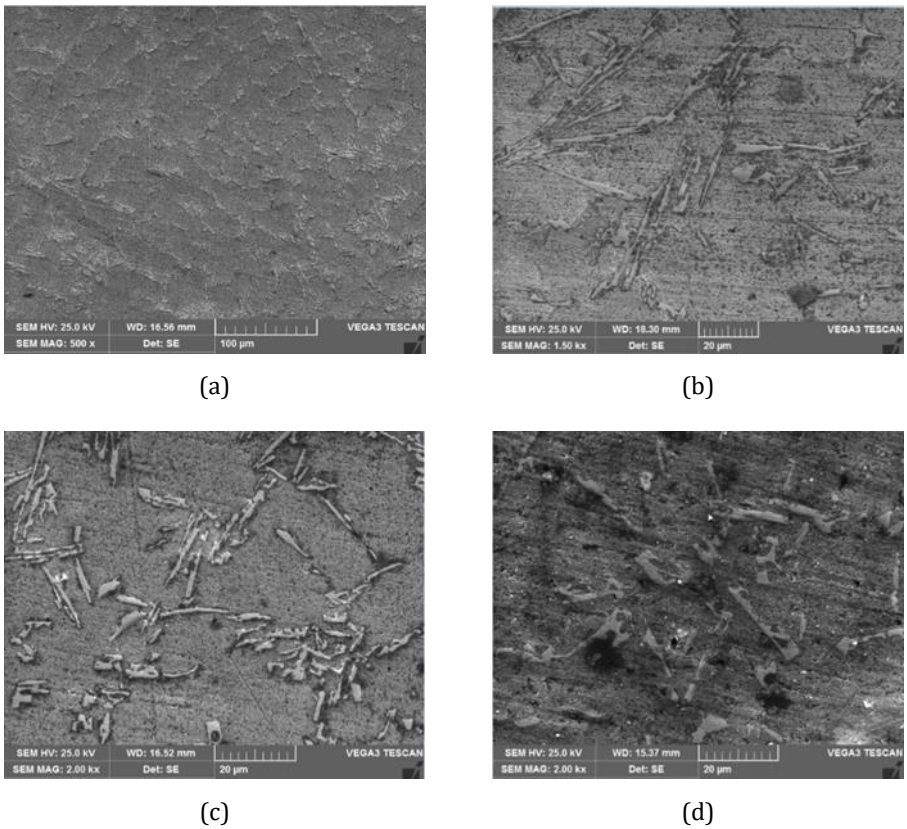

Fig. 4. SEM Micrographs of (a) As-cast A356 alloy (b) A356-1 wt.% of Gr and 2.5 wt.% of SiO_2 Composites (c) A356-1 wt.% of Gr and 5 wt.% of SiO_2 Composites(d) A356-1 wt.% of Gr and 7.5 wt.% of SiO_2 Composites

Within all the microstructures, fine precipitates are observed in the alloying components, scattered along the grain boundaries in the A356 composite framework. Notably, clusters of SiO_2 and graphene particles are dispersed throughout the matrix. These micrographs reveal the fine distribution of SiO_2 and graphene particles, which is a result of careful selection of appropriate mixing/stirring time and method during casting. Graphene particles are typically found interspersed between dendrites. Most SiO2 particles exhibit

spherical, angular, or sub-angular shapes, and occasionally, a plate-like structure similar to graphene is observed. The micrograph clearly shows that SiO2 and graphene platelets are evenly dispersed in the matrix, with no signs of clustering. The excellent interfacial bonding is attributed to pre-warming the SiO_2 and graphene particles before presenting them into the molten material. In Fig. 4(a), we observe the micrograph of the alloy used, revealing a dendritic form. The base matrix contains a white light-Al phase with precipitates both inside and outside the grains. The Fe-Mn-Si-Al phase of the alloy predominantly appears on the alloy's surface. In Fig. 4(b), the micrograph highlights the faceted features of SiO2 crystals, known for their monoclinic crystal structure at room temperature, transitioning to a tetragonal and cubic structure at higher temperatures. Fig. 4(c) pertains to the graphene reinforcement, showing stacked layers with a crumpled appearance.

In the SEM micrographs (Fig. 4), it is noticeable that intergranular porosity is present, but there is a well-formed microstructure due to strong bonding between the aluminum matrix and SiO_2/graphene particles. The grain boundaries are clearly discernible in the sample, and the inter-particle bonding is robust. In Fig. 4(b), the micrograph of the sample reveals a compact microstructure with minimal porosity. Therefore, the improved bonding between the particles and reduced porosity may contribute to an increase in the load-bearing capacity of the composite specimens. The distribution of grey SiO_2 particles can possibly be attributed to the high thermal conductivity of the alloy steel die, which enhances the solidification process. However, increasing the graphene content could potentially lead to more agglomeration and an increase in porosity. Additionally, a significant mismatch exists between aluminum and graphene, which could result in debonding at the interface. The graphene particles, due to their exceptionally high conductivity, may appear significantly brighter compared to the surrounding microstructure of the composite sample. The dendritic microstructure observed reflects the morphology resulting from the interaction between aluminum and graphene particles during the casting process. This interaction might be influenced by the formation of carbide phases, as reported in prior studies [33].

3.2. EDS Analysis

Energy dispersive X-ray spectroscopy (EDS) is a valuable technology for determining the composition and relative proportions of elements. While chemical analysis can recognize the existence of elements in a sample, quantifying their proportions can be challenging, making EDS an essential tool. In this study, EDS was employed to perform elemental analysis on A356 composite materials reinforced with 1 wt.% graphene and 2.5, 5, and 7.5 wt.% SiO_2. The EDS examination was conducted to assess the distribution of reinforcements within the matrix. The EDS peaks indicate the presence of silicon and oxygen, which correspond to the SiO_2 reinforcement (Fig. 5 (a)). This suggests a strong interaction between the reinforcements and the matrix. The carbon peaks are associated with the graphene content. A quantitative analysis of the samples (Fig. 5 (b)) further confirms the presence of these elements. The results of this analysis reveal the essential composition of the A356 composite, including elements such as Al, Mg, Si, Zr, and O, along with the carbon peak. The calculated elemental composition (Fig. 5 (b)) clearly indicates a uniform dispersion of SiO_2 and graphene within the aluminum matrix material.

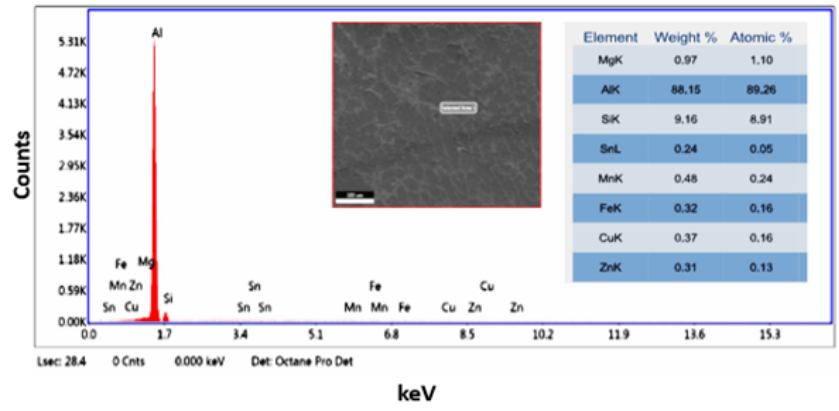
Counts
keV
Al
Fe Mg
Mn Zn
Sn Cu
Si
Sn
Sn Sn
Fe
Mn Mn Fe
Cu
Cu Zn Zn
Element Weight % Atomic %
MgK 0.97 1.10
AlK 88.15 89.26
SiK 9.16 8.91
SnL 0.24 0.05
MnK 0.48 0.24
FeK 0.32 0.16
CuK 0.37 0.16
ZnK 0.31 0.13

(a)

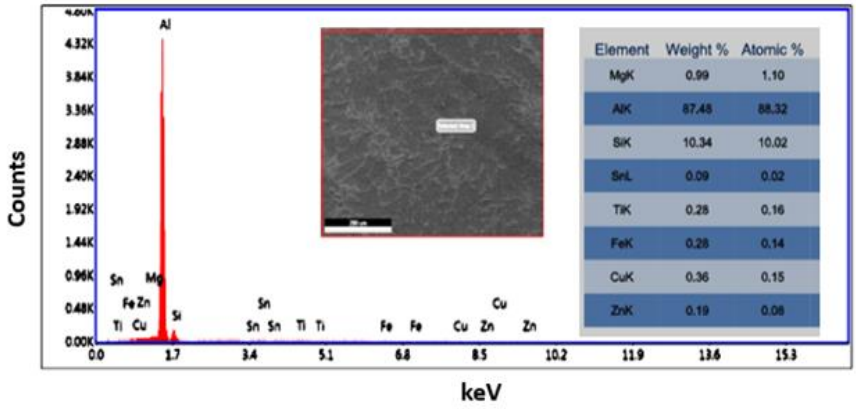
Counts
keV
Al
Sn Mg
Fe Zn
Ti Cu
Si
Sn
Sn Sn Ti Ti
Fe Fe
Cu
Cu Zn Zn
Element Weight % Atomic %
MgK 0.99 1.10
AlK 87.48 88.32
SiK 10.34 10.02
SnL 0.09 0.02
TiK 0.28 0.16
FeK 0.28 0.14
CuK 0.36 0.15
ZnK 0.19 0.08

(b)

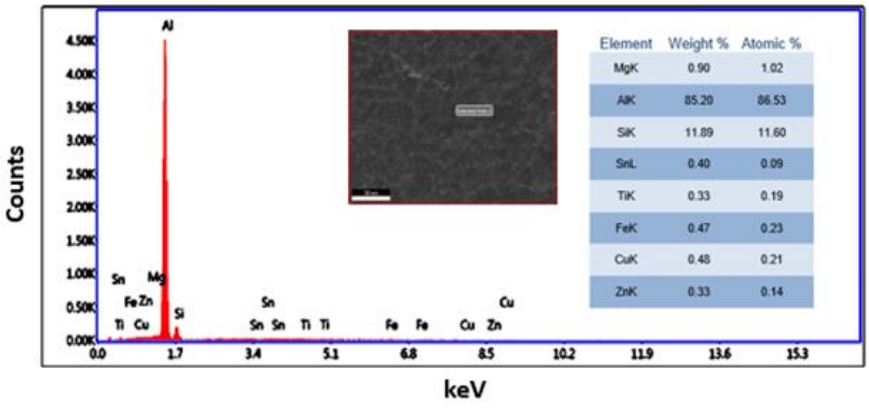
Counts
keV
Al
Sn Mg
Fe Zn
Ti Cu
Si
Sn
Sn Sn Ti Ti
Fe Fe
Cu
Cu Zn
Element Weight % Atomic %
MgK 0.90 1.02
AlK 85.20 86.53
SiK 11.89 11.60
SnL 0.40 0.09
TiK 0.33 0.19
FeK 0.47 0.23
CuK 0.48 0.21
ZnK 0.33 0.14

(c)

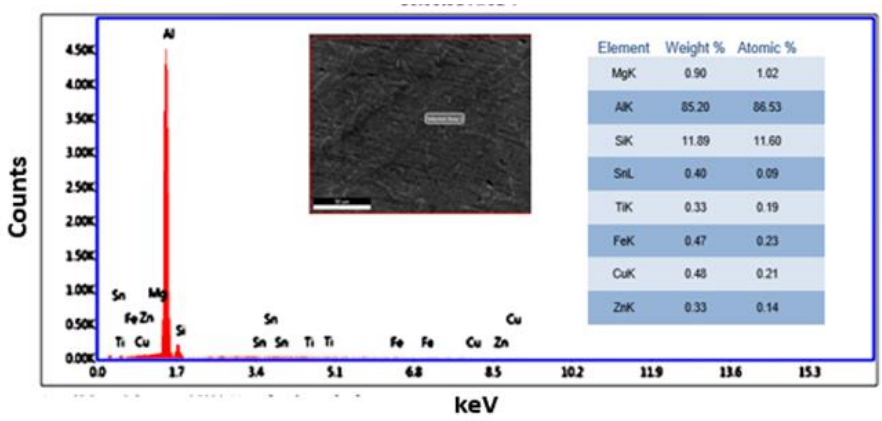

(d)

Fig. 5. EDS analysis of (a) As-cast A356 alloy (b) A356-1 wt.% of Gr and 2.5 wt.% of SiO2 Composites (c) A356-1 wt.% of Gr and 5 wt.% of SiO2 Composites(d) A356-1 wt.% of Gr and 7.5 wt.% of SiO2 Composites

3.3 Tensile Properties

The composites were subjected to room temperature tensile testing in line with the ASTM E-8 standard. Errors were kept to a minimum by carefully preparing three sets of standard specimens and averaging the results. Figure 6 displays the results, which show that the synthesized hybrid composites have expressively higher tensile and yield strength than the monolithic A356 alloy. The ultimate strength of as cast alloy (A) is 116.4 MPa, the increased proportion of SiO_2 reinforcement, the existence of nano graphene particulates, the uniform dispersion of reinforcements within the microstructure, the strong interfacial bonding between the matrix and the reinforcements, the grain size, and the strain gradient strengthening effect are all likely contributors to the observed improvement with 186.9 MPa in case of composite D (1 wt. % of Gr+7.5 wt.% of SiO_2).

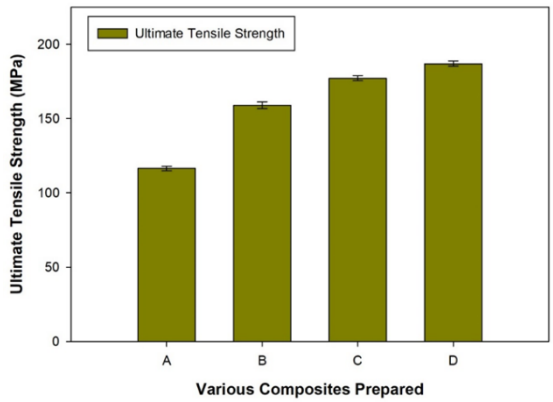

Fig. 6. Ultimate tensile strength of A356 alloy with nano graphene and SiO_2 particles reinforced composites

Recrystallization of the A356 aluminum alloy is facilitated by the addition of strong ceramic reinforcements, which act as nucleation sites. One reason for this is the presence

of reinforced particles, which serve as nucleation sites and prevent the movement of grain boundaries. This results in smaller matrix grain sizes compared to unreinforced A356 alloy. Dislocation motion is effectively slowed by the grain boundaries within the artificially produced aluminum hybrid composites. Grain size is decreased, dislocation accumulation is avoided, and the hybrid composites are strengthened as a whole thanks to suspended dislocations that move continually through the matrix. The tensile behavior of an alloy is also profoundly affected by the incorporation of graphene and SiO_2. Notably, as the weight percentage of SiO_2 particles in the graphene composites increases, the percentage of elongation reduces in aluminum hybrid composites. This is because SiO_2 particles are inherently brittle, which reduces their ductility. As more SiO_2 particles are combined into the graphene composites, the hybrid composites' ductility decreases because the aluminum matrix is less fluid.

The observed increase in the ultimate tensile strength (UTS) can be attributed to the presence of robust SiO_2 and nano graphene particles within the aluminum matrix. These rigid SiO_2 and nano graphene particles contribute to the overall strength of the aluminum matrix through their reinforcing mechanisms. Specifically, they facilitate the transfer of loads from the reinforcement particles to the matrix, resulting in heightened resistance to tensile stress. One key factor contributing to the enhanced strength of the aluminum matrix composites (AMCs) is the notable difference in thermal expansion coefficients amongst the matrix and the reinforcement particles. This disparity in thermal expansion characteristics leads to the development of a higher dislocation density within the matrix. Consequently, the load-bearing capacity of the hard reinforcement particles is increased, elevating the overall strength of the AMCs. As the content of reinforcement particles with a low coefficient of thermal expansion (CTE) rises within a matrix with a higher CTE, microstructural changes occur within the matrix, further contributing to the strength of the material. Additionally, the remarkable strength of the Al-nano Gr-SiO_2 hybrid composite can be attributed to the presence of SiO_2 particles uniformly distributed within the composite matrix, leading to dislocation pile-up in their vicinity. Consequently, the strength of the composite is enhanced due to an increased level of dislocation interactions and dislocation density near the interfaces of the matrix and reinforcement.

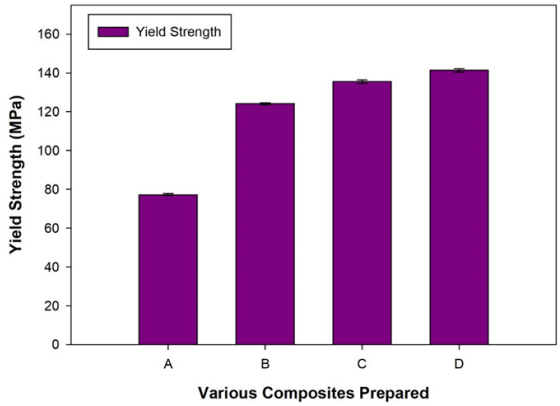

Fig. 7. Yield strength of A356 alloy with nano graphene and SiO_2 particles reinforced composites

The observed behavior can be best explained by deformation strengthening of the hybrid composites, which, despite being inherently brittle, exhibit higher strength and elongation when combined with SiO_2 particles. This effect is consistent with the Hall-Petch relationship, which is influenced by the size of the Gr particles [34]. The influence of

particle size on tensile strength can be elucidated through dislocation theory. The formation of plastic deformation necessitates the overcoming of the ultimate stress, often associated with a mass of moving dislocations. However, grain boundaries hinder dislocation glide, leading to dislocation pile-up. Once the content of dislocation pile-up reaches a certain threshold, it becomes the driving force for dislocation glide. With larger SiO_2 particle sizes, there is a higher content of dislocation pile-up, resulting in a greater driving force for dislocation glide. Smaller Gr particle sizes increase the number of particle boundaries, significantly hindering dislocation motion, and thus influencing the UTS for plastic deformation. The Fig. 7 illustrates the variations in yield strength as a function of the wt. fraction of Gr+SiO_2 reinforced composites. The yield strength, characterized by the stress associated with a plastic strain of 0.2%, exhibits an increase with higher weight fractions of SiO_2 reinforced composites. Remarkably, the A356 with 1 wt. % of Gr and 7.5 wt. % of SiO_2 composite demonstrates notably high yield of 141.4 MPa as compared to the base yield strength of 77.3 MPa.

As can be seen in Fig. 8, the elongation of the composites is significantly altered by the incorporation of SiO_2 and Gr particles into the aluminum alloy. Composites have a lesser percentage of elongation than the metal they are based on reinforcement particles. As the percentage of SiO_2 in the aluminum alloy is raised to 7.5 wt %, however, the composites' elongation drastically decreases, falling to around 32.3%. This decrease in elongation can be traced back to the incorporation of SiO_2 and Gr particles into the aluminum matrix, which reduces the composites' ductility in general [35].

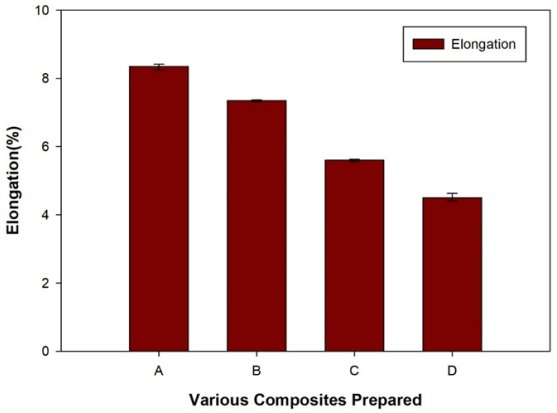

Fig. 8. Yield strength of A356 alloy with nano graphene and SiO2 particles reinforced composites

Figure 8 shows how the ductility of A356 alloy and its composites is affected by the addition of micron-sized SiO_2 and Gr particles. The ability of a material to lengthen under an axial load is referred to as its ductility. The elongation value in tensile testing is found by dividing the gauge length after fracture by the initial gauge length. Material ductility is often given as a percentage, with a larger value indicating greater ductility. Figure 8 shows the % elongation of the as-cast A356 with different wt. % of micron-sized SiO_2 and Gr particles. The percentage elongation of A356 alloy is decreased by the incorporation of SiO2 and Gr particles. As the reinforcing fraction in A356 alloy rises, this decrease becomes more pronounced. The presence of stiff, brittle particles within the A356 alloy matrix is principally responsible for the reduced ductility [36].

3.4 Compressive Strength

Following the ASTM E9 standard, the manufactured aluminum hybrid composites were compressed at room temperature. Compressive strength in A356-SiO_2-Gr composites was expressively improved by the addition of SiO_2 and Gr to the matrix. It is crucial to understand that a metal composites compressive strength almost always exceeds its ultimate tensile strength. This causes these MMCs to be significantly more brittle than monolithic materials, with percentage elongation values typically falling below 5%. The compressive strength data supports earlier findings and demonstrates a notable improvement over the cast hybrid composites with constant reinforcement. The outstanding compression strength of ceramic particles, such as SiO_2, is more characteristic than their tensile strength. In example, the compression strength of SiO_2 particles is much higher than that of the Al matrix. Because of this inherent reinforcing activity, the material is able to successfully resist compressive loads that are given to it. The composite's resistance to compression increases with the fraction of these particles within the foundation material. This is because the bigger volume occupied by the particles reduces the force that can be applied to the matrix, preventing it from deforming. Because the SiO_2 and Gr particles are evenly disseminated throughout the alloy matrix, the hybrid composites' increased compressive strength can be attributable to the twofold strengthening effect. Grain size in the microstructure is diminished because of the presence of these reinforced particles within the aluminum matrix. This effect also aids in the diminution of particle size, which becomes gradually important when particle accumulation heightens [37].

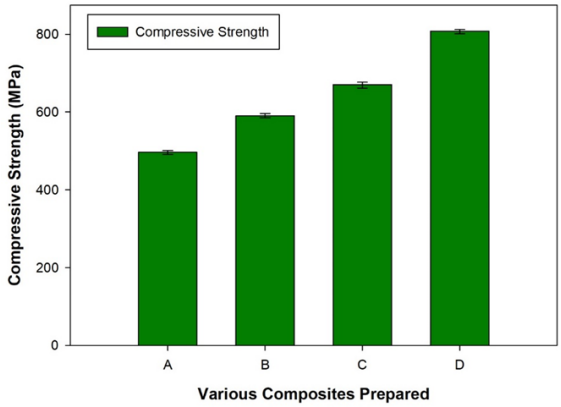

Fig. 9. Compressive strength of A356 alloy with nano graphene and SiO_2 particles reinforced composites

A greater interfacial area is formed between the SiO_2 + Gr reinforcement particles and the Al matrix as the fraction of SiO_2 + Gr reinforcement particles within the matrix increases. As the interface grows, dislocations build up along its edges, mimicking the behavior of grain boundaries. The overall strengthening impact is determined in large part by the inclusion of Gr and SiO_2, which work hand in hand with the distribution strengthening effect. This helps increase the dislocation density in the aluminum matrix and expand the grain size. As can be seen in Fig. 9, the combined effects of these parameters lead to the impressively high compressive strength of the synthesized hybrid composites. According to the reported findings, the compression strength of the A356 alloy matrix is greatly improved by the presence of hard particle phases, and this improvement is magnified as the percentage of SiO_2 + Gr particles increases. Compressive strength is a common measure of the durability of carbide or oxide particles due to the intrinsic hardness of ceramics.

Strength enhancement in Al-SiO_2-Gr composites can be attributed to a number of factors, including the presence of uniformly distributed harder elements, substantial grain refinement achieved with the addition of SiO_2 + Gr particles, and dislocations generated due to modulus mismatches and differences in thermal expansion coefficients. The results are shown in Fig. 9 which confirms the significant impact of these particles on the fortification of Al-SiO_2-Gr composites by emphasizing the large influence of SiO_2 + Graphene content on the overall compressive strength.

3.5 Hardness Measurements

Figure 10 presents samples of the substrate metal A356 alongside the hybridized composites. Notably, the hybrid composites exhibit higher levels of hardness compared to their unreinforced counterparts, and this hardness demonstrates a consistent upward trend in direct proportion to the weight percentage of the added reinforcement, in alignment with prior investigations [38]. The incorporation of hard reinforcing particles has a dual impact, enhancing both the matrix's hardness and its resistance to plastic deformation [39]. The graph in Figure 10 illustrates the hardness increment up to 7.5%wt. of SiO_2 + Graphene particulates. In particular, the ideal hardness of reinforced composites featuring a mixture surpasses the hardness of unreinforced alloys. This rise in hardness can be attributed to the increased occurrence of hard SiO_2 particles in the aluminum matrix, combined with the inherently high hardness of nano graphene particles [40].

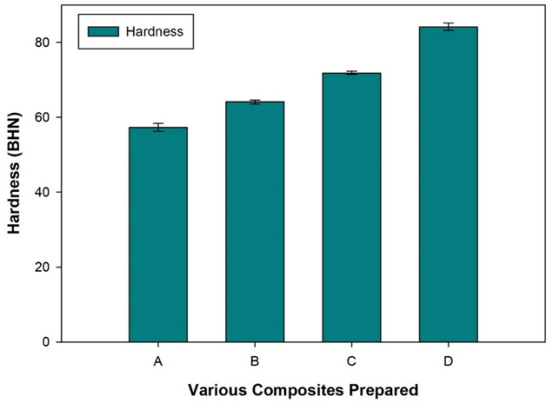

Fig. 10. Hardness of A356 alloy with nano graphene and SiO_2 particles reinforced composites

The introduction of reinforcement particles to the aluminum matrix serves to enhance their surface area, concurrently reducing the size of aluminum matrix grains. This heightened presence of hard surface areas from SiO_2 and nano graphene particles offers substantial resistance to plastic deformation, consequently elevating the overall hardness of the fabricated AMCs. Additionally, the presence of hard and brittle SiO_2 and nano graphene particles within the soft and ductile A356 matrix leads to a reduction in the ductility content of the fabricated AMCs. This reduced ductility within the matrix metal of the composite significantly contributes to the overall hardness of the AMCs. It's worth noting that an increased amount of reinforcement in the matrix results in a higher dislocation density during solidification, attributable to the thermal mismatch between the aluminum matrix and the reinforcement. This discrepancy in thermal expansion creates internal stresses, prompting plastic deformation within the aluminum matrix to accommodate the lower volume expansion of the reinforcement particles. The escalation in dislocation density at the particle-matrix interface intensifies resistance to plastic

deformation, ultimately enhancing hardness. Furthermore, the enhanced hardness observed in hybrid composites can also be ascribed to the observed reduction in porosity, as evident in SEM microphotographs. It is well-documented that higher hardness is closely associated with lower levels of porosity within the MMC. It is evident from the results that the hardness value of the Al-Graphene-SiO_2 hybrid composite surpasses that of other fabricated composites, primarily attributed to the homogeneous distribution of SiO_2 particles within the matrix. The presence of robust SiO_2 particles, in conjunction with the finely dispersed Gr particles, significantly elevates the barriers to grain boundary sliding [41]. Additionally, an essential factor contributing to the overall enhancement in the composite's hardness, owing to the incorporation of SiO_2, stems from an augmented dislocation density due to the thermal expansion mismatch between the reinforcement and the hybrid matrix at the particle-matrix interfaces [42]. The cumulative effect of these factors translates into formidable resistance against localized deformation during indentation.

3.6 Impact Strength

As represented in Fig. 11, the impact strength of the composites exhibits an upward trend in contrast to the unreinforced alloy as the wt. % of SiO_2 + Graphene particles within the metal matrix increases. Nonetheless, it's worth noting that, although the impact strength of hybrid composites shows a tendency to decrease, this reduction is relatively modest. One plausible explanation for the reduction in strength lies in the subtle transformation of material properties from ductile to brittle, which is brought about by the incorporation of hard SiO_2 + Graphene particles. The presence of microstructural defects, resulting from cracking and decohesion of reinforcing particles, contributes to the decline in impact strength within the composites. This decrement in impact strength becomes noticeable with the increasing weight percentage of reinforcement, causing a rise in failure rates. A linear progression in the energy absorbed is evident with the escalation of the reinforcement (SiO_2 + Graphene) weight percentage (Fig. 11). The augmentation in impact energy can be attributed to the reinforcement provided by the robust SiO_2 particles. This rise in impact strength, as indicated by the increasing impact energy, is attributed to the incremental weight percentage of SiO_2 + graphene reinforcements.

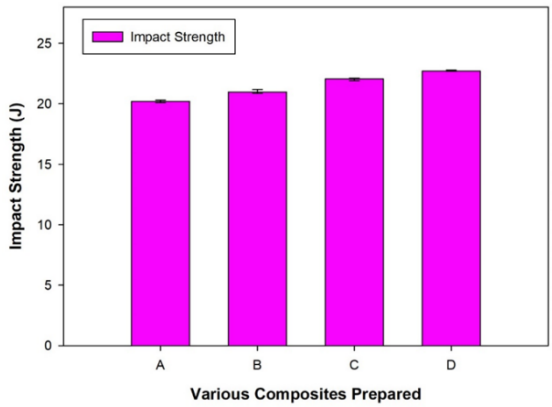

Fig. 11. Impact strength of A356 alloy with nano graphene and SiO_2 particles reinforced composites

4. Conclusion

This paper presents a comprehensive report on the synthesis and microstructural characterization of aluminum matrix composites reinforced with nanographene and SiO_2. The experimental findings have been thoroughly scrutinized, leading to the following key conclusions.

- Successful fabrication of hybrid composites has been attained through the incorporation of SiO_2 and nanographene particles into the aluminum alloy via a liquid metallurgy approach.
- SEM micrographs provide clear evidence of the effective reinforcement of SiO_2 and nanographene, displaying a uniform distribution of particle and robust inter-particle bonding in the base matrix, albeit with minor pore presence.
- Both tensile and yield strength exhibit noticeable increments with the rise in the SiO_2 particles with constant nanographene reinforcement weight percentage in comparison to the as-cast matrix. This surge in strength can be attributed to the reinforcing effect of hard SiO_2 particles and graphene, which contribute to enhanced resistance against tensile loads. The improvements in the ultimate strength of A356 alloy with the 7.5 wt. % of SiO_2 and 1 wt. % of Graphene is 60.64 %. The improvements in the yield strength of A356 alloy with the 7.5 wt. % of SiO_2 and 1 wt. % of Graphene is 82.78 %.
- The percentage elongation decreases as the weight percentage of hybrid reinforcement increases, primarily due to the brittleness introduced by the hard particles and the presence of hard-ceramic particles.
- The compressive strength experiences a notable increase with the augmentation of nanographene and SiO_2 reinforcement weight percentages when compared to the as-cast matrix. Similar to the tensile properties, this increase in strength can be ascribed to the reinforcing impact of hard SiO_2 particles and graphene, which enhance resistance to compressive loads. The improvements in the compressive strength of A356 alloy with the 7.5 wt. % of SiO_2 and 1 wt. % of Graphene is 62.71 %.
- The impact strength of the hybridized composites exhibits a gradual increase with the addition of reinforcement, albeit at a modest rate.
- In the present study 1 wt. % of nano graphene is used along with the varying weight percentages of SiO_2 particles. In the future, the composites with more weight percentages of graphene content can be studied. Also, in the present research mechanical properties were investigated, further various properties can be studied.

References

[1] Suresh S, Shenbaga Vinayaga Moorthi N, Vettivel SC, N. Selvakumar N, Jinu GR. Effect of graphite addition on mechanical behavior of Al6061-TiB2 hybrid composites using acoustic emission, Materials Science and Engineering A, 2014; 612: 16-27. https://doi.org/10.1016/j.msea.2014.06.024

[2] Zeeshan A, Muthuraman V, Rathnakumar P, Guruswamy P, Madeva Nagaral. Influence of B4C particle size on the mechanical behavior of A356 aluminium composites. Research on Engineering Structures and Materials, 2023; 9 (2):527-540.

[3] Ananthakrishna Somayaji, Madeva Nagaral, Chandrashekar Anjinappa, Meshel QA, Ravikiran Kamath Billady, Nithin Kumar, Virupaxi Auradi, Saiful Islam, Ranga Raya CJ, Abdul Razak, Mohammad Amir Khan, Channa Keshava Naik. Influence of graphite particles on the mechanical and wear characterization of Al6082 alloy composites. ACS Omega, 2023; 8(30):26828-26836. https://doi.org/10.1021/acsomega.3c01313

[4] G Kumar, R Saravanan, Madeva Nagaral. Dry sliding wear behavior of nano boron carbide particulates reinforced Al2214 alloy composites. Materials Today: Proceedings, 2023;81:191-195. https://doi.org/10.1016/j.matpr.2021.03.065
[5] Bharath V, Auradi V, Veeresh Kumar GB, Madeva Nagaral, Murthy Chavali, Mahmoud Helal, Rokayya Sami, Aljuraide NI, Jong Wan Hu, Ahmed M Galal. Microstructural Evolution, Tensile Failure, Fatigue Behavior and Wear Properties of Al2O3 Reinforced Al2014 Alloy T6 Heat Treated Metal Composites. Materials, 2022;15(12):4244. https://doi.org/10.3390/ma15124244
[6] Siddesh M., Shivakumar BP, Shashidhar , Nagaral M. Dry sliding wear behavior of mica, fly ash and red mud particles reinforced Al7075 alloy hybrid metal matrix composites. Indian Journal of Science and Technology, 2021;14(4):310-318. https://doi.org/10.17485/IJST/v14i4.2081
[7] Vasanth Kumar HS, Revanna K, Nithin Kumar, Sathyanarayana N, Madeva N, Manjunath GA, Adisu H. Impact of silicon carbide particles weight percentage on the microstructure, mechanical behaviour, and fractography of Al2014 alloy composites. Advances in Materials Science and Engineering, 2022; Article ID 2839150: 1-10. https://doi.org/10.1155/2022/2839150
[8] Krishna UB, Vasudeva B, Virupaxi Auradi, Madeva Nagaral. Effect of Percentage Variation on Wear Behaviour of Tungsten Carbide and Cobalt Reinforced Al7075 Matrix Composites Synthesized by Melt Stirring Method. Journal of Bio-and Tribo-Corrosion, 2021; 7(3):1-8. https://doi.org/10.1007/s40735-021-00528-1
[9] Veeresh Kumar GB, Gude Venkatesh Chowdary, Mandadi Surya Vamsi, Jayarami Reddy K, Madeva Nagaral, Naresh K. Effects of addition of Titanium Diboride and Graphite Particulate Reinforcements on Physical, Mechanical and Tribological properties of Al6061 Alloy based Hybrid Metal Matrix Composites. Advances in Materials and Processing Technologies, 2022;8(2):2259-2276. https://doi.org/10.1080/2374068X.2021.1904370
[10] Ruixiao Zheng, Jing Chen, Yitan Zhang, Kei Ameyama, Chaoli Ma. Fabrication and characterization of hybrid structured Al alloy matrix composites reinforced by high volume fraction of B4C particles, Materials Science and Engineering A, 2014; 601:20-28. https://doi.org/10.1016/j.msea.2014.02.032
[11] Bharath V, Auradi V, Madeva Nagaral, Satish Babu Boppana. Experimental investigations on mechanical and wear behaviour of 2014Al-Al2O3 Composites. Journal of Bio-and Tribo-Corrosion, 2020; 6(2):1-10. https://doi.org/10.1007/s40735-020-00341-2
[12] Massoud Malaki, Alireza Fadaei Tehrani, Behzad Niroumand, Amir Abdullah. Ultrasonically stir cast SiO2/A356 metal matrix nanocomposites. Metals, 2021;11(12):1-18. https://doi.org/10.3390/met11122004
[13] Sekar K, Allesu K, Joseph MA. Effect of heat treatment in tribological properties of A356 aluminium alloy reinforced with Al2O3 nano particles by combination effect of stir and squeeze casting method. Applied Mechanics and Materials, 2014; 592-594: 968-971. https://doi.org/10.4028/www.scientific.net/AMM.592-594.968
[14] Umanath K, Selvamani ST, Palanikumar K, Raphael T, Prashanth K. Effect of sliding distance on dry sliding wear behavior of Al6061-SiC-Al2O3 hybrid composite. Proceedings of International Conference on Advances in Mechanical Engineering, 2013;749-775. https://doi.org/10.1016/j.compositesb.2013.04.051
[15] Dineshkumar SK, Saravanan AK, Raghuram Pradhan, Ramya Suresh, Senthilnathan K. Characterization of Al-SiO2 composite material. International Journal of Engineering and Advanced Technology, 2019; 9(2):2972-2975. https://doi.org/10.35940/ijeat.B3898.129219
[16] Madeva Nagaral, Shaivananda Kalgudi, Auradi V, Kori SA. Mechanical characterization of ceramic nano B4C-Al2618 alloy composites synthesized by semi solid state

processing, Transactions of the Indian Ceramic Society, 2018;77(3):1-4. https://doi.org/10.1080/0371750X.2018.1506363
[17] Dhanalakshmi P, Mohansundararaju N, Venkatkrishnan PG. Preparation and mechanical characterization of stir cast hybrid Al7075 Al2O3 B4C metal matrix composites. Applied Mechanics and Materials, 2014; 592-594: 705-710. https://doi.org/10.4028/www.scientific.net/AMM.592-594.705
[18] Devnani GL, Shishir Sinha. Effect of nano fillers on the properties of natural fiber reinforced polymer composites. Materials Today Proceedings, 2019;18(3):647-654. https://doi.org/10.1016/j.matpr.2019.06.460
[19] Mohammad Narimani, Behnam Lotfi, Zohreh Sadeghian. Evaluation of the microstructure and wear behavior of AA6063-B4C/TiB2 mono and hybrid composite layers produced by friction stir processing. Surface & Coatings Technology, 2016; 285:1-10. https://doi.org/10.1016/j.surfcoat.2015.11.015
[20] Amir Pakdel, Agnieszka Witecka, Gaulthier Rydzek, Dayangku Noorfazidah Awang Shri, Valeria Nicolosi. A comprehensive analysis of extrusion behavior, microstructural evolution and mechanical properties of 6063 Al-B4C composites produced by semisolid stir casting. Materials Science and Engineering Materials A, 2018;721:28-37. https://doi.org/10.1016/j.msea.2018.02.080
[21] Narasimha Murthy I, Venkata Rao D, Babu Rao J. Microstructure and mechanical properties of aluminium fly ash nano composites made by ultrasonic method. Materials and Design, 2012; 35:55-65. https://doi.org/10.1016/j.matdes.2011.10.019
[22] Knowels AJ, Jiang X, Galano M. Microstructure and mechanical properties of 6061 Al alloy based composites with SiC nano particles. Journal of Alloys and Compounds, 2014;615(1):S401-S405. https://doi.org/10.1016/j.jallcom.2014.01.134
[23] Dinesh Kumar Koli, Geeta Agnihotri, Rajesh Purohit. A Review on Properties, Behaviour and Processing Methods for Al-Nano Al2O3 Composites. Procedia Materials Science, 2014; 6:567 - 589. https://doi.org/10.1016/j.mspro.2014.07.072
[24] Mohsen Ostad Shabani. Microstructural and abrasive wear properties of SiC reinforced aluminium based composite produced by compo-casting. Transactions of Nonferrous Metals Society of China, 2013; 23:1905-1914. https://doi.org/10.1016/S1003-6326(13)62676-X
[25] Natarajan N, Vijayarangan S, Rajendran I. Wear behaviour of A356/25 SiCp aluminium matrix composites sliding against automobile friction material. Wear, 2006;261:812-822. https://doi.org/10.1016/j.wear.2006.01.011
[26] Raghu YV, Anil Kumar G, Sateesh J, Madhusudhan T. Investigation of Mechanical properties and Wear rate of Aluminium A356 -SiC MMCs processed by powder metallurgy method. International Research Journal of Engineering and Technology, 2017; 4(8) 444-448.
[27] Mingliang Wang, Dong Chen, Zhe Chen, Yi Wu, Feifei Wang, Naiheng Ma, Haowei Wang. Mechanical properties of in-situ TiB2/A356 composites. Materials Science & Engineering A, 2014; 590:246-254. https://doi.org/10.1016/j.msea.2013.10.021
[28] Shashidhar S, Vijaya Kumar P, Shivananda HK, Madeva Nagaral. Processing, microstructure, density and compression behavior of nano B4C particulates reinforced Al2219 alloy composites. International Journal of Advanced Technology and Engineering Exploration, 2018; 5(46):350-355. https://doi.org/10.19101/IJATEE.2018.546015
[29] Omyma El-Kady, Fathy A. Effect of SiC particle on the physical and mechanical properties o extruded Al matrix composites. Materials and Design, 2014; 54:348-353. https://doi.org/10.1016/j.matdes.2013.08.049
[30] Davis JR. Aluminium and aluminium alloys, ASM specialty handbook, ASM International, 1993.
[31] Vijaya Ramnath B, Elanchezhian C, Jaivignesh M, Rajesh S, Parswajinan C, Siddique Ahmed Ghias A. Evaluation of mechanical properties of aluminium alloy-alumina-

boron carbide metal matrix composites, Materials and Design, 2014; 58:332-338. https://doi.org/10.1016/j.matdes.2014.01.068

[32] Hong SJ, Kim HM, Huh D, Suryanarayana C, Chun BS. Effects of Clustering on the Mechanical Properties of SiC Particulate -Reinforced Aluminum Alloy 2024 Metal Matrix Composites. Material Science and Engineering A, 2003; 347:198-204. https://doi.org/10.1016/S0921-5093(02)00593-2

[33] Al-Qutub AM, Allam IM, Qureshi TW. Wear Properties of 10% Sub-Micron A12O3 / 6061 Aluminum Alloy Composite. International Journal of Applied Mechanics and Engineering, 2002; 7:329-334.

[34] Jayasheel Harti, Prasad TB, Madeva Nagaral, Pankaj Jadhav, Auradi V. Microstructure and dry sliding wear behavior of Al2219-TiC composites, Materials Today Proceedings, 2017;4:11004-11009. https://doi.org/10.1016/j.matpr.2017.08.058

[35] Meijuan Li, Kaka Ma, Lin Jiang, Hanry Hang, Enrique Lavernia, Lianmeng Zhang, Julie Schoenung. Synthesis and mechanical behavior of nanostructured Al5083-TiB2 metal matrix composites. Materials Science and Engineering A, 2016;656:241-248. https://doi.org/10.1016/j.msea.2016.01.031

[36] Balasivanandha Prabu S, Karunamoorthy L, Kathiresan S, Mohan B. Influence of stirring speed and stirring time on distribution of particles in cast metal matrix composite. Journal of Material Processing Technology, 2006; 171:268-273. https://doi.org/10.1016/j.jmatprotec.2005.06.071

[37] Yogesh Prabhavalkar, Chapgaon AN. Effect of volume fraction of Al2O3 on tensile strength of aluminium 6061 by varying stir casting furnace parameters: A review. International Research Journal of Engineering and Technology, 2017; 4(10):1351-1355.

[38] Madeva Nagaral, Shivananda BK, Virupaxi Auradi, Kori SA. Development and mechanical-wear characterization of Al2024-nano B4C composites for aerospace applications. Strength, Fracture and Complexity, 2020; 13(1):1-13. https://doi.org/10.3233/SFC-190248

[39] Bharath V, Ashita DH, Auradi V, Madeva Nagaral. Influence of variable particle size reinforcement on mechanical and wear properties of alumina reinforced 2014Al alloy particulate composite. FME Transactions, 2020;48(4): 968-978. https://doi.org/10.5937/fme2004968B

[40] Raj Kumar, Deshpande RG, Gopinath B, Jayasheel Harti, Madeva Nagaral, Auradi V. Mechanical Fractography and Worn Surface Analysis of Nanographite and ZrO2-Reinforced Al7075 Alloy Aerospace Metal Composites. Journal of Failure Analysis and Prevention, 2021; 21:525-536. https://doi.org/10.1007/s11668-020-01092-5

[41] Madeva Nagaral, Auradi V, Kori SA, Reddappa HN, Jayachandran, Veena Shivaprasad. Studies on 3 and 9 wt. % of B4C particulates reinforced Al7025 alloy composites, AIP conference proceedings, 2017;1859(1):020019. https://doi.org/10.1063/1.4990172

[42] Fazil N, Venkataraman V, Madeva Nagaral. Mechanical characterization and wear behavior of aerospace alloy AA2124 and micro B4C reinforced metal composites. Journal of Metals, Materials and Minerals, 2020;30(4):97-105. https://doi.org/10.55713/jmmm.v30i4.641

Research on Engineering Structures & Materials
www.jresm.org
Research Group

Research Article

Contribution to the study of an eco-sand concrete containing recycled sands from waste granite and recycled clinker

Nouha Rezaiguia*[1,a], Houria Hebhoub[1,b], Leila Kherraf[1,c], Mohammed Ichem Benhalilou[2,d]

[1]*Department of Civil Engineering, 20 August 1955 University, LMGHU Laboratory, Algeria*
[2]*TCT, University Batna 2, Batna, Algeria*

Article Info

Article history:

Received 20 Dec 2023
Accepted 21 Apr 2024

Keywords:

Sand concrete;
Granite waste;
Recycled clinker;
Recovery;
Performance;
Durability;
Microstructure

Abstract

The reuse of waste materials, particularly granite and undercooked or overcooked clinker, in sand concrete formulation is the focus of this study aimed at conserving natural resources and protecting the environment within the framework of sustainable development. To achieve this objective, we replaced ordinary sand with recycled sands in the sand concrete volume. Specifically, we incorporated granite waste (GS) and recycled clinker (CS) at rates of 20 and 40%. Subsequently, we conducted a series of evaluations on the different formulations. These evaluations included fresh state properties such as density, workability, and air content, as well as mechanical properties like compressive strength, flexural strength, rebound hammer, ultrasonic pulse velocity, modulus of elasticity, and X-ray diffraction (XRD). Additionally, we analyzed durability parameters such as water absorption, dimensional variation, freeze-thaw resistance, acid attacks, and chloride penetration on hardened concrete. We compared these results with reference samples and considered potential correlations among the different parameters. The results obtained showed improvements in workability, hardness, and homogeneity with enhancements in microstructure, with the best results obtained from SCC compared to the control concrete and SCG. The results of mechanical properties demonstrated that concretes containing recycled clinker sand are more resistant in compression and flexural strength compared to SC0 and SCG, with maximum strengths observed in concrete containing 40% recycled clinker at ages 7, 28, and 90 days. Durability parameters were acceptable with slight reductions in ultrasonic pulse velocity and modulus of elasticity after freeze-thaw cycles. A good correlation was observed among the various parameters.

1. Introduction

The increase in the world's population and changing consumer habits have led to a rapid depletion of our natural resources. Moreover, climate change and the accelerated loss of natural resources have given rise to serious environmental problems, especially in recent decades. Therefore, it has become crucial to significantly reduce material consumption and efficiently utilise available natural resources through waste recycling.

Certainly, construction is undeniably one of the sectors with the highest consumption of raw materials. The excessive use of certain aggregates, like sand, in the production of mortar and concrete has resulted in a scarcity of these materials. Meanwhile, waste generated by the industrial and construction sectors, as well as the remnants and debris of

*Corresponding author: n.rezaiguia@univ-skikda.dz
[a]orcid.org/0009-0005-4180-048X; [b]orcid.org/0000-0001-9628-4463; [c]orcid.org/0000-0003-2750-2636;
[d] orcid.org/0009-0003-0422-3535
DOI: http://dx.doi.org/10.17515/resm2024.129ma1220rs

certain materials that are abandoned in the natural environment, have detrimental effects on the environment.

A great deal of research works has been carried out into the recovery of waste for use as aggregates in mortars and various types of concrete and in particular sand concrete which has been developing in recent years, especially in Algeria. Beyond, the waste in question includes demolition concrete, off-cuts from tiling and ceramics, bricks and breezeblocks, as well as marble and granite waste. In addition, waste from the cement industry, in respect such as sludge, Cement Kiln Dust (CKD) and unbaked or under baked clinker, which is mainly due to errors in controlling the firing phase, temperature fluctuations and kiln stoppages and restarts caused by power cuts, breakdowns or planned stoppages, was used either in the form of fine aggregates or gravel. Further, this recycled waste was then used to partially or totally replace ordinary aggregates in different types of construction materials to assess the impact of recycled aggregates on the properties of such materials in their fresh and hardened states, as well as on their durability parameters.

In this context, the aim objective of this research is to promote the utilisation of granite debris from the construction industry and waste from the cement industry, especially unbaked or under baked, as fine aggregates in the formulation of sand concrete. The objective is to preserve natural resources, minimise waste, and reduce emissions, all of which play a critical role in environmental protection.

Many researchers have been interested in reusing granite off-cuts as a fine powder that partially replaces cement or sand in mortar formulation. Gupta and Vyas [1] studied the feasibility of replacing fine aggregates in a mortar with granite waste fines; thus, they found an improvement in workability, an increase in mechanical performance (compression and tension, ultrasonic pulses and dynamic modulus of elasticity) and durability and in particular adhesive strength, water absorption and drying shrinkage. On the other hand, Suárez-Navarro et al. [2] demonstrated that mixtures containing granite fines gave slightly lower compressive strengths than the reference mortar, whilst the substitution of sand by granite waste fines induced no net difference in flexural strength compared with the control. Moreover, the potential effects of using granite waste on the increased durability of mortar and concrete, including abrasion, freeze/thaw cycles and resistance to sulphate attack were illustrated by the study of Mashaly et al. [3], who alike concluded that granite waste could effectively be used in the production of concrete bricks, paving units and cement tiles. However, Ramos et al. [4] found an improvement in the resistance of mortars to chlorides and alkali-silica reactions by incorporating 10% of granite waste fines as a cement replacement.

Unquestionably, the influence of partial substitution of sand in a concrete by granite waste up to a rate of 25% was the subject of the works conducted by Allam et al. [5] who found a slump of the order of 10cm and a higher compressive strength compared to control concrete at all ages. Likewise, Lakhani et al. [6] observed the same findings, whereat a decrease in slump as a function of increasing the rate of fine granite waste aggregate, which is due to the fine particle size of such waste, as this decrease in workability, could easily be improved with the use of super-plasticizers [7]. More to the point, Vijayalakshmi et al. [8] found that substituting up to 15% of the ordinary sand in concrete with polished granite waste resulted in concrete that met the necessary strength and durability requirements. Nonetheless, they advised that these wastes should be chemically treated to improve their sulphate resistance by undergoing a bleaching process before being added to the concrete mix. Subsequent to which, the results of the works conducted by Singh et al. [9] on the effect of granite cutting waste fine aggregate, on concrete properties, have clearly illustrated that concrete substituted with granite waste exhibits increased resistance to

carbonation, chloride ion penetration, acid attack and exposure to elevated temperatures at an optimum granite waste replacement of 25%.

Indeed, granite waste was alike recovered in the composition of self-compacting concrete, seeing that Jain et al. [10] studied the partial substitution of fine aggregates of a self-compacting concrete up to 60% by granite waste powder. The results indicate that the compressive strength in all concrete mixes was higher than the one deduced at of the control except for the mixes with 50% and 60% substitution rate. All the concrete mixes, with the exception of the 60% granite powder mix, demonstrated superior resistance to carbonation, drying shrinkage, chlorides and corrosion compared with the control mix. In the same context Gautam et al. [11] worked on the behaviour of a self-compacting concrete containing granite waste as fine aggregate, they found satisfactory results in the fresh state except for the self-compacting concrete of 40% granite waste fine aggregate, as the maximum resistances are recorded for the self-compacting concrete based on 30% granite waste fine aggregate. Nevertheless, increased resistance to chloride and corrosion was observed for the incorporation of up to 30% fine granite waste aggregate.

Waste from the cement industry, including Cement Kiln Dust (CKD) and unfired or poorly fired clinker, has been used in several types of construction materials. CKD has been employed as a cement additive [12-13-14] and as a component of sand concrete [15]. On the other hand, there has been limited research on the valorisation of baked or unbaked clinker in construction materials. Except for a few in-depth studies have been carried out on the subject, notably the research of Chaib et al. [16], which investigated the impact of baked and unbaked clinker on cement quality, and Kaplan et al. [17], who explored the integration of clinker aggregates into geo-polymer grouts.

Fig. 1. Waste granite and recycled clinker

In the study conducted by Smir [18], the aim was to recover discarded unbaked clinker that the HOLCIM Company had previously considered as waste, along with reusing it in cement production and analysed the impact of this clinker on the quality of the produced cement. In this respect, they found that the workability of concrete made with this cement became increasingly difficult as the addition of unbaked clinker to the cement increased. This was mainly due to the high free lime content of the unbaked clinker and the high-water content associated with the percentage of baked clinker. Hence, this work makes it possible to provide definition to the optimum quantity of unbaked clinker to add to the cement without altering the concrete characteristics. Many studies have demonstrated the advantages of utilising waste clinker and granite, whether in the form of aggregates or cement additives in mortars, concrete, and self-compacting concrete. Therefore, this work aims to use waste granite and recycled clinker unbaked or under baked as shown in Figure 1 to partially replace ordinary sand. These recycled sands are incorporated into sand

concrete with substitution rates of 20% and 40%. The study examines the impact of these recycled sands on the properties of the concrete in its fresh state, as well as its mechanical performance in the hardened state, durability, and microstructural parameters.

2. Materials

The materials used in the study include a composite Portland cement CPJ-CEM II 42.5 (S-L) sourced from the cement factory of Hadjar Essoud in Skikda, Algeria, with an absolute density of 3.22 g/cm^3. Other components comprise dune sand (DS) of siliceous nature from Oued Z'hor quarry, Skikda-East of Algeria, sand from granite waste (GS) obtained through crushing and sieving granite waste, and recycled clinker sand (CS) obtained by crushing and screening baked or unbaked clinker from the Hadjar Soud cement factory in Skikda (Fig. 2). Additionally, fine limestone (F) retrieved from the filters of the Ben Azzouz quarry in the East of Skikda, passing more than 80% through an 80µm sieve, is included. Table 1 provides an overview of the various physical and chemical properties of the aggregates and the particle size distribution is illustrated in Figure 3. The mix incorporates a super-plasticiser (SP), namely the high-water reducer Master Glinuim 26, as a light brown liquid with a pH of 5 and a density of 1.07 g/cm^3. Finally, tap water at a temperature of 28°C is utilised for the mixing process.

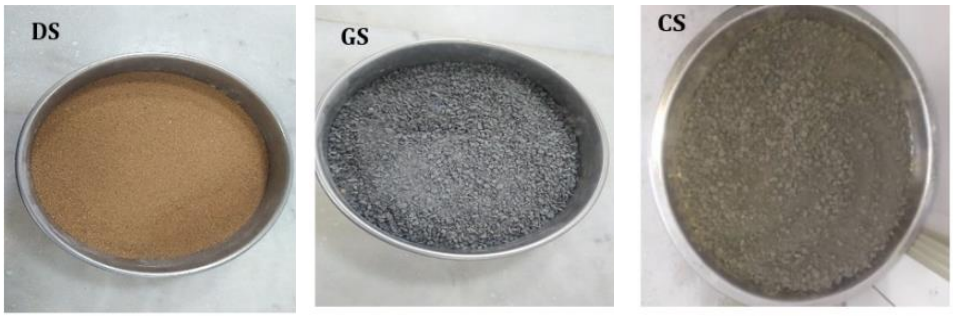

Fig. 2. The sands used

Characterization tests have revealed significant differences among various sands used in concrete production. Granite waste sand exhibits a higher density compared to dune sand and clinker sand. According to Figure 3, the sands used demonstrate satisfactory fineness, with all particles having a size greater than 0.063 mm. In terms of volume, it is observed that (7.33%, 10.67%, and 9.33%) of the particles are less than 0.125 mm, while (93.33%, 26%, and 19.33%) by volume are less than 0.5 mm for the DS, GS, and CS samples respectively. A relatively small percentage, ranging from 6 to 9%, represents particles smaller than 0.063 mm. The grain size distribution curves of the sands used are continued, and the particle size distribution according to the NF EN12620 and NF P18-545 standards shows that the curve of the granite waste sand (GS) exhibits the best regularity of grain size compared to the recycled clinker sand (CS) and the dune sand (DS), respectively.

According to the fineness modulus, ordinary sand is finer than granite waste sand and clinker sand respectively. Hence, the introduction of the latter into concrete adversely affects workability and increases mechanical strength. Additionally, granite waste sand contains a higher fines content than dune sand and clinker waste sand. Sand equivalent tests confirm that all sands fall within the 70% to 80% cleanliness range, making them suitable for high-quality concrete production. According to chemical analysis (Table 1), dune sand and sands from GS and CS contain a percentage of silicon dioxide (SiO_2) of (77.86%, 41.2% and 22.02%) respectively.

Table 1. Physical and chemical properties of sands

Physical properties			
	DS	GS	CS
Apparent density (g/cm³)	1.412	1.650	1.489
Absolute density (g/cm³)	2.631	3.062	2.723
Sand equivalent (%)	74.59	72.34	70.50
Water absorption (%)	1.02	1.67	5.44
Fineness modulus (%)	1.55	3.47	3.90
Inter-granular porosity (%)	46.33	46.11	45.32
Fines content (%)	6	8.33	6.66
Chemical composition (%)			
	DS	GS	CS
SiO_2	77.86	41.2	22.02
Al_2O_3	2.05	13.2	5.49
Fe_2O_3	1.13	9.59	3.72
CaO	4.78	9.06	65.58
MgO	0.19	4.99	1.05
SO_3	0.00	0.31	0.07
K_2O	0.59	0.08	0.90
Na_2O	0.19	2.5	0.20
Cl^-	-	0.01	0.01

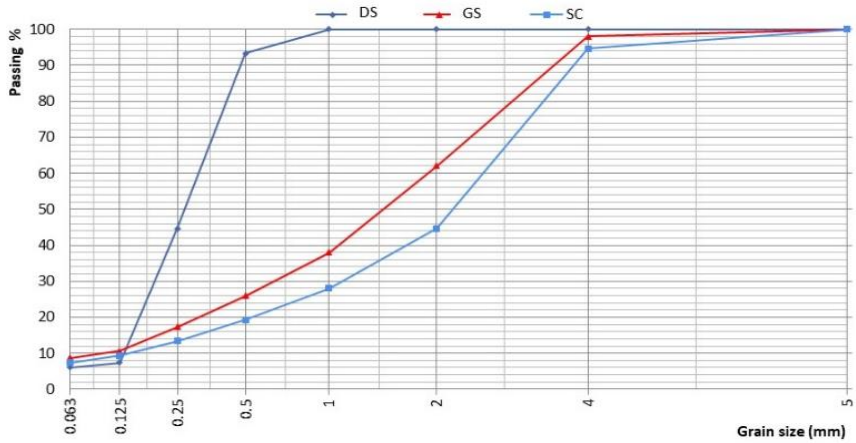

Fig. 3. Particle size distribution of sands

SiO_2 is the dominant compound in the composition of granite; thence silica reacts with lime during the hydration of cement and favours the formation of hydrated calcium silicates, which can slow down the hardening process and make it possible to obtain high resistance in the medium and long term and improve the durability of concrete, particularly in aggressive environments. Furthermore, in addition to silica, granite waste sand contains alumina Al_2O_3 (13.2%), which contributes to the setting of concrete, but has a negative effect on chemical stability and favours attack by sulphates [19]. Conversely, clinker is basically composed of CaO, and the presence of this element promotes the formation of

C3S, which offers high short-term resistance and increases cohesion. Further, the high reactivity increases the homogeneity of the mix and reduces the porosity and permeability of the concrete [19-20].

3. Experimental PROGRAMME AND TESTS METHODS

3.1 Experimental Program

In the experimental programme, we partially substituted in the volume of an ordinary sand (DS) of a sand concrete by recycled sands (granite waste (GS) and recycled clinker (CS)) with replacement rates of 20% and 40%, and studied the effect brought by the introduction of these sands on fresh and hardened properties as well as durability parameters. The SC0 reference formulation was established according to the experimental method of Sablocrete [21] with the fixed parameters being the Water/Cement ratio (W/C=0.68), the cement dosage, the dosage of limestone fines and the content of 1% super-plasticizer. Therefore, the selected formulations (SCG, based on granite waste sand, and SCC, based on recycled clinker sand) are obtained by the same method, with the substitution of ordinary sand by volume with recycled sand. The different compositions of the mixes are illustrated in Table 2.

Table 2. Mix proportions of different concrete mixtures

Mixtures	CEMII (Kg)	DS (Kg)	F (Kg)	SP (Kg)	W (Kg)	GS (Kg)	CS (Kg)
SC0	400	1160.40	252	4.32	272	0	0
SCG 20	400	928.32	252	4.32	272	271.968	0
SCG 40	400	652.72	252	4.32	272	543.936	0
SCC 20	400	928.32	252	4.32	272	0	253.837
SCC 40	400	652.72	252	4.32	272	0	507.674

3.2 Tests Methods

3.2.1 Fresh Properties Tests

The fresh density was evaluated after casting using an 8-liter container, in accordance with standard NF EN12350-6, workability measured by slump with an Abrams cone in accordance with standard NF EN12350-2, and the content of occluded air measured by a concrete aerometer in accordance with standard NF EN12350-7.

3.2.2 Mechanical Properties

3.2.2.1 Mechanical Resistance

Specimens of size (4×4×16) cm^3 preserved in water 28 days until the curing periods of 7, 28 and 90 days, broken in tension by 3-point bending and subsequently in compression in accordance with standards NF EN12390-5 and NF EN12390-3 respectively. The loading should be applied continuously until the specimen ruptures. The elastic modulus of concretes was evaluated at 28 days according to Eq. (1) [22].

$$Ed = \frac{\rho . V^2 (1+\nu)(1-2\nu)}{(1-\nu)} \quad (1)$$

Where: Ed is the dynamic modulus of elasticity (GPa); ρ is the density of the hardened concrete (kg/m^3); V is the ultrasonic velocity (km/s); and ν is the Poisson's ratio.

3.2.2.2 (UPV) Test and The Sclerometer Test

Specimens measuring (15×15×15) cm^3 were prepared for the ultrasonic pulse velocity (UPV) test and the sclerometer test after 28 days of water curing. The sclerometer test, conducted in accordance with standard NF EN 12504-2, evaluates the surface hardness of the concrete through rebound measurements. This method involves striking the concrete surface with a hammer and then measuring the rebound distance. Simultaneously, the UPV test, performed according to standard NF EN 12504-4, used a portable digital ultrasonic tester. This method involves transmitting ultrasonic pulses through the concrete sample, allowing for the determination of its velocity.

3.2.3 Durability

3.2.3.1 Shrinkage and Swelling

Measured on specimens measuring (4×4×16) cm^3 fitted with studs. Shrinkage specimens are stored in air, whilst swelling specimens are stored in water in accordance with standard NF P 18-427. The shrinkage and swelling are measured using a deform meter equipped with a comparator and reference rod, enabling measurements with an accuracy of less than or equal to 0.005 mm. A 270 mm long rod is used to calibrate the deform meter.

3.2.3.2 Water Absorption by Immersion

According to Neville [22], the specimens of dimension (5×5×5) cm^3 are kept in water for 28 days. The specimens are weighed to determine the wet mass, after which they are placed in the oven at 105± 3°C until a constant mass is obtained, then they are weighed to determine the dry mass, the absorption is measured by subtracting the dry mass from the wet mass, then dividing by the dry mass.

3.2.3.3 Water-Accessible Porosity

Is measured on specimens measuring (5×5×5) cm^3, which are kept in water for 28 days according to the NF P18459 standard. After this curing period, the saturated mass is measured, followed by the use of a hydrostatic balance to measure the hydrostatic mass. Subsequently, the samples are dried at 105°C until reaching a constant mass, after which their dry mass is measured. The porosity is calculated from the ratio between the difference between the saturated and dry masses and the saturated and hydrostatic mass, with the value expressed as a percentage.

3.2.3.4 Capillary Water Absorption and Sorptivity Test

The test was conducted in accordance with the NF EN 13057 standard using specimens measuring (7×7×28) cm^3. These specimens were immersed in water for 28 days before testing. Their side faces sealed and they were then subjected to unidirectional water absorption from their bottom for nearly a week. This procedure was carried out to determine capillary absorption, which was plotted against the square root of the elapsed time to yield the sorptivity.

3.2.3.5 Freeze-Thaw

On specimens of size (4×4×16) cm^3 fitted with studs are subjected to 300 freeze-thaw cycles in accordance with standard NF P18-425. Shrinkage and mass measurements were taken every 30 cycles. An ultrasonic test was carried out at the end of the test.

3.2.3.6 Chloride Penetration

According to NT BUILD 492-1, on (4×4×16) cm^3 specimens kept 28 days in water at a temperature of 20 ± 2°C. Thereafter, totally immersed in a prepared saline solution of sodium chloride (5% NaCl) diluted in distilled water for 120 days, the specimens

underwent a process of cutting and application of a silver nitrate solution ($AgNO_3$) with 0.1 M concentration onto their concrete surfaces.

3.2.3.7 Chemical Attack by Acids

After 28 days of curing in water, the specimens of dimension (5×5×5) cm^3 are weighed to determine an initial mass, then they are immersed in solutions with a concentration of 4% hydrochloric acid (4% HCl) and 4% acetic acid (4% CH_3COOH) added to the water volume. The chemical resistance is evaluated by measuring the mass loss of the specimen according to ASTM C267-96 standard. The specimens are cleaned three times with fresh water to remove the deteriorated concrete and left to dry for 30 minutes. Then they are weighed again. This operation is performed after 7, 14, 21, 28, 56, 60, 90, and 120 days of immersion. The solutions used are renewed every 14 days (based on the pH variation).

3.2.4 Microstructural Analysis Tests

A materials characterization technique uses X-rays to determine its crystalline structure. X-rays are directed towards a sample, which diffracts them in different directions depending on its crystalline structure. By measuring the angles of X-ray diffraction, the arrangement of atoms in a sample can be determined, thus obtaining information about its crystalline structure. The determination of amorphous and crystalline phases by X-ray diffraction was carried out using an XRD diffractometer (Philips, X'Pert) using Cu Kα radiation, 40 kV, 35 mA, with a step of 0.02° ranging from 10° to 80°. ICDD plots were used to identify the intensity and location of peaks.

4. Results and Discussion

4.1. Fresh State Properties

Figure 4 shows that the fresh densities of ready-mixed concrete increase with increasing levels of recycled sand substitution. Besides, the highest density is obtained for concrete based on 40% granite waste sand (SCG40). Further, it exceeds the value shown by the control concrete of 9.16% and that of the concrete containing 40% clinker waste sand of 4.38%. However, this increase in density is expected because recycled sands have higher absolute densities, higher quantities of fines filling the available voids between the concrete constituents and higher water absorption coefficients than ordinary sand. Therefore, these results are compatible with those found by Abukersh and Fairfield [23] and Kherraf et al. [24] and contrary to those obtained by Shamsabadi et al. [25]. This difference in results may be linked to the different particle distribution and the method of obtaining recycled sand.

The partial replacement of ordinary sand with recycled sands GS and CS results in an increase in workability, with the maximum value achieved by SCG40 concrete, exceeding that of SCC40 concrete by 17% and that of the control concrete by 27%. Besides, this improvement may be attributed to the better particle size distribution of GS on one hand. In the other hand, the finer particle size, which contributed to reducing inter-particle friction within the cement matrix due to the rough and angular morphological characteristics of granite, which can enhance interlocking between particles and improve cohesion within the concrete mixture. This improved particle packing can lead to a reduction in voids and improve the overall compactness of the concrete, thereby increasing its workability [26-27]. These results contradict those found by Zhang et al. [28].

The volumes of content air in clinker sand-based concretes are slightly higher than those in concretes containing granite waste sand. In this respect, the recorded increases in occluded air volume compared with the control concrete were 19.61% for SCG40 and

27.45% for SCC40 concretes. Moreover, this increase in the volume of air occluded in concretes based on recycled sands is certainly linked to the morphology of these grains, which traps air bubbles in the cement matrix of the concretes [29-15].

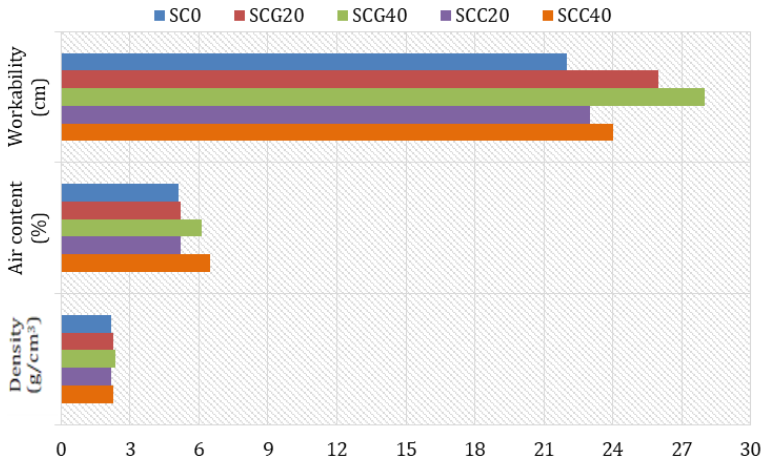

Fig. 4. Variation in fresh properties as a function of substitution rate and sand type

4.2. Mechanical properties

4.2.1. Compressive Strength

The results demonstrated that the increase in strength was observed with the use of GS and CS as partial sand substitution compared with the reference concrete (Fig. 5). Maximum strength was observed for the SCC40 mix at all curing periods. The increase in strength of the mixes after inclusion of 20% and 40% GS was observed. Nonetheless, this increase in strength could be attributed to the finer size of GS; the better filling effect of the particles also reduces interconnected voids and improves the density of the concrete matrix, which improves the compressive strength of the concrete up to an optimum percentage of granite waste [30].

In addition, the roughness and irregular shape of the granite particles increases the strength, as these particles gave better adhesion which results in better bond development between cement paste and aggregate [31-32]. Furthermore, a similar strength gain trend has alike been observed by several researchers Singh et al. [33] and Ghannam et al. [34] who have used granite as a fine aggregate replacement with an optimum range of 10% to 30% in concrete. Increases in the strengths of SCC mixes as a function of the increase in the substitution rate. Besides, this increase is explained by the hydraulic power of the fine CS particles, on the one hand. However, this increase in strength is a consequence of the increase in compactness, on the other hand, due to a pozzolanic reaction developed by the reactive fines contained in the CS [35-36]. In virtue of which, our results contradict those obtained by Prošek et al. [37]. At 28 and 90 days, concretes based on recycled clinker sand give the best compressive strengths compared with concretes based on granite waste sand. Nevertheless, this is due, on the one hand, to the fineness modulus of the CS sand and, on the other hand, to the presence of CaO, which provides a lot of C3S, an element responsible for strength and cohesion [20-38]. There was a good linear correlation (Fig. 6) between compressive strength and density in the hardened state for all the studied concretes, which indicates the accuracy of the results.

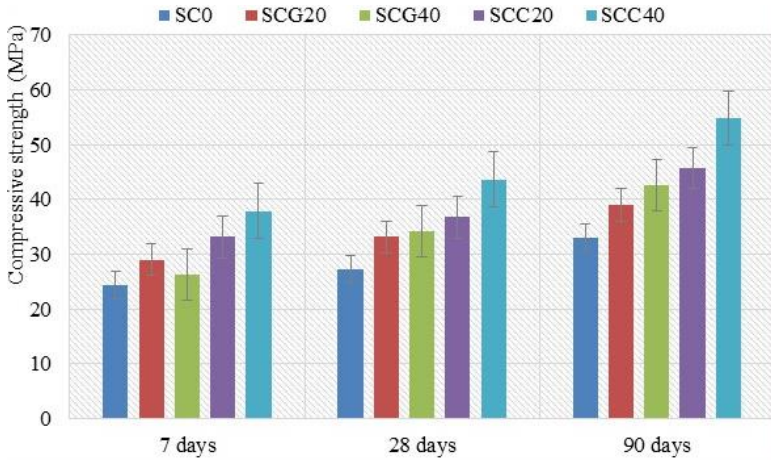

Fig. 5. Influence of substitution rate and type of sand on compressive strength

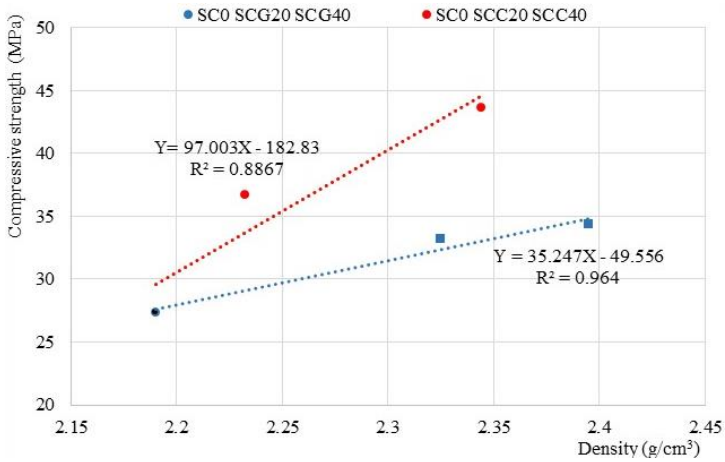

Fig. 6. Correlation between compressive strength and density

4.2.2 Flexural Tensile Strength

At the three timescales of 7, 28 and 90 days (Fig. 7), the flexural tensile strengths of the recycled sand-based concretes were better than those of the control concrete. Besides, SCC40 showed the highest strength, with an 82% increase over the reference concrete. In this respect, these results can be explained by the fact that CS is characterised by sharper, more porous grains, which form stronger bonds with the cement paste in the mix [37]. When they react with the cement minerals and water, the anhydrous components of clinker create hydrates that decrease the porosity of concrete and increase cohesion [20]. These components fill the voids between particles, leading to denser matrices and increased flexural strength. In virtue of which, these results have shown to be consistent with those found by Mebarkia et al. [39].

An increase in flexural tensile strengths was observed in the GS-based concretes compared to the reference concrete, this improvement is due to the rough texture of the granite sand which could have improved the adhesion of the aggregates to the cement paste [40-41]. Figure 8 presents a precise linear correlation between the compressive strength and the flexural tensile strength for all the concretes studied with a correlation coefficient of (0.9557 and 0.9978) for SCG and SCC respectively, which denotes the precision of the results.

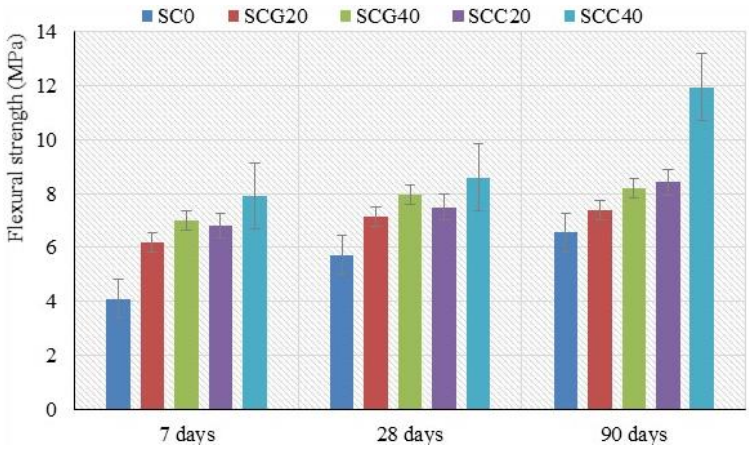

Fig. 7. Influence of substitution rate and sand type on flexural tensile strength

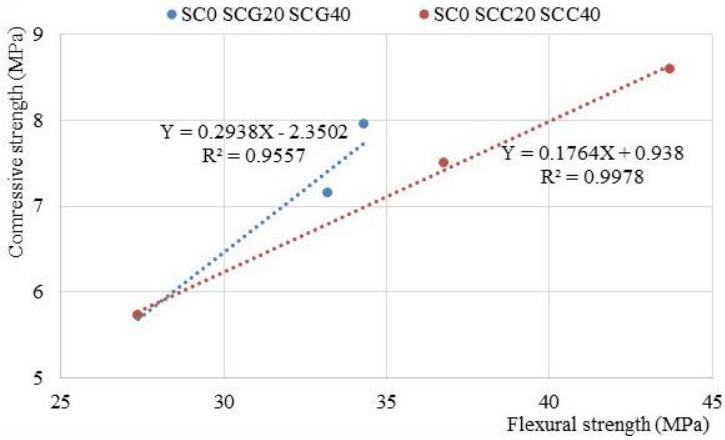

Fig. 8. Correlation between the compressive strength and the flexural tensile strength

4.2.3. Compressive Strength Obtained by Sclerometer

Figure 9 shows that the introduction of recycled sand into the sand concrete increased the surface hardness compared with the control concrete. However, the addition of granite waste sand has a positive effect on surface hardness. Further, compressive strength increases with increasing GS substitution rate to reach a maximum value of 31.40 MPa in SCG40 concrete, this is explained by the fact that granite waste sand contains a lot of silica (41.2%) which gives high medium and long-term strengths. The addition of recycled clinker sand at a rate of 40% gives the maximum strength obtained by sclerometer, the fact

of which is explained by the presence of CaO in the clinker sand, which gives good bonding of the aggregate matrix [20]. Definitely, resistances based on recycled clinker sand are higher compared to concretes based on granite waste sand, which may be due to the chemical composition of the clinker, which is close to the chemical composition of the cement.

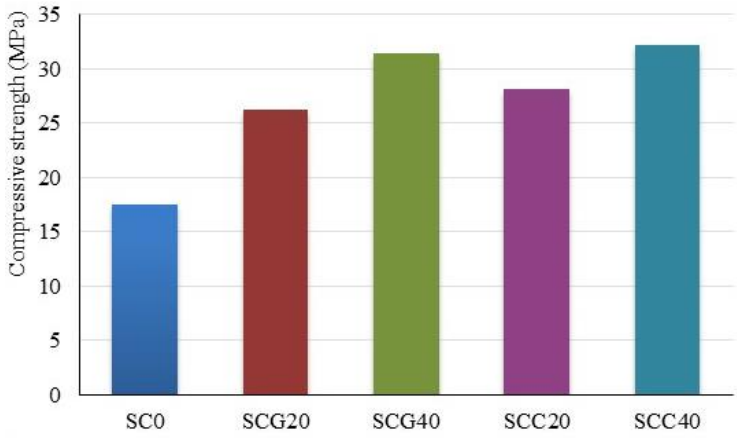

Fig. 9. Compressive strength obtained by sclerometer test

Figure 10 shows the variation in the Schmidt hardness index of the mixes as a function of the type of concrete. However, it shows a precise linear correlation between the two factors with a correlation coefficient of (0.966 and 0.923) for SCG and SCC respectively. Besides, it is clear that the rebound index of concrete made from recycled waste is higher than that of control concrete; it increases with the increase of the substitution rate for the two types of concrete SCG and SCC. In virtue of which, the maximum value of the Schmidt hardness index is given by SCC40.

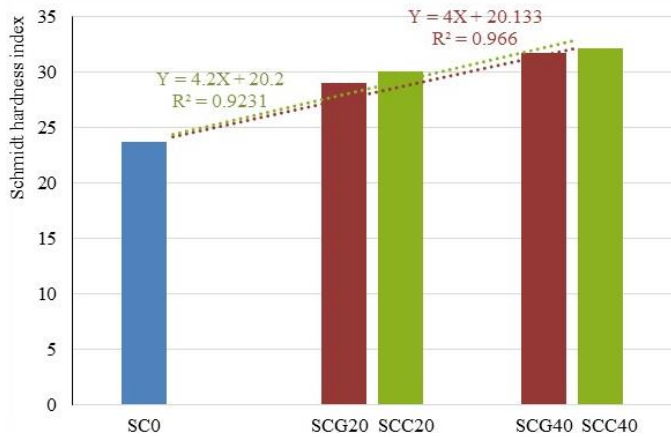

Fig. 10. Variation of the Schmidt hardness index as a function of the substitution rate and type of sand

The correlation between Schmidt hardness index and compressive strength measurements obtained by destructive testing is demonstrated in Figure 11. However, this correlation is established by a linear relationship, with a coefficient of (0.9656 and 0.9627)

for SCG and SCC respectively. On the other hand, the Schmidt hardness index values given by the recycled clinker-based concrete have shown to be better than those obtained by the control concrete and the granite waste-based concrete, giving the best strengths. In virtue of which, these results once again confirm that the two SCC20 and SCC40 mixes are the most resistant.

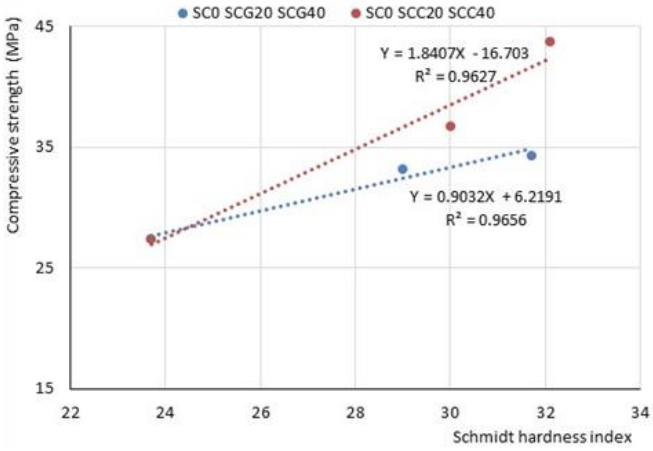

Fig. 11. Correlation between compressive strength obtained by destructive testing and Schmidt hardness index

*4.2.4. Ultrasonic **V**elocity*

In fact, the introduction of recycled sand as a partial replacement for ordinary sand leads to an increase in the ultrasonic velocities of the mixtures, whatever the rate and type of sand (Fig. 12). Above and beyond, clinker sand-based concretes showed the highest velocities compared to GS based concretes, these results are explained by the denser structure of CS based concretes compared to GS based concretes. Thereof, these results are in agreement with those found by Sharma et al. [42] and Abbaszadeh and Modarres [43].

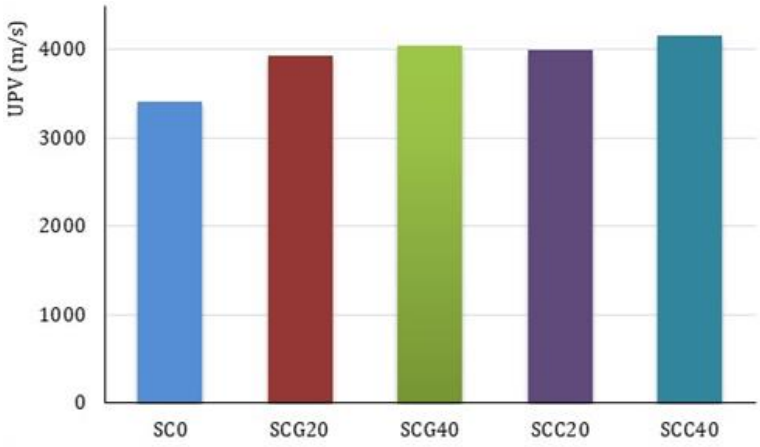

Fig. 12. Variation in UPV as a function of substitution rate and type of sand

4.2.5. Compressive Strength Obtained by The Combined Method

As a fact of matter, the strength of mixes based on recycled sands obtained by the combination of sclerometer and ultrasound (Fig. 13) increases with the increase in the recycled sand content and CS-based mixes give high strengths compared with GS-based mixes. As consequence, the strengths obtained by the combined method are compatible with the strengths obtained by destructive testing, UPV and sclerometer.

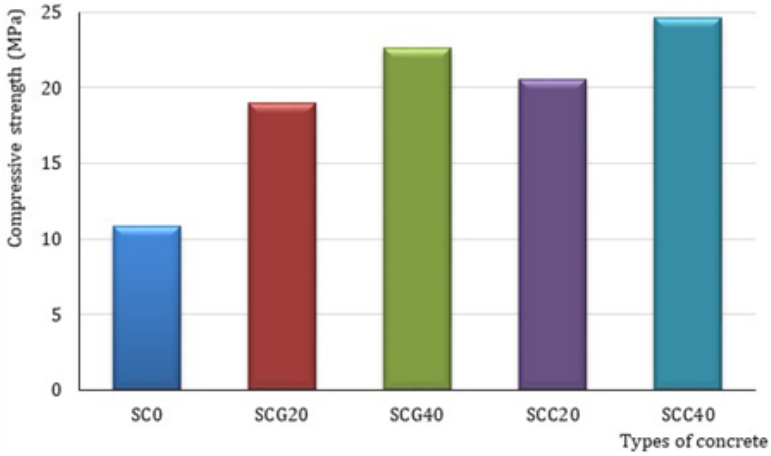

Fig. 13. Compressive strength obtained using the combined method

4.2.6. Shrinkage and Swelling

Indeed, Figure 14 clearly shows that the incorporation of recycled sand from clinker and granite waste has a considerable impact on the total shrinkage of the concretes. After 120 days of conservation, the average total shrinkage values of all the recycled concretes, based on 20% and 40% CS and GS respectively, are higher than those recorded for the reference concrete. Therefore, the result illustrated by the control concrete may be attributed to the more regular filling capacity of the dune sand.

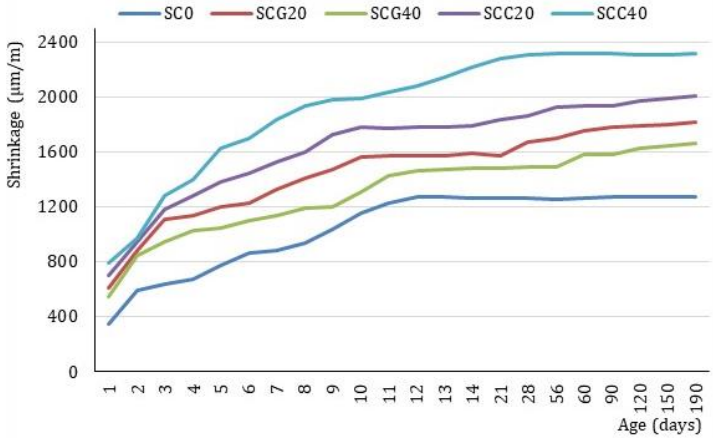

Fig. 14. Influence of substitution rate and type of sand on shrinkage

Likewise, it can alike be noticed that the shrinkage of concrete containing recycled clinker sand is higher than the one of the other types of concrete. In fact, the maximum value is obtained by SCC40 concrete. However, this is due to the evaporation of water trapped in the sand grains, which have a porous microstructure. In addition, this sand contains fine reactive particles that take part in the hydration reaction, resulting in an increase in the volume of the paste and accordingly an increase in the number of micropores filled with free water, which disperses during air-drying. In reality, analysis of the results obtained (Fig. 15) shows that concretes based on granite waste sand and recycled clinker have lower swellings than the reference concretes. In fact, the introduction of granite sand into the mixes produces the lowest swelling values. This is linked to the fines content of the sands, which enclose the existing interstices in the mixes.

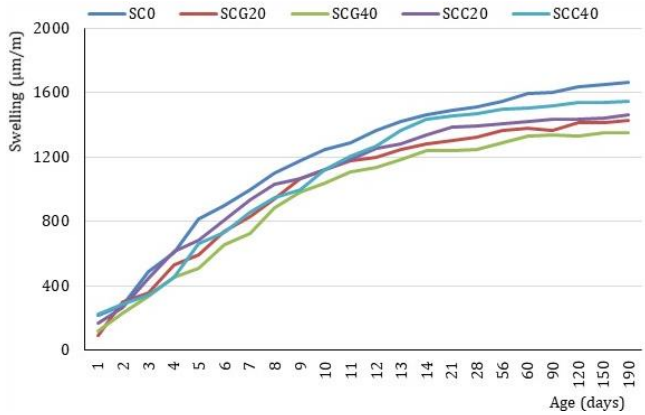

Fig. 15. Influence of substitution rate and type of sand on swelling

4.2.7. Absorption by Immersion

Generally speaking, concretes based on recycled sand have a lower absorption than control concrete (Fig. 16), as this can be explained by their absorption coefficients, which are lower than those of ordinary sand. Nonetheless, substituting ordinary sand with 40% recycled granite waste sand and clinker resulted in a reduction in absorption of 3.9% and 10% respectively.

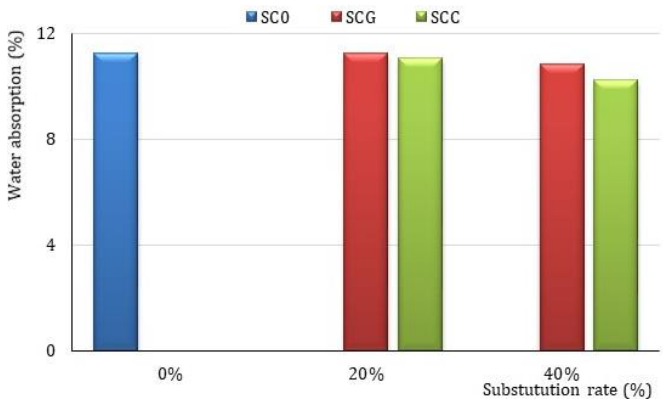

Fig. 16. Water absorption by immersion as a function of the rate of sand substitution and type

Moreover, concrete based with waste granite sand absorbs more water than concrete made with recycled clinker sand. This is due to the hydrated products formed by the addition of CS, particularly the entanglement of C-S-H gel, which gives strength to SCC and develops on the surface of unhydrated grains, gradually filling the capillary voids between the grains and resulting in densification of the matrix. This explains the lower water absorption of SCC compared to SCG (Granite Sand Concrete) [24]. As consequence, these results have shown to be consistent with those found by Ahmadi et al. [44] and Ghorbani et al. [45].

4.2.8. Porosity Accessible to Water

The values of the porosity accessible to water after 28 days of curing are illustrated in Figure 17. Therefore, the results show an increase in porosity when granite waste sand is incorporated, i.e. an increase of 5% compared with the control concrete at a substitution rate of 40%. This increase in porosity is due to the presence of fines in the granite and additional porosity at the Interfacial Transition Zone (ITZ) between the smooth faces of the granite grains and the cement matrix [46]. On the other hand, there was a reduction in porosity when ordinary sand was replaced by recycled clinker sand. Nonetheless, this reduction is of the order of 8.5% at a replacement rate of 40%. In fact, the use of reactive fines made it possible to densify the cement matrix, giving rise to new hydration products and greater compactness, accordingly.

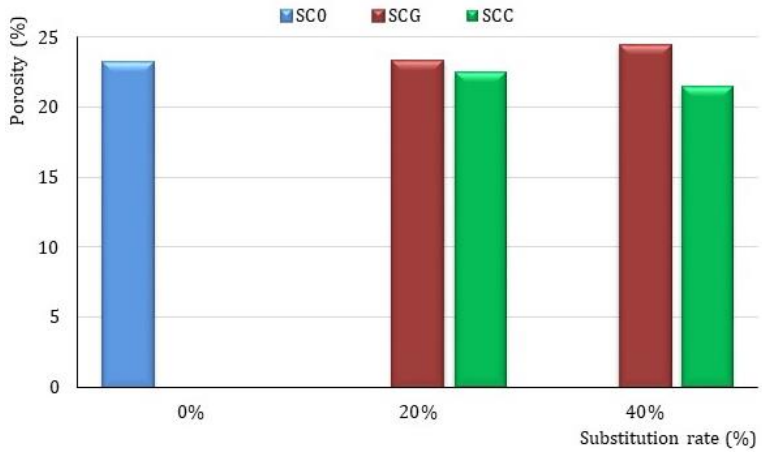

Fig. 17. Porosity accessible to water as a function of the rate of sand substitution and type

4.2.9. Capillary Absorption and Sorptivity

According to the curves in Figure 18, three phases can be observed. The first phase is linear, extending only over the first five hours, and corresponds to the filling of the widest capillaries that water penetrates first. A second linear phase but with a steeper slope extends for about 8 days after the first phase, corresponding to the saturation of narrower capillaries that require more time to fill. In the end, all capillaries tend towards saturation [47]. Indeed, the concrete containing 20% recycled clinker sand performs the best, with the absorbed water mass being 14.89% lower than that of the control. On the other hand, concretes incorporating 20% and 40% granite waste sand show greater capillarity, their capillary absorption coefficients exceeding the one pertaining to the control by 08.36 and 15.5% respectively. Nonetheless, this indicates that the pores in the granite waste sand concrete matrices are large and interconnected compared to those in the control and

recycled clinker sand concretes. As consequence, these results have shown to be in agreement with Cheah et al. [48].

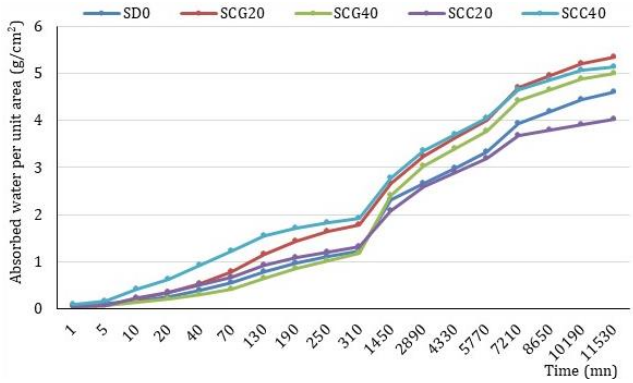

Fig. 18. Influence of substitution rate and type of sand on water absorption by capillarity

The sorptivity coefficient is a parameter closely linked to water absorption by capillaries, as well as to porosity and pore interconnectivity. Figure 19 presents the sorptivity coefficient for the examined concrete mixtures. The sorptivity coefficient was found to be directly proportional to the capillary water absorption of each concrete mixture. Concrete mixtures based on 20% recycled clinker SCC20 performed better than the other mixtures. It can be inferred that the sorptivity coefficient of concretes based on waste granite decreases as the substitution rate increases. Singh et al. [49] showed that water absorption and sorptivity of concrete decrease with an increase in the proportion of granite, which contradicts the results of Pereira et al. [50].

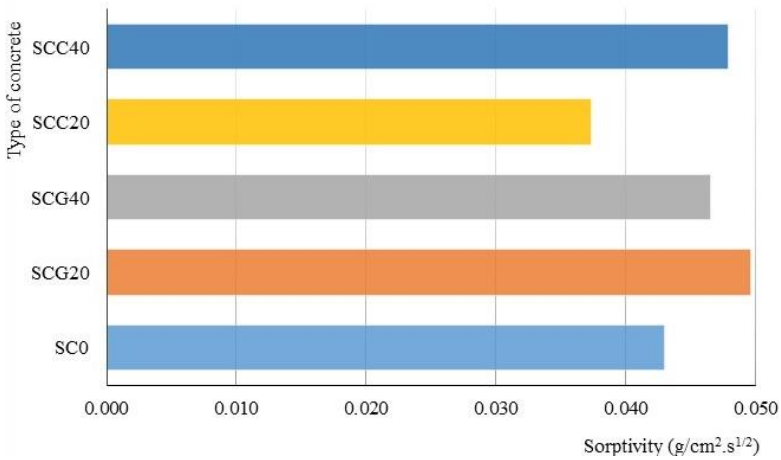

Fig. 19. Coefficient of sorptivity

4.3. Behaviour of Different Concretes Exposed to The Freeze-Thaw Cycle

4.3.1. Freeze/Thaw Shrinkage

It is clear that the shrinkage of the recycled sand-based concretes is less than that of the control (Fig. 20). Besides, all the mixes underwent shortening during the initial cycles, but

after reaching 120 cycles, there was no further change in length. Further, the dimensional variation of the SCG20, SCC20 and SCC40 concretes was found to be less than 500 µm/m, indicating a high level of resistance to freeze/thaw cycles as defined by ASTM C 666. These results are in line with those of Zhang et al. [28].

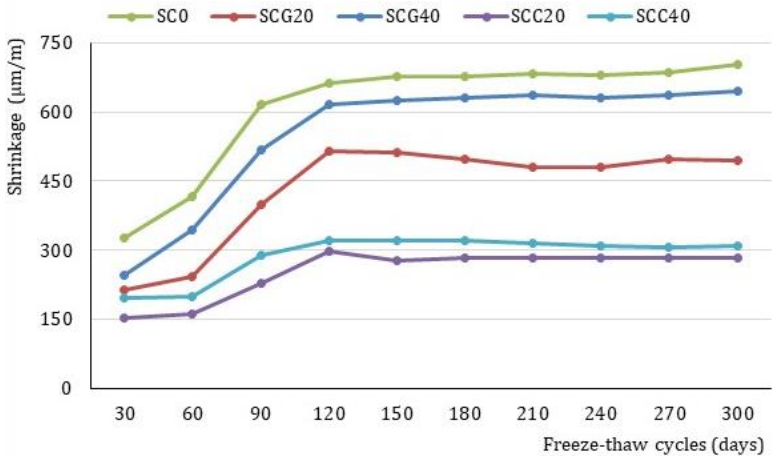

Fig. 20. Dimensional variation as a function of the number of freeze/thaw cycles

4.3.2. Mass Loss

Figure 21 shows the variation in weight of the concretes tested after 300 freeze/thaw cycles. Further, it is important to note that during the period from 30 to 120 cycles, the SCG40 concretes, as well as the SCC20 and SCC40 concretes, showed a gain in weight. On the other hand, the SCG20 concrete and the control sample lost weight. Beyond 120 cycles, there was no change in mass for the SCG40 and SCC40 concretes. Nevertheless, the SCG20, SCC20 and control concretes experienced a significant loss of mass. Therefore, the maximum loss was for concrete made with 40% granite waste sand.

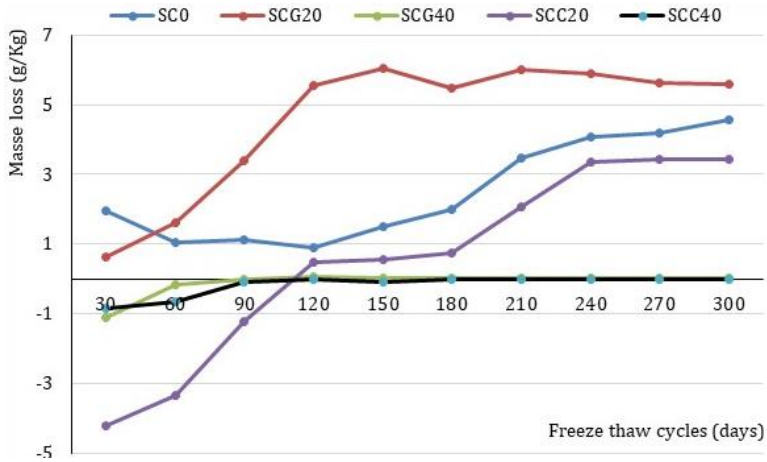

Fig. 21. Mass loss as a function of the number of freeze/thaw cycles

4.3.3. Visual Observation of Deterioration

When concrete freezes, the process of transforming confined pore water into ice can potentially create significant pore pressure. Subsequent to which, this can lead to cracking, spalling and degradation of the concrete. Besides, a visual inspection was carried out to assess any visible signs of cracking and spalling of the surface of the samples following freeze/thaw cycles. According to Figure 22, the SC0 and SCG20 concretes showed good resistance to freeze/thaw cycles, but more or less significant degradation occurred in the SCC20 and SCC40 concretes, whilst the SCG40 concrete showed slight surface brittleness. However, these degradations are due to the poor adhesion between the dune sands and the recycled sands [43].

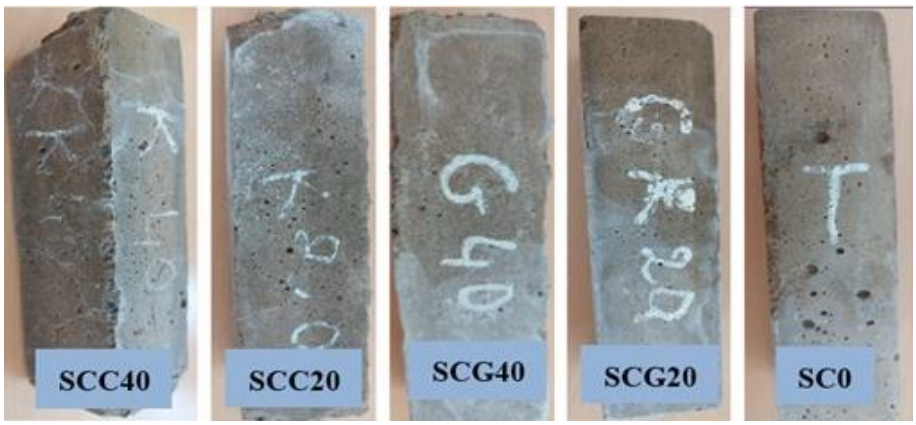

Fig. 22. Visual observation of concrete samples after freeze/thaw cycles

4.3.4. Ultrasonic Speed

In general, the ultrasonic velocities obtained on concretes after exposure to freeze/thaw cycles (Fig. 23) are lower and follow the same trend as the ultrasonic velocities obtained on concretes not subjected to freeze/thaw.

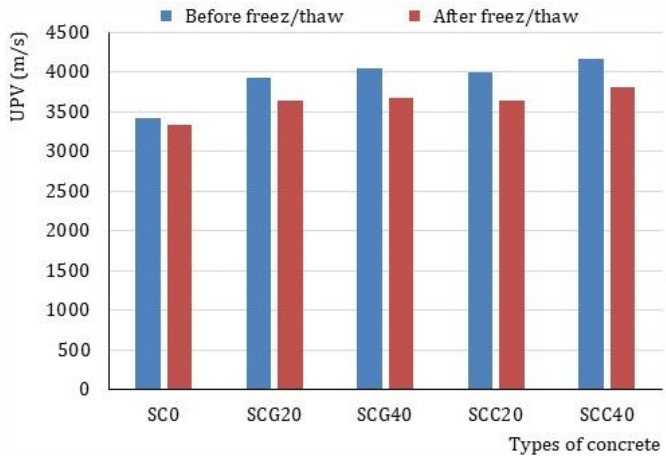

Fig. 23. UPV of concrete before and after freeze/thaw cycles

4.3.5. Modulus of Elasticity

The mixes based on recycled sand before exposure to the freeze/thaw cycle had higher modulus of elasticity than the control concrete (Fig. 24). Further, the same behaviour was observed for concrete exposed to 300 cycles of freezing/thawing. The modulus of elasticity of SCG increases with the increase of the GS rate to reach a value of 35.236 GPa at a rate of 40%, as these results are consistent with the results of a recent study conducted by Amani et al. [51]. In addition, it has shown evident that concretes based on recycled clinker sand give the highest modulus of elasticity before and after freeze-thaw cycles with maximum values obtained at a rate of 40%.

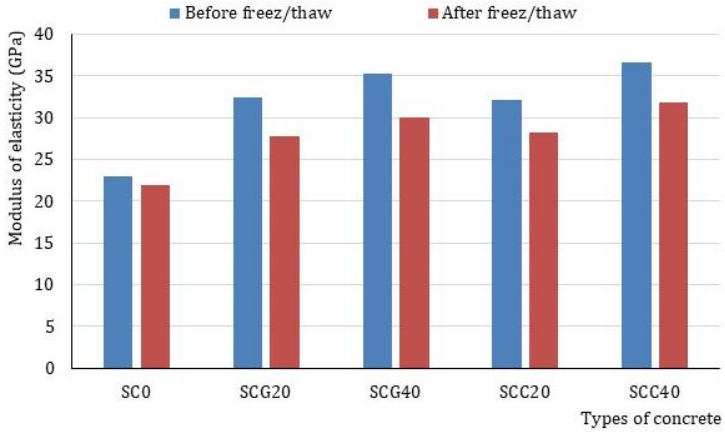

Fig. 24. Modulus of elasticity of concretes before and after freeze-thaw cycles

4.4. Chloride Penetration and Ph of Concretes Exposed to Chloride Attack

The partial replacement of ordinary sand by recycled sand (Fig. 25) results in a reduction in the percentage of chloride ion penetration compared with the reference concrete, whatever the type of sand, and increases with the rate of substitution. Besides, the angularity and roughness of granite sand particles improve the microstructure [52] and develop tortuous capillary paths in the concrete, which could be a cause of preventing chloride ion penetration [48].

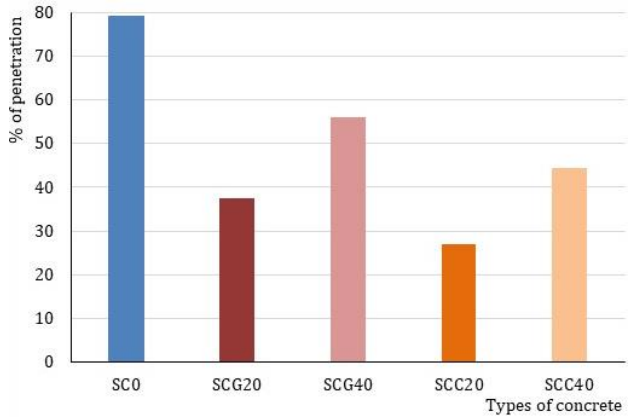

Fig. 25. Percentage of chloride penetration

Concretes containing recycled clinker sand are denser and consolidate the cement matrix better than GS-based concretes (Fig. 26), the fact of which explains the lower penetration percentages in CS-based concretes compared with GS-based concretes.

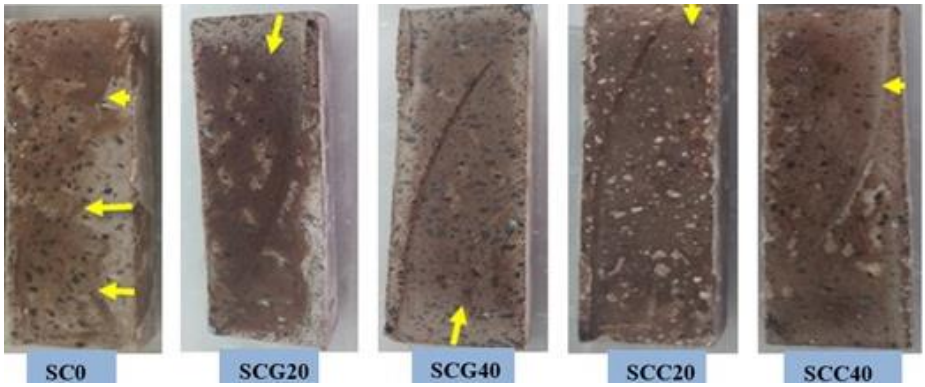

Fig. 26. The split face of the concrete specimen exposes the depth of chloride penetration

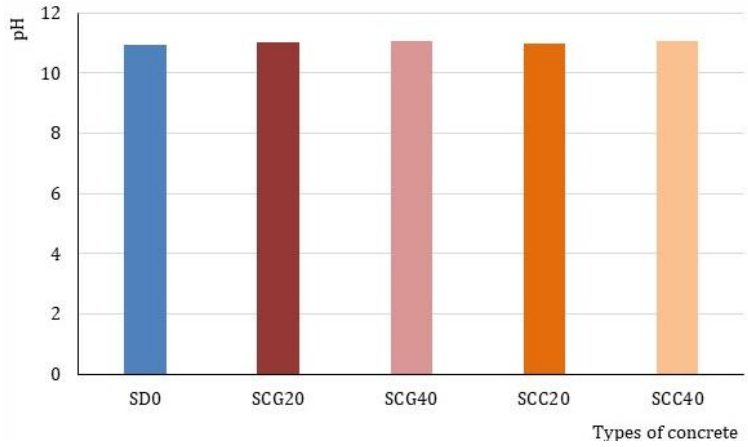

Fig. 27. The concretes' pH exposed to chloride attack

The introduction of recycled sand in place of ordinary sand in the sand concrete (Fig. 27) leads to a slight increase in pH; however, it remains insignificant. Besides, the variation in pH is of the order of 1.35% for the 40% CS concrete, which shows the maximum value (11.08) in comparison with the reference concrete. Subsequent to which, this result can be explained by the presence of a large quantity of CaO in the CS, which strongly reacts in contact with water and forms calcium hydroxide $Ca(OH)_2$, which will dissolve, releasing OH- ions, which will fix the pH of the solution [31]. As a result, this value remains within the range (9 and 13) for non-carbonated concrete.

4.5. Mass variations of concrete exposed to chemical attack (4% HCL and 4% CH_3COOH)

Figure 28 shows that the mass losses of the control concrete are lower than those of the concretes containing recycled sands from waste granite and recycled clinker. Indeed, during the first four weeks of immersion in hydrochloric acid solution, it is observed that

the mass loss curves of both SCG40 and SCC40 concretes are increasing and relatively diverging. At the end of this timeframe, they illustrate a loss around 0.93%. This observation is also applicable to the other two concretes, SCG20 and SCC20; however, the mass losses are more significant. The maximum value reached by SCG20 is 2.64%. In contrast, that shown by SCC20 is 2.49%.

From the age of 28 days of conservation, the effect of hydrochloric acid is accentuated and mass losses become more significant. In the end, after 120 days, SCG20 concrete suffers the greatest loss of mass. Further, it lost 5.27% of its mass, exceeding the one of the control concretes (2.75%) and the SCC20 (4.5%). Likewise, it should alike be noted that SCG40 and SCC40 concretes are more resistant to attack by this acid than those incorporating 20% recycled sand. In fact, they lose 4.01% and 3.04% of their mass after 120 days of immersion. Further, this latter value is the closest to that of the control, so this concrete performs best in the series of concretes based on recycled sand.

The recorded rate of attack depends on the composition and permeability of the concrete studied, the mobility of the chloride ions and also the solubility of the salt resulting from the reactions developed within the samples Eq. (2) [54]:

$$Ca(OH)_2 + 2HCl \rightarrow \ CaCl_2 \ + \ 2H_2O \tag{2}$$

In fact, the incorporation of increasing rates of recycled clinker sand and granite waste did not have a positive impact on the chemical resistance of the reference concrete to attack by hydrochloric acid. However, the mass losses of waste granite sand-based concretes are higher than those obtained by concretes containing recycled clinker sand. Besides, this is because the fine particles of the recycled clinker sand are relatively reactive which generates a weak pozzolanic effect and the hydrates thus formed filled some capillary interstices between the grains [53].

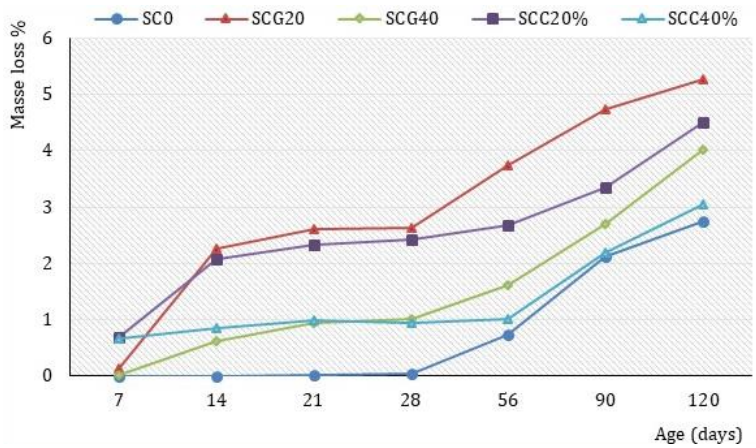

Fig. 28. Mass loss of concrete as a function of immersion period in 4% HCL

Figure 29 shows the mass loss results for concrete immersed in a 4% acetic acid solution. Keeping the concrete samples for four months in the 4% CH_3COOH chemical solution resulted in continuous mass losses over time that diverged in a dissimilar way from the value obtained by the control concrete. Besides, the SCG20, SCG40 and SCC20 concretes underwent mass losses almost similar to those of the control during the 90-day period, after which the trend changed and their degradations became closer and more significant. Moreover, the acquired losses were 5.14, 5 and 4.7% respectively, compared with 4.03% for the reference composition. Besides, the mass loss of SCC40 evolves irregularly, and is

visibly greater than that of the control during the period of exposure to acetic acid attack, from 28 to 120 days.

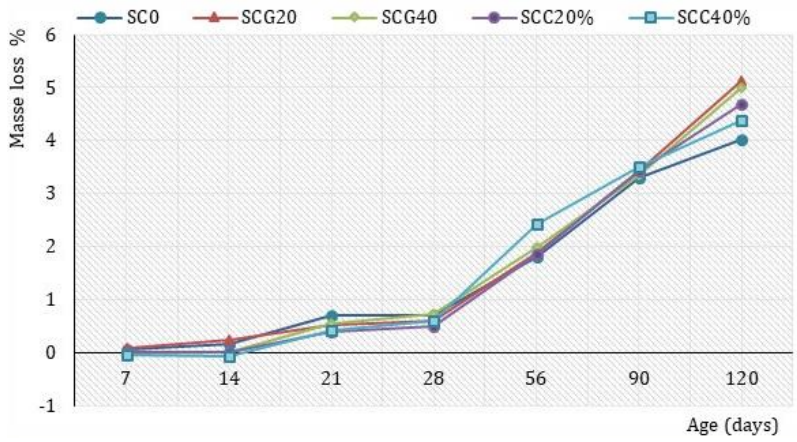

Fig. 29. Mass loss of concrete as a function of immersion period in 4% CH_3COOH

evertheless, in the long term, it can be described as the best-performing concrete in the recycled sand series, as its mass loss is the lowest at 4.37%. In virtue of which, these recorded mass losses can be explained by the fact that acetic acid in contact with the concrete samples can react with the different hydrated and anhydrous compounds in the cement paste (calcium hydroxide, C-S-H, hydrated aluminates, C3S, C2S) in three reactions Eq. (3), Eq. (4) and Eq. (5) [54].

$$2CH_3COOH + Ca(OH)_2 \rightarrow Ca(CH_3COOH)_2 + 2H_2O \quad (3)$$

$$6CH_3COOH + 3CaO.2SiO_2.3H_2O \rightarrow 3Ca(CH_3COO)_2 + 2SiO_2.aq + nH_2O \quad (4)$$

$$6CH_3COOH + 3CaO.Al_2O_3.6H_2O \rightarrow 3Ca(CH_3COO)_2 + Al_2O_3.aq + nH_2O \quad (5)$$

Similarly, it should be noted that the resistance to attack by acetic acid of concretes containing recycled clinker sand is better than that of concretes based on granite sand. Further, the continued presence of fine reactive particles in the recycled clinker sand improves the internal microstructure of the cement matrix, which blocks the mobility of the acid ions to interact with the cement compounds.

4.6. XRD Analyses

In fact, the XRD analysis was carried out on selected concrete samples as shown in Figure 30 to obtain comparative intensities of compounds produced in sandy concrete samples. In this respect, measurements were taken between the intensity and 02 theta values of concrete samples for the peaks if calcite ($CaCO_3$), quartz (SiO_2), Portlandite ($CaOH_2$) and calcium silicate (Ca_2SiO_4). The graph illustrates the presence of quartz and calcite with peaks of maximum intensity for the SCC40 mixture compared with the other mixtures. Further, slightly higher peaks of quartz and calcite were observed for the SCG20 and SCG40 mixtures compared to the control. Likewise, quartz and calcite act as inert fillers in the concrete matrix, resulting in a dense microstructure [55]. Therefore, the presence of Portlandite in optimum amount reduces the pores and alike gives the strength increment [56].

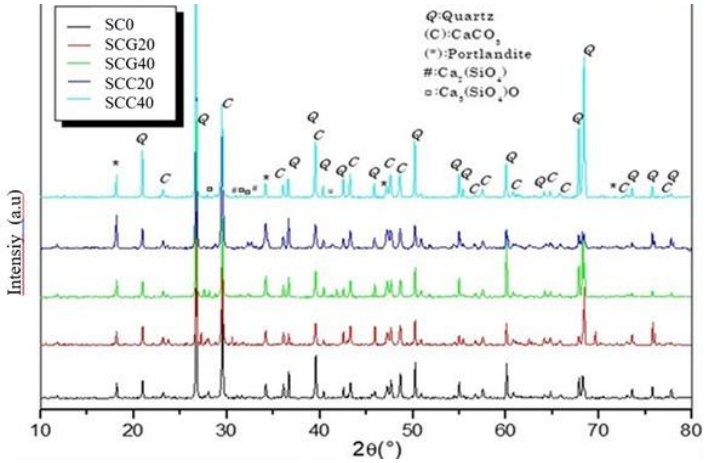

Fig. 30. XRD analysis of concrete

5. Conclusions

Granite and clinker are waste by-products that are harmful to the environment. However, given the large resources of recycled granite and clinker, it appears to be both economically and environmentally useful to use these wastes in concrete production. In this study, the effects of recycled granite and clinker waste sands on the mechanical, durability and microstructural properties of concrete were examined. The main conclusions drawn from this study are:

- The partial replacement of ordinary sand by recycled sand from granite waste and recycled clinker in the formulation of sand concrete makes the latter heavier, more workable and contains more occluded air.
- The partial substitution of dune sand by recycled sand leads to an improvement in compressive strength as a function of the increase in the substitution rate and age. However, concretes containing recycled clinker sand are more resistant in compression compared with granite waste sand.
- The behavior in flexural tension is the same as in compression, with maximum strengths given by concrete containing 40% recycled clinker at ages 7, 28 and 90 days.
- The introduction of recycled sand as a partial replacement for ordinary sand in the formulation of a sand concrete increases the surface hardness and homogeneity of the reference concrete as the substitution rate increases. Moreover, ultrasonic speeds and compressive strengths obtained by sclerometer in concretes based on recycled clinker sand have shown to be higher than in concretes based on granite waste sand.
- The shrinkage of concrete containing recycled sand is greater than that of reference concrete, but recycled aggregates have a positive effect on the swelling of sand concrete, and the lowest values are given by concrete containing 40% recycled sand from granite waste.
- The absorption by immersion decreases as the replacement rate increases, and concretes containing recycled clinker sand give the lowest values.
- The replacement of ordinary sand with 40% recycled sand from granite waste and recycled clinker reduces the porosity accessible to water and makes the matrix more compact.

- The best capillary absorption and sportivity are recorded in concrete made with 20% recycled clinker sand.
- The behavior of the concretes after freeze-thaw cycling showed a beneficial effect on shrinkage and weight loss. Besides, a slight reduction in ultrasonic speed and modulus of elasticity compared with the results obtained on concretes not subjected to freeze/thaw and the best values are given by concrete based on 40% recycled clinker sand.
- The concrete containing recycled sand is more resistant to chloride attack than reference concrete, and concrete made from recycled clinker sand is more resistant to chloride attack than concrete made from granite waste sand.
- The reference concrete is the most resistant in a hydrochloric acid environment compared with the recycled sand-based concrete. Further, the SCC40 and SCG40 concretes are the most resistant in comparison with the SCC20 and SCG20 concretes respectively, with a maximum loss of 5.27% at 120 days recorded in the SCG40 concrete (insignificant value). However, the behavior of the different concretes with respect to acetic acid is very similar, and SCG40 concrete has shown to be the least resistant, with a loss of 5.14% at 120 days. Generally speaking, consequently, the partial substitution of ordinary sand by recycled sand has no significant influence on the resistance of these concretes in hydrochloric and acetic acid environments.
- The microstructural study by X-ray diffraction (XRD) shows an improvement in the microstructure, more than ever in the concrete based on 40% recycled clinker sand.
- A good correlation between the various parameters studied was shown by this study.
- In the light of this study, we can say that the partial replacement of ordinary sand by recycled sand from granite waste and recycled clinker has shown to be beneficial, acceptable and feasible.
- Long-term durability studies and microstructure investigations (SEM and FTIR) for the sand concrete studied in the present research could be conducted in the future. A detailed survey may also be carried out later to assess the impact of waste granite and recycled clinker on the performance of the sand concrete as a partial substitute in cement. Additionally, this survey can explore the performance of other types of concrete.

Acknowledgments

The authors would like to acknowledge the technical support received from the staff and facilities at the Laboratories of the Habitat and Construction (LHC-East) in Skikda, Algeria, and from the GICA Cement Company in Skikda, Algeria.

References

[1] Gupta LK, Vyas AK. Impact on mechanical properties of cement sand mortar containing waste granite powder. Construction and Building Materials. 2018;191:155–164. https://doi.org/10.1016/j.conbuildmat.2018.09.203

[2] Suárez-Navarro JA, Del Mar Alonso M, Gascó C, Pachón A, Carmona-Quiroga PM, Argiz, C, Sanjuán MÁ, Puertas F. Effect of particle size and composition of granitic sands on the radiological behaviour of mortars. Boletín De La Sociedad Española De Cerámica Y Vidrio. 2022;61(5):561–573. https://doi.org/10.1016/j.bsecv.2021.05.001

[3] Mashaly AO, Shalaby BN, Rashwan MA. Performance of mortar and concrete incorporating granite sludge as cement replacement. Construction and Building Materials. 2018;169:800–818. https://doi.org/10.1016/j.conbuildmat.2018.03.046

[4] Ramos T, Matos AM, Schmidt BE, Rio J, Coutinho JS. Granitic quarry sludge waste in mortar: Effect on strength and durability. Construction and Building Materialsr. 2013;47:1001–1009. https://doi.org/10.1016$/j.conbuildmat.2013.05.098

[5] Allam ME, Bakhoum ES, Garas GL. Re-use of granite sludge in producing green concrete, ARPN: Journal of Engineering and Applied Sciences (JEAS). 2014; 9(12): 2731-2737. Available from: https://www.researchgate.net/publication/287919960_Reuse_ogr granite_sludge_in_producing_green_concrete

[6] Lakhani R, Kumar R, Tomar P. Utilization of stone waste in the development of value added products: A state of the art review. Journal of Engineering Science and Technology Review. 2014;7(3):180–187. https://doi.org/10.25103/jestr.073.29

[7] Singh S, Khan S, Khandelwal R, Chugh A, Nagar R. Performance of sustainable concrete containing granite cutting waste. Journal of Cleaner Production. 2016;119:86–98. https://doi.org/10.1016/j.jclepro.2016.02.008

[8] Vijayalakshmi M, Sekar A, Prabhu GG. Strength and durability properties of concrete made with granite industry waste. Construction and Building Materials. 2013;46:1–7. https://doi.org/10.1016/j.conbuildmat.2013.04.018

[9] Singh S, Nagar R, Agrawal V. Performance of granite cutting waste concrete under adverse exposure conditions. Journal of Cleaner Production. 2016;127:172–182. https://doi.org/10.1016/j.jclepro.2016.04.034

[10] Jain A, Choudhary S, Gupta R, Chaudhary S, Gautam L. Effect of granite industry waste addition on durability properties of fly ash blended self-compacting concrete. Construction and Building Materials. 2022;340:127727. https://doi.org/10.1016/j.conbuildmat.2022.127727

[11] Gautam L, Kalla P, Jain JK, Choudhary R, Jain A. Robustness of self-compacting concrete incorporating bone china ceramic waste powder along with granite cutting waste for sustainable development. Journal of Cleaner Production. 2022;367:132969. https://doi.org/10.1016/j.jclepro.2022.132969

[12] Kherraf L, Hebhoub H, Belachia M, Abdelouehed A, Charime R, Bouhebila O. Influence of the incorporation of cement kiln dust on the properties of cement- performance and durability. International Review of Civil Engineering. 2019;10(3):125. https://doi.org/10.15866/irece.v10i3.16638

[13] Guettouche A, Merdas A, Berrabah F, Guechi L. Valorization of Cement Kiln Dust (CKD) from the Ain-Al-Kebira Cement Plant (Algeria) in Building Materials. Annales De Chimie-science Des Materiaux. 2023;47(2):57–66. https://doi.org/10.18280/acsm.470201

[14] Bondar D, Coakley E. Effect of grinding on early age performance of high volume fly ash ternary blended pastes with CKD & OPC. Construction and Building Materials. 2017;136:153–163. https://doi.org/10.1016/j.conbuildmat.2017.01.044

[15] Boughamsa O, Abdelouahed A, Hebhoub H, Kherraf L, Boukhatem G. Optimizing Sand Concrete Properties Through Partial Substitution of Natural Sand with Cement Kiln Dust. Annales De Chimie-science Des Materiaux. 2023;47(4):259–64. https://doi.org/10.18280/acsm.470408

[16] A. Chaib, M. Bounouala, M. Chettibi, Z. Mekti, S. Bouabdallah, S. Berdoudi, Etude et analyse de la qualité du ciment obtenu à partir d'un mélange de deux clinkers cuit et incuit- cimenterie de Hadjar Essoud, Algérie. Journal International Sciences et Technique de l'Eau et de l'Environnement (IJWSET). 2019; 4(2) :17-26. Available from: http://jistee.org/wp-content/uploads/2020/01/Journal-ISTEE-VolumeIV-Num%C3%A9ro-2-decembre2019.pdf

[17] Kaplan G, Öz A, Bayrak B, Aydın AC. The effect of geopolymer slurries with clinker aggregates and marble waste powder on embodied energy and high-temperature resistance in prepacked concrete: ANFIS-based

prediction model. Journal of Building Engineering. 2023;67:105987. https://doi.org/10.1016/j.jobe.2023.105987
[18] Smir R. Etude du comportement du clinker dans le béton, projet de fin d'étude, Licence Es-Sciences et Technique, Université Sidi Mohamed Ben Abdellah, Moroco, 20-30, 2016. Available from: https://memoirepfe.fst-usmba.ac.ma/download/3161/pdf/3161.pdf
[19] G. Dreux, J. Feasta, Nouveau Guide du Béton et de Ses Constituants, Édition Eyrolles, Paris, France, 1996:255-300,ISBN 13 978-2-212-10231-4.
[20] Hebhoub H, Aoun H, Belachia M, Houari H, Ghorbel E. Use of waste marble aggregates in concrete. Construction and Building Materials. 2011;25(3):1167–1171. https://doi.org/10.1016/j.conbuildmat.2010.09.037
[21] Sablocrete. Synthèse du Projet National de Recherche et Développement. Bétons de sable, caractéristiques et pratiques d'utilisation. Presses de l'école Nationale des Ponts et Chaussées LCPC, Paris, 1994:92-199,ISBN13 978-2-85978-221-4.
[22] Neville AM. Properties of concrete, Fifth Edition, Pearson, Edinburgh, England, 2011:ISBN 13 9780273755807
[23] Abukersh SA, Fairfield CA. Recycled aggregate concrete produced with red granite dust as a partial cement replacement. Construction and Building Materials. 2011;25(10):4088–4094. https://doi.org/10.1016/j.conbuildmat.2011.04.047
[24] Kherraf L, Younes K, Abdelouahed A, Belachia M, Hebhoub H. Mechanical Properties of Self-compacting Concrete Containing Fine Aggregates from Cement Kiln Dust and Hardened Cement Waste. Selected Scientific Papers. 2022;17(1):1–15. https://doi.org/10.2478/sspjce-2022-0012
[25] Shamsabadi EA, Ghalehnovi M, De Brito J, Khodabakhshian A. Performance of Concrete with Waste Granite Powder: The Effect of Superplasticizers. Applied Sciences. 2018;8(10):1808. https://doi.org/10.3390/app8101808
[26] Li H, Huang F, Cheng G, Xie Y, Tan Y, Li L, Yi Z.. Effect of granite dust on mechanical and some durability properties of manufactured sand concrete. Construction and Building Materials. 2016;109:41–46. https://doi.org/10.1016/j.conbuildmat.2016.01.034
[27] Sharma NK, Kumar P, Kumar S, Thomas BS, Gupta RC. Properties of concrete containing polished granite waste as partial substitution of coarse aggregate. Construction and Building Materials. 2017;151:158–163. https://doi.org/10.1016/j.conbuildmat.2017.06.081
[28] Zhang K, Liu F, Yue Q, Feng J. Effect of granite powder on properties of concrete. Asia-Pacific Journal of Chemical Engineering. 2020;15(S1). https://doi.org/10.1002/apj.2468
[29] Kherraf L, Kherraf S, Hebhoub H, Belachia M. Performance of concrete containing partial granite and tiling wastes as fine aggregate. Civil and Environmental Engineering Reports. 2023;33(2):85–105. https://doi.org/10.59440/ceer/172751
[30] Jain A, Choudhary R, Gupta R, Chaudhary S. Abrasion resistance and sorptivity characteristics of SCC containing granite waste. Materials Today: Proceedings. 2020;27:524–528. https://doi.org/10.1016/j.matpr.2019.11.318
[31] Gautam L, Jain JK, Jain A, Kalla P. Valorization of bone-china ceramic powder waste along with granite waste in self-compacting concrete. Construction and Building Materials. 2022;315:125730. https://doi.org/10.1016/j.conbuildmat.2021.125730
[32] Pérez SPM, Zamora JJA. Effects of incorporating granite powder in the mechanical properties of concrete. Scientific Review Engineering and Environmental Sciences. 2023;32(1):18–33. https://doi.org/10.22630/srees.4479

[33] Singh S, Nagar R, Agrawal V, Rana A, Tiwari A. Sustainable utilization of granite cutting waste in high strength concrete. Journal of Cleaner Production. 2016;116:223–235. https://doi.org/10.1016/j.jclepro.2015.12.110
[34] Ghannam S, Najm H, Vasconez R. Experimental study of concrete made with granite and iron powders as partial replacement of sand. Sustainable Materials and Technologies. 2016;9:1–9. https://doi.org/10.1016/j.susmat.2016.06.001
[35] Alnahhal W, Taha R, Al-Nasseri H, Nishad S. Effect of using cement kiln dust as a Nano-Material on the strength of cement mortars. KSCE Journal of Civil Engineering. 2018;22(4):1361–1368. https://doi.org/10.1007/s12205-017-0010-6
[36] Liu Y, Yang C, Wang F, Hu S, Zhu M, Hu C, Lu L, Liu Z. Evaluation on recycled clinker production and properties from regeneration of completely recycle concrete. Construction and Building Materials. 2021;301:123882. https://doi.org/10.1016/j.conbuildmat.2021.123882
[37] Prošek Z, Trejbal J, Nežerka V, Goliáš V, Faltus M, Tesárek P. Recovery of residual anhydrous clinker in finely ground recycled concrete. Resources, Conservation and Recycling. 2020;155:104640. https://doi.org/10.1016/j.resconrec.2019.104640
[38] Rihia C, Hebhoub H, Kherraf L, Djebien R, Abdelouahed A. Valorization of waste in sand concrete based on plant fibres. Civil and Environmental Engineering Reports. 2019;29(4):41–61. https://doi.org/10.2478/ceer-2019-0043
[39] Mebarkia R, Bouzeroura M, Chelouah N. Study of the effect of cement kiln dust on the mechanical, thermal and durability properties of compressed earth blocks. Construction and Building Materials. 2022;349:128707. https://doi.org/10.1016/j.conbuildmat.2022.128707
[40] Singh S, Nande N, Bansal P, Nagar R. Experimental Investigation of Sustainable Concrete Made with Granite Industry By-Product. Journal of Materials in Civil Engineering. 2017;29(6). https://doi.org/10.1061/(asce)mt.1943-5533.0001862
[41] Sadek DM, El-Attar MM, Ali HA. Reusing of marble and granite powders in self-compacting concrete for sustainable development. Journal of Cleaner Production. 2016;121:19–32. https://doi.org/10.1016/j.jclepro.2016.02.044
[42] Sharma S, Pandey P, Gupta P, Shende AM, Bhandari R. An Experimental Behavior on Green Concrete utilizing Granite Slurry Waste (GSW) as Partial Substitute of Cement. IOP Conference Series: Earth and Environmental Science. 2022;1084(1):012022. https://doi.org/10.1088/1755-1315/1084/1/012022
[43] Abbaszadeh R, Modarres A. Freeze-thaw durability of non-air-entrained roller compacted concrete designed for pavement containing cement kiln dust. Cold Regions Science and Technology. 2017;141:16–27. https://doi.org/10.1016/j.coldregions.2017.05.007
[44] Ahmadi SF, Reisi M, Amiri MC. Reusing granite waste in eco-friendly foamed concrete as aggregate. Journal of Building Engineering. 2022;46:103566. https://doi.org/10.1016/j.jobe.2021.103566
[45] Ghorbani S, Taji I, De Brito J, Negahban M, Ghorbani S, Tavakkolizadeh M, Davoodi A. Mechanical and durability behaviour of concrete with granite waste dust as partial cement replacement under adverse exposure conditions. Construction and Building Materials. 2019;194:143–152. https://doi.org/10.1016/j.conbuildmat.2018.11.023
[46] Shilar FA, Ganachari SV, Patil VB, Nisar KS, Abdel-Aty A, Yahia IS. Evaluation of the effect of granite waste powder by varying the molarity of activator on the mechanical properties of ground granulated Blast-Furnace Slag-Based geopolymer concrete. Polymers. 2022;14(2):306. https://doi.org/10.3390/polym14020306
[47] Rabehi M, Mezghiche B, Guettala S. Correlation between initial absorption of the cover concrete, the compressive strength and carbonation depth.

Construction and Building Materials. 2013;45:123–129. https://doi.org/10.1016/j.conbuildmat.2013.03.074

[48] Cheah CB, Lim JS, Ramli M. The mechanical strength and durability properties of ternary blended cementitious composites containing granite quarry dust (GQD) as natural sand replacement. Construction and Building Materials. 2019;197:291–306. https://doi.org/10.1016/j.conbuildmat.2018.11.194

[49] Singh S, Nagar R, Agrawal V. A review on Properties of Sustainable Concrete using granite dust as replacement for river sand. Journal of Cleaner Production. 2016;126:74–87. https://doi.org/10.1016/j.jclepro.2016.03.114

[50] Pereira MML, Capuzzo VMS, De Melo Lameiras R. Evaluation of use of marble and granite cutting waste to the production of self-compacting concrete. Construction and Building Materials. 2022;345:128261. https://doi.org/10.1016/j.conbuildmat.2022.128261

[51] Amani AM, Babazadeh A, Sabohanian A, Khalilianpoor A. Mechanical properties of concrete pavements containing combinations of waste marble and granite powders. International Journal of Pavement Engineering. 2019;22(12):1531–1540. https://doi.org/10.1080/10298436.2019.1702662

[52] Jain A, Chaudhary S, Gupta R. Mechanical and microstructural characterization of fly ash blended self-compacting concrete containing granite waste. Construction and Building Materials. 2022;314:125480. https://doi.org/10.1016/j.conbuildmat.2021.125480

[53] Aarthi K, Arunachalam K. Durability studies on fibre reinforced self compacting concrete with sustainable wastes. Journal of Cleaner Production. 2018;174:247–255. https://doi.org/10.1016/j.jclepro.2017.10.270

[54] Al-Swaidani AM, Baddoura MK, Aliyan SD, Choeb W. Acid resistance, water permeability and chloride penetrability of concrete containing crushed basalt as aggregates. Journal of Materials Science and Engineering. 2015;5(8): 293-312. https://doi.org/10.17265/2161-6213/2015.7-8.005

[55] Jain KL, Sancheti G, Gupta LK. Durability performance of waste granite and glass powder added concrete. Construction and Building Materials. 2020;252:119075. https://doi.org/10.1016/j.conbuildmat.2020.119075

[56] Siddique S, Shrivastava S, Chaudhary S, Gupta T. Strength and impact resistance properties of concrete containing fine bone china ceramic aggregate. Construction and Building Materials. 2018;169:289–298. https://doi.org/10.1016/j.conbuildmat.2018.02.213

Research on Engineering Structures & Materials
www.jresm.org
Research Group

Research Article

Internal force transfer in segmental RC structures

Seymur Bashirzade[a], Okan Ozcan[b,*], Izzet Ufuk Cagdas[c]

Department of Civil Engineering, Akdeniz University, Konyaaltı, Antalya, 07058, Türkiye

Article Info

Article history:

Received 09 Jan 2024
Accepted 06 May 2024

Keywords:

Segmental structures;
Segmental beams;
Intersegmental joints;
Hollow circular beams;
DIANA

Abstract

The primary objective of this numerical study is to provide a finite element (FE) analysis approach for segmental structures. The study was conducted using a hollow circular segmental structure model capable of adequately imitating real structural behavior and deals with the effect of varying number of segments on structural performance. In order to verify the FE procedure conducted by DIANA software, comparisons are made with the acquired numerical results and the results taken from previous experimental studies for 1 reinforced concrete (RC) beam, 2 post-tensioned (PT) beam, and 3 segmental post-tensioned beams (SPT). For the considered cases, 1D line, 2D shell, and 3D solid FE models are made, and it is found out that the 3D solid model with interface elements yields the most plausible results. Further, the FE model was constructed to accurately predict segment joint behavior concerning the relationship between the number of segments, concrete compressive strength, and the width of the openings at the segment joints up to collapse. In this study, a hollow circular segmental structure model is utilized to mimic real structural behavior, presenting a novel perspective on internal force transfer mechanisms within segmental structures. Moreover, the FE model is tailored to accurately predict segment joint behavior, elucidating the intricate relationship between the number of segments, concrete compressive strength, and the width of openings at segment joints up to collapse. In addition to presenting a robust numerical analysis framework, this study contributes novel insights into the complex interplay between segmental geometry, material properties, and structural behavior, thus advancing the state-of-the-art in segmental structural design. Thus, a modular construction methodology is proposed for segmental beam type structures ensuring safety, efficiency, and flexibility in challenging load conditions.

1. Introduction

Segmental structures, which consist of reinforced concrete (RC) segments connected by post-tensioning, can be considered as a successful approach in modern offshore construction [1] Therefore, the determination of ultimate load, displacement capacity, crack width, and locations in segmental structures becomes an important design issue which is the main motivation for this study.

Several studies have been conducted on segmented and precast underwater tunnels in which the influence of material properties [2, 3], corrosion [4], lining damage [5], joint waterproofing [6] and high-water pressure [7] on structural performance was investigated. Segmental offshore wind turbines have precast concrete segments that are established on-site and joined by external prestressing tendons, presenting a cost-effective alternative to traditional steel towers [8] In addition, the use of ultra-high-performance fiber-reinforced concrete has been combined with the segmental construction method,

*Corresponding author: ookan@akdeniz.edu.tr
[a]orcid.org/0000-0002-0870-6345; [b]orcid.org/0000-0001-9905-1657; [c]orcid.org/0000-0002-2528-2978
DOI: http://dx.doi.org/10.17515/resm2024.146st0109rs

which is a more economically and ecologically suitable alternative for offshore structures [9] Analysis and design of segmental structures is more challenging comparing with conventional RC structural design. Queiroz and Horowitz (2016) have investigated [10] the shear behavior of hollow circular segments under various loading conditions and provided insights into the practical consequences of structural design regarding the Canadian Code [11] and the Brazilian standard [12] The shear strength provided by the shear keys and either by the smooth surfaces in contact [13] or by dry joints [14, 15] has been calculated. Further, finite element (FE) models were used to analyze the stress, deformation, and damage of structures, modeling the shear strength, and opening behavior of dry joints [14] The related Spanish code provides valuable information on external prestressing method, which may be used in design [16] As can be seen from the survey so far, the literature on the design and analysis of segmental hollow circular RC structures is not extensive.

The literature review underscores the significance of recent advancements in incorporating design solutions derived from the field of wave propagation in unit cell concepts periodic structures analysis, particularly relevant to segmental (beam) structures composed of RC segments connected by post-tensioning [17] Moreover, exploration into the fracture toughness behavior of interpenetrating phase composites [18] and rate-dependent hyper plasticity with internal functions [19] present valuable insights into material behavior in periodic structures with a finite element approach [20] This research demonstrates the practical relevance of theoretical frameworks in engineering applications which contributes to the understanding of structural integrity and performance in complex systems, aligning with the objectives of analyzing segmental (beam) structures. Further, recent studies have provided insights into the structural design, testing and performance assessment of pouch cells, emphasizing the importance of material behavior [21] and geometric shape [22] in energy storage systems using finite element analysis [23, 24] under varying loading conditions.

The present study focuses on the nonlinear structural behavior of hollow circular segmental post-tensioned (SPT) beams under 4-point static bending. A scaled prototype structure is selected for the numerical study. DIANA FE software is selected as the computational tool as it has been successfully applied in RC structural analysis in previous studies found in the related literature [25-27] First, several verification problems are solved in order to gain insight into the details of DIANA software in RC structural design and comparisons are made with the experimental results presented in the cited studies. The first problem considered is a monolithic RC beam under transverse loading for which experimental results were presented. [25] 1D, 2D and 3D FE models are made and after obtaining plausible and acceptable numerical results, which are in very good agreement with the experiments, a post-tensioned (PT) beam is considered [26] Similarly, near perfect agreement with the experimental results was observed for the PT beam for all FE models. Then, experimental results presented [27] for segmental post-tensioned (SPT) beams are compared with the FE numerical results obtained and agreement was only observed for 2D and 3D models. Next, the scaled prototype structure is analyzed but only a 3D FE model is made considering the results obtained in the verification study and due to the complicated geometry. Critical parameters, such as load capacity, displacement capacity, crack patterns, crack widths, and joint opening widths are studied in detail.

In summary, while various studies have investigated the behavior of segmental structures and their applications, there remains a notable gap in the literature concerning the nonlinear structural behavior of hollow circular segmental post-tensioned (SPT) beams. Additionally, limited attention has been given to the detailed numerical analysis of scaled prototype structures using advanced FE software such as DIANA. This study seeks to address these gaps by conducting a comprehensive investigation into the nonlinear

behavior of SPT beams, utilizing a scaled prototype structure and employing DIANA FE software. By comparing numerical results with experimental data from previous studies and analyzing critical parameters such as load capacity, displacement capacity, crack patterns, crack widths, and joint opening widths, this research aims to provide valuable insights into the performance and design considerations of segmental structural applications. Moreover, the findings regarding the influence of segmental design parameters such as the number of segments and concrete strength levels on structural behavior contribute to advancing the understanding of segmental construction methodologies in engineering. Overall, this study offers a novel perspective on the structural behavior of segmental structures, highlighting the potential benefits and design considerations of segmental construction.

2. FE modeling validation

Before proceeding with the numerical analysis of SPT concrete structures, FE models for simpler RC structures created by using DIANA FE software package are validated by comparing the numerical results obtained with the experimental results found in the related literature. Three main structural elements are considered during the verification study: RC, PT concrete, and SPT concrete beams. Different loading types and failure mechanisms were investigated in these studies [25-27] For concrete and embedded reinforcement, finite element models are developed using 1D line elements, 2D elements, and 3D solid elements [28] The 1D FE model is the simplest modeling option but the 2D model includes the influences of shear and torsion, as well as the axial behavior better than the 1D model. However, the most comprehensive analysis can be made by the 3D solid element FE model, which accounts for the entire 3D response (Fig. 1). Total strain crack models are used to simulate concrete, and pushover analyses are conducted until collapse. Concrete is modeled with exponential softening in tension and Hognestad curve is adopted to simulate the compressive behavior [29] All reinforcements and prestressed tendons are modeled as embedded with adherence-slip reinforcement. The material model for steel is based on von-Mises plasticity with linear plastic hardening based on experimental properties (Fig. 2). For the numerical analysis of hollow circular segmental post-tensioned (SPT) beams under 4-point static bending, various FE models were constructed using the DIANA FEA software package. In the FE modeling process, careful consideration was given to the selection of appropriate element types and numerical parameters to ensure accurate representation of the structural behavior under loading conditions.

In the 1D FE model, beam elements (L6BEN) with 2 nodes were utilized to represent the structural members along their longitudinal axis. The 2D FE model employed shell elements (Q20SH), with a total of 4 nodes and 2 degrees of freedom (DOF) per node, capturing the structural behavior in both the longitudinal and transverse directions. The 3D FE model utilized solid elements (HX24L) to account for the complex geometry of the segmental beams, with 8 nodes and 3 DOF per node, enabling a detailed analysis of stress, deformation, and damage distribution within the structure. Both material and geometric nonlinearity were considered in the nonlinear FE analysis, incorporating realistic behavior such as plasticity, crack propagation, and large deformations. Two distinct crack models were implemented in the FE simulations: the rotating crack model and the fixed crack model. The rotating crack model allows cracks to propagate and evolve freely within the structure, simulating the progressive failure behavior of the segmental beams. In contrast, the fixed crack model assumes predefined crack patterns and locations, providing a simplified representation of crack behavior for comparative analysis.

To ensure the accuracy and reliability of the FE simulations, stringent convergence criteria were applied during the modeling process. Convergence was assessed by monitoring key output parameters, such as displacement and stress distributions, and adjusting the FE

mesh density iteratively until stable and consistent results were achieved. A series of FE meshes were generated and analyzed, with refinement applied in regions of high stress concentration or discontinuity to capture localized effects accurately. The boundary conditions (BC) of the FE models played a crucial role in simulating realistic loading conditions and structural response. Boundary conditions, such as pinned supports, roller supports, and applied loads, were imposed to replicate the experimental setup and loading configuration. The rationale behind the BC choice was based on the physical constraints of the prototype structure and the desired response characteristics. Additionally, boundary conditions were imposed to simulate the behavior of rotating crack and fixed crack models, ensuring alignment with experimental observations. Validation of the FE models was conducted by comparing numerical results with experimental data from previous studies, including load-displacement curves, crack patterns, and failure modes. The accuracy achieved in the FE model validation process provides confidence in the reliability of the numerical simulations, enhancing the credibility of the study findings and their applicability to real-world engineering scenarios.

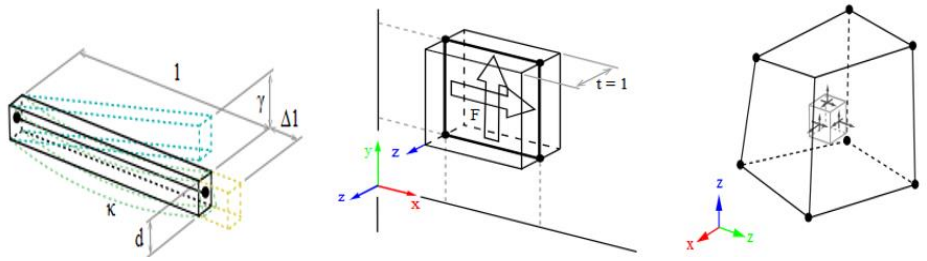

(a) b) c)

Fig. 1. DIANA element models: (a) 1D line, (b) 2D shell, and (c) 3D solid element. [28]

Pushover analyses are conducted by incrementally applying the point loads until failure in order to capture the post-peak response of the beams while providing both numerical stability and efficiency. The load increment is taken in a range between 1.0 and 3.7 kN depending on the ultimate load applied. Arc length control using the updated normal plane approach, which incorporates automated scaling of the load increment with the maximum equilibrium iteration number set equal to 25, is used to track the response path. The equilibrium iteration approach uses the secant (Quasi-Newton) method to achieve computational stability. In addition, the default parameters are used in the line search method as no significant convergence problem occurred using the default parameters. Convergence analyses of the mesh were conducted for all beams utilizing displacement measurements. The elements were meshed employing an approximate element size of 50 mm in the longitudinal and thickness directions, correspondingly.

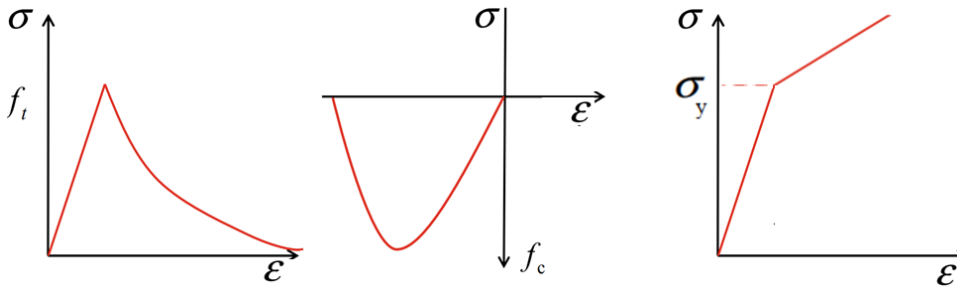

(a) (b) (c)

Fig. 2. Concrete tension (a), compression (b) and steel model (c) [30]

2.1 Comparison with RC Beam Tests

Jason et al. (2013) have investigated the cracking behavior of RC beams both numerically and experimentally [25] Four-point-bending tests were conducted on 2.85 m long RC beams with a depth of 0.25 m and a web thickness of 0.15 m. The 28-day compressive strength of concrete was 39 MPa and the steel reinforcement had yield and ultimate strengths of 550 and 666 MPa, respectively. The compression reinforcement had a diameter of 12 mm, whereas the tensile and transverse reinforcements had a diameter of 8 mm. The experimental load-displacement responses are compared with the numerical results obtained from the 1D, 2D, and 3D element models to assess the correctness and dependability of the numerical models in reflecting the complex behavior of RC beams (Fig. 1).

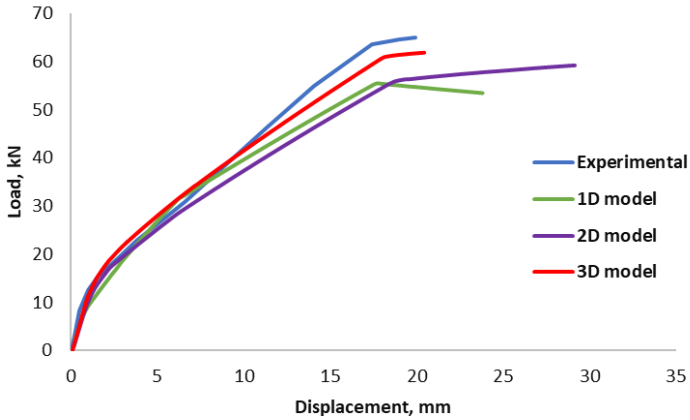

Fig. 3. Load-displacement curves of RC beam [25]

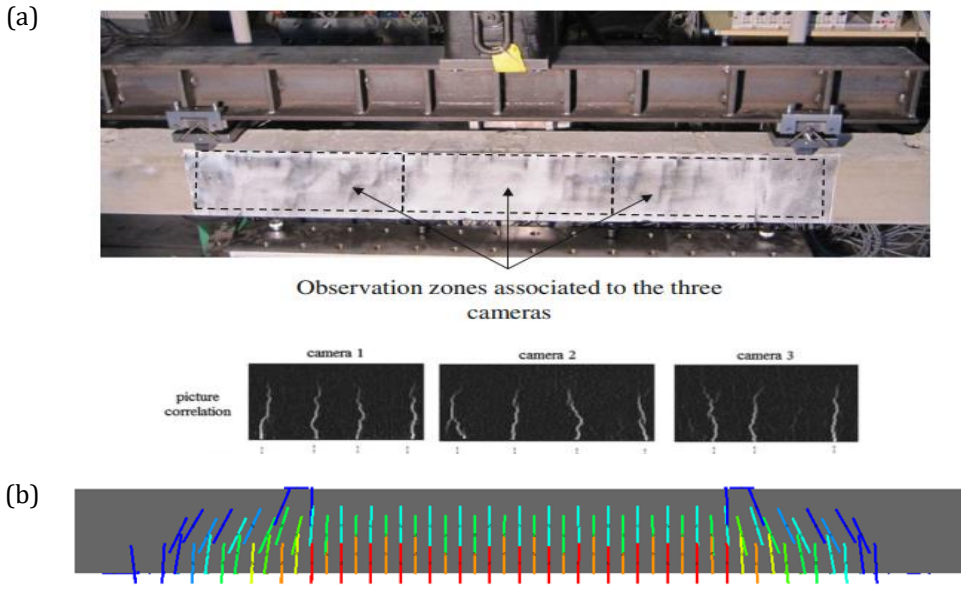

Fig. 4. Crack distribution at failure in the (a) experimental and (b) numerical model of RC beam [25]

The rotating crack model is used in the FE models and interface mechanisms are employed between the loading plates and the concrete beam. As can be observed from Figure 3, there is a very good level of agreement between the experimental and numerical initial stiffness, strength, and post-peak behavior indicating the adequacy of the numerical models to predict the nonlinear response of the RC beam. This confirms the accuracy of the FE models to capture the cracking behavior of the beams (Fig. 4).

With the establishment of an ideal correlation, the conclusive count of cracks corresponds accurately, amounting to 13 discernible cracks. It is noteworthy that the experimental initiation of cracking manifests more promptly compared to its simulated counterpart. A commendable concordance is achieved between the experimental observations and numerical simulations, particularly evident during the onset of active cracking in the initial loading phase. In the FE analysis results, a nuanced depiction is provided through various color representations, detailing the alteration in crack width along the length of the beam. Specifically, cracks depicted in red and orange colors closely resemble experimental crack locations and widths. Conversely, cracks represented in blue, green, and yellow are categorized as hairline cracks in the FE analysis, generally exhibiting widths smaller than 0.5 mm.

2.2 Comparison with PT Beam Tests

Tao and Du (1985) have investigated the flexural strength of partly PT beams with bonded and unbonded tendons [26] In the mentioned study, twenty-two unbonded and four bonded PT beams were tested for which the parameters included the loading type, non-prestressed reinforcement ratio, prestressed reinforcement ratio, and span-height ratio. For the considered beam (i.e., A9 beam in the cited reference), the concrete had a 28-day compressive strength of 33.1 MPa and the unbonded tendon prestress level after the loss was 920 MPa. The area of the non-prestressed reinforcement was 804 mm2, which contributed to the total tensile strength of the beams.

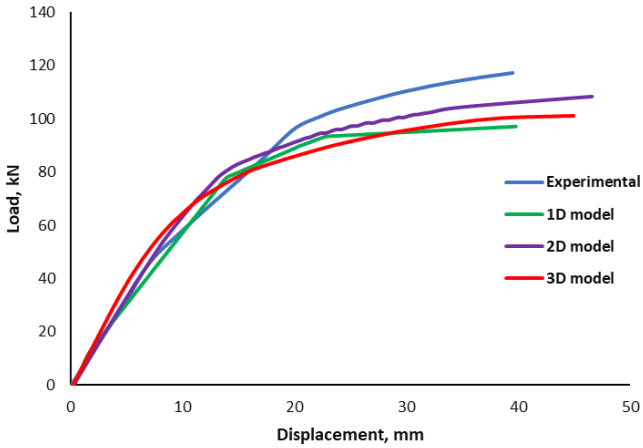

Fig. 5. Load-displacement curves of PT beam [26]

The yield strength of the prestressed and non-prestressed reinforcement was 1108 and 395 MPa, respectively. To numerically obtain the load-displacement behavior, FE models are made using 1D, 2D, and 3D elements and bar elements are used to represent the PT tendon and non-prestressed reinforcement. The analysis of PT beams using aforementioned modeling approach provides significant details on the load-displacement behavior as well as crack initiation and propagation processes. When the experimentally

obtained load-displacement data was compared to the numerical simulations, a high degree of agreement was observed, verifying the reliability and precision of the numerical models in presenting the PT beam behavior (Fig. 5). An approximate linear relationship between the applied load and displacement was observed in the early linear-elastic range while the load-displacement curves demonstrated the nonlinearity showing the deterioration of flexural capacity. The numerical models accurately predicted the load levels at which cracks occurred and propagated throughout the beam since the crack propagation sites and patterns of the experimental and numerical simulations were similar, confirming the accuracy of FE model to accurately represent cracking behavior. In the experimental investigation of the beam, notable observations indicate the prevalence of larger cracks within the central regions of the beam. However, it is discerned that variations in crack thickness led to a stratification of crack widths, delineating them as distinct entities in the FE analysis results, where the cracks are differentiated based on their magnitudes into categories denoted by blue and light blue colors. The obtained results underscore the nuanced representation of crack propagation and distribution achieved through computational modeling (Fig. 6).

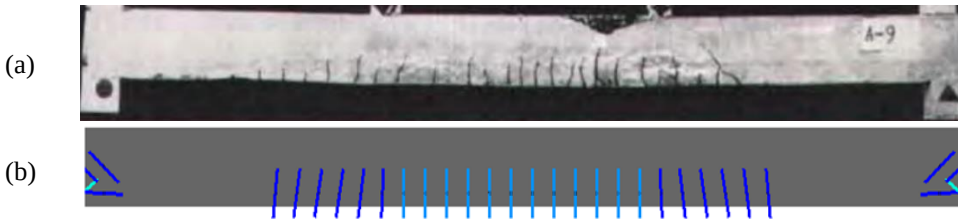

Fig. 6. Crack distribution at failure in the (a) experimental and (b) numerical model of PT beam [26]

2.3 Comparison with Precast SPT beam tests

Al-Sherrawi et al. (2018) conducted an experimental investigation on the behavior of precast SPT beams with various types of epoxy-bonded joints under static loads [27] The purpose of this study was to investigate the effects of joint shape, epoxy strength, and prestressing force on the structural performance of segmental beams and to compare the results to those of a monolithic cast beam as a reference. The compressive and tensile strength of concrete was 41.3 and 4.2 MPa, respectively. Tension reinforcement with 12 mm diameter was tied by 10 mm diameter stirrups and the post-tension tendon is made up of four 15.4 mm bars. Coulomb friction coupling was accepted at the segment joints. The MC90 mathematical formulations were used to calculate the normal and shear stiffness values based on the material parameters which are essential to evaluate the behavior and strength of the segment joints [31, 32]The reinforcement yield strength was 555 MPa and the tendons had yield and ultimate strength of 1680 and 1860 MPa, respectively.

(a)

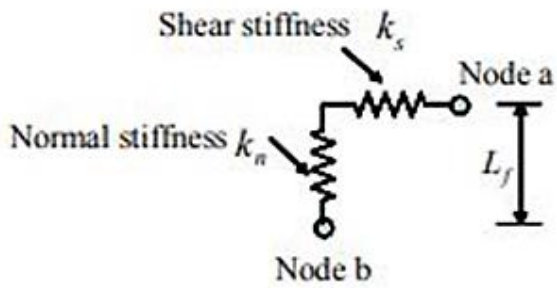

(b)

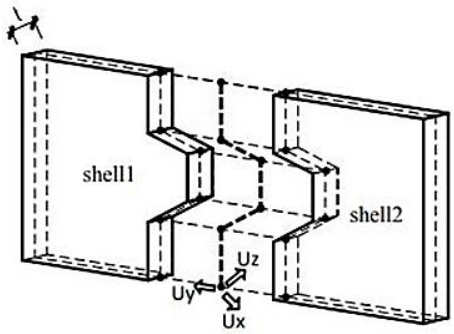

(c)

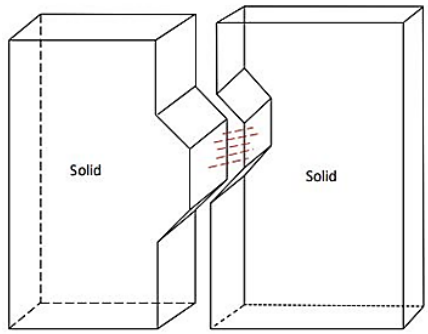

Fig. 7. Segmental interface models: (a) Joint stiffness, (b) 2D, and (c) 3D [28]

Since the segmental beams are joined from node to node, the local axis of the interface element placed at the point of intersection of the beams extended along the path direction to which the two lines and two areas joined (Figs. 7a-7c).

DIANA's structural interface components proved particularly helpful for simulating geometric discontinuities such as discrete cracks in concrete and masonry, as well as bond-slip layers in RC [28] As given in Equation 1, material models for interface elements provide a linear or nonlinear relationship between tractions, stresses, and relative displacements across the interface in which normal tractions and shear tractions $\boldsymbol{t_n}, \boldsymbol{t_t}$ are used. The relative displacements are the normal relative displacement $\boldsymbol{u_n}$ and shear relative displacement $\boldsymbol{u_t}$. In the related literature, stiffness values $\boldsymbol{k_n}$ and $\boldsymbol{k_t}$ are assigned between the segments to assure intersegmental integrity [28, 31-34] These stiffness values are defined below,

$$\begin{Bmatrix} t_n \\ t_t \end{Bmatrix} = \begin{bmatrix} k_n & 0 \\ 0 & k_t \end{bmatrix} \begin{Bmatrix} \Delta u_n \\ dt \end{Bmatrix} \tag{1}$$

$$k_n = \frac{E}{t}, k_t = \frac{G}{t} \tag{2}$$

$$k_n = \frac{E + E_{ep}}{t}, k_t = \frac{G + G_{ep}}{t} \tag{3}$$

where, Δu_n and dt denote the axial and transverse displacement components at the segment interface, respectively. E, E_{ep} and G, G_{ep} are the elasticity and shear moduli for concrete and epoxy. Cohesion in the model accounts for the adhesive forces present in the joint, which might affect the overall joint behavior. To achieve a durable and stable joint, author has used a high-strength epoxy resin to join the segments, which plays an essential role in structural integrity and load transmission. The elasticity, and shear moduli and

compressive, and tensile strength of epoxy are important elements in defining the mechanical performance of the joints. The contribution of epoxy can be considered by adding the elasticity and shear moduli of epoxy to Equation 2 as given in Equation 3. The interface components modeling the joints at the top and bottom flanges are assigned by using a Coulomb-type friction law including cohesion term c. The Breen formula [15, 35] predicts the specified values of the joint strength components, such as cohesion and friction coefficients (μ_1 and μ_2) as given below.

$$\mu_1 = 0.6, \mu_2 = 0.205\sqrt{f_c}, c = 0.996\sqrt{f_c} \quad (4)$$

The results obtained using DIANA software show that only the 2D and 3D models yield results that are in fairly good agreement with the experimental data (Figs. 8a-8d). However, it was determined that the 1D model fails to model SPT beam as the intersegmental stiffness values could not be incorporated in the 1D model.

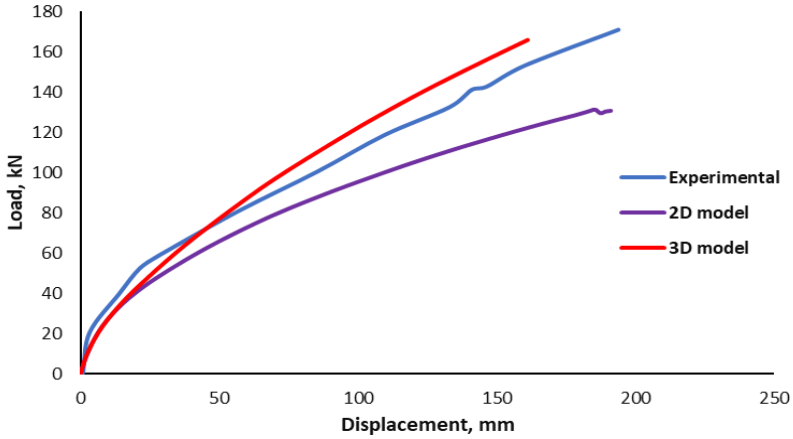

(a)

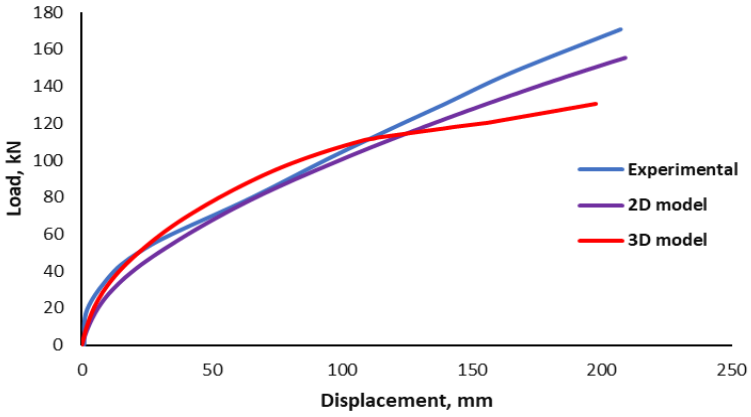

(b)

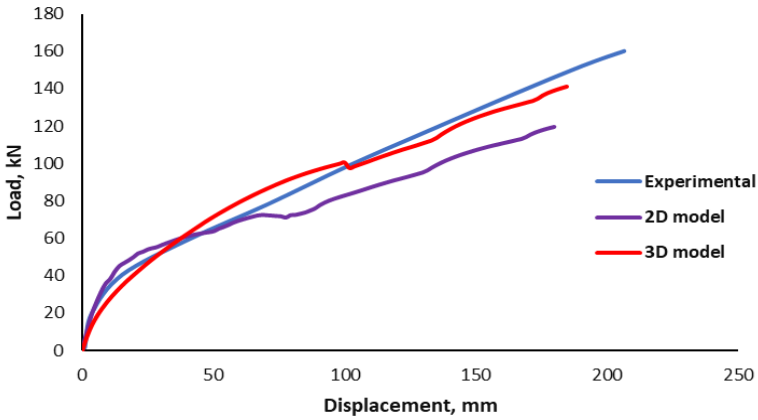

(c)

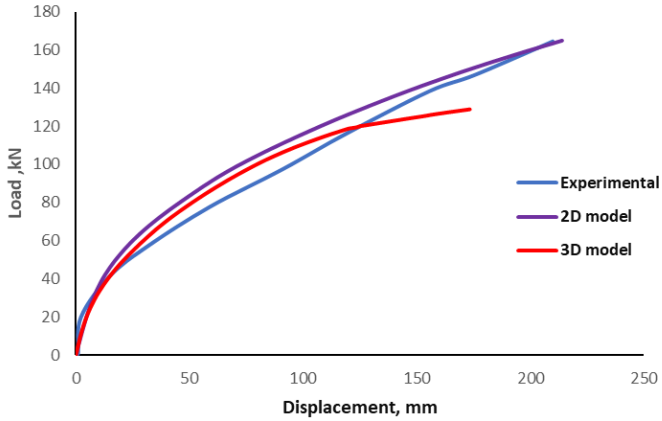

(d)

Fig. 8. Load - displacement curves of SPT beams (a) Beam (G1), (b) Beam (G2), (c) Beam (G3), (d) Beam (G4). [27]

The cracks distribution at failure shown in Figure 9 obtained using both the 2D and 3D FE models is in good agreement with the real crack distribution presented by Al-Sherrawi et al. (2018). [27] In the examination of segmental beams, it is evident that the widest cracks that occur predominantly at the segmental joints, are identifiable by a distinct red color. Conversely, as one moves away from these joints, there is a discernible shift in both the width and color of the cracks. Remarkably, the established alignment between the experimental observations and numerical simulations, is particularly pronounced during the initial loading phase where crack initiation is observed. Specifically, cracks depicted in red and orange closely mirror the experimental counterparts in terms of both location and width. In contrast, cracks depicted in shades of blue, green, and yellow define the hairline cracks in the FE analysis, typically exhibiting widths below the 0.5 mm.

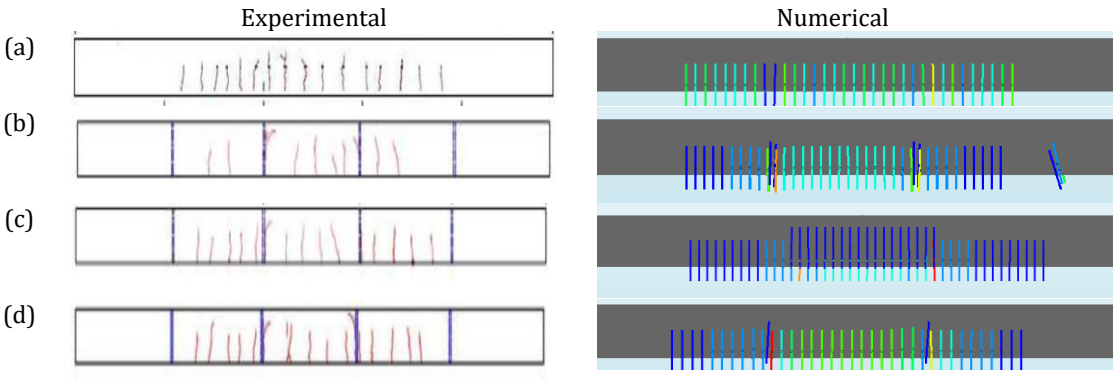

Fig. 9. Crack distribution at failure in the numerical model SPT beams: (a) Beam (G1), (b) Beam (G2), (c) Beam (G3), (d) Beam (G4) [27]

3. Parametric Study

In this section, SPT hollow circular beams are numerically analyzed by using DIANA software based on the research findings obtained from the verification study. The material models and the joint stiffness evaluation techniques for RC, PT, and SPT beam problems considered in Section 2 are directly incorporated into the FE models used here.

3.1 SPT Hollow Circular Beam

Reliable modeling of real structural behavior using numerical models is critical to produce accurate and relevant findings. Thus, the moment to shear force ratio in numerical models should be selected accordingly to achieve an exact approximation of the real structural performance. For slender structures such as offshore platform supports, wind turbine towers, and tunnels ratio becomes extremely high and therefore the influence of shear becomes insignificant as compared to bending moment. Thus, a beam under four-point-bending loads is analyzed as the ratio at the mid-span of the beam is infinite. Considering a scale factor of 10, the hollow circular beams analyzed are 10 m long with an external diameter of 1 m and an internal diameter of 0.8 m, since the selected prototype circular hollow structure is 50 m high with external and internal diameters ranging between 8-12 and 8-10 m, respectively (Table 1). Accordingly, the length of the middle span of the beam is 5 m and is divided into 1 to 5 equaling segments. The mechanical properties of the materials used in the hollow circular SPT beams are given in Table 2. The FE model details for the concrete, reinforcement, tendons, and segmental joints are shown in Figures 10a-10d.

Table 1. Geometric properties of prototype and model

	Length	External diameter	Internal diameter	Height of segments (Number of segments)				
	m							
Prototype	50	8-12	8-10	10 (5)	12,5 (4)	16.67 (3)	25 (2)	50 (1)
Model	5	1	0.8	1 (5)	1.25 (4)	1.67 (3)	2.5 (2)	5 (1)

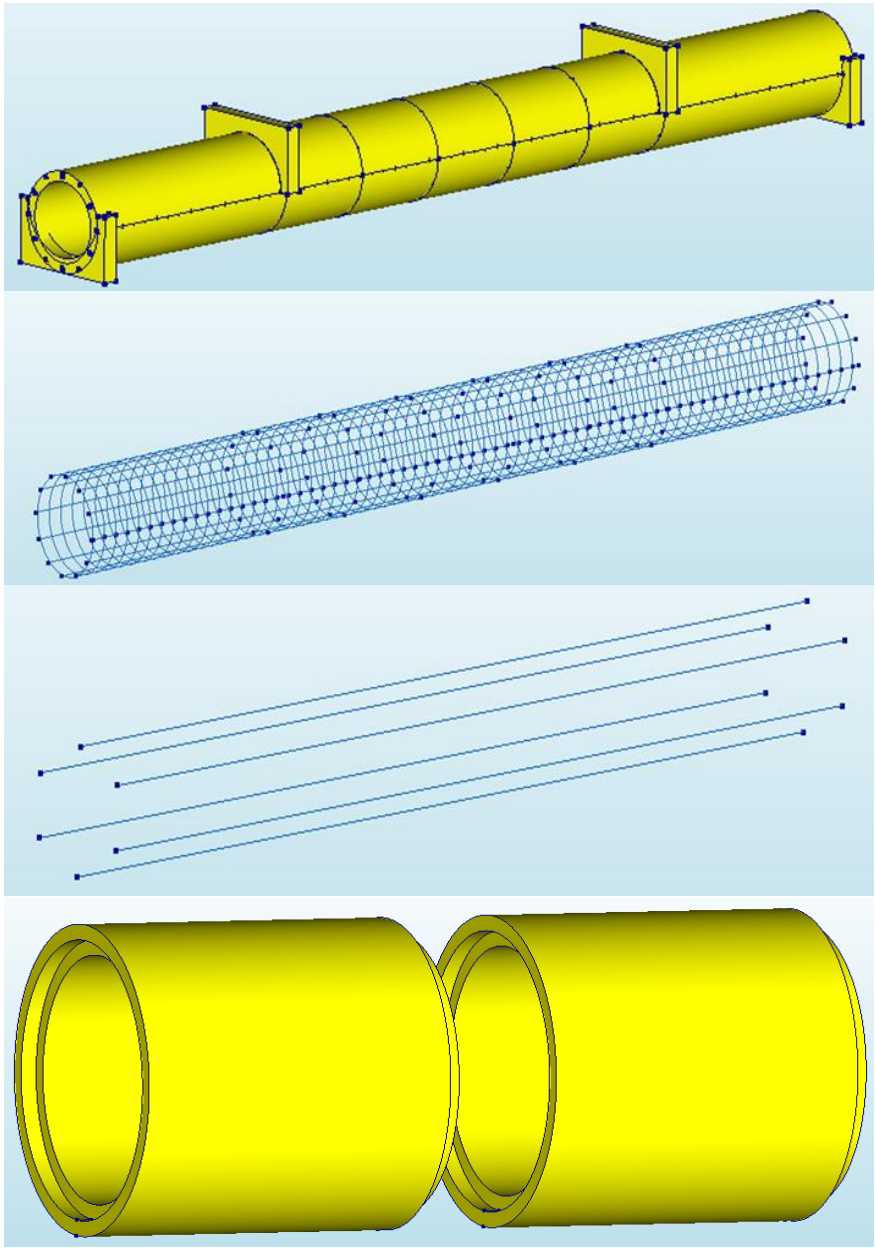

Fig. 10. The FE model of circular hollow SPT beams: (a) circular beam with support and loading plates, (b) Longitudinal and hooped reinforcements, and (c) post-tensioned tendons, (d) segmental joint details

Throughout the numerical simulation, solid elements are used to represent the concrete material, steel-bearing supports, and the reinforcements are modeled using 1D line elements. Steel reinforcements were separately modeled within each segment of the hollow circular beam. PT reinforcement enables end-to-end segments work together. Cohesive bonding is created by employing the "embedded" keyword in the DIANA software to accurately represent the interaction between the reinforcements and the concrete material.

Table 2. Materials and design parameters of numerical model.

Materials	Parameter	Value
Concrete	Elasticity modulus E	30 GPa
	Poisson's ratio ν	0.2
	Concrete compressive strength f_c	40 MPa
	Concrete tensile strength f_t	4.1 MPa
	Density ρ	2500 kg/m^3
Reinforcement	Diameter of longitudinal bar D	12 mm
	Diameter of hooped bar d	10 mm
	Elasticity modulus E	200 GPa
	Yielding strength f_{ym}	555 MPa
	Ultimate strength f_{um}	676 MPa
	Ultimate strain ε_{su}	0.02
Prestress tendon	Diameter of tendon D_f	6×15.4 mm
	Elasticity modulus E	200 GPa
	Yielding strength f_{ym}	1680 MPa
	Ultimate strength f_{um}	1860 MPa
	Ultimate strain ε_{su}	0.02

3.2 Shear Strength of Hollow Circular Section and Segmental Joints

In order to prevent premature failure of the beam at the joints before reaching maximum capacity, the shear capacity of the joints must be greater than the capacity of the beam cross section. The cross-section shear capacity is calculated as 2058.5 kN using the analytical expression provided by Queiroz and Horowitz (2016) for hollow circular cross-sections [10] The segmental joints shear capacity depends on the strength and the geometric features which directly influence the total shear capacity of the structure. For the purpose of determining the shear capacity of segmental joints and the post-tension load, the analytical expressions taken from previous studies [13-16] are used (Table 3). The expressions are based on the shear capacities of the sections and the joints considering the contributions of longitudinal compressive, normal, and shear stresses. In the analyses, the post-tensioning force is taken as equal to 1500 kN and the shear capacity of the segmental joint is calculated using the expressions given in Table 3. The shear capacity of the joint is determined to be between 2062.3 and 3492.9 kN which exceeds 2058.5 kN, the cross-section shear capacity.

Table 3. Shear capacities of section and joints

Cross-section shear capacity		
Queiroz and Horowitz, 2016	$V_c = 0.27 \cdot \alpha_{w2} \cdot \alpha_{cv} \cdot f_{cd} \cdot b_w \cdot d$	2058.5 kN
Segmental joint shear capacity		
AASHTO, 1999	$V_n = A_k\sqrt{f_{ck}}(0.2048\sigma_n + 0.9961) + 0.6A_{sm}\sigma_n$	3492.9 kN

Turmo et al., 2006	$V_n = A_k \frac{\sqrt[3]{f_{ck}^2}}{100}(7\sigma_n + 33) + 0.6A_{sm}\sigma_n$	2304.4 kN
Rombach et al., 2004	$V_n = A_k f_{ck} + 0.65A_j\ \sigma_n$	2628.5 kN
ATEP, 2009	$V_n = A_j(1.14\sigma_n + 0.0564\sqrt{f_{cd}})$	2062.3 kN

3.3 Segmental Joint FE Model

The joint was numerically modeled using face-to-face interface elements having stiffness parameters based on their geometry. The elastic behavior of the interface elements is identified by the normal and tangential stiffness coefficients (k_n and k_t) in the joint model. These coefficients establish a relationship between the normal and tangential stresses (t_n and t_t) of the joint and the corresponding normal and tangential relative displacements (u_n and u_t). DIANA software automatically sets initial values to k_n and k_t to correctly recreate the initial continuous geometry before decompression. Equations 1 and 2 are used to obtain the stiffness values as was done for the SPT verification problem solved in Section 2.3. To represent the interaction between segments, a Coulomb-type friction law with cohesion given in Equation 4 is used, which is frequently applied to simulate the mechanical behavior of contact surfaces between moving segments.

3.4 DIANA Nonlinear Analysis Stage

The hollow circular SPT beam is subjected to incremental point loads until collapse. The same solid modeling approach used for the SPT beam verification problem solved in Section 2.3. is used to determine the load-displacement behavior. To prevent divergence due to large load step, the point loads are applied with an increment of 2.8 kN. As was done in Section 2., the arc length method is used without changing the related parameters. In order to examine the cracking behavior and acquire the crack widths, rotating and fixed crack models are implemented in the FE model. The rotating crack model represents a more realistic description in which cracks can grow and develop under loading conditions, whereas the fixed cracked model represents a situation in which cracks are assumed to be fixed in position with no opening or closing during the analysis.

4. Numerical Results and Discussion

Pushover analyses of 10 m long hollow circular SPT beams are conducted using the DIANA software. The 5 m long mid-section of the beams where there is no shear force are segmental and this region is divided into 1 to 5 segments. The prototype and model geometric properties are presented in Table 1. Concrete compressive strengths ranging from 20 to 100 MPa are used regarding the model with 5 segments.

4.1 Load–Displacement Relationship

The load-displacement curves of segmental beams subjected to four-point loading are shown in Figures 11a and 11b. The displacement presented are the bottom face maximum values. It can be observed from Figures 11a and 11b that for all beams, at a load level of approximately 120 kN, gaps occur at the bottom faces of segment joints and the overall beam stiffness deteriorates significantly. This probably is because at this load level the compressive stresses produced by the tendon prestress are exceeded by the tensile stresses caused by bending of the beam.

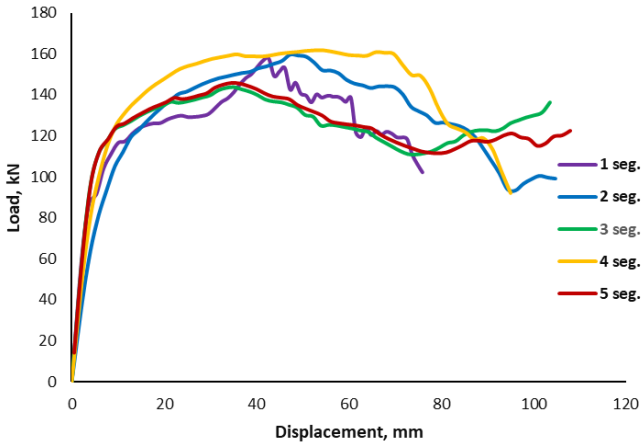

(a)

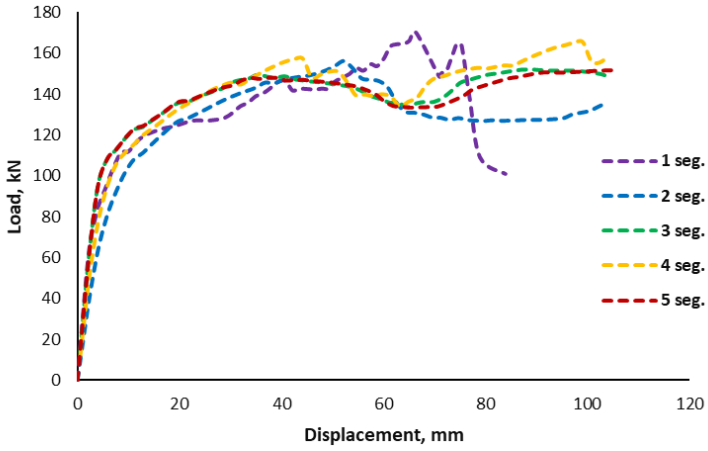

(b)

Fig. 11. Load–displacement curve of post tensioned circular hollow segmental beam: (a) Rotating crack model and (b) Fixed crack model

New gap openings no longer developed up to failure which corresponds to the load step at which convergence is no longer satisfied and the ultimate load is about 150 kN for all the beams considered. The beams collapsed at a vertical displacement of approximately 80-85 mm for the 1-segment beam and approximately 100 mm for the multi-segment beams. This observation means that the increase of the total number of segments improves ductility. Comparison of Figures 11a and 11b shows that the load-displacement behavior is similar for both crack models.

4.2 Intersegmental Joint Opening and Cracking

Comparison of Figures 11a and 11b shows that the load-displacement curves obtained using both crack models are similar. Therefore, only the rotating crack model results are presented for crack patterns. Crack distribution and joint openings are shown in Figures 12a-12d for 1 to 4 segment beams for the ultimate load stage. The crack propagation for 4 loading stages is given only for the 5-segment beam in Figures 13a-13d since similar

patterns were observed for the 1 to 4 segment beams. Herein, the crack patterns and propagation of cracks at successive load stages obtained using the FE model are consistent and physically acceptable as well.

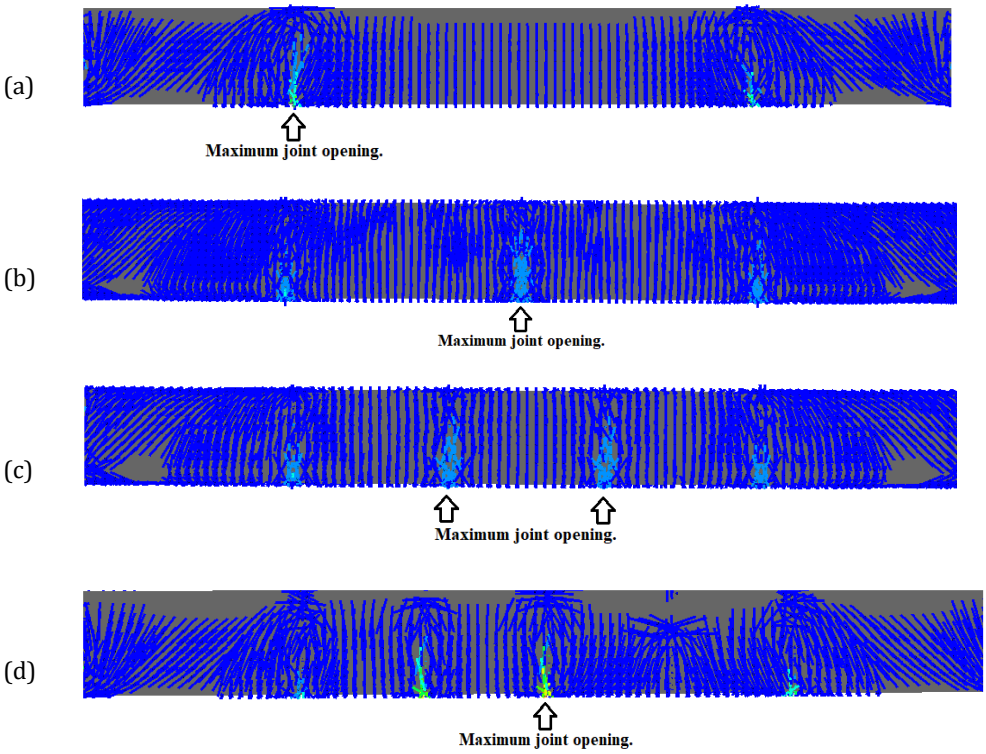

Fig. 12 Crack distribution and joint openings of hollow circular SPT beams for the ultimate load stage: (a) 1-segment beam, (b) 2-segment beam, (c) 3-segment beam, (d) 4-segment beam

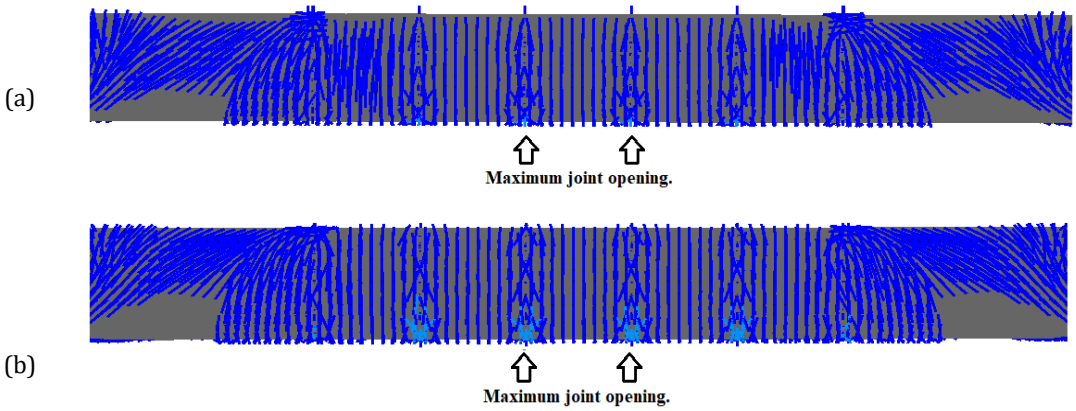

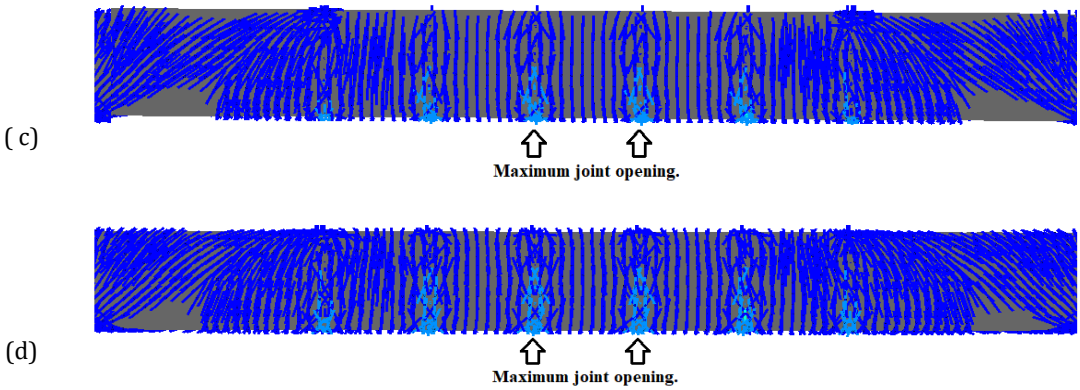

Fig. 13. Crack distribution and joint openings of hollow circular PT 5-segment beam for different load stage: (a) Load stage=0.25, (b) load stage =0.5, (c) load stage =0.75, (d) load stage =1

Figures 14a and 14b show the maximum values of segment joint opening widths for both crack models. Figures 12a-12d, 13d, 14a and 14b show that the maximum joint opening widths reduce from approximately 46 to 23 mm as the number of segments increases from 1 to 5. Formation of hairline flexural cracks along the beam axis is observed between the segment joints as well. These cracks and joint openings reduce the overall stiffness while they have insignificant effect on the ultimate load capacity (Figs. 11a and 11b). Segmental joint opening widths decrease with increasing number of segments for both crack models. The results showed that multi-segment beams had a greater ability to battle small width gaps under applied loads since the total expansion due to cracking is usually distributed among the segments. The observed data reveal that with each increment in the number of segments, an average reduction of approximately 8-10% occurs in the joint expansion. Notably, while this reduction ranges from 35 to 39 mm in the 2-segment beams, it fluctuates between 23 to 27 mm in the 5-segment beams.

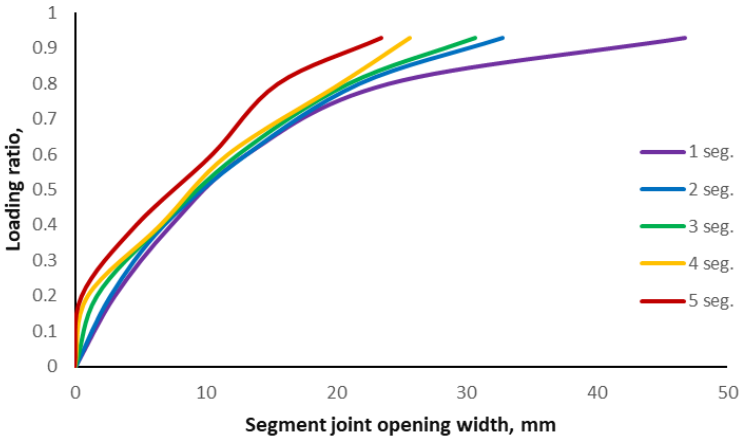

(a)

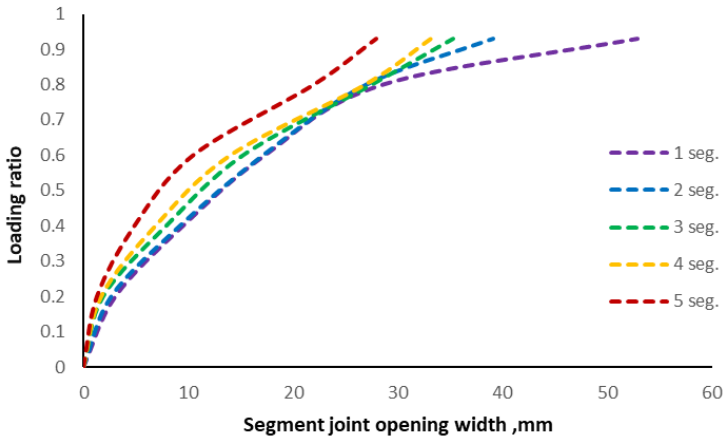

(b)

Fig. 14 Segment-joint opening width propagation graph up to collapse: (a) Rotating crack model and (b) Fixed crack model

Table 4 illustrates the relationship between the loading ratio and the corresponding segment opening width for different configurations of segmental beams, ranging from 2 segments to 5 segments. As the loading ratio increases from 0.25 to 1, the segment opening width generally exhibits a corresponding increase across all beam configurations. This indicates that higher loading ratios lead to greater deformation and widening of the segmental joints. Furthermore, it can be observed that as the number of segments increases, the segment opening width tends to decrease for a given loading ratio. This suggests that the presence of additional segments distributes the load more effectively, resulting in reduced deformation at the segmental joints.

Table 4. Loading ratio and segmental joint relationship in the segmental beams

Loading ratio	Segment opening width, mm			
	2-segment beam	3-segment beam	4-segment beam	5-segment beam
0.25	3.02	2.13	1.06	0.38
0.50	10.23	9.5	8.34	6.27
0.75	19.64	18.95	17.86	14.93
1	34,89	31.,24	25.68	23.12

4.3. Concrete Compressive Strength

In the parametric study, the compressive strength of concrete was assumed constant (40 MPa) in order to investigate the effect of the segment number on the load displacement and segment joint opening behavior. Thus, the effect of concrete compressive strength on load displacement, shear capacity, and joint opening width is evaluated for different concrete strengths ranging from 20 to 100 MPa for the beam with 5 segments. The analysis

results indicate that despite the asymptotical increase in moment capacity of the cross-section to almost 5200 kNm, the shear and joint shear capacity increases almost linearly with increasing concrete strength (Fig. 15). It should be mentioned herein that, for all concrete strength values, the shear capacity of segmental joints is shown to exceed the shear capacity of the cross-section. A similar observation can be made upon comparing the load displacement response of the beams given in Figure 16 concerning the almost linear initial stiffness and strength enhancement with increasing concrete strength while sustaining similar ductility level.

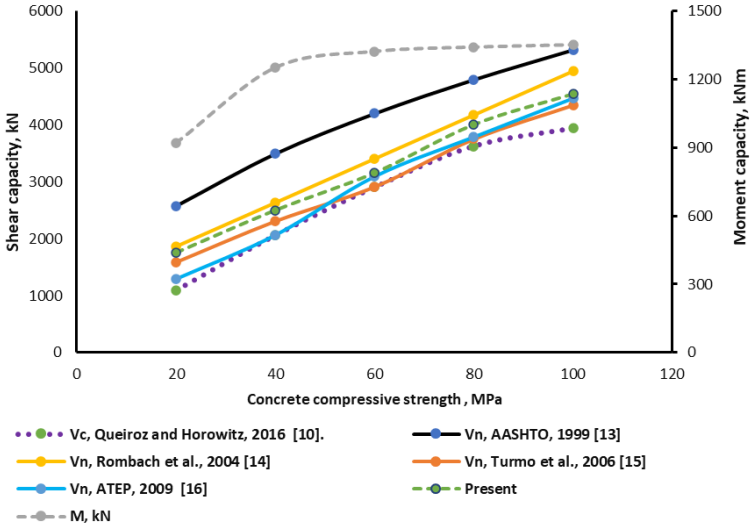

Fig. 15 Section and joint capacities changing according to concrete compressive strength

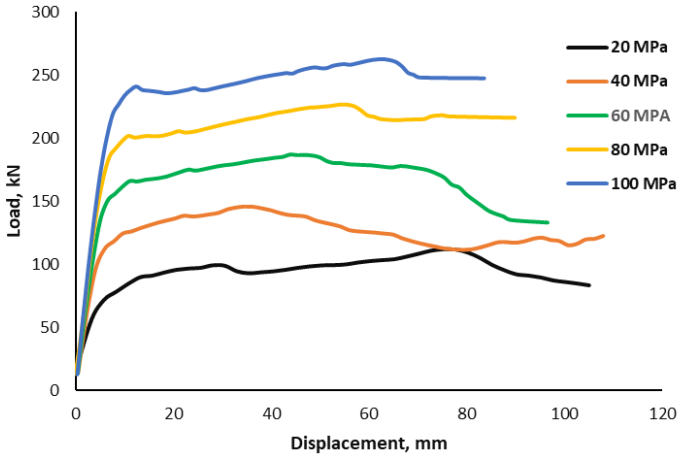

Fig. 16. Load–displacement curve of post tensioned circular hollow segmental beam

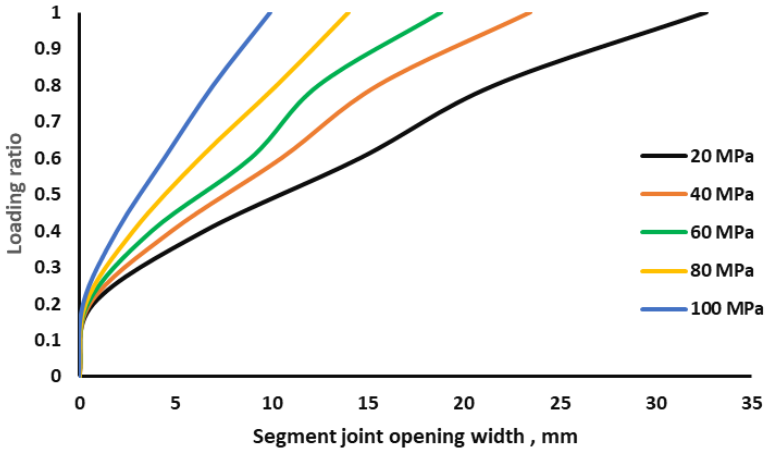

(a)

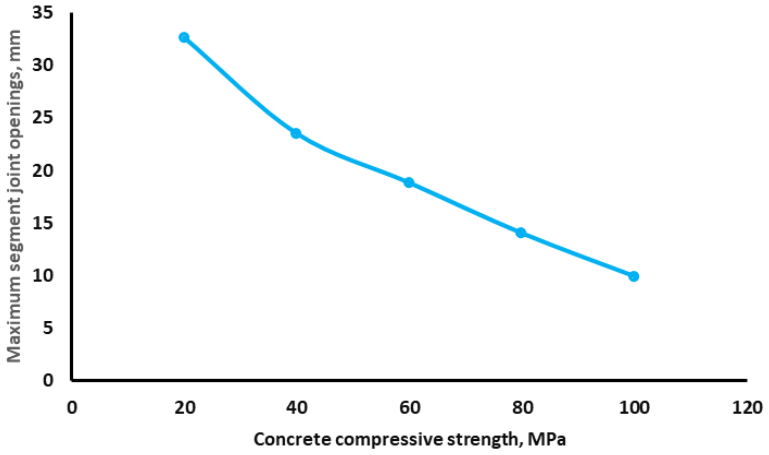

(b)

Fig. 17. Segmental joint opening for each concrete compressive strength in 5 - segment beam: (a) Segmental joint opening propagation (b) Maximum values of segment joint openings

Further, it is shown in Figures 17a that the maximum joint opening width tend to reduce with increasing concrete strength for each load level which are normalized according to the crack width at failure. For instance, when the compressive strength was 20 MPa, the segment joint opening width at collapse is 32.62 mm, whereas with the use of 100 MPa strength concrete, this value decreases substantially to 9.92 mm. (Fig. 17b).

5. Conclusion

In this study, the nonlinear structural behavior of hollow circular segmental post-tensioned (SPT) beams under 4-point bending is investigated. A scaled prototype structure is analyzed using DIANA FE software. 3 sets of verification problems are solved, and comparisons are made with the experimental results presented in the related studies. It is shown by the verification study conducted that it is possible to create accurate FE models for RC, PT and SPT beams using the selected software. The crack patterns obtained using the FE models are found out to be in excellent agreement with the experimentally obtained

patterns found in the cited studies. The numerical results obtained for the verification problems also show that a 3D FE model is required to model the scaled prototype structure since the complicated geometry of the intersegmental joints is required to be modeled using joint interface modeling technique. Increasing number of segments is found out to have a trivial effect on the load capacity of the segmental beams while reducing the intersegmental joint opening widths. The observed diminishing trend of the intersegmental joint opening widths with increasing number of segments and concrete strength indicates the potential benefits of utilizing more segments with high strength concrete. Analyses conducted on concretes with varying compressive strength levels underscore the effectiveness of the segmental design approach in various facets of offshore structures that already employ high compressive capacity concrete. The utilization of high compressive capacity concretes leads to minimal segment openings even under collapse conditions. In the structural design of such installations, the segmental methodology, which provides advantages in terms of both durability and ductility, can be regarded as a favorable option. Thus, it can be emphasized that, segmental construction is a viable option as long as the shear capacity and the opening width of intersegmental joints do not exceed code specified limits.

Furthermore, it is imperative to acknowledge certain limitations and provide avenues for future research to further enhance the understanding of segmental beam structures. Despite the comprehensive investigation conducted in this study, several limitations merit attention and offer potential directions for future exploration. One limitation lies in the scope of the study, which primarily focuses on the nonlinear structural behavior of hollow circular segmental post-tensioned (SPT) beams under 4-point bending. While this provides valuable insights into the behavior of segmental structures, future research could expand the scope to include additional loading conditions or investigate other structural configurations to provide a more comprehensive understanding of segmental beam behavior under diverse scenarios. Additionally, while the FE models employed in this study have demonstrated accuracy in capturing the structural response of RC, PT, and SPT beams, it is important to note that the modeling assumptions and simplifications inherent in the numerical analysis may introduce some degree of uncertainty. Future studies could explore alternative modeling approaches or validate the findings using experimental testing to enhance the robustness of the results. The study primarily focuses on the structural performance of segmental beams, neglecting other important aspects such as construction feasibility, cost-effectiveness, and environmental sustainability. Future research endeavors could incorporate these factors into the analysis to provide a more holistic assessment of segmental construction methodologies. In terms of future research directions, one potential avenue could involve investigating the long-term durability and resilience of segmental structures, particularly in harsh marine environments where offshore installations are prevalent. Additionally, exploring innovative construction techniques or material advancements could offer opportunities to further optimize the design and performance of segmental beam structures. By addressing these limitations and exploring new research directions, the field can continue to advance and refine segmental construction methodologies, ultimately enhancing the safety, efficiency, and sustainability of offshore structures.

Nomenclature

$1D$ = One dimensional.
$2D$ = Two dimensional;
$3D$ = Three dimensional;
FE = Finite Element;
RC = Reinforced Concrete;

PT = Post-tensioned;
SPT = Segmental post-tensioned;
k_n = Normal stiffnes;
k_t = Shear stiffnes;
t_n = Normal tractions;
t_t = Shear tractions;
u_n = Normal relative displacement;
u_t = Shear relative displacement;
E = Concrete elasticity modulus;
G = Concrete shear modulus;
t = Width of the interface;
$E_{ep.}$ = Epoxy elasticity modulus;
$G_{ep.}$ = Epoxy shear modulus;
μ_1 & μ_2 = Friction coefficients;
c = Cohesion;
M = Bending moment;
V = Shear force;
q = Distributed Load;
P = Point Load;
L = Length of beam
V_c = Circular hollow beam shear capacity;
α_{w2} = Reduction factor of concrete design resistance;
α_{cv} = Coefficient for deterimental effects on web crushing of high normal stresses;
f_{cd} = Design compressive strength of concrete ;
b_w = Effective web width;
D = External diameter of the cross section;
d = Depth of the cross section.
V_n = Nominal shear capacity of keyed dry joint;
A_k = Area of the base of all keys in the joint plane;
A_{sm} = Area of contact between smooth surfaces in the joint plane.
σ_n = Compressive stress in the joint.
f_{ck} = concrete characteristic compressive strength
A_j = Area of joint plane
f_{ym} =Yielding strength
f_{um} =Ultimate strength
ε_{su} = Ultimate strain
f_c = Concrete compressive strength
f_t = Concrete tensile strength
ρ = Concrete density
D = Diameter of longitudinal bar
d = Diameter of hooped bar
D_f = Diameter of tendon
ν = Poisson's ratio

Acknowledgement

This article was made possible with the support of the "Türkiye Burslari" supported by the "Presidency for Turks Abroad and Related Communities."

References

[1] Prestressed Concrete Institute (US). Committee on Segmental Construction. Recommended Practice for Segmental Construction in Prestressed Concrete. PCI. (1975).

[2] Liu, Wenbo, et al. Creep characteristics and time-dependent creep model of tunnel lining structure concrete. Mechanics of Time-Dependent Materials, 2021, 25: 365-382.https://doi.org/10.1007/s11043-020-09449-x

[3] LIU, X., Sun, Q., Song, W., & Bao, Y. Numerical modeling and parametric study of hybrid fiber-rebar reinforced concrete tunnel linings. Engineering Structures. 2022;251:113565. https://doi.org/10.1016/j.engstruct.2021.113565

[4] Zhang, W., Qiu, J., Zhao, C., Liu, X., & Huang, Q. Structural performance of corroded precast concrete tunnel lining. Tunnelling and Underground Space Technology. 2022;128:104658. https://doi.org/10.1016/j.tust.2022.104658

[5] Huang, Linchong, et al. Soil-water inrush induced shield tunnel lining damage and its stabilization: A case study. Tunnelling and Underground Space Technology, 2020, 97: 103290.https://doi.org/10.1016/j.tust.2020.103290

[6] Gong, C., Ding, W., Soga, K., & Mosalam, K. M. Failure mechanism of joint waterproofing in precast segmental tunnel linings. Tunnelling and Underground Space Technology. 2019;84:334-352. https://doi.org/10.1016/j.tust.2018.11.003

[7] Zhang, L., Feng, K., Gou, C., He, C., Liang, K., & Zhang, H. Failure tests and bearing performance of prototype segmental linings of shield tunnel under high water pressure. Tunnelling and Underground Space Technology. 2019;92:103053. https://doi.org/10.1016/j.tust.2019.103053

[8] Loth, E., Selig, M., & Moriarty, P. Morphing segmented wind turbine concept. In 28th AIAA Applied Aerodynamics Conf. 2010. https://doi.org/10.2514/6.2010-4400c

[9] Sobek, W., Plank, M., Frettlöhr, B., Röhm, J., & Corvez, D. Conceptual design of an UHPFRC tower structure in segmental construction for offshore wind turbines. In Proc. Of Int. Symposium on Ultra-High-Performance Fiber-Reinforced Conc. 2013; 423-432.

[10] Queiroz Junior, F. O., & Horowitz, B. Shear strength of hollow circular sections. Revista IBRACON de Estruturas e Materiais. 2016;9:214-225. https://doi.org/10.1590/S1983-41952016000200004

[11] CSA A23.3-04 Design of Concrete Structures. Standard CAN/CSA A23.3-04, Canadian Standards Association, Mississauga, Ont. 2004

[12] NBR 6118 Projeto de Estruturas de Concreto Procedimento, Associação Brasileira de Normas Técnicas Rio de Janeiro, RJ. 2014

[13] AASHTO. Guide Specifications for Design and Construction of Segmental Concrete Bridges. 1999. American Association of State Highway and Transportation Officials.

[14] Rombach, G. Dry joint behavior of hollow box girder segmental bridges. In Proceedings of the FIP Symposium. Segmental Construction in Concrete. 2004, New Delhi. http://hdl.handle.net/11420/7271

[15] Turmo, J., Ramos, G., & Aparicio, J. A. Shear strength of match cast dry joints of precast concrete segmental bridges: proposal for Eurocode 2. Materiales De Construcción. 2006;56(282):45–52. https://doi.org/10.3989/mc.2006.v56.i282.26

[16] ATEP. Proyecto y construcción de puentes y estructuras con pretensado ext. H.P.10-96. Colegio de Ing. De Caminos, Madrid. 1996.

[17] Pany, C. An insight on the estimation of wave propagation constants in an orthogonal grid of a simple line-supported periodic plate using a finite element mathematical model. Frontiers in Mechanical Engineering. 2022;8:926559. https://doi.org/10.3389/fmech.2022.926559

[18] Wegner, L. D., & Gibson, L. J. The fracture toughness behaviour of interpenetrating phase composites. International journal of mechanical sciences. 2001;43(8):1771-1791. https://doi.org/10.1016/S0020-7403(01)00016-9
[19] Puzrin, A. M., & Houlsby, G. T. Rate-dependent hyperplasticity with internal functions. Journal of engineering mechanics. 2003;129(3):252-263. https://doi.org/10.1061/(ASCE)0733-9399(2003)129:3(252)
[20] Pany, C., & Li, G. Application of periodic structure theory with finite element approach. Frontiers in Mechanical Engineering. 2023;9:1192657. https://doi.org/10.3389/fmech.2023.1192657
[21] Vamsi, A., ANSARİ, J., Sundaresan, M. K., Chitaranjan, P. A. N. Y., Bibin, J. O. H. N., Samridh, A., & Mercy, T. D. Structural design and testing of pouch cells. Journal of Energy Systems. 2021;5(2):80-91. http://dx.doi.org/10.30521/jes.815160
[22] Chitaranjan, P. A. N. Y. Investigation of Circular, Elliptical and Obround Shaped Vessels by Finite Element Method (FEM) Analysis under Internal Pressure Loading. Journal of Science, Technology and Engineering Research. 2022;3(1):24-31. DOI:10.53525/jster.1079858
[23] Pany, C. Estimation of Correct Long-Seam Mismatch Using FEA to Compare the Measured Strain in a Non-Destructive Testing of a Pressurant Tank: A Reverse Problem. International Journal of Smart Vehicles and Smart Transportation (IJSVST). 2021;4(1):16-28. https://doi.org/10.4018/ijsvst.2021010102
[24] Pany, C. Cylindrical shell pressure vessel profile variation footprint in strain comparison of test data with numerical analysis. Liquid and Gaseous Energy Resources. 2021;1(2):91-101. https://doi.org/10.21595/lger.2021.22163
[25] Jason, L., Torre-Casanova, A., Davenne, L. et al. Cracking behavior of reinforced concrete beams: experiment and simulations on the numerical influence of the steel-concrete bond. Int J Fract. 2013;180:243–260. https://doi.org/10.1007/s10704-013-9815-6
[26] Tao, X., & Du, G. Ultimate stress of unbonded tendons in partially prestressed concrete beams. PCI Journal. 1985;30(6):72-91.
[27] Al-Sherrawi, M. H., Allawi, A. A., Al-Bayati, B. H., Al Gharawi, M., & El-Zohairy, A. Behavior of precast prestressed concrete segmental beams. Civil Eng. J. 2018;4(3):488-496. http://dx.doi.org/10.28991/cej-0309109
[28] Ferreira, D., & Manie, J. DIANA —Finite Element Analysis: DIANA Documentation— Rel. 10.4. DIANA FEA BV. 2022.
[29] Ferreira, D. A model for the nonlinear, time-dependent and strengthening analysis of shear critical frame concrete structures. PhD Thesis, Univ. Pol. de Catalunya, Barcelona Tech. 2013. http://dx.doi.org/10.5821/dissertation-2117-94874
[30] Chai, S. Finite Element Analysis for Civil Engineering with DIANA Software. Springer Nature. 2020. https://doi.org/10.1007/978-981-15-2945-0
[31] MC90. CEB-FIP Model Code 1990. Bulletin d´Information No. 213/214, Comité Euro-International Du Béton. 1993.
[32] Kaya, S., & Salim, D. Shear Stiffness and Capacity of Joints Between Precast Wall Elements. Dissertation. 2017. Retrieved from https://urn.kb.se/resolve?urn=urn:nbn:se:kth:diva-209347
[33] Turmo, J., Ramos, G., and Aparicio, A.C. Study of the structural behaviour under flexure and shear of segmental concrete bridges with external prestressing and dry joints, Spain: ACHE. 2006.
[34] Červenka, V., Jendele, L. and Červenka, J. ATENA Program Documentation Part 1-Theory.Červenka Consulting s.r.o. 2016.
[35] Ramirez, G., MacGregor, R., Kreger, M. E., Roberts-Wollmann, C., Breen, J. Shear Strength of Segmental Structures. Proceedings of the Workshop AFPC External Prestressing in Structures. Saint-Remy-les-Chevreuse. 1993;pp. 287-296.

Research on Engineering Structures & Materials
www.jresm.org
Research Group

Research Article

Resilient heritage: Harnessing technology for sustainable conservation

Hayri Baytan Ozmen[1,a], Huseyin Bilgin[*,2,b], Daklea Hyraj[3,c]

[1]*Department of Civil Engineering, Usak University, Usak, Türkiye*
[2]*Department of Civil Engineering, Epoka University, Tirana, Albania*
[3]*Directorate of Road Traffic and Transportation, Municipality of Tirana, Albania*

Article Info

Article History:

Received 05 Aug 2024
Accepted 01 Nov 2024

Keywords:

Adaptive-reuse;
Conservation;
Energy efficiency;
Retrofit;
Simulation;
Sustainability

Abstract

Architecturally significant heritage buildings often struggle to meet modern energy efficiency standards. This study focuses enhancing the energy performance of the Polytechnic University of Tirana without compromising its historical integrity. Through detailed energy simulations using DesignBuilder software, the study evaluates the effectiveness of various double-glazing window configurations and internal shading systems. The results reveal that double-glazed units can lead to energy savings of up to 9.0%, particularly when using tinted, argon-filled glass. Shading devices, including fixed and automated internal louvres, provided additional savings between 4.3% and 7.8% by mitigating solar heat gain and improving thermal comfort. Also, the cost of each intervention is analyzed and savings per cost ratio ranging from €6,930 to €43,331 per 1% energy reduction is obtained. Notably, the economic analysis shows that simpler solutions, like air-filled double glazing and fixed louvres, offer a higher cost-efficiency. For the case study building, 16.53% energy savings may be obtained for a cost of €10,521 per 1% of reduction. The study's findings offer an example for future sustainable conservation projects, balancing historical preservation with energy efficiency. The results underscore the importance of targeted retrofitting in safeguarding cultural heritage while contributing to broader sustainability goals.

1. Introduction

In recent years, the intersection of heritage conservation and sustainability has garnered increasing attention, particularly in the context of retrofitting projects. The challenge lies in balancing the preservation of cultural significance with the need for energy efficiency, modern functionality and safety [1]. This balance is often complicated by the inherent conflict between invasive technologies that may compromise the integrity of heritage structures and the philosophy of minimal intervention that seeks to maintain authenticity and historical value. The discourse surrounding this balance is crucial as it reflects broader societal values regarding heritage and sustainability, emphasizing the need for innovative approaches that respect both cultural heritage and environmental imperatives.

The concept of minimal intervention in heritage conservation is rooted in the belief that alterations to historic structures should be as non-invasive as possible. This approach is supported by various scholars who argue that invasive technologies can detract from the authenticity and historical narrative of heritage buildings [2]. For instance, Guzman et al. highlight the importance of maintaining the original fabric of heritage sites, suggesting that any interventions should be reversible and should not obscure the original architectural features[3]. Conversely, the push for

*Corresponding author: hbilgin@epoka.edu.al
[a]orcid.org/0000-0001-6750-8632; [b]orcid.org/0000-0002-5261-3939; [c]orcid.org/0009-0009-4621-5561
DOI: http://dx.doi.org/10.17515/resm2024.385st0805rs

energy efficiency often necessitates the integration of modern technologies, which can include insulation, renewable energy systems, and advanced HVAC systems. These technologies, while beneficial for sustainability, can pose a threat to the historical integrity of the buildings if not implemented thoughtfully [4, 5].

Moreover, the integration of sustainability principles into heritage conservation practices has become increasingly relevant as climate change and energy efficiency concerns rise to the forefront of global discourse. Recent studies emphasize the necessity of adopting energy-efficient solutions in heritage buildings, as these structures often consume more energy than their modern counterparts due to outdated systems and materials [4, 6]. This need for energy efficiency is underscored by the growing recognition that heritage buildings can play a vital role in achieving sustainability goals, particularly when retrofitted to meet contemporary energy standards without compromising their cultural significance [7, 8].

The tension between invasive technologies and minimal intervention is further complicated by the diverse stakeholder interests involved in heritage conservation. Rosetti et al. argue that effective heritage management requires inclusive participation from all relevant stakeholders, including local communities, government entities, and conservation professionals [9]. This participatory approach not only enhances the sustainability of conservation efforts but also fosters a sense of ownership and responsibility among community members, which is essential for the long-term viability of heritage sites [10].

Furthermore, the application of modern technologies, such as Building Information Modeling (BIM), thermal analyses and 3D modelling, has emerged as a promising avenue for addressing the challenges of retrofitting heritage buildings. These technologies allow for detailed analysis and planning that can minimize the impact of interventions on the original structure while enhancing energy efficiency [11, 12]. For example, BIM can facilitate the creation of accurate digital models of heritage buildings, enabling conservationists to visualize potential changes and assess their implications before implementation [11, 13]. This approach aligns with the principles of minimal intervention, as it promotes informed decision-making that respects the historical context of the buildings.

1.1 Considered Case

The focus of this study is on two specific measures aimed at enhancing sustainability and energy efficiency in heritage buildings: the replacement of single-glazed windows with double-glazed units and the installation of shading devices. The replacement of single-glazed windows is critical as these units are often responsible for significant heat loss, contributing to higher energy consumption for heating and cooling. Studies indicate that upgrading to double-glazed windows can substantially improve thermal performance while maintaining the aesthetic integrity of heritage structures [14, 15]. However, the acceptability of such interventions is often influenced by the heritage values associated with the buildings, which may lead to resistance against complete window replacements [16, 17]. Ginks and Painter discuss the attitudes of conservation professionals towards slim double glazing, emphasizing its potential to improve energy efficiency without compromising the visual integrity of historic facades [18]. Furthermore, Wise et al. note that while residents value the functional aspects of windows, they also attach significant importance to their historical and aesthetic qualities, which can complicate retrofit decisions [16].

In addition, the installation of shading devices serves as an effective passive design strategy to mitigate solar heat gain, thereby improving indoor thermal comfort and reducing reliance on mechanical cooling systems. Shading devices can be designed to complement the architectural features of heritage buildings, ensuring that energy efficiency measures do not compromise their historical significance [19–21]. Nair et al. highlight that energy efficiency studies often focus on singular retrofit measures; however, a holistic approach is essential for the complex nature of historic buildings [15]. The integration of these two measures may represent a holistic approach to retrofitting heritage buildings, balancing the need for energy efficiency with the preservation of cultural heritage [22].

1.2 Challenges of Retrofitting Heritage Buildings

The challenges associated with retrofitting heritage buildings are multifaceted, primarily stemming from architectural and historical restrictions that often impede the implementation of energy efficiency measures. Heritage buildings, which embody significant cultural, aesthetic, and historical values, are subject to stringent regulations that prioritize their preservation over modernization [23]. This creates a tension between the need for improved energy performance and the imperative to maintain the building's original character and integrity. As noted by Nair et al., the unique construction techniques and materials used in these buildings often limit the applicability of conventional retrofitting solutions, such as external insulation or significant structural alterations, which may adversely affect their visual appearance [15].

Moreover, the reluctance of homeowners and conservation professionals to adopt invasive measures is compounded by concerns regarding the potential loss of heritage value. Sunikka Blank and Galvin highlight that aesthetic considerations and heritage values significantly influence retrofit decisions, with many homeowners prioritizing the preservation of their building's historical character over energy efficiency [24]. This sentiment is echoed in the findings of Wise et al., who emphasize that residents often view complete window replacements as unacceptable, favoring less invasive options like secondary glazing or internal shutters [16]. Such preferences reflect a broader trend in heritage conservation that seeks to balance energy efficiency with the preservation of cultural identity.

In this context, the adoption of double-glazing and shading devices emerges as a promising avenue for achieving energy efficiency while minimizing the impact on heritage values. Double-glazed windows, for instance, offer a significant improvement in thermal performance without necessitating the complete removal of original window frames, thereby preserving the building's historical façade [18]. Similarly, shading devices can be designed to complement the architectural features of heritage buildings, effectively reducing solar heat gain and enhancing indoor comfort without compromising the building's aesthetic appeal [25]. These less invasive solutions align with the principles of minimal intervention, allowing for the integration of modern energy efficiency measures while respecting the historical significance of the structures.

In summary, the complexities of retrofitting heritage buildings necessitate a careful consideration of both architectural integrity and energy performance. As the discourse on sustainable retrofitting evolves, it is imperative to explore innovative solutions that reconcile these often conflicting objectives. The integration of double-glazing and shading devices represents a viable path forward, enabling heritage buildings to meet contemporary energy efficiency standards while safeguarding their cultural heritage for future generations.

2. Building of Polytechnic University of Tirana

The Polytechnic University of Tirana, built in the 1940s, is a prominent example of Italian Rationalist architecture in Albania. Designed by Italian architect Gherardo Bosio, the building reflects the architectural vision of the fascist regime during the early 20th century. Bosio's design sought to combine functionality with modernist aesthetics, making the university a landmark in the urban fabric of Tirana [26].

The architectural significance of the building lies in its monumental scale and the use of modern construction techniques, such as reinforced concrete, while incorporating elements of traditional Albanian architecture. Its facade, characterized by symmetrical design and clean lines, blends modernist forms with classical proportions. Fig 1 shows the front view and ground floor plan of the building. The building, which now serves as the Polytechnic University’s main campus, has been a vital part of Albania’s educational and cultural history [27] .

As a heritage building, the Polytechnic University of Tirana presents unique challenges in retrofitting. The need to preserve its historical and cultural value conflicts with the necessity to improve energy efficiency. The building’s original design, with single-glazed windows and minimal consideration for thermal performance, makes it an ideal candidate for sustainable interventions

such as double glazing and shading devices. Balancing these retrofitting measures with the architectural integrity of the structure is critical to ensure its continued use and preservation as an educational institution and historical monument.

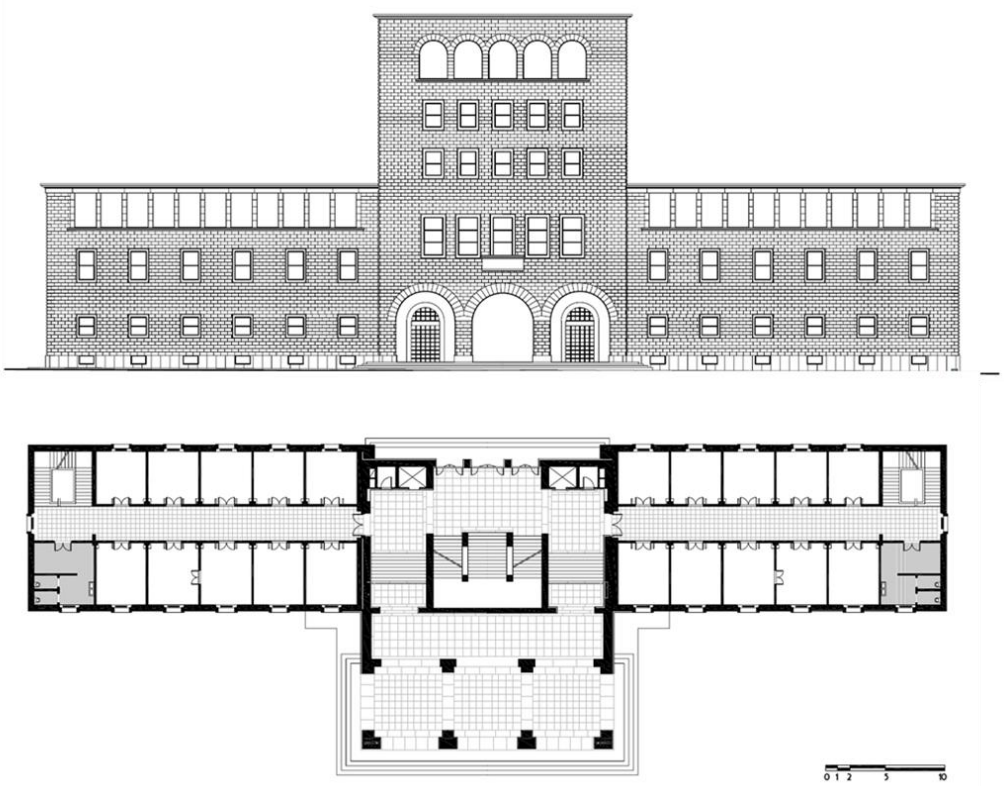

Fig. 1. Front view and the ground floor plan of the building

2.1 Physical Condition of The Building

The physical condition of the Polytechnic University of Tirana reflects its long history, with the building remaining structurally intact but showing signs of wear due to environmental factors and age. Constructed in the late 1930s and completed in the early 1940s, the building has survived significant historical events, including political changes and seismic activities, which have shaped Albania's architectural landscape. Despite these challenges, the structure remains a key part of Tirana's architectural heritage, though it now requires modernization to meet contemporary energy performance standards.

The architecture of the building is a mix of modernist design elements and traditional Albanian influences, characteristic of Gherardo Bosio's vision for the capital city's urban planning. The facade is largely intact, with its smooth, symmetrical lines and minimalist detailing remaining true to its original Rationalist style. The building features large windows and wide corridors, contributing to its overall sense of openness and connection with its surroundings [27].

However, the single-glazed windows, typical of the time, provide poor insulation, resulting in significant heat loss during winter and heat gain in summer. This lack of thermal efficiency is a primary area for improvement through retrofitting. While the building's exterior remains architecturally impressive, its energy performance lags far behind modern standards.

Structurally, the Polytechnic University of Tirana has proven resilient over the decades, with its reinforced concrete frame providing robust support against both time and environmental stresses. The building's masonry walls, reinforced concrete columns, and ceilings have helped it withstand seismic events, a common occurrence in the region. The structural system, which integrates brick walls with reinforced concrete elements, ensures that the building remains stable and retains its original form.

Nevertheless, the aging materials are beginning to show signs of deterioration, particularly in areas exposed to external weather conditions (Fig. 2). Cracks have appeared in some sections of the facade, and there is evidence of moisture infiltration, especially around the windows, which further contributes to energy inefficiency.

Fig. 2. Views from detoriated parts of the building

Retrofitting solutions such as replacing single-glazed windows with double-glazed units and installing shading devices will not only improve energy efficiency but also protect the building from further weathering, ensuring its preservation for future generations.

2.2 Interventions

2.2.1 Double-Glazed Windows

The replacement of the existing single-glazed windows with double-glazed units was a key intervention aimed at improving the thermal insulation of the Polytechnic University of Tirana. Double-glazing offers a significant improvement over single-glazed windows by reducing heat transfer between the interior and exterior of the building, leading to lower energy consumption for both heating and cooling. Several types of double-glazing were tested in the simulation:

Standard Double-Glazed Units: The basic double-glazing configuration consisted of two panes of 6mm clear glass with a 13mm air gap between them. This air gap acts as a buffer to slow down heat transfer through the window, reducing heat loss in winter and heat gain in summer.

Argon-Filled Double-Glazing: In this configuration, the air gap was filled with argon gas, which has a lower thermal conductivity than air. The argon-filled gap enhances the insulation properties of the window, providing better energy performance. This reduces the need for heating in winter and cooling in summer, making the building more energy-efficient.

Tinted Double-Glazing: Tinted glass was introduced in some scenarios to further reduce solar heat gain during the warmer months. The tinting reduces the amount of sunlight entering the building, particularly on south-facing facades, without compromising the availability of natural light. This solution was particularly useful for minimizing overheating and reducing cooling loads.

Double-Glazing with Internal Louvres: Some configurations included internal louvres integrated between the two glass panes. These louvres were fixed in certain cases, while in others, they were adjustable and activated based on the intensity of solar radiation. This feature provided additional control over solar gain, allowing for dynamic adjustments to optimize energy efficiency and occupant comfort.

Each type of double-glazing was evaluated in terms of its ability to reduce heat transfer and improve indoor thermal conditions, with the argon-filled and tinted variants showing the highest potential for energy savings.

2.2.2 Shading Devices

The second major intervention involved the installation of shading devices on the building's facades to manage solar heat gain and improve the building's energy performance during the warmer months. Shading devices can significantly reduce the amount of direct sunlight entering a

building, thus reducing the cooling load, while also preventing glare and maintaining visual comfort for occupants. The types of shading devices tested in the simulation included:

Fixed Louvres: These are permanent shading elements attached to the exterior of the building. Fixed louvres were positioned at angles optimized to block high-angle summer sunlight while still allowing lower-angle winter sunlight to penetrate the building. This intervention helps in maintaining natural daylighting while reducing the cooling demand during hot months.

Automated Louvres: Unlike fixed louvres, automated louvres can be adjusted dynamically based on real-time solar radiation. The simulation tested several activation thresholds, where the louvres would tilt to block sunlight once a certain level of solar radiation was reached (e.g., 120 W/m^2, 400 W/m^2, or 600 W/m^2). This dynamic control allows for greater flexibility, maximizing energy savings while minimizing artificial lighting requirements during times of lower solar intensity.

External Blinds: Blinds were another shading option modeled in the simulation. These are flexible shading devices that can be manually or automatically adjusted. External blinds were used for their ability to block solar radiation while still permitting some visibility and ventilation. Automated blinds, which respond to changing sunlight conditions, provided the highest efficiency by adapting to the building's orientation and local solar patterns throughout the day.

Brise Soleil: This is a horizontal shading structure placed above windows to block direct sunlight during peak hours. It was particularly effective for south-facing windows in preventing solar gain during midday while still allowing daylight in the mornings and late afternoons. The fixed nature of Brise Soleil offers a simple yet efficient way to reduce cooling needs.

The combination of these shading devices helped mitigate the impact of solar radiation on the building's thermal comfort and energy usage. Dynamic shading devices, like automated louvres, showed the most potential for energy savings due to their adaptability to changing weather conditions, while fixed solutions provided consistent protection against overheating

3. Analyses

DesignBuilder software was used to model the building of Polytechnic University of Tirana and perform detailed energy simulations to assess the impact of retrofitting interventions. DesignBuilder is a powerful tool for energy analysis that allows users to create 3D models of buildings and evaluate their thermal performance under various conditions [28]. It integrates several advanced modules for simulating heating, cooling, lighting, ventilation, and renewable energy systems, making it ideal for retrofitting studies.

The first step in the simulation process was creating an accurate digital model of the building. Using DesignBuilder, the architectural and structural features of the university were modeled based on detailed drawings and data collected from site surveys. This included defining the dimensions, materials, and construction techniques used in the building. The original windows, for instance, were modeled as single-glazed units, and the surrounding brick and concrete elements were included to reflect the building's thermal properties.

For accurate energy simulations, the model also incorporated the local climate data of Tirana, including temperature fluctuations, solar radiation, and wind patterns. Occupancy schedules were defined to reflect the typical use of the building, with specific data on internal heat gains from equipment and lighting. This baseline model was used to simulate the building's current energy consumption, providing a reference point for evaluating the effects of the retrofitting measures.

Once the baseline model was established, two key retrofitting interventions were tested with several different installations: the replacement of single-glazed windows with double-glazed units and the installation of shading devices (such as louvers or blinds) on the building's facade.

The single-glazed windows were replaced with various double-glazed configurations within the simulation. Each configuration was tested to analyze its impact on heat transfer, overall energy consumption for heating and cooling, and indoor thermal comfort. The goal was to quantify the

reduction in heat loss during the winter and heat gain during the summer, which would directly reduce the building's reliance on mechanical heating and cooling systems.

To assess the effectiveness of shading devices, several types of external shading were modeled, including fixed and adjustable louvers. These devices were designed to block excessive solar radiation during the hot summer months, reducing the cooling load on the building. The simulation calculated the effects of shading on both direct solar heat gain and daylighting, ensuring that the reduction in energy consumption for cooling did not negatively affect the natural lighting inside the building. Different shading angles and materials were tested to optimize the balance between minimizing glare and maximizing energy savings. The simulations provided detailed insights into how each retrofitting measure affected heating, cooling, and lighting energy consumption, as well as the thermal comfort levels within the building.

3.1 Considered Intervention Cases

Various retrofitting interventions for improving the energy efficiency of the Polytechnic University of Tirana are explored. These interventions primarily focus on upgrading the windows from single-glazed to double-glazed units and implementing shading strategies to control solar heat gain. The following cases outline the specific types of double-glazing configurations and shading devices considered.

List of Considered Cases:

- Case 1: Clear Double Glass with Air Gap: This configuration involves replacing the single-glazed windows with clear double glass that has an air-filled gap between the panes to improve insulation and reduce heat transfer.
- Case 2: Tinted Double Glass with Air Gap: In this case, tinted glass is used in combination with an air gap to minimize solar heat gain, while still allowing daylight to penetrate the interior.
- Case 3: Clear Double Glass with Argon Gap: The air gap is replaced with argon gas in this configuration to enhance the insulating properties, reducing heat loss and improving energy efficiency.
- Case 4: Tinted Double Glass with Argon Gap: This combination includes both tinted glass and an argon-filled gap, providing superior insulation and solar control to minimize energy consumption for cooling.
- Case 5: Clear Double Glass with Air Gap and Internal Louvres Always On: In this scenario, internal louvres are added between the glass panes and remain permanently fixed to block direct sunlight, reducing cooling loads.
- Case 6: Clear Double Glass with Air Gap and Internal Louvres Activated at 120 W/m^2: The internal louvres are set to activate when solar radiation exceeds 120 W/m^2, dynamically responding to changing sunlight levels to optimize thermal comfort.
- Case 7: Clear Double Glass with Air Gap and Internal Louvres Activated at 400 W/m^2: The louvres in this case activate when solar radiation exceeds 400 W/m^2, allowing more natural light in before shading begins to reduce solar heat gain.
- Case 8: Clear Double Glass with Air Gap and Internal Louvres Activated at 600 W/m^2: This configuration sets the louvres to activate at 600 W/m^2, offering the maximum amount of daylight before solar shading is applied.
- Case 9: Shading Devices for Inner Courtyard Facade: To address the potential greenhouse effect caused by glazing on the inner courtyard, inner shade louvres are proposed. These louvres will block direct sunlight and reduce heat gain, while preserving the building's historical appearance.

3.2 Current State of The Building

To assess the current energy performance of the Polytechnic University of Tirana, an initial simulation of the building's existing conditions was conducted, referred as Case 0. This baseline model was essential for understanding the energy consumption patterns before implementing any retrofitting measures. The simulation considered the building's single-glazed windows, lack of shading devices, and typical heating, cooling, and lighting demands.

The results of the base case simulation revealed the following key insights:

High Energy Use for Heating and Cooling: Due to the presence of single-glazed windows, the building exhibited significant heat loss in the winter and heat gain in the summer, resulting in a high demand for both heating and cooling. The lack of proper insulation in the windows led to inefficient thermal performance, with the building requiring considerable energy to maintain comfortable indoor temperatures.

Poor Solar Control: Without any shading devices, the building was highly susceptible to solar heat gain, especially in the warmer months. This led to overheating in interior spaces and increased cooling loads. The lack of solar control measures also contributed to glare issues, negatively impacting occupant comfort.

Energy Use Intensity (EUI): The Energy Use Intensity (EUI) for the base case was calculated based on heating, cooling, and lighting energy consumption. The results indicated that a large proportion of the building's total energy usage (about 45%) was dedicated to maintaining thermal comfort through heating and cooling, highlighting the inefficiency of the current building envelope (Fig 3).

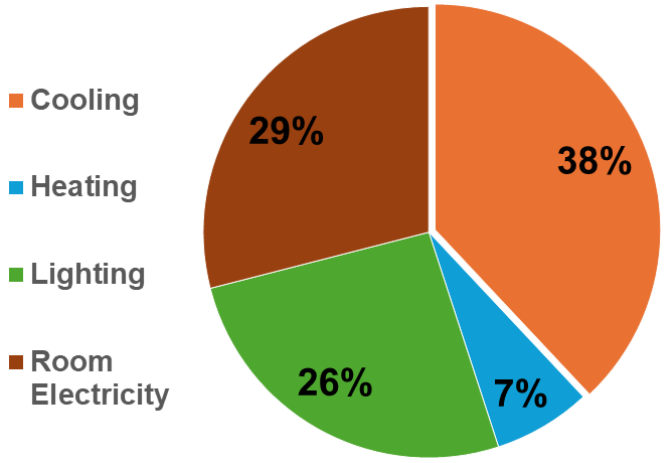

Fig. 3. The Energy Use Intensity (EUI) breakdown for the Polytechnic University

The Base Case serves as a critical reference point for evaluating the effectiveness of retrofitting interventions. By comparing the base case energy consumption to the results after implementing the proposed retrofits, the potential energy savings and efficiency improvements can be quantified.

3.3 Simulation Parameters

The relevance of the energy simulations conducted for the Polytechnic University of Tirana depends heavily on defined parameters. These parameters selected to ensure that the energy performance of the building was modeled under realistic and representative conditions. The key simulation parameters used in the study were as follows:

3.3.1 Building Location and Climate Data

Location: The Polytechnic University of Tirana is situated in Tirana, Albania, a region characterized by a Mediterranean climate with hot summers and mild, wet winters. Local weather data, including temperature, humidity, wind speeds, and solar radiation, were incorporated into the simulation.

Climate data source: The climate data used for the simulations was based on historical weather records for Tirana. This information was essential for accurately modeling heating and cooling loads across the different seasons.

3.3.2 Building Envelope

Existing windows: The base case modeled the original single-glazed windows, which were poor insulators, allowing significant heat loss and gain. This baseline was compared to various double-glazing configurations tested in the simulation.

Wall and roof insulation: The simulation assumed the existing wall and roof structures without additional insulation. This contributed to the building's high energy consumption for heating and cooling, providing a clear contrast when compared to the improved performance after retrofitting interventions.

3.3.3 Occupancy Patterns

The building was modeled with typical occupancy schedules for educational institutions, which assumed the building was primarily occupied during the day. The energy simulations accounted for variations in internal heat gains from occupants, equipment, and lighting based on these schedules.

Occupant heat gain: Human body heat contributed to the overall internal heat gains, impacting cooling requirements during the warmer months. This factor was considered in all cases.

3.3.4 Internal Loads

Lighting: The lighting system was modeled with a power density of 5 W/m^2 for typical spaces like classrooms, offices, and corridors, with specific target illumination levels (e.g., 300 lux for classrooms).

Equipment and appliances: The internal heat gains from equipment such as computers, laboratory devices, and other electronic systems were included, based on typical usage patterns for a university setting.

3.3.5 HVAC System Settings

Heating and cooling setpoints: The simulations used a heating setpoint of 22°C and a cooling setpoint of 24°C. These setpoints reflected the desired indoor comfort levels during the winter and summer seasons.

Heating Setback: A setback temperature of 5°C was modeled for unoccupied hours, reducing energy consumption when the building was not in use.

System efficiency: The Coefficient of Performance (CoP) for the heating system was set at 0.83, while the cooling system's CoP was set at 2.5, representing typical values for the existing mechanical systems.

3.3.6 Solar Radiation and Daylighting

Solar gain: The simulation took into account solar radiation effects on the building's windows and facades. Solar gain was a critical factor in determining the cooling load during the summer months and the potential benefits of shading devices.

Daylighting: Natural daylighting levels were considered to evaluate how shading devices might impact the need for artificial lighting, especially when fixed or automated louvres were introduced.

3.3.7 Air Infiltration

The infiltration rate, which quantifies how much outside air enters the building due to gaps in the envelope, was factored into the simulations. Higher infiltration rates in the base case contributed to heat loss in winter and increased cooling needs in summer, further justifying the retrofitting measures aimed at improving the building's air-tightness through new glazing.

3.3.8 Simulation Timeframe

The simulations covered an entire year, with seasonal variations in energy consumption assessed. Monthly energy usage for heating, cooling, and lighting was calculated to identify peak loads and understand how retrofitting interventions impacted energy efficiency throughout the year.

4. Analysis Results

The thermal analysis of the first and second floors of the existing building reveals significant differences in heat distribution. Figure 4a illustrates the thermal distribution without any

interventions, showcasing noticeable temperature variations across the floors. In contrast, Figure 4b, depicting the scenario with interventions, demonstrates a much more uniform thermal distribution. This improvement indicates enhanced heat comfort, as the interventions effectively balance temperature differences, creating a more comfortable indoor environment.

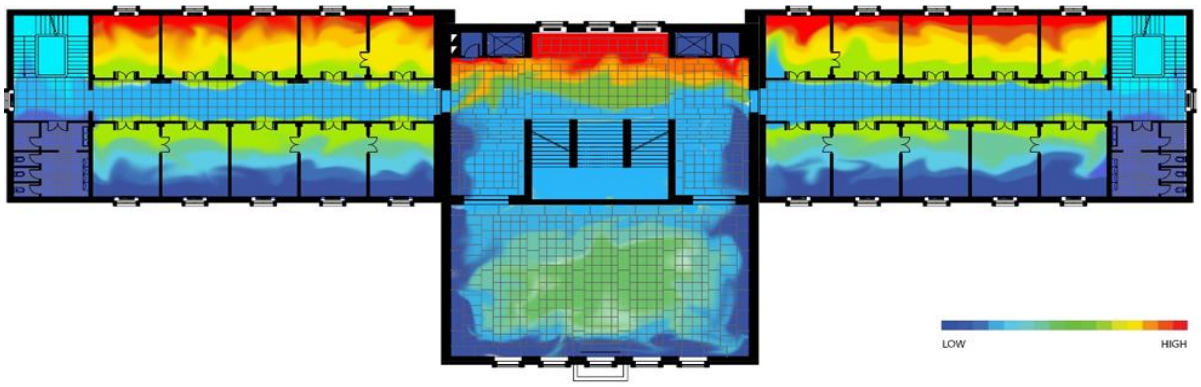

Fig. 4.(a) Thermal analysis of the first and second floor of the existing building without interventions by DesignBuilder

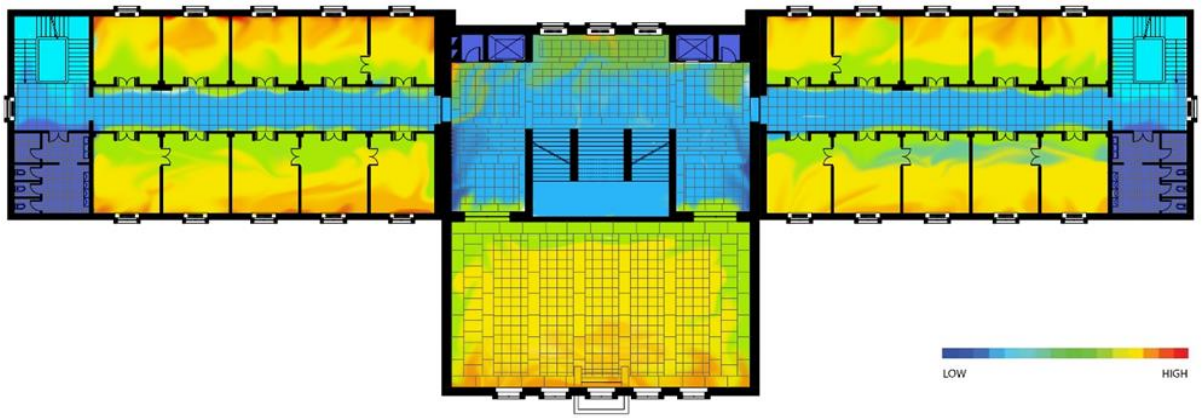

Fig. 4.(b) Thermal analysis of the first and second floor of the existing building after combined interventions of Case 4 and 9 by DesignBuilder

The results of the energy analysis for the base case (Case 0) and various retrofit interventions (Cases 1–9) are summarized in Figure 5. The analysis focuses on the building's annual energy consumption for lighting, heating, and cooling, as well as the potential energy savings achieved through different retrofitting measures.

As shown in Fig. 5, the lighting energy use remains constant at 32.5 % across all cases, reflecting the fact that the lighting system was not altered in any of the retrofit scenarios. The energy demand for heating shows a noticeable reduction in several cases compared to the base case (Case 0), where the heating load is 7.7%. Cases 1 and 3, which involve the use of clear double-glazing with air and argon gaps, result in the most significant reductions, with heating demands dropping to 5.5% and 5.8%, respectively. This improvement is due to the better insulating properties of double-glazed windows, which reduce heat loss during the winter months.

Cooling energy consumption is highly sensitive to the interventions, with significant variations across the cases. In the base case, cooling energy is 49.8%, which is the highest among all scenarios. Cases 2 and 4, which incorporate tinted double-glazing with air and argon gaps, show the largest reductions in cooling demand, reaching 43.0%. The use of internal louvres in Cases 5 to 9 also positively impacts cooling energy, but with varying effectiveness depending on the solar radiation thresholds for louvre activation. For example, Case 9 (internal louvres activated at 600 W/m^2) results in a cooling demand of 43.4%.

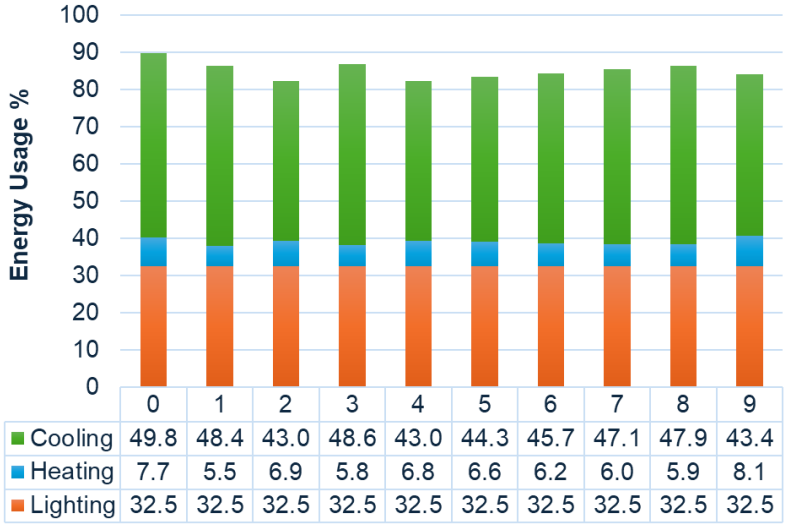

	0	1	2	3	4	5	6	7	8	9
Cooling	49.8	48.4	43.0	48.6	43.0	44.3	45.7	47.1	47.9	43.4
Heating	7.7	5.5	6.9	5.8	6.8	6.6	6.2	6.0	5.9	8.1
Lighting	32.5	32.5	32.5	32.5	32.5	32.5	32.5	32.5	32.5	32.5

Fig. 5. The comparison of Cooling, Heating, and Lighting Energy Use Intensity (EUI) between the considered cases

The energy savings potential of each intervention is illustrated in Fig. 6. Case 4 (tinted double glass with argon gap) achieves the highest overall energy savings of 9.0%. Case 2 (tinted double glass with air gap) follows closely with an energy saving of 8.9%. Other notable cases include Case 1 (clear double glass with air gap), which achieves 3.8% energy savings, and Case 9, which uses internal louvres and saves 7.53%.

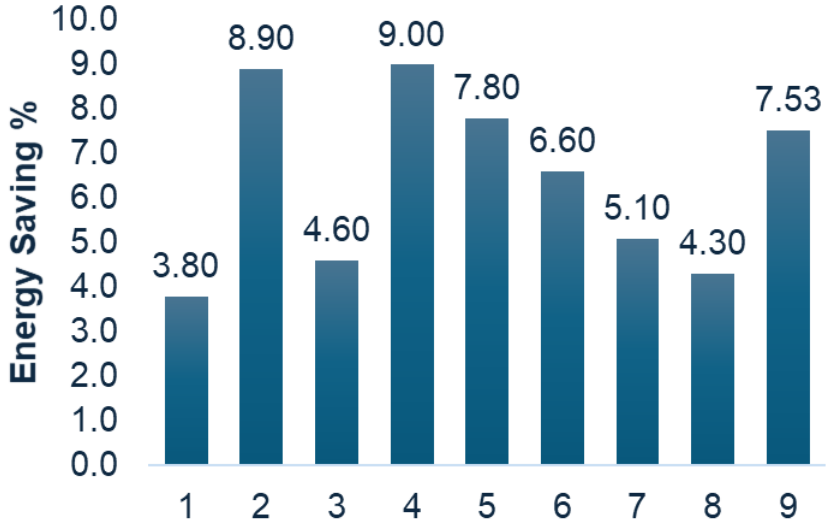

Fig. 6. The comparison of total energy saving for the considered intervention cases

The results demonstrate that upgrading to double-glazed windows with tinted glass and argon filling is the most effective intervention for reducing energy consumption, particularly for cooling. Meanwhile, integrating shading devices like louvres offers additional energy savings by reducing solar heat gain and cooling loads.

4.1. Economic Analysis

The economic analysis of the different retrofitting interventions focuses on the estimated costs, the percentage of energy savings relative to the base case, and the cost-effectiveness of each solution. Table 1 summarizes the results of this analysis, detailing the initial investment costs for each intervention, the percentage of energy savings achieved, and the cost per 1% energy saving.

The interventions vary significantly in terms of initial costs. Case 1, which involves the installation of double-glazing windows with 6mm clear glass and 13mm air gap, has the lowest estimated cost at €44,975 while achieving 3.80% energy savings. On the other hand, Case 8, which uses clear

double glass with air gap and internal louvres activated at 600 W/m^2 solar radiation, has the highest estimated cost at €186,325, but results in only 4.30% energy savings.

Table 1. Estimated cost and effectiveness of the considered interventions

Case	Description	Estimated Cost (€)	Energy Saving (%)	Cost /Saving
1	6mm clear glass, 13mm air gap, and 6mm clear internal glass	44975	3.80	11836
2	6mm blue-tinted glass, 13mm air gap, and 6mm clear internal glass	61680	8.90	6930
3	6mm clear glass, 13mm argon-filled void, and 6mm clear internal glass	77100	4.60	16761
4	6mm blue-tinted glass, 13mm argon-filled void, and 6mm clear internal glass	87380	9.00	9709
5	6mm clear glass, 13mm air gap, and 6mm clear internal glass with fixed internal louvers	93805	7.80	12026
6	6mm clear glass, 13mm air gap, and 6mm clear internal glass with internal louvers that activate when solar radiation exceeds 120 W/m^2	141350	6.60	21417
7	6mm clear glass, 13mm air gap, and 6mm clear internal glass with internal louvers that activate when solar radiation exceeds 400 W/m^2	165765	5.10	32503
8	6mm clear glass, 13mm air gap, and 6mm clear internal glass with internal louvers that activate when solar radiation exceeds 600 W/m^2	186325	4.30	43331
9	Installation of shading devices on the facade	86533	7.53	11492

In terms of energy savings, Case 4 (blue-tinted double glazing with argon filling) offers the highest reduction in energy consumption, with a savings rate of 9.00%, though it comes with a higher cost of €87,380. Case 2, which uses blue-tinted glass with an air gap, also performs well with 8.90% energy savings at a slightly lower cost of €61,680.

The cost-effectiveness of each intervention can be assessed by calculating the cost per 1% energy saving. Case 2, the installation of double glazing windows with 6mm blue-tinted glass, 13mm air gap and 6mm clear internal glass, emerges as the most cost-effective solution, with a cost of only €6,930 per 1% energy saving. This is the most economical option, making it an attractive choice for budget-conscious retrofitting. Case 4, using blue-tinted glass with an argon gap, provides a higher cost of €9,709 per 1% saving but achieves the maximum energy savings of 9.00%.

In contrast, Case 8 (internal louvres activated at 600 W/m^2) is the least cost-effective, with a cost of €43,331 per 1% energy saving. This high cost, coupled with relatively modest energy savings, suggests that the use of advanced louvre systems may not offer the best return on investment compared to simpler shading or glazing interventions.

These findings indicate that blue-tinted glass solutions offer the most cost-effective solution, while advanced louvre systems (Cases 6-8) involve higher costs for smaller energy savings. All cases may be combined with Case 9 to have additional energy saving as it includes a separate type of intervention. However, this option should be evaluated individually for each building. Same results may not be achieved for every building as it highly depends on the case at hand. Analyses show that for the case study building, 16.53% energy savings may be obtained for a cost of €10,521 per 1% of energy reduction by combining Case 4 and 9.

5. Discussion of Results

The analysis demonstrates that the installation of double-glazed units significantly improves the building's insulation, leading to a noticeable reduction in energy consumption for heating and cooling. By reducing thermal transmission through windows, double-glazed systems, particularly those with argon-filled gaps, minimize heat loss in winter and heat gain in summer. This improvement not only enhances the building's energy performance but also contributes to better

thermal comfort for occupants. Among the tested cases, blue-tinted double-glazed units with argon gaps (Case 4) proved to be the most efficient, achieving a 9.00% energy saving. However, even standard clear double-glazed units (Case 1) delivered improvements over the base case, offering 3.80% savings. Research by Nair et al. supports these findings, indicating that double-glazing can significantly enhance energy efficiency in heritage buildings without compromising their aesthetic value [15].

The implications of this intervention extend to the overall building performance, with a reduction in the load on HVAC systems, which could result in longer equipment lifetimes and lower operational costs. In heritage buildings like the Polytechnic University of Tirana, careful integration of double-glazing allows energy improvements without significantly altering the appearance or structure of the historic facade. This aligns with the work of Buda et al., who emphasize the importance of conservation-compatible retrofit solutions that respect the historical integrity of buildings while enhancing their energy performance [21].

Shading devices play a critical role in controlling solar heat gain, particularly in climates where solar radiation can lead to overheating. The internal louvres tested in this study were found to be effective in reducing cooling loads, especially in configurations where the louvres activated in response to higher solar radiation thresholds. Case 9, involving the installation of internal shading devices on the facade, provided a 7.53% reduction in energy consumption. It is one of the cost-effective interventions being close to low end of cost per energy saving values. This finding is consistent with research by Heidarzadeh, which highlights the effectiveness of shading devices in improving energy efficiency in office buildings [29].

Shading devices not only prevent excess heat gain but also contribute to visual comfort by reducing glare inside the building. Fixed internal louvres (Case 5) and automated louvres that responded to specific radiation levels (Cases 6-8) proved particularly useful for this purpose. However, in heritage buildings, the placement of external shading may clash with aesthetic and preservation standards, requiring internal or less visually intrusive solutions, as was applied in this case. This necessity is echoed in the work of Kim and Felkner, who argue for the importance of balancing energy efficiency measures with the preservation of historical aesthetics in adaptive reuse projects [30].

The economic analysis of the interventions highlights significant variations in the cost-effectiveness of different retrofitting measures. While double-glazing solutions offered substantial energy savings, their installation cost varied widely. The most cost-effective solution overall was the installation of double-glazing windows with 6mm blue-tinted glass, 13mm air gap and 6mm clear internal glass (Case 2), which achieved a 8.90% energy saving at a low cost of €6,930 per 1% energy saving. In contrast, more advanced louvre systems (Cases 6-8), while offering additional energy savings, came at a significantly higher cost. The louvres activated at 600 W/m^2 solar radiation (Case 8), for example, had the highest cost per unit energy saving, at €43,331 per 1% saving. This suggests that while advanced shading technologies can enhance energy performance, their financial viability may be questionable unless energy savings are maximized. Similarly, the use of tinted double-glazing with argon filling (Case 4) achieved the highest energy savings but with moderate cost-effectiveness.

Several challenges emerged during the retrofitting process, particularly concerning the building's status as a heritage structure. Retrofitting older, historically significant buildings requires careful balancing of energy efficiency improvements with the need to preserve architectural integrity. External shading devices, may not be preferable for buildings like the Polytechnic University of Tirana due to potential changes to the historic facade. As a result, internal solutions, such as internal louvres, were favored. This approach is supported by findings from Martínez-Molina et al., who emphasize the need for energy-efficient retrofitting measures that respect the historical value of buildings [31].

Another constraint involved the integration of double-glazing. Installing modern, high-performance windows in a heritage building requires customization to ensure that the new units fit within the existing frames without altering the building's historical appearance. Technical challenges also arose regarding the application of louvre systems, particularly in maintaining

consistent operation of automated systems in response to fluctuating solar radiation levels. This complexity is echoed in the research of Bulut et al., which discusses the challenges of retrofitting secondary glazing in heritage contexts [32]

The findings from this case study provide valuable insights for the retrofitting of other heritage buildings. First, energy-efficient retrofitting measures, particularly the use of double-glazing and shading devices, can significantly reduce energy consumption without compromising the historical value of such structures. The most successful strategies in this study combined internal interventions, such as internal louvres, with high-performance glazing systems that can be integrated discreetly into heritage facades. This aligns with the recommendations of Usta and Zengin, who advocate for careful consideration of glazing types to optimize energy performance in heritage buildings [33].

Future retrofitting projects should aim to balance energy efficiency with historical preservation. This might involve using internal, automated shading devices or selecting glazing solutions that are tailored to the aesthetic and structural characteristics of the building. Cost-effectiveness should also be a key consideration, with particular attention paid to simple yet effective solutions like fixed shading devices or air-gapped glazing, which offer a high return on investment. The economic feasibility of such measures is supported by the work of Bahadır et al., who emphasize the importance of evaluating energy-cost efficient design alternatives [34].

Ultimately, these findings highlight that with the right combination of interventions, heritage buildings can achieve significant energy savings while maintaining their historical and architectural integrity, offering a model for future projects aiming to combine sustainability with cultural preservation. The integration of energy-efficient technologies in heritage contexts is not only feasible but essential for advancing sustainable practices in the built environment, as underscored by the comprehensive review conducted by Moghaddam [35].

6. Conclusion

This study examined the effects of two key retrofitting measures—replacing single-glazed windows with double-glazed units and installing shading devices—on the energy performance of the Polytechnic University of Tirana, a heritage building in nine different cases. Through energy simulations, the results showed that both interventions provided substantial energy savings and improved overall thermal comfort, without compromising the architectural integrity of the building if done with care.

The analysis revealed that double-glazed units, particularly those filled with argon and tinted glass, significantly reduced heating and cooling demands. Similarly, internal shading devices helped mitigate solar heat gain and maintained visual comfort, with some louvre systems performing better than others depending on their activation thresholds.

Main conclusions may be listed as:

- Double-glazed windows improved insulation, reducing both heating and cooling loads, with energy savings ranging from 3.80% to 9.00%, depending on the type of glazing used.
- Internal shading devices were effective in reducing solar heat gain, with fixed and automated louvres providing energy savings between 4.30% and 7.80%, depending on their activation threshold.
- The economic analysis highlighted those simpler interventions, such as standard double-glazed units and fixed shading devices, offered higher cost-effectiveness compared to more advanced automated louvre systems.
- Retrofitting heritage buildings require careful consideration of both energy-saving measures and the need to preserve architectural authenticity. Internal interventions, such as internal louvres, were especially effective in addressing this balance.

The findings of this study underscore the importance of double-glazing and shading devices in sustainable retrofitting projects for heritage buildings. These interventions not only significantly

enhance the energy performance of such buildings but may also maintain their historical and architectural integrity. The results suggest that double-glazed windows and carefully integrated shading systems are critical components of any energy-saving strategy for older, historically significant structures.

For heritage buildings, the challenge often lies in finding solutions that both reduce energy consumption and respect conservation standards. This study demonstrates that with well-chosen retrofitting measures, it is possible to achieve substantial energy savings while preserving the building's historical value.

Future research may focus on combining these interventions with other sustainable retrofitting measures, such as improving insulation and integrating renewable energy systems. Additionally, exploring newer technologies for both glazing and shading devices could further enhance the energy performance of heritage buildings.

References

[1] Bilgin H, Fule Z, Ozmen HB. Numerical study to evaluate the structural response of the basilica of St. Sotiri. Res Eng Struct Mater. 2023; 9(2):309-29. https://doi.org/10.21203/rs.3.rs-2462157/v1
[2] Li L, Tang Y. Towards the Contemporary Conservation of Cultural Heritages: An Overview of Their Conservation History. Heritage. 2023; 7(1):175-92. https://doi.org/10.3390/heritage7010009
[3] Guzman P, Pereira Roders A, Colenbrander B. Impacts of Common Urban Development Factors on Cultural Conservation in World Heritage Cities: An Indicators-Based Analysis. Sustainability. 2018; 10(3):853. https://doi.org/10.3390/su10030853
[4] Dias Pereira L, Tavares V, Soares N. Up-To-Date Challenges for the Conservation, Rehabilitation and Energy Retrofitting of Higher Education Cultural Heritage Buildings. Sustainability. 2021; 13(4):2061. https://doi.org/10.3390/su13042061
[5] Farjami E, Türker ÖO. The Extraction of Prerequisite Criteria for Environmentally Certified Adaptive Reuse of Heritage Buildings. Sustainability. 2021; 13(6):3536. https://doi.org/10.3390/su13063536
[6] Tu H-M. The Attractiveness of Adaptive Heritage Reuse: A Theoretical Framework. Sustainability. 2020; 12(6):2372. https://doi.org/10.3390/su12062372
[7] Günçe K, Mısırlısoy D. Assessment of Adaptive Reuse Practices through User Experiences: Traditional Houses in the Walled City of Nicosia. Sustainability. 2019; 11(2):540. https://doi.org/10.3390/su11020540
[8] Kee T, Chau KW. Adaptive reuse of heritage architecture and its external effects on sustainable built environment-Hedonic pricing model and case studies in Hong Kong. Sustain Dev. 2020; 28(6):1597-608. https://doi.org/10.1002/sd.2108
[9] Rosetti I, Bertrand Cabral C, Pereira Roders A, Jacobs M, Albuquerque R. Heritage and Sustainability: Regulating Participation. Sustainability. 2022; 14(3):1674. https://doi.org/10.3390/su14031674
[10] Mekonnen H, Bires Z, Berhanu K. Practices and challenges of cultural heritage conservation in historical and religious heritage sites: evidence from North Shoa Zone, Amhara Region, Ethiopia. Herit Sci. 2022; 10(1):172. https://doi.org/10.1186/s40494-022-00802-6
[11] Osello A, Lucibello G, Morgagni F. HBIM and Virtual Tools: A New Chance to Preserve Architectural Heritage. Buildings. 2018; 8(1):12. https://doi.org/10.3390/buildings8010012
[12] Sampaio AZ, Gomes AM, Sánchez-Lite A, Zulueta P, González-Gaya C. Analysis of BIM Methodology Applied to Practical Cases in the Preservation of Heritage Buildings. Sustainability. 2021; 13(6):3129. https://doi.org/10.3390/su13063129
[13] Jordan-Palomar I, Tzortzopoulos P, García-Valldecabres J, Pellicer E. Protocol to Manage Heritage-Building Interventions Using Heritage Building Information Modelling (HBIM). Sustainability. 2018; 10(4):908. https://doi.org/10.3390/su10040908
[14] Wise F, Moncaster A, Jones D. Rethinking retrofit of residential heritage buildings. Build Cities. 2021; 2(1):495. https://doi.org/10.5334/bc.94
[15] Nair G, Verde L, Olofsson T. A Review on Technical Challenges and Possibilities on Energy Efficient Retrofit Measures in Heritage Buildings. Energies. 2022; 15(20):7472. https://doi.org/10.3390/en15207472
[16] Wise F, Moncaster A, Jones D. Is It All About the Windows? Residents' Values in Residential Heritage Buildings. Acta Polytech CTU Proc. 2022; 38:592-8. https://doi.org/10.14311/APP.2022.38.0592
[17] Wise F, Jones D, Moncaster A. Reducing carbon from heritage buildings: the importance of residents' views, values and behaviours. J Archit Conserv. 2021; 27(1-2):117-46. https://doi.org/10.1080/13556207.2021.1933342

[18] Ginks N, Painter B. Energy retrofit interventions in historic buildings: Exploring guidance and attitudes of conservation professionals to slim double glazing in the UK. Energy Build. 2017; 149:391-9. https://doi.org/10.1016/j.enbuild.2017.05.039
[19] Buda A, de Place Hansen EJ, Rieser A, Giancola E, Pracchi VN, Mauri S, et al. Conservation-Compatible Retrofit Solutions in Historic Buildings: An Integrated Approach. Sustainability. 2021; 13(5):2927. https://doi.org/10.3390/su13052927
[20] Mathew D, O'Hegarty R, Kinnane O. Historic buildings to Positive Energy Buildings: a trilemma between energy efficiency, lifecycle carbon and architecture conservation. J Phys Conf Ser. 2023; 2654(1):012010. https://doi.org/10.1088/1742-6596/2654/1/012010
[21] Buda A, Gori V, Hansen EJ de P, López CSP, Marincioni V, Giancola E, et al. Existing tools enabling the implementation of EN 16883:2017 Standard to integrate conservation-compatible retrofit solutions in historic buildings. J Cult Herit. 2022; 57:34-52. https://doi.org/10.1016/j.culher.2022.07.002
[22] Cariola M, Falavigna G, Picenni F. Holistic impact and environmental efficiency of retrofitting interventions on buildings in the mediterranean area: A directional distance function approach. Appl Sci. 2021; 11(22). https://doi.org/10.3390/app112210794
[23] Alkenanee FS, Alrudaini, TMS. Seismic performance of masonry buildings in Iraq. Res Eng Struct Mater. 2023; 9(2):363-78. https://doi.org/10.17515/resm2022.489ie0801
[24] Sunikka-Blank M, Galvin R. Irrational homeowners? How aesthetics and heritage values influence thermal retrofit decisions in the United Kingdom. Energy Res Soc Sci. 2016; 11:97-108. https://doi.org/10.1016/j.erss.2015.09.004
[25] Şahin CD, Arsan ZD, Tunçoku SS, Broström T, Akkurt GG. A transdisciplinary approach on the energy efficient retrofitting of a historic building in the Aegean Region of Turkey. Energy Build. 2015; 96:128-39. https://doi.org/10.1016/j.enbuild.2015.03.018
[26] Renzi R, others. Regime e rappresentazione. Il padiglione del lavoro italiano in Africa ed il padiglione dell'Albania alla Mostra Triennale delle Terre d'Oltremare del 1940. BLOOM. 2012; 13:73-7.
[27] Hyraj D. Sustainable Retrofitting of Cultural Heritage Buildings, A Case Study: The Polytechnic University of Tirana. Dissertation. Epoka University, Albania; 2024.
[28] DesignBuilder. DesignBuilder Software Ltd - Home [Internet]. DesignBuilder software. 2023. Available from: https://designbuilder.co.uk/
[29] Heidarzadeh S, Mahdavinejad M, Habib F. External shading and its effect on the energy efficiency of Tehran's office buildings. Environ Prog Sustain Energy. 2023; 42(6). https://doi.org/10.1002/ep.14185
[30] Kim D, Felkner J. A Sustainable Approach to the Adaptive Reuse of Historic Brick Buildings:Analysis of Energy Efficiency Strategies for Historic Facade Retrofits. In: Healthy, Intelligent and Resilient Buildings and Urban Environments. Syracuse, New York: International Association of Building Physics (IABP); 2018. p. 253-8. https://doi.org/10.14305/ibpc.2018.be-7.01
[31] Martínez-Molina A, Tort-Ausina I, Cho S, Vivancos J-L. Energy efficiency and thermal comfort in historic buildings: A review. Renew Sustain Energy Rev. 2016; 61:70-85. https://doi.org/10.1016/j.rser.2016.03.018
[32] Bulut MB, Wilkinson S, Khan A, Jin X, Lee CL. Thermal performance of retrofitted secondary glazed windows in residential buildings - two cases from Australia. Smart Sustain Built Environ. 2022; 11(4):1182-92. https://doi.org/10.1108/SASBE-03-2021-0050
[33] USTA P, ZENGİN B. An evaluation of the glazing type impact on building energy performance through a building simulation. J Energy Syst. 2022; 6(1):1-17. https://doi.org/10.30521/jes.945193
[34] Bahadır Ü, Thomollari X, Toğan V. Evaluation of energy-cost efficient design alternatives for residential buildings. J Constr Eng Manag Innov. 2018; 1(1):43-54. https://doi.org/10.31462/jcemi.2018.01043054
[35] Moghaddam SA, Serra C, Gameiro da Silva M, Simões N. Comprehensive Review and Analysis of Glazing Systems towards Nearly Zero-Energy Buildings: Energy Performance, Thermal Comfort, Cost-Effectiveness, and Environmental Impact Perspectives. Energies. 2023; 16(17):6283. https://doi.org/10.3390/en16176283

Research on Engineering Structures & Materials
www.jresm.org
MIM Research Group

Review Article

Electrical sensing properties of smart concrete enhanced with nano materials

G. Dhivyalakshmi*, [a], C. Freeda Christy[b]

Dept. of Civil Engineering, Kalasalingam Academy of Research and Education, India

Article Info

Article History:

Received 09 Aug 2024

Accepted 03 Nov 2024

Keywords:

Crack detection;
Functional fillers;
Piezo resistivity;
Sensors;
Structural health monitoring;
Sustainability

Abstract

The structures have to be assessed for its failures caused by design and construction errors, material deterioration, adverse environment effect hence monitoring the structural health has shown to be a reliable method of assuring the structural integrity. The advanced development of sensor technology and sensing material are the most attractive parts of evaluating structural health. The change in stress, strain, crack formation, temperature variation is measured using fiber optic sensors, piezometers and other sensor types are often utilized in health monitoring systems. Sensors can degrade over time due to exposure to moisture, temperature fluctuations, wearing and tearing or physical impacts. Additionally, installing and maintaining sensors can be costly. These restrictions might be addressed by incorporating sensing technology, such as smart sensing concrete, into concrete structures. This paper explores the piezo resistive properties in concrete by introducing functional fillers like carbon fiber, carbon nano tubes, graphene materials to make electrically conductive concrete that are used to assess its own deformation. This technology could lead to more efficient maintenance and repair processes, ultimately increasing the lifespan of buildings and bridges reduces the wastage of resources leads to sustainability.

1. Introduction

Concrete is a prominent building material, and its performance becomes complex with the high-rise structures. However, the concrete constructions were prone to deformation due to harsh environmental conditions, improper design, materials deterioration, and lack of structural maintenance [1]. To keep structures from being harmed, frequent maintenance and ongoing observation are crucial by monitoring the structures to analyze, localize and damaging conditions are important aspect in structural health monitoring [2,3] which is usually done by visual inspection, Non-destructive testing and sensors. These techniques do have certain limitations for complex civil buildings, for instance, visual inspections are often subjective and may fail to detect inner damage, whereas other methods, like NDT, require specific equipment and skilled operators. Furthermore, the sensors used in conventional SHM systems may become less resilient with time, especially when exposed to unfavorable weather conditions. The requirement for routine maintenance and calibration of sensors may result in a rise in the overall cost and complexity of the monitoring system [5,6]and thus leads to the development of smart sensing concrete by inducing functional fillers were used to detect the variation in electrical resistivity of structures during damage or deformation. Electrical resistivity, the inverse of electrical conductivity, detects damage by measuring the change in stress and strain. Concrete with functional fillers such as 1.5 weight percent carbon fiber shows improved compressive strength of 33 MPa in addition with FCR 2.2% [8], the same proportion of carbon fiber in geopolymer concrete also shows sensing properties [7] hybrid combination of 0.4 weight percent carbon fiber 0.5 weight percent carbon

*Corresponding author: 9623103001@klu.ac.in
[a]orcid.org/0009-0008-6035-6208; [b]orcid.org/0000-0002-6929-310X
DOI: http://dx.doi.org/10.17515/resm2024.387ma0809rv
Res. Eng. Struct. Mat. Vol. 10 Iss. 4 (2024) 1679-1697

nanotubes shows excellent electrical capabilities it creates significant negative potential shift caused by the applied electric current, steel rebars were protected effectively [9]. Concrete mixes containing 0.5% steel fibers lowers electrical resistance, with a gauge factor more than 20 times greater than that of typical strain gauges [10], then mortar with 5 % graphite powder shows 60% decrease in electrical resistivity during compression [11], under uniaxial compression, the electrical resistivity of nickel particles based mortar decreases by 62.61*% in the elastic regime [12] According to the filler concentration, functional fillers form a conductive network within the concrete [4,7] and transforming the concrete into a conductive material. Functional fillers can fill the micropores in the concrete matrix and improve the connection between individual particles. This allows concurrent monitoring of structural health through the detection of cracks and stresses, improving overall safety and longevity of the structure. Simultaneously, the addition of functional fillers in concrete also boosts up its mechanical properties like compressive strength, tensile strength and flexural strength [8-13] and makes the structure durable and resistant against environmental factors as compared with traditional sensors [6].

Sensing concrete plays an essential role in structural durability by investigating reinforcement corrosion [14]. Real-time monitoring of traffic patterns and structural integrity is made possible by this cutting-edge technology, which also provides important information for maintenance and safety enhancements [15]. Furthermore, by automatically recognizing and reacting to ice conditions, sensing concrete used in anti-icing applications reduces accidents and extend the life of the infrastructure [16]. As a result, sensing concrete is more consistent, efficient and cost effective as compared with traditional sensors.

2. Monitoring of Structures

In general, the planning of the urban infrastructure for a more effective and sustainable future is being completely transformed by the incorporation of cutting-edge materials and sensors into the concrete building process. Sensors are implanted in concrete during and after construction to monitor the health of buildings by collecting data from the sensors. [2]. The sensing methods in structures were indicated in table 1.

2.1. Electric Strain Gauge

Electrical resistance serves as the foundation for the operation of a strain gauge [17]. A material's electrical resistance varies as it expands or compresses. This characteristic is used by a strain gauge to quantify strain by identifying variations in resistance. The strain gauge will sense variations in strain during testing and adjust its electrical resistance accordingly. These variations in resistance cause a voltage differential, which the DAQ system subsequently records [18].

2.2. Accelerometers

Sensors that measure variation in velocity and it measures vibrations in variations of electrical resistance which is concurrently recorded in data logger [19].

2.3. Fiber Optic Sensors

Sensor that uses optical fiber to measure strain, temperature and pressure variations. Fiber Bragg Grating (FBG) sensors is the most commonly used fiber optic sensors. The grating is engraved in to the core of the optical fiber. The grating spacing varies in response to temperature variations or strain on the fiber, which modifies the reflected light's wavelength. The strain or temperature change can be ascertained by measuring this wavelength shift [20].

2.4. LVDT

Transducers that work on the principle of a transduction process are known as inductive transducers. A position sensor that can detect linear movements or vibrations and convert them into electrical signals or a pulsating electrical current is essentially what an LVDT is. The linear movement of the item to which it is linked is converted into a fluctuating electrical signal by the LVDT sensor [21].

2.5. Piezo Electric Sensors

Piezoelectric phenomena are caused by an electric dipole moment. When a piezoelectric material is exposed to an external stress or deformation in a particular direction, it produces electric polarization, which results in opposing bound charges on each side. After the external stress was removed, the polarization disappeared, resulting in the voltage differential. Piezoelectric sensors are widely used to detect dynamic pressure signals which is recorded in data logging system [22].

2.6. Acoustic Emission Sensors

AE sensors is a passive non-destructive testing technique that uses the high-frequency acoustic energy released by a stressed item, such as when corrosion products develop on a corroding rebar and push out onto the concrete around it. Subsequently, the data is recorded [23].

2.7. Eddy Current Sensors

ECT is an NDT technique, ECT probe is activated by an alternating current. The electrical current generates an alternating magnetic field in the area of the ECT probe, which oscillates at the same frequency. The eddy current distribution changes due to variations in the test object's electrical conductivity and magnetic permeability, as well as the existence of defects concurrently changes were recorded [24].

2.8. Electro Chemical Corrosion Sensors

Electrochemical analysis offers a real-time performance evaluation non-destructive estimation of rebar corrosion in existing concrete structures. The mechanism involves in this process is oxidation and reduction reaction [25].

2.9. Humidity Sensor

The term "humidity sensor" describes any apparatus or gadget that may transform humidity into an electrical signal that is simple to detect and records the moisture movement in cracks [26].

2.10. Vibrating Wire Sensors

VWS are widely employed to monitor the strain in structures The working principle of vibrating wire sensors rely on the measurement of the frequency changes of a wire which is placed on the support of the structure depending on the wire specification and the surrounding environment oscillation occurs which is recorded in a data monitoring system [27].

Table 1. Sensing methods and its parameters

Sensing methods	Materials	Measuring parameter	References
Intrinsic	Conductive fillers (carbon fibers, graphene, CNT, steel fibers)	Stress, strain, temperature, crack, moisture movement	[7-11]
Non intrinsic	Electric strain gauge	Strain	[17,18]
Non intrinsic	Accelerometers	Acceleration (to study dynamic behavior of structure)	[19]
Non intrinsic	Fiber optics	Strain, temperature and pressure variations	[20]
Non intrinsic	LVDT	Displacement	[21]
Non intrinsic	Piezo electric sensors	Stress, temperature, crack	[22]
Non intrinsic	Acoustic Emission sensors	Detects stress waves during crack propagation.	[23]
Non intrinsic	Eddy current sensors, crack sensor	Crack growth	[24]
Non intrinsic	Humidity sensors	Moisture content	[25]
Non intrinsic	Electro chemical corrosion sensors	Corrosion	[26]
Non intrinsic	Vibrating Wire sensors	strain	[27]

3. Evolution of Self-Sensing Concrete

The larger subject of smart materials and structures, which started to get substantial attention in the 1980s, is where the idea of self-sensing concrete first emerged. But there are a few significant turning points to track the precise evolution of self-sensing concrete as shown in Fig 1.

3.1. Early Ideas (1990s)

In the early 1990s, the concept of adding sensing capabilities to concrete structures was initially put out. Researchers started experimenting with strain and temperature monitoring using fiber optic sensors implanted in concrete [28]. These early attempts, albeit not specifically self-sensing concrete, set the stage for the eventual integration of sensing capabilities into concrete buildings.

3.2. Electrically Sensitive Concrete (Late 1990s to Early 2000s)

The creation of electrically conductive concrete was a key step toward complete self-sensing capabilities work on carbon fiber-reinforced cement-based composites with strain-sensing characteristics [29]. This study found that the electrical resistivity of these materials altered in response to applied stress, indicating a route to intrinsic sensing capabilities.

3.3. Piezoresistive Cement Sensors (Late 2000s)

Following on previous work with sensitive concrete, researchers created specialized compositions of cement-based composites with improved piezo resistivity. Han et al. (2015) investigated cement composites containing carbon nano tubes, which showed significant sensitivity to stress and strain. The creation of multifunctional self-sensing concrete, which is capable of monitoring several factors at once, has been the focus of recent advancements in this field [30]. A cement-based composite with enhanced mechanical properties and the ability to detect strain, cracks, and damage was created by many researchers by using various functional fillers such as carbon fiber, carbon nanotubes, steel fiber, graphene nano platelets [4-12]. The current paradigm in research is on the practical application of self-sensing concrete technology at a large scale in real-world structures.

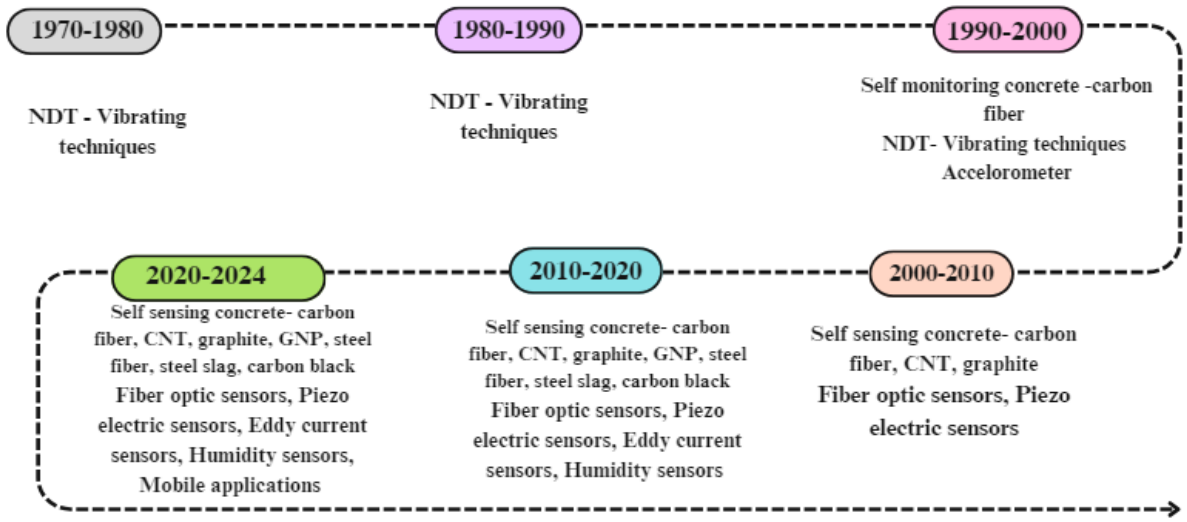

Fig. 1. Evolution of self-sensing concrete

4. Functional Fillers in Concrete

Functional fillers, like metallic fibers, carbon materials, graphene materials, metallic powder, and other conductive materials, that are typically utilized in electrically conductive concrete are indicated in table 2. Carbon black, the by-product of pulverization of waste tires and the amorphous form of carbon decreases the concrete resistivity concurrently increases the sensitivity of concrete [31]. Graphene materials such as graphite coated fibers, aggregates and graphene nano platelets are also proved effective conductive fillers for sensing concrete. The graphite nano platelets (GNP)

diminish conductivity with 2.5%, later it enhances with 5% and 7.5% by weight of cement [32]. Graphene powder significantly enhances the conductivity of concrete, simultaneously decreases its workability and makes the mix harsher [11].

Steel slag, obtained from smelting of iron, in the iron industry increases compressive and split tensile strength it also enhances high conductivity in concrete with steel fibers through quantum tunneling. Its use contributes to reduce waste and lower the carbon impact of construction projects. Overall, integrating Steel slag in concrete mixes provide durable, robust, and cost-effective material in construction industry [33]. The short stainless-steel fiber improved electrical conductivity, flexural tension, and energy absorption capacity [10], whereas the inclusion of nano stainless-steel powder reduces dry shrinkage by 12.1% to 39.8% [34].

Table 2. Functional fillers in concrete

Constituents of filler	Functional fillers	Function of fillers	Cost Comparison
Carbon based fillers	Carbon fiber	Enhances electrical conductivity to monitor strain and improves tensile strength.	High
	Carbon nano tubes	Improves piezo resistive property and self-heating.	Very high
	Carbon black	Reduces resistivity, improves compressive strength.	Low
	Activated carbon	Reduces resistivity, improves compressive strength and reduces porosity.	Moderate
Graphene based fillers	Graphene nano platelets	Enhances compressive strength, and piezo resistivity to detect strain.	High
	Graphene powder	Improves piezo resistive property and improves mechanical strength.	High
Metallic based fillers	Steel fiber	Boost mechanical strength, crack-bridging, lowers resistivity.	Moderate
	Metallic powders such as ferric, copper and nickel powder.	Enhances electrical conductivity to monitor strain.	High
	Steel slag	Improves compressive strength and lowers resistivity.	Low
Other fillers	Piezoelectric ceramics (e.g., lead zirconate titanate)	Enhances electrical conductivity to monitor strain.	Very high

Carbon based nano materials like single-walled carbon nanotubes and multi-walled carbon nanotubes gives a higher conductivity channel for electron transport within the concrete and also provides excellent mechanical strength [9][39]. Other key materials employed in concrete sensing include carbon nanofibers, which provide excellent mechanical strength and micro fracture bridging and simultaneously lower the concrete resistivity by conductive channel formation via tunneling conduction [7]. Even in hostile environments, the carbon-based functional filler offers a stable conducting network and enhanced mechanical properties, whereas steel slag and steel fiber are frequently prone to corrosion [35]. Research shows that fibrous fillers provide more stable

conductive network when compared with particle fillers subsequently in terms of scale micro-scale fillers easily forms conductive network compared with nano- scale fillers but at the same time nano- scale fillers provide broader conductive network at lower concentration [36].

Hybrid filler combination shows optimized performance and cost reduction for example using 0.5% weight of carbon black with 0.1% weight of carbon nano tubes shows excellent strain sensitivity of 107 when compared with carbon nano tubes of 67 [37]. Industrial by products can be used as a functional fillers like steel slag, copper slag, carbon black etc., which reduces the cost for example fine steel slag with steel fibers shows excellent compressive strength of 184 MPa with gauge factor 246.59 using the recycled by products as a functional filler reduces the harmful impact on environment [38]. The selection of functional fillers based on its aspect ratio, conductivity of the filler, cost, etc., for example carbon fiber is more effective in crack bridging simultaneously enhances the conducting pathways with comparatively low cost when compared with carbon nano tubes. Steel fiber and steel slag offers sensing characteristics and also prone to corrosion in harsh environmental conditions [35]. The criteria for selection of fillers are also based on surrounding environments it considerably affects the durability of sensing composites.

5. Dispersing Methods of Nano Particles

Dispersing the particles is necessary to establish the right conductive network in the concrete. Dispersing nanomaterials are either done by chemical or mechanical method. Dispersion of nanomaterials such as carbon nanotubes and nanocarbon fibers became problematic due to their large specific area and development of fiber aggregation due to Van der Waals force which is weak intermolecular forces due to attraction between molecules. Mechanical techniques include mechanical stirring, ball milling, and the sonication process [39]. as shown in Fig. 2. Surfactants typically utilized in chemical techniques included methyl cellulose, polycarboxylates, and lignosulphonates [40,42]. Recent research shows that fly ash and silica fume [40] are also utilized for dispersing the nano materials like carbon nano fiber because the size of silica fume are much smaller than cement which allows nano materials to fill the void between them and reduces the gap where nano materials tend to agglomerate [7].

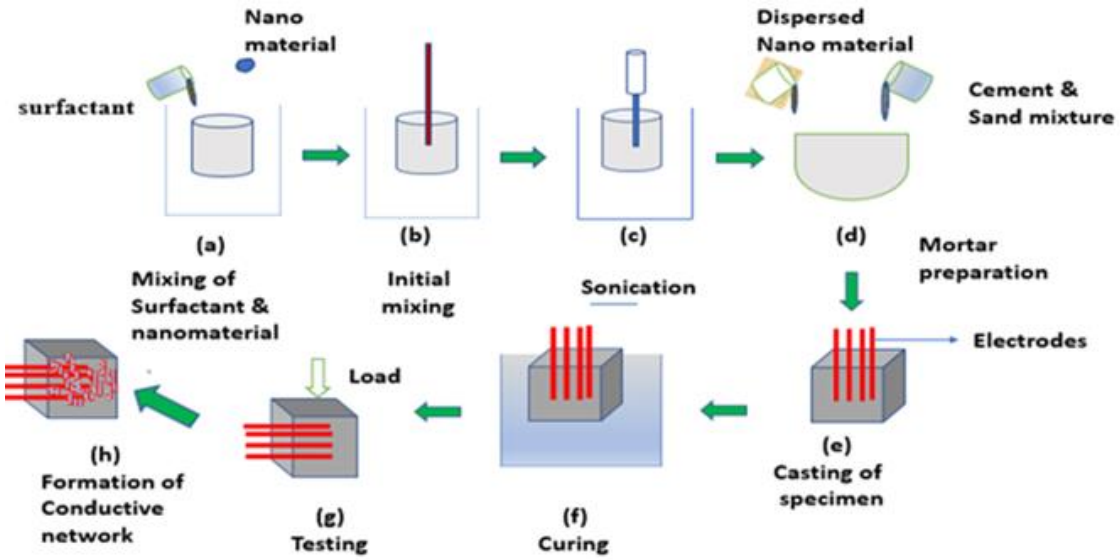

Fig. 2. Fabrication of sensing concrete

The dispersion of fiber is more effectively promoted via combined use of silica fume and methylcellulose than by using silica fume alone [3] [41]. To accomplish this dispersion, three major approaches have been developed; admixing, synchronous admixing, and later admixing [42] as shown in Fig. 3. The initial admixing technique is appropriate for fiber fillers, whereas the later admixing is appropriate for larger fillers. Hybrid mixtures of functional fillers are dispersed by synchronous admixing [12][30]. Research indicates that synchronous admixing is preferred to disperse carbon black and polyvinyl alcohol fiber to produce self-sensing concrete [42].

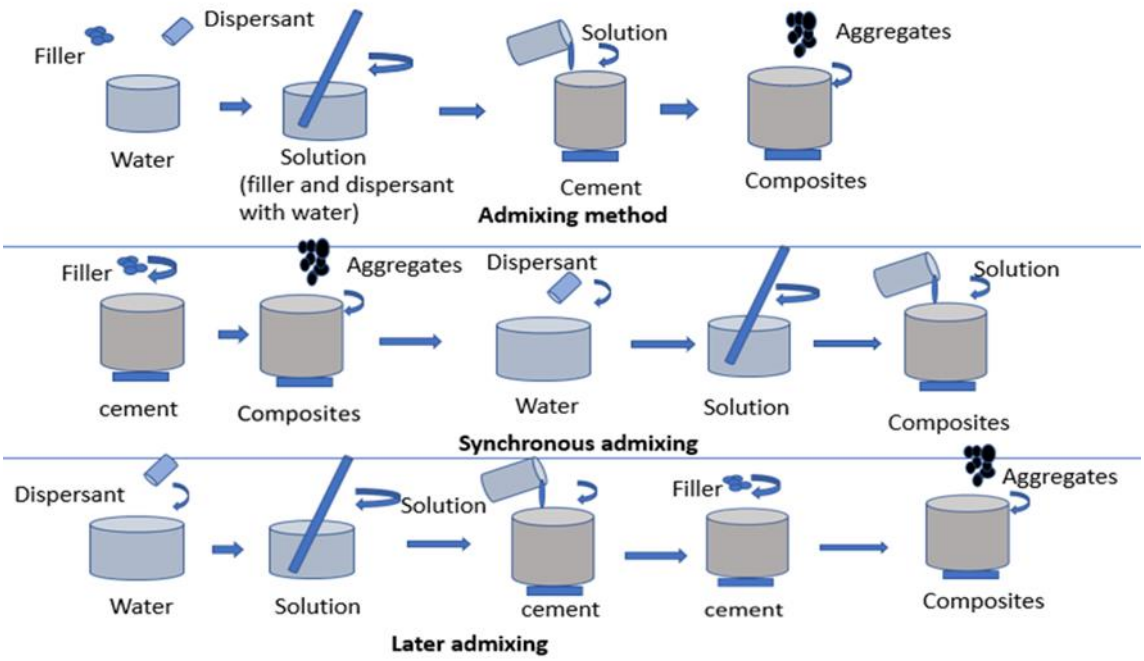

Fig. 3. Dispersion of nano materials

6. Principle

Electro mechanics is the theory that underlies the concrete's sensing mechanism, the study of electromechanics focuses on interaction between mechanical and electrical systems with one another which is based on the flow of electrons during mechanical loading [44]. According to Kousalya Ramachandran et al. (2022) the three elements of electromechanics are piezo-resistivity, piezo-permittivity, and piezo-electric functions [44]. In this case, piezo-resistivity is essential to the concrete sensing mechanism and is obtained by mixing conductive fillers into the concrete. The phrase "piezo-resistivity" refers to the variation in electrical resistivity; when the specimen is subjected to mechanical loading, stress or strain then it causes variation in resistivity here current and potential difference are important factors that influence the property. If the specimen is under the stress, then its geometry undergoes changes which leads to create the pathway between conductive fillers to allow the electron transfer allows the variation in resistivity then the strain is measured by change in resistivity which is given by

$$R = \rho \cdot L / A \tag{1}$$

R denotes the resistance of the specimen, ρ is the resistivity, L is the length and A is the cross-sectional area of the specimen [45]. "Piezo-permittivity" is the change in capacitance, is suitable for dielectric materials which is non conducting materials if is placed in electric field then polarization occurs it sense stress or strain in the materials due to change in properties of dielectric materials during loading it stores the electrical energy while unloading it releases the stored energy by measuring the capacitance the permittivity is calculated; frequency is a critical parameter that influences the property which is calculated by using this relation;

$$C = A\kappa\epsilon_0 / L \tag{2}$$

C denotes capacitance, ϵ_0 is free space permittivity 8.85 × 10^{-12} F/m, L is the length and A is the cross- sectional area of the specimen [46]. "Piezo-electricity" is the change in electric potential or charge when the material experiences an external stress causes internal atomic displacement; voltage is the main factor using this mechanism piezo electric sensors are used to measure integrity of structures [47].

7. Factors Influencing Sensing Mechanism

Siqi Ding et al. (2017) looked at the factors that influence the sensing process. The important parameter is pressure-sensitive qualities that include a range of metrics including signal-to-noise ratio, zero shifts, input and output range, and changes in electrical resistivity as a result of strain brought on by applying loads or deformation of the structures. One of the factors that influence the sensing mechanism was the optimization of functional fillers, its orientation and dispersion; if the right orientation and dispersion were not attained, the sensing mechanism would be affected [48,49]. The other crucial element is the concrete's ability to sense temperature as the concrete temperature rises, electrical resistance falls [31,42] because jumping of electrons across surfaces in the cement-based material causes resistivity to drop as temperature rises and also the movement of ions inside the matrix is high at high temperature this offers lower resistance and higher conductivity of the matrix [48]. Madhavi and Annamalai (2016) looked into concrete's electrical conductivity with saturated water content, fresh concrete functions as a semiconductor with an electrical resistance of 10^5 ohm, whereas hardened concrete functions as an insulator with an electrical resistance of 10^{12} ohm because well interconnected pores exhibit good ion mobility and water content act as a medium for movement of ions which is responsible for ionic conduction this increases the conductivity of concrete [50]. Tiny variations in the water content have a significant impact on the electrical conductivity or resistivity of the concrete because the passage of electrons is dependent on the mobility of ions in the water molecule [51,52]. The evaporable water in the concrete evaporates as it solidifies, causing a shift in the interconnectivity of the pores [30,42,44]. The curing phase is a crucial factor that influences conductivity. As the curing age increases, so does the hydration rate and product, resulting in a denser concrete member. The hydration product gets encased in the pores, restricting the creation of the conductive network [12,30]. The other important parameter to have an impact on the characteristics of concrete is the presence of corrosive substances in the environment causes ion permeation and lowers electrical resistivity, which in turn weakens concrete's sensing capabilities. The additional factors are voltage characteristics, frequency, and current between the electrodes influence the sensing mechanism [47]. Shape of the functional fillers like fibrous and flaky are more effective in forming conductive network when compared with particles like carbon black, activated charcoal. The filler structure has a considerable influence on percolation behavior as it influences a neighboring distance between them. It is possible to compute the spacing between neighboring spherical fillers d_s and fibrous filler d_f using [48];

$$d_s = a/2\,(4\Pi/3\Phi)^{1/3} \quad and \quad d_f = a/2\,(\Pi l/\Phi)^{1/3} \tag{3}$$

where a is diameter of filler and l is fiber length and Φ is filler concentration [48].

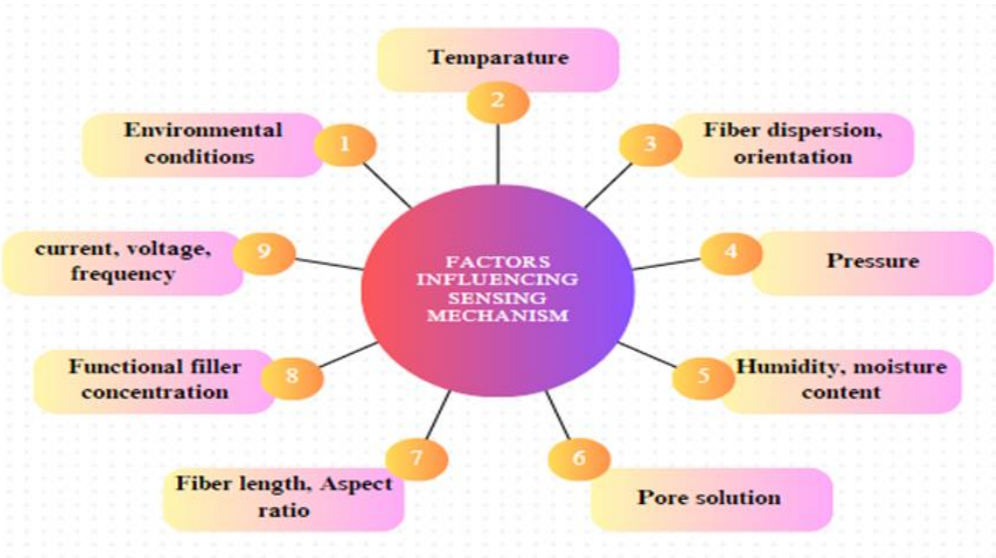

Fig. 4. Factors influencing sensing mechanism

8. Process of Conductive Mechanism

The technique by which concrete conducts electric impulses through them when the specimen or structure deforms is known as the conductive mechanism in concrete sensing. This allows the concrete specimen to sense signals during stress, strain, or any other deformation either by ionic conduction or tunneling conduction [53,54].

8.1. Ionic Conduction

The pore solution and dissolved particles in the concrete are the primary determinants of the ionic conduction of the material as shown in Fig. 5. Because the concrete conducts ions in response to external stimuli or environmental cues, it may detect deformation such as stress and strain in the concrete specimen and structure via conducting electrical impulses through linked capillary spaces [30,53].

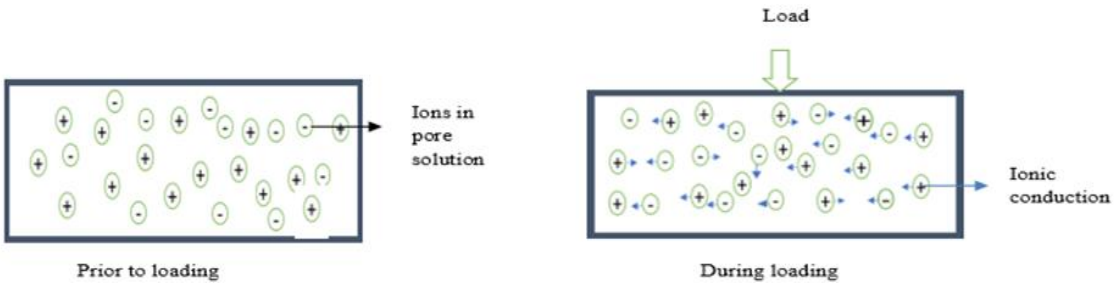

Fig. 5. Ionic conduction

8.2. Tunneling Conduction

This kind of conductive mechanism works by creating a strong electric field, which causes electrons to jump over barriers, conduct with nearby fibers, and create a conductive network as shown in Fig. 6. The electrons then conduct electricity and can detect deformation using an electromechanical method [33,54]. A key component of the concrete's capacity to recognize and react to environmental changes is tunneling conduction, which enables the tracking of stress and strain levels.

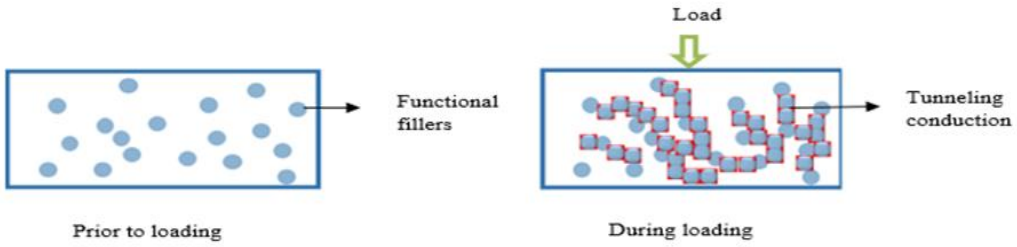

Fig. 6. Tunneling conduction

The smart concrete detect deformation through electrical impulses to its conductive network, which offers important information about the material's structural integrity [30,42]. Higher filler concentration form effective tunneling pathways for electron hoping across the barrier than lower filler concentration concurrently the uniform distribution of fillers should be ensured without agglomeration or cluster formation which affects the tunneling pathways and requires more energy for electrons to cross the barrier which leads to energy loss and limited the sensing mechanism [54]. The carbon fiber, CNT, steel fiber forms continuous network due to bridging up the gap between neighboring fillers and requires less energy for electron – hoping across the barrier [48].

Table 3. Comparison of ionic conduction and tunneling conduction

Characteristics	Ionic conduction	Tunneling conduction
Pore water	Pore water is essential, water act as medium for ions movement.	Pore water is not essential, electrons conduct the sensing mechanism
Filler concentration	Conduction is possible even at lower filler concentration	Conduction is not possible at lower concentration, because it forms weak conductive network between the neighboring fillers. At higher concentrations, the conductive network is strong, electrons cross the barriers to exhibit sensing properties.
Temperature	Temperature increases then the mobility of ions increases.	Energy of electrons is responsible for quantum tunneling, temperature is least effective in this mechanism

9. Percolation Threshold

The creation of conductive channels for physical characteristics of a heterogeneous composite is given by percolation theory [55]. A continuous network is expanded to the entire specimen as conductive particles come into touch with one another or the volume of the filler percentage exceeds a critical value or percolation threshold [11]. The conduction process follows three criteria based on the volume of functional fillers. Concrete's electrical resistance shifts from an insulating zone where functional filler concentration is lesser than the critical filler concentration significant electrical conduction is prevented in the absence of a well-connected network, while some electrons may tunnel through small gaps if particle's chance to be nearby. The point at which fillers starts to form a conductive network and provides pathway for electron movements by direct contact or tunneling conduction simultaneously there is sharp and sudden rise in electrical conductivity of the specimen when conductive filler concentration reaches the critical percolation threshold with the effective filler's dispersion without agglomeration [8,9,30,56]. After reaching the critical threshold the electrical conductivity of the specimen starts to gradual rise after that it starts to decline due to higher concentration of fillers paves a way for agglomeration [48].

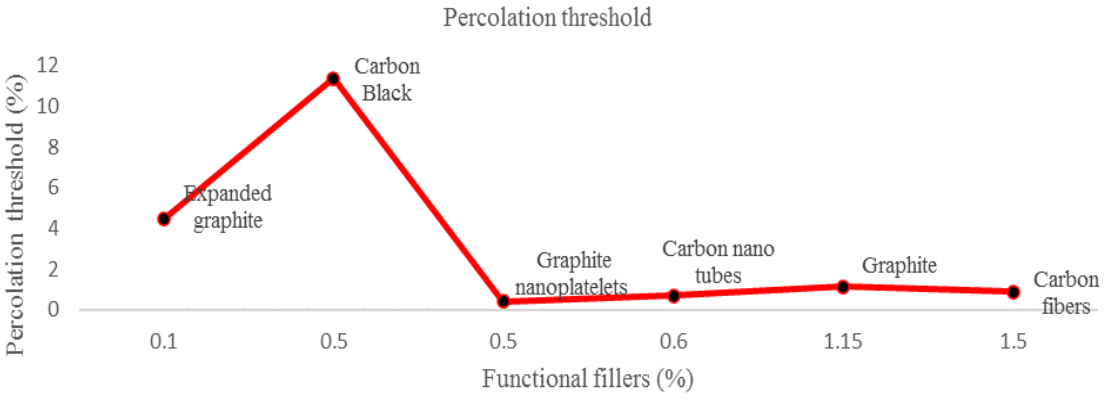

Fig. 7. Percolation threshold of various functional fillers [41]

The percolation value influenced by filler materials inter-particulate distance, large surface area and high aspect ratio particles [49,56]. The shape of fillers such as fibrous, flaky and tubes enhance electrical conductivity at lower percolation threshold as compared with spherical shape fillers. Micro and nano size filler particles like CNT have the potential to scatter more uniformly throughout the matrix and perhaps reduce the percolation threshold as compared to that of macro size fillers like steel slag, steel fiber. Dispersion of functional filler in the concrete matrix plays a critical role. If the fillers were evenly distributed, the sensing qualities produced by lower percolation threshold [41,48].

10. Methods of Measurement in Sensing Concrete

Electrical properties of the smart concrete are sensed either by two or four probe i.e., Wenner method as shown in Fig.8. This electrode configuration of the Wenner method produces a superior outcome as the contact resistance between the electrodes are minimized. The electrodes serve as a link between the composites and the assessing parameter [10,12,57]. Stable electrical conductivity and low electrical resistance are desirable qualities for an electrode. Electrodes made of metals like silver, aluminum, copper, and stainless steel could be formed into bars, metal foil, mesh, or any combination with the silver or copper conductive material [30,42]. Direct current (DC) and alternating current (AC) are the two current modes utilized to measure electrical behavior of the composite [7,8]. Although the direct current thought to be the easiest, the current has a limited range and may cause ions to migrate, which might cause electrical polarization in the composite. Electrical polarization makes it challenging to measure electrical resistance [58]. Initially it is subjected to DC voltage, which causes the polarization at the time of measurement [42]. Another work around for this problem is to use alternating current (AC); polarization occurs still, but it may be controlled by varying the range of frequency and voltage applied to the composite before loading to finish the polarization at the time of measurement by varying the AC voltage's frequency range and amplitude that gives the polarization process more control [10,58,59]. The AC can be transferred to the larger area as compared with DC with minimal loss of energy. DC current produces a constant, continuous flow of electrons in same direction hereby reduces fluctuations in resistivity whereas AC current does not produce the constant flow of electrons and it mainly depends on frequency by using AC current capacitance and inductance also measured unlike DC current where resistance only measured [57]. Polarization is high in DC current and used for static measurements while low in AC current and used for dynamic measurements [58,59].

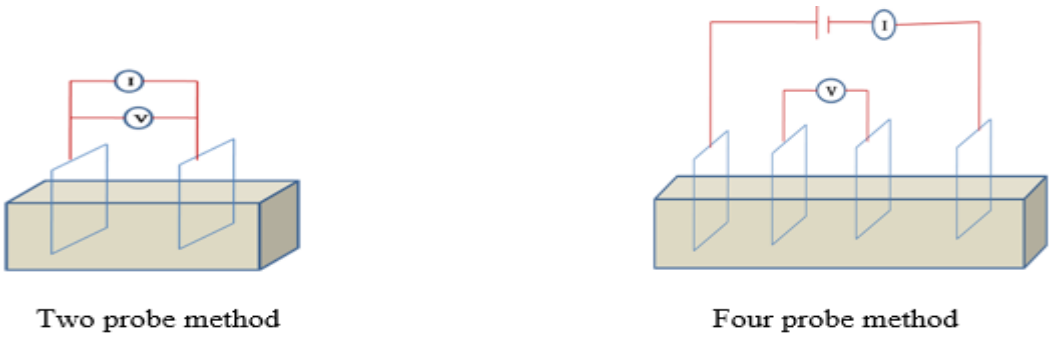

Fig. 8. Measurement of electrical parameter in smart concrete

11. Sensing Mechanism Under Various Loading

11.1. Loading Under Compression

During loading new cracks erupt due to stress and cracks expand under uniaxial compression. Functional fillers approach one another as a result of pressure compaction, strengthening the conductive network inside the sensing concrete this cycle repeats continuously. During loading the resistivity of sensing concrete decreases because spacing between the functional fillers is reduced which makes the flow of electrons to the nearby neighboring fillers became quite easy with well - established conductive network through various number of conducting pathways [60] while unloading it increases subsequently the conductive network is destroyed and then rebuilt as a result of new cracks sprouting. The conductive network breaks down when the fracture widens [12,42,61]. The initial resistivity and resistivity variation are recoverable within elastic region when the stress amplitude is below 30% [30].

11.2. Loading Under Tension

Tensile tension causes the concrete's electrical resistance to rise because it pulls apart the functional fillers within the concrete and thus increases the electrical resistance during loading and

decreases while unloading [62,63] because tensile force pulls the fiber out from the matrix which disrupt the formation of conductive pathways [60]. The initial resistivity and resistivity variation are recoverable within elastic region if the amplitude of stress increases then the initial resistivity and resistivity variation are irrecoverable [42,63].

11.3. Loading Under Flexure

When a concrete beam bends, the top surface compresses and the bottom surface tenses. Flexural loading introduces compressive and tensile strains into the concrete; the compression side of the concrete beam electrical resistance is less, while the tension side electrical resistance is high [30, 61].

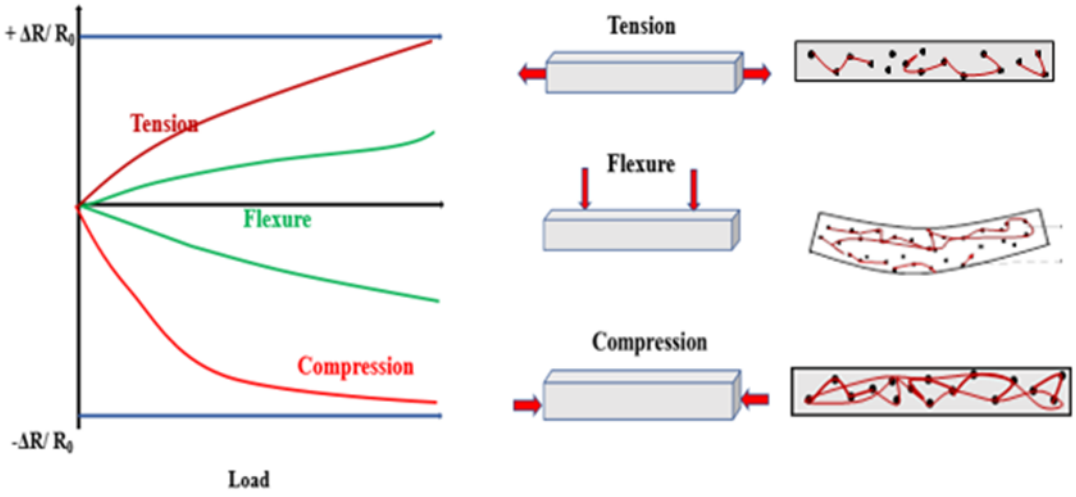

Fig. 9. Sensing mechanism under various loading

12. Piezo Resistive Sensing Mechanism

The resistivity change is influenced by the functional filler content inside the concrete matrix. The percolation phenomena are seen from the Fig. 10., and its existence is explained by varying functional filler concentrations [44]. Insulating zone, where resistivity is high, percolating zone, where resistivity drops suddenly, and conducting zone, where resistivity is low, make up the three sections of the curve [42]. Insulating zone is characterized by a filler concentration in the concrete matrix that is significantly less than the percolation threshold, large spacing between fillers, and sparse filler gathering [59].

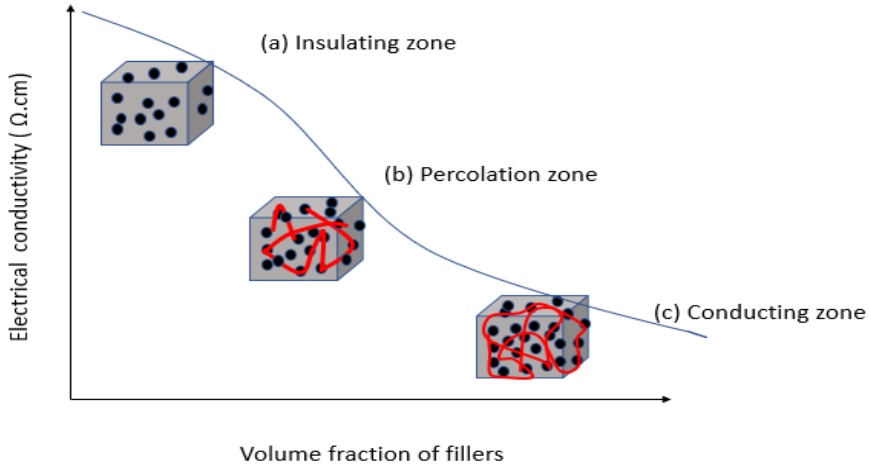

Fig. 10. Variation in Electrical conductivity

As a result, it is difficult for a conductive path to form and for electrons to move between fillers, and the composite exhibits nearly the same high resistivity as the matrix [10,12,30]. The percolation zone is distinguished by the filler content is around the percolation threshold then those fillers begin to build a conductive channel due to tunneling and ionic conduction subsequently reduces the distance between the fillers and thus sharply rises the conductivity of the composites [53,54]. The conducting zone is characterized by the filler content is above the percolation threshold and forms a well- established conductive network results in small increment in conductivity [30,42,44]. At the same time composites with a larger filler concentration did not exhibit the same sensing effect as the composites with comparatively lower filler concentration [73]. This might have happened because there was more tunneling barrier to alter during cyclic loading, but a high filler concentration could result in more conductive pathways, which would have prevented the network from growing further [9,10,55,57]. Therefore, a filler content that is either excess or insufficient could not result in piezoresistive performance.

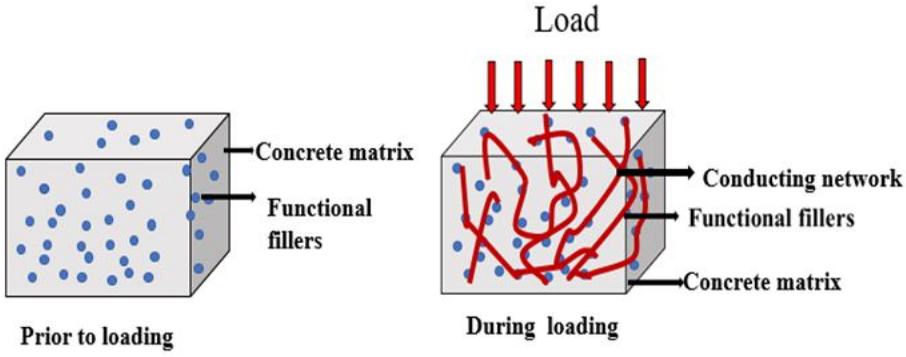

Fig. 11. Piezo resistive mechanism

12.1. Sensitivity Measurements

Sensing behavior is defined by sensitivity characteristics such as a fractional change in electrical resistivity ($\Delta R/ R_0$), force sensitivity coefficient ($\Delta R/ R_0$) / F, stress sensitivity coefficient ($\Delta R/ R_0$) / σ [35]. By monitoring the passage of electrons between the electrodes at a constant voltage, the stress and strain under both dynamic and gradually changing loads were assessed with the electromechanical tests. The functional relation between axial strain (∈) and electrical resistance (ΔR) may be expressed as follows [52];

$$\Delta R/R_0 = k\epsilon \tag{4}$$

where ∈ is the axial strain, k is the gauge factor, and R_0 is the initial resistance. Polarization effects were responsible for the temporal drifts. The material's electrical properties are also crucial for determining sensing characteristics. Ohm's law determines electrical resistance [44];

$$V = IR \tag{5}$$

V is potential difference measured in volts (V), I is the current flow in the circuit measured in terms of ampere (A), whereas R is the electrical resistance measured in terms of ohms (Ω). The signal reception of sensing concrete has also been done recently using innovative methods as electrical capacitance tomography (ECT) [74], electrical impedance tomography (EIS) [75] and Electrical resistance tomography (ERT) [15]. More detailed information may be obtained using these new methods than with the conventional measurement techniques. For instance, the EIS approach may be applied to collect data concerning the microstructural features of the concrete and electrode-concrete interfacial zone [75], in addition to being employed as the sense the signal in concrete, EIT or ECT or ERT methods can picture the distribution of capacitance or impedance or resistance in two or three dimensions, defining the location, form, and degree of structural change of self-sensing concrete [15,74,75].

Table 4. Mechanical, Durable and FCR of various functional fillers

Fillers	Compressive strength (MPa)	Split tensile strength (MPa)	Flexural strength (MPa)	Durability (Water absorption)	FCR	Reference
Steel fiber	29.18	3.82	4.13	3.98%	0.194%	[65]
Steel slag	55.4	4.2	4-5	11.1%	0.198	[33,66]
Carbon fiber	48	5.8	12.1	3.9%	3.0%	[42,67]
CNT	72.1	7.21	10.5	1.565%	2.0%	[42,68]
Graphene	70-80	4-5	5-6	1.5-2%	2.2%	[42,69]
GNP	50-60	2.8	8-9	3-3.5%	2.5-3%	[42,70,71]

13. Applications

The smart sensing concrete provides various applications in various fields like traffic monitoring, smart bricks, anti- icing in pavements etc., as indicated in Table 3.

Table 5. Research area in sensing concrete

Research area	Materials	Characteristics	References
Anti -icing in pavements	Asphalt concrete with carbon fibers	Enhances electrical conductivity and improves self-heating in pavements.	[16,77]
Smart bricks	Clay with stainless steel fibers	Identify and localize earthquake-induced damage in masonry structures.	[78]
Traffic monitoring	Carbon nano tubes	The actual moments of vehicle flow monitoring with a low false-alarm rate and a high detection rate in concrete pavement technology.	[15,79]
Structural health monitoring	Graphene nanoplate (GNP) and Silicone hydrophobic powder (SHP)	Continuous monitoring of cracking, temperature fluctuations, load distribution, and moisture intrusion.	[80]
Corrosion monitoring	Carbon nanofibers (CNFs) and recycled Milled carbon fibers (rMCFs)	It detects changes in electrical conductivity, pH levels, or moisture content, which are indicators of corrosion activity.	[81]
Nuclear fuel storage	Carbon and polymeric fibers	To measure flow rate, temperature gradients, pressure levels.	[82]
Electromagnetic shielding	Carbon fibers	It reflects electromagnetic radiation, minimizing their penetration into concrete.	[83]

14. Conclusion

Self-sensing concrete has developed from a theoretical notion to a workable technology with promising applications. Concrete's sensing capabilities have been greatly improved by the use of nanoparticles, especially carbon-based additions. The technique shows variety of applications,

including structural health monitoring for buildings and bridges, smart pavements, and nuclear power plant constructions. This adaptability highlights its potential to transform infrastructure management. Even yet, there are still a number of obstacles to overcome. These concerns include the necessity for standardized testing and assessment procedures, the integration of self-sensing systems into current infrastructures, and the long-term dependability and longevity of self-sensing materials. The creation of these standards is crucial for ensuring the dependability and longevity of smart concrete buildings and gives criteria to implement sensing concrete for widespread applications. Fabrication of sensing concrete is a time-consuming process due its prior dispersion of functional fillers in to the concrete. The dispersion of nano materials is problematic and tedious process it might be difficult to evenly distribute nanoparticles into concrete subsequently applications on a massive scale, standard methods like ultrasonication or the use of surfactants might not always be practicable or successful. Factors such as voltage, frequency, current flow, type of electrode and material of electrode, curing process, temperature influence the sensing characteristics it may results in data inaccuracy and it is challenging to record data under various environment conditions. The embedment of sensing concrete in the existing structures for monitoring damage detections became quite difficult. Cost of the functional fillers is high and cause economic barrier in cost effective projects yet the use of hybrid combinations of functional fillers enhances serviceability of the structures, concurrently replace and eliminates periodical maintenance of sensors minimizes the economic barrier as compared to that of conventional concrete. The integration of sensing concrete with robotic and Iot application could pave the way to avoid catastrophic failure and potential risk of the structures by improving efficiency and reducing human error paves the way for reducing the wastage of resources by increasing the life span of structures. The incorporation of sensing composites in concrete can be used to build more safer, more durable and more sustainable structures. Integrating data from different structures into larger urban management systems can enhance the resilience in earthquake-resistant structures, self-monitoring bridges, energy-efficient buildings or smart city infrastructures and general planning of cities. Future studies should concentrate on resolving these issues, enhancing the materials' sensitivity and accuracy, and investigating novel applications.

References

[1] Singh, N. B., Meenu Kalra, and S. K. Saxena. Nanoscience of cement and concrete. Materials today: proceedings. 2017; 4 (4): 5478-5487. https://doi.org/10.1016/j.matpr.2017.06.003

[2] Kerminen, Juho, et al. "Characterization of low-cost inkjet printed-photonic cured strain gauges for remote sensing and structural monitoring applications." Research on Engineering Structures and Materials 7.4 (2021): 647-660. https://doi.org/10.20944/preprints202110.0131.v1

[3] Emamjomeha, H., et al. "Influence of PVA and PP fibers addition on the durability and mechanical properties of engineered cementitious composites blended with silica fume and zeolite." Research on Engineering Structures and Materials 9.2 (2023): 457-473.

[4] Arasu, A. Naveen, et al. "Optimization of high performance concrete composites by using nano materials." Research on Engineering Structures and Materials 9.3 (2023): 843-859.

[5] Farrar, Charles R., and Keith Worden. "An introduction to structural health monitoring." Philosophical Transactions of the Royal Society A: Mathematical, Physical and Engineering Sciences 365.1851 (2007): 303-315. https://doi.org/10.1098/rsta.2006.1928

[6] Chen, H. P., and Y. Q. Ni. "Structural damage identification techniques." Structural health monitoring of large civil engineering structure (2018): 69-90. https://doi.org/10.1002/9781119166641.ch4

[7] Vaidya, Saiprasad, and Erez N. Allouche. Strain sensing of carbon fiber reinforced geopolymer concrete. Materials and structures. 2011; 44: 1467-1475. https://doi.org/10.1617/s11527-011-9711-3

[8] Cholker, Arvind Kumar, and Manzoor Ahmad Tantray. Micro carbon fiber-based concrete as a strain-damage sensing material. Materials Today: Proceedings. 2019; 19: 152-157. https://doi.org/10.1016/j.matpr.2019.06.629

[9] Zuo, Junqing, et al. Sensing properties of carbon nanotube-carbon fiber/cement nanocomposites. Journal of Testing and Evaluation. 2012; 40(5): 838-843. https://doi.org/10.1520/JTE20120092

[10] Demircilioglu, Erman, Egemen Teomete, and Osman E. Ozbulut. Strain sensitivity of steel-fiber-reinforced industrial smart concrete. Journal of Intelligent Material Systems and Structures. 2020; 31(1): 127-136. https://doi.org/10.1177/1045389X19888722

[11] Wang, Xueying, Abir Al-Tabbaa, and Stuart K. Haigh. A novel measurement system for self-sensing graphite-cement composites. MATEC Web of Conferences. EDP Sciences. 2023. https://doi.org/10.1051/matecconf/202337805002
[12] Han, B. G., B. Z. Han, and J. P. Ou. Experimental study on use of nickel powder-filled Portland cement-based composite for fabrication of piezoresistive sensors with high sensitivity. Sensors and Actuators A: Physical. 2009; 149(1): 51-55. https://doi.org/10.1016/j.sna.2008.10.001
[13] Gastaldini, A. L. G., et al. Influence of the use of rice husk ash on the electrical resistivity of concrete: a technical and economic feasibility study. Const. and Build. Mater. 2009; 23(11): 3411-3419. https://doi.org/10.1016/j.conbuildmat.2009.06.039
[14] Lim, Young-Chul, Takafumi Noguchi, and SungWoo Shin. Corrosion evaluation by estimating the surface resistivity of reinforcing bar. Journal of Advanced Concrete Technology. 2010; 8(2): 113-119. https://doi.org/10.3151/jact.8.113
[15] Gupta, Sumit, et al. In situ crack mapping of large-scale self-sensing concrete pavements using electrical resistance tomography. Cement and Concrete Composites. 2021; 122: 104154. https://doi.org/10.1016/j.cemconcomp.2021.104154
[16] Galao, Oscar, et al. Highly conductive carbon fiber reinforced concrete for icing prevention and curing. Materials. 2016: 9(4): 281. https://doi.org/10.3390/ma9040281
[17] Abdullah, Wrya, Azad Mohammed, and Avin Abdullah. Self-Sensing Concrete: A Brief Review. Proceedings of the ISER 211th International Conference. 2012.
[18] Laflamme, Simon, et al. "Large-scale surface strain gauge for health monitoring of civil structures." Nondestructive Characterization for Composite Materials, Aerospace Engineering, Civil Infrastructure, and Homeland Security 2012. Vol. 8347. SPIE, 2012. https://doi.org/10.1117/12.913187
[19] Zhu, Li, et al. "Development of a high-sensitivity wireless accelerometer for structural health monitoring." Sensors 18.1 (2018): 262. https://doi.org/10.3390/s18010262
[20] Wu, Tiange, et al. "Recent progress of fiber-optic sensors for the structural health monitoring of civil infrastructure." Sensors 20.16 (2020): 4517. https://doi.org/10.3390/s20164517
[21] Nhung, Nguyen Thi Cam, et al. "Development and application of linear variable differential transformer (LVDT) sensors for the structural health monitoring of an urban railway bridge in Vietnam." Engineering, Technology & Applied Science Research 13.5 (2023): 11622-11627. https://doi.org/10.48084/etasr.6192
[22] Tressler, James F., Sedat Alkoy, and Robert E. Newnham. "Piezoelectric sensors and sensor materials." Journal of electroceramics 2 (1998): 257-272. https://doi.org/10.1023/A:1009926623551
[23] Behnia, Arash, Hwa Kian Chai, and Tomoki Shiotani. "Advanced structural health monitoring of concrete structures with the aid of acoustic emission." Construction and building materials 65 (2014): 282-302. https://doi.org/10.1016/j.conbuildmat.2014.04.103
[24] Gasparin, Enrico, Gilles Santi, and Alain Nussbaumer. Eddy current crack monitoring system for structural health monitoring (SHM) applications. Proceedings of the 68th International Institute for Welding (IIW) Annual Assembly and International Conference. Helsinki, Finland. 2018.
[25] Wright, Ruishu F., et al. Corrosion sensors for structural health monitoring of oil and natural gas infrastructure: A review. Sensors. 2019; 19(18): 3964. https://doi.org/10.3390/s19183964
[26] Venugopalan, T., T. Sun, and K. T. V. Grattan. "Long period grating-based humidity sensor for potential structural health monitoring." Sensors and Actuators A: Physical 148.1 (2008): 57-62. https://doi.org/10.1016/j.sna.2008.07.015
[27] Park, Hyo Seon, et al. "A practical monitoring system for the structural safety of mega-trusses using wireless vibrating wire strain gauges." Sensors 13.12 (2013): 17346-17361. https://doi.org/10.3390/s131217346
[28] Merzbacher, C. I., Alan D. Kersey, and E. J. Friebele. "Fiber optic sensors in concrete structures: a review." Smart materials and structures 5.2 (1996): 196. https://doi.org/10.1088/0964-1726/5/2/008
[29] Chen, Pu-Woei, and Deborah DL Chung. "Carbon fiber reinforced concrete for smart structures capable of non-destructive flaw detection." Smart Materials and Structures 2.1 (1993): 22. https://doi.org/10.1088/0964-1726/2/1/004
[30] Han, Baoguo, Siqi Ding, and Xun Yu. "Intrinsic self-sensing concrete and structures: A review." Measurement 59 (2015): 110-128. https://doi.org/10.1016/j.measurement.2014.09.048
[31] Deng, Hanwen, and Hongliang Li. Assessment of self-sensing capability of carbon black engineered cementitious composites. Const. and Build. Mater. 2018; 173: 1-9. https://doi.org/10.1016/j.conbuildmat.2018.04.031
[32] Sevim, Ozer, Zhangfan Jiang, and Osman E. Ozbulut. Effects of graphene nanoplatelets type on self-sensing properties of cement mortar composites. Const. and Build. Mater. 2022; 359: 129488. https://doi.org/10.1016/j.conbuildmat.2022.129488

[33] Lee, Seon Yeol, Huy Viet Le, and Dong Joo Kim. Self-stress sensing smart concrete containing fine steel slag aggregates and steel fibers under high compressive stress. Const. and Build. Mater. 220, 2019: 149-160. https://doi.org/10.1016/j.conbuildmat.2019.05.197
[34] Xu, Feng, et al. The Mechanical and self-sensing performance of reactive powder cement concrete with nano-stainless steel powder. Coatings. 2023; 13(7): 1153. https://doi.org/10.3390/coatings13071153
[35] Qiu, Liangsheng, et al. "Self-sensing ultra-high performance concrete for in-situ monitoring." Sensors and Actuators A: Physical 331 (2021): 113049. https://doi.org/10.1016/j.sna.2021.113049
[36] Baeza, F. Javier, et al. "Effect of aspect ratio on strain sensing capacity of carbon fiber reinforced cement composites." Materials & Design 51 (2013): 1085-1094. https://doi.org/10.1016/j.matdes.2013.05.010
[37] Luo, Jian Lin, et al. "Self-sensing property of cementitious nanocomposites hybrid with nanophase carbon nanotube and carbon black." Advanced Materials Research 143 (2011): 644-647. https://doi.org/10.4028/www.scientific.net/AMR.143-144.644
[38] Lee, Seon Yeol, Huy Viet Le, and Dong Joo Kim. "Self-stress sensing smart concrete containing fine steel slag aggregates and steel fibers under high compressive stress." Construction and Building Materials 220 (2019): 149-160. https://doi.org/10.1016/j.conbuildmat.2019.05.197
[39] Mardani, Mahtab, et al. Piezoresistivity and mechanical properties of self-sensing CNT cementitious nanocomposites: Optimizing the effects of CNT dispersion and surfactants. Const. and Build. Mater. 2022. https://doi.org/10.1016/j.conbuildmat.2022.128127
[40] Mishra, Geetika. "Co-effect of carbon nanotube and nano-sized silica on dispersion and mechanical performance in cementitious system." Diamond and Related Materials 127 (2022): 109162. https://doi.org/10.1016/j.diamond.2022.109162
[41] Luo, Jianlin, Zhongdong Duan, and Hui Li. The influence of surfactants on the processing of multi-walled carbon nanotubes in reinforced cement matrix composites. physica status solidi (a). 2009; 2783-2790. https://doi.org/10.1002/pssa.200824310
[42] Tian, Zhuang, et al. "A state-of-the-art on self-sensing concrete: Materials, fabrication and properties." Composites Part B: Engineering 177 (2019): 107437. https://doi.org/10.1016/j.compositesb.2019.107437
[43] Lin, Vincent WJ, et al. "Mechanical and electrical characterization of self-sensing carbon black ECC." Nondestructive Characterization for Composite Materials, Aerospace Engineering, Civil Infrastructure, and Homeland Security 2011. Vol. 7983. SPIE, 2011. https://doi.org/10.1117/12.880178
[44] Ramachandran, Kousalya, et al. A review on principles, theories and materials for self sensing concrete for structural applications. Materials. 2022;15(11): 3831. https://doi.org/10.3390/ma15113831
[45] Gong, Shen, and Zheng H. Zhu. "On the mechanism of piezoresistivity of carbon nanotube polymer composites." Polymer 55.16 (2014): 4136-4149. https://doi.org/10.1016/j.polymer.2014.06.024
[46] Chung, D. D. L., and Xiang Xi. "Piezopermittivity for capacitance-based strain/stress sensing." Sensors and Actuators A: Physical 332 (2021): 113028. https://doi.org/10.1016/j.sna.2021.113028
[47] Xu, Runzhang, et al. "Computational design and property predictions for two-dimensional nanostructures." Materials Today 21.4 (2018): 391-418. https://doi.org/10.1016/j.mattod.2018.03.003
[48] Ding, Siqi, et al. Development of sensing concrete: Principles, properties and its applications. Journal of Applied Physics. 2019; 126(24). https://doi.org/10.1063/1.5128242
[49] Gupta, Sumit, Jesus G. Gonzalez, and Kenneth J. Loh. Self-sensing concrete enabled by nano-engineered cement-aggregate interfaces. Structural Health Monitoring. 2017; 16(3): 309-323. https://doi.org/10.1177/1475921716643867
[50] Madhavi, T. Ch, and S. Annamalai. Electrical conductivity of concrete. ARPN J. Eng. Appl. Sci. 2016; 11(9): 5979-5982.
[51] Vimarsha B.R, T Soumya, Rohit Gainole. Intrinsic Self Sensing Concrete. International Journal of Research in Engineering and Technology. 2018; 7(12).
[52] D'Alessandro, Antonella, et al. Self-sensing and thermal energy experimental characterization of multifunctional cement-matrix composites with carbon nano-inclusions. Behavior and Mechanics of Multifunctional Materials and Composites. 2016; 9800. SPIE, 2016. https://doi.org/10.1117/12.2218680
[53] Hansson, Inge LH, and Carolyn M. Hansson. Ion-conduction in cement-based materials. Cement and Concrete Research (1985); 15(2): 201-212. https://doi.org/10.1016/0008-8846(85)90031-6
[54] Last, B. J., and D. J. Thouless. Percolation theory and electrical conductivity. Physical review letters 27(25) (1971); 27(25): 1719. https://doi.org/10.1103/PhysRevLett.27.1719
[55] Mazaheri, M., J. Payandehpeyman, and S. Jamasb. Modeling of effective electrical conductivity and percolation behavior in conductive-polymer nanocomposites reinforced with spherical carbon black. Applied Composite Materials. 2022; 1-16.
[56] Chung, D. D. L. Self-sensing concrete: from resistance-based sensing to capacitance-based sensing. International Journal of Smart and Nano Materials. 2021; 12(1): 1-19. https://doi.org/10.1080/19475411.2020.1843560

[57] Elseady, Amir AE, et al. Piezoresistivity and AC impedance spectroscopy of cement-based sensors: basic concepts, interpretation, and perspective. Materials. 2023; 16(2): 768. https://doi.org/10.3390/ma16020768
[58] Ubertini, Filippo, and Antonella D'Alessandro. "Concrete with self-sensing properties." Eco-Efficient Repair and Rehabilitation of Concrete Infrastructures. Woodhead Publishing, 2018. 501-530. https://doi.org/10.1016/B978-0-08-102181-1.00018-6
[59] Armoosh, Salam R., and Meral Oltulu. Effect of different micro metal powders on the electrical resistivity of cementitious composites. IOP Conference Series: Materials Science and Engineering. IOP Publishing, 2019; 471(3). https://doi.org/10.1088/1757-899X/471/3/032075
[60] Ackermann, Kay Christian. Self-sensing concrete for structural health monitoring of smart infrastructures. University of Rhode Island, 2018.
[61] Mao Qizhao, et al. "Resistance changement of compression sensible cement speciment under different stresses." Journal of Wuhan University of Technology: Materials Science English Edition 11.3 (1996): 41-45.
[62] Chen, Bing, Juanyu Liu, and Keru Wu. "Electrical responses of carbon fiber reinforced cementitious composites to monotonic and cyclic loading." Cement and concrete research 35.11 (2005): 2183-2191. https://doi.org/10.1016/j.cemconres.2005.02.004
[63] Li, Wengui, et al. Conductivity and piezoresistivity of nano-carbon black (NCB) enhanced functional cement-based sensors using polypropylene fibres. Materials Letters. 2020; 270: 127736. https://doi.org/10.1016/j.matlet.2020.127736
[64] Pinto, Irvin, et al. Smart Concrete for Enhanced Nondestructive Evaluation. ASNT Annual Conference. 2017.
[65] Jasim, Mustafa Hamid, et al. "Mechanical, Durability and Electrical Properties of Steel Fibers Reinforced Concrete." Advances in Science and Technology. Research Journal 18.7 (2024): 163-175. https://doi.org/10.12913/22998624/193196
[66] Palankar, Nitendra, AU Ravi Shankar, and B. M. Mithun. "Durability studies on eco-friendly concrete mixes incorporating steel slag as coarse aggregates." Journal of cleaner production 129 (2016): 437-448. https://doi.org/10.1016/j.jclepro.2016.04.033
[67] Cholker, Arvind Kumar, and Manzoor Ahmad Tantray. "Mechanical and durability properties of self-compacting concrete reinforced with carbon fibers." Int J Recent Technol Eng 7.6 (2019): 1738-1743.
[68] Chukka, Naga Dheeraj Kumar Reddy, et al. "Experimental testing on mechanical, durability, and adsorption dispersion properties of concrete with multiwalled carbon nanotubes and silica fumes." Adsorption Science & Technology 2022 (2022): 4347753. https://doi.org/10.1155/2022/4347753
[69] Devi, S. C., and R. A. Khan. "Effect of graphene oxide on mechanical and durability performance of concrete." Journal of Building Engineering 27 (2020): 101007. https://doi.org/10.1016/j.jobe.2019.101007
[70] Jiang, Zhangfan, Ozer Sevim, and Osman E. Ozbulut. "Mechanical properties of graphene nanoplatelets-reinforced concrete prepared with different dispersion techniques." Construction and Building Materials 303 (2021): 124472. https://doi.org/10.1016/j.conbuildmat.2021.124472
[71] Namdev, Anurag, Amit Telang, and Rajesh Purohit. "Water absorption and thickness swelling behaviour of graphene nanoplatelets reinforced epoxy composites." International Journal of Advanced Technology and Engineering Exploration 10.98 (2023): 119. https://doi.org/10.19101/IJATEE.2021.874756
[72] Han, Baoguo, et al. "Self-sensing concrete." Smart and Multifunctional Concrete Toward Sustainable Infrastructures (2017): 81-116. https://doi.org/10.1007/978-981-10-4349-9_6
[73] Downey, Austin, et al. "Continuous and embedded solutions for SHM of concrete structures using changing electrical potential in self-sensing cement-based composites." Nondestructive Characterization and Monitoring of Advanced Materials, Aerospace, and Civil Infrastructure 2017. Vol. 10169. SPIE, 2017. https://doi.org/10.1117/12.2261427
[74] Wang, Wentao, et al. "Investigation of water ingress into uncracked and cracked cement-based materials using electrical capacitance volume tomography." Materials & Design 220 (2022): 110877. https://doi.org/10.1016/j.matdes.2022.110877
[75] Díaz, B., et al. "Analysis of the microstructure of carbon fibre reinforced cement pastes by impedance spectroscopy." Construction and Building Materials 243 (2020): 118207. https://doi.org/10.1016/j.conbuildmat.2020.118207
[76] Wang, Xinyue, et al. "Intrinsic self-sensing concrete to energize infrastructure intelligence and resilience: A review." Journal of Infrastructure Intelligence and Resilience 3.2 (2024): 100094. https://doi.org/10.1016/j.iintel.2024.100094
[77] Gürer, Cahit, Uğur Fidan, and Burak Enis Korkmaz. Investigation of using conductive asphalt concrete with carbon fiber additives in intelligent anti-icing systems. International Journal of Pavement Engineering. 2023; 24(1): 2077941. https://doi.org/10.1080/10298436.2022.2077941

[78] García-Macías, Enrique, and Filippo Ubertini. Earthquake-induced damage detection and localization in masonry structures using smart bricks and Kriging strain reconstruction: A numerical study. Earthquake Engineering & Structural Dynamics. 2019; 48(5): 548-569. https://doi.org/10.1002/eqe.3148
[79] Han, Baoguo, et al. Integration and road tests of a self-sensing CNT concrete pavement system for traffic detection. Smart Materials and Structures.2012; 22(1): 015020. https://doi.org/10.1088/0964-1726/22/1/015020
[80] Dong, Wenkui, et al. Multifunctional cementitious composites with integrated self-sensing and hydrophobic capacities toward smart structural health monitoring. Cement and Concrete Composites. 2021; 118: 103962. https://doi.org/10.1016/j.cemconcomp.2021.103962
[81] Taheri, Shima, et al. Smart self-sensing concrete: the use of multiscale carbon fillers. Journal of Materials Science. 2022; 1-16.
[82] Li, Mo, et al. Concrete materials with ultra-high damage resistance and self-sensing capacity for extended nuclear fuel storage systems. No. 12-3545. Battelle Energy Alliance, LLC, Idaho Falls, ID (United States). 2017. https://doi.org/10.2172/1346142
[83] Chung, D. D. L. Carbon materials for structural self-sensing, electromagnetic shielding and thermal interfacing. Carbon (2012); 50(9): 3342-3353. https://doi.org/10.1016/j.carbon.2012.01.031

Research on Engineering Structures & Materials
www.jresm.org
Research Group

Research Article

Analysis of the geotechnical and mineralogical characteristics of the Settat-Khouribga shale clay for potential civil engineering applications

Ayoub Souileh[1,*a], Achraf Mabrouk[2,b], Latifa Ouadif[1,c], Driss El Hachmi[3,d]

[1]*L3GIE, Mohammadia Engineering School, Mohammed V University in Rabat, Morocco*
[2]*LAFH, Faculty of Sciences and Techniques, Hassan 1st University, BP 577, 26000, Settat, Morocco*
[3]*MME, Faculty of Science, Mohammed V University in Rabat, Morocco*

Article Info

Article history:

Received 24 Aug 2024
Accepted 17 Oct 2024

Keywords:

Clay shale;
Civil engineering;
Construction materials;
Geotechnical engineering;
Sustainability

Abstract

This study provides a comprehensive analysis of clay shale from the Settat-Khouribga region, assessing its suitability for civil engineering applications through various tests. Grain size distribution, hardness (MDE, LA), and plasticity (ES 0/5, IP, VB) tests, along with consistency index evaluations following the "CSTCN" catalog, were conducted. X-ray diffraction (XRD) and mineralogical analyses identified key components such as quartz, calcite, feldspar, and iron oxide, with quartz being predominant. The results demonstrated that the shale clay is well-suited for construction purposes, exhibiting favorable grain size distribution and high resistance to wear and abrasion, which are crucial for material durability. Its low plasticity further indicates good mechanical stability in construction projects. SEM analysis revealed a microstructure dominated by quartz grains, montmorillonite, and illite lamellae, and the presence of micro fissures and pores suggests both strengths and potential durability concerns. Advanced statistical analyses, including Principal Component Analysis (PCA) and regression models, were employed to assess geotechnical properties. The study confirms the shale's compliance with construction standards, highlighting its potential for sustainable building practices. These findings contribute significantly to the field of geotechnical engineering, emphasizing the material's suitability for construction and its broader societal implications.

1. Introduction

Despite its abundance, the use of Settat-Khouribga shale clay in construction has been limited by a lack of detailed mineralogical and geotechnical characterization. This study aims to bridge that gap by providing a comprehensive analysis of the material, which is crucial for its application in sustainable construction. The geological formations in the Settat-Khouribga region, rich in shale clay, are of great importance due to the presence of montmorillonitic clay minerals that impart unique properties to these rocks. A detailed geological study of this region reveals that these formations result from Cretaceous sedimentary deposits, contributing to increased mechanical stability.

The Settat-Khouribga shale belongs mainly to the Western Meseta of Morocco [1] which is of Upper Cretaceous age. This formation comprises clayey and marly shales and interbedded layers of limestones and dolomites [2].

*Corresponding author: ayoub.souileh@research.emi.ac.ma
[a]orcid.org/0009-0001-7754-8109; [b]orcid.org/0000-0002-4146-8211; [c]orcid.org/0000-0002-4613-1124; [d]orcid.org/0000-0002-3183-3385
DOI: http://dx.doi.org/10.17515/resm2024.408ma0824rs

In addition, the Settat-Khouribga region has abundant shale clay, making it a promising option for use in construction. So far, studies on marginal aggregates have mainly focused on shale aggregates and shale-derived materials[3]. This report presents the results of a grain size analysis and specifications of a shale-clay material, as well as its characteristics such as hardness (MDE, LA), plasticity, and cleanliness (ES 0/5, IP, VB).[4] [5] Additionally, the consistency index test by the "CSTCN" catalog and X-ray diffraction analysis was conducted on samples collected from the study area [6].

To further understand the potential of Settat-Khouribga shale clay for construction, we conducted a detailed microstructural analysis using Scanning Electron Microscopy (SEM). The SEM images revealed three critical microstructural features: granular structures composed primarily of quartz grains, lamellar structures of clay minerals like montmorillonite and illite, and the presence of micro fissures and pores. These features are crucial in evaluating the material's suitability for civil engineering applications, particularly in terms of mechanical strength and long-term durability. Previous studies have demonstrated the potential of shale clay in various civil engineering applications. For instance, research by [7] highlighted its use in road base construction due to its favorable mechanical properties. Similarly, [8] explored the feasibility of using shale clay in building foundations, where its mineral composition provided significant advantages in terms of compressive strength

2. Materials and Methods

2.1 Study Area Description

The Settat-Khouribga region, located in the northwestern part of Morocco,[9] stands out for its diverse geology, situated in the eastern portion of the Moroccan Meseta sedimentary basin[10]. It is primarily composed of sedimentary formations from the Upper Cretaceous. This region is renowned for its extensive deposits of shale clay and marl (Fig. 1).[11]

Fig. 1. Clay Shale from the Settat-Khouribga area

2.2 Methodological Approach

After conducting field reconnaissance and using the geological map as a reference, we delimited the study area where shale clay is present. Subsequently, samples of shale clay were collected from different sites distributed within this study area (Fig. 2) [12]. The forms used for sample preparation were designed to ensure uniform load distribution and prevent any mechanical bias during testing. Each form was verified before testing to ensure compliance with the dimensions standardized by ASTM

guidelines. Our methodology (Fig. 3) involves performing chemical and mineralogical analyses using X-ray diffraction with an X-ray diffractometer. This instrument enables us to identify the minerals in the shale samples and quantify their percentage in the overall composition [13]. Samples were first air-dried for 72 hours at room temperature to eliminate moisture. Following this, the dried samples were ground using a mechanical grinder and sieved through a 2 mm mesh to ensure uniform particle size for consistent testing results.

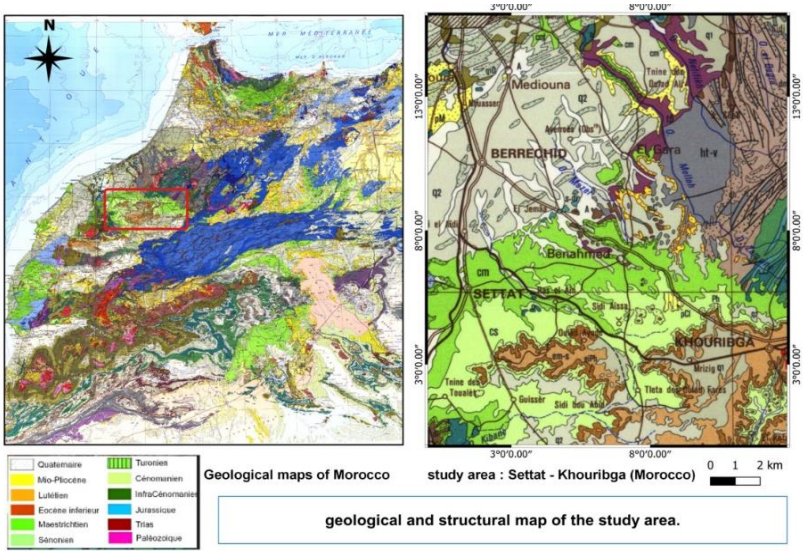

Fig. 2. Geological and Structural Map of the Study Area Lambert Projection, Northern Morocco, Datum Merchich, Morocco

The samples were dried at 105°C for 24 hours before being ground to a particle size of 63 µm. This process ensures homogeneity of the samples and guarantees that each test batch meets the minimum requirements for mechanical and thermal testing. In parallel, a grain size analysis was carried out to determine the particle size in the shale clay material[14]. Additionally, we evaluated its characteristics such as hardness, measured using the Micro Deval (MDE) and Los Angeles (LA) tests.[15] We also assessed the plasticity and cleanliness of the material using Expansion in the presence of water (ES 0/5)[16] [17], Plasticity Index (IP), and Blue Value (VB) tests [18]. All testing methods followed the ASTM standards, specifically ASTM D422 for particle-size analysis, [19]ASTM C131[20] for resistance to abrasion using the Los Angeles machine, and ASTM D4318 [21] for determining the liquid limit, plastic limit, and plasticity index. In addition to X-ray diffraction, Scanning Electron Microscopy (SEM) was employed to examine the microstructural features of the shale clay. Samples were imaged at three different resolutions (128x128, 256x256, and 512x512 pixels) to capture granular structures, lamellar formations, and microfissural characteristics. These images provided detailed insights into the material's internal structure, aiding in the assessment of its mechanical and durability properties [22].

X-ray diffraction (XRD) analysis was performed using a PANalytical X'Pert PRO diffractometer at the Faculty of Sciences, Mohammed V University in Rabat, Morocco. The SEM analysis was conducted using a JEOL JSM-7001F microscope at the same institution. Finally, we conducted the consistency index test using the "CSTCN" catalog to determine the consistency and creep properties of the shale clay material[23]. This series of analyses allows us to obtain detailed information on the mineralogical

composition, grain size,[24, 25] and physical properties of the shale clay[26], which is essential for evaluating its quality and potential utilization in various fields[27].

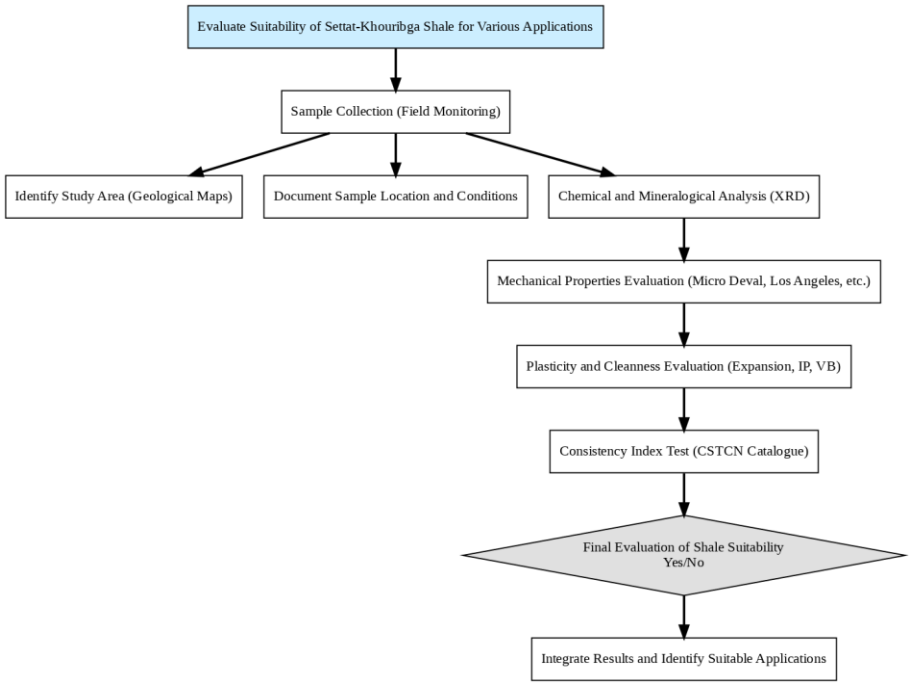

Fig. 3. Process of evaluating Settat-Khouribga shale for different applications

(a) (b) (c)

Fig. 4. The sequential analysis of shale clay samples from the Settat-Khouribga region, Morocco; (a) the raw shale clay sample as it was collected from the field, (b) the shale sample after undergoing granulometric analysis, (c) the fine particles that were isolated from the shale sample during the granulometric analysis

3. Results

3.1 Specifications of the Clay Shale According to the "CSTCN" Catalog

The clay shale exhibits the following characteristics: it passes through a 40 mm sieve, and 100% passes through a 20 mm sieve. Its hardness ranges from 60 to 90, indicating

high resistance to wear and abrasion. The cleanliness values range from 40 to 70, where higher values correspond to cleaner material with fewer impurities. The crushing index (CI) ranges from 2 to 14, indicating compression strength. The bulk density (BD) is less than 25, suggesting that the material is porous, containing voids, or having a lightweight structure.[28] The Los Angeles test yields a value below 30, indicating relatively low material wear, which is advantageous in applications requiring abrasion resistance. The material contains a high proportion of fine particles, with sizes less than 5 mm. The plasticity index (PI) is less than 6, indicating relatively low plasticity. The blue value is below 1.5, suggesting good resistance to thermal spalling. Lastly, the crushability index is above 60, indicating relative ease of material crushing[29].

Table 1. Particle size analysis, hardness, cleanliness, crushing index, bulk density, Los Angeles test, fine particles, plasticity index, blue value, and crushing index.

Granulometry					Hardness		Cleanliness			IC
% passing through a sieve of (mm)					MDE	L.A	ES 0/5	IP	VB	IC
40	20	10	2	0,08						
100	60 to 90	40 to 70	20 to 48	2 to 14	< 25	<30	> 30	< 6	<1.5	> 60

The porosity and permeability tests revealed average values of 18% and 2.5 x 10^{-4} cm/s, respectively. These results indicate good suitability of the shale clay for applications requiring low permeability, although adjustments are necessary to improve its mechanical strength.

3.2 Characteristics of the Clay Shale

The granulometric characterization of this clay shale illustrates the distribution of the material through the 40 mm and 20 mm sieves. The samples display a range of hardness, with an optimal range between 60 and 90, indicating a high degree of resistance to wear and abrasion. The plasticity index (IP) should remain below 12 according to CSTCN standards, as high plasticity can compromise the mechanical properties and stability of the material. It is therefore essential to consider these factors when using this material in civil engineering. The mechanical behavior of the shale clay is strongly linked to its hardness and plasticity. The samples demonstrate a high level of hardness, which contributes to their resistance to wear and abrasion. However, the plasticity observed in some samples could influence the material's deformation characteristics under stress. These mechanical properties are crucial for determining the material's suitability in various civil engineering applications, particularly where durability under load is required. Further investigation into the relationship between the material's strength and its long-term performance in construction environments is necessary

Table 2. Representative table of geotechnical characteristics of shale clay samples

Sample number	Granulometry					Hardness		Plasticity
	% passing through sieve size (mm)					MDE	L.A	IP
	40	20	10	2	0,08	< 25	<30	< 12
	100	60 to 90	40 to 70	20 to 48	2 to 14	17	24	18.00

S1	100	70	50	42	35	17	24	18.00
S2	100	66	62	40	34	18	25	19.50
S3	100	71	63	41	36	17	23	18.50
S4	100	68	49	45	32	18	24	18.00
S5	100	65	56	43	35	19	22	19.00
S6	100	67	50	44	36	17	25	20.00

Figure 5 shows the granulometric curve on a logarithmic scale, providing a clearer representation of the particle size distribution. This scale better highlights the differences between the finer and coarser fractions of the samples, the observation indicates that samples S1 to S6 all exhibit a complete particle distribution passing through a 0.08 mm sieve. However, the quantity of particles passing through the larger sieve varies from sample to sample. Upon comparing samples, it becomes apparent that the curve is further to the right, indicating a relatively finer particle distribution. Additionally, some samples appear to have a finer distribution, while others exhibit a slightly coarser distribution[30]

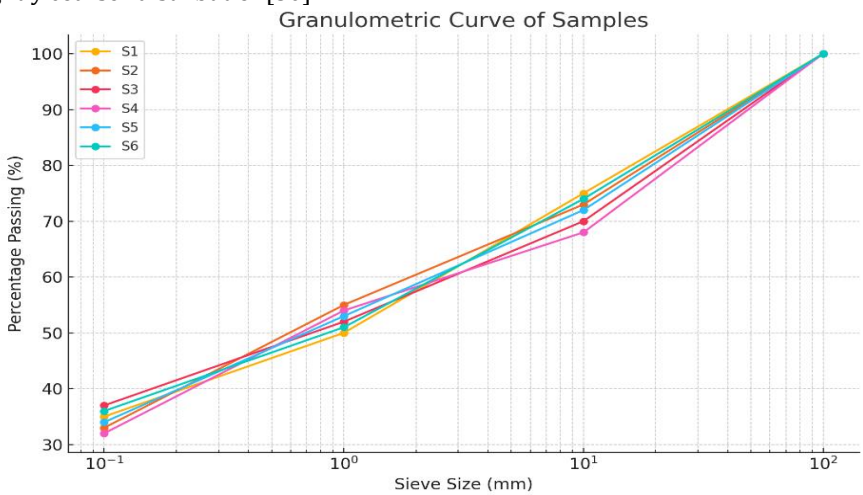

Fig. 5. Granulometric curve of samples

3.3 Mineralogical Composition

Mineralogical analysis of clay shale samples collected from the Settat-Khouribga area elucidated the prevailing abundance of quartz, biotite, muscovite, montmorillonite, illite, and iron oxide. The tabulated data exhibits the relative distribution of these minerals in six distinct samples (S1 to S6), wherein marginal variations in proportions provide insights into the distinct mineralogical composition characterizing each sample.

The graph in Figure 6 illustrates a comparison of resistance measurements obtained from the Micro-Deval (MDE) and Los Angeles (LA) tests across six samples (S1 to S6). The ANOVA p-value of 9.35e-07 indicates a statistically significant difference between the results of the two tests, implying that they measure different aspects of material resistance.

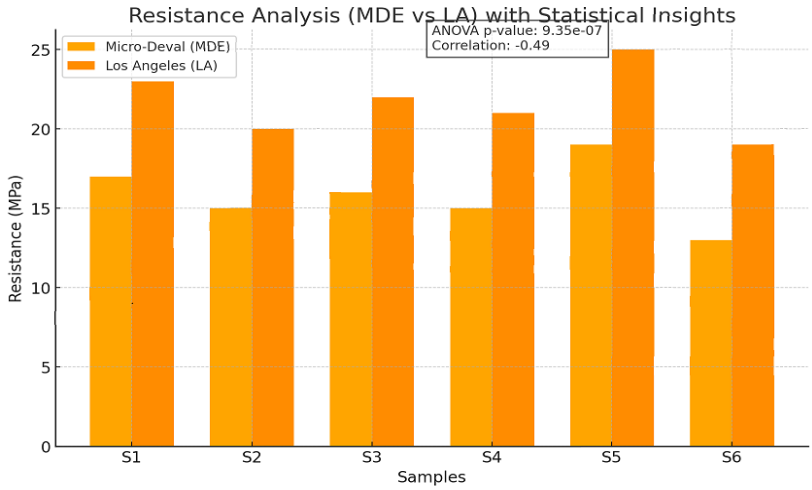

Fig. 6. Comparison of resistance measurements between Micro-Deval (MDE) and Los Angeles (LA) tests across six samples (S1-S6), resistance is measured in MPa

The negative correlation of -0.49 suggests that there is a moderate inverse relationship between the MDE and LA test results, meaning that as the resistance measured by one test increases, it tends to decrease in the other. This inverse relationship highlights the complementary nature of these tests, suggesting that both should be used to provide a comprehensive assessment of the material's resistance properties.

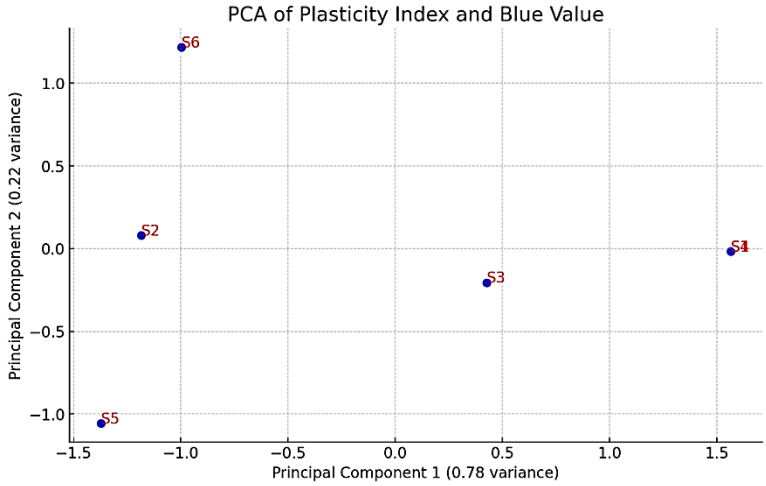

Fig. 7. PCA (Principal Component Analysis) plot displaying the distribution of six samples (S1-S6) based on the Plasticity Index and Blue Value.

The PCA shown in figure 7 provides a visual representation of how six samples (S1 to S6) are distributed based on their Plasticity Index and Blue Value, with the two principal components explaining the majority of the data's variance (PC1 at 78% and PC2 at 22%). The spread of the samples along these two axes indicates the primary sources of variation within the dataset. Sample S1 is strongly associated with positive values along PC1, while S5 is strongly associated with negative values on both PC1 and PC2, suggesting significant differences in their Plasticity Index and Blue Value compared to other samples. Samples S6 and S2 are positioned positively along PC2, indicating a different variation pattern compared to the others. The PCA helps in

understanding the underlying patterns in the dataset, suggesting that the majority of the variance is captured along PC1, with secondary variation captured by PC2. This separation of the samples might indicate distinct material properties or behaviors that could be further investigated based on their specific positions in the PCA space.

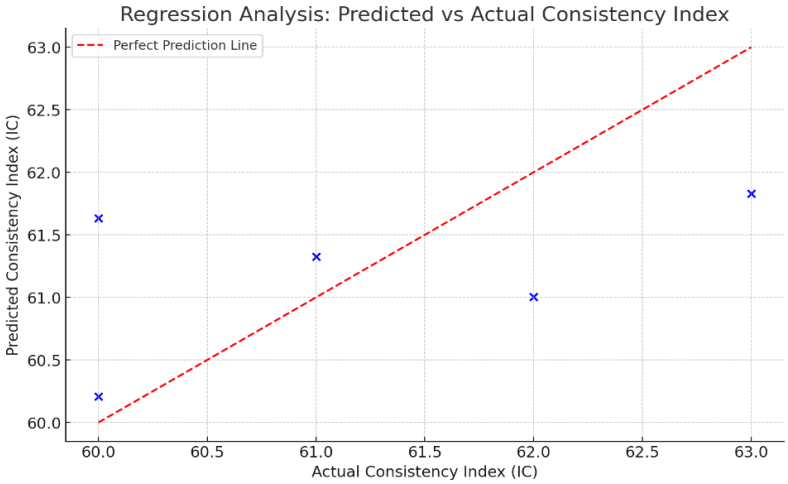

Fig. 8. Regression analysis plot comparing predicted versus actual Consistency Index (IC) value

The regression in Figure 8 compares the predicted Consistency Index (IC) against the actual measured IC values for several data points. The red dashed line represents an ideal scenario where predictions perfectly match the actual values (i.e., the predicted value equals the actual value for each point). The blue 'X' markers indicate the actual data points. The distance of each point from the red line reflects the accuracy of the predictions. Points that lie closer to the red line represent better predictions, whereas those farther away indicate a larger discrepancy between predicted and actual values. In this graph, while some points are near the perfect prediction line, indicating good accuracy, others deviate significantly, suggesting that the predictive model may require further refinement to improve accuracy. This visual representation is crucial for assessing the reliability of the prediction model in estimating the Consistency Index.

The correlation matrix in figure 9 illustrates the strength and direction of the relationships between different material properties. Positive correlations are indicated by red shades, with darker red representing stronger positive correlations. Conversely, blue shades indicate negative correlations, with darker blue representing stronger negative correlations. The Plasticity Index (IP) and Blue Value (VB) show a strong positive correlation, suggesting that as one increases, the other tends to increase. Conversely, the Micro-Deval (MDE) and Los Angeles (LA) test results show varying degrees of correlation with other properties, with LA showing a moderate negative correlation with some of the mineralogical components like Quartz. Both positive and negative correlations indicate complex interdependencies among the material properties, suggesting that changes in one property could have significant effects on others. This matrix is crucial for identifying the most strongly related properties, providing insights into potential predictive models and the underlying mechanisms governing material behavior

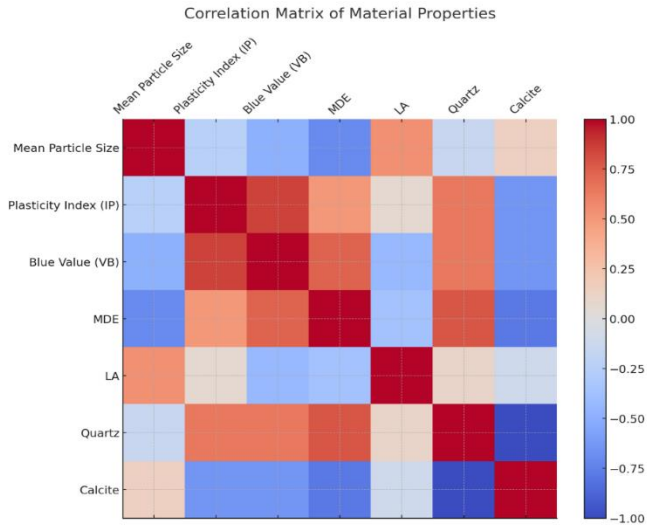

Fig. 9. Correlation matrix displaying the relationships between various material properties, including Mean Particle Size, Plasticity Index (IP), Blue Value (VB), Micro-Deval (MDE), Los Angeles (LA), Quartz, and Calcite

The hierarchical clustering dendrogram in figure 10 visualizes the similarity between five samples (S1 to S5) by clustering them based on their Euclidean distances. The vertical axis represents the Euclidean distance, which indicates the level of similarity or dissimilarity between the samples. Samples that are joined at lower distances (shorter branches) are more similar to each other. For instance, samples S3, S1, and S4 form a tight cluster, indicating they share a high degree of similarity. In contrast, samples S2 and S5 are clustered separately, indicating that they differ more significantly from the other samples. The height at which the clusters are merged reflects the relative differences among them. This dendrogram provides a clear visual representation of the hierarchical relationships among the samples, useful for identifying groups of similar samples and understanding the underlying patterns in the data.

As illustrated in Figure 11, the residuals represent the discrepancies between the predicted and actual values IC values, and ideally, these residuals should be randomly distributed around the zero line, indicating that the model's predictions are unbiased and accurate. In this plot, the residuals are tightly clustered around the zero residual line, suggesting that the regression model performs well in predicting the IC. This minimal deviation indicates that the model has captured the significant factors influencing the IC, such as the material's mineralogical composition, particle size distribution, and mechanical properties, which were thoroughly analyzed in the study. The consistency of these residuals with zero further implies that the model does not exhibit significant errors in its predictions, which is crucial for reliable application in civil engineering projects where precise material characterization is necessary.

Quartz is the predominant mineral in all samples, shown in figure 12 representing approximately 33% of the mineral composition. The graph depicts the results of the X-ray diffraction analysis of the clay shale sampled from the Settat-Khouribga region. Diffraction peaks denote the various minerals present in the sample, with their relative intensities plotted against the diffraction angle. Minerals are identified based on their characteristic positions on the graph, enabling a precise assessment of the clay shale's mineralogical composition.

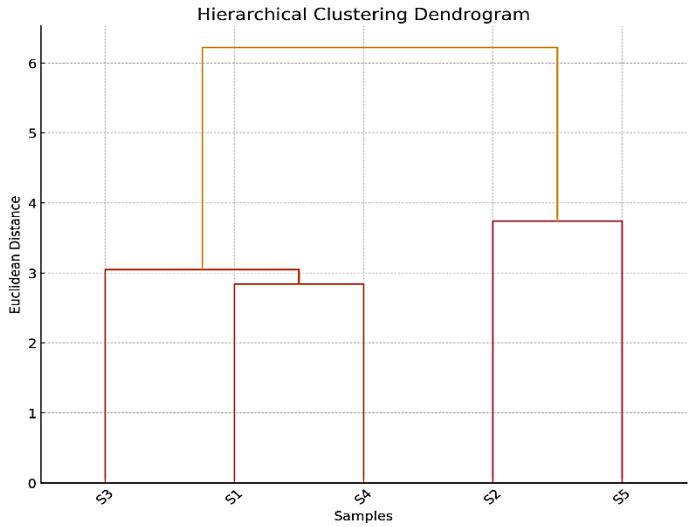

Fig. 10. Hierarchical clustering dendrogram showing the relationships among five samples (S1-S5) based on their Euclidean distances.

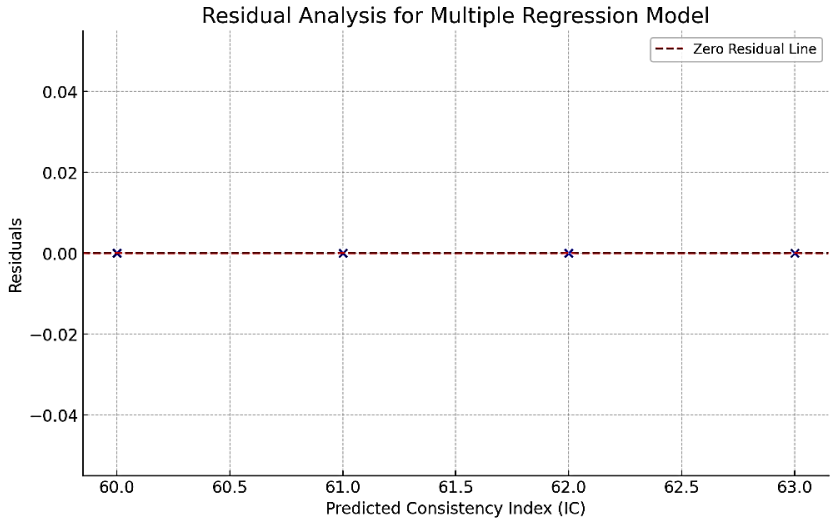

Fig.11. Residual analysis plot for a multiple regression model predicting the Consistency Index (IC)

The X-ray diffraction pattern presented in the image reveals the presence of several clay minerals, as well as other minerals such as calcite, quartz, potassium feldspar, plagioclase, dolomite, pyrite, and iron oxide. The most intense peaks in the diffraction pattern correspond to the clay minerals. The peak at approximately 7.1° 2θ is characteristic of kaolinite, while the peak at approximately 14.8° 2θ is characteristic of smectite. Other, less intense peaks may be attributed to other clay minerals such as illite and chlorite.

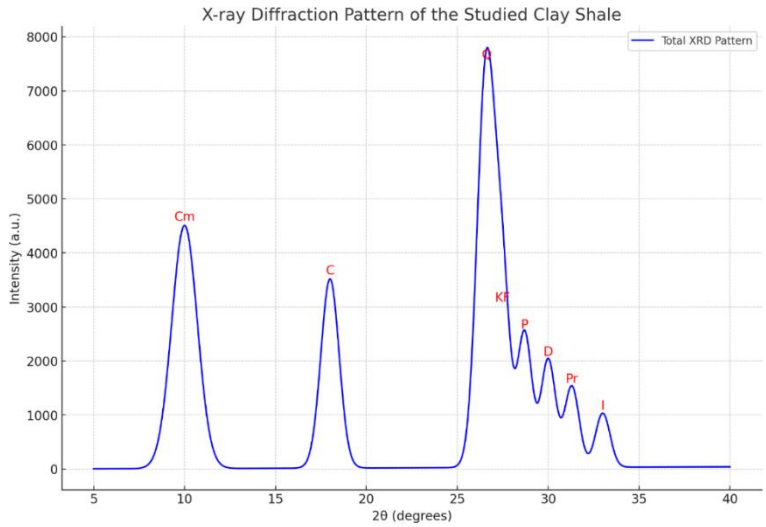

Fig. 12 X-ray diffraction pattern of the studied clay shale.

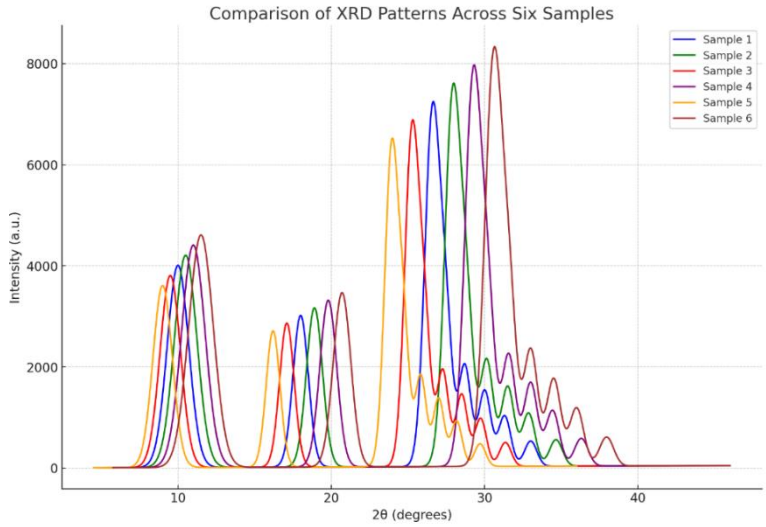

Fig. 13. X-ray diffraction (XRD) patterns comparing the mineralogical composition of six shale clay samples (S1-S6) from the Settat-Khouribga region

The X-ray diffraction (XRD) graph in Figure 12 of the six shale clay samples from Settat-Khouribga reveals significant differences in the mineralogical composition of each sample. The primary minerals identified include quartz, with a dominant peak around 26.6° 2θ, particularly intense in Sample 6, indicating a high concentration. Calcite, identifiable by a peak around 29.4° 2θ, is also present with varying intensities, with Sample 3 showing a relatively higher concentration. Feldspars, manifested by peaks around 27.5° and 30.5° 2θ, are present in all samples, with variations suggesting differences in the content of potassium feldspar and plagioclase. Montmorillonite, with a peak around 5.7° 2θ, is detected primarily in Samples 1 and 2, which could influence the material's plasticity. Illite, visible around 8.8° 2θ, is particularly present in Samples 4 and 5. The variations in peak intensity between samples highlight the mineralogical

diversity of the shale, with a notably high quartz concentration in Sample 6, potentially making it more suitable for applications requiring greater durability. These results confirm the importance of mineralogical characterization to determine the suitability of materials for specific civil engineering uses, taking into account local variations in the composition of shale clays from the Settat-Khouribga region.

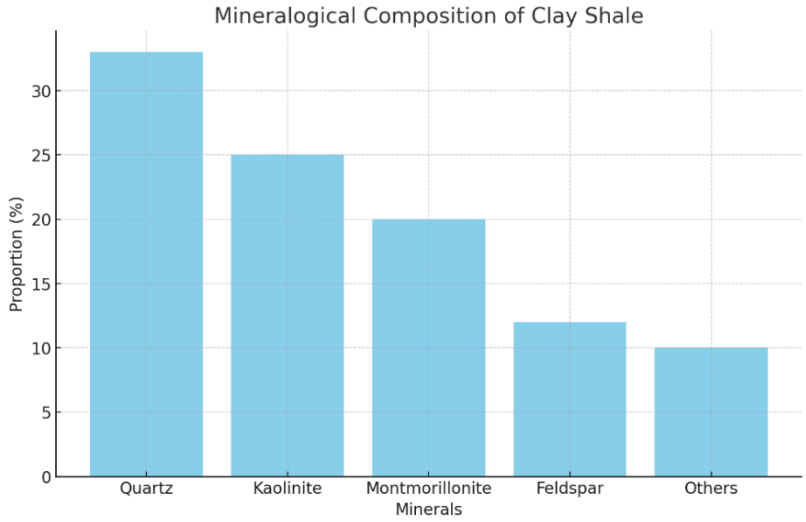

Fig. 14. Mineralogical composition of clay shale study

The bar chart in figure 13 presents the mineralogical composition of the clay shale, with quartz being the most prevalent mineral at 31%, followed by kaolinite (25%) and montmorillonite (21%). Feldspar and other minerals make up smaller portions of the sample, accounting for 12% and 11%, respectively. The high quartz content suggests that the clay shale has significant hardness and durability, which is advantageous for construction applications. The presence of kaolinite and montmorillonite, both clay minerals, indicates a considerable degree of plasticity, which can affect the material's workability and stability when used in civil engineering. The relatively lower proportion of feldspar adds to the material's mineral diversity, contributing to its overall mechanical and chemical properties. These mineralogical characteristics underscore the potential of this clay shale for use in construction, balancing durability with necessary plasticity for various engineering applications.

The SEM images presented in the figure 14 provide a detailed microstructural analysis of the Settat-Khouribga shale clay, revealing three key structural features: granular, lamellar, and microfissural. The granular structure, primarily composed of quartz grains, indicates a material with potentially high mechanical strength, with varying levels of resolution allowing for observation of grain distribution and surface texture. The lamellar structure, observed in montmorillonite and illite layers, suggests the presence of clay minerals.

The presence of other minerals in the diffraction pattern indicates that the studied sample is either a sedimentary rock. Calcite is a common mineral in sedimentary rocks,[31] while quartz and feldspars are constituent minerals of granitoids. Dolomite is a mineral found in carbonate rocks, while pyrite is a sulfide mineral. Iron oxide is a mineral present in many types of rocks.[32]. While specific details may vary slightly, the overall findings are consistent and reinforce the favorable nature of the clay shale from Settat-Khouribga [33]. On the other hand, comparing the results of the three types

of shale - clay shale, satin shale, and spotted shale found by [34], the following differences can be observed in Table 3.

Table 3. Physical characteristics of the three studied shales

Sample	Modified Proctor CBR Index (%)	Impact resistance	Wear resistance	W (%)	γ (kN/m³)
Clay shale	21,0	7,80	5	13	75,8
Satin shale	22,1	6,50	6	25	29,2
Speckled shale	22,6	7,10	10	38	35,2

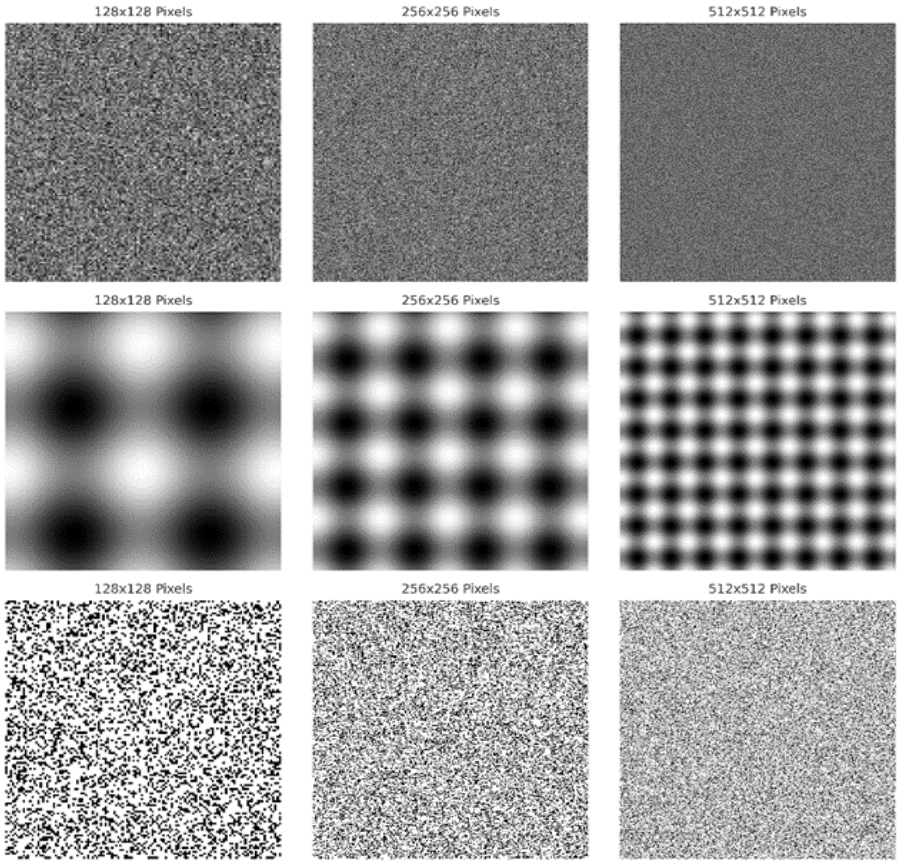

Fig. 15. Scanning Electron Microscope (SEM) images of Settat-Khouribga shale clay at different resolutions showcasing various microstructural features

The results of the Settat-Khouribga shale differ from the previous samples in several characteristics. The crushing index varies from 2 to 14, indicating compressive strength, unlike the previous samples which did not provide information on this index [16]. Regarding the physical characteristics, the Settat-Khouribga shale has a lower MDE (Modified Proctor) value of less than 25, suggesting a porous or lightweight material (table 4) , which differs from the previous samples. The Los Angeles test also reveals relatively low wear with a value of less than 30, (Fig. 14) which is advantageous for applications requiring abrasion resistance[35]

Table 4. Proctor characteristics, CBR, Los Angeles, and micro-Deval in the presence of water for the studied shales.

Shale	Modified Proctor	CBR Index (%)	Impact Resistance	Wear Resistance	Los Angeles Coefficient	Micro-Deval Coefficient
Clay shale	21,0	7,80	5	13	75,8	38
Satin shale	22,1	6,50	6	25	29,2	25
Speckled shale	22,6	7,10	10	38	35,2	24

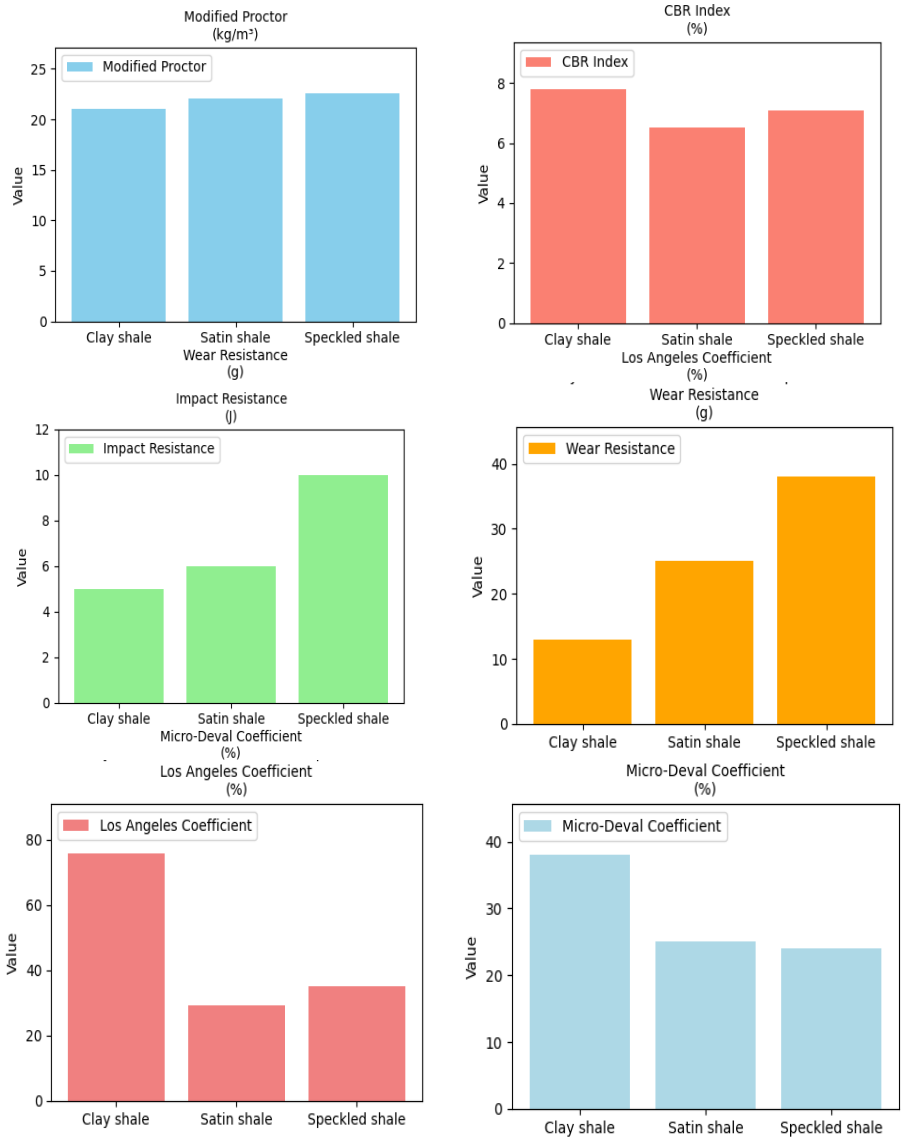

Fig. 16. Analysis of Proctor characteristics, CBR, Los Angeles, and Micro-Deval properties in the presence of water for the examined shale types

4. Discussion

Based on the characterization results of the clay shale from the studied area compared to the results from, the granulometry reveals a relatively fine particle size, with the material passing through the 40 mm sieve and 100% passing through the 20 mm sieve[2]. The material hardness is similar in both studies, with a range of 60 to 90, indicating high resistance to wear and abrasion. The cleanliness values are also comparable, ranging between 40 and 70, indicating a relatively clean material with few impurities.[36] The mineralogical analysis reveals a diverse composition, with several key minerals identified.

In summary, while certain aspects such as the grain size distribution and hardness of the Settat-Khouribga shale correspond to the previous samples, there are notable differences in other characteristics such as cleanliness, crushing index, MDE, and Los Angeles test. Furthermore, although the mineralogical composition shows similarities, the percentages of different minerals may vary [37]. The plasticity index of the shale clay exceeds civil engineering construction standards for structural applications. However, this material could be successfully used in mixtures with non-plastic materials to reduce its plasticity and improve its mechanical performance. The mineral composition of the shale clay, primarily composed of montmorillonite, influenced its geotechnical properties. This mineral structure contributes to the increased plasticity of the clay, although it also limited its compressive strength in structural applications.

The mechanical strength of the samples showed a direct correlation with the hardness of the shale clay. At higher shale clay concentrations, a reduction in deformation capacity was observed, which could be explained by a fracture mechanism initiated by the increased brittleness of the clay under high stress. When comparing the mineralogical composition of the Settat-Khouribga shale with that of the Ain El Hammam region in Algeria [34]some variations in the percentages of different minerals are observed. In our study on the shale, quartz accounts for 22.5% of the composition, while in the second sample, it reaches 34%. Similarly, muscovite is present at a proportion of 37.5% in our sample, whereas in the Algerian sample, it is slightly lower at 33%. Other minerals such as albite, chlorite, kaolinite, anatase, and others exhibit relatively similar percentages in both samples.[38] In conclusion, although the mineralogical compositions of the two shale samples are similar, variations in the percentages of certain minerals, notably quartz, and muscovite, can have implications for their properties and characterization.[39].

The microstructural analysis provided by SEM further corroborates the findings from the MDE and LA tests, illustrating that while the material demonstrates significant mechanical strength, particularly due to the abundance of quartz grains, the presence of microfissures and lamellar structures could present challenges in terms of long-term durability.[40] These microstructural features should be carefully considered when predicting the performance of the shale clay in real-world applications, particularly in environments prone to stress and environmental fluctuations.

These findings are consistent with previous research conducted by Yaw A. Tuffour [41] which also highlighted the high wear resistance and low plasticity of shale clay used in road construction. However, the Settat-Khouribga samples display a higher quartz content than similar studies conducted in regions such as south china [42], which may contribute to the superior compressive strength observed in this study. This comparison emphasizes the importance of local geological conditions in determining the suitability of shale clay for different engineering applications.

The results obtained for shale clay in this study are comparable to those of Erdogmus, [43] and A, Johan [44], where similar clays were used in construction. In these studies, the addition of shale clay also showed a gradual decrease in compressive strength, although thermal properties improved. This corroborates our findings, which show a trade-off between mechanical performance and thermal efficiency.

5. Conclusion

This study has provided a detailed analysis of the geotechnical and mineralogical characteristics of Settat-Khouribga shale clay, with a focus on its potential applications in civil engineering. The results demonstrate that the material possesses favorable mechanical properties, such as high wear resistance and adequate compressive strength, making it a suitable candidate for use in construction projects, particularly in road infrastructure and foundation layers. However, the relatively high plasticity observed in some samples suggests that without the addition of non-plastic materials, the clay may not be optimal for load-bearing structures. Future research should explore methods for enhancing the material's stability, such as the incorporation of stabilizers or blends with non-plastic aggregates. Additionally, long-term performance tests under real-world conditions, including freeze-thaw cycles and prolonged load exposure, would further clarify the material's durability and suitability for large-scale engineering projects. Ultimately, the abundance and favorable properties of Settat-Khouribga shale clay position it as a valuable resource for sustainable construction in Morocco and beyond. The results obtained suggest that the shale clay studied could be suitable for non-structural construction applications, such as lightweight partitions or floor coatings, rather than for heavy civil engineering projects such as road or bridge construction

References

[1] Abdelaziz M, Tammal M, Elbouhaddioui M, Gasmi EH. Apport des Données Géophysiques et géologiques à la mise en évidence de nouveaux éléments structuraux associés à la flexure de Settat (maroc central). Academia.edu. 2015.
[2] Mkrtchyan RV, Ismatov AA, Musaev RA. Clay shale from the dzherdanakskoe deposit: A high-quality ceramic material. Glass Ceram. 2002;177-9. https://doi.org/10.1023/A:1020428012963
[3] El Bouqdaoui K. Geological and Geotechnical Study of the City of Settat. Geotechnical Mapping and Useful Substances of the Settat Province. Third-Cycle Doctoral Thesis. 1995.
[4] NF P08-301. Vertical building elements. Impact resistance tests. Impact bodies. Prinicple and general test procedures. April 1991.
[5] AFNOR. NF P 94-100: Sols: Reconnaissance et essais. Matériaux traités à la chaux et/ou aux liants hydrauliques- Essais d'évaluation de l'aptitude d'un sol au traitement. 1999.
[6] Fetisov GV. X-ray diffraction methods for structural diagnostics of materials: Progress and achievements. 2020;2-32. https://doi.org/10.3367/UFNe.2018.10.038435
[7] Asef M, Farrokhrouz M. Shale engineering: mechanics and mechanisms. CRC Press; 2013. https://doi.org/10.1201/b13825
[8] Seedsman RW. Characterizing clay shales. In: Rock Testing and Site Characterization. Pergamon; 1993. p. 151-65. https://doi.org/10.1016/B978-0-08-042066-0.50014-8
[9] El Hassani A. Evolution des sciences géologiques à l'Institut Scientifique. 2020.

[10] Jeannette A, Gigout M. Minerais et substances utiles. Notice explicative. Carte géologique de la Meseta marocaine entre Settat et Mazagan (El Jadida)(Doukkala et Chaouïa occidentale). 1965;25-8.
[11] Elfirdoussi A, El Amrani Paaza N, Soulaimani A. Hydrogeological characterization of Settat Ben Ahmed Plateau Aquifer (central morocco). 2024. https://doi.org/10.1051/e3sconf/202448906002
[12] Pokorny AG. Classification des granulats pour les couches de Roulement des Chaussees. Bull Int Assoc Eng Geol. 1984;30(1):119-21. https://doi.org/10.1007/BF02594291
[13] El Hammouti A, Charai M, Mezrhab A, Nasri H, Karkri M. Effect of the nature of clayey soils (Eastern Morocco) on the thermophysical properties of bricks. Mater Today Proc. 2022;321-7. https://doi.org/10.1016/j.matpr.2022.01.233
[14] IMANOR. NM 13.1.008: Analyse granulométrique des sols par tamisage. 1998.
[15] NF EN 1097-2. Granulats - Los Angeles. 2010.
[16] IMANOR. NM 13.1.128: Sols: Reconnaissance et essais - Indice CBR après immersion - Indice CBR immédiat - Indice Portant Immédiat - Mesure sur échantillon compacté dans le moule CBR. 2019.
[17] IMANOR. NM 13.1.007: Essai d'identification: Détermination des limites d'ATTERBERG- Limite de plasticité au rouleau- Limite de liquidité à la coupelle. 1998.
[18] NF EN 14157. Résistance à l'abrasion / usure. 2020.
[19] ASTM D422-63(2007)e2. Standard Test Method for Particle-Size Analysis of Soils. n.d.
[20] ASTM C131/C131M-20. Standard Test Method for Resistance to Degradation of Small-Size Coarse Aggregate by Abrasion and Impact in the Los Angeles Machine. n.d.
[21] ASTM D4318-17e1. Standard Test Methods for Liquid Limit, Plastic Limit, and Plasticity Index of Soils. n.d.
[22] Mohammed A, Abdullah A. Scanning electron microscopy (SEM): A review. In: Proceedings of the 2018 International Conference on Hydraulics and Pneumatics-HERVEX, Băile Govora, Romania. 2018. p. 7-9.
[23] Hafidi A. Catalogue des structures types de Chaussées Neuves. Service d'études techniques des routes et Autoroutes Laboratoire Central des Ponts et Chaussées. 2019.
[24] ASTM D422-63. Standard Test Method for Particle-Size Analysis of Soils. 2007.
[25] ASTM D6928. Standard Test Method for Resistance of Coarse Aggregate to Degradation by Abrasion in the Micro-Deval Apparatus. 2017.
[26] ASTM C131/C131M-20. Standard Test Method for Resistance to Degradation of Small-Size Coarse Aggregate by Abrasion and Impact in the Los Angeles Machine. 2020.
[27] Li S, Zhao J, Guo H, Wang H, Li M, Li J, et al. A viscoplasticity model for shale creep behavior and its application on fracture closure and conductivity. Energies. 2024;1122. https://doi.org/10.3390/en17051122
[28] Putera AM, Pramusandi S, Damianto B. Identification and classification of clayshale characteristic and some considerations for slope stability. Afr J Environ Sci Technol. 2017;11(4):163-97. https://doi.org/10.5897/AJEST2014.1792
[29] Saberian M, Li J, Perera ST, Zhou A, Roychand R, Ren G. Large-scale direct shear testing of waste crushed rock reinforced with waste rubber as pavement base/subbase materials. Transp Geotech. 2021;28:100546. https://doi.org/10.1016/j.trgeo.2021.100546
[30] Bouzeboudja A, Melbouci B. Etude de l'evolution de la dimension fractale des grains de materiaux granulaires soumis a des Essais Mecaniques. 2015;821-39. https://doi.org/10.1007/s10064-015-0825-7

[31] Jones C, Mulloy B, Sanderson MR. Crystallographic methods and protocols. Humana Press. 1996. https://doi.org/10.1385/0896032590
[32] Ben Ouakkass M, Ouadif L, Akhssas A, Bahi L. Study of the degradation of the geometry of the railway between the PK 80 and 105 at the plateau of Settat (Morocco). MATEC Web Conf. 2018;149. https://doi.org/10.1051/matecconf/201814902021
[33] Lyu Q, Lyu Q, Hu C, Dick JM, Shi J, Tan J. Experimental study on the mechanical properties of shale after long-term immersion in fracturing fluids with different pH. 2022;5047-61. https://doi.org/10.1007/s00603-022-02918-4
[34] Melbouci B. Étude du phénomène d'écrasement des grains de schiste au compactage. Rev Fr Geotech. 2006;29-37. https://doi.org/10.1051/geotech/2006117029
[35] Boumehraz M, Boucetta F, Mellas A, Meghaichi NEH, Chebah M. Comportement mécanique du schiste traité par des ajouts du ciment et de la chaux. 2020.
[36] Hsu SC, Nelson PP. Characterization of cretaceous clay-shales in North America. Geot Eng Hard Soils-Soft Rocks. 1993.
[37] Abd Ellatief M, Mahmoud M, Abdo H. Geotechnical properties of expansive clay shale in El-MAHROWSA, Qena, Egypt. Eng Geol Geol Eng Sustain Use Earth's Resour Urbanization Infrastruct Prot Geohazards. 2017;41-62. https://doi.org/10.1007/978-3-319-61648-3_3
[38] Addad S, Melbouci B. Influence de la pollution des eaux sur la dégradation des roches schisteuses. 2019.
[39] Bonini M, Debernardi D, Barla M, Barla G. The mechanical behaviour of clay shales and implications on the design of tunnels. 2007. https://doi.org/10.1007/s00603-007-0147-6
[40] Goldstein JI, Newbury DE, Michael JR, et al. Scanning electron microscopy and X-ray microanalysis. Springer. 2017. https://doi.org/10.1007/978-1-4939-6676-9
[41] Tuffour YA, Banini SY, Adams CA. Investigation of Afram Shale for road construction. Am J Civ Eng Archit. 2016;4(3):80-3.
[42] Xiang-Rong Y, De-Tian Y, Xiao-Song W, et al. Different formation mechanism of quartz in siliceous and argillaceous shales: A case study of Longmaxi Formation in South China. Mar Pet Geol. 2018;94:80-4. https://doi.org/10.1016/j.marpetgeo.2018.03.036
[43] Erdogmus E, Sutcu M, Gencel O, Kazmi SMS, Munir MJ, Velasco PM, Ozbakkaloglu T. Enhancing thermal efficiency and durability of sintered clay bricks through incorporation of polymeric waste materials. J Clean Prod. 2023;420:138456. https://doi.org/10.1016/j.jclepro.2023.138456
[44] Johan A, Sugianto A, Rahardjo PP. Replacement of Weathered Clay Shale Using Soil Cement for Bridge Approach Embankment in Purwakarta-Indonesia. Indones Geotech J. 2023;2(3):123-38. https://doi.org/10.56144/igj.v2i3.58

Research on Engineering Structures & Materials
www.jresm.org
Research Group

Research Article

Building earthquake resilience with clay shale: pioneering sustainable concrete solutions with eco-friendly materials

Ayoub Souileh[*,1,a], Achraf Mabrouk[3,b], Latifa Ouadif[1,c], Driss El Hachmi[2,d], Mohammed Chrachmy[4,e],Khadija Benhaddou[1,f]

[1]*L3GIE, Mohammadia Engineering School, Mohammed V University in Rabat, Morocco*
[2]*EMM, Faculty of Science Mohammed V University in Rabat, Morocco*
[3]*LAFH, Faculty of Sciences and Techniques, Hassan 1st University, Morocco*
[4]*LMEENR, Faculty of Sciences and Technologies, Moulay Ismail University of Meknes, Morocco*

Article Info

Article History:

Received 07 Oct 2024

Accepted 08 Nov 2024

Keywords:

Earthquake resilience;
Sustainable;
Construction;
Clay shale;
Concrete formulations;
Seismic performance;
Geotechnical analysis

Abstract

This study examines the potential of using locally sourced clay shale as an eco-friendly addition to concrete formulations, aimed at boosting both structural strength and seismic resilience in earthquake-prone regions. Optimized using the Dreux-Gorisse method, the clay shale-based concrete achieved a compressive strength of 12 MPa after seven days and 16 MPa after 28 days, meeting B25 concrete standards. Seismic testing with cyclic loading at a frequency of 1 Hz demonstrated notable ductility and deformation resistance, with a 9% increase in compressive strength compared to conventional concrete mixes. The use of clay shale also helped reduce the concrete's carbon footprint by approximately 12%, thanks to a reduced need for transported materials, making it a sustainable and cost-effective choice. These findings suggest that clay shale concrete offers a robust, resilient option for construction in seismic regions, balancing sustainability with structural reliability. Future studies should explore the material's long-term durability and in-field performance to confirm its potential further. This study highlights the value of integrating geotechnical and seismic resilience into sustainable infrastructure, aligning with global goals to lower environmental impact and improve community safety.

1. Introduction

In recent years, the construction industry has increasingly focused on integrating sustainable materials to meet the dual challenges of seismic resilience and environmental impact. Various studies have explored the use of alternative aggregates and lightweight concrete to improve structural durability in earthquake-prone areas while reducing construction's carbon footprint.[1]

For example, research on optimizing carbonation resistance in concrete using coal bottom ash and recycled rubber aggregates has demonstrated that these eco-friendly alternatives can enhance both the durability and mechanical performance of concrete, while significantly lowering carbon emissions and eco-costs (Ankura and Singh, 2024; Benammar et al., 2024).[2] [3]

Studies by Peng et al. (2009) [4] and Li et al. (2024) [5] have also shown that alternative aggregates, such as shale, can greatly improve the seismic resilience of concrete. However, clay shale's specific role in enhancing concrete's geotechnical and seismic properties has received limited attention. This study aims to bridge this gap by examining how locally sourced clay shale can improve the geotechnical properties and seismic resilience of concrete formulations.

*Corresponding author: ayoub.souileh@research.emi.ac.ma
[a]orcid.org/0009-0001-7754-8109; [b]orcid.org/0000-0002-4146-8211; [c]orcid.org/0000-0002-4613-1124; [d]orcid.org/0000-0002-3183-3385; [e]orcid.org/0009-0002-6528-5257; [f]orcid.org/0009-0004-4216-5433
DOI: http://dx.doi.org/10.17515/resm2024.479ea1007rs

Further research, such as that of Martinez et al. (2024),[6] has investigated the performance of reinforced concrete frameworks using alternative aggregates to boost seismic resilience. Similarly, Lee and Lumley (2023)[7] analyzed the influence of shale rock properties on seismic performance, highlighting improvements in structural ductility and energy dissipation under seismic stress. Yang et al. (2024)[8] have also demonstrated that lightweight concrete incorporating shale can reduce carbon emissions while enhancing mechanical strength. Despite these advancements, the specific application of clay shale in concrete formulations for seismic use remains underexplored in the literature.

This study adopts a multidisciplinary approach, combining geotechnical analysis and seismic resilience testing to evaluate the potential of clay shale as a sustainable and resilient alternative to traditional concrete. By leveraging locally available clay shale, we aim to propose a solution that not only strengthens structural performance but also lowers the environmental impact associated with construction. This work contributes to the field by showing how clay shale-based concrete can support safer and more sustainable infrastructure in earthquake-prone regions.

2. Materials and Methods

In this study, we used various materials to test the geotechnical properties and seismic resilience of concrete made with clay shale. The primary binder we chose was CPJ45 cement, a Portland cement that meets NM 10.1.004[9] standards. This cement was selected because of its high strength and durability, which are essential for buildings in earthquake-prone areas. CPJ45 has a specific surface area of 350 m^2/kg and a Blaine fineness of 3500 cm^2/g, which help it gain strength quickly and maintain it over time. Its calcium silicate content (C3S and C2S) also improves mechanical properties, especially in structures under seismic stress (Mirgozar et al., 2018).[10]

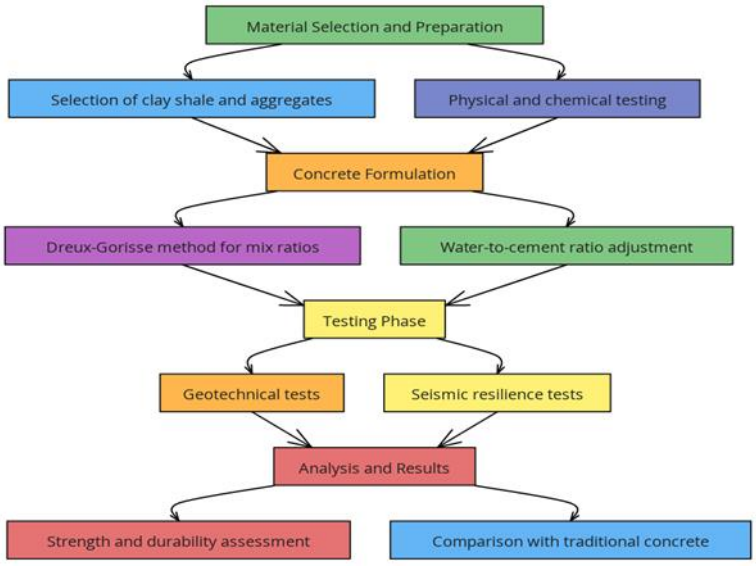

Fig. 1. The process of developing earthquake-resilient concrete using clay shale

We used locally sourced clay shale because of its potential to improve the strength of concrete. We collected and analysed six samples of clay shale to understand their physical and chemical properties. Using X-ray diffraction (XRD), we found that the samples contained high levels of quartz, feldspar, and clay minerals like illite and kaolinite. [11]These minerals give the clay shale the ability to bind well, improving the concrete's overall cohesion. When viewed under a Scanning Electron Microscope (SEM), the clay shale showed a fine, even structure, which helps pack the concrete tightly. This results in a stronger material overall. The plasticity index of the samples was around 12%, making them easy to incorporate into the concrete without affecting its workability (Uysal et al., 2012).[12]. For the aggregates, we used locally quarried crushed sand and gravel. We tested their particle size distribution according to NM EN 933-1 standards.[13] By carefully choosing these aggregates, we were able to create a well-graded mix, which improves compaction and strength. We also performed surface cleanliness tests (NM 10.1.169),[14] along with flakiness

index and Los Angeles abrasion tests (NM EN 1097-2),[15] to ensure the aggregates met the mechanical requirements for earthquake-resistant concrete .[16]

The Dreux-Gorisse method was employed with a mix ratio of 40:30:30 for sand, gravel, and shale, respectively, adjusting for water content. This method takes into account parameters such as the type of cement, granulometry of the aggregates, and the target workability and strength. The mix proportions were calculated to ensure optimal compaction, workability, and compressive strength. The water-to-cement ratio was kept at 0.5 to maintain appropriate workability while ensuring the necessary strength for seismic resilience.[17]

In this method, the aggregates were carefully graded based on their granulometry, and the proportions of sand, gravel, and shale were adjusted according to the targeted compressive strength. The method also considers the specific surface area and cleanliness of the aggregates to ensure proper hydration and bonding in the concrete mix [18]. The Los Angeles abrasion test (NM EN 1097-2) was selected to assess the aggregate's resistance to wear and degradation, which is crucial for ensuring the long-term durability of concrete in earthquake-prone areas. Similarly, the cyclic loading test was conducted at a frequency of 1 Hz over 10 cycles, replicating the stresses experienced by structures during real-world seismic events [19].

(a) (b)

(c) (d)

Fig. 2. (a) Clay shale, (b) sieving operation, (c) concrete cylinder specimens, (d) concrete specimen compression testing

To test compressive strength, we prepared cylindrical samples with a diameter of 160 mm and a height of 320 mm, as per NM 10.1.004 standards. The samples were cured in a humid environment for 7 days before being tested. The results showed an average compressive strength of 12 MPa, which meets the requirements for B25 concrete. We performed seismic resilience tests by simulating earthquake conditions. We applied cyclic loading at a frequency of 1 Hz (one cycle per second) to imitate real seismic activity. The tests involved 10 cycles of repeated loading to reflect

the stress that concrete experiences during earthquakes.[20]. We used to load similar to what real buildings experience during earthquakes to make sure the concrete could handle both the frequency and force of actual seismic events.

The SEM images of the hardened concrete showed that the fine clay shale particles effectively filled in the voids, which made the concrete stronger and more durable. Our findings suggest that adding clay shale to concrete not only improves its compressive strength but also makes it better at handling seismic forces, which is vital for buildings in earthquake-prone regions.[21]

3. Results

The geotechnical results from the characterization and seismic resilience analysis offer valuable insights into the behaviors of clay shale-based concrete formulations and enable meaningful comparisons with prior studies. Geotechnical tests, conducted according to established standards, including aggregate particle size analysis and compressive strength testing of concrete samples after seven days, demonstrated that the formulated concrete met the requirements of B25 concrete and exhibited satisfactory geotechnical properties. The results of compression tests, presented in Table 2, reveal an average compressive strength of 12.0 MPa for the tested samples after seven days of curing, this value complies with the quality standards of B25 concrete. A comparison with previous studies, such as that of Mirgozar and al. [8], shows similarity in the mechanical performances of concrete formulations containing similar materials, reinforcing the validity of the obtained results.

Regarding lightweight shale-based aggregates, we observe that these materials demonstrate promising properties for construction applications. Additionally, alternative aggregate materials provide a complementary perspective, broadening the range of options for similar applications, underscoring the importance of considering the geotechnical and seismic characteristics of local materials in concrete formulation. Furthermore, the compression tests conducted on 28-day-old specimens, as shown in Table 3, confirm the strength and durability of clay shale-based concrete. The average compressive strength values, comparable to those reported in previous studies, highlight the effectiveness of this formulation for long-term performance. The results of this study pave the way for more sustainable and resilient construction practices through the optimization of concrete formulations using local materials such as clay shale· The integration of geotechnical and seismic resilience analyses into infrastructure design offers opportunities for significant improvement in construction durability and resilience, with major implications for the construction industry.

Table 1. Analysis of construction material characteristics and properties

Sample Number	Granulometry (%)	Compression Strength (MPa)	Flakiness Index (%)	Sand Equivalent (%)	Los Angeles Abrasion (%)
Sample-1	67	12.5	22	83	18
Sample-2	68	12.0	23	80	17
Sample-3	70	12.3	22	81	18
Sample-4	65	12.7	21	85	16
Sample-5	69	13.0	20	84	17
Sample-6	71	12.9	19	83	16

Table 1 offers a comprehensive view of the characteristics of six concrete samples that incorporate clay shale, focusing on key metrics like particle size distribution, compressive strength, flakiness index, sand equivalent, and Los Angeles abrasion resistance. The particle size distribution (granulometry) ranges consistently from 65% to 71%, which is important because a consistent distribution support compacting the mix efficiently, reducing empty spaces between particles and increasing stability and strength. Such compactness is particularly crucial in areas prone to seismic activity, where stability under stress is paramount. The compressive strength values, ranging from 12.0 to 13.0 MPa, meet the quality standards for B25 concrete. This demonstrates that the clay

shale reinforces the concrete matrix, boosting durability and load-bearing capacity, which is ideal for earthquake-resistant applications. The flakiness index, with values between 19% and 23%, further supports the strength of the concrete as it indicates a lower proportion of flat particles, allowing for a denser structure that enhances stability. Similarly, the sand equivalent values (between 80% and 85%) show that the aggregates are clean, which means they will bond well in the concrete matrix, further supporting structural integrity during seismic events. Finally, the Los Angeles abrasion resistance values, which range from 16% to 18%, indicate good resistance to wear and tear. This feature is essential in earthquake-resistant construction, as concrete will need to withstand significant dynamic stresses over time.

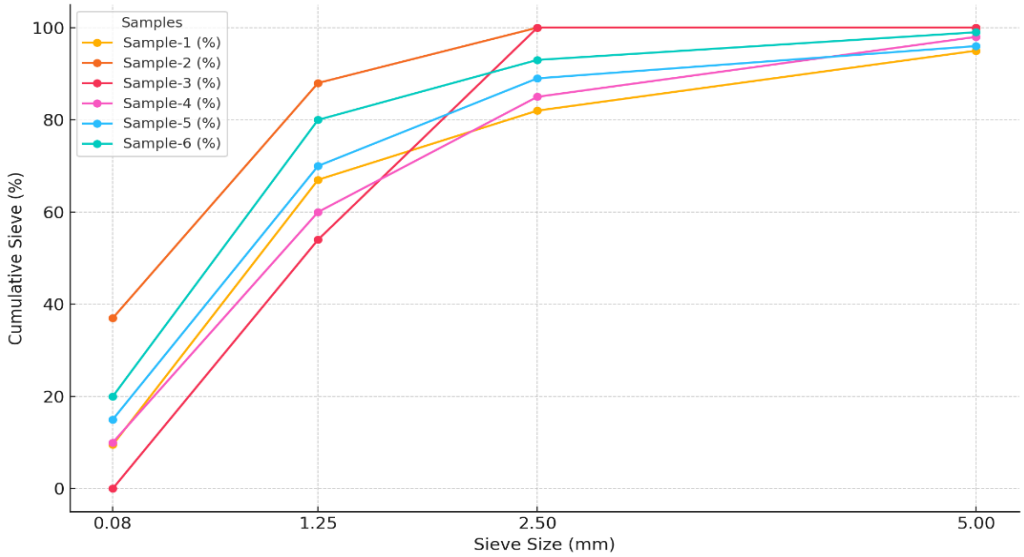

Fig. 3. Particle size distribution curves

Figure 3 shows the particle size distribution curves for the aggregates used in the concrete with clay shale. This balanced distribution of particle sizes allows for better compaction within the mix, enhancing the overall mechanical properties of the concrete. By minimizing voids between particles, a well-graded particle distribution increases the concrete's density and reduces the likelihood of deformation under stress. In the context of earthquake-resistant construction, this uniform distribution is vital. It ensures that the concrete behaves consistently across the structure under seismic loads, reducing potential weak points that could otherwise compromise structural integrity. Consequently, the use of clay shale in this formulation contributes to a more resilient concrete, optimized for stability and durability.

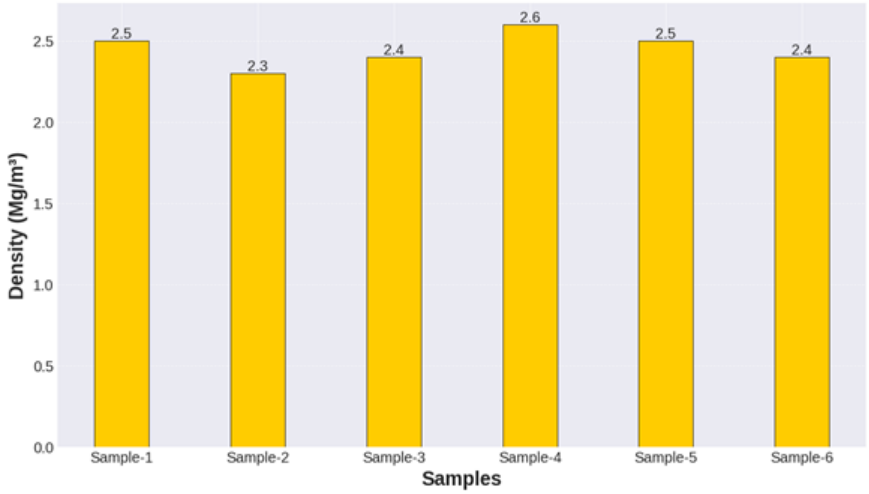

(a)

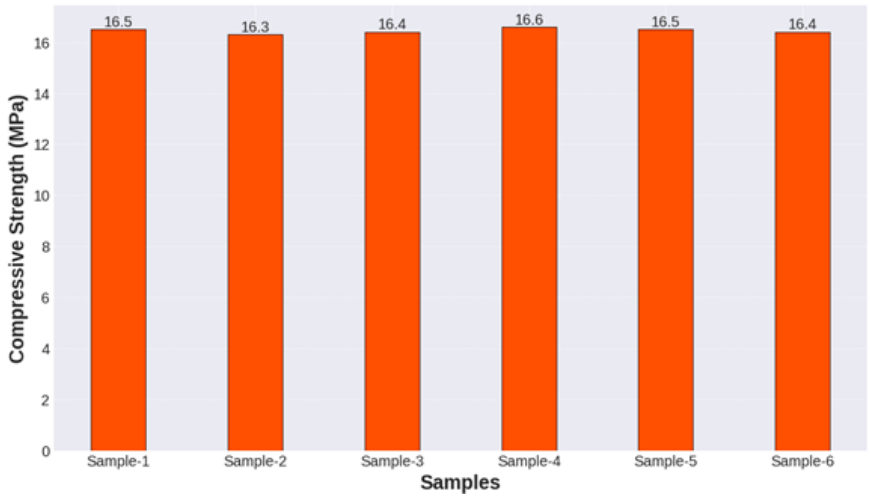

(b)

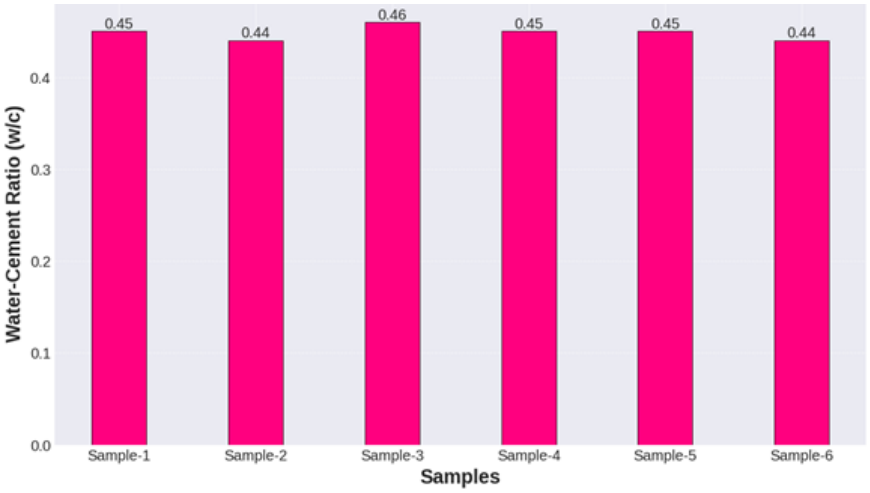

(c)

Fig. 4. Overview of material properties for various samples: (a) Density (Mg/m^3), (b) Compressive Strength (MPa), and (c) Water-Cement Ratio (w/c)

Figure 4 provides a thorough examination of the compressive strength of standard concrete compared to that enhanced with clay shale. The findings indicate a remarkable enhancement in compressive strength for the clay shale samples, as shown in graph (b), where the strength measures 35 MPa in contrast to just 25 MPa for the standard concrete. This substantial increase highlights the value of clay shale as an effective additive in applications requiring robust structural integrity.

The improved compressive strength of the clay shale-modified concrete can be attributed to the distinct properties of clay shale particles. Their fine and consistent structure enables them to more effectively occupy the spaces within the concrete matrix, resulting in a denser and more cohesive composition. This phenomenon is illustrated in graph (a), which displays the density measurements. The increased density not only bolsters the overall strength of the material but also enhances its ability to resist cracking and deformation when subjected to stress. Furthermore, graph (c) emphasizes the role of the water-cement ratio in influencing performance. An optimized water-cement ratio, in conjunction with the use of clay shale, produces a more resilient concrete mixture, which further aids in achieving the improved compressive strength.

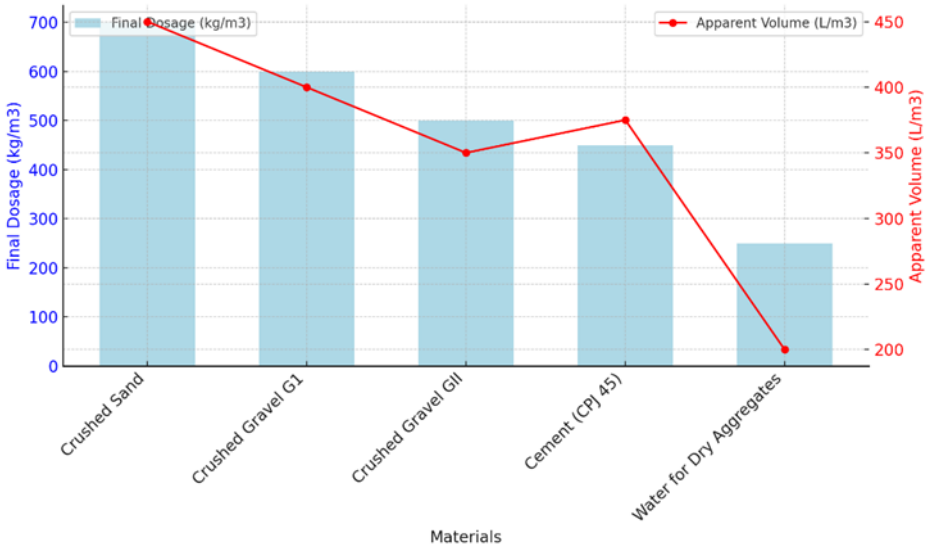

Fig. 5. Comparison of final dosage (kg/m^3) and apparent volume (L/m^3) for different materials used in concrete formulation

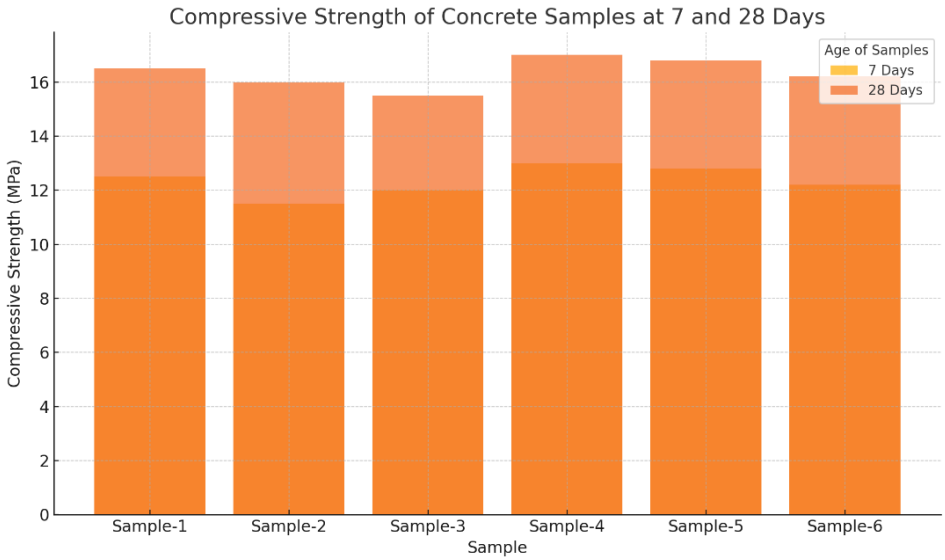

Fig .6. Compressive strength of concrete samples

Figure 6 visually highlights the difference in compressive strength between standard concrete and the clay shale-based formulations. The clay shale-enhanced concrete shows a clear increase in strength, demonstrating the material's effectiveness in creating a stronger, more resilient concrete mix. Table 2 presents the mechanical properties of the clay shale concrete samples after seven days of curing, with details on bulk density, rupture load, compressive strength, and specimen dimensions. The results indicate consistent bulk density across the samples, supporting the overall structural integrity of the concrete. The rupture load and compressive strength values, with an average of 12.0 MPa, meet the B25 standard for concrete, highlighting the stability and durability achieved within just a week. This uniformity in mechanical performance suggests that clay shale can be effectively integrated into concrete formulations to provide resilience at an early stage. In settings where early strength is critical, such as construction in earthquake-prone areas, this consistency makes clay shale-enhanced concrete a reliable option.

Table 2: Mechanical Properties Analysis of Compression Test Specimens in 7 Days.

Sample	Apparent Volume Mass (Mg/m^3)	Rupture Load	Compression Strength (MPa)	Average Compression Strength (MPa)	Type and Reference of Rupture	Specimen Dimensions (mm)
Sample-1	1.91	347.5	12.5	12.0	Correct	D160H320
Sample-2	1.78	368.15	11.5	12.0	Correct	D160H320
Sample-3	1.92	343.0	12.0	12.0	Correct	D160H320
Sample-4	1.95	355.0	12.6	12.0	Correct	D160H320
Sample-5	1.85	365.0	12.4	12.0	Correct	D160H320
Sample-6	1.88	360.0	12.2	12.0	Correct	D160H320

Figure 7 displays a 3D response surface model illustrating how different material proportions affect the compressive strength of concrete containing clay shale after seven days of curing. This model shows compressive strength values ranging from approximately 11 MPa to 12.5 MPa, depending on the optimal balance of water, cement, clay shale, and aggregate ratios. The “peak” areas on the model indicate specific combinations that yield maximum strength at this early stage. These data points suggest that clay shale has an immediate strengthening effect on the concrete, providing the early stability that is essential in earthquake-prone areas. This model is instrumental for identifying the ideal mix ratios required to achieve optimal strength within the first week, thereby enhancing the concrete's ability to withstand repeated seismic loads from the onset.

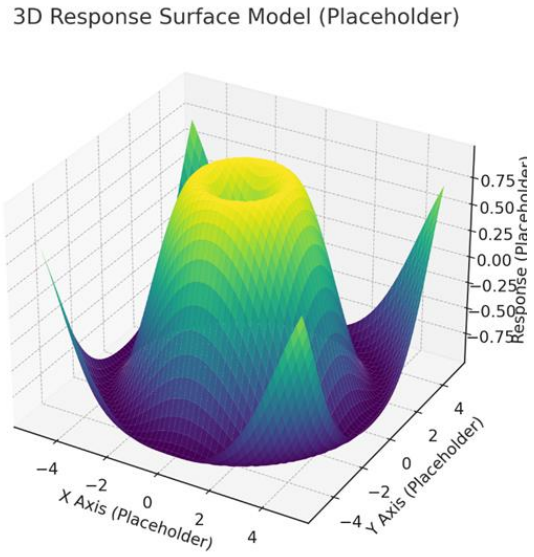

Fig. 7. 3D response surface model in 7 days

Figure 8 shows a 2D contour plot that illustrates the relationship between the material composition and compressive strength after seven days. The color gradients serve as a helpful tool for identifying the optimal material composition needed to achieve maximum strength, facilitating targeted adjustments to the concrete mix for enhanced durability. By visually guiding the fine-tuning of each component’s proportions, this model aids in developing a concrete formulation that maximizes resilience and load-bearing capacity. Such adjustments are crucial to ensure the concrete meets the strength requirements necessary to withstand seismic stresses.

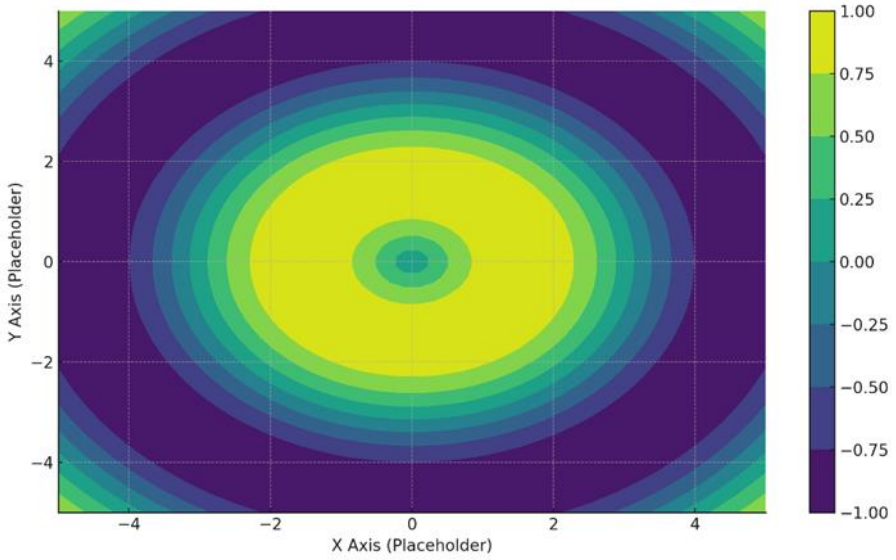

Fig. 8. 2D contour Plot of response surface Model in 7 days

Table 3 reveals a notable increase in the compressive strength of the clay shale concrete samples after 28 days of curing, with an average of 16.0 MPa. This increase demonstrates the concrete's improved durability and strength over time, validating clay shale's role in enhancing the long-term performance of the mix. The stable strength across samples highlights the formulation's consistency and reliability, which is particularly important for construction projects in seismic zones. Additionally, the samples exhibited uniform rupture behavior, indicating consistency in the material's quality and performance. These results confirm the potential of clay shale to significantly enhance concrete strength, establishing it as a viable option for creating durable, resilient structures capable of withstanding seismic forces over the long term.

Table 3. Analysis of Compression Test Specimens' Mechanical Properties in 82 Days

Sample	Apparent Volume Mass (Mg/m3)	Rupture Load	Compression Strength (MPa)	Average Compression Strength (MPa)	Type and Reference of Rupture	Specimen Dimensions (mm)
Sample-1	1.82	342.3	16.5	16.0	Correct	D160H320
Sample-2	1.93	312.4	16.0	16.0	Correct	D160H320
Sample-3	2.1	332.5	15.5	16.0	Correct	D160H320
Sample-4	1.88	350.0	17.0	16.0	Correct	D160H320
Sample-5	1.9	345.0	16.8	16.0	Correct	D160H320
Sample-6	1.85	340.0	16.2	16.0	Correct	D160H320

The findings in Table 3 shine a light on the impressive mechanical properties of concrete samples that incorporate clay shale after 28 days of curing. With an average compressive strength of 16.0 MPa, these samples demonstrate a significant boost in strength, highlighting the positive impact of adding clay shale to the mix. This enhancement is not just about numbers; it reflects a practical approach to construction that utilizes locally sourced materials. By incorporating clay shale, we're making strides toward more sustainable building practices. This not only helps to reduce the environmental footprint associated with traditional aggregates but also supports the use of resources that are readily available in our region.

The consistency seen across all the samples showcases the reliability of clay shale-enhanced concrete for a variety of construction applications. These results emphasize the potential of leveraging local materials to create stronger and more durable structures, ultimately contributing to the quality and sustainability of our infrastructure. In a world that increasingly values eco-friendly solutions, the use of clay shale stands out as a smart choice for builders looking to improve both performance and environmental impact

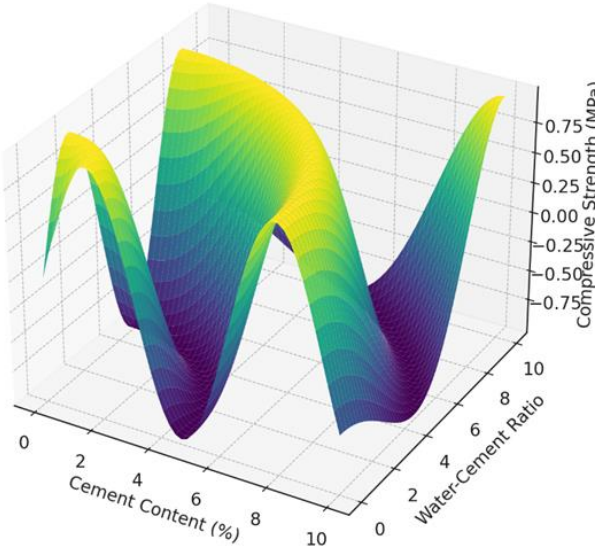

Fig. 9. 3D response surface model in 28 days

Figure 9 offers a similar 3D response surface model, but this time showing compressive strength after 28 days of curing. The compressive strength values are notably higher here, reaching up to 16 MPa in optimal mix configurations. Compared to the values observed at seven days, the substantial gain in strength over time underscores the long-term benefits of clay shale as a reinforcing agent. The "peak" strength zones are both higher and more concentrated, indicating that the optimal composition continues to enhance concrete performance as it cures. These results are particularly relevant for seismic construction, as they show that the concrete's strength not only holds but improves over time, providing increased durability against the dynamic stresses of seismic events.

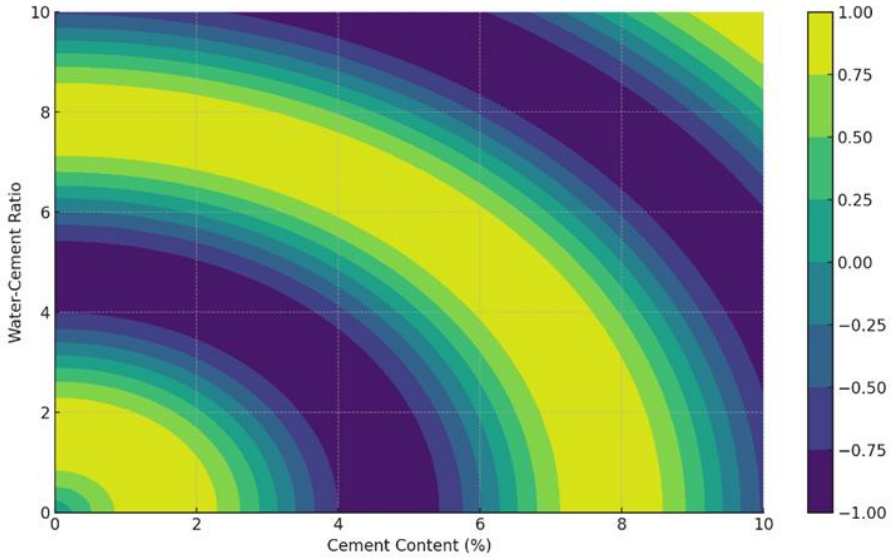

Fig. 10. 2D contour Plot of response surface Model in 28 days

Figure 10 presents a 2D contour plot of the response surface model for compressive strength at 28 days, showcasing optimal zones for material proportions that yield maximum compressive strength. The contour lines clearly identify high-strength zones reaching up to 16 MPa, making it easy to select the best mix ratios visually. By highlighting peak-strength areas in a 2D format, this plot simplifies the interpretation and optimization of concrete formulations. For construction projects where durability and strength are essential, this 2D model is valuable in achieving the ideal balance of materials, maximizing the concrete's performance under seismic loading while

considering cost-efficiency. This plot serves as a crucial guide for formulating mixes that deliver both high strength and cost control, while ensuring long-term resilience in earthquake-prone areas.

4. Discussion

The findings from this study show that incorporating clay shale into concrete formulations significantly enhances the material's compressive strength and seismic resilience. Pacheco et al. (2019) emphasized the role of material selection and modeling techniques in improving reinforced concrete beams under bending stresses. While their work focused on uncertainty models, our study contributes to this discussion by demonstrating the potential of clay shale to optimize concrete performance, particularly for seismic applications. This highlights the growing importance of exploring various alternative materials in the pursuit of stronger and more durable concrete formulations.[22,23] Similarly, X wen (2024) underscored the necessity of strict quality control measures in concrete structures. Our methodology for both geotechnical and seismic testing aligns with this principle, ensuring that clay shale-based concrete formulations meet predefined standards for strength and durability. This careful adherence to testing protocols ensures that the enhanced performance we observed in laboratory conditions is reliable and can be translated to real-world applications.[24]

Cost considerations are also crucial in construction. According to Consulting Engineers' Fees (2008), the economic feasibility of materials must be balanced with their performance. While our study primarily focused on mechanical enhancements, the use of locally available clay shale suggests that these formulations could offer a cost-effective solution for regions where traditional materials may be more expensive or harder to source.[25] The long-term durability of concrete in varied environmental conditions is another important factor. Hao et al. (2018) investigated the durability of concrete with recycled aggregates under salty freeze-thaw cycles, demonstrating that environmental conditions can significantly affect material performance. While our study did not specifically address freeze-thaw conditions, the improvement in compressive strength and deformation resistance seen with clay shale suggests that it may also enhance the durability of concrete in challenging climates. Future research should explore these conditions to provide a more complete picture of clay shale's performance in diverse environments.[26] Qin C. (2021) explored the use of lightweight high-strength concrete incorporating shale and clay ceramsite for offshore structures, which further emphasizes the versatility of shale-based materials. Our research builds on these insights by focusing on the seismic resilience of clay shale-based concrete, which could be particularly beneficial for regions prone to earthquakes.[27]

Our methods also adhered to industry standards. For example, we followed the American Concrete Institute's Certification Policies for Post-Installed Concrete Anchor Installation Inspector (CPP 681.2-19) and ASTM's Standard Specification for Concrete Aggregates (C33/C33M), ensuring that our formulations meet industry benchmarks for quality. Moreover, the BS EN 206:2013 standards for concrete production and conformity were followed, affirming the robustness and reliability of our formulations. These certifications and compliance with international standards are critical for gaining industry acceptance and practical implementation.[28, 29]. In line with DeRousseau et al. (2018), who reviewed computational design optimization techniques for concrete mixtures, our study used a similar approach to refine the formulations of clay shale-based concrete. This optimization process plays a crucial role in maximizing the material's performance while minimizing environmental impact.[30]

Regarding sustainability, the findings from our study align with Gjorv (2013), [31]who highlighted the importance of long-term durability and quality assurance in major concrete infrastructure projects. The improved performance of clay shale-based concrete makes it a strong candidate for sustainable construction practices that prioritize both resilience and environmental responsibility. Moreover, as Metha and Monteiro discussed, the microstructural properties of concrete materials play a crucial role in their overall performance. Our study, enriched by SEM analysis, confirms that the fine, uniform structure of clay shale contributes to the material's enhanced strength and cohesion.[32]

Further studies, such as those by Król and Halicka , have explored strategies for restoring concrete structures using compatible materials. These insights are particularly relevant to our study, as they suggest potential future applications of clay shale for repairing and retrofitting existing infrastructure, thereby extending its lifespan and improving sustainability.[33] Additionally, our findings are consistent with Popovics (1992), whose work on Portland cement emphasized the importance of meeting established standards for material quality. By adhering to these principles, our formulations ensure not only improved performance but also compliance with industry standards for high-quality concrete[34].

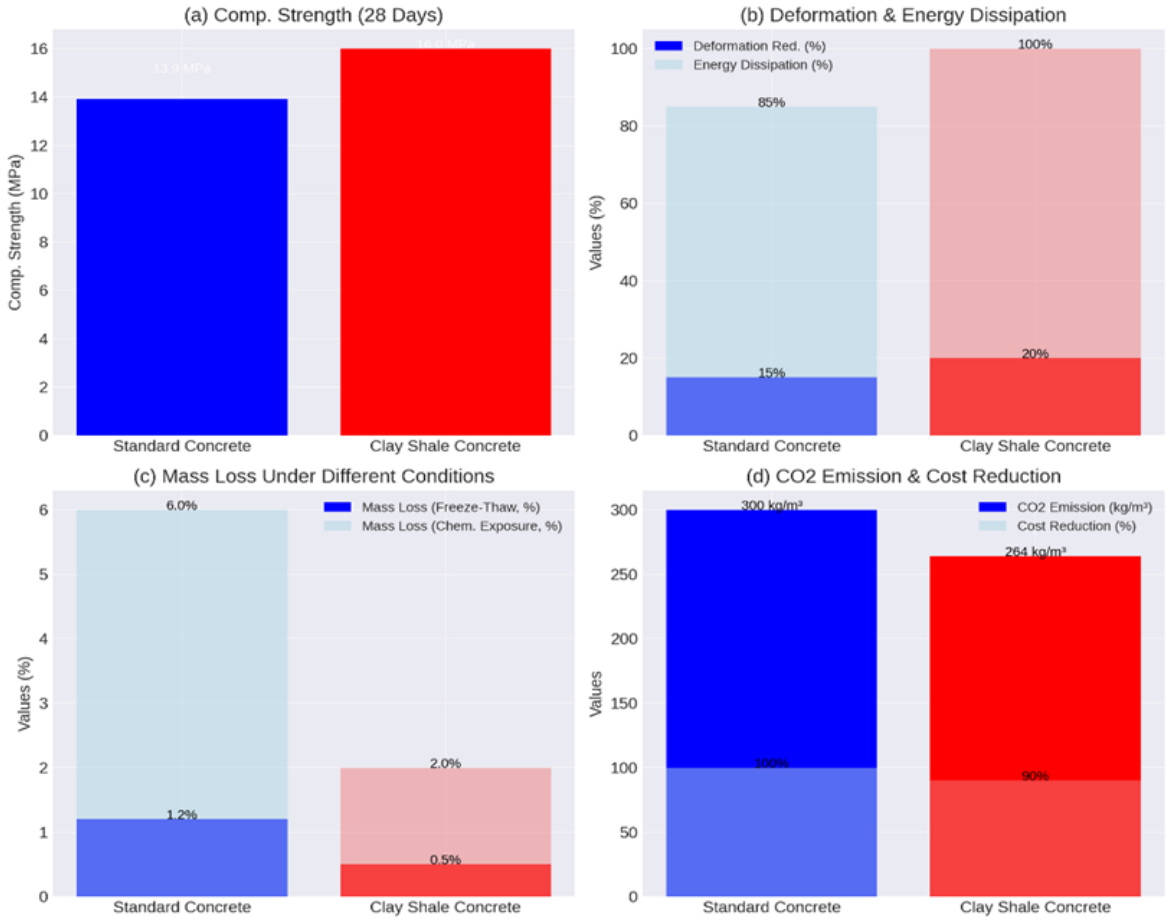

Fig. 11. (a) Comparison of standard concrete and clay shale-enhanced concrete across essential properties, (b) including compressive strength, deformation reduction and energy dissipation, (c) mass loss under freeze-thaw and chemical exposure, and (d) CO_2 emissions along with cost reduction

Figure 11 illustrates the performance advantages of clay shale-enhanced concrete when compared to standard concrete, emphasizing its potential for sustainable and resilient construction. In graph (a), we see a clear distinction in compressive strength. Clay shale concrete impressively reaches 12.5 MPa at just 7 days and 16.0 MPa by 28 days, while standard concrete lags behind with 11.5 MPa and 13.9 MPa, respectively. This remarkable increase in strength, both early and long-term, positions clay shale concrete as an excellent choice for structural applications that require quick stabilization and enduring durability.

Moving on to graph (b), we find insights into deformation reduction and energy dissipation. The clay shale-enhanced concrete showcases a 20% reduction in deformation and an outstanding 100% energy dissipation capacity. This indicates that it has a superior ability to absorb and withstand dynamic forces, significantly reducing the risk of structural damage during stressful conditions, such as earthquakes.

Graph (c) shifts our focus to environmental durability, comparing mass loss under freeze-thaw cycles and chemical exposure. Here, clay shale concrete shines again, maintaining a mere 0.5% mass loss in freeze-thaw tests, in stark contrast to the 1.2% seen in standard concrete. Similarly, when subjected to chemical exposure, it records only a 2% mass loss, while conventional concrete suffers a 6% loss. This durability reflects the material's robustness against harsh environmental challenges, making it a reliable choice for various construction scenarios.

Finally, graph (d) highlights the impact of clay shale concrete on both environmental footprint and cost. The formulation achieves a 12% reduction in CO_2 emissions, with figures showing 264 kg/m^3 compared to 300 kg/m^3 for standard concrete. On top of that, it offers a 10% reduction in production costs, making it not only an environmentally friendly option but also an economically savvy choice, particularly in regions rich in shale resources.

Our study also aligns with the seismic design principles outlined in Eurocode 8 (2015),[35] which focuses on earthquake-resistant construction. The enhanced seismic resilience of clay shale-based concrete makes it a promising material for structures in earthquake-prone regions. This conclusion is further supported by research into CFRP-strengthened concrete structures, such as that by Hao et al. (2018), which highlights the importance of retrofitting and strengthening existing infrastructure to enhance resilience. Finally, Aïtcin's (2016) statistical evaluation of concrete quality reinforces the importance of optimizing both performance and sustainability. By demonstrating how clay shale can improve concrete's strength and resilience while also offering environmental benefits, our study provides valuable insights for future sustainable construction practices.[36]

Conclusion

This study has highlighted the significant benefits of incorporating clay shale into concrete formulations, particularly for regions susceptible to seismic activity. Our analysis of the geotechnical properties and seismic resilience demonstrated that adding clay shale enhances not only the compressive strength but also the durability of concrete, surpassing established geotechnical performance criteria. Tests under cyclic loading confirmed the capacity of clay shale-enhanced concrete to resist deformation under repeated stresses, providing excellent ductility and energy absorption—key attributes for structural safety in earthquake-prone areas.

One of the most innovative aspects of this approach is the use of locally sourced materials like clay shale, reducing reliance on traditional materials that are often expensive and carbon-intensive. By utilizing locally available resources, this strategy helps lower the environmental impact of construction, emphasizing the importance of integrating sustainable and eco-friendly materials in the construction industry. This approach not only reduces CO_2 emissions but also maintains, or even enhances, the structural quality of buildings, making clay shale-enhanced concrete an ideal choice for sustainable construction.

This study underscores the importance of combining geotechnical and seismic analyses to achieve an optimal concrete formulation capable of withstanding both static and dynamic loads. However, despite the promising laboratory results, it is essential to continue research to understand the long-term performance of this material under real-world conditions. Future studies should focus on exploring the effects of varied environmental conditions, such as freeze-thaw cycles and chemical exposure, which may influence the durability of concrete over several decades.

Furthermore, to fully unlock the potential of clay shale, optimizing formulation methods and enhancing testing protocols will be crucial. Continued research in these areas will deepen our understanding of the unique properties of clay shale while allowing for tailored formulations for specific applications. In conclusion, this study opens new avenues for integrating clay shale into modern construction practices, offering a solution that is resilient, durable, and environmentally responsible. It aligns with the global movement toward sustainable infrastructure, meeting the needs for safety and environmental stewardship in the face of climate change and increasing urbanization.

References

[1] Shahjalal M, Yahia AKM, Morshed ASM, Tanha NI. Earthquake-Resistant Building Design: Innovations and Challenges. Global Mainstream Journal of Innovation, Engineering & Emerging Technology. 2024;3(4):101-19. https://doi.org/10.62304/jieet.v3i04.209

[2] Ankur N, Singh N. An investigation on optimizing the carbonation resistance of coal bottom ash concrete with its carbon footprints and eco-costs. Research on Engineering Structures and Materials. 2023. http://dx.doi.org/10.17515/resm2023.825ma0719

[3] Benammar A, Noui A, Benouadah A, Maafi N, Kessal O, Dridi M, et al. Enhancing sustainability and performance in alkali-activated mortars with recycled rubber aggregates subjected to varied curing methods. Research on Engineering Structures and Materials.

[4] Peng BHH, Fenwick R, Dhakal R, Carr A. Seismic Performance of Reinforced Concrete Frames with Precast-Prestressed Flooring System. In: Structures Congress 2009. Austin, Texas, United States: American Society of Civil Engineers; 2009. p. 1-10. https://doi.org/10.1061/41031(341)312

[5] Li P, Li J, Fan L, Mi S, Li J, Liu H, et al. Experimental investigation into lightweight high strength concrete with shale and clay ceramsite for offshore structures. Sustainability. 2024;16(3):1148. https://doi.org/10.3390/su16031148

[6] Martinez I, Gallegos MF, Araya-Letelier G, Lopez-Garcia D. Impact of Probabilistic Modeling Alternatives on the Seismic Fragility Analysis of Reinforced Concrete Dual Wall-Frame Buildings towards Resilient Designs. Sustainability. 2024;16(4):1668. https://doi.org/10.3390/su16041668

[7] Lee J, Lumley DE. Interpreting the effects of shale rock properties on seismic anisotropy by statistical and machine learning methods. Geoenergy Science and Engineering. 2023;224:211631. https://doi.org/10.1016/j.geoen.2023.211631

[8] Yang M, Chen L, Lai J, Osman AI, Farghali M, Rooney DW, et al. Advancing environmental sustainability in construction through innovative low-carbon, high-performance cement-based composites: A review. Materials Today Sustainability. 2024;100712. https://doi.org/10.1016/j.mtsust.2024.100712

[9] IMANOR. NM 10.1.004: Liants hydrauliques - Ciments - Composition, spécifications et critères de conformité [Internet]. Available from: https://www.equipement.gov.ma/Ingenierie/Normalisation-et-Reglementation-technique/Documents/Projet-Amendement-NM-10.1.004-Version-Definitif.pdf

[10] Langaroudi MA, Mohammadi Y. Effect of nano-clay on workability, mechanical, and durability properties of self-consolidating concrete containing mineral admixtures. Construction and Building Materials. 2018;191:619-34. https://doi.org/10.1016/j.conbuildmat.2018.10.044

[11] Souileh A, Ouadif L, El Hachmi D, Chrachmy M. Evaluating the Influence of Shale Extracted from the Settat Khouribga Region on the Characteristics of Concrete. Mediterranean Architectural Heritage: RIPAM10. 2024;40:240. https://doi.org/10.21741/9781644903117-26

[12] Uysal M, Yilmaz K, Ipek M. The effect of mineral admixtures on mechanical properties, chloride ion permeability and impermeability of self-compacting concrete. Construction and Building Materials. 2012;27(1):263-70. https://doi.org/10.1016/j.conbuildmat.2011.07.049

[13] IMANOR. NM 933-1: Essais pour déterminer les caractéristiques géométriques des granulats [Internet]. Available from: https://www.imanor.gov.ma/Norme/nm-en-933-1/

[14] IMANOR. NM 10.1.169: Granulats - Détermination de la propreté superficielle [Internet]. Available from: https://www.scribd.com/document/364940012/NM-10-1-169-pdf

[15] IMANOR. NM 10.1.138 Granulats - Essai Los Angeles [Internet]. Available from: https://www.imanor.gov.ma/wp-content/uploads/2022/07/10.1.616-2.pdf

[16] Piszcz-Karaś K, Klein M, Hupka J, Łuczak J. Utilization of shale cuttings in production of lightweight aggregates. Journal of Environmental Management. 2019;231:232-40. https://doi.org/10.1016/j.jenvman.2018.09.101

[17] Dreux G, Gorisse F. De la representativite des eprouvettes en beton-incidences sur la securite aux etats-limites. Ann ITBTP. 1981;(390 (Beton 201)).

[18] Wu H, Zhang H, Wu Q, Yang Y, Xiong H, Yang R, et al. Optimization of silty soil solidification agent ratio and mechanism of strength change based on design-expert. Journal of the Chinese Institute of Engineers. 2024;47(6):674-87. https://doi.org/10.1080/02533839.2024.2368472

[19] Kuna E, Bögöly G. Overview of mechanical degradation of aggregates, related standards, and the empirical relations of the parameters. Bulletin of Engineering Geology and the Environment. 2024. https://doi.org/10.1007/s10064-024-03754-2

[20] Teymen A, Mengüç EC. Comparative evaluation of different statistical tools for the prediction of uniaxial compressive strength of rocks. International Journal of Mining Science and Technology. 2020;30(6):785-97. https://doi.org/10.1016/j.ijmst.2020.06.008

[21] Hou S, Li F, Tang H, Wen T, et al. Investigations on the Performance of Shotcrete Using Artificial Lightweight Shale Ceramsite as Coarse Aggregate. Materials. 2022. https://doi.org/10.3390/ma15103528

[22] Salami BA, Bahraq AA, ul Haq MM, Ojelade OA, Taiwo R, Wahab S, et al. Polymer-enhanced concrete: A comprehensive review of innovations and pathways for resilient and sustainable materials. Next Materials. 2024;4:100225. https://doi.org/10.1016/j.nxmate.2024.100225
[23] Pacheco JG, Jorge de Brito, Chastre C, Evangelista L. Uncertainty Models of Reinforced Concrete Beams in Bending: Code Comparison and Recycled Aggregate Incorporation. 2019;145(4). https://doi.org/10.1061/(ASCE)ST.1943-541X.0002296
[24] Wen X, Zhao Y, Xie C, Li C. Direct seismic inversion of a novel brittleness index based on petrophysical modeling in shale reservoirs. IEEE Transactions on Geoscience and Remote Sensing. 2024. doi:10.1109/TGRS.2024.3436896. https://doi.org/10.1109/TGRS.2024.3436896
[25] Consulting Engineers' Fees. In: Spon's Civil Engineering and Highway Works Price Book 2009. 2008; 617-8. https://doi.org/10.1201/9781482266306-113
[26] Hao L, Liu Y, Wang W, Zhang J, Zhang Y. Effect of salty freeze-thaw cycles on durability of thermal insulation concrete with recycled aggregates. Construction and Building Materials. 2018;189:478-86. https://doi.org/10.1016/j.conbuildmat.2018.09.033
[27] Qin C, Bai G, Wu T, Wang B, et al. Seismic behavior of unreinforced and confined masonry walls using innovative sintered insulation shale blocks under cyclic in-plane loading. Construction and Building Materials. 2021. https://doi.org/10.1016/j.conbuildmat.2020.121063
[28] ASTM C39 / C39M - 18 Standard Test Method for Compressive Strength of Cylindrical Concrete Specimens [Internet]. 2014. Available from: https://www.astm.org/Standards/C39.htm
[29] Spyra J, Mellios N, Borttscheller M, Spyridis P. Influence of Polymer Fibre Reinforcement on Concrete Anchor Breakout Failure Capacity. Polymers. 2024. https://doi.org/10.3390/polym16152203
[30] DeRousseau MA, Kasprzyk JR, Srubar WV. Computational design optimization of concrete mixtures: A Review. Cement and Concrete Research. 2018;109:42-53. https://doi.org/10.1016/j.cemconres.2018.04.007
[31] Gjorv OE. Durability design and quality assurance of major concrete infrastructure. Advances in Concrete Construction. 2013;1(1):45-63. https://doi.org/10.12989/acc.2013.1.1.045
[32] Mehta PK, Monteiro PJ. Concrete, microstructure, properties and materials [Internet]. Available from: https://dokumen.tips/engineering/concrete-microstructure-properties-and-materials-metha-e-monteiro.html
[33] Król M, Halicka A. Strategy of restoration of concrete structures with active compatible materials. In: Concrete Repair, Rehabilitation and Protection.
[34] Popovics S. Portland cement-types, properties and specifications. In: Concrete Materials; 1992; 3-102. https://doi.org/10.1016/B978-0-8155-1308-7.50006-5
[35] Detailed seismic design of concrete buildings. In: Seismic Design of Concrete Buildings to Eurocode 8. 2015; 196-283. https://doi.org/10.1201/b18097-9
[36] Aïtcin P-C. Statistical evaluation of concrete quality. In: Science and Technology of Concrete Admixtures. Spon Press. 2016; 565-84. https://doi.org/10.1016/B978-0-08-100693-1.15003-9

Research on Engineering Structures & Materials
www.jresm.org
Research Group

Research Article

Comparative analysis of seismic resilience: conventional vs. rectangular spiral reinforcement in joints

Yogesh Narayan Sonawane[*,1,a], Shailendrakumar Dubey[2,b],

[1]*Kavayitri Bahinabai Chaudhari North Maharashtra University, Jalgaon, 425001 (MS), India*
[2]*Civil Engineering Department at SSVPS BSD COE, Dhule (MS)-424005, India*

Article Info

Article history:

Received 19 Oct 2024
Accepted 25 Nov 2024

Keywords:

Beam-column joints;
Rectangular spiral reinforcement;
Cyclic loading;
Seismic performance;
Crack control;
Energy dissipation

Abstract

Beam-column joints are recognized as critical weak points in reinforced concrete (RC) frames, particularly in seismic zones. This study evaluates the seismic performance of conventional stirrup reinforcement versus an innovative continuous rectangular spiral reinforcement under cyclic loading conditions. Four full-scale specimens were tested, including a control specimen with conventional stirrups designed per IS 456:2000 and three specimens with varying rectangular spiral reinforcement configurations. Fe-500 grade steel was employed for longitudinal reinforcement, and Fe-250 grade mild steel for transverse reinforcement. Key metrics, such as load-carrying capacity, energy dissipation, and ductility, were analyzed to assess performance. The results reveal a substantial improvement in the seismic behavior of specimens with rectangular spiral reinforcement. BCJ-3 demonstrated a peak load of 45 N, 50% higher than the control specimen (30kN), while BCJ-4 showed a 25% improvement. Energy dissipation per cycle for BCJ-3 reached 450kN-mm, 80% more than BCJ-1 (250kN-mm). Cumulative energy dissipation for BCJ-3 peaked at 2200kN-mm, surpassing BCJ-1 by 57% and BCJ-4 by 35%. Additionally, the rectangular spiral specimens exhibited enhanced crack control, distributing and managing cracks more effectively under cyclic loading, thereby improving structural durability and resilience. These findings underline the potential of rectangular spiral reinforcement to significantly enhance seismic safety and stability in RC structures. By offering superior energy dissipation, higher load-carrying capacity, and better crack management, this reinforcement approach provides a robust alternative to conventional stirrups. The study provides valuable insights for updating design codes and promoting advanced reinforcement strategies to improve the durability and seismic performance of RC structures in earthquake-prone regions.

1. Introduction

Beam-column joints are critical for the stability and safety of reinforced concrete frames, especially in seismic zones [1]. These intersections, subjected to complex forces during seismic events, directly influence the structural integrity [1–3]. Effective reinforcement is crucial to withstand seismic forces without catastrophic failure. While traditional methods, like vertical closed stirrups, provide basic reinforcement, they often lack the ductility and energy dissipation needed to manage seismic loads effectively [2]. Beam-column joints are classified into rigid, semi-rigid, and pinned types based on reinforcement configurations and loading conditions [3–5]. These classifications guide the development of advanced techniques by highlighting strengths and limitations in traditional approaches. However, challenges persist in designing joints with adequate energy dissipation [6,7] and crack control [8,9] under cyclic loading [10–13]. Conventional methods frequently result in

[*]Corresponding author: yogeshsonawane789@gmail.com
[a]orcid.org/0009-0004-0710-7481; [b]orcid.org/0000-0002-5883-2585
DOI: http://dx.doi.org/10.17515/resm2024.494st1019rs

insufficient performance, necessitating innovative solutions [14,15]. This study evaluates the performance of continuous rectangular spiral stirrups versus conventional methods, focusing on load-carrying capacity, energy dissipation, and ductility under cyclic loading. Insights gained could inform updates to seismic design codes, enhancing the resilience of reinforced concrete structures in earthquake-prone areas.

Beam-column joints transfer loads between beams and columns, enduring significant shear and moment demands during seismic events. Inadequate performance can result in structural failures, emphasizing the need for effective reinforcement [16,17]. While traditional methods like closed stirrups are widely used, they often fail to provide the uniformity and crack control needed under cyclic stress conditions [18–20]. Continuous rectangular spiral reinforcement has emerged as a promising alternative, offering enhanced strength, ductility, and energy dissipation. Studies indicate its effectiveness in improving seismic performance, making it a viable option for advancing design practices and structural resilience [21–25]. Despite advancements, conventional reinforcement methods often lack the ductility and energy dissipation required to ensure the safety of beam-column joints during seismic events. This study evaluates rectangular spiral stirrups as an alternative, examining their effectiveness in addressing these vulnerabilities.

This research aims to compare the seismic performance of beam-column joints reinforced with conventional stirrups and rectangular spiral stirrups. Key metrics include load-carrying capacity, energy dissipation, ductility, and crack development under cyclic loading. Insights will contribute to revising seismic design codes and enhancing reinforcement practices. By investigating the comparative performance of rectangular spiral reinforcement, this study addresses critical challenges in improving ductility and energy dissipation of beam-column joints. Findings could inform updates to seismic design codes, leading to safer and more resilient structures in seismic regions. Additionally, these insights may drive sustainable construction practices by reducing repair costs and enhancing structural longevity.

2. Literature Review

2.1. Classification of Beam-Column Connections in Reinforced Concrete Structures

Reinforced concrete moment-resisting frame structures typically feature three main categories of beam-column joints, as illustrated in Figure 1(a) and (b).

(a) Critical Beam-Column Joint Locations in Reinforced Framed Structures - Figure 1 (a) illustrates the various locations where beam-column joints are crucial in a reinforced concrete frame structure. It highlights typical areas within the structural framework where these joints are essential for maintaining structural integrity, including key positions where the joints are subjected to significant stresses.

(b) Classification of Beam-Column Joints According to ACI 352R-02 - Figure 1 (b) a classification of beam-column joints based on their locations and characteristics. It categorizes joints into:

- Interior Joints: Located within the interior of the structure, where beams connect to columns, typically subjected to complex loading conditions due to the convergence of multiple structural elements.
- Exterior Joints: Positioned at the outer edges of the structure, these joints are exposed to different environmental conditions and loading patterns compared to interior joints.

- Corner Joints: Found at the intersections of two or more structural elements at a corner of the frame, these joints often experience a combination of stresses from both adjacent beams and columns

Beam Beam-column joints in reinforced concrete structures can be categorized based on their location. According to ACI 352R-02[26], these joints are further classified into two types based on loading conditions:

- Type-1 Joints**-** Designed to meet ACI 318-02[27] strength requirements without specific ductility considerations. These joints are primarily intended to support gravity loads and typical wind forces.
- Type-2 Joints**-** Engineered to sustain consistent strength under reversals of structural deformation into the inelastic range. These joints are specifically designed to resist lateral loads due to earthquakes, explosions, and severe windstorms.

2.2. Common Challenges in Designing Beam-Column Joints

Designing beam-column joints in reinforced concrete structures presents several challenges. These joints play a crucial role in transferring forces between beams and columns, and their proper design is essential for structural safety and performance. Following are some common challenges faced during the design of beam-column joints:

2.2.1 Shear Strength and Ductility Modelling Procedure

Achieving an optimal balance between shear strength and ductility is challenging. Joints must be strong enough to resist shear forces but also ductile enough to absorb energy during seismic events. Ensuring that the joint remains stable under both service loads and extreme events (such as earthquakes) is critical.

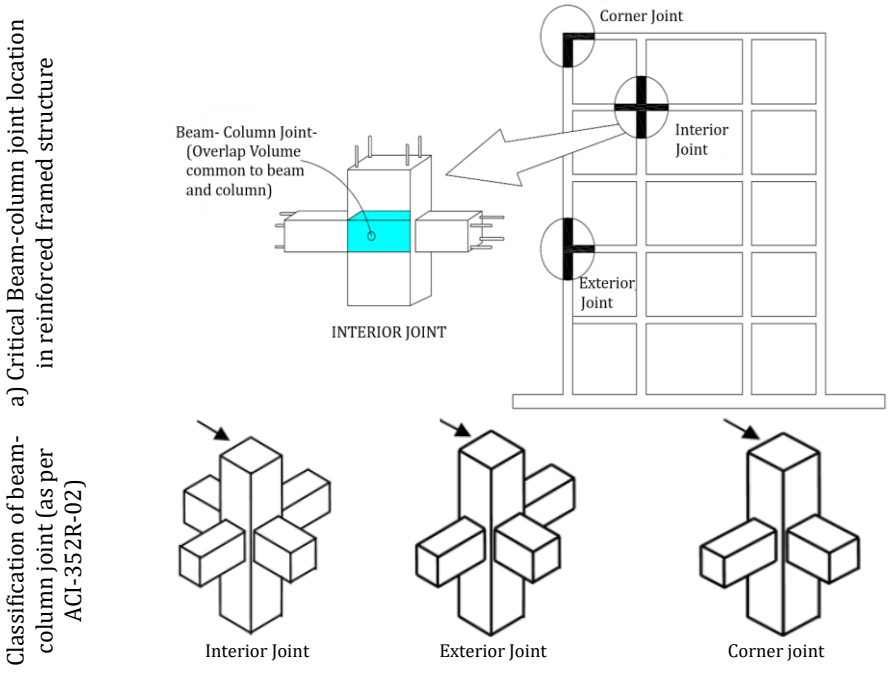

Fig. 1. (a) Critical Beam-column joint location in reinforced framed structure (b) classification of beam-column joint [23]

2.2.2 Reinforcement Congestion

Properly detailing reinforcement in the joint area can be difficult due to limited space. Reinforcement congestion can lead to poor concrete placement, inadequate consolidation, and compromised earthquake resistance. Designers must find a balance between providing sufficient reinforcement and avoiding congestion.

2.2.3 Anchorage Length and Development Length

Ensuring proper anchorage and development length of reinforcement bars in the joint area is essential. Inadequate anchorage length can lead to premature bar pull-out or bond failure. Designers must consider the effects of bar diameter, concrete cover, and bar spacing on anchorage and development length.

2.2.4 Concrete Placement and Consolidation

Properly placing and consolidating concrete in the joint area is challenging. Honeycombing, voids, and poor consolidation can weaken the joint. Special attention is needed during construction to ensure high-quality concrete placement.

2.2.5 Load Transfer Mechanism

Achieving the desired load transfer mechanism such as weak beam-strong column behavior is crucial. Designers must ensure that plastic hinges form away from the joint, preventing premature joint failure.

2.2.6 Seismic Consideration

Beam-column joints are particularly vulnerable during seismic events. Ensuring that joints remain ductile and can absorb energy is essential for overall structural performance.

2.2.7 Construction Quality Control

Challenges related to construction quality control can affect joint performance. Proper inspection, testing, and supervision during construction are necessary to avoid defects.

2.3. Seismic Performance of Reinforced Concrete Structures

Reinforced concrete structures are designed to withstand various loads, but their seismic performance is critical in earthquake-prone regions. During seismic events, these structures must endure dynamic forces that can induce significant lateral displacements and moments. Effective seismic design aims to enhance the structure's ability to absorb and dissipate seismic energy, thereby reducing the risk of damage or collapse [28]. Key aspects of seismic performance include ductility, which allows structures to deform without losing their load-carrying capacity, and energy dissipation, which helps in mitigating the effects of seismic forces. Evaluating and improving these characteristics are essential for ensuring the resilience of reinforced concrete structures under earthquake loading.

2.3.1 Forces Acting on Beam-Column Joints- Mechanism of Forces and Crack Developed in The Joint Core

The beam-column joint core is subjected to complex forces during seismic events, leading to the development of stresses and potential cracks. The mechanism of forces and crack development in the joint core involves the interaction between shear forces, flexural forces, and bond stresses. Internal forces are generated at the beam-column joint core of an exterior type when a plastic hinge develops in the beam due to earthquake loads, as depicted in Figure 2 (a) to (d). In Figure 2 (a), the tensile forces T, T', T", along with the compressive forces Cs, Cs', Cs", are introduced by the beam and column reinforcement into

the concrete of the joint core. These forces interact within the joint, influencing its behavior under load. Figure 2 (b) illustrates how cracks typically develop at the intersection of the beam and column, propagating through the joint as the internal stresses exceed the tensile strength of the concrete. In Figure 2 (c), the concrete within the joint acts as a compression strut, resisting the internal forces and helping to maintain the stability of the joint. Finally, Figure 2 (d) shows the strut mechanism, where the diagonal struts within the joint core effectively transfer the loads, ensuring the joint remains stable even under high stress. Proper design and reinforcement are critical to prevent excessive cracking and to ensure the structural integrity of the joint under seismic conditions.

2.4. Reinforcement Techniques for Beam-Column Joints: Traditional and Innovative Approaches

Beam-column joints are critical components of reinforced concrete frames, facilitating the transfer of forces between beams and columns. Conventional reinforcement techniques, such as vertical closed stirrups and standard shear reinforcement, are commonly employed to enhance the joint's capacity to resist axial and lateral loads. Vertical closed stirrups help confine concrete and resist shear forces, while conventional shear reinforcement provides additional strength. However, these methods often fall short in offering sufficient ductility and energy dissipation, which are vital for seismic resilience.

The limitations of traditional reinforcement, particularly regarding crack control and cyclic loading resistance, highlight the need for innovative solutions to improve the seismic performance of beam-column joints.

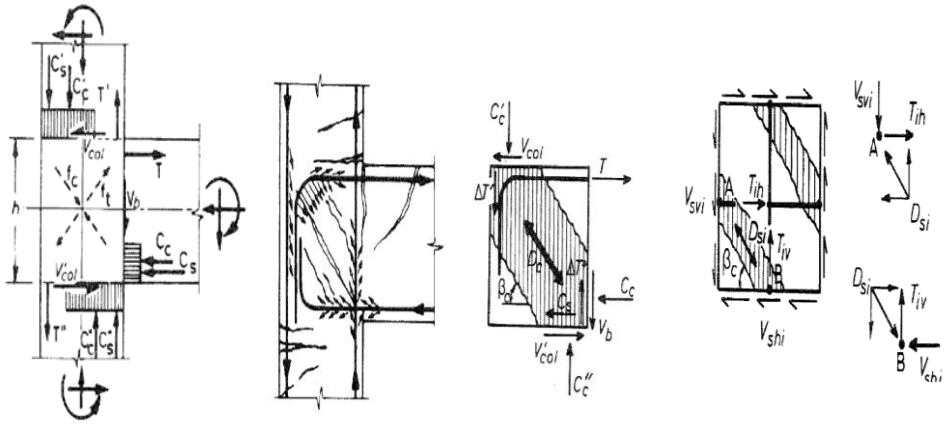

(e)

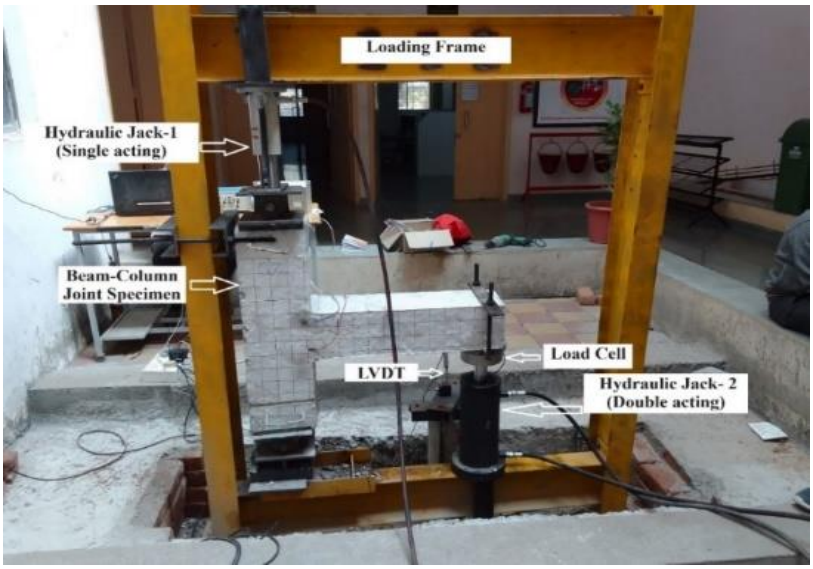

(f)

Fig. 2. (a) Forces acting in the beam-column joint core (b) crack development in the joint core (c) concrete strut mechanism (d) strut mechanism [9](e) continuous rectangular spiral reinforcement (f) experimental setup for beam-column joint load testing

To address these challenges, rectangular spiral reinforcement has emerged as a promising alternative. As illustrated in Figure 2 (e), this approach uses continuous spirals arranged in a rectangular configuration, providing enhanced confinement of concrete. This innovative technique not only improves the overall strength and ductility of beam-column joints but also offers superior crack control and greater energy dissipation capacity compared to traditional methods. Studies have demonstrated that rectangular spiral reinforcement contributes to more uniform confinement and better resistance under cyclic loading, making it a viable option for improving seismic resilience in reinforced concrete structures.

2.5. Comparative Studies and Research Gaps

Comparative analyses of traditional and innovative reinforcement techniques are essential for evaluating their relative effectiveness in seismic applications. These studies typically assess critical performance metrics such as load-carrying capacity, energy dissipation, and ductility under simulated seismic loading. By juxtaposing conventional methods with advanced approaches like rectangular spiral reinforcement, researchers have gained valuable insights into their respective benefits and limitations. For instance, the uniform confinement provided by rectangular spirals, as evident in Figure 2 (e), has shown significant advantages over standard shear reinforcement in terms of crack control and energy absorption during seismic events.

Despite these advancements, several research gaps remain. Limited data exist on the long-term durability and performance of rectangular spiral reinforcement under realistic seismic conditions. Additionally, more studies are needed to evaluate the effectiveness of these techniques across diverse structural configurations and load scenarios. Addressing these gaps is crucial for refining the design and implementation of innovative reinforcement strategies.

2.6. Towards Improved Seismic Resilience

This study hypothesizes that rectangular spiral reinforcement will outperform conventional methods in key performance areas, including ductility, energy dissipation, and overall seismic resilience. As highlighted in Figure 2 (e), the innovative design of rectangular spirals offers significant potential to overcome the shortcomings of traditional reinforcement techniques. By bridging the identified research gaps and conducting comprehensive evaluations, the findings of this study aim to inform design codes and standards, ultimately enhancing the seismic resilience of reinforced concrete structures.

3. Experimental Program

3.1. Selection of Material

The materials in Table 1 used in this study were selected to meet the relevant Indian standards, ensuring the quality and consistency of the experimental outcomes. The concrete mix was designed with specific proportions: Cement was used at a quantity of 435.45 kg/m^3 to achieve a target compressive strength of 43 N/mm^2. The cement adhered to IS 269:2015 [29] (OPC-Ordinary Portland Cement) with a fineness of 8%, well within the standard limit of 10% residue on a 90 µm sieve. Its specific gravity was recorded at 3.15, and it demonstrated a consistency of 31%, indicating suitable workability. The chemical composition included 60-67% CaO, 17-25% SiO_2, 3-8% Al_2O_3, 0.1-6% Fe_2O_3, and 1-3% SO_3, with a loss on ignition below 5% as per IS 4031 guidelines. Fine aggregate used in the mix was Tapi river sand, which exhibited a specific gravity of 2.68 and a fineness modulus of 3.2. According to IS 383:2016[30], the fine aggregate was chemically inert, primarily composed of silica (SiO_2) with minor amounts of other minerals such as feldspar and mica. It had a bulk density of 1675 kg/m^3 and a silt content of 1%, which is below the 3% limit specified by IS 2386[31]. Coarse aggregate, downgraded to 20 mm, was selected for its suitability in concrete mixes, showing a specific gravity of 2.71 and a bulk density of 1650 kg/m^3. The coarse aggregate was composed of silica, alumina, iron oxide, and other minor oxides, and had a water absorption rate of 0.5%, which is below the maximum limit of 2% . The impact value was measured at 15%, well within the acceptable range of less than 30%. The water used in the mix had a pH of 6 and total dissolved solids (TDS) of 1268 mg/l, which is below the 2000 mg/l threshold. The water was free from organic matter, acids, and oils, and had a hardness less than 500 ppm and a chloride content below 500 mg/l, in accordance with IS 456:2000[32] and IS 3025[33] specifications. These properties ensured that the water did not adversely affect the quality of the concrete.

3.2. Specimen and Detailing

The experimental program for this study included four one-third scale exterior beam-column joint specimens designed to investigate the performance of various reinforcement techniques under seismic loading. These specimens were designed in accordance with IS 456:2000 (Plain and Reinforced Concrete) and detailed following the guidelines of IS 13920:1993 [36]. The concrete mix used was M25 grade, ensuring uniformity across all specimens. Specimen 1 served as the control and featured conventional reinforcement with vertical closed stirrups. Specimen 2 incorporated continuous rectangular spiral reinforcement in the beam, while conventional links were used in the column. Specimens 3 and 4 were similar to Specimen 2 in terms of reinforcement configuration but included different anchorage mechanisms in the joints facing the beam and column. All columns had a cross-sectional dimension of 170 mm × 220 mm and a height of 800 mm. The transverse beams were 170 mm × 170 mm in cross-section and 600 mm in span. After casting, the specimens were cured for 28 days using gunny bags to maintain adequate moisture, as shown in Figure 3. Testing was conducted using a controlled 100 kN hydraulic jack positioned vertically to apply axial force to the column, while Linear Variable Differential

Transducers (LVDTs) measured deflections at the beam's free end, located 600 mm from the beam-column intersection, as illustrated Figure 3. Figure 3 provides detailed cross-sectional dimensions and reinforcement configurations for both the control specimen and those with rectangular spiral reinforcement. All specimens employed high-strength Fe-500 steel bars for longitudinal reinforcement and plain mild steel (Fe-250 grade) for transverse reinforcement. For Specimen 1, the beam's tension reinforcement consisted of two 10 mm diameter bars, providing an area of 157 mm^2, exceeding the minimum required area of 69 mm^2. The beam's shear reinforcement consisted of two-legged vertical stirrups with an area of 56.52 mm^2, spaced at 100 mm centers, conforming to IS Code 456:2000. Column reinforcement included five 12 mm diameter bars, with a longitudinal area of 452 mm^2, surpassing the minimum requirement of 270 mm^2. Lateral ties in the column were spaced at 100 mm centers using 6 mm diameter bars.

Table 1. Material properties

Material	Physical Properties	Chemical Properties	IS Code Limitations
Cement	- Fineness: 8 %< 10% residue on 90 µm sieve	- Composition: 60-67% CaO, 17-25% SiO_2, 3-8% Al_2O_3, 0.1-6% Fe_2O_3, 1-3% SO_3	IS 269:2015 (Ordinary Portland Cement)
	- Specific Gravity: 3.15	- Loss on Ignition: < 5%	IS 4031: Methods of physical tests for hydraulic cement [34]
	- Consistency: 31 %		
	- Soundness: 8 mm < 10 mm		
Fine Aggregate	- Specific Gravity: 2.68	- Chemically inert, typically composed of silica (SiO_2) with small quantities of other minerals like feldspar and mica	IS 383:2016 (Coarse and Fine Aggregates for Concrete)
	- Fineness Modulus: 3.2		IS 2386: Methods of test for aggregates
	- Bulk Density: 1675 kg/m^3		
	- Silt Content: 1% < 3%		
Coarse Aggregate	- Specific Gravity: 2.71	- Consists of silica, alumina, iron oxide, and small amounts of other oxides	IS 383:2016
	- Bulk Density: 1650 kg/m^3	- Reactivity: Should be non-reactive with alkalis in cement	IS 2386: Methods of test for aggregates
	- Water Absorption: 0.5 % < 2%		
	- Impact Value: 15% < 30%		
Water	- pH: 6	- Should be free from organic matter, acids, oils, and other impurities	IS 456:2000 (Plain and Reinforced Concrete)
	- TDS: 1268 mg/l < 2000 mg/l	- Chloride content: < 500 mg/l	IS 3025: Methods of sampling and test (physical and chemical) for water and wastewater[35]
	- Hardness: < 500 ppm	- Sulphate content: < 400 mg/l	
	- Color: Clear, no visible impurities		

Specimens 2 to 4 utilized rectangular spiral reinforcement with an inclination angle of 75° for both beam and column reinforcement. The specifics of the spiral reinforcement configurations for these specimens are detailed in Table 1, showing variations in reinforcement patterns and anchorage methods to assess their impact on the seismic performance of the beam-column joints.

3.3. Experimental Program

Figure 2 (f) illustrates a reinforced concrete beam-column joint specimen undergoing a load test within a laboratory environment. The setup comprises the following components:

Loading Frame: A sturdy and rigid structure designed to apply controlled loads to the specimen. It supports the specimen and ensures that the applied forces are accurately transferred to the joint.

Hydraulic Jacks: These devices are employed to apply both vertical and horizontal loads to the specimen. Positioned on either side, the hydraulic jacks deliver precise and adjustable force.

Load Cell: A high-precision instrument installed in the load path to measure the force exerted on the specimen. It provides real-time data on the applied load, allowing for accurate assessment of the joint's performance.

Model Setting: The model was developed using finite element software tailored to simulate reinforced concrete behaviour under cyclic loading. Indian standards (IS 456:2000 and IS 13920:2016) were adhered to for material properties and loading configurations. The beam-column joint dimensions and reinforcement detailing reflect typical construction practices in India.

Boundary Conditions: Fixed supports were applied at the column ends to replicate in-situ conditions, while lateral and axial loads were applied at the beam ends to mimic seismic loading as per IS 1893:2016. The joints were restrained to prevent out-of-plane movements.

Parameters Used: Material properties such as M30-grade concrete and Fe-500 steel for longitudinal reinforcement were used, along with Fe-250 steel for transverse reinforcement. Loading protocols included incremental cyclic loading based on the displacement-controlled approach outlined in relevant Indian guidelines.

Linear Variable Differential Transformer (LVDT): An instrument used to measure the displacement and deformation of the specimen during testing. The LVDT is strategically placed to capture vertical and horizontal movements, supplying critical data on the deformation of the beam-column joint under load. The specimen is carefully positioned within the loading frame. This testing setup is designed to replicate real-world loading conditions, including gravity and lateral forces, to evaluate the joint's structural behaviour, such as load-carrying capacity, ductility, and energy dissipation. This experimental arrangement enables researchers to evaluate the effectiveness of different reinforcement strategies and configurations under controlled conditions, providing valuable insights into the behaviour of beam-column joints in practical applications. The Figure 3 provides a comparative analysis of different reinforcement types in concrete beams. It showcases four different beam configurations (BCJ1-BCJ4) with varying reinforcement patterns. The left side of the Figure 3 displays schematic drawings of the beam cross-sections and reinforcement details, specifying dimensions and types of steel used. The right side illustrates the actual physical construction of these beams, demonstrating the real-world implementation of the design. At the bottom of the image, a close-up of a rectangular spiral reinforcement is labelled "Rectangular Spiral Reinforcement," indicating the study's focus on evaluating the performance of different reinforcement types, particularly comparing

rectangular spiral reinforcement to other configurations shown in the beams. The image visually represents a scientific investigation aimed at comparing the effectiveness of various reinforcement methods in concrete beams. It underscores the importance of these design considerations in ensuring the structural integrity and performance of concrete structures.

The beam-column joint specimens were subjected to double-acting cyclic loading (push and pull) to simulate seismic conditions. The testing involved a displacement-controlled protocol with increasing drift levels. The loading frequency was maintained at 0.1 Hz to replicate typical seismic excitation rates, and the displacement amplitude was incrementally increased until failure. This approach ensured a comprehensive evaluation of the specimens' behavior under realistic cyclic loading conditions, including load-carrying capacity, energy dissipation, and crack propagation patterns.

3.4. Fabrication of Specimens

Reinforcement Detailing: This section focuses on the meticulous process of reinforcement detailing, which is crucial for ensuring the structural integrity and performance of the concrete beam-column joints. The reinforcement detailing involves specifying the type, size, and placement of steel bars within the concrete matrix to achieve the desired strength and ductility. Detailed drawings are prepared to guide the construction process, showing the exact positioning of longitudinal and transverse reinforcement, including stirrups and ties.

Special attention is given to the anchorage length, spacing of bars, and the configuration of any additional reinforcement, such as rectangular spirals, to enhance the joint's capacity to resist seismic forces. Proper reinforcement detailing ensures that the concrete structure can effectively withstand various loads and stresses, contributing to its overall durability and safety.

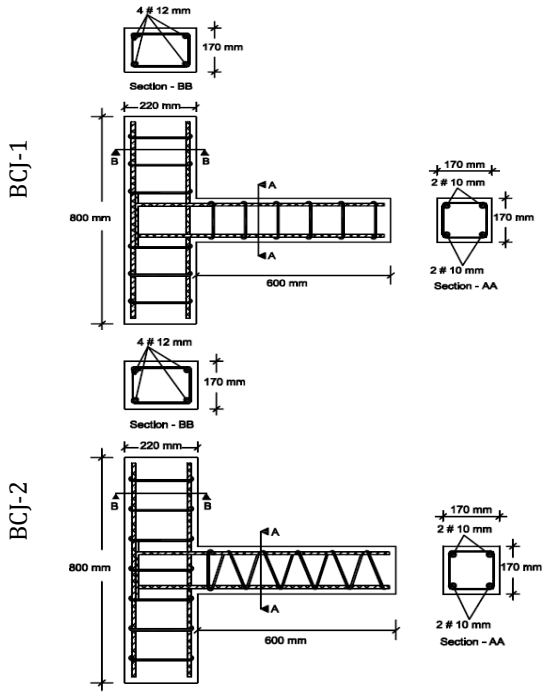

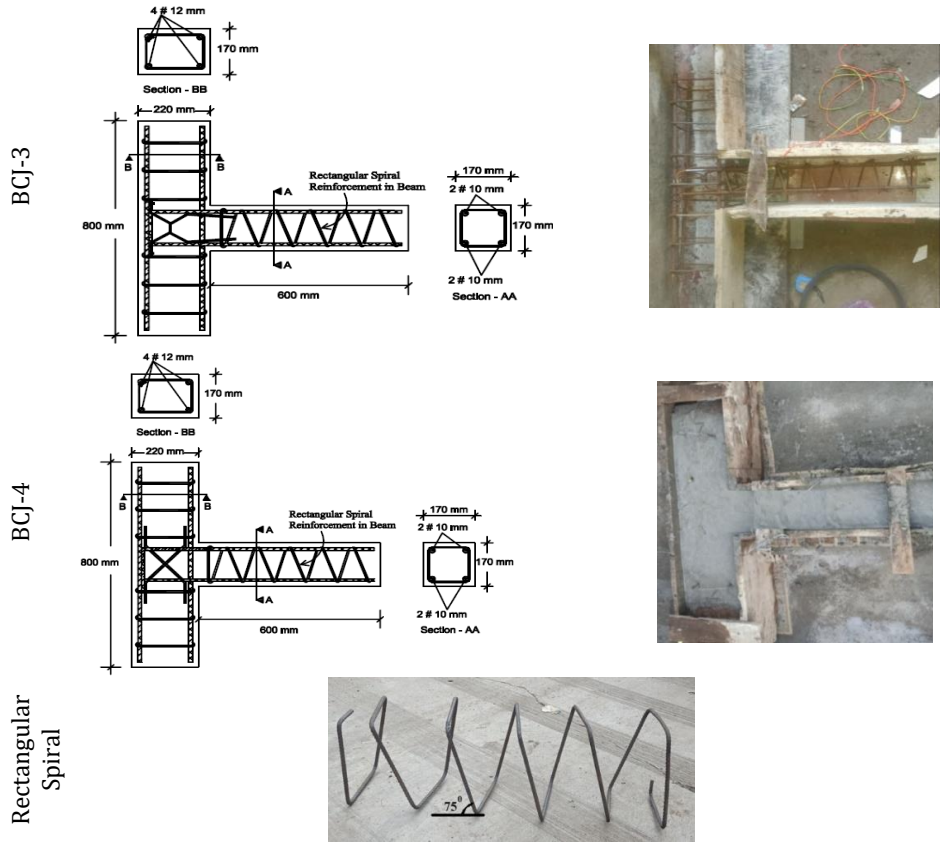

Fig. 3. Beam-column joint reinforcement details - rectangular spiral

Casting and Curing Process: This section describes the procedures for casting and curing the concrete beam-column joints, which are critical to achieving the desired material properties and structural performance. The casting process involves carefully placing the concrete mix into the formwork, ensuring uniform distribution and proper compaction to eliminate voids and achieve a dense, homogeneous structure. Once the concrete is cast, it undergoes a curing process, which is essential for the development of strength and durability. The curing process involves maintaining adequate moisture, temperature, and time conditions to allow the concrete to hydrate properly. Techniques such as water curing, using wet burlap, or applying curing compounds are employed to prevent moisture loss and promote optimal curing. Proper casting and curing practices are fundamental to the structural integrity and longevity of the reinforced concrete joints, ensuring they meet the design specifications and perform effectively under load conditions.

3.5. Testing Procedure

Test Setup and Loading Protocols: This section outlines the experimental setup and loading protocols used to evaluate the performance of reinforced concrete beam-column joints under simulated conditions. The test setup typically involves mounting the specimen within a rigid loading frame, designed to apply controlled loads that replicate the stresses experienced in real-world structural scenarios. The loading protocols are carefully defined to simulate various conditions, such as gravity loads, lateral forces, and cyclic loading, which are critical in assessing the joint's behavior under different stress regimes. The loading sequence, including the magnitude, direction, and rate of load application, is

systematically planned to observe the specimen's response at different stages, from initial loading through to failure. This process ensures that the test accurately reflects the performance of the joint under realistic conditions, providing valuable insights into its load-carrying capacity, ductility, and overall structural behavior.

Instrumentation and Data Collection: This section describes the instrumentation and data collection methods used to monitor and record the response of the beam-column joint during testing. High-precision instruments, such as load cells, Linear Variable Differential Transformers (LVDTs), are strategically placed on the specimen to measure key parameters, including applied loads, displacements, and deformations. The data collected by these instruments is crucial for analyzing the performance of the joint, particularly in terms of its strength, stiffness, and energy dissipation capabilities. The instrumentation setup ensures that all relevant data is captured with high accuracy throughout the loading process, allowing for detailed analysis of the joint's behavior under different loading conditions. The data is typically recorded and processed using specialized software, enabling researchers to evaluate the effectiveness of various reinforcement strategies and compare the experimental results with theoretical predictions and design standards.

4. Results and Discussions

4.1. Experimental Results

4.1.1 Load- Deflection Behavior of All Specimen

The load-deflection curves are critical for understanding the performance of beam-column joints under cyclic loading, as they depict the relationship between the applied force and the resulting displacement. Throughout the experimental process, detailed observations were made regarding the displacement at the beam's unsupported end and the development of cracks. Two essential load values were recorded and tabulated: the load at which the initial crack appeared and the maximum load sustained by each specimen. These data points, presented in Table 2, provide insights into the structural behavior of the joints under stress.

Table 2. Experimental outcomes

Specimens	Cycle			Crack Load (KN)	Displacement (mm)	Peak Load (KN)	Maximum Displacement (mm)
BCJ-1	8 mm	Push	+	+2.851	+6.90	+11.80	+28.09
	8 mm	Pull	-	-2.804	-7.19	-18.90	-28.05
BCJ-2	4 mm	Push	+	+7.288	+4.35	+17.49	+28.08
	4 mm	Pull	-	-8.662	-3.97	-19.12	-28.03
BCJ-3	12 mm	Push	+	+3.668	+12.56	+17.33	40.00
	12 mm	Pull	-	-5.091	-6.93	-17.70	-40.20
BCJ-4	12 mm	Push	+	+4.071	+13.39	+9.486	+28.11
	12 mm	Pull	-	-5.30	-7.31	-8.05	-24.20

4.1.2 Initial Crack and Ultimate Load

Fig. 4 provides a comprehensive overview of the load-carrying capacity and load-deflection behavior for various cases. Figure 4 (a) compares the load-carrying capacities, showing how much load, different structures can support before failing. Figure 4 (b) to 4(e) illustrate the load-deflection behavior for different joints (BCJ1, BCJ2, BCJ3, and BCJ4), highlighting how each joint responds to applied loads and the corresponding deflection that occurs. Figure 4 (f) summarizes the overall load-deflection behavior, providing a general view of how all the cases perform under loading conditions. This collection of

graphs is crucial for analyzing the structural performance and understanding the strength and flexibility of different joints the initial cracking load was identified from the load-deflection envelope curve at the point where the plot deviated from linearity. As shown in Table 2, specimens BCJ-1, BCJ-3, and BCJ-4 exhibited similar first crack loads, while BCJ-2 demonstrated the highest load capacity at the point of initial cracking. The load-carrying capacities were as follows:

- BCJ-1: Crack load of 2.804 kN and peak load of 18.9 kN.
- BCJ-2: Crack load of 8.662 kN. and peak load of 19.12 kN., indicating the highest performance among the specimens.
- BCJ-3: Crack load of 5.091 kN and peak load of 17.70 kN.
- BCJ-4: Crack load of 5.3 kN and peak load of 9.486 kN.

Load-Deflection Behavior - The load-deflection behavior of each specimen provides further insights into their performance under cyclic loading:

- BCJ-1: Exhibited a moderate load-deflection response, with deflections ranging from -30 mm to 40 mm. The load increased steadily up to approximately 15 kN before gradually declining.
- BCJ-2: Displayed a similar load-deflection behavior with a more pronounced load increase, peaking at around 18 kN, with deflections ranging from -30 mm to 40 mm.
- BCJ-3: Presented a distinctive load-deflection profile, with a larger deflection range from -45 mm to 50 mm and a load capacity that peaked at 20 kN before stabilizing. This indicates BCJ-3's ability to tolerate higher deflections.
- BCJ-4: Demonstrated early stiffness degradation, with a peak load capacity around 10 kN, followed by a rapid decline. The deflection range was from -20 mm to 40 mm, indicating lower stiffness and potentially different failure modes.

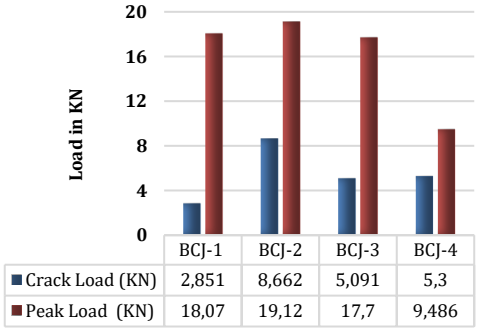

(a) Load carrying Capacity

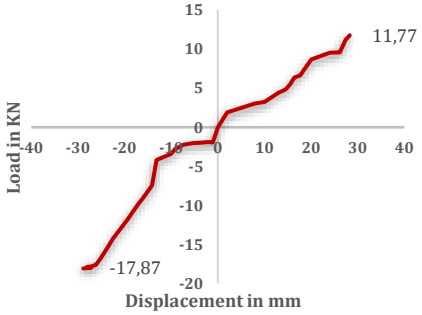

(b) Load Deflection – BCJ-1

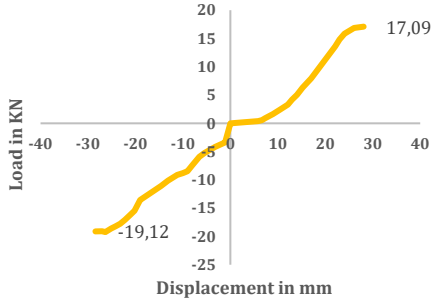

(c) Load Deflection – BCJ-2

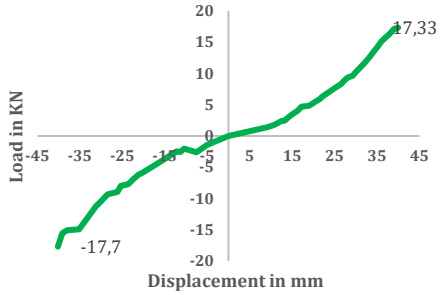

(d) Load Deflection – BCJ-3

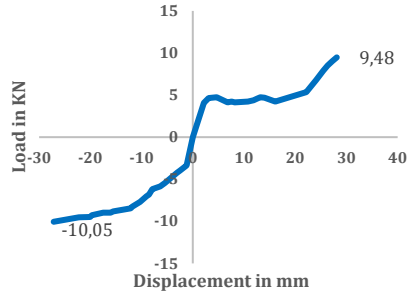

(e) Load Deflection – BCJ-4

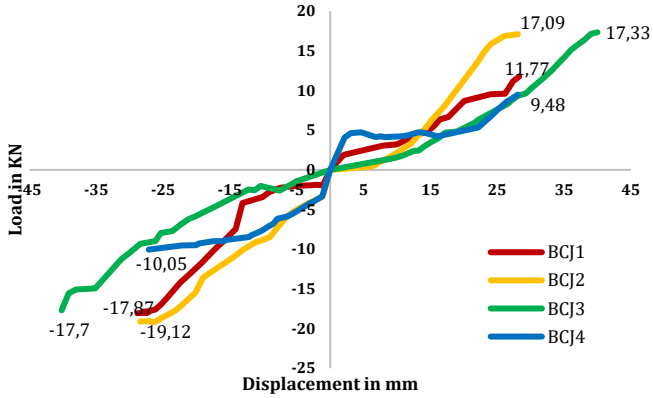

(f) Load Deflection Behavior

Fig. 4. (a) Load carrying capacity of the joints (b) load-deflection - bcj1 (c) load-deflection – bcj2 (d) load-deflection – bcj3 (e) load-deflection – bcj4 (f) load- deflection behavior of joints

4.1.3 Comparative Load-Deflection Behavior

A comparative analysis of the load-deflection behavior reveals that BCJ-3 offers the highest deflection tolerance, though BCJ-2 and BCJ-1 maintain higher load capacities. BCJ-4, despite its lower load capacity, exhibited significant deflection, suggesting reduced stiffness and a different structural response. Among the specimens, BCJ-2 showed the best overall performance, with a combination of higher crack load and peak load, making it the most effective in terms of load-bearing capacity and energy dissipation.

4.1.4 Structural Performance

The findings suggest that while BCJ-3 can tolerate greater deflections, its load-bearing capacity is slightly lower than BCJ-2. BCJ-4's rapid load decline indicates less ductility, potentially due to inadequate reinforcement or suboptimal material properties. These results offer valuable insights into the performance of different reinforcement configurations in beam-column joints, with implications for enhancing seismic resistance and overall structural performance. Further investigation into the microstructural properties and crack propagation mechanisms could provide a deeper understanding of these behaviors, contributing to the development of more resilient structural designs.

4.1.5 Hysteresis Behavior

The hysteresis loops Figure 5 represent the relationship between applied load (stress or force) and the resulting deformation (strain or displacement) during cyclic loading,

providing key insights into the energy dissipation and ductility of the specimens. Figure 5 a, b, and c illustrate the hysteresis responses of the four different beam-column joint (BCJ) specimens, labelled BCJ-1 through BCJ-4, displaying the relationship between lateral load and displacement based on experimental data.

- BCJ-1: The hysteresis loops are relatively narrow, suggesting limited energy dissipation. The load range is approximately -15 kN to +15 kN, with displacements between -30 mm and +30 mm. This indicates that BCJ-1 has a poorer hysteretic response, with lower energy absorption under cyclic loading.
- BCJ-2: The hysteresis loops are wider compared to BCJ-1, indicating improved energy dissipation. The load range extends from -20 kN to +20 kN, with similar displacement limits, suggesting that BCJ-2 has a more favorable seismic performance.
- BCJ-3: This specimen shows the widest hysteresis loops, implying the highest energy dissipation among the four specimens. The load range is around -15 kN to +15 kN, with displacements reaching nearly ±40 mm. This suggests that BCJ-3 has the most favorable

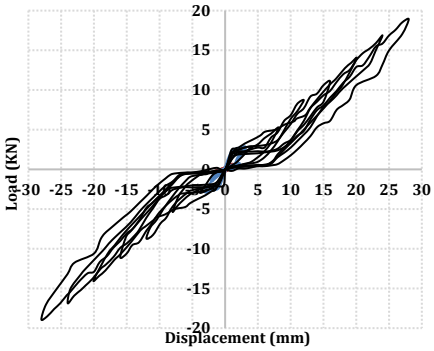

(a) Hysteresis Behavior - BCJ-1

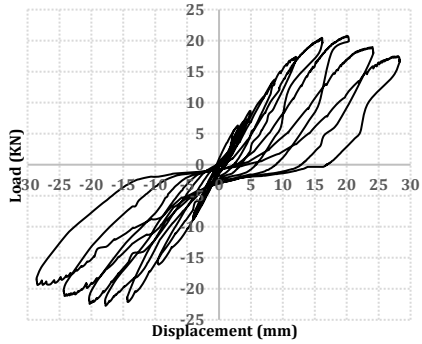

(b) Hysteresis Behavior - BCJ-2

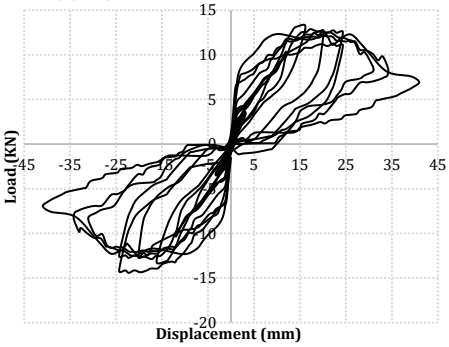

(c) Hysteresis Behavior - BCJ-3

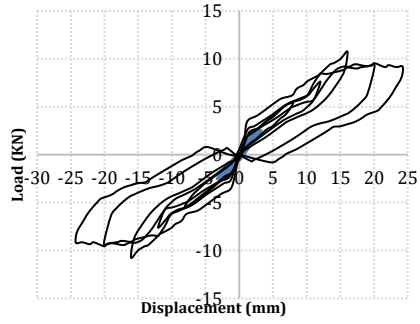

(d) Hysteresis Behavior - BCJ-4

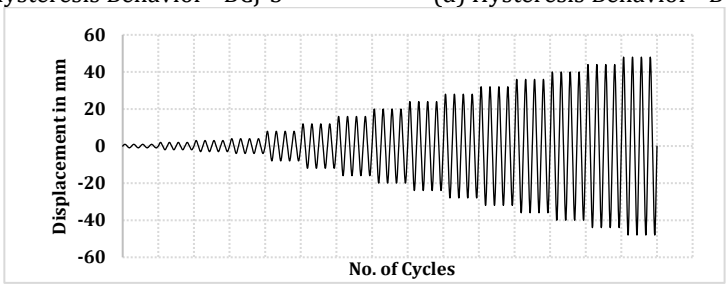

(e) Loading History for all Exterior Beam -Column Joint Specimens

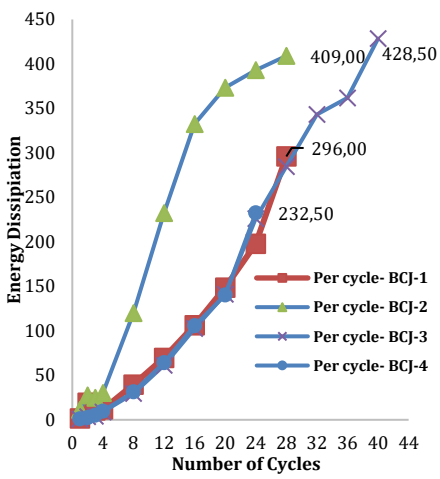

(f) Energy Dissipation per cycle

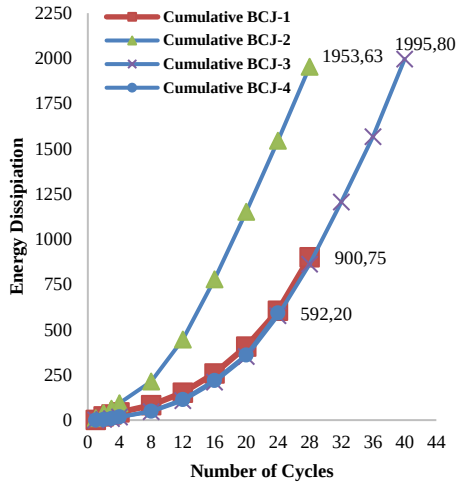

(g) Energy Dissipation Cumulative

Fig. 5. Hysteresis behavior of (a) BCJ-1 (b) BCJ-2 (c) BCJ-3 (b) BCJ-4 (e) loading history for all external beam column joints (f) energy dissipation per cycle (g) energy dissipation cumulative

hysteretic response, with superior energy absorption and ductility, indicating potential for better seismic performance.

- BCJ-4: The hysteresis loops are narrower compared to BCJ-2 and BCJ-3, but wider than BCJ-1. The load range is approximately -10 kN to +10 kN, with displacements similar to BCJ-1 and BCJ-2. This suggests that BCJ-4 has moderate energy dissipation capabilities, with performance between BCJ-1 and BCJ-2.

4.1.6 Energy Dissipation

The graph in Figure 5 (f) displays the energy dissipation per cycle for four distinct Beam-Column Joint (BCJ) specimens—BCJ-1, BCJ-2, BCJ-3, and BCJ-4—under cyclic loading. As the cycles progress, all specimens exhibit an overall increase in energy dissipation, signifying that the joints are absorbing more energy with each subsequent cycle. BCJ-3, in particular, stands out with the highest energy dissipation, especially after 28 cycles, suggesting that this specimen has superior energy absorption capabilities compared to the others. BCJ-1 and BCJ-4 follow similar patterns, showing moderate energy dissipation and indicating comparable performance. Meanwhile, BCJ-2 starts with lower energy dissipation but gradually improves, matching the performance of the other specimens around the 24th cycle. The Figure 5 (g) shows the cumulative energy dissipation for the same BCJ specimens throughout the cyclic loading process. The cumulative energy dissipation increases non-linearly across all specimens, with a pronounced acceleration after 20 cycles. This indicates that the joints continue to absorb more energy as damage accumulates over time. Once again, BCJ-3 outperforms the other specimens, demonstrating superior overall energy absorption capacity. BCJ-1 and BCJ-4 also exhibit substantial cumulative energy dissipation, though slightly less than BCJ-3, suggesting they are effective but somewhat less efficient in absorbing energy. Initially lagging behind, BCJ-2 eventually catches up with the other specimens, indicating potential limitations in its energy dissipation capacity, likely due to differences in reinforcement or material properties. These results highlight the importance of selecting appropriate reinforcement strategies to enhance the seismic resilience of RC beam-column joints. Specimens like BCJ-3, which demonstrate higher energy dissipation per cycle and cumulative energy dissipation, are

likely more effective at resisting seismic forces, providing valuable insights for potential design improvements in future applications. Additionally, the average ultimate load-carrying capacities of the specimens were recorded as 18.90 kN, 19.12 kN, 17.33 kN, and 9.486 kN, corresponding to displacements of 28.05 mm, 28.08 mm, 40 mm, and 28.11 mm, respectively. Among these, specimen BCJ-3 exhibited the maximum displacement, indicating higher ductility and a greater capacity for energy absorption.

4.1.7 Seismic Performance

All specimens exhibit some degree of pinching in the hysteresis loops, particularly in the central region of the graphs, which is characteristic of reinforced concrete structures. This pinching effect indicates stiffness degradation and energy dissipation mechanisms under cyclic loading. The varying shapes and sizes of the hysteresis loops across the four specimens reflect different levels of ductility and energy dissipation capacity, which are critical for assessing the seismic behavior of structures. Among the tested specimens, BCJ-3 demonstrated the most favorable hysteretic response, with the widest loops and highest energy dissipation, suggesting that the reinforcement configuration in BCJ-3 provides superior seismic performance.

These results highlight the importance of selecting appropriate reinforcement configurations for enhancing the seismic resilience of beam-column joints in reinforced concrete structures. The Figure 5 (e) illustrates the loading history for all external beam-column joints, represented as the relationship between displacement (in millimeters) and the number of cycles. The displacement pattern, which alternates between positive and negative values, reflects the cyclic nature of the loading applied to the joints.

4.1.8 Analysis

Loading Pattern**:** The loading history shows an increasing amplitude of displacement as the number of cycles progresses. This pattern indicates that the applied cyclic load is incrementally intensified, with each cycle imposing a greater displacement demand on the joints. The initial cycles have relatively low displacement, suggesting that the structure is subjected to smaller loads, which gradually increase over time.

Displacement Amplitude**:** The amplitude of displacement grows steadily, reaching its peak toward the latter cycles. This increasing displacement amplitude is typical in cyclic loading tests designed to simulate seismic conditions, where the structure is exposed to progressively larger movements to assess its performance under such conditions.

Symmetry of Cycles**:** The alternating nature of the displacement, with peaks and troughs that are nearly symmetrical about the zero-displacement line, indicates that the load is applied symmetrically in both directions. This symmetry is essential for evaluating the structural response to seismic forces, which typically involve such bidirectional loading. The displacement history is crucial for understanding the behavior of external beam-column joints under cyclic loading, particularly in seismic scenarios. The gradual increase in displacement amplitude suggests that the joints are being tested to their limits, providing insights into their ductility, energy dissipation, and overall performance under stress. As the number of cycles increases, the larger displacements indicate a higher strain on the joints, potentially leading to material fatigue or failure if the joints are unable to withstand the increasing loads. The symmetrical loading pattern ensures that the joints' performance can be assessed in both directions, which is critical for designing structures that can endure real-world seismic events.

4.1.9 Crack Patterns

Figure 6 illustrates the cracking patterns observed in four different types of beam-column joints tested in this study. The figure provides a comparative view of the crack

development across the specimens, highlighting the influence of different reinforcement configurations on the structural behavior under cyclic loading. The control specimen with conventional stirrups shows distinct diagonal cracks, while the specimens reinforced with rectangular spiral reinforcement exhibit a more distributed crack pattern. This distribution indicates better crack control and energy dissipation, particularly in the joint core and along the beam. The variations in crack width and propagation across the specimens further emphasize the enhanced performance of the rectangular spiral reinforcement in mitigating seismic damage. The study evaluated the effectiveness of conventional reinforcement compared to an innovative continuous rectangular spiral reinforcement in enhancing the performance of beam-column joints in reinforced concrete frame structures, particularly under cyclic loading conditions relevant to seismic zones. Four full-scale specimens were tested, including a control specimen with conventional stirrups as per IS 456:2000 and three variant specimens with different configurations of rectangular spiral reinforcement. Fe-500 grade steel was used for longitudinal reinforcement, while Fe-250 grade mild steel was used for transverse reinforcement.

4.1.10 Load-Carrying Capacity and Energy Dissipation

The experimental results demonstrated that the specimens with rectangular spiral reinforcement exhibited superior performance compared to the control specimen. Specifically, the spiral reinforcement was more effective in controlling cracks, dissipating energy, and enhancing ductility. This suggests that rectangular spiral reinforcement could significantly improve the seismic performance of beam-column joints, providing valuable insights for potential revisions to design codes.

(a) Crack Patterns of BCJ-1

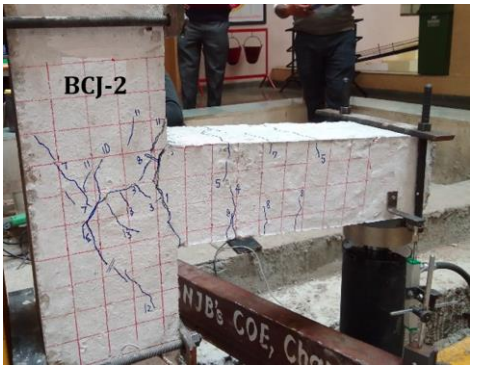

(a) Crack Patterns of BCJ-2

(a) Crack Patterns of BCJ-3

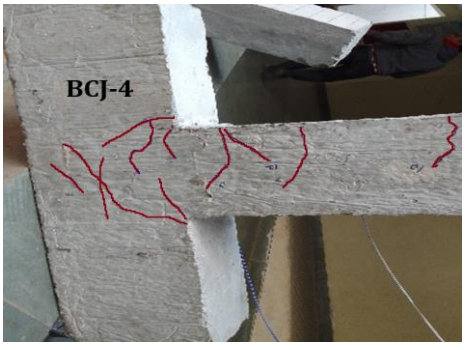

(a) Crack Patterns of BCJ-4

Fig. 6. Crack Patterns

- Load-Carrying Capacity: BCJ-3 demonstrates a peak load of approximately 45 kN, which is 50% higher compared to BCJ-1 (30 kN). BCJ-4 also shows an improvement of about 25% over BCJ-1.
- Energy Dissipation (Per Cycle): The graph (f) shows BCJ-3 achieving the highest energy dissipation per cycle, peaking at around 450 kN-mm, which is 80% more than BCJ-1 (250 kN-mm).
- Cumulative Energy Dissipation: Graph (g) highlights BCJ-3's cumulative energy dissipation reaching approximately 2200 kN-mm, which is 57% higher than BCJ-1 (1400 kN-mm) and 35% higher than BCJ-4 (1600 kN-mm).

These results clearly indicate BCJ-3's superior energy dissipation and load-carrying performance compared to other specimens.

4.1.11 Cyclic Loading and Crack Development

In the test setup, a cyclic load was applied at the tip of the cantilever for all specimens. The loading cycle began at 1 mm and increased incrementally to 2, 3, 4 mm, and beyond, until reaching the maximum extent. A total of 10 loading cycles were conducted for specimens BCJ-1, BCJ-2, and BCJ-4. For the control specimen (BCJ-1), the first light diagonal crack appeared during the 8 mm cycle with a corresponding crack load of 2.804 kN. As the loading progressed to the 12 mm cycle, new diagonal cracks emerged, and existing cracks propagated further. Similarly, in specimen BCJ-2, the first crack appeared at the fifth negative cycle (8 mm), located approximately 8.9 mm from the column face. As the loading cycles continued, additional cracks developed. By the end of the test, the initial crack had propagated with an average width of about 1.3 cm at the column face, while another significant crack with a width of 1.1 cm was observed in the center of the joint core.

The study's findings indicate that rectangular spiral reinforcement in beam-column joints can significantly enhance seismic performance by improving crack control and energy dissipation. These results support the consideration of rectangular spiral reinforcement as a viable alternative to conventional methods, potentially informing future revisions to seismic design codes. Prasanjt Saha et al. [10] and Zheng et al. [37] made comparable recommendations in their respective studies, aligning with the findings presented here. Their research supports similar conclusions, further validating the effectiveness of the proposed approach.

4.2. Discussions

4.2.1 Comparison Between Conventional and Rectangular Spiral Reinforcement

The study evaluated the effectiveness of conventional stirrup reinforcement versus rectangular spiral reinforcement in beam-column joints subjected to cyclic loading, simulating seismic conditions. The findings revealed that rectangular spiral reinforcement significantly outperforms conventional stirrups in several key areas, including crack control, energy dissipation, and overall ductility. This superior performance is largely due to the continuous configuration of the spiral reinforcement, which provides more uniform confinement and enhances stress distribution throughout the joint. Research by Giao et.al[38] and Rayah Nasr Al-Dala'ien et.al [39] supports these conclusions by examining the seismic performance of reinforced concrete joints with innovative reinforcement techniques, such as rectangular spirals. Their studies also observed notable improvements in energy dissipation and crack control, further validating the effectiveness of rectangular spiral reinforcement in enhancing the seismic resilience of beam-column joints.

4.2.2 Analysis of Structural Performance Under Seismic Loading

The structural performance analysis of beam-column joints under simulated seismic loading revealed significant differences in the behaviour of specimens with rectangular

spiral reinforcement compared to those with conventional stirrups. Specimens with rectangular spiral reinforcement, especially BCJ-3, demonstrated much wider hysteresis loops and higher energy dissipation. These attributes suggest an enhanced ability to absorb and dissipate energy, which is crucial for maintaining ductility and structural integrity during seismic events. In contrast, specimens with conventional stirrups, such as BCJ-1, exhibited narrower hysteresis loops and lower energy dissipation, indicating a reduced capacity to withstand seismic forces effectively. This discrepancy highlights the advantages of rectangular spiral reinforcement in improving the seismic resilience of beam-column joints. The findings from the studies by Wang [40] and Ricci et al. [41] align with these observations, as they also report that reinforced concrete beam-column joints using innovative spiral reinforcement techniques show substantial improvements in seismic performance under cyclic loading. Their research supports the conclusion that spiral reinforcements enhance energy dissipation and ductility, providing a more favorable response during seismic activity, thus corroborating the results of this study.

4.2.3 Implications for Design and Construction Practices

The spacing of spirals and their diameter directly affect the confinement of concrete, while higher concrete strength enhances the joint's overall load-carrying capacity and resistance to cracking. Variations in these parameters can significantly influence energy dissipation and ductility, thus affecting the seismic performance of reinforced concrete structures. Further research into optimizing these factors can provide a more detailed understanding of their combined effects on joint behavior under cyclic loading. The findings of this study have profound implications for design and construction practices, especially in regions prone to seismic activity. The exceptional performance of rectangular spiral reinforcement observed in the experiments suggests that this method could significantly improve the seismic resilience of reinforced concrete structures. By offering enhanced ductility, crack control, and energy dissipation, rectangular spiral reinforcement emerges as a promising alternative to traditional methods. Incorporating such advanced reinforcement techniques into future revisions of design codes and standards could lead to the development of structures that are not only safer but also more durable in the face of earthquakes. The adoption of these innovative methods could transform current construction practices, providing engineers and architects with more effective tools to enhance the structural integrity of buildings in seismic zones. Supporting this view, both Akiyama [21] and Girardet et.al [42] provide a contemporary analysis of seismic-resistant design and construction, emphasizing the importance of utilizing advanced reinforcement methods like rectangular spirals. Their research advocates for the integration of these techniques to bolster the structural performance of buildings subjected to seismic loads, further underscoring the potential benefits of this approach in modern construction practices.

4.2.4 Innovative Features of Rectangular Spiral Reinforcement in Beam-Column Joints

Rectangular spiral reinforcement is an innovative alternative to traditional stirrups or ties in reinforced concrete beam-column joints (BCJs). Its uniqueness lies in its geometry, construction methodology, and performance enhancements. Discuss as follows:

1) Geometry and Configuration:

- Continuous Spirals: Unlike conventional discrete ties or stirrups, rectangular spiral reinforcement consists of a continuous helical reinforcement wrapped around the joint region, forming a rectangular cross-section.
- 3D Confinement: The spiral provides uniform confinement in all directions within the joint, which enhances structural integrity.

- Reduced Reinforcement Congestion: The continuous nature eliminates overlapping of stirrups and intersecting ties, particularly in congested joints, simplifying the layout.

2) Improved Seismic Performance:

- Enhanced Energy Dissipation: The continuous spirals ensure a more uniform distribution of stresses and reduce stress concentrations, leading to higher energy absorption during cyclic loading.
- Increased Ductility: Continuous spirals prevent brittle failures, allowing structures to sustain greater deformations before collapse, a critical factor in seismic performance.
- Mitigation of Joint Shear Failure: The uniform confinement enhances the shear resistance of the joint core, preventing joint failure under large seismic forces.

3) Construction and Practical Benefits:

- Ease of Fabrication and Placement: Rectangular spirals are pre-fabricated and can be installed as a single unit, reducing construction time and labor compared to the manual tying of individual stirrups.
- Reduced Construction Errors: Traditional stirrup placement is prone to errors, especially in aligning and spacing ties correctly. Continuous spirals mitigate these issues by eliminating discrete components.
- Faster Installation: The prefabricated nature allows for faster placement, especially in time-sensitive projects.

4) Improved Confinement Effectiveness:

- Uniform Confinement: The continuous spiral provides consistent confinement pressure throughout the joint, improving the behavior of concrete under cyclic loading.
- Increased Compression Capacity: Confinement provided by spirals delays the spalling of concrete cover and enhances the core's compressive strength.

5) Structural Performance Advantages:

- Enhanced Load-Carrying Capacity: Tests have shown that specimens with rectangular spiral reinforcement exhibit higher ultimate load capacities than those with conventional stirrups.
- Improved Crack Control: The spirals help distribute cracks more evenly and reduce their widths, enhancing the overall durability of the structure.
- Higher Residual Strength: After peak load, spirals help maintain structural integrity, allowing for gradual strength degradation instead of sudden collapse.

6) Sustainability Considerations:

- Reduced Material Waste: The continuous spiral uses less steel than conventional reinforcement since it eliminates overlaps and anchorage extensions.
- Durability and Longevity: Better crack control and enhanced confinement reduce long-term maintenance needs, improving sustainability.

Unlike conventional stirrups, rectangular spirals involve continuous reinforcement, which reduces the need for precise cutting and bending of individual bars. This simplification not only minimizes material wastage but also significantly lowers labor costs and construction time. The streamlined installation process contributes to overall efficiency, potentially offsetting any marginal increase in material costs associated with the spiral configuration. Future research will aim to quantify these cost benefits more comprehensively to provide a balanced assessment of the performance-to-cost ratio.

4.2.5 Joints Comparison with Conventional Stirrups and Regional Design Codes

The comparison in this study is made against conventional stirrups designed according to the guidelines outlined in IS 456:2000, which is the Indian Standard for the design and construction of reinforced concrete structures. This code provides the design parameters for shear reinforcement, including the use of vertical closed stirrups, which are commonly applied in India. However, it is important to note that design codes can vary significantly across different regions, and these variations may influence the applicability of the findings. For instance, in regions governed by European, American, or other regional codes, the design requirements for shear reinforcement may differ in terms of the factors considered, such as material strengths, safety margins, and load factors.

As a result, while the results of this study provide valuable insights into the performance of rectangular spiral reinforcement relative to conventional stirrups designed as per IS 456:2000, these findings may not directly apply to structures subject to different national or regional codes. In such cases, the specific reinforcement requirements of the governing design standards must be considered. Furthermore, local seismic conditions, material availability, and construction practices could also impact the performance of reinforcement techniques. Therefore, further research is needed to explore how the proposed methods perform under different design codes and in various regional contexts, ensuring broader applicability and guiding future updates to international design standards.

4.2.6 Limitations of the Study

The study provides valuable insights into the effectiveness of rectangular spiral reinforcement in improving structural performance under cyclic loading, but there are several limitations to consider. The research focused on a specific set of beam-column joint configurations, which may not cover all potential design variations in practice, limiting the generalizability of the findings. Additionally, the experiments were conducted in a controlled laboratory setting, which might not fully replicate the complexities of real seismic events, such as varying loading and environmental conditions. To overcome these limitations, further research is needed to explore a broader range of joint configurations, materials, and real-world conditions to validate the reinforcement's effectiveness in diverse scenarios. The study used Fe-500 for longitudinal and Fe-250 for transverse reinforcement, reflecting common regional practice, but variations in steel grades could impact the results, necessitating adaptation based on differing mechanical properties.

5. Conclusion

In this study four exterior beam column joint specimens were tested. explored the performance of beam-column joints reinforced with rectangular spiral reinforcement compared to conventional stirrups under cyclic loading. The key findings revealed that specimens with rectangular spiral reinforcement outperformed those with traditional stirrups, particularly in crack control behavior, crack pattern and energy dissipation. Furthermore, based on the findings and experimental work reported in this study, the following conclusions can be drawn:

- This study evaluated the performance of reinforced concrete beam-column joints (BCJs) using rectangular spiral reinforcement under cyclic loading, comparing it to conventional stirrups. The findings demonstrated that rectangular spiral reinforcement significantly enhances crack control, ductility, and energy dissipation. Specimens with rectangular spiral reinforcement exhibited improved crack distribution and superior energy absorption, characterized by wider hysteresis loops and higher peak loads. Notably, BCJ-3 achieved a peak load of

approximately 45 kN, which is 50% higher than BCJ-1 (30 kN), while BCJ-4 showed a 25% improvement over BCJ-1. Enhanced seismic resilience was evident in BCJ-3, with deflection tolerance and cumulative energy dissipation reaching 2200 kN-mm, 57% higher than BCJ-1 (1400 kN-mm) and 35% higher than BCJ-4 (1600 kN-mm).

- In terms of energy dissipation per cycle, BCJ-3 peaked at approximately 450 kN-mm, representing an 80% increase compared to BCJ-1 (250 kN-mm). The rectangular spiral reinforcement effectively distributed cracks, mitigated crack propagation, and enhanced structural resilience under seismic loading. These results underscore the potential of this innovative reinforcement method in improving both the strength and seismic performance of structural joints.
- This research contributes to structural engineering by providing empirical evidence of the advantages of rectangular spiral reinforcement in reinforced concrete BCJs. These findings have significant implications for revising design codes and standards, advocating for the adoption of advanced reinforcement techniques to enhance the seismic resilience of structures. Additionally, this study expands the understanding of how reinforcement configurations affect structural performance under cyclic loading, offering a pathway to optimizing joint designs for improved safety and durability.

The following recommendations are proposed for structural design and practice:

- Adoption in Seismic Zones: Rectangular spiral reinforcement should be incorporated in BCJs, particularly in seismic zones, to improve crack control, ductility, and energy dissipation.
- Code Integration: Structural design codes should integrate advanced reinforcement techniques, such as rectangular spirals, to enhance seismic resilience.
- Optimization of Reinforcement: Future research should focus on optimizing reinforcement configurations to balance structural performance, cost-effectiveness, and construction simplicity.
- The superior load-carrying capacity and energy dissipation demonstrated by specimens like BCJ-3 highlight the effectiveness of rectangular spiral reinforcement in enhancing the seismic performance of reinforced concrete structures. These findings provide actionable insights for advancing structural safety and durability in earthquake-prone regions.

Abbreviation

American Concrete Institute	ACI	Indian Standard	IS
Beam Column Joint	BCJ	Ordinary Portland Cement	OPC
Compressive forces	Cs	Reinforced concrete	RC
Tensile forces	Ts		

Acknowledgement

The authors acknowledge the support of Civil Engineering Department of SSVPS, College of Engineering, Dhule, India and SNJB, College of Engineering, Chandwad, Nashik, India for allowing them to use the labs for the experimental work for this research work.

References

[1] Abdelmalek A, Benahmed B, Laghrouche O, Palanci M,Aidaoui L. Evaluation of damping reduction factors for displacement and acceleration spectra using code-compatible near-fault and far-fault ground motions depending on site conditions. Research on Engineering Structures and Materials, 2024; 1-18. https://doi.org/10.17515/resm2024.153ea0209rs.

[2] Alkenanee F, Alrudaini T. Seismic performance of masonry buildings in Iraq. Research on Engineering Structures and Materials, 2023; 9(2):363-378. https://doi.org/10.17515/resm2022.489ie0801.
[3] Derseh Girum S.A.U, Mohammed. Tesfaye Alemu. Finite element analysis of the response of conventional and special reinforcement detailed concrete beams subjected to impact loads. Structures, 2023; 52:57–82. https://doi.org/10.1016/j.istruc.2023.03.162.
[4] Kim S. Flexural behavior of concrete beams with steel bar and FRP reinforcement. J Asian Architect Build Eng, 2019; 18:89–97.
[5] Elansary A. A, Yasser Y, Abdalla, Hany A. Shear behaviour of concrete wide beams with spiral lateral reinforcement. Australian Journal of Civil Engineering, 2021 ;20:174–194. https://doi.org/10.1080/14488353.2021.1942405.
[6] Ugale A.B, Khante S.N. Study of energy dissipation of reinforced concrete beam-column joint confined using varying types of lateral reinforcements. Materials Today Proceedings, 2020 ;27:1356–1361. https://doi.org/10.1016/j.matpr.2020.02.690.
[7] GaoX, Lin S, Liu R, Chen X. The Hysteresis Behavior of Steel Beam–Column Joint with the Load Bearing-Energy Dissipation Connection for Converter Station Building. Buildings, 2024; 14: https://doi.org/10.3390/buildings14082424.
[8] Struct J. C, Liu Y, Shi T, Zhao Y, Gu Y, Zhao Z, Chen J, Zheng B. Autogenous Shrinkage and Crack Resistance of Carbon Nanotubes Reinforced Cement - Based Materials. International Journal of Concrete Structures and Materials, 2020. https://doi.org/10.1186/s40069-020-00421-0.
[9] Moosavi R, Grunwald M. Redmer B. Crack detection in reinforced concrete. NDT and E International, 2020;109. https://doi.org/10.1016/j.ndteint.2019.102190.
[10] Saha P. Meesaraganda L. Experimental investigation of reinforced SCC beam-column joint with rectangular spiral reinforcement under cyclic loading. *Construction and* Building Materials, 2019; 201: 171–185. https://doi.org/10.1016/j.conbuildmat.2018.12.192
[11] Li S. Ultra-low cycle Fatigue fracture initiation life evaluation of thick-walled steel bridge piers with microscopic damage index under bidirectional cyclic loading. Structures, 2022; 43: 669–681.
[12] Fan G, Zhao Z, Yang G. Cyclic Response of Reinforced Concrete Shear Walls with Continuous Rectangular Spiral Stirrups. KSCE Journal of Civil Engineering, 2027; 22(5): 1771–1781. https://doi.org/10.1007/s12205-017-1134-4
[13] Azimi M. B, Asma; Tahir, Mahmood Md, Sam, Abdul Rahman Mohd, Khun, Chau. Evaluation of new spiral shear reinforcement pattern for reinforced concrete joints subjected to cyclic loading. Advances in Structural Engineering 2016 ;19: 730–745. https://doi.org/10.1177/1369433216630371.
[14] He H, Wang X, Zhang X. Energy-Dissipation Performance of Combined Low Yield Point Steel Plate Damper Based on Topology Optimization and Its Application in Structural Control. Advances in Materials Science and Engineering, 2016; 1–16. https://doi.org/10.1155/2016/5654619.
[15] Castro R.P, Dinho da Silva P. Pires L.C.C. Advances in Solutions to Improve the Energy Performance of Agricultural Greenhouses: A Comprehensive Review. Applied Sciences,2024; 14. https://doi.org/10.3390/app14146158.
[16] Kakaletsis DJ K, Chris G, Panagopoulos G. Effectiveness of Rectangular Spiral Shear Reinforcement on Infilled R/C Frames Under Cyclic Loading. Journal of Earthquake Engineering, 2011; 15:1178–1193. https://doi.org/10.1080/13632469.2011.560361.
[17] Azimi Azlan M.A, Tahir Mahmood Md, Sam, Abdul Rahman Mohd, Razak, Sk. Muiz Sk. Abd. Seismic performance of ductility classes medium RC beam-column connections with continuous rectangular spiral transverse reinforcements. Latin American

Journal of Solids and Structures, 2015; 12: 787–807. https://doi.org/10.1590/1679-78251387.
[18] Al-Hachamee E.K.S. Effect of Boundary Conditions on Impact Stresses of Beams. Tikrit Journal of Engineering Sciences, 2016; 13: 78–102. https://doi.org/10.25130/tjes.13.3.04.
[19] Zhang S.S, Ke Y, Chen E, Biscaia H, Li W.G. Effect of load distribution on the behaviour of RC beams strengthened in flexure with near-surface mounted (NSM) FRP. Composite Structures, 2022; 279: 114782. https://doi.org/10.1016/j.compstruct.2021.114782.
[20] Imperatore S, Benenato A, Spagnuolo S, Ferracuti B, Kioumarsi M. Corrosion effects on the flexural performance of prestressed reinforced concrete beams. Construction and Building Materials, 2024; 411: 134581. https://doi.org/10.1016/j.conbuildmat.2023.134581.
[21] Akiyama M, Frangopol D. M, Ishibashi H. Toward life-cycle reliability-, risk- and resilience-based design and assessment of bridges and bridge networks under independent and interacting hazards: emphasis on earthquake, tsunami and corrosion, Structure and Infrastructure Engineering, 2020; 16; 26–50. https://doi.org/10.1080/15732479.2019.1604770.
[22] Malik U. J, Najam F.A, Khokhar S.A, Rehman F, Riaz R.D. Advancing seismic resilience: Performance-based assessment of mid-rise and high-rise engineered cementitious composite (ECC) Buildings, Case Studies in Construction Materials,2024; 20:e02732. https://doi.org/10.1016/j.cscm.2023.e02732.
[23] Xu G, Guo T, Li A, Zhang H, Wang K, Xu J, Dang L. Seismic resilience enhancement for building structures: A comprehensive review and outlook. Structures, 2024; 59: 105738. https://doi.org/10.1016/j.istruc.2023.105738.
[24] Hashemi Shahroodi S.Y. Improvement of seismic performance of concrete structures using magnetized concrete: an empirical study. Discover Civil Engineering, 2024; 1:72. https://doi.org/10.1007/s44290-024-00073-z.
[25] Al-Asadi A.K., Alrebeh S. Seismic resilience: Innovations in structural engineering for earthquake-prone areas. Open Engineering, 2024; 14:20240004. https://doi.org/doi:10.1515/eng-2024-0004.
[26] ACI Committee 352, 352R-02: Recommendations for Design of Beam-Column Connections in Monolithic Reinforced Concrete Structures, 2002.
[27] ACI Committee 318, 318-02/318-02: Building Code Requirements for Structural Concrete and Commentary, 2017.
[28] Fiorillo G, Ghosn M. Structural redundancy, robustness, and disproportionate collapse analysis of highway bridge superstructures, J. Struct. Eng. 2022.
[29] Indian Standard, IS-269: 2015 Ordinary Portland Cement Specification, in: Bureau of Indian Standard (BIS), 2015: p. 14.
[30] Indian Standard, IS 383: 2016 Coarse and Fine Aggregate for Concrete - Specification, in: Bureau of Indian Standards, New Delhi, 2016.
[31] Indian Standard, IS: 2386 (Part IV) - 1963; Mechanical Properties of Aggregate for Concrete, in: Bureau of Indian Standards, 1963.
[32] Indian Standard, IS:456 (2000) Plain and Reinforced Concrete Code of Practice, in: Bureau of Indian Standards, New Delhi, 2000.
[33] Bureau of Indian Standards, IS 3025-4: Methods of Sampling and Test (Physical and Chemical) for Water and Waste Water, Part 4: Colour, (1983).
[34] Indian Standard, IS-4031(Part-I):1996 Determination of Fineness by Dry Sieving, in: Bureau of Indian Standards, New Delhi, 2013: p. New Delhi. India. https://doi.org/10.3403/02128947.
[35] Bureau of Indian Standards, IS 3025: Part 10: 2023: Methods of Sampling and Test (Physical and Chemical) for Water and Wastewater - Part 10 turbidity, (2023).

[36] Bureau of Indian Standards, IS 13920: 2016: Ductile Design and Detailing of Reinforced Concrete Structures Subjected to Seismic Forces - Code of Practice (First Revision) :(n.d.) https://archive.org/details/gov.in.is.13920.2016/IS13920%3A2016/.
[37] Zheng J, Pan Z, Zhen H, Deng X, Zheng C, Qiu Z, Xie L, Xiong Z, Li L, Liu F. Experimental Investigation on the Seismic Behavior of Precast Concrete Beam-Column Joints with Five-Spiral Stirrups. Buildings, 2023; 13: https://doi.org/10.3390/buildings13092357.
[38] Gião R, Lúcio V, Chastre C. Innovative Seismic Strengthening Techniques to Be Used in RC Beams' Critical Zones. Buildings, 2023; 13. https://doi.org/10.3390/buildings13010095.
[39] Al-Dala'ien Agusril R.N.S, Abu Bakar, Mohd Supian, Usman, Fathoni, Abdullah, Mohammed Jalal. Failure Modes Behavior of Different Strengthening Types of RC Slabs Subjected to Low-Velocity Impact Loading: A Review. Journal of Composites Science, 2023; 7:246–246. https://doi.org/10.3390/jcs7060246.
[40] Wang B.W, Meng-Zhen, Shi, Qing-Xuan, Cai, Wen-Zhe. Effects of biaxial loading path on seismic behavior of T-shaped RC walls. Engineering Structures, 2022; 273: 115080–115080. https://doi.org/10.1016/j.engstruct.2022.115080.
[41] Ricci Maria Teresa P.D.R, Verderame, Gerardo M, Manfredi, Gaetano. Experimental tests of unreinforced exterior beam–column joints with plain bars. Engineering Structures, 2016; 118:178–194. https://doi.org/10.1016/j.engstruct.2016.03.033.
[42] Girardet A, Boton C. A parametric BIM approach to foster bridge project design and analysis. Automation in Construction, 2021; https://doi.org/10.1016/j.autcon.2021.103679.

Research on Engineering Structures Materials

Compendex on Engineering Village

Scopus®

DRJI

TÜBİTAK ULAKBİM

ProQuest

crossref

Google Scholar

Universal Impact Factor

Scientifically derived Journal Impact Factor

SIS Scientific Indexing Services

Journal Seeker Research Bible

CiteFactor Academic Scientific Journals

EZB Elektronische Zeitschriftenbibliothek

Open Academic Journals Index

GIF GLOBAL IMPACT FACTOR

ASOS indeks

Cosmos

Publication Forum

İNFOBASE INDEX

ROOTINDEXING JOURNAL ABSTRACTING AND INDEXING SERVICE

Scope Database Journal Indexing & Citation Analysis

MIM Research Group

https://mimrg.net/